

# Molecular Tools for Tunable Photonics

DOCTORAL THESIS

Thesis report submitted by

**Edurne Avellanal Zaballa**

For the degree of Doctor

with "INTERNATIONAL DOCTORATE" mention

and

Basque C2 certificate

Supervisors: Dr. Jorge Bañuelos and Dr. Leire Gartzia Rivero

Leioa, December 2020



Jadanik gurekin ez daudenei, baina beti egongo direnei



# AGRADECIMIENTOS

---

Cuando decidí apostar por la investigación y comenzar la tesis más de uno me dijo que tenía que tener ilusión. Y realmente creo que haber mantenido esa ilusión intacta durante estos cuatro años me ha ayudado a terminar este proyecto que creemos útil para el avance de la ciencia, y por ende, de la sociedad. Por ello, en primer lugar querría agradecer a mis directores de tesis Jorge y Leire por su apoyo incondicional y por haberme guiado en esta ardua tarea. No solo me han enseñado aspectos totalmente desconocidos de la química para mí, sino que también han contribuido a mi desarrollo como persona. Quién me diría a mí que al principio de todo este viaje terminaría aprendiendo tanto y sobre tan diversos temas, y lo que nos queda aún por descubrir.

Del mismo modo también me gustaría dar las gracias al Gobierno Vasco por la concesión de la beca predoctoral, ya que sin ella todo esto habría sido imposible, sin olvidarme de los servicios Generales de la Facultad de Ciencia y Tecnología de la UPV/EHU (SGIker) por todas las medidas realizadas, en especial las referentes a cálculos teóricos.

Sin embargo, nada de esto habría sido posible sin la colaboración de los grupos de síntesis orgánica que nos proporcionan las muestras para su posterior caracterización. Es por ello que me gustaría agradecerles su gran trabajo y dedicación a los grupos del Prof. Eduardo Peña de la Universidad de Guanajuato, de las Prof. M<sup>a</sup> José Ortiz y la Dra. Antonia Agarrabeitia (en especial a Alejandro y Ágata) y del Prof. Santiago de la Moya (en especial a César, Josué y Christopher) de la Universidad Complutense de Madrid, y del Prof. Cristóbal López y Prof. Ana Gómez, y del Prof. José Luis Chiara (en especial a Alberto), del Instituto de Orgánica General (IQOG-CSIC) de Madrid. También me gustaría agradecerle a la Prof. Inmaculada García-Moreno del Instituto de Física-Química "Rocasolano" (CSIC) por las medidas de espectroscopia láser realizadas, y en especial al Dr. Luis Cerdán, por su inagotable paciencia a la hora de ayudarme a entender la caracterización laser de las moléculas orgánicas.

Además, no me gustaría olvidarme de toda la gente que me hizo sentir como en casa durante mi estancia en Lausanne (Suiza). Gracias a todo el grupo de la Prof. Clémence Corminboeuf (en especial a Sergi y María) del "École Polytechnique Fédérale de Lausanne" por hacer más pequeña esa brecha entre el mundo teórico y el experimental.

Muchas gracias a mis compañeras del Laboratorio de Espectroscopia Molecular Iñigo, Teresa, Virginia, Hegoi, Rebeca, Edu, Ruth, Ainhoa, Xabi, Carolina y Jon por hacer mucho más ameno y divertido este largo viaje.

Por supuesto a mis amigas de toda la vida las que dicen llamarse "Ferminas", a los chicos locos que nos complementan tan bien y a las "Angugulas de Norte" por hacerme reír y por preocuparse por mí. A Lidia, Amaia, Xabi (Txo), Ager, Nahia e Imanol, porque con vosotros empezó todo.

Finalmente, a mi familia Aita, Amatxu y Llelle por no dejarme tirar la toalla nunca y por apoyarme siempre.

Zuri ere, Amaia, azkenengo urte bitxi samar honetan agertzearen eta nire bizitzari kolore ukitze bat ematearren.

Mila esker bihotz-bihotzez.



# ABSTRACT

---

Dye chemistry is witnessing a renewed recognition as a valuable tool to design smart photonic applied materials. In particular, the recent avenues in organic chemistry allow the access to new tailor made molecular structures. Against this background, in this thesis we aimed to design, characterize and apply a new generation of organic dyes as fluorophores and photosensitizers for photonic purposes. Instead of using different dyes for each target application, the herein applied strategy was based on the use of a specific molecular scaffold, where, after suitable chemical modifications of its chromophoric core, the photonic performance can be modulated in a controlled way depending on the searched application field. To this aim, we selected BOron DIPYrrromethene (BODIPY) as molecular platform to tackle diverse photonic applications, even if they sometimes imply opposite photophysical properties. This modern dye outstand by its chemical accessibility and tunable photophysical properties ready and finely modulated by structural factors. A rational design of its molecular structure allows the development of red- and near infrared-emitting dyes for tunable lasers, fluorescent sensors for the detection of biomolecules, and fluorescent probes for biomaging, as well as non-fluorescent singlet oxygen photosensitizers for therapy in biomedicine. The design was extended to the combination of several dyes into one single molecular structure, where new photophysical phenomena as energy and charge transfer, and excitonic couplings, are induced. These complex and challenging multichromophoric dyes show a remarkable behavior as improved dye lasers, optically active systems, light harvesters and molecular antennae. The research activity was focused in the design of novel BODIPY-based molecular structures using computational tools, and mainly in the computationally assisted photophysical and lasing characterization of the synthesized fluorophores and photosensitizers. A deep understanding of the interplay between the molecular structure and the photonic performance, as well as unraveling the key underlying photophysical mechanisms in each application field, result essential to improve the photonic performance and redesign optimized photoactive dyes. We hope that the herein reported guidelines could serve as inspiration and settle the bases to sketch smart and advanced organic molecules for applied photonics.





# LABURPENA

---

Koloratzaileen kimika erraminta baliotsu gisa onarpenaren lekuko izaten ari da aplikagarriak diren material fotoniko adimentsuak diseinatzeko. Kimika organikoan sortutako bide sintetiko desberdinek egitura molekular berrien sorkuntza erraztu dituzte, bereziki neurria egindakoak. Hori dela eta, gure helburua tesi honetan aplikazio fotonikoetan fluoroforo eta fotosentikortzaile gisa jarduten duten koloratzaile organiko belaunaldi berri baten diseinua eta karakterizazioa da. Aplikazio xede bakoitzerako koloratzaile ezberdinak erabili beharrean, hemen erabilitako estrategia egitura molekular espezifiko bat abiapuntu bezala hartzea izan zen, non, nukleo kromoforikon aldaketa kimiko egokiak egin ostean, jarraitutako aplikazio arloaren arabera funtzio fotonikoa kontrolpean modulatzeko posible izan zen. Horregatik BORO DIPYrrometeno (BODIPY) koloratzailea eredu molekular gisa aukeratu zen aplikazio fotoniko desberdinei aurre egiteko, baita kontrako propietate fotofisikoa beharrezkoak zirenean ere. Gaur egungo koloratzaile hau bere eskuragarritasun kimikoagatik eta bere egiturazko faktoreen bitarteko propietate fotofisiko sintonizagarriengatik nabarmentzen da. Bere egitura molekularren diseinu aproposak eremu gorrian eta infragorri hurbilean igortzen duten koloratzaileen garapena ahalbidetzen du. Azken hauek laser sintonizagarri, biomolekulak detektatzeko sentso fluoreszente eta bioirudirako proba fluoreszente gisa aplikatu daitezke, baita biomedikuntzan terapiarako oxigeno singletea sortzeko gai diren eta fluoreszenteak ez diren fotosentikortzaile gisa ere. Bere diseinua egitura molekular bakar batean koloratzaile anitzen konbinazioaren bitartez hedatu zen, non energia zein karga transferentzia eta akoplamendu exzitonikoak bezalako prozesuak induzitu ziren. Koloratzaile multikromoforiko konplexu eta erronkari hauek koloratzaile-laser aurreratu, optikoki aktiboak diren sistema, argi biltzaile eta antena molekular gisa jokaera aparta erakusten dute. Ikerketaren aktibitatea BODIPYetan oinarritutako egitura molekular berritzaileen diseinuan zentratu zen erraminta konputazionalak erabiliz, eta batez ere sintetizatutako fluoroforo eta fotosentikortzaileen karakterizazio fotofisikoa eta laser-karakterizazioan, laguntza konputazionalari esker. Egitura molekularren eta funtzio fotonikoaren arteko elkarrekintzari buruzko ulermena, baita aplikazio arlo bakoitzean gertatutako fenomeno fotofisikoen argibidea ere, ezinbestekoak dira jokabide fotonikoa hobetzeko eta koloratzaile fotoaktibo aurreratuak berriz diseinatzeko. Lan honetan islatutako jarraibideak fotonika aplikatuan molekula organiko adimentsuak eta aurreratuak garatzeko oinarriak finkatzea eta inspirazio gisa baliagarriak izatea espero dugu.



# RESUMEN

---

La química de colorantes está presenciando un renovado reconocimiento como herramienta valiosa para diseñar materiales fotónicos inteligentes prácticos. Las recientes rutas sintéticas en química orgánica han permitido el acceso a nuevas estructuras moleculares, en particular las hechas a la medida. En este contexto, nuestro objetivo en esta tesis es diseñar, caracterizar y aplicar una nueva generación de colorantes orgánicos como fluoróforos y fotosensibilizadores con fines fotónicos. En lugar de usar diferentes colorantes para cada propósito de aplicación, la estrategia empleada aquí se basó en el uso de un punto de partida molecular específico, donde, tras adecuadas modificaciones químicas de su núcleo cromofórico, la función fotónica pudo ser modulada de una manera controlada dependiendo del campo de aplicación que se quería perseguir. Es por ello que se eligió el colorante BORO-DIPYRROMETENO (BODIPY) como patrón molecular para hacer frente a diferentes aplicaciones fotónicas, incluso cuando a veces implicaban propiedades fotofísicas opuestas. Este colorante moderno sobresale por su accesibilidad química y sus propiedades fotofísicas sintonizables mediante factores estructurales. Un diseño lógico de su estructura molecular permite el desarrollo de colorantes capaces de emitir en la región roja e infrarroja cercana para ser aplicados como láseres sintonizables, sensores fluorescentes para la detección de biomoléculas, y pruebas fluorescentes para bioimagen, así como fotosensibilizadores no fluorescentes capaces de generar oxígeno singlete para terapia en biomedicina. Su diseño se amplió a través de la combinación de numerosos colorantes en una única estructura molecular, donde los nuevos fenómenos fotofísicos como la transferencia de energía y carga, y los acoplamientos excitónicos, son impulsados. Estos colorantes multicromofóricos complejos y desafiantes presentan un comportamiento excepcional como láseres de colorante mejorados, sistemas ópticamente activos, captadores de luz y antenas moleculares. La actividad investigadora se centró en el diseño de estructuras moleculares novedosas basadas en BODIPY mediante el uso de herramientas computacionales, y principalmente mediante la caracterización láser y fotofísica asistida computacionalmente de los fluoróforos y fotosensibilizadores sintetizados. Un entendimiento más profundo acerca de la interacción entre la estructura molecular y la función fotónica, así como el desciframiento de los mecanismos fotofísicos que ocurren en cada campo de aplicación, resultan esenciales para mejorar el comportamiento fotónico y rediseñar colorantes fotoactivos optimizados. Esperemos que las pautas reflejadas en este trabajo puedan servir como inspiración y fijen las bases para desarrollar moléculas orgánicas inteligentes y avanzadas para la fotónica aplicada.



# ABBREVIATIONS

---

AA	Amino Acids
BINOL	1,1-binaphtol
BODIPY	Boron Dipyrromethene
CD	Circular Dichroism
CPL	Circularly Polarized Luminescence
CR	Charge Recombination
CS	Charge Separation
CYS	Cysteine
DFT	Density Functional Theory
DSSC	Dye-Sensitized Solar cell
ECD	Electronic Circular Dichroism
EET	Excitation Energy Transfer
FRET	Förster Resonance Energy Transfer
G	<i>Gauche</i> (bent)
GSH	Glutathione
HCYS	Homocysteine
HOMO	Highest Occupied Molecular Orbital
ICT	Intramolecular Charge Transfer
ISC	Intersystem Crossing
LE	Locally Excited
LIF	Laser-Induced Fluorescence
LSC	Luminescent Solar Concentrator
LUMO	Lowest Unoccupied Molecular Orbital
MO	Molecular Orbital
MRI	Magnetic Resonance Imaging
NB	Nile Blue
NIR	Near-Infrared
$^1\text{O}_2$	singlet oxygen
OPO	Optical Parametric Oscillator

## Abbreviations

---

ORTEP	Oak Ridge Thermal Ellipsoid Plot
OSC	Organic Solar Cell
PS	Photosensitizer
PCM	Polarizable Continuum Model
PDI	Perylendiimide
PDT	Photodynamic Therapy
PET	Photoinduced Electron Transfer
RISC	Reverse Intersystem Crossing
$S_0$	ground state
$S_1$	first excited singlet state
SBCT	Symmetry-Breaking Charge Transfer
SCRF	Self Consistent Reaction Field
SOCT	Spin-Orbit Coupling charge Transfer
STED	Stimulated Emission Depletion
$T$	<i>Trans</i> (extended)
$T_1$	first triplet excited state
TAC	Time-to-Amplitude Converter
TADF	Thermally Activated Delayed Fluorescence
TBET	Through-Bond Energy Transfer
TC-SPC	Time-Correlated Single-Photon Counting
TD	Time-Dependent
UV	Ultraviolet
Vis	Visible

# Table of Contents

---

<b>Introduction</b> .....	<b>1</b>
Objectives.....	9
Structure of the thesis.....	10
<b>Methodology and Experimental Techniques</b> .....	<b>15</b>
I. Dyes and Sample Preparation .....	16
II. Experimental Techniques.....	16
Ultraviolet-visible light absorption spectroscopy.....	17
Fluorescence spectroscopy.....	17
Time-correlated single-photon counter.....	18
Singlet oxygen generation .....	20
Laser measurement setup.....	21
Cyclic voltammetry.....	22
III. Quantum Mechanical Calculations .....	22
Geometry optimization and frontier orbitals.....	23
Absorption profile .....	24
Solvent effect.....	24
<b>CHAPTER 1: Laser Dyes and Cation Sensors Based on Novel BODIPYs</b> .....	<b>27</b>
1.1. <i>N</i> -BODIPYs as Laser Media.....	29
1.2. <i>N</i> -BODIPYs as Cation Sensors.....	33
<b>CHAPTER 2: Red and NIR Emitting Laser Dyes</b> .....	<b>41</b>
2.1. Red Lasers Based on Benzofuran-Fused BODIPYs.....	43
2.1.1. Photophysical properties.....	44
2.1.2. Lasing properties .....	48
2.1. Aza-BODIPYs as NIR Lasers .....	50
2.2.1. <i>F</i> -aza-BODIPYs.....	51
2.2.2. <i>O</i> - and <i>C</i> -aza-BODIPYs.....	54
2.2.3. Lasing properties .....	55

<b>CHAPTER 3: Fluorescent Probes, Sensors and Photosensitizers for Bioimaging and Therapy</b> .....	<b>61</b>
3.1. Water-Soluble BODIPY-Labeled Carbohydrates .....	63
3.1.1. Photophysical properties .....	64
3.1.2. Lasing properties.....	67
3.2. Sensing of Amino Acids Bearing Thiol .....	68
3.3. Halogen-Free Singlet Oxygen Photosensitizer .....	73
<b>CHAPTER 4: Bis-BODIPYs Laser Dyes with Chiroptical Response</b> .....	<b>79</b>
4.1. Structure and Conformation .....	81
4.2. Photophysical Properties .....	83
4.3. Chiroptical Properties .....	90
4.4. Lasing Properties .....	90
<b>CHAPTER 5: Multichromophoric Energy Transfer Antennae</b> .....	<b>95</b>
5.1. Red/NIR Aza-BODIPY-BODIPY Cassettes.....	97
5.1.1. Photophysical properties .....	98
5.1.2. Lasing properties.....	101
5.2. Panchromatic Cassettes with Red Emission.....	104
5.2.1. Photophysical properties .....	104
5.2.2. Lasing properties.....	109
5.3. All-BODIPY Based Pentad and Hexad Laser Dyes.....	110
5.3.1. Photophysical properties .....	111
5.3.2. Lasing properties.....	115
<b>Conclusions</b> .....	<b>121</b>
<b>Outlook</b> .....	<b>123</b>
<b>List of Publications (ANNEXES)</b> .....	<b>125</b>



---

## Introduction

---

We have an amazing ability to read and judge people within seconds of meeting them. "First impressions last". Every day, from the moment we wake up in the morning until we sleep at night, we are able to distinguish myriad of colors around us. We use colors in daily life and they tell stories about ourselves; they give us power to manipulate our appearance and environment. Indeed, color has never occupied such an important part in our lives as it does today. Overall, dyes and pigments have been used to provide color to objects, since they are able to absorb light in the ultraviolet-visible-near-infrared (UV-Vis-NIR) spectral region. Both inorganic and organic pigments produced magnificent colors involving dyes from flora and fauna sources<sup>[1]</sup>. These first earth pigments produced mainly yellow ochre, red ochre and black colors and were found in geometrical patterns in the Blombos Cave in South Africa 70000 years ago<sup>[2]</sup>. It was not until 1856 that the first synthetic dye called "mauveine" was discovered by W. H. Perkin<sup>[3]</sup> while trying to find a route to synthesize quinine, a drug used to cure malaria. Although mauveine became a commercial product only for a few years, it led to the huge development of new revolutionizing industry<sup>[4]</sup> which consequently increased the demand of synthetic dyes to a large extent.

In the late 1900's dyes in general found extensive modern applications in an increasing range of scientific research areas. With this sudden growth of interest, the need for new emerging dyes, which could challenge the power and versatility of the formers improving their limitations, caused a great revolution. That is why nowadays dye chemistry<sup>[5,6]</sup> has revived and is in the spotlight, being most of these molecules synthetic organic dyes, and employing them successfully in a great deal of molecular devices driven by light<sup>[7-10]</sup>.

This success owed basically to the development of three distinguishable but at the same time complementary research fields: organic chemistry, computational chemistry and technological advancement. Firstly, many contemporary synthetic routes have been designed<sup>[11,12]</sup> to modulate the structure of chromophores and graft different functional groups into them leading to sophisticated organic dyes in search of different functionalities and applications. Such modern synthetic strategies have not only accelerated the preparation of unique compounds, but also allowed the exploration of chemotypes inaccessible through conventional pathways. Secondly, the advances in computational resources allow the performance of larger and complex theoretical calculations in shorter time scales. This breakthrough progress boosted the computational chemistry as a tool to theoretically simulate and predict the behavior of molecules and help in the search of specific properties, since advanced theoretical methods can be applied to study complex molecules and processes. Computational chemistry<sup>[13,14]</sup> is totally appropriate for the design of new compounds guiding their synthesis and saving on time and resources (especially economical ones). Moreover, it enables us to solve classically intractable chemistry problems helping to answer unresolved questions about phenomena. Lastly, the technological improvements done in advanced spectroscopic techniques enable the study and unraveling of light-guide ultrafast phenomena (even in the femtoseconds scales) underlying in photoactive devices. As a matter of fact, the improvements in microspectroscopy enable to surpass the resolution limit imposed by the diffraction limit ( $\lambda/2$ ), (the Nobel Prize in Chemistry 2014 for the development of super-resolved fluorescence microscopy) allowing the detection of one single particle or molecule (nanoscopy) thanks to the Stimulated Emission Depletion (STED) through the combination of two excitation lasers<sup>[15]</sup> and the consecutive scans with laser irradiation in the same region<sup>[16,17]</sup> (Figure 1).

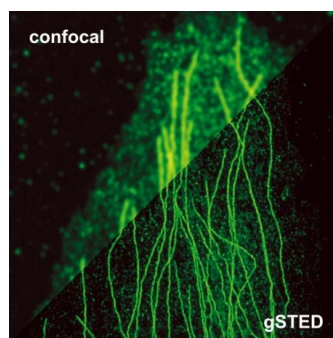


**Figure 1.** Resolution comparison between the images achieved through confocal microscopy (above) and STED (down)<sup>[18]</sup>.

Therefore, at present there is a wide chart of organic dyes available along the UV-Vis-NIR spectral region<sup>[19]</sup>, being those able to emit bright light the most attractive ones. That is to say, some of them are able to show fluorescence<sup>[20]</sup>, a particular phenomenon of luminescence where, after light absorption, an electron returns from the singlet state ( $S_1$ ) to the ground state ( $S_0$ ) with the loss of energy emitted as light (photon). These organic molecules are called fluorophores and they can be employed in a wide range of applications. They are actively tested as photoactive media of dye lasers. Laser (*Light Amplification by Stimulated Emission of Radiation*) is a device which emits light thanks to the optical amplification process based on the stimulated emission of electromagnetic radiation, producing one more photon than in spontaneous emission<sup>[21]</sup>. In comparison with ordinary light, lasers possess monochromatic and coherent radiation which enables to focus the light in a particular point, obtaining high amounts of energy per surface area. These beneficial properties make this light source essential for our daily life, being applied in many fields such as industry<sup>[22]</sup> or medicine<sup>[23]</sup>. Furthermore, organic lasers (organic dyes as active medium, Figure 2a)<sup>[24]</sup> are attractive owing to their broad laser bands, which enable to tune the wavelength<sup>[25]</sup> of the laser signal among a broad spectral range and the generation of ultrashort pulses. Thanks to the aforementioned development of organic chemistry, there is a wide battery of organic laser dye families currently available<sup>[26]</sup> covering the whole visible electromagnetic spectrum (Figure 2b).

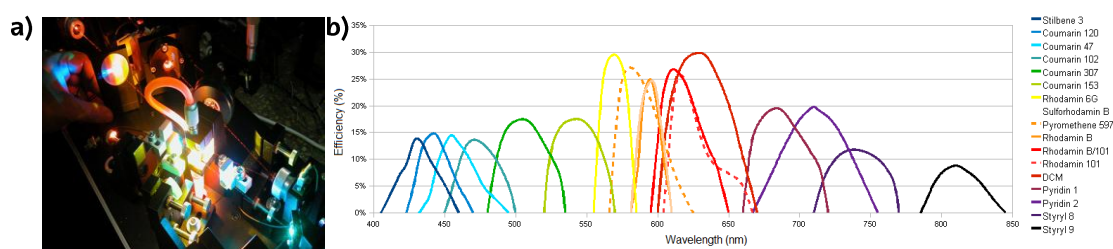


**Figure 2. a)** Laser containing an organic dye solution as active medium. **b)** Laser emission spectra of some dyes with tunable output signal along different wavelength range<sup>[27]</sup>.

Another application of the fluorescent dyes and, surely the most studied and renowned one, is their use as fluorescent probes for bioimaging<sup>[28,29]</sup>. In that regard, organic molecules are biocompatible and able to absorb and emit light efficiently and in a bright and stable manner, all of them essential qualities to develop competitive fluorescent probes. These dyes are led specifically to the desired organelle or anchored to the biomolecule of interest<sup>[30]</sup>, allowing their real-time positioning<sup>[31]</sup> and the monitoring of dynamic biochemical processes tracking the emission of light through fluorescence microspectroscopy (fluorescent imaging, Figure 3). To favor the labeling of the target organelle or biomolecule, the fluorophore is decorated with functional groups to promote the biorecognition of specific binding sites or enable covalent linkage with biomolecules or bioreceptors.

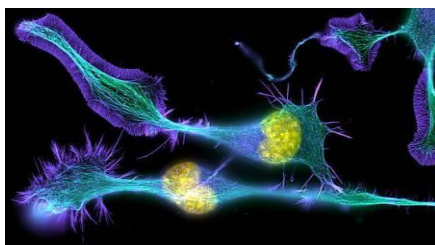


**Figure 3.** Neuronal cell image achieved through fluorescence microscopy<sup>[32]</sup>.

And that is not all, among all the strategies accessible for sensing purposes, fluorescent chemosensors (Figure 4) emerge as the best choice<sup>[33]</sup>. This type of sensors translates straightforwardly chemical information, like the concentration of an analyte, into analytical information, just following the emission signal at real time. For this purpose, the fluorophore should be functionalized with a recognition site for the target analyte.

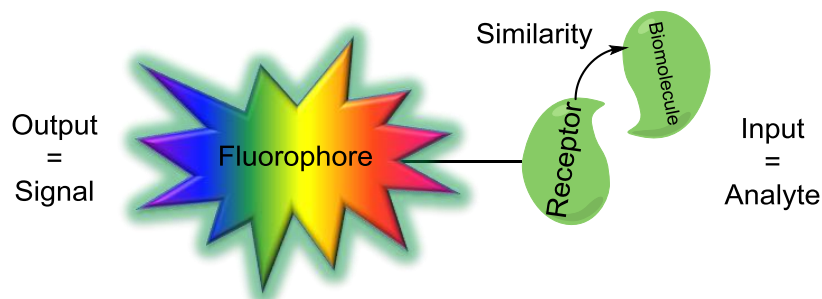


**Figure 4.** Operating principle of analyte-responsive fluorophore-receptor systems.

On the other hand, chromophores with smaller or almost non fluorescent capacities can sometimes lead to new opportunities and show interesting photophysical properties, being applicable for example as photosensitizers (PS), where their main role is

to absorb light efficiently to trigger alternative processes afterwards. One of their applicability concerns the photodynamic therapy (PDT)<sup>[34]</sup> to treat the detrimental diseases of cancer. In such treatment, the photosensitizer agent is metabolized and activated by light of a specific wavelength. Such photoactivation implies the generation of oxidative singlet oxygen<sup>[35]</sup> ( $^1\text{O}_2$ ) from the available bioenvironmental oxygen (Figure 5). This reactive cytotoxic entity attacks the tumor tissues, which are photodamaged irreversibly<sup>[36]</sup>. When the irradiation ceases, the cytotoxic activity disappears and the surrounding organelles are not affected<sup>[37]</sup>. Therefore, this treatment is by far more selective than the current radiotherapy and chemotherapy as healthy cells remain undamaged.

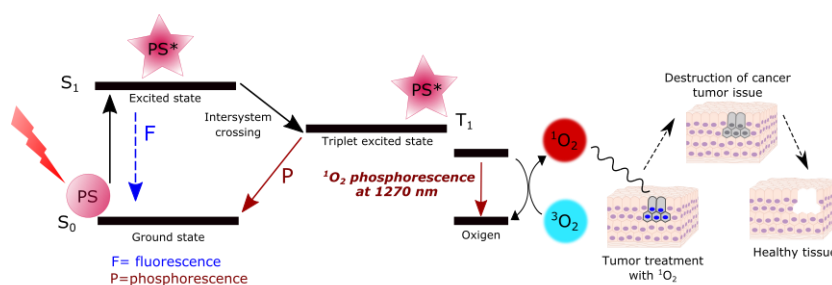


**Figure 5.** Scheme of the formation of the cytotoxic reactive  $^1\text{O}_2$  agent via excitation of the photosensitizer accompanied by the sketch representing the tumor destruction process.

Photosensitizers are also employed in solar cells or photovoltaic devices. Up to now inorganic semiconductors, such as silicon<sup>[38]</sup>, have been responsible for the conversion of solar radiation into useful electric or chemical energy. Nevertheless, their efficiency to absorb light (mainly in the visible part of the electromagnetic spectrum) is quite poor (requiring a certain thickness, increasing the price of the device) and their manufacturing is expensive and generates undesired residues. To tackle all of these problems dyes working as sensitizers can be introduced in solar cells leading to dye-sensitized solar cells (DSSC)<sup>[39]</sup> or in solar concentrators, leading to luminescent solar concentrators (LSC)<sup>[40]</sup>. In a traditional solar cell, the inorganic semiconductor acts as source of photoelectrons and provides electric field to separate the charges and create a current. However, in DSSCs and LSCs, the bulk of semiconductor is only used as a charge transporter and photoelectrons are provided by photosensitive dyes. Thus, after sunlight absorption by the dye, the semiconductor is activated through an electron transfer. In some cases there is no inorganic semiconductor and the solar cell is fully organic (OSCs)<sup>[41]</sup>, where different functional groups acting as electron donors (such as thiophene) and acceptors are joined to boost charge separation<sup>[42]</sup> and obtain stabilization.

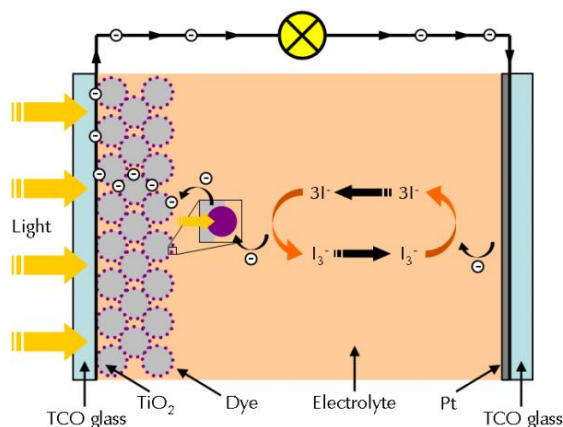
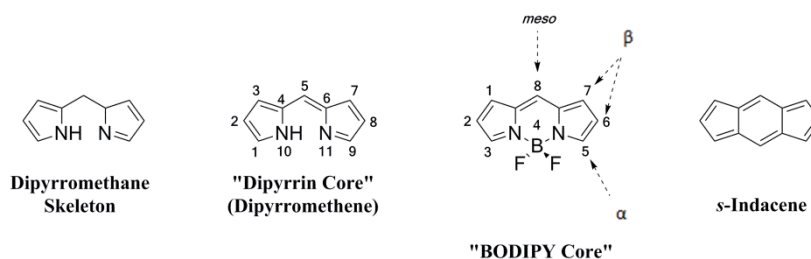


Figure 5. Simplified setup of a dye-sensitized solar cell<sup>[43]</sup>.

Due to the huge number of areas where the organic chromophores are applied by the scientific community, there is no available just one fluorophore suitable for every application. Actually the efforts in dye chemistry are oriented to find versatile molecular scaffolds prone to tailor-made functionalized. That is, instead of developing different dyes for each target application, take a given molecular structure which can be applied in a myriad of application fields after a rational design and proper functionalization. On that subject, the understanding of the correlation between photophysical profiles and structural design must be established. By determining the relationships between the molecular structure and the resultant photophysical properties, chromophores with exact and accurately predictable properties can be developed. Thus, the discovery of a single new fluorophore, whilst being potentially useful, is only significant in a broader sense if it has room for structural modification. In this regard, 4,4-difluoro-4-bora-3a,4a-diaza-s-indacene dyes (renowned by the distinctive noun of BODIPY, and also known as "porphyrin's little sister"), first described in 1968 by Kreuzer and Treibs<sup>[44]</sup>, are in the forefront as modern and applied fluorophores owing to the chemical versatility<sup>[45]</sup> afforded by its boron-dipyrrin core and the deeply tunable photophysical properties<sup>[46]</sup> controlled by the substitution pattern.

BODIPY dye is a cyanine cyclic molecule. Its chromophoric core features a conjugated  $\pi$ -system formed by a polymethine chain with two terminal amine groups chelated by a difluoroboron bridge (Figure 6). The dipyrin framework is the responsible for the main electronic transition, whereas the coordinated BF<sub>2</sub> unit restricts the conformational flexibility of the dipyrin structure, keeping it planar to enhance the aromaticity and fluorescence emission since non-radiative relaxation channels related to internal conversion are vanished<sup>[47]</sup>. The numbering of any substituents in BODIPY follows

rules set up for the *s*-indacene (carbon polycycle), and position 8 sometimes is referred as *meso*-position by analogy to porphyrinic systems (Figure 6).



**Figure 6.** Scheme of the structures of dipyrromethane, dipyrromethene, BODIPY core with its corresponding IUPAC numbering and *s*-indacene skeletons.

Many desirable photophysical properties arise from this unique framework. As a result of its robust core, BODIPY dyes commonly demonstrate strong absorption bands with extinction coefficients frequently around  $100000 \text{ M}^{-1}\cdot\text{cm}^{-1}$  and high fluorescence quantum yields (close to 1.00) and laser efficiencies (higher than 50%) in the green-yellow region of the visible electromagnetic spectrum<sup>[48]</sup>. What is more, this fluorophore shows high photostability with a reasonable tolerance to a continuous and hard irradiation regime<sup>[49]</sup>. These photophysical properties are outstanding for fluorescence and laser purposes owing also to the practically negligible population of the triplet-state<sup>[50]</sup> and its low probability to aggregate in organic media<sup>[51]</sup>.

Compared to other known dipyrin complexes, BODIPY is characterized by very high chemical stability and decomposes only under very strong acidic or basic conditions. Therefore, for many researchers BODIPY has turned into the cornerstone of their projects, being ready exploitable for a multitude of synthetic routes<sup>[52-55]</sup>. Indeed, its success relies on its chromophoric core which is able to suffer from different reactions (Figure 7), like Knoevenagel, Pd-mediated cross couplings and nucleophilic substitutions, among others<sup>[56]</sup>. Moreover, this direct functionalization allows the modulation of the photophysical signatures of the resulting derivative<sup>[57]</sup>. All these facts support and explain the exhaustive chemical transformations carried out at its dipyrin moiety, designing a large number of unique derivatives with different functional groups. This chameleonic character of this dye explains its success in a vast number of applications as fluorophores in tunable lasers<sup>[26]</sup>, light harvesters<sup>[58]</sup>, optoelectronics<sup>[59]</sup>, fluorescent sensors<sup>[60]</sup> and probes<sup>[61]</sup> for diagnosis or as photosensitizers in photovoltaic devices<sup>[62]</sup> and in photodynamic therapy<sup>[63,64]</sup> in biomedicine, where the requirements of photoactive

molecule are completely opposite and the molecular structure of the BODIPY should be chemically adapted to induce the requested photophysical property by a rational design.

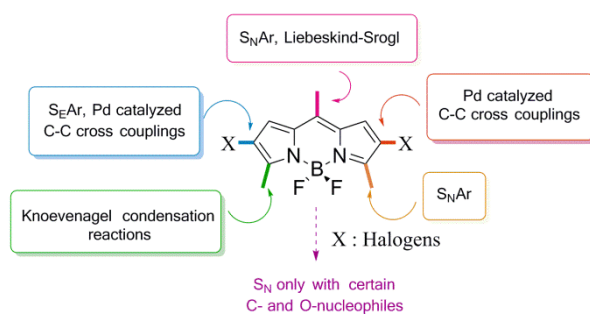


**Figure 7.** Multiple reactivity variety offered by the BODIPY core.

Against this context, in the herein reposted thesis we use molecular tools for the development of a new generation of BODIPY-based dyes with tunable and tailor-made photophysical properties to be applied in a wide range of photonic applications.



## Objectives

The main aim of this thesis is the understanding of the complex interplay between molecular structure and photophysical properties of BODIPY based dyes. Such knowledge allows a deep but controlled modulation of their photonic performance and apply them in fields related with photonics (lasers, light harvesters, chiral activity) and biotechnology (fluorescent probes for diagnosis, fluorescent sensors for detection, and photosensitizers for therapy). Thus, we focus on the unraveling of the molecular structure guided photophysical phenomena underlying in each application fields. The feedback provided by the computationally assisted spectroscopic study enables the redesign of the molecules with tailor-made substitution patterns in single dyes or molecular assemblies in multichromophoric dyes to improve their workability as fluorophores, chiral agents, lasers or photosensitizers. A summary of the specific objectives pursued in this thesis is briefly presented below:

- Unravel the impact of the chemical modification around the boron atom into the photophysical and laser signature of BODIPYs.
- Evaluate the suitability of the conducted molecular approaches to shift the absorption and emission bands of the BODIPY towards longer wavelengths to develop red and near infrared emitting fluorophores and lasers.
- Increase the water solubility of BODIPYs via the fluorescent tagging of carbohydrates to apply them as fluorescent probes for bioimaging.
- Determine the suitability of a red-emitting BODIPY as fluorescent sensor for thiolated amino acids.
- Evaluate the performance of a symmetrical covalently linked BODIPY dimer as heavy atom free singlet oxygen photosensitizer for photodynamic therapy of cancer.
- Determine the intramolecular interaction of bridged symmetrical bis-BODIPYs through chiral and achiral tartaric spacers as lasers and chiral agents.
- Evaluate the molecular structure control of the energy transfer in molecular assemblies to develop light harvesters and energy transfer lasers with long wavelength emission.

## Structure of the thesis

The thesis is divided in five chapters. The ordering of the chapters has been made according to criterion of ascending complexity of the molecular structure. Thus, we start with single dyes bearing different substitution patterns to modulate their photonic performance. Afterwards we introduce multichromophoric dyes ranging from molecular assemblies composed exclusively of BODIPYs (bis-BODIPYs) to more complex molecular architectures combining different dyes (coumarin, perylene and mainly BODIPY).

- Chapter 1; we studied a set of dyes where the fluorine atoms at the boron center are replaced by nitrogens. We focus on the impact of the substitution pattern at the boron atom into the spectroscopic signatures of the BODIPY paying attention to the possibility of inducing electron transfer processes. These *N*-BODIPYs are intended as dye lasers and solid state emitters.
- Chapter 2; this section is oriented to shift the spectral band of the BODIPY to long-wavelengths and attain red and NIR-emitting dyes as lasers with superior performance than the commercially available ones in each spectral window. To this aim two complementary approaches are tested: conformationally restricted BODIPYs bearing fused benzofuran rings and polyarylated aza-BODIPYs.
- Chapter 3; this chapter is oriented to biophotonics. We aim to develop BODIPY-based dyes for diagnosis, sensing and therapy. Therefore, to achieve water-soluble fluorescent probes BODIPYs are labeled with carbohydrates. On the other hand, to achieve fluorescent sensors sensitive to the presence of thiolated amino acids in the surrounding media, the BODIPY core is decorated with unsaturated esters. Finally, singlet oxygen photosensitizers for therapy or theragnosis are designed by the direct linkage of a pair of identical BODIPYs.
- Chapter 4; following the strategy of designing complex dyes to induce new photophysical phenomena, a pair of BODIPY dyes are connected through tartaric acid as an optical active spacer. The stereochemical properties of the bridge do not only rule the chiral response, but also the intramolecular excitonic interactions, which control simultaneously the spectroscopic properties and laser performance of the bis-BODIPYs.

- Chapter 5; finally, different dyes able to undergo energy transfer processes are combined in a single molecular structure as broadband light harvesters and laser emitters in the red-edge of the electromagnetic spectrum. To this aim different approaches have been tested. First, the energy acceptor perylene red decorated with coumarins and blue- and green-emitting BODIPYs as energy donors. Secondly, the aza-BODIPYs described in chapter 2 linked with green-emitting BODIPYs as energy donors. Lastly, we studied all-BODIPY-based multichromophoric dyes bearing many energy donors and acceptors. We pay special attention to the effect of the molecular structure of the assembly (spacer and linkage positions) into the photophysical signatures.

At the end, we present the general conclusions and future perspectives accompanied by the published articles (annex) derived from this thesis.

## Bibliography

- [1] Rasmussen, S. C.; *Chemical Technology in Antiquity*, American Chemical Society, Washington, DC, 1<sup>st</sup> Ed., 7, 197-217, **2015**.
- [2] Barnett, J. R.; Miller, S.; Pearce, E.; *Opt. Laser. Technol.*, **2006**, 38, 445-453.
- [3] Plater, M. J.; *J. Chem. Res.*, **2015**, 39, 251-259.
- [4] Hunger, K.; *Industrial Dyes: Chemistry, Properties and Applications*, WILEY-VCH, Weinheim, 1<sup>st</sup> Ed., **2003**.
- [5] Waring, D. R.; Hallas, G.; *The Chemistry and Application of Dyes*, Plenum Press, New York, 1<sup>st</sup> Ed., **1990**.
- [6] Batchelor, S. N.; *Color. Technol.*, **2015**, 131, 81-93.
- [7] Golshan, M.; Rostami-Tapeh-Esmail, E.; Salami-Kalajahi, M.; Roghani-Mamaqani, H.; *Eur. Polym. J.*, **2020**, 137, 109933.
- [8] Umezawa, K.; Citterio, D.; Suzuki, K.; *Anal. Sci.*, **2014**, 30, 327-349.
- [9] Baroncini, M.; Silvi, S.; Credi, A.; *Chem. Rev.*, **2020**, 120, 200-268.
- [10] Bushuyev, O. S.; Aizawa, M.; Shishido, A.; Barrett, C. J.; *Macromol. Rapid. Commun.*, **2018**, 39, 1700253.
- [11] Levi, L.; Müller, T. J. J.; *Chem. Soc. Rev.*, **2016**, 45, 2825-2846.
- [12] de Moliner, F.; Kielland, N.; Lavilla, R.; Vendrell, M.; *Angew. Chem. Int. Ed.*, **2017**, 56, 3758-3769.
- [13] Lewars, E. G.; *Computational Chemistry*, Springer, New York, 3<sup>rd</sup> Ed., **2016**.
- [14] McArdle, S.; Endo, S.; Apuru-Guzik, Al.; Benjamin, S. C.; Yuan, X.; *Rev. Mod. Phys.*, **2020**, 92, 015003.
- [15] Hell, S.W.; *Angew. Chem. Int. Ed.*, **2015**, 54, 8054-8066.
- [16] Betzig, E.; *Angew. Chem. Int. Ed.*, **2015**, 54, 8034-8053.
- [17] Moerner, W. E.; *Angew. Chem. Int. Ed.*, **2015**, 54, 8067-8093.
- [18] <https://www.picoquant.com/applications/category/life-science/sted>
- [19] Davis, L. D.; Raines, R. T.; *ACS Chem. Biol.*, **2014**, 9, 855-866.
- [20] Lakowicz, J. R.; *Principles of Fluorescence Spectroscopy*, Springer, New York, 3<sup>rd</sup> Ed., **2006**.
- [21] Silfvast, W. T.; *Laser Fundamentals*, Cambridge University Press, Cambridge, 2<sup>nd</sup> Ed., **2004**.
- [22] Lawrence, J.; *Advances in Laser Materials Processing*, Elsevier, Amsterdam, 2<sup>nd</sup> Ed., **2017**.
- [23] Cheng, Y. C.; Fan, X.; *Adv. Optical Mater.*, **2019**, 7, 1900377.
- [24] Schäfer, F. P.; *Dye Lasers*, Springer, New York, 1<sup>st</sup> Ed., **1990**.
- [25] Duarte, F. J.; *Tunable Laser Applications*, CRC Press, Boca Raton, 3<sup>rd</sup> Ed., **2017**.
- [26] Kuehne, A. J. C.; Gather, M. C.; *Chem. Rev.*, **2016**, 116, 12823-12864.
- [27] <https://www.radiant-dyes.com/index.php/products/laser-dyes/list-of-laser-dyes>
- [28] Yin, J.; Ma, Y.; Li, G.; Peng, M.; Lin, W.; *Coord. Chem. Rev.*, **2020**, 412, 213257.
- [29] Terai, T.; Nagano, T.; *Eur. J. Physiol.*, **2013**, 465, 347-359.
- [30] Wu, X.; Shi, W.; Li, X.; Ma, H.; *Acc. Chem. Res.*, **2019**, 52, 1892-1904.
- [31] Dong, Y.; Chen, Z.; Hou, M.; Qi, L.; Yan, C.; Lu, X.; Liu, R.; Xu, Y.; *Spectrochim. Acta A Mol. Biomol. Spectrosc.*, **2020**, 224, 117456.
- [32] <https://www.nikonsmallworld.com/galleries/2004photomicrographycompetition/differentiating-neuronal-cells-actin-microtubules-and-dna>
- [33] Wu, D.; Sedgwick, A.C.; Gunnlaugsson, T.; Akkaya, E.U.; Yoon, J.; James, T.D.; *Chem. Soc. Rev.*, **2017**, 46, 7105-7123.
- [34] Chilakamarthi, U.; Giribabu, L.; *Chem. Rec.*, **2017**, 17, 775-802.
- [35] Ogilby, P. R.; *Chem. Soc. Rev.*, **2010**, 39, 3181-3209.
- [36] Dougherty, T. J.; Gomer, C. J.; Henderson, B. W.; Jori, G.; Kessel, D.; Korbelik, M.; Moan, J.; Peng, Q.; *J. Natl. Cancer Inst.*, **1998**, 90, 889-905.
- [37] Dolmans, D. E.; Fukumura, D.; Jain, R. K.; *Nat. Rev. Cancer*, **2003**, 3, 380-387.

- [38] Yamaguchi, M.; Lee, K. H.; Araki, K.; Kojima, N.; *J. Phys. D: Appl. Phys.*, **2018**, *51*, 133002.
- [39] Sharma, K.; Sharma, V.; Sharma, S. S.; *Nanoscale Res. Lett.*, **2018**, *13*, 381.
- [40] Tummeltshammer, C.; Portnoi, M.; Mitchell, S. A.; Lee, A. T.; Kenyon, A. J.; Tabor, A. B.; Papakonstantinou, I.; *Nano Energy*, **2017**, *32*, 263-270.
- [41] Yeh, N.; Yeh, P.; *Renew. Sust. Energ. Rev.*, **2013**, *21*, 421-431.
- [42] Tamai, Y.; *Polym. J.*, **2020**, *52*, 691-700.
- [43] <https://www.gamry.com/application-notes/physechem/dssc-dye-sensitized-solar-cells>
- [44] Treibs, A.; Kreuzer, F. H.; *Justus Liebig's Ann. Chem.*, **1968**, *718*, 208-223.
- [45] Ulrich, G.; Ziesel, R.; Harriman, A.; *Angew. Chem. Int. Ed.*, **2008**, *47*, 1184-1201.
- [46] Loudet, A.; Burgess, K.; *Chem. Rev.*, **2007**, *107*, 4891-4932.
- [47] Ziesel, R.; Ulrich, G.; Harriman, A.; *New J. Chem.*, **2007**, *31*, 496-501.
- [48] Bañuelos, J.; *Chem. Rec.*, **2016**, *16*, 335-348.
- [49] Ahmad, M.; King, T. A.; Ko, D. K.; Cha, B. H.; Lee, J.; *Opt. Comm.*, **2002**, *203*, 327-334.
- [50] Goorman, A. A.; Hamblett, I.; King, T. A.; Rahn, M. D.; *J. Photochem. Photobiol. A.*, **2000**, *130*, 127-132.
- [51] López-Arbeloa, F.; López-Arbeloa, T.; López-Arbeloa, I.; *J. Photochem. Photobiol. A.*, **1999**, *121*, 177-182.
- [52] Boens, N.; Verbelen, B.; Ortiz, M. J.; Jiao, L.; Dehaen, W.; *Coord. Chem. Rev.*, **2019**, *399*, 213024.
- [53] Lakshmi, V.; Sharma, R.; Ravikanth, M.; *Rep. Org. Chem.*, **2016**, *6*, 1-24.
- [54] Clarke, R. G.; Hall, M. J.; *Advances in Heterocyclic Chemistry, Recent Development in the synthesis of BODIPY Dyes*, Elsevier, Cambridge, 1<sup>st</sup> Ed., 128, **2019**.
- [55] Jean-Gérard, L.; Vasseur, W.; Scherniniski, F.; Andrioletti, B.; *Chem. Commun.*, **2018**, *54*, 12914-12929.
- [56] Boens, N.; Verbelen, B.; Dehaen, W.; *Eur. J. Org. Chem.*, **2015**, 6577-6595.
- [57] López-Arbeloa, F.; Bañuelos, J.; Martínez, V.; Arbeloa, T.; López-Arbeloa, I.; *Int. Rev. Phys. Chem.*, **2005**, *24*, 339-374.
- [58] Yousaf, M.; Zarate, X.; Schott, E.; Lough, A. J.; Koivisto, B. D.; *RSC Adv.*, **2018**, *8*, 28533-28537.
- [59] Poddar, M.; Misra, R.; *Coord. Chem. Rev.*, **2020**, *421*, 213462.
- [60] Wu, D.; Sedgwick, A. C.; Gunnlaugsson, T.; Akkaya, E. U.; Yoon, J.; James, T. D.; *Chem. Soc. Rev.*, **2017**, *46*, 7105-7123.
- [61] Kowada, T.; Maeda, H.; Kikuchi, K.; *Chem. Soc. Rev.*, **2015**, *44*, 4953-4972.
- [62] Ivaniuk, K.; Pidluzhna, A.; Stakhira, P.; Baryshnikov, G. V.; Kovtun, Y. P.; Hotra, Z.; Minaev, B. F.; Agren, H.; *Dyes Pigm.*, **2020**, *175*, 108123.
- [63] Turksoy, A.; Yildiz, D.; Akkaya, E. U.; *Coord. Chem. Rev.*, **2019**, *379*, 47-64.
- [64] Prieto-Montero, R.; Prieto-Castañeda, A.; Sola-Llano, R.; Agarrabeitia, A. R.; García-Fresnadillo, D.; López-Arbeloa, I.; Villanueva, A.; Ortiz, M. J.; de la Moya, S.; Martínez-Martínez, V.; *Photochem. Photobiol.*, **2020**, *96*, 458-477.



---

## Methodology and Experimental Techniques

---

In this section the preparation of dye samples and the different spectroscopic and electrochemical techniques, as well as computational calculations used for recording and understanding their photonic performance are detailed.

The herein studied organic dyes have been synthesized by specialized research groups in the field (specified hereafter). In the same way, the laser characterization has been carried out by the research group headed by Prof. Inmaculada García-Moreno (Instituto de Física-Química "Rocasolano", IQFR-CSIC, Madrid), albeit for long-wavelength emitting dyes the laser properties were registered in our laboratory as mentioned later on. In this regard, we must acknowledge gratefully Dr. Luis Cerdán (IQFR-CSIC) for technical support to ready our laser setup. Therefore, the research job carried out in this thesis is mainly related to the spectroscopic characterization and theoretical calculations, in close collaboration with different research groups.

## I. DYES AND SAMPLE PREPARATION

The BODIPY chromophores presented in the herein work are novel and non-reported to date. Their synthesis has been carried out by expert research groups on the field: Prof. Eduardo Peña from Universidad de Guanajuato in Mexico, Prof. M<sup>a</sup> Jose Ortiz and Prof. Santiago de la Moya from the Universidad Complutense de Madrid (UCM), and Prof. Cristobal López and Dr. José Luis Chiara from the Instituto de Química Orgánica General (IQOG-CSIC) from Madrid. The studied molecular structures of each BODIPY are summarized in each chapter along the discussion and their synthetic process details are explained in the corresponding appended articles.

The photophysical properties were registered in diluted solutions (around  $2 \cdot 10^{-6}$  M), prepared by adding the corresponding solvent to the residue from the adequate amount of a concentrated stock solution in acetone, after vacuum evaporation of this solvent. In this way the reabsorption/reemission phenomena and aggregation processes are avoided<sup>[1-3]</sup>. The concentration effect was analyzed just diluting a concentrated solution in a given solvent. The preparation of the stock was started by weighting around 1 mg of the solid using Sartorius SECURA125-1S analytical balance ( $\pm 0.01$  mg).

On the other hand, laser emission and efficiency was studied in ethyl acetate by varying the concentration from 1 mM to 0.1 mM while keeping all the experimental parameters constant. Once the most efficient solution is known, around 30  $\mu$ L of volume of this solution is employed to study its photostability. All organic solvents were of spectroscopic grade (Merck and Scharlau) and the used water was deionized and distilled.

## II. EXPERIMENTAL TECHNIQUES

The study of the photophysical properties of the dyes in different solvents was carried through spectroscopic techniques. Therefore, UV-Vis absorption spectrophotometer and emission spectrofluorimeter (steady state and time correlated) were employed. The spectra were registered in diluted solutions (around 2  $\mu$ M) contained in 1 cm optical-path rectangular quartz cells carefully sealed at 20-25 °C temperature. The spectroscopic properties of the concentrated solutions were recorded using narrower



cuvettes (from 0.1 cm to 0.001 cm) to maintain the same optical density than in diluted solutions. Besides, to further minimize the undesired reabsorption and reemission phenomena, the corresponding fluorescence spectra were registered in front-face configuration instead of the typical right-angle configuration.

### **Ultraviolet-visible light absorption spectroscopy**

Absorption spectra were recorded on a double beam UV-Vis Varian model CARY 4E spectrophotometer. This spectrophotometer has two lamps; halogen lamp (Vis region) and another deuterium one (UV region), which are automatically exchanged at 350 nm. In the same way, it has a double monochromator and double diffraction grating of 1200 lines/mm with a resolution of  $\pm 0.1$  nm. The detector is a photomultiplier Hamamatsu R928. The absorption spectra for dye solutions were recorded in transmittance from 200 nm to 800 nm at 300 nm/min sweep speed with 0.1 s integration time and slits width of 0.5 nm.

The experimental absorption measurements allow to calculate the molar absorption coefficient ( $\epsilon$ ), which is one dimension of the absorption probability, following the Beer-Lambert law. To this aim, the maximum absorbance of the sample ( $A$ ), its concentration and the optical-path of the cell (1 cm) must be known (Equation 1).

$$A = \epsilon \cdot c \cdot l \quad (1)$$

### **Fluorescence spectroscopy**

After exciting the sample, the fluorescence signal is recorded measuring the emitted light intensity in right-angle for diluted solutions and front-face for the concentrated ones. The fluorescence and excitation spectra were recorded on an Edinburgh Instruments spectrofluorimeter (model FLSP 920). The spectrofluorimeter is composed of the following parts: 1) continuous xenon flash lamp (450 W); 2) double monochromator to improve the resolution of the excitation and emission wavelength; and 3) Hamamatsu R928-P photomultiplier as a detector, which is highly sensitive at long wavelengths. The latter bears a Peltier, not only to cool electronically, but also to decrease the back noise and enhance the signal-to-noise ratio. The fluorescence spectra were

recorded at 300 nm/min sweep speed with a resolution of  $\pm 0.5$  nm. The fluorescence spectra were corrected from the wavelength dependence on the detector sensibility.

Fluorescence quantum yield values ( $\phi$ ) can be obtained using the corrected fluorescence spectra and a suitable commercial dye (Exciton, laser grade) as a reference (see each case in the experimental section of the corresponding article attached to the annex). To this aim, is essential to measure under the same conditions both fluorescence spectra of the sample and the reference. The area under the curve ( $E_{fl}$ ) of the fluorescence spectra of the sample and reference (ref subscript) must be known. The absorbed light intensity ( $A$ ) values at the excitation wavelength are also necessary. When the reference and the sample are measured in different solvents, a correction factor is used considering the refractive index ( $\eta$ ) (Equation 2)<sup>[1]</sup>.

$$\phi = \phi^{ref} \cdot \frac{E_{fl}}{E_{fl}^{ref}} \cdot \frac{1 - 10^{-A^{ref}}}{1 - 10^{-A}} \cdot \frac{\eta^2}{\eta_{ref}^2} \quad (2)$$

On the other hand, when the dye concentration is higher than  $10^{-6}$  M the absolute method was applied to obtain the quantum yield value by using an integrating sphere coupled to the spectrofluorimeter and using the solvent as reference.

In molecular antennae, the efficiency of the energy transfer process between the donor (D) and the acceptor (A) is calculated via the decrease of the fluorescence ability of the donor. So, the fluorescence quantum yield of the donor before ( $\phi_D^0$ ) and after ( $\phi_D$ ) linking covalently to de acceptor must be known (Equation 3).

$$\phi_{EET} = 1 - \frac{\phi_D}{\phi_D^0} \quad (3)$$

### Time-correlated single-photon counter

The lifetime ( $\tau$ ) of the excited state is registered by measuring the decrease of the emission light intensity along the time after the excitation of the sample. Radiative decay curves were recorded with the time-correlated single-photon counting technique (TC-SPC) using a multichannel plate detector (Hamamatsu C4878) as implemented in the aforementioned spectrofluorimeter. Fluorescence emission was monitored at the

maximum emission wavelength after excitation by means of a wavelength-tunable Fianium Supercontinuum laser (time resolution of picoseconds).

Single-photon counter measures the time passed between the moment when the laser pulse excites the sample (start) and the moment when the first photon emitted by the sample arrives to the detector (stop) in order to determine the fluorescence lifetime. The time measures consist on the electric potential difference created between start and stop signals. Afterwards, the amplitude of such voltage is related with the time thanks to a time-to-amplitude converter (TAC) and is registered as a count. The use of a multichannel detector allows to record more than one photon (or more than one count) at the same time, since each channel is related to single voltage amplitude. Thanks to the repetition of this process a counts histogram is obtained thorough the channels (in proportion to the created voltage, the time passed between start and stop signals)<sup>[4-5]</sup>. In this way, the decay curve represents only the %2 of the recorded counts, in order to avoid the counts accumulated before.

These fluorescence deactivation decay curves were obtained when the amount of counts was at least 10.000 at the maximum. The influence of the excitation source was eliminated by its measurement through a scatter solution (Ludox colloidal suspension), since it allows the detection of the excitation light at 90°. The fluorescence lifetime was obtained after the deconvolution of the instrumental response signal from the recorded decay curves by means of an iterative method (Equation 4). Before this fitting the Marquadt algorithm was applied to remove the aforementioned laser influence.

$$Fit = A \cdot B_1 \cdot e^{-\frac{t}{\tau_1}} + B_2 \cdot e^{-\frac{t}{\tau_2}} + B_3 \cdot e^{-\frac{t}{\tau_3}} + B_4 \cdot e^{-\frac{t}{\tau_4}} \quad (4)$$

According to this formula,  $B_i$  is a preexponential factor which controls the statistical weight of each exponential, and  $\tau_i$  is the lifetime value corresponding to each exponential slope.

The goodness of the exponential fit was controlled by statistical parameters; the chi-square ( $\chi^2$ ) must be under the value 1.3 and the analysis of the residuals<sup>[6-8]</sup>. The latter can be seen by naked eye. For the definition of the chi-square free scale ( $\nu$ ), deviation from the calculations ( $R(t_i)$ ) and deviation from the experimental respond ( $R_c(t_i)$ ) are needed (Equation 5).

$$\chi^2 = \frac{1}{V} \cdot \sum \left[ \frac{R(t_i) - R_c(t_i)}{R(t_i)} \right]^2 \quad (5)$$

The radiative ( $k_{fl}$ ) and non-radiative ( $k_{nr}$ ) rate constants were calculated from the fluorescence quantum yield and lifetime (Equation 6 and 7).

$$K_{fl} = \frac{\phi}{\tau} \quad (6) \quad K_{nr} = \frac{1 - \phi}{\tau} \quad (7)$$

### Singlet oxygen generation

The photoinduced production of  $^1\text{O}_2$  was determined by direct measurement of the luminescence (phosphorescence) at 1276 nm with a NIR detector integrated in the aforementioned spectrofluorimeter (InGaAs detector, Hamamatsu G8605-23), cooled at low temperature (77 K) by an Optisa DN cryostat and ITC 601 external temperature controller (Oxford Instruments). Owing to the low intensity of this emission the slits were widened, the integration time was increased and up to 5 scans were accumulated.

The  $^1\text{O}_2$  signal was registered in front configuration (front-face),  $40^\circ$  and  $50^\circ$  to the excitation and emission beams, respectively and leaned  $30^\circ$  to the plane formed by the direction of incidence and registration in cells of 1 cm. The signal was filtered by a low cut-off of 850 nm to remove fluorescence.  $^1\text{O}_2$ -generation quantum yield ( $\phi_\Delta$ ) was determined using the following equation (8):

$$\phi_\Delta = \phi_\Delta^r \cdot (\alpha^r / \alpha^{Ps}) \cdot (Se^{Ps} / Se^r) \quad (8)$$

where  $\phi_\Delta^r$  is the quantum yield of  $^1\text{O}_2$  generation for the used reference. Phenalenone was used as reference for visible irradiation (510 nm). The singlet-oxygen quantum yield of phenalenone in chloroform and toluene is  $\phi_\Delta = 0.98^{[9]}$  and  $\phi_\Delta = 0.92^{[10]}$ , respectively. Factor  $\alpha = 1 - 10^{-Abs}$ , corrects the different amount of photons absorbed by the sample ( $\alpha^{Ps}$ ) and reference ( $\alpha^r$ ). Factor Se is the intensity of the  $^1\text{O}_2$  phosphorescence signal of the sample ( $Se^{Ps}$ ) and the reference ( $Se^r$ ) at 1276 nm.  $^1\text{O}_2$  quantum yields were averaged from 5 concentrations between  $10^{-6}$  M and  $10^{-5}$  M.

## Laser measurement setup

Liquid solutions of dyes in ethyl acetate were contained in 1 cm optical-path rectangular quartz cells carefully sealed to avoid solvent evaporation during experiments. The liquid solutions were transversely pumped with a wavelength tunable optical parametric oscillator (OPO) coupled to the third harmonic (355 nm) of a Q-switched Nd:YAG laser (Lotis TII 2134) at a repetition rate of 1 Hz<sup>[11]</sup>. The exciting pulses were linefocused onto the cell using a combination of positive and negative cylindrical lenses ( $f = 15$  cm and  $f = -15$  cm, respectively) perpendicularly arranged. The plane parallel oscillation cavity (2 cm length) consisted of a 90% reflectivity aluminium mirror acting as back reflector, and the lateral face of the cell acting as output coupler (4% reflectivity). The pump and output energies were detected by an Ophir powermeter (Figure 8).

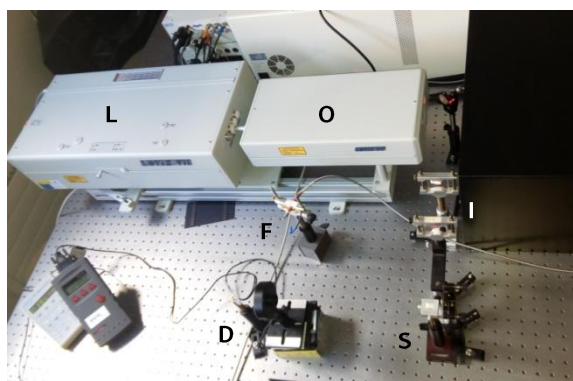


**Figure 8.** Laser measurement setup: L, Nd:YAG laser; O, wavelength tunable OPO; I, lenses; S, support for the cuvette; D, detector; F, optical fiber.

The photostability of the dyes in ethyl acetate solution was evaluated by using a pumping energy and geometry exactly equal to that of the laser experiments. We used spectroscopic quartz cuvettes with 0.1 cm optical-path to allow for the minimum solution volume ( $V_S = 30 \mu\text{L}$ ) to be excited. The lateral faces were grounded, whereupon no laser oscillation was obtained. The photostability was monitored by the decrease in laser-induced fluorescence (LIF) intensity. In order to facilitate comparisons independently of the experimental conditions and sample, the photostability was defined as the accumulated pump energy absorbed by the system ( $E_{\text{dose}}$ ), per mole of dye, before the output energy falls to a 90% its initial value. In terms of experimental parameters, this energy dose, in units of  $\text{GJ} \cdot \text{mol}^{-1}$ , can be expressed as Equation (9):

$$E_{\text{dose}}^{90} (\text{GJ} \cdot \text{mol}^{-1}) = \frac{E_{\text{pump}} (\text{GJ}) \cdot (1 - 10^{-\epsilon CL}) \cdot \sum_{\# \text{ pulses}} f}{CV_S} \quad (9)$$

where  $E_{\text{pump}}$  is the energy per pulse,  $C$  is the molar concentration,  $\varepsilon$  is the molar absorption coefficient in units of  $\text{M}^{-1}\cdot\text{cm}^{-1}$ ,  $L$  is the optical-path of the cuvette expressed in cm,  $V_S$  is the solution volume, in liters, within the cuvette, and  $f$  is the ratio between the LIF intensity after #pulses and the LIF intensity in the first pulse. It can be shown that  $\Sigma f$  accounts for the reduction in pump absorption due to species photodegradation. To speed up the experiment the pump repetition rate was increased up to 10 Hz. The fluorescence emission was monitored perpendicular to the exciting beam, collected by an optical fiber (see F section in Figure 8), and imaged onto a spectrometer (USB2000+ from Ocean Optics), the same used to record the laser spectra.

### Cyclic voltammetry

Electrochemical properties were measured by cyclic voltammetry (Metrohm Autolab) using three-electrode setup with a platinum disk (diameter 3 mm) or layer (surface of 8 x 7.5 mm) working electrode, platinum wire as counter electrode and Ag/AgCl as reference electrode. A 0.1 M solution of tetrabutylammonium hexafluorophosphate (TBAPF<sub>6</sub>) in dry acetonitrile was used as the electrolyte solvent in which the compounds were dissolved to achieve a concentration of 0.5-1 mM. All redox potentials were reported vs ferrocene as internal standard. The solutions were purged with argon and all the measurements were performed under an inert atmosphere.

## III. QUANTUM MECHANICAL CALCULATIONS

Mathematical simulations based on computational chemistry are employed in order to study the behavior of atoms and molecules at microscopic level. The computational methods used in the herein project are based on quantum mechanics, where the molecules are described through the interaction between the core and electrons, and the molecular geometry through the nuclear arrangement of minimum energy. In the herein section these methods have been employed for the optimization of the geometries, charge density calculations, visualization of the molecular orbital (MOs) distribution and electronic transition determination, taking into account the solvent effect in all of them.

Considering the number of atoms of the herein tested BODIPY molecules, the most suitable option is the *Density Functional Theory* (DFT)<sup>[12]</sup>. In this case, in order to solve the Schrödinger Equation, the electronic energy is determined thanks to the electronic density, but without calculating the wave function. Indeed, DFT methods consider the electronic correlation, not considered in *ab initio* methods based on Hartree-Fock, showing the best balance between computational cost and accuracy for the theoretical study of BODIPY chromophore<sup>[13]</sup>.

### Geometry optimization and frontier orbitals

Ground state geometries ( $S_0$ ) were optimized with DFT using mainly the range separated hybrid B3LYP functional (formed by the non-local correlation provided by Lee, Yang and Parr (LYP)<sup>[14]</sup> expression and the hybrid method Becke<sup>[15]</sup> with 3 parameters), since it is one of the best functional available for DFT to treat molecules bearing many atoms and balancing accuracy and computational cost. However, and specially for the multicromophoric systems, we used alternatively the  $\omega$ B97XD functional<sup>[16]</sup>. This functional considers the dispersion correction, which is essential in long-range interaction systems<sup>[17,18]</sup>.

Once the geometry of  $S_0$  is optimized, the excited state ( $S_1$ ) geometry was optimized using the time-dependent (TD)<sup>[19,20]</sup> method and the same functional.

For both functionals, the double valence basis set 6-31G was used (each inner shell is represented by a single basis function taken as a sum of six Gaussians and each valence orbital is split into inner and outer parts described by three and one Gaussian function, respectively)<sup>[21]</sup>. In order to improve the accuracy of the calculation the triple valence basis set 6-311G<sup>[22]</sup> was also employed. Depending on the size of the molecule and the requested accuracy in the calculation, the basis sets were enlarged with polarization functions<sup>[23]</sup> (\*) and diffuse functions<sup>[24]</sup> (+). The geometries were considered as energy minima when the corresponding frequency analysis did not give any negative value.

From the optimized geometries, the analysis of the charge distribution and molecular dipole moments of the molecules was performed using ChelpG method. The energies and contour maps of the molecular orbitals (mainly, *Highest Occupied Molecular*

*Orbital*, HOMO and *Lowest Unoccupied Molecular Orbital*, LUMO) were also determined from the ground state optimized geometries.

### **Absorption profile**

The absorption spectra are based on the Franck-Condon transition, a vertical transition from the ground state to the excited state. For the simulation of the absorption profile and transition moment once again the starting point is the optimized geometry of the ground state. To study the spectral characteristics of one vertical transition between two energy levels TD method was used with B3LYP or  $\omega$ B97XD functionals, depending on the system, and the aforementioned basis set. This calculation also allows the prediction of the circular dichroism (CD) spectra and the corresponding Cotton effect.

### **Solvent effect**

The presence of the solvent was considered in all the conducted theoretical simulations by means of the self consistent reaction field (SCRF)<sup>[25]</sup> method. In that theoretical solvation process the surrounding of the environment is taken as an homogeneous field which respond to the charge of the dye in the solvent via the polarizable continuum model (PCM)<sup>[26,27]</sup>. The latter defines the cavity as spheres overlapped and centered in the atoms. In other words, it only considers the common interactions between the solvent and solute, introducing the charge separation in the surface of the cavity according to the dielectric constant of the solvent.

All of the calculations were performed using GAUSSIAN 16<sup>[28]</sup> as implemented in the computational cluster "ARINA" of the UPV/EHU.



## Bibliography

- [1] Demas, J. N.; Crosby, G. A.; *J. Phys. Chem.*, **1971**, 75, 991-1024.
- [2] López-Arbeloa, I.; *J. Photochem.*, **1980**, 14, 97-105.
- [3] Parker, C. A.; *Photoluminescence of Solutions*, Elsevier, Amsterdam, 1<sup>st</sup> Ed., **1968**.
- [4] Demas, J. N.; *Excited State Lifetime Measurements*, Academic Press, New York, **1983**.
- [5] O'Connor, D. V.; Phillips, D.; *Time-Correlated Single Photon Counting*, Academic Press, London, **1984**.
- [6] Boens, N.; van de Zegel, M.; De Schryver, F. C.; *Chem. Phys. Lett.*, **1984**, 111, 340-346.
- [7] Favre, A.; Tyrrell, R.; Cadet, J.; *From Photophysics to Photobiology, The time-correlated single photon counting technique as a tool in photobiology*, Elsevier, Amsterdam, **1987**.
- [8] Van de Zegel, M.; Boens, N.; Daems, D.; De Schryver, F. C.; *Chem. Phys.*, **1986**, 101, 311-335.
- [9] Schmidt, R.; Tanielian, C.; Dunasbach, R.; Wolff, C.; *J. Photochem., Photobiol. A.*, **1994**, 79, 11-17.
- [10] Martí, C.; Jürgens, O.; Cuenca, O.; Casals, M.; Nonell, S.; *J. Photochem., Photobiol. A.*, **1996**, 97, 11-18.
- [11] Whinnery, J. R.; *Acc. Chem. Res.*, **1974**, 7, 225-231.
- [12] Kohn, W.; Becke, A. D.; Parr, R. G.; *J. Phys. Chem.*, **1996**, 100, 12974-12980.
- [13] Foresman, J. B.; Frisch, A.; *Exploring Chemistry with Electronic Structure Methods*; Gaussian, Inc., Wallingford, CT, 3<sup>rd</sup> Ed., **2015**.
- [14] Lee, C.; Yang, W.; Parr, R. G.; *Phys. Rev. B.*, **1988**, 37, 785-789.
- [15] Becke, A. D.; *J. Chem. Phys.*, **1996**, 104, 1040-1046.
- [16] Chai, J. D.; Head-Gordon, M.; *Phys. Chem. Chem. Phys.*, **2008**, 10, 6615-6620.
- [17] Brémond, É.; Savarese, M.; Su, N. Q.; Pérez-Jiménez, A. J.; Xu, X.; Sncho-Gracia, J. C.; Adamo, C.; *J. Chem. Theory Comput.*, **2016**, 12, 459-465.
- [18] Jensen, S. R.; Saha, S.; Flores-Livas, J. A.; Huhn, W.; Blum, V.; Goedecker, S.; Frediani, L.; *J. Phys. Chem. Lett.*, **2017**, 8, 1449-1457.
- [19] Wiberg, K.B.; Stratmann, R.E.; Frisch, M.J. *Chem. Phys.* **1998**, 297, 60.
- [20] Hirata, S.; Lee, T.J.; Head-Gordon, M.J. *J. Chem. Phys.* **1999**, 111, 8904.
- [21] Rassolov, V. A.; Ratner, M. A.; Pople, J. A.; Redfern, P. C.; Curtiss, L. A.; *J. Comput. Chem.*, **2001**, 22, 976-984.
- [22] Krishnan, R.; Binkley, J. S.; Seeger, R.; Pople, J. A.; *J. Chem. Phys.*, **1980**, 72, 650-654.
- [23] Frisch, M. J.; Pople, J. A.; Binkley, J. S.; *J. Chem. Phys.*, **1984**, 80, 3265-3269.
- [24] Clark, T.; Chandrasekhar, J.; Spitznagel, G. W.; von Ragué Schleyer, P.; *J. Comput. Chem.*, **1983**, 4, 294-301.
- [25] Klamt, A.; Schuurmann, G.; *J. Chem. Soc. Perkin Trans.*, **1993**, 2, 799-805.
- [26] Tomasi, J.; Persico, M.; *Chem. Rev.* **1994**, 94, 2027-2094.
- [27] Miertus, S.; Scrocco, E.; Tomasi, J.; *Chem. Phys.* **1981**, 55, 117-129.
- [28] Frisch, M. J.; Trucks, G. W.; Schlegel, H. B.; Scuseria, G. E.; Robb, M. A.; Cheeseman, J. R.; Scalmani, G.; Barone, V.; Petersson, G. A.; Nakatsuji, H.; Li, X.; Caricato, M.; Marenich, A. V.; Bloino, J.; Janesko, B. G.; Gomperts, R.; Mennucci, B.; Hratchian, H. P.; Ortiz, J. V.; Izmaylov, A. F.; Sonnenberg, J. L.; Williams-Young, D.; Ding, F.; Lipparini, F.; Egidi, F.; Goings, J.; Peng, B.; Petrone, A.; Henderson, T.; Ranasinghe, D.; Zakrzewski, V. G.; Gao, J.; Rega, N.; Zheng, G.; Liang, W.; Hada, M.; Ehara, M.; Toyota, K.; Fukuda, R.; Hasegawa, J.; Ishida, M.; Nakajima, T.; Honda, Y.; Kitao, O.; Nakai, H.; Vreven, T.; Throssell, K.; Montgomery, J. A., Jr.; Peralta, J. E.; Ogliaro, F.; Bearpark, M. J.; Heyd, J. J.; Brothers, E. N.; Kudin, K. N.; Staroverov, V. N.; Keith, T. A.; Kobayashi, R.; Normand, J.; Raghavachari, K.; Rendell, A. P.; Burant, J. C.; Iyengar, S. S.; Tomasi, J.; Cossi, M.; Millam, J. M.; Klene, M.; Adamo, C.; Cammi, R.; Ochterski, J. W.; Martin, R. L.; Morokuma, K.; Farkas, O.; Foresman, J. B.; Fox, D. J.; Gaussian, Inc., Wallingford CT, **2016**.



## CHAPTER 1

---

# Laser Dyes and Cation Sensors Based on Novel BODIPYs

---

Fluorescent dyes have become unavoidable recently and ubiquitous in many light-driven devices. In fact, the discovery of BODIPY revolutionize the synthetic dye era with regard to organic chemistry. BODIPY functionalization has been exploded through myriad of synthetic routes<sup>[1]</sup>. However, the direct functionalization of BODIPYs at the boron center has not been evaluated in depth<sup>[2-4]</sup>, although such functionalization makes these chromophores even more appealing<sup>[5-8]</sup>, since water solubility could be improved for biological applications<sup>[9]</sup> and laser photostability could be enhanced<sup>[10]</sup>, just to mention a few. This straightforward functionalization at the boron atom replacing the fluorine atoms (*F*-BODIPYs) has hitherto been accomplished by nucleophilic substitutions with certain alkyl and alkoxy-based moieties leading to the corresponding *C*- and *O*-BODIPYs, respectively<sup>[11-14]</sup>. Nevertheless, a low amount of new derivatives have been obtained satisfactorily<sup>[15]</sup>. Although the boron atom does not take part in the delocalized  $\pi$ -system, the replacement of the highly electronegative fluorine atoms by moieties with different electron withdrawing forces could easily rearrange the electronic density at the chromophore. What is more, when this extremely electronegative atom is substituted, a noteworthy drop of the stability of these dyes is observed. Therefore, this atom exchange

at the boron position increases the electron density and reduces its Lewis acidity, lessening its capability to be chelated by the dipyrroin moiety.

To improve this handicap, new synthetic alternatives should be carried out. Up to now, electron-poor functional groups have been mainly employed<sup>[13]</sup>. Nitrogen is an appealing candidate to replace the at-boron fluorine atoms since its structural and electronic properties are between those of carbon and oxygen. Nonetheless, nitrogen atom displays different key bonding features such as higher reactivity, different bond directionality and enhanced bond valence, which allows raising the number of pendant moieties around the BODIPY chromophore. In this sense, more postfunctionalization choices can be reached, as *N*-BODIPYs, unlike *C*- and *O*-BODIPYs. The former derivatives can have linked up to three substituents or even can be quaternized, gaining much more control of the photophysics simultaneously. On that subject, the herein chapter reveals an unprecedented synthetic route for the replacement of strongly electronegative fluorine atoms by nitrogen atoms. Synthetic access to these systems has been gained through a judicious design focused on stabilizing the involved diaminoboron chelate. Thus, a new unveiled chromophore family has been reported for the first time: *N*-BODIPYs (diaminoboron dipyrromethenes). In this context, the discovery of *N*-BODIPYs paves the way towards unexplored frontiers, since its properties have never been studied and its potential is rather difficult to predict. So, this strategy opens up novel avenues for multifunctionalization expanding at the same time the range of applications.

In the herein chapter we have synthesized successfully a battery of new dyes (Figure 1.1) with different *N*-substitution pattern studying the differences between symmetric and asymmetric structures (**NBDP1a** vs **NBDP1d** and **NBDP1b** vs **NBDP1c**) and among closed rigid and open structures (**NBDP1a**, **NBDP1d**, **NBDP1e** vs **NBDP1f**) in order to unravel the interplay between the molecular structure and the photophysical properties. Thus, in the following sections, we first present a brief description of the outstanding photophysical and lasing properties of these *N*-BODIPYs compared to the parent available *F*-BODIPY (PM567) (section 1.1). Afterwards, we also discuss the findings around this synthetic strategy towards the design of dyes applied for chemosensing of cations (section 1.2). More information can be found in **Chemistry - A European Journal** attached to the annex I.

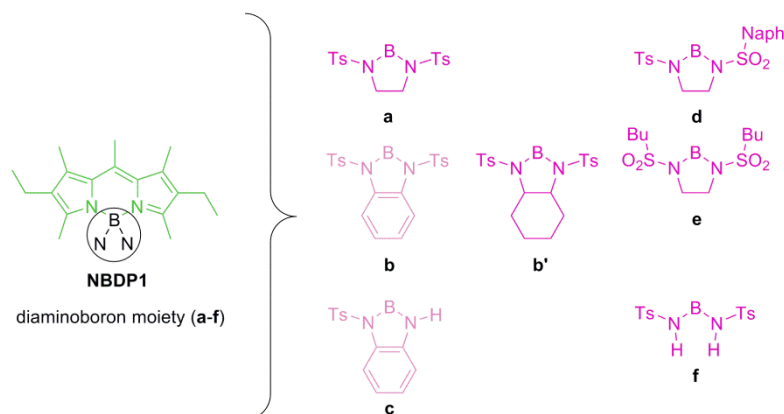


**Figure 1.1.** Novel set of *N*-BODIPYs derived from commercial PM567 dye (Ts = *p*-toluenesulfonyl (tosyl), Naph = 2-naphthyl, Bu = butyl).

### 1.1. *N*-BODIPYs AS LASER MEDIA

These *N*-BODIPYs show an absorption band centered roughly at 525 nm due to the electronic transition occurring on the conjugated system of the cyanine, being independent of the distinct pendant moieties around the nitrogen atoms at the boron bridge. The tethered sulfonylated amines at the boron center instead of fluorine atoms slightly shifts bathochromically the absorption band (less than 10 nm), whereas the spectral profile fully reminds to the parent *F*-BODIPY (PM567), exhibiting their characteristic vibronic shoulder<sup>[16]</sup>. Thus, the nature of the delocalized  $\pi$ -system has not been suffered from the alterations of the sulfonylated amine groups linked to the boron atom. Such slight spectral shift is attributed to the rearrangement of the charge density in the cyanine chromophore, since a resonant interaction has been excluded owing to the fact that more pronounced changes should have been observed and the boron bridge does not take part in the delocalized  $\pi$ -system. While no significant changes are recorded for the absorption properties, the fluorescence signatures depend markedly on the chemical modifications around the nitrogen atoms of their diaminoboron moieties. All *N*-BODIPYs display an emission peaked at around 540 nm following the expected trend and matching the fluorescence emission of the reference PM567. However, on the one hand **NBDP1a**, **NBDP1d**, **NBDP1e** and **NBDP1f** dyes provides bright emission, regardless of the tosylated diaminoboron moiety being cyclized in a five-membered spiro ring or not and the peripheral substitution at the sulfonyls showing fluorescence quantum yields higher than 0.75 and lifetimes values superior to PM567, almost independent of the solvent polarity (Table 1.1). On the other hand, the fusion of a phenyl at the said spiro ring

sharing the boron center in **NBDP1b** and **NBDP1c** promotes the opposite behavior and their fluorescence response is almost negligible. Therefore, in this section we will focus on the former set of dyes as promising candidates for dye lasers, whereas the last set of dyes are not suitable as photoactive media for lasers and will be analyzed in the next section 1.2.

**Table 1.1.** Photophysical properties of newly synthesized *N*-BODIPYs dissolved in polar/protic (trifluoroethanol) and less polar (ethyl acetate) solvents. For comparison purposes, photophysical data of commercial PM567 are also included.

Dye	$\lambda_{ab}$ <sup>a)</sup> [nm]	$\epsilon_{max}$ <sup>b)</sup> [10 <sup>4</sup> M <sup>-1</sup> cm <sup>-1</sup> ]	$\lambda_{fl}$ <sup>c)</sup> [nm]	$\phi$ <sup>d)</sup>	$\tau$ <sup>e)</sup> [ns]
<b>PM567</b>					
Ethyl Acetate	517.0	7.6	533.0	0.84	5.78
F <sub>3</sub> -ethanol	516.0	6.9	532.5	0.82	6.94
<b>NBDP1a</b>					
Ethyl Acetate	526.5	6.5	543.5	0.83	7.65
F <sub>3</sub> -ethanol	525.0	5.9	540.0	0.80	9.53
<b>NBDP1b</b>					
Ethyl Acetate	529.0	4.3	546.5	0.009	0.11 (99.4%) – 5.84 (0.6%)
F <sub>3</sub> -ethanol	527.5	3.7	543.0	0.046	0.60 (98.8%) – 6.99 (1.2%)
<b>NBDP1c</b>					
Ethyl Acetate	524.5	2.5	540.5	0.004	-
F <sub>3</sub> -ethanol	523.5	2.0	538.0	0.131	1.95 (65.5%) – 7.33 (34.5%)
<b>NBDP1d</b>					
Ethyl Acetate	527.0	6.3	544.5	0.80	7.70
F <sub>3</sub> -ethanol	526.5	5.8	544.0	0.74	9.73
<b>NBDP1e</b>					
Ethyl Acetate	523.5	5.0	540.5	0.80	7.19
F <sub>3</sub> -ethanol	521.5	5.8	538.5	0.77	8.99
<b>NBDP1f</b>					
Ethyl Acetate	528.0	5.9	547.0	0.76	7.64
F <sub>3</sub> -ethanol	526.5	5.6	545.5	0.80	9.53

<sup>a)</sup>Absorption peak wavelength; <sup>b)</sup>Maximum molar extinction coefficient; <sup>c)</sup>Fluorescence peak wavelength; <sup>d)</sup>Quantum yield; <sup>e)</sup>Fluorescence lifetime.

The spiranic design (**NBDP1a**, **NBDP1d** and **NBDP1e**) limits the conformational flexibility of the dyes<sup>[17]</sup>, diminishing the probability of non-radiative relaxation channels from the excited state. In this line of reasoning, one may expect poorer fluorescence ability for the non-spiranic **NBDP1f** on account of the higher structural flexibility and greater conformational freedom<sup>[18, 19]</sup>. Nevertheless, it seems that such a large tosyl group and the steric hindrance exerted by the methyl groups at BODIPY positions 3 and 5 suffice to hinder the aforementioned free turn and a minor fall is barely observed (Table 1.1). In fact, the optimized geometry (B3LYP/6-31G\*) for all of these four compounds indicates that both tosyl fragments are disposed in an orthogonal way regarding the dipyrin plane, even if this orthogonal arrangement is more evident in spiranic compounds. Furthermore,

this disposition is in good agreement with the solid-state geometry determined experimentally by X-ray diffraction (Figure 1.2).

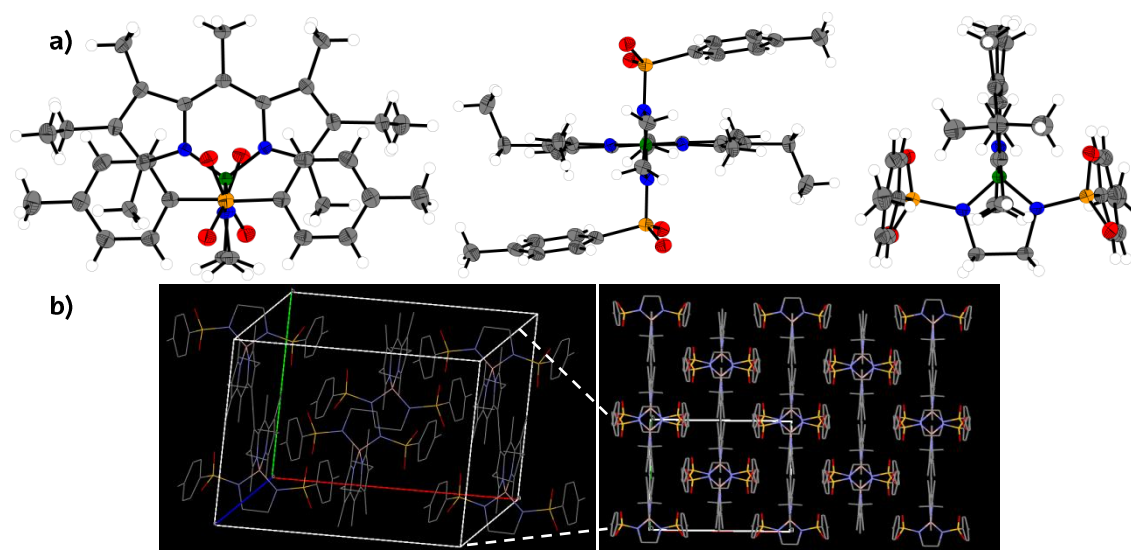


**Figure 1.2.** a) Oak Ridge Thermal Ellipsoid Plot (ORTEP) diagram in different views and b) X-ray crystalline packing of N-BODIPY **NBDP1a** (right) and an amplified view of the selected region (left) (boron atoms in green, nitrogens in blue, oxygens in red and sulfurs in orange).

This type of arrangement in these four compounds avoids the formation of aggregates and chromophoric interactions. The disposition of the tosyl groups flanking the dipyrromethene moiety, prevents potential interactions of the chromophoric core, such as,  $\pi$ - $\pi$  stacking, and promotes the preservation of its photophysical properties even in the aggregated state. It is possible to appreciate a significant fluorescence response in the solid crystalline state (absolute quantum yield of around 3% for **NBDP1a** vs almost negligible fluorescent response for the commercial ones). The study of these objects by fluorescent microspectroscopy reveals particles of variable size (some of them reaching lengths up to several hundred of micrometers) with quite homogenous and right-angled shapes displaying fluorescence emission peaked at around 600 nm, 50-60 nm bathochromically shifted with respect to those in solution (Figure 1.3). This shift is probably due to the presence of strong re-absorption/re-emission effects assisted by the possible existence of small defects that act as energy traps, according to the short Stokes shifts registered (about  $600\text{ cm}^{-1}$ ). In other words, this fluorescence response in the solid state is exclusively inherent to the monomeric emission and not to the presence of new aggregated states<sup>[14, 20]</sup>, considering that dipyrin chromophores are far away from each other (centre-to-centre distance  $>10\text{ \AA}$ , see Figure 1.2) vanishing the probability of intermolecular interactions (e.g., exciton coupling). This is of great assistance in order to develop tunable lasers in the solid state (microlasers), since it is usually necessary to

introduce the dyes in solid guest matrixes to afford the necessary spacing between the chromophores and avoid losses in the lasing performance, with its consequent experimental unforeseen difficulty<sup>[21]</sup>.

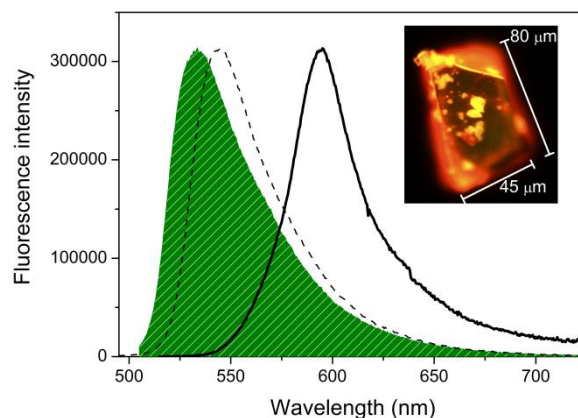


**Figure 1.3.** Fluorescence images of representative crystals of **NBDP1d** together with its fluorescence spectra in solid state (bold lines) upon irradiation at 470/40 nm. For comparison the corresponding spectra recorded from diluted solution (dashed lines) and PM567 emission spectra (green filled) both in ethyl acetate are also included.

The fact that these four compounds exhibit greater molar absorption probability at 532 nm (second harmonic of Nd:YAG laser which is used to pump transversally these dyes) comparing to the fluorinated counterpart PM567,  $5.0\text{--}6.0 \times 10^4 \text{ M}^{-1} \text{ cm}^{-1}$  vs  $1.8 \times 10^4 \text{ M}^{-1} \text{ cm}^{-1}$ , adds another noticeable advantage with a view to laser dye development, which cannot be set aside, since it decreases the threshold to record laser emission. In this way, **NBDP1a**, **NBDP1d**, **NBDP1e** and **NBDP1f** display an improved laser emission in solution centered at 569 nm (Figure 1.4) diminishing from 1.00 to 0.35 mM the required dye concentration for optimal pumping conditions.

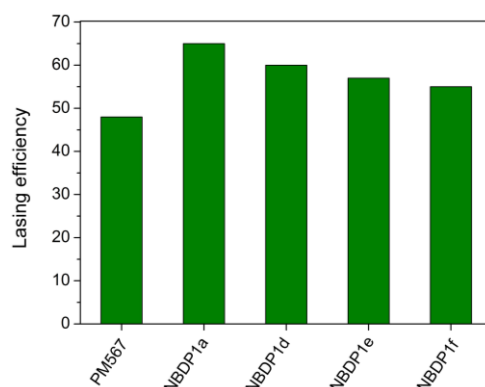


**Figure 1.4.** Lasing efficiencies of the N-BODIPYs which can act as laser media in comparison with the reference PM567.

In order to support the valuable technological progress of these N-BODIPYs, the performance of dye **NBDP1a** as distributed feedback (DFB) laser was studied<sup>[22]</sup>. For this



purpose, this dye and the reference PM567 were doped in a poly(-methyl methacrylate) (PMMA) film and their results were compared. After pumping the devices at well above the threshold, 0.2 nm width DFB laser emission at around 567 nm was observed. If we focus on the pump intensity, it is possible to conclude that **NBDP1a** has a lower DFB laser threshold than PM567 ( $17 \text{ kWcm}^{-2}$  vs  $28 \text{ kWcm}^{-2}$ ). Furthermore, when pumped at well above the said thresholds, a two-fold enhancement in output intensity is recorded for the *N*-BODIPY. As a result, the herein synthesized *N*-BODIPYs surpass the performance as lasing devices in solution as well as in the solid-state of the nowadays commercially available dyes.

## 1.2. *N*-BODIPYs AS CATION SENSORS

As aforementioned, the sole fusion of a benzene ring to the spiranic diazaboracycle (**NBDP1b** and **NBDP1c**) provokes abrupt changes in the fluorescence features (see Table 1.1). Even if the position of the spectral bands has been barely altered, not only the absorption probability has dropped, but also the fluorescence ability has been reduced drastically (fluorescence quantum yield close to 0%, Table 1.1). As a matter of fact, a bi-exponential fitting is required for the proper adjustment of the fluorescence decay curve of the compound **NBDP1b** (Figure 1.5), where the main contribution derives from the shortest lifetime (around 100 ps). Such tendencies are more noticeable in the case of the asymmetric derivative which contains a non-tosylated amine (**NBDP1c**), displaying even lower absorption probability (between  $2.0\text{-}3.0 \cdot 10^4 \text{ M}^{-1} \text{ cm}^{-1}$  vs  $7.6 \cdot 10^4 \text{ M}^{-1} \text{ cm}^{-1}$  for PM567) and virtually negligible fluorescence response (being actually not feasible the registration of its fluorescence decay curve).

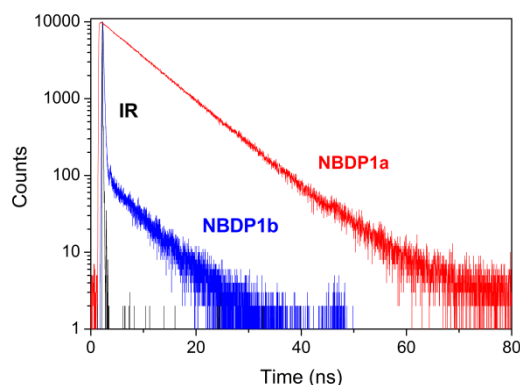


**Figure 1.5.** Fluorescence decay curves of the *N*-BODIPYs **NBDP1a** (red) and **NBDP1b** (blue) in ethyl acetate.

These findings state that the union of such benzene aromatic ring to the spiranic cycle propels the appearance of an extra non-radiative deactivation process which is responsible of the fluorescence quenching. The fusion of the phenyl to the spiranic ring enables the electronic coupling between the amines leading to a delocalized electron rich group pendant at the boron atom. In effect, theoretical calculations predict that the deactivation mechanism corresponds to a photoinduced electron transfer (PET) process<sup>[23]</sup>. In **NBDP1c**, bearing one amine non-tosylated, theoretical simulations point that HOMO is localized in the new fragment linked to the boron atom, that is to say, the occupied molecular orbital belonging to the dianiline with one tosyl group is settled between the BODIPY frontier molecular orbitals responsible of the visible transition (Figure 1.6). As a result, after excitation an electronic transfer takes place from the fragment joined to the boron to the BODIPY, avoiding its radiative deactivation. In the case of **NBDP1b**, bearing both amines tosylated, the diaminoboron moiety is less electron-donor, decreasing its HOMO energy below the energy gap corresponding to the BODIPY (Figure 1.6). In this energy distribution the reductive PET process is less thermodynamically favored, but still viable since the energy gap between the HOMO (now located at the BODIPY) and the low-lying HOMO-1 (placed at the diaminoboron moiety) is within 0.1 eV. Such low energy barrier enables PET to compete effectively with the fluorescence emission.

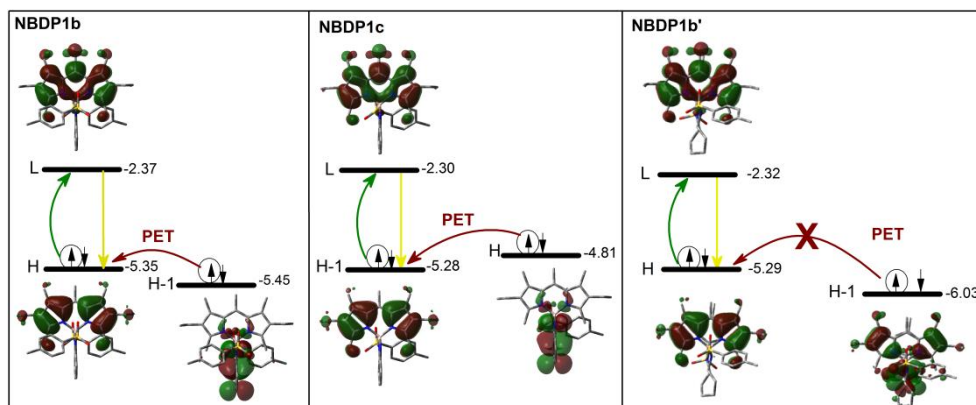


**Figure 1.6.** Theoretically predicted (B3LYP/6-31G\*) energy diagrams (in eV) of the molecular orbitals involved in the main electronic transition as well as in the fluorescence quenching PET of **NBDP1b**, **NBDP1b'** and **NBDP1c**.

In order to reinforce this explanation, both theoretically and experimentally, the fusion of a non-aromatic ring to the spiranic cycle was considered (compound **NBDP1b'**)<sup>[24]</sup>. In this case, instead of a benzene ring one cyclohexane unit has been joined, and this mere structural change provokes drastic enhancement of the fluorescence ability, from being non-fluorescent (**NBDP1b**) to being highly fluorescent with efficiencies

and lifetimes as high as those observed for the rest of the *N*-BODIPYs in section 1.1 ( $\phi > 0.95$  and  $\tau > 7$  ns). Thus, it can be said that PET process cannot take place as theoretical calculations reaffirm (see Figure 1.6). The benzene ring of the fluorophore **NBDP1b** enables a global resonant interaction with both diamines and tosyl groups, so that the pendant moiety at the boron atom is electron rich and, thus, electron donor. On the contrary, the sole replacement of the benzene by a cyclohexane moiety avoids the resonance between aminetosyl groups. As a consequence, the less electron donor character decreases considerably the energy level of its HOMO-1 (0.58 eV), not interfering with the HOMO-LUMO gap of the BODIPY, hampering the PET process (energetic barrier around 0.74 eV) and recovering the high fluorescence ability of the BODIPY.

The electron-rich diaminoboron moiety responsible of the low fluorescent response of **NBDP1b** and **NBDP1c** can be serviceable as receptor to interact with cations and protons for sensing purposes<sup>[25,26]</sup>, since such interaction should modulated the PET viability and this could be reflected in the fluorescence response. As a matter of fact, the fast, sensible and non-invasive detection of ions in human being is of great interest and very important so as to follow and understand plenty of biochemical processes<sup>[27]</sup>. Moreover, cations like  $H^+$ ,  $Na^+$ ,  $Mg^{2+}$ ,  $Ca^{2+}$ ,  $Zn^{2+}$  or  $Fe^{2+}$  take part in many processes such as neuron communication mechanisms, modulation of the cellular activity, homeostasis or enzymatic metabolism<sup>[25]</sup>. Of course, the detection of heavy cations ( $Hg^{2+}$ ,  $Pb^{2+}$  and  $Cd^{2+}$ ) is also fundamental because they are harmful for our bodies. In this regard, fluorescence is a suitable tool to translate the chemical information (presence and amount of cation) into analytical information (fluorescent signal). As a proof of concept, we evaluated theoretically the performance of **NBDP1c**, bearing an amine with less sterical hindrance and more accessible to cations, as fluorescent sensor. As can be seen in the Figure 1.7, after the protonation of the non-tosylated amine, PET process is not energetically viable anymore. Under this new condition, HOMO is now placed along the BODIPY core and is energetically far away from HOMO-1 (around 0.6 eV), which is now localized on the pendant moiety linked to the boron. This new reorganization of the molecular orbitals makes the PET process thermodynamically unworkable and turns dye **NBDP1c** into a potential off/on (absence of cation, PET allowed/presence of cation, PET suppressed) switch, ideal for the detection of cations through an enhancement of the fluorescence emission<sup>[28,29]</sup>.

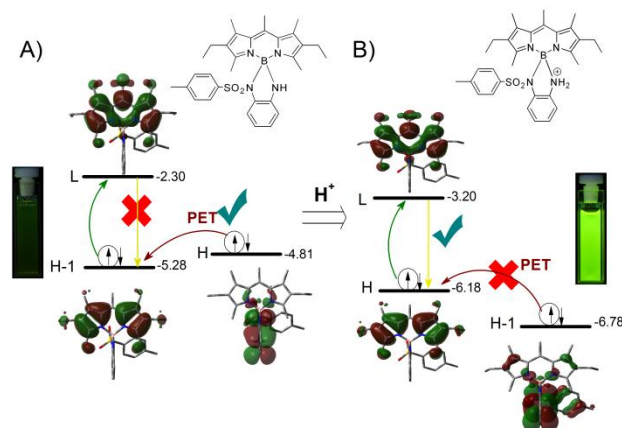


**Figure 1.7.** Computationally ( $B3LYP/6-31G^*$ ) aided energy diagrams (in eV) of the molecular orbitals involved in compound **NBDP1c** before (A) and after (B) its protonation.

Against this theoretical background, we tested experimentally the fluorescent response of **NBDP1c** against a battery of monovalent, divalent and trivalent metal cations (around 25 equivalents of cation per dye molecule). Evaluating the fluorescence response of this screening (Figure 1.8), one can conclude that the presence of monovalent cations, with the exception of the proton, as well as some divalent cations ( $Ca^{2+}$ ,  $Mg^{2+}$ ,  $Ni^{2+}$  and  $Zn^{2+}$ ) diminishes even more the fluorescence emission. This issue can occur on account of the excess of such cations which promotes the presence of an extra non-radiative deactivation such as intersystem crossing by the intermolecular heavy atom effect, charge-transfer phenomena, or collisional effects. So, the design of this *N*-BODIPY is not appropriate for the detection of these cations. Nevertheless, the addition of protons and ions such as  $Co^{2+}$ ,  $Fe^{2+}$ ,  $Fe^{3+}$  and  $Cr^{3+}$  induces a huge impact on the increase of the fluorescence signal (Figure 1.8), supporting the theoretical hypothesis explained before and suggesting that this fluorophore is valuable as switches for the detection of the latter set of cations. In fact, this set of cations present the sufficient positive charge density to interact electrostatically with the amine groups and eliminate the fluorescence quenching induced by PET. Such charge density depends on the solvation volume of each ion. So, the greater solvation shell possess the cation, the less charge density should be boosted and this cation is not going to be able to create the necessary electrostatic interaction with the electron lone pair on the amine moiety in order to eliminate the PET process. Therefore, dye **NBDP1c** can operate as cation sensor for ions with high charge density, and even as a proton sensor.

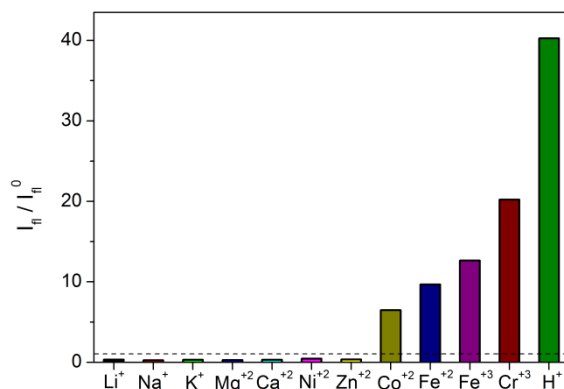


**Figure 1.8.** Ratio between the fluorescence intensity (at 535 nm) with an excess of cation ( $10^{-4}$  M) and the signal recorded without cation ( $I_f^0$ ) for diluted solutions of **NBDP1c** ( $4 \cdot 10^{-6}$  M).

Titration measurements were performed to study its sensibility (Figure 1.9). In all experiments tested herein; that is when proton,  $\text{Co}^{2+}$  or  $\text{Cr}^{3+}$  are added, there is a progressive increase of the fluorescence intensity in concordance with the cation concentration until it reached a maximum response (between 1 and  $4 \cdot 10^{-4}$  M). After that saturation point, if we continue increasing the concentration, the fluorescence intensity starts going down owing to the huge excess of metal ions, which enables the activation of the aforementioned non-radiative relaxation pathways. Even so, this sensor presents high sensitivity especially to the presence of  $\text{Cr}^{3+}$  cations, as the fluorescence intensity increases up to 70-fold. Moreover, the detection limit registered for this cation was well below  $10^{-5}$  M reaching the nanomolar scale. It is also highly important to mention that higher proton concentration was needed to reach the same maximum fluorescence response showed by  $\text{Cr}^{3+}$  ( $1.8$  vs  $5 \cdot 10^{-5}$  M, respectively), demonstrating that **NBDP1c** is more sensible to the presence of  $\text{Cr}^{3+}$  ions than it is for protons.

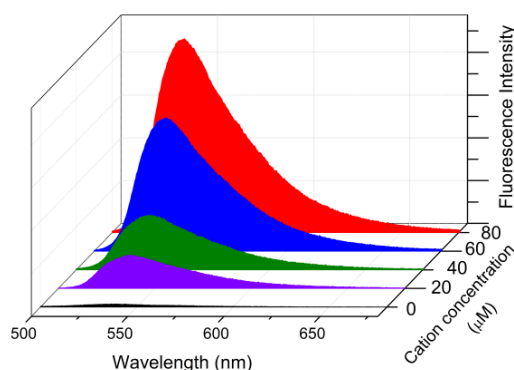


**Figure 1.9.** Fluorescence spectra corresponding to the titration of diluted ethanolic solutions of **NBDP1c** (dye concentration  $4 \cdot 10^{-6}$  M) with different concentrations of  $\text{Cr}^{3+}$ .

To sum up, it has been tested that electron-poor amine moieties based on tosylated amines are required to stabilize *N*-BODIPY dyes. Moreover, small structural changes around the pendant functionality at the boron atom drastically change the fluorescence response. In this sense, on the one hand, we have shown that *N*-BODIPYs, spiranic or not, lead to bright chromophores even in the solid crystalline state, with prominent lasing capacities in both liquid and solid state (surpassing 60% laser efficiencies) improving the laser performance of PM567. On the other hand, the sole arylation of the spiranic diamminoboron moiety arouses the presence of a PET process that eliminates the fluorescence emission completely. However, the electrostatic binding of cations to the amine suppresses the PET, recovering the bright fluorescence of the dye. Therefore, reversible on-off switches have been designed for the detection of cations and protons in the surrounding environment. So, it is clear that a specific fitting of the electronic properties at the boron atom results crucial to expand the applications of these fluorophores towards the development of improved photonic materials with multiple applications in the field of biomedical and environmental monitoring. Indeed, and taking advantage of the claimed postfunctionalization advantages featuring the amines at the boron center, we are currently working in the design of smart dyes bearing there suitable chromophores to induce energy transfer processes for light collectors and emitters, optically active moieties for circularly polarized absorption (ECD) and luminescence (CPL), and specific functionalities for selective recognition of targeted biomolecules or organelles as fluorescence probes of bioimaging.

## Bibliography

- [1] Boens, N.; Verbelen, B.; Dehaen, W.; *Eur. J. Org. Chem.*, **2015**, 6577-6595.
- [2] Jiang, X. D.; Zhang, J.; Furuyama, T.; Zhao, W.; *Org. Lett.*, **2012**, 14, 248-251.
- [3] Nguyen, A. L.; Bobodova-Parvanova, P.; Hopfinger, M.; Fronczek, F. R.; Smith, K. M.; Vicente, M. G. H.; *Inorg. Chem.*, **2015**, 54, 3228-3236.
- [4] Ulrich, G.; Goze, C.; Goeb, S.; Retailleau, P.; Ziesse, R.; *New J. Chem.*, **2006**, 30, 982-986.
- [5] Courtis, A. M.; Santos, S. A.; Guan, Y.; Hnedricks, A.; Ghosh, B.; Szantai-Kis, D. M.; Reis, S. A.; Shah, J. V.; Mazitschek, R.; *Bioconjugate Chem.*, **2014**, 25, 1043-1051.
- [6] Florès, O.; Pliquett, J.; Galan, L. A.; Lescure, R.; Denat, F.; Maury, O.; Pallier, A.; Bellaye, P. S.; Collin, B.; Mème, S.; Bonnet, C. S.; Bodio, E.; Goze, C.; *Inorg. Chem.*, **2020**, 59, 1306-1314.
- [7] Wang, M.; Zhang, G.; Kaufman, N. E. M.; Bobodova-Parvanova, P.; Fronczek, F. R.; Smith, K. M.; Vicente, M. G. H.; *Eur. J. Org. Chem.*, **2020**, 971-977.
- [8] Durán-Sampedro, G.; Agarrabeitia, A. R.; Cerdán, L.; Pérez-Ojeda, M. E.; Costela, A.; García-Moreno, I.; Esnal, I.; Bañuelos, J.; López-Arbeloa, I.; Ortiz, M. J.; *Adv. Funct. Mater.*, **2013**, 23, 4195-4205.
- [9] Yang, L.; Fan, G.; Ren, X.; Zhao, L.; Wang, J.; Chen, Z.; *Phys. Chem. Chem. Phys.*, **2015**, 9167-9172.
- [10] Jagtap, K. K.; Shivran, N.; Mula, S.; Naik, D. B.; Sarkar, S. K.; Mukherjee, T.; Maity, C. K.; Ray, A. K.; *Chem. Eur. J.*, **2013**, 19, 702-708.
- [11] Manzano, H.; Esnal, I.; Marques-Matesanz, T.; Bañuelos, J.; López-Arbeloa, I.; Ortiz, M. J.; Cerdán, L.; Costela, A.; García-Moreno, I.; Chiara, J. L.; *Adv. Funct. Mater.*, **2016**, 26, 2756-2769.
- [12] Ziessel, R.; Ulrich, G.; Haefele, A.; Harriman, A.; *J. Am. Chem. Soc.*, **2013**, 135, 11330-11344.
- [13] Brizet, B.; Bernhard, C.; Volkova, Y.; Rousselin, Y.; Harvey, P. D.; Goze, C.; Denat, F.; *Org. Biomol. Chem.*, **2013**, 11, 7729-7737.
- [14] Abdulhadi El-Ali, H. A.; Jing Jing, J.; Zhang, X.; *RSC Adv.*, **2019**, 9, 16246-16251.
- [15] Bodio, E.; Goze, C.; *Dyes Pigm.*, **2019**, 160, 700-710.
- [16] Boens, N.; Verbelen, B.; Ortiz, M. J.; Jiao, L.; Dehaen, W.; *Coord. Chem. Rev.*, **2019**, 399, 213024.
- [17] Sánchez-Carnerero, E. M.; Gartzia-Rivero, L.; Moreno, F.; Maroto, B. L.; Agarrabeitia, A. R.; Ortiz, M. J.; Bañuelos, J.; López-Arbeloa, I.; de la Moya, S.; *Chem. Commun.*, **2014**, 50, 12765-12767.
- [18] Jiménez, J.; Ruth Prieto-Montero, R.; Maroto, B. L.; Moreno, F.; Ortiz, M. J.; Oliden-Sánchez, A.; López-Arbeloa, I.; Martínez-Martínez, V.; de la Moya, S.; *Chem. Eur. J.*, **2020**, 26, 601-605.
- [19] Sola-Llano, R.; Jiménez, J.; Avellanal-Zaballa, E.; Johnson, M.; Cabrerros, T. A.; Moreno, F.; Maroto, B. L.; Muller, G.; Bañuelos, J.; Cerdán, L.; García-Moreno, I.; de la Moya, S.; *Dyes Pigm.*, **2019**, 170, 107662.
- [20] Bozdemir, Ö. A.; Al-Sharif, H. T.; McFarlane, W.; Waddell, P. G.; Benniston, A. C.; Harriman, A.; *Chem. Eur. J.*, **2019**, 25, 15634-15645.
- [21] Gierschner, J.; Varghese, S.; Park, S. Y. *Adv. Opt. Mater.*, **2016**, 4, 348-364.
- [22] Samuel, I. D. W.; Turnbull, G. A.; *Chem. Rev.*, **2007**, 107, 1272-1295.
- [23] Bissel, R. A.; Prasanna da Silva, A.; Nimal-Gunaratne, H. Q.; Mark-Lynch, P. L.; Maguire, G. E. M.; McCoy, C. P.; Samankumara-Sandanayake, K. R. A.; *Fluorescence PET (photoinduced electron transfer) sensors*, Topics in Current Chemistry, Springer, Berlin, 168, **1993**.
- [24] Ray, C.; Schad, C.; Avellanal-Zaballa, E.; Moreno, F.; Bañuelos, J.; Maroto, J. L.; de la Moya, S.; *Proceedings*, **2019**, 41, 54, 1-9.
- [25] Valeur, B.; Leray, I.; *Coordination Chemistry Reviews*, **2000**, 205, 3-40.
- [26] Boens, N.; Leen, V.; Dehaen, W.; *Chem. Soc. Rev.*, **2012**, 41, 1130-1172.
- [27] Motagues, M. E.; Martínez-Manez, R.; Sancenon, F.; *Chem. Soc. Rev.*, **2011**, 40, 2593-2643.
- [28] Bozdemir, Ö. A.; Guliyev, R.; Buyukcakir, O.; Selcuk, S.; Kolemen, S.; Gulseren, G.; Nalbantoglu, T.; Boyaci, H.; Akkaya, E. U.; *J. Am. Chem. Soc.*, **2010**, 132, 8029-8036.
- [29] Sui, B.; Tang, S.; Liu, T.; Kim, B.; Belfield, K. D.; *ACS Appl. Mater. Interfaces*, **2014**, 6, 18408-18412.





## CHAPTER 2

---

### Red and NIR Emitting Laser Dyes

---

Among the frequencies of electromagnetic radiation which cover the electromagnetic spectrum, those photons with the suitable energy to emit red light are indispensable in technological fields such as telecommunications and in biomedicine owing to the low interference of this radiation source with the surroundings<sup>[1-4]</sup>. In that regard, we have to take into account that the ideal working range for both applications is located at the red-edge of the electromagnetic spectrum (650-900 nm for the so called “biological window”) and even in the NIR region (800-1600 nm for the “telecom range” in particular). In biomedicine this type of light penetrates more deeply into biological tissues (up to 2-5 cm), minimizing the photo-damage of the samples and at the same time, avoiding background interferences related to the auto-fluorescence of surrounding biomolecules and enhancing the resolution in bioimaging<sup>[5]</sup>.

In technology, fiber optics enables communication and optical spectroscopy to be performed on sites inaccessible by the conventional one, reaching large distances, for instance<sup>[6]</sup>. So, displaying high fluorescence signal in the red-edge and even in the NIR is of paramount importance. In this regard, nowadays organic dyes are a suitable approach to this aim due to their chemical versatility<sup>[7]</sup>. Therefore, it is extremely necessary the search of red-NIR organic fluorophores able to tolerate long laser irradiations, boosting their operative lifetime<sup>[8,9]</sup>.

Against this background, a number of parameters and attributes must be evaluated when it concerns the design of a new chromophore for a specific application. For the issue addressing in the herein chapter, our prototype dye has to possess bright emission efficiencies at long wavelengths and/or high photostability under intense irradiation conditions. At present, there is a wide range of fluorescent dyes emitting in different regions of the visible electromagnetic spectrum (Figure 2.1)<sup>[10]</sup>. However, in most cases the photostability is not the desired one and the emission is far from the red-edge of the visible spectral region and the NIR. Cyanine-based<sup>[11]</sup> dyes (including porphyrins and phthalocyanines) for instance, can emit fluorescence deep in the red-edge, even reaching the NIR, but these fluorophores have some drawbacks for its optimal performance, such as; (i) tedious synthetic and purification procedures; (ii) low fluorescence efficiency (owing to their conformationally flexible structures which promotes non-radiative deactivation funnels further favored by their intrinsic push-pull character<sup>[12]</sup>); (iii) poor photostability owing to photobleaching; and (iv) limited chemical versatility for postfunctionalization.

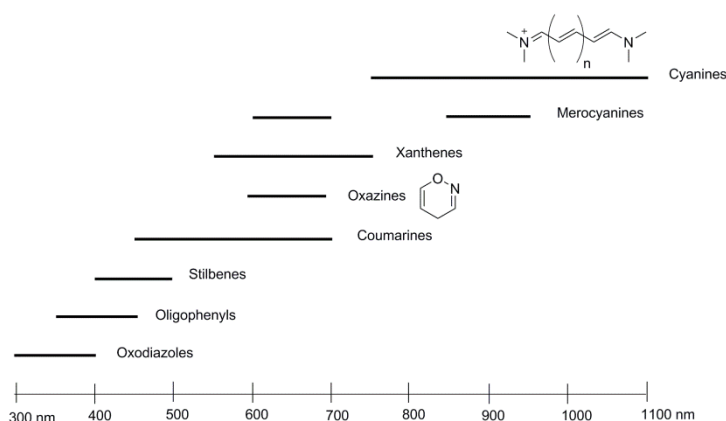


**Figure 2.1.** Nowadays commercially available dyes covering the whole visible spectrum.

Therefore, the research of new molecular structures is focused on shifting the spectral bands to the reddest possible region of the visible spectrum and magnify their tolerance with a view to a prolonged exposure of intense laser irradiation<sup>[13]</sup>. To this aim, in the herein chapter we propose two different approximations to satisfy this object. In order to achieve a large bathochromic shift of both absorption and emission bands, one useful option could be to reduce the HOMO-LUMO gap of the BODIPY by extending their conjugation system through aromatic frameworks, characterized by their excellent photophysical properties and robustness<sup>[14]</sup>. These aromatic rings can be either fused to the dipyrin core, leading to conformationally restricted BODIPYs, or connected to the core via single bond enabling resonant interactions between the dipyrin and these peripheral groups<sup>[15,16]</sup>. In the first strategy, in which the BODIPY core is merged with

aromatic rings, fused bis-BODIPYs are obtained (Figure 2.2). The second pathway, inspired in the structural changes undertaken in porphyrines to obtain phthalocyanines, leads to the aza-BODIPYs where the *meso* carbon is replaced by a nitrogen atom<sup>[17]</sup>. Such simple modification induces pronounced bathochromic shifts, which can be even enlarged through the aforementioned modifications to span the delocalized  $\pi$ -system<sup>[18]</sup>. Indeed, aza-BODIPY dye family stands out as a promising alternative to design bright, stable, compact and smaller NIR emitters than phthalocyanines<sup>[19]</sup> for instance (Figure 2.2).

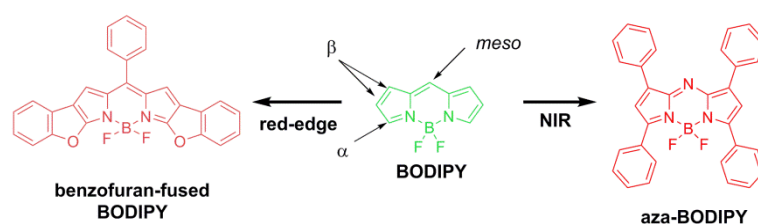


**Figure 2.2.** Two possible approaches based on the BODIPY core modification to push its spectral bands towards the red-edge of the visible spectrum and the NIR region.

As our aim is to develop a set of laser dyes covering the spectral region of interest for biophotonic applications ranging from 650 to 750 nm, in the following sections we proposed the dyes based on benzofuran-fused BODIPYs as laser dyes emitting in the far-red region of the visible (section 2.1), whereas the poliarilated aza-BODIPYs are better suited for the NIR spectral region (section 2.2). Hereafter, we overview the photophysical and laser properties of these novel BODIPYs and we put their photonic performance into context by comparison with other commercially available laser dyes working in the same spectral region. More information can be found in **The Journal of Organic Chemistry** and in **Chem-Photo-Chem**, respectively, attached to the annex II.

## 2.1. RED LASERS BASED ON BENZOFURAN-FUSED BODIPYs

As mentioned in Chapter 1, BODIPY dye offers a very versatile dipyrin core. On this matter, good leaving functional groups like halogen heteroatoms could be added to positions 3-5 and 2-6, that is  $\alpha$  and  $\beta$  positions (Figure 2.2), in order to enable the later fusion of heterocycles, specifically, furanes. With views to the further extension of the  $\pi$ -system, additional aromatic rings like benzene could be introduced creating benzofuran-fused BODIPYs (Figure 2.3). As a matter of fact, this structure is going to be the main platform to design a new family of benzofuran-fused BODIPY dyes with different

variations at the aryl group anchored at the *meso*-position (**RED22-26**) and in the benzofuran substitution pattern (**RED34-36**). So as to reach even lower energies, a larger conjugation system has been successfully designed (see compound **RED37** in Figure 2.3). Moreover, after the incorporation of two phenolic biomolecules into the BODIPY core compounds **RED41** and **RED42** were synthesized, demonstrating the applicability of the synthetic methodology.

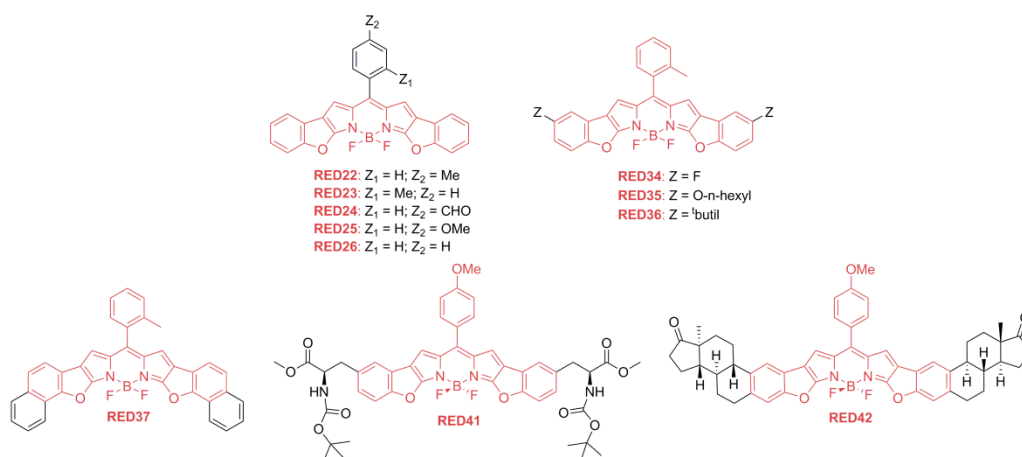


Figure 2.3. New family of benzofuran-fused BODIPYs.

### 2.1.1. Photophysical properties

The fusion of benzofuran rings to the 2, 3 and 5, 6 positions of the dipyrin core occasions strong bathochromic shifts of both spectral bands (up to 83 nm in absorption and 87 nm in fluorescence) and surprisingly a high absorption probability, being twice of those recorded for simpler BODIPYs (with molar extinction coefficients around  $20 \cdot 10^4 \text{ M}^{-1} \cdot \text{cm}^{-1}$ ), on account of the spanning of the aromaticity (Figure 2.4).

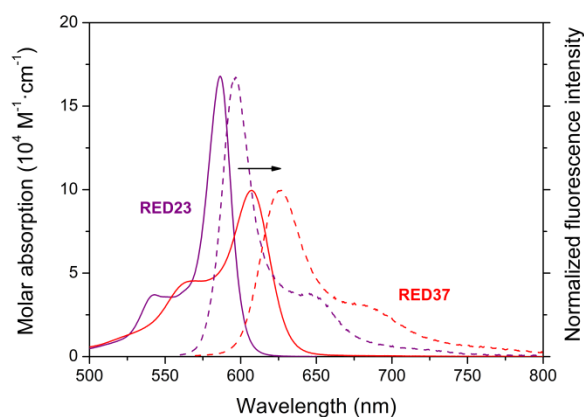
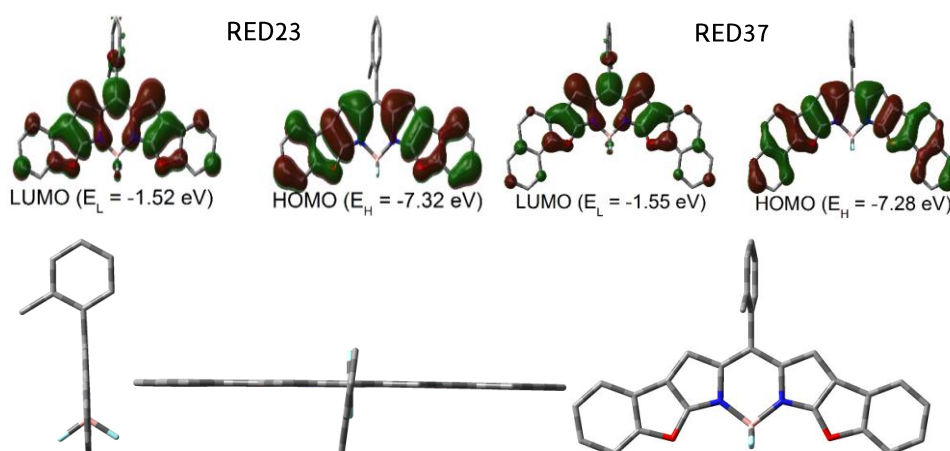


Figure 2.4. Absorption (solid lines) and normalized fluorescence (dashed lines) spectra of dye **RED23** and **RED37** ( $2 \mu\text{M}$ ) in ethyl acetate.

In fact, the theoretical calculations (using long-range corrected density functional method,  $\omega$ B97XD/6-311G\*\*) predict an increase of the  $\pi$ -system delocalization which encompasses all the conjugated aromatic rings. And these effects, in turn, are only consequence of the fused aromatic rings because the contribution of the *meso*-aryl group is minor and only appears in the LUMO orbital (Figure 2.5), as this ring does not take part in the delocalized  $\pi$ -system due to its twisted disposition. Moreover, it has no effect in the spectral band positions (Table 2.1). As a matter of fact, not only the compound bearing methyl group in the *ortho* position of the 8-phenyl (**RED23**) places this ring almost orthogonal to the dipyrin core due to the steric hindrance, but also dyes **RED22**, **RED24**, **RED25** and **RED26** collocates their *meso*-phenyl ring twisted (about  $60^\circ$ ), in the four latter cases owing to the steric hindrance caused by the hydrogens at positions 1 and 7. Although one may expect compounds **RED22**, **RED25** and **RED26** to present quenched fluorescence response in comparison to **RED23** owing to the presence of unconstrained 8-aryl fragments with conformational freedom<sup>[20]</sup>, the obtained results wreck this hypothesis. In this case, the extension of the  $\pi$ -system through the aromatic fused rings displaces the electronic density far away from the key *meso* position (Figure 2.5), preventing the quenching pathway related to this motion<sup>[21]</sup>. As a result, these four compounds are extremely fluorescent independently of the solvent polarity, with high quantum yields and lifetime values ( $\phi > 0.85$  and  $\tau \approx 4$  ns, see Table 2.1). Indeed, these dyes are characterized by a high conformational restriction due to the cyclization of the substituent, which hinders at the same time the non-radiative relaxation processes. Furthermore, these chromophores remain planar (Figure 2.5) in spite of the ensuing structural stress even upon excitation, resulting in small Stokes shifts.



**Figure 2.5.** Theoretically calculated ( $\omega$ B97XD/6-311G\*\*) contour maps and energies of the frontier orbitals for compounds **RED23** and **RED27** together with different views of the optimized ground state geometry of **RED23** (left and right) and **RED37** (middle).

Although these dyes share the same chromophoric unit (dipyrrin fused with benzofurans), they differ in their *meso*-substitution, but, even so, they present similar fluorescence response (Table 2.1) regardless of the conformational mobility of the 8-aryl group (unconstrained, twisting angle of the phenyl of 60° in dyes **RED22** and **RED26**, or constrained, orthogonal *o*-tolyl in **RED23**) or its functionalization (electron donor *p*-methoxy in **RED25**). The only exception to the rule is the **RED24** which has a *para*-formylated 8-aryl group and shows lower fluorescence response in comparison to the others (Table 2.1), which is even lower at polar surroundings (quantum yields lessen from 0.63 in cyclohexane to 0.39 in ethyl acetate). Taking into account that the presence of an oxygen heteroatom at the  $\alpha$ -pyrrolic position makes the benzofuran to be prone to act as an electron donor and that this compound bears a weak electron-withdrawing group at the 8-aryl moiety, this combination could strengthen the formation of an intramolecular charge transfer (ICT) process<sup>[16]</sup> which is able to compete with the radiative decay. In fact, excitation (HOMO  $\rightarrow$  LUMO) implies the shift of electronic density from the benzofuran to the dipyrrin core anticipating the viability of charge transfer. This hypothesis is reinforced from the fact that in compounds **RED22** and **RED25**, in which the substituents at *para* position are electron donors, the probability for the ICT to be switched on is mostly avoided. Furthermore, this tendency is more obvious in polar media due to the large charge separation in the aforementioned ICT process, whose energy level changes a lot depending on the solvent polarity, mainly in polar media where the low-lying ICT is further stabilized.

**Table 2.1.** Photophysical properties of red-emitting benzofuran-fused BODIPYs dissolved in cyclohexane.

RED	$\lambda_{ab}$ [nm]	$\epsilon_{max}$ [10 <sup>4</sup> M <sup>-1</sup> ·cm <sup>-1</sup> ]	$\lambda_{fl}$ [nm]	$\Delta\nu_{st}$ <sup>a)</sup> [cm <sup>-1</sup> ]	$\phi$	$\tau$ [ns]
<b>22</b>	548.5	21.5	596.5	345	0.88	4.09
<b>23</b>	586.5	21.5	595.5	260	0.88	4.21
<b>24</b>	592.5	13.7	612.0	540	0.63	2.47
<b>25</b>	583.5	20.0	593.5	290	0.88	4.10
<b>26</b>	586.0	15.6	597.5	330	0.84	3.99
<b>34</b>	581.5	17.3	590.0	250	0.95	4.02
<b>35</b>	592.0	19.0	603.0	310	0.96	4.12
<b>36</b>	591.5	23.2	602.0	295	0.89	4.11
<b>37</b>	613.0	12.9	625.0	315	0.81	4.31
<b>41</b>	586.5	18.0	596.5	285	0.81	3.94
<b>42</b> <sup>b)</sup>	596.5	17.9	611.5	410	0.88	4.04

<sup>a)</sup> Stokes shifts; <sup>b)</sup> RED42 was insoluble in cyclohexane; thus, the reported data were recorded in diethyl ether.

Although fluorophores **RED34**, **RED35** and **RED36** differ from the previous ones concerning the substitution pattern, these dyes display very similar photophysical properties showing almost identical absorption and fluorescence wavelengths and slightly higher quantum yields and lifetime values (Table 2.1). That is, the presence of heteroatoms, like fluorine in dye **RED34**, or alkyl groups, like *tert*-butyl in **RED36**, maintains a high fluorescence response independently of the surrounding media. However, when alkoxy chains are linked to the chromophore (**RED35**), there is a slump in the fluorescence signatures, decreasing the quantum yields from 0.96 in cyclohexane to 0.73 and 0.29 in ethyl acetate and methanol, respectively. In the same way, the lifetime also sees its values declined from 4.12 ns in cyclohexane to 3.81 and 1.67 ns in ethyl acetate and methanol, respectively. Such a tendency is consistent with the activation of the ICT process once again, which quenches the emission from the locally excited (LE) state.

The fusion of more rings to the benzofuran (**RED42** and specially **RED37**, which comprises up to seven aromatic rings) implies an additional bathochromic shift, reaching fluorescence bands centered at 625 nm (Figure 2.4). Despite the geometrical stress imposed by the fusion of aromatic rings, the theoretical calculations predict that the chromophore remains planar and rigid (Figure 2.5). Although the fluorescence signatures stay similar for dye **RED41** irrespective of the surrounding media ( $\phi \approx 0.80$  and lifetime values about  $\tau \approx 2$  ns), in the case of **RED37** and **RED42** the fluorescence response only remains high in cyclohexane (Table 2.1). In these two cases, an increase of the solvent polarity lead to a moderate decline of quantum yield values (0.69 and 0.48 in ethyl acetate and methanol, respectively for **RED37** and 0.61 and 0.52 for **RED42**) accompanied by shorter lifetime values (similar values in non-polar media, see Table 2.1, but 3.17 ns and 3.71 ns in methanol for **RED37** and **RED42**, respectively). In media with higher polarity, where the interactions are stronger, the planarity of these two compounds could be slightly distorted. Thus, the level of the internal conversion relaxation is likely to grow with a consequent reduction in the fluorescence ability.

### 2.1.2. Lasing properties

Taking into account the high fluorescence efficiency showed by these red-emitting dyes and with a view to fulfill our objective, their performance as active media for tunable lasers was tested at different concentrations. All of them were solved in ethyl acetate in order to avoid solubility setbacks, with the exception of **RED42**, in which the required concentration to accomplish laser emission was impossible to reach. In general, at high concentrations the lasing properties follow the photophysical trends and strong laser emissions are recorded spanning the far-red spectral region from 615 nm to 660 nm, and reaching 685 nm for **RED37**. These laser emission lines appear far away from the absorption and fluorescence signals (around 70 nm and 50 nm bathochromically shifted, respectively), being these shifts much stronger than those recorded for typical BODIPY dyes (about 40 nm and 20 nm, respectively)<sup>[22]</sup>. However, at low concentrations or low pump energies the laser signals appear in the expected position for BODIPYs. Because of that, in these compounds it is possible to register dual laser emission (Figure 2.6) depending on the dye concentration (between 0.25 - 0.50 mM). This phenomenon could be ascribed to the high propensity of these kinds of fluorophores with flat molecular geometries to stack each other, leading to the formation of excited states aggregates, favored by the high pump energy of the high-optical density active media. That is to say, the presence of these aggregates (photoinduced excimers or superexciplexes) is only detected under strong pumping and not under standard excitation conditions like those used for the registration of photophysical properties<sup>[23]</sup>. Therefore, the laser emission recorded at high concentrations corresponds to an aggregated state and the one recorded at low concentrations corresponds to the pertinent monomeric form (Figure 2.6). So, it is possible to widen the tuning range<sup>[24]</sup> playing with the dye concentration or the pump energy, having a custom-made laser for the desired application.

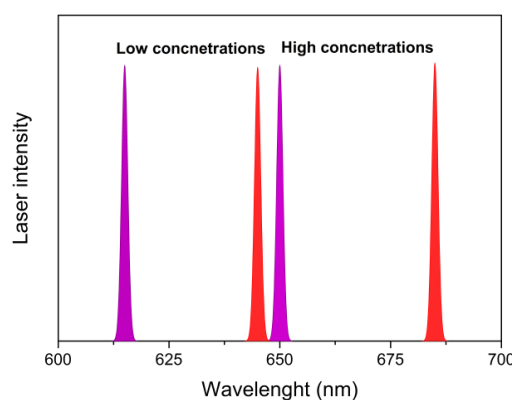


**Figure 2.6.** Laser spectra (dual emission depending on the dye concentration) of dye **RED23** (purple) and **RED37** (red) in ethyl acetate.



Following the same trend, the higher lasing efficiencies (approaching 50%) were recorded for those dyes showing the higher fluorescence efficiencies (Figure 2.7), being dyes **RED24** and **RED37** the ones displaying the poorest results. Another point worth mentioning is their photostability, a key parameter ruling the operative lifetime of a dye and a light-driven device. To estimate this, we measure the amount of energy required to reduce the laser induced fluorescence a 10% (that is to retain a 90% of the initial signal). All the dyes show a reasonable tolerance to a continuous and hard irradiation regime, being exceptional in some cases (Figure 2.7). The lowest photostabilities correspond to the dyes bearing the 8-phenyl *para*-substituted (with methoxy in **RED25** and **RED41** and formaldehyde **RED24**), whereas the highest ones relate to those dyes bearing substituents in the benzofuran moiety (fluorine, *tert*-butyl or aliphatic alcoxy in **RED34-36**, respectively). On this matter, dye **RED34** shows the highest tolerance (reaching 7.4 GJ/mol) owing to the stability provided by the strongly bounded fluorine atoms, which ensure a long-lasting emission<sup>[25]</sup>.

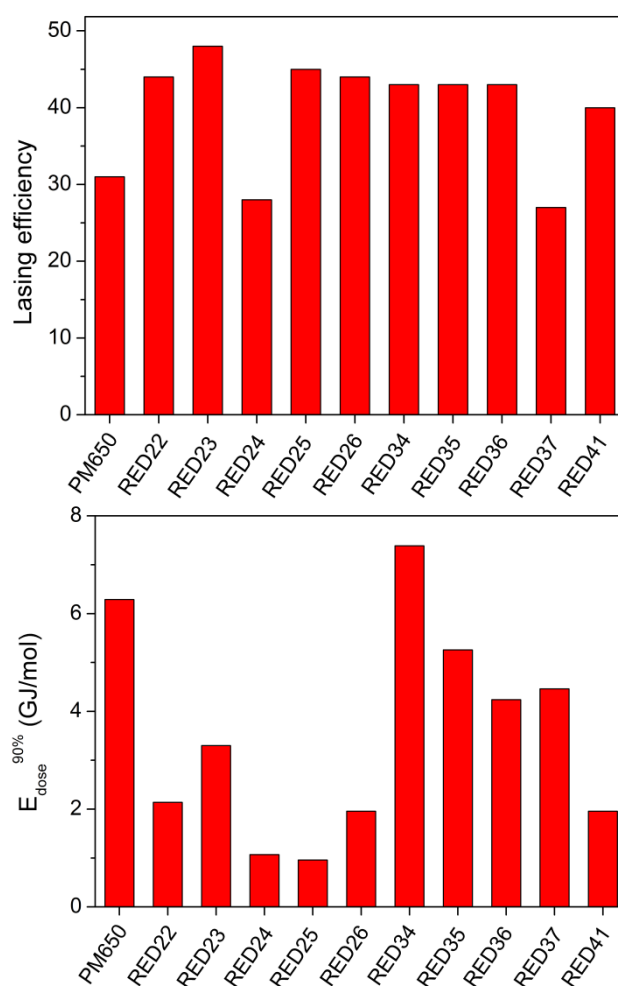


**Figure 2.7.** Lasing efficiency and photostability of red-emitting benzofuran-fused BODIPYs in ethyl acetate at the optimum dye concentration (from 0.50 to 0.75 mM).

To contextualize these results, we compare them with the commercially available BODIPY dye PM650<sup>[26]</sup>, working in the same spectral region (Figure 2.7). BODIPY PM650 bears a cyano group at the *meso*-position which is a good electron withdrawing substituent. This functional group is the responsible of the high photostability (6.3 GJ/mol) assigned to this commercial dye, since its electronegative character decreases the reactivity against the ambient oxygen involved in the photo-oxidative degradation mechanism<sup>[27]</sup>. However, this functional group also bolsters the charge separation facilitating the non-radiative deactivation channel, that is, the ICT process. Generally speaking, all the dyes tested herein have slightly lower photostability values (from 1 to 5 GJ/mol) than that showed by PM650 (> 6 GJ/mol) except for the **RED34** whose value is even higher (Figure 2.7). However, in terms of lasing efficiency, this battery of compounds (with the exception of **RED24** and **RED37**) shows notably improved signatures in comparison with the commercially available dye.

Therefore, it has been proved that the new synthesized set of chromophores with extended aromatic frameworks is able to improve light harvesting in the red-edge of the electromagnetic spectrum with largely enhanced absorption probabilities. Moreover, these compounds are useful for shifting both, fluorescence and laser bands to the red edge of the visible spectrum, reaching almost 100% of fluorescence efficiencies and lasing efficiencies higher than 40% in the best cases. The most striking signature is that with these systems it is possible to widen the tuning range of the laser (just by varying the dye-concentration) thanks to the formation of excited-state aggregates retaining at the same time the long-lasting emission efficiencies typical of BODIPYs, and overcoming for the first time the limitations inherent to most of the commercially available dyes (such as cyanines or oxazines) working in this spectral region.

## 2.2. Aza-BODIPYs as NIR LASERS

As mentioned before, the search of highly efficient and stable far-red and near-infrared light-emitting sources is a remaining challenge in (bio)photonics owing to the inherent advantages that this kind of radiation holds. One of the most actively tested approach to this aim is the replacement of the central *meso*-carbon of the BODIPY by an aza group<sup>[18]</sup>. This minimal change on the BODIPY core leads to a pronounced bathochromic shift, since the electronegative character of this atom stabilizes the LUMO

state, and as a consequence the energy gap is reduced<sup>[17,18]</sup>. The combination of this strategy with the extension of the  $\pi$ -system through the link of peripheral aromatic substituents generates a synergistic effect, pushing the emission fluorescence deeper into longer wavelengths (**NIR1-4-F**). In order to improve the fluorescence response a new battery of  $\pi$ -extended aza-BODIPYs has been performed, in which the boron atom has been successfully replaced with cyano and alcoxy groups (**NIR1-4-C** and **NIR1-4-O**) (Figure 2.8).

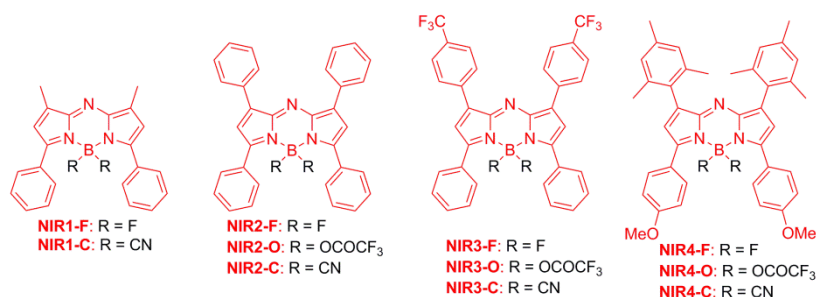
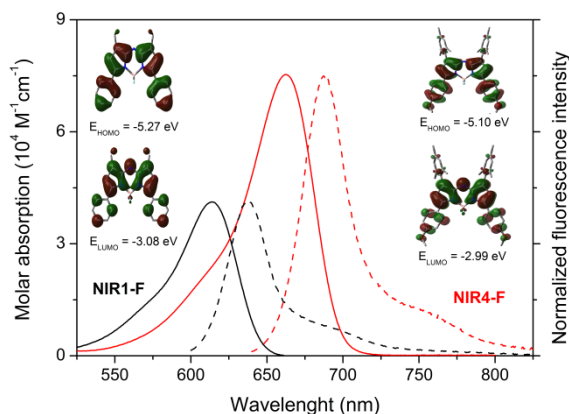


Figure 2.8. New battery of  $\pi$ -extended aza-BODIPYs.

### 2.2.1. F-aza-BODIPYs

The further the  $\pi$ -system is extended, the further bathochromic shift is achieved (Table 2.2). This is the main reason to explain the reddest shift showed by the **NIR4-F** among the herein tested F-aza-BODIPYs. Although the aromatic rings at positions 1 and 7 do not take part in the conjugation system due to their orthogonal disposition supported by the steric hindrance imposed by the methyl groups, the functionalization with anisoles at positions 3 and 5 pushes even more the spectral bands deeper into lower energies (absorption band centered at 670 nm and emission one at around 695 nm) (Figure 2.9). So the combination of the replacement at *meso*-position by an aza group together with the decoration of the dipyrin core with electron rich aromatic moieties is a fruitful strategy to manage the desired goal.



**Figure 2.9.** Absorption (solid lines) and normalized fluorescence (dashed lines) of dye **NIR1-F** and **NIR4-F** in cyclohexane. Calculated frontier orbitals from the ground state optimized geometries (B3LYP/6-311G\*) are also included.

**NIR1-F** displays quite lower value than for the benzo-furan fused BODIPYs (section 2.1), but despite its moderate absorption ability, this compound presents acceptable fluorescence parameters especially in non-polar solvents (Table 2.2). When the polarity of the solvent grows this response is diminished (quantum yield and lifetime value down to 0.18 and 1.44 ns in methanol, respectively). It is generally accepted that a red-shift implies that the ground and excited state gap is reduced, and this in turn, increases the rate of radiationless transitions such as the internal conversion (energy gap law)<sup>[28]</sup>. Nevertheless, apart from that, in these compounds a specific interaction takes place with the hydrogen atoms of the polar protic solvents<sup>[29]</sup>. The point is that when the *meso*-carbon atom is replaced by a nitrogen, this atom becomes the most electronegative one in the whole molecule (Figure 2.10), as it has been proved by theoretical calculations (B3LYP/6-311G\*). Thus, this atom is readily available to create hydrogen bonds with alcohols, endorsing the recorded fluorescence slump results in these solvents.

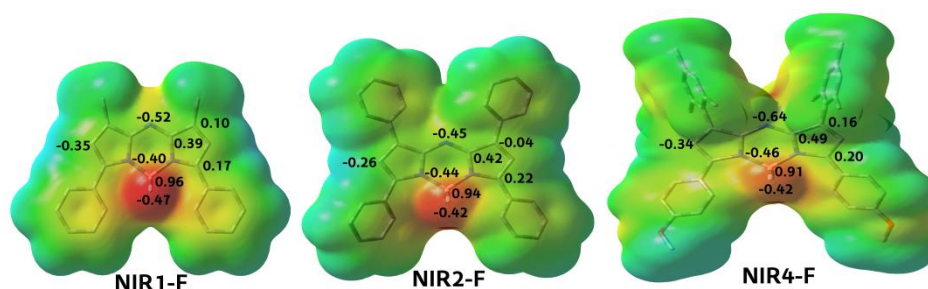


**Figure 2.10.** Electrostatic potential mapped onto the electronic density (positive in blue and negative in red), together with the corresponding CHelpG charge distribution (B3LYP/6-311G\*) along the chromophoric core for the F-aza-BODIPYs (**NIR 1-F**, **NIR2-F** and **NIR4-F**). The corresponding chromophoric charges of **NIR3-F** are not included because they are very similar to the structurally related **NIR2-F**.

The extension of the aromaticity brings with it a shift towards lower energies and an increase of the absorption probability (Table 2.2). But this red shift goes hand in hand also with a decrease in the fluorescence response, as it has been reported for compound **NIR2-F**<sup>[30]</sup>. In this sense, the free motion of the phenyls at positions 1 and 7 is responsible of this drop<sup>[31]</sup>. In contrast, slightly improved fluorescence response can be achieved when the same phenyls are functionalized with *para*-trifluoromethyl groups (**NIR3-F**), since their electron withdrawing character<sup>[32]</sup> counteracts the effect of the phenyl motion. Nonetheless, it is important to highlight that the latter two dyes' fluorescence response suffer from less changes than **NIR1-F** when the solvent polarity is increased (quantum yield values from 0.19 to 0.12 in cyclohexane and methanol, respectively for **NIR3-F**), owing to the fact that the presence of the twisted phenyls makes the aza-group less accessible to the H-bonding.

**Table 2.2.** Photophysical properties of NIR emitting aza-BODIPYs dissolved in ethyl acetate.

NIR	$\lambda_{ab}$ [nm]	$\epsilon_{max}$ [10 <sup>4</sup> M <sup>-1</sup> ·cm <sup>-1</sup> ]	$\lambda_{fl}$ [nm]	$\phi$	$\lambda_{la}$ <sup>a)</sup> [nm]	%Eff <sup>b)</sup>
<b>1-F</b>	614.0	3.2	639.0	0.32	647.0	13
<b>1-CN</b>	604.0	5.5	638.0	0.22	644.0	13
<b>2-F</b>	645.0	8.6	66.08	0.12	681.0	16
<b>2-OCOCF<sub>3</sub></b>	646.0	5.6	671.5	0.47	689.0	19
<b>2-CN</b>	652.5	7.3	670.0	0.46	686.0	12
<b>3-F</b>	654.5	8.6	682.0	0.15	690.0	20
<b>3-OCOCF<sub>3</sub></b>	655.0	6.7	687.0	0.44	696.0	16
<b>3-CN</b>	653.5	7.3	677.0	0.12	692.0	16
<b>4-F</b>	669.0	7.8	696.0	0.46	708.0	23
<b>4-OCOCF<sub>3</sub></b>	678.0	7.9	708.5	0.49	720.0	33
<b>4-CN</b>	667.0	5.6	703.5	0.31	717.0	29

<sup>a)</sup> Laser wavelength; <sup>b)</sup> Laser efficiency. Compound **NIR1-O** could not be isolated owing to its chemical instability.

**NIR4-F**, bearing bulky mesityls at positions 1 and 7 and anisoles at positions 3 and 5 is the reddest one and both quantum and lifetime values have been ameliorated significantly (Table 2.2) on account of the structural rigidity afforded by conformational restrictions, being the best results among all tested *F*-aza-BODIPYs. In spite of this improvement, this structural change does not avoid the aforementioned drawback in polar protic solvents like alcohols (fluorescence emission and lifetime drops to 0.28 and 2.3 ns in methanol, respectively). Furthermore, in **NIR4-F** the charge of the aza atom is even higher and the lone pair of the aza group is more accessible to the solvent due to the perpendicular dispositions of the adjacent phenyl rings (Figure 2.10).

### 2.2.2. O- and C-aza-BODIPYs

As it has been exposed in Chapter 1 (for the *N*-BODIPYs) and with a view to enhance the fluorescence response<sup>[33]</sup>, fluorine atoms of these aza-BODIPYs can be replaced by electron withdrawing moieties like cyano (**NIR1-4-C**) and trifluoroacetoxy (**NIR1-4-O**). Taking into account Chapter 1, one may expect similar spectral band positions when the fluorine atoms are replaced since the boron bridge does not take part in the delocalized  $\pi$ -system, and the recent results suggest that this issue depends markedly on the substitution pattern at the dipyrin core (Table 2.2.).

Surprisingly, and compared to their parent *F*-aza-BODIPYs, the recorded fluorescence emission for the *O*-aza-BODIPYs in low polar solvents is better (Figure 2.11), being most remarkable the two which have unconstrained 1,7-aryls (**NIR2-O** and **NIR3-O**), where the quantum yield results have been doubled or even tripled (Table 2.2). Thus, this variation at the boron atom is suitable at least in non polar solvents. However, once again the fluorescence response in alcohols is limited, which results in even lower quantum yields. In this case, such replacement at the *meso* position implies a significant charge redistribution which increases the negative charge at the nitrogen atom (up to -0.69 in dye **NIR4-O**, the highest among the herein tested dyes). So, once again this atom is ready available to H-bonding, even in presence of sterically hindered adjacent phenyl groups.

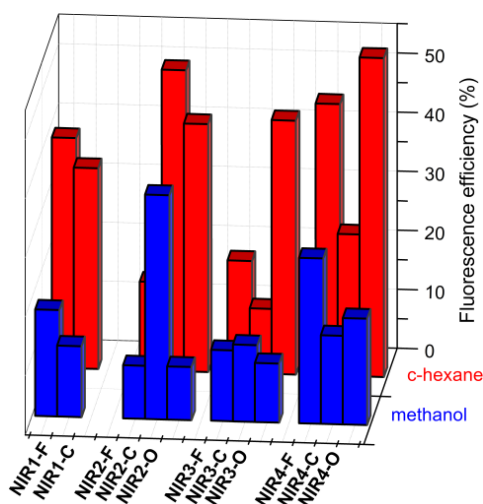


**Figure 2.11.** Evolution of the fluorescence efficiency of the novel *O*-aza-BODIPYs and *C*-aza-BODIPYs with regard to their parent *F*-aza-BODIPYs in non-polar (cyclohexane) and polar/protic (methanol) solvents.

On the other hand, in general *C*-aza-BODIPYs do not improve the fluorescence response in comparison with the former *F*-BODIPYs. As an exception compound **NIR2-C** presents an outstanding performance in both polar and non-polar solvents. What is more,

in this case the cyano group provokes this dye to have the lowest negative charge around the aza group (-0.37) among the herein tested aza-BODIPYs, blocking the availability for H-bonding interaction and avoiding such quenching pathway. Therefore, **NIR2-C** becomes the best fluorophore of the herein developed set of compounds in terms of fluorescence response.

Thus, while *O*-aza-BODIPYs are suitable in order to enhance the fluorescence response of *F*-aza-BODIPYs in non polar solvents, *C*-aza-BODIPYs are a way out for a successful emission in polar media.

### 2.2.3. Lasing properties

In view of the photophysical properties of these dyes we studied their performance as laser dyes. All these aza-BODIPYs show laser emission deep in the red-edge of the visible spectrum, from 645 nm to 720 nm in correlation with the fluorescence emission wavelengths (Figure 2.12A and Table 2.2), reaching deeper laser emissions in comparison to the benzofuran-fused BODIPYs (section 2.1). According to the laser efficiencies, **NIR2-F** and **NIR3-F** display a remarkable laser performance, being even higher than **NIR1-F**, despite the fact that this last one presented higher fluorescence response. This contradiction can be explained if we notice the short lifetime values of the first two dyes, as a fast decay enhances the population inversion and promotes the stimulated emission<sup>[34]</sup>. Still, **NIR4-F** shows the higher lasing efficiency (reaching values of 33%) among all the *F*-aza-BODIPYs in agreement with its fluorescence response (Table 2.2).

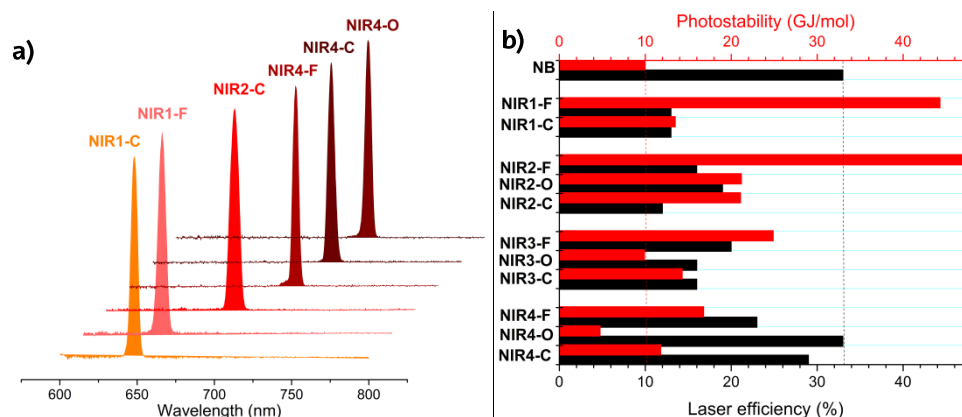


**Figure 2.12. a)** Evolution of the normalized laser spectra of some of the novel aza-BODIPYs **and b)** comparison of both laser efficiency and photostability of the herein tested aza-BODIPYs with the commercial dye Nile Blue (NB) under strong irradiation.

It is important to highlight that the modification around the boron bridge is not very effective as a strategy to improve the lasing efficiency, providing similar values (C-aza-BODIPYs) or just slightly higher (O-aza-BODIPYs) than those recorded for the non-modified ones. Nevertheless, compound **NIR4-O** shows not only the reddest laser emission, but also the highest laser efficiency among all the tested dyes. These results are in line with the photophysical results as this dye displays also the best fluorescence performance.

However, the most striking discovery in the herein aza-BODIPYs is the trend followed by their photostability, where surprisingly the most stable ones under strong and long laser irradiation are those with the lower lasing efficiencies (Figure 2.12B and Table 2.2). In general terms, all fluorophores (despite compound **NIR4-O**) require at least more than 10 GJ/mol of energy in order to reduce their laser induced fluorescence in a 10%. What is more, F-aza-BODIPYs are the most stable ones, retaining 90% of the laser output after receiving around 47 GJ/mol (see compound **NIR2-F**). In fact, it seems that the free motion of the 1,7-phenyl dissipates the energy excess during the pumping process. So, in terms of photostability the modification at the boron bridge is not recommendable.

If we compare these results with a commercially available oxazine Nile Blue (NB), which emits its fluorescence in a similar spectral region (around 690 nm), we can conclude that in general the herein aza-BODIPYs show lower laser efficiencies but better photostable response. That is to say, NB displays remarkable high laser efficiency but limited photostability (Figure 2.12B) and only some of the tested dyes (**NIR4-F**, **NIR4-O** and **NIR4-C**) reach similar laser efficiencies. Nevertheless, these chromophores are able to tolerate by far higher energies under strong pumping conditions. Moreover, compounds **NIR1-F** and **NIR2-F** show four times stronger photostability than the reference compound (Figure 2.12B), supporting their viability as bright and long lasting active media for laser and bioimaging purposes.

Once again, it has been demonstrated that the rich and versatile chemistry of BODIPYs is a suitable tool to design a chart of photoactive dyes which can be applied as efficient and stable tunable lasers within the spectral window ranging from 600 to 720 nm. For the far-red region of the visible conformationally restricted benzofuran-fused BODIPYs appear as suitable candidates. Its flat and rigid aromatic framework is endowed with a huge absorption probability of the pumping light and avoids non-radiative deactivation funnels, yielding efficient (approaching the 50%) and stable laser signals in the spectral



range 600 - 650 nm. To further push the laser emission towards the NIR region polyarylated aza-BODIPYs are preferred. Surprisingly, the chemical modification at the boron atom is not a recommended strategy since it markedly decreases the stability of the dye. Therefore, the *F*-aza-BODIPYs are the best approach since they outstand by their high photostability and they display notable laser emission efficiencies in wavelengths ranging from 645 to 720 nm.

Furthermore, these molecular scaffolds might be envisaged as promising fluorescent and long-lasting probes for bioimaging applications, once properly functionalized to promote selective recognition, and as building blocks to design light-harvesting arrays undergoing energy transfer to improve their photonic performance.

## Bibliography

- [1] Pansare, V.; Hejazi, S.; Faenza, W.; Prud'homme, R. K.; *Chem. Mater.*, **2012**, *24*, 812–827.
- [2] Poddar, M.; Misra, R.; *Coordination Chemistry Reviews*, **2020**, *421*, 213462.
- [3] Yuan, L.; Lin, W.; Zheng, K.; He, L.; Huang, W.; *Chem. Soc. Rec.*, **2013**, *42*, 622–661.
- [4] Luo, S.; Zhang, E.; Su, Y.; Cheng, T.; Shi, C.; *Biomaterials*, **2011**, *32*, 7127–7138.
- [5] Geddes, C. D.; *Reviews in Fluorescence, Organized assemblies probed by fluorescence spectroscopy*, Springer, Berlin, 1<sup>st</sup> Ed., **2017**.
- [6] Wang, X.; Wolfbeis, O. S.; *Anal. Chem.*, **2016**, *88*, 203–227.
- [7] Martenic, I.; Eliseeva, S. V.; Petoud, S.; *Journal of Luminescence*, **2017**, *189*, 19–43.
- [8] Grossi, M.; Morgunova, M.; Cheung, S.; Scholz, D.; Conroy, E.; Terrile, M.; Panarella, A.; Simpson, J. C.; Gallagher, W. M.; O'Shea, D. F.; *Nat. Commun.*, **2016**, *7*, 10855.
- [9] Liu, J.; Sun, Y. Q.; Zhang, H.; Shi, H.; Shi, Y.; Guo, W.; *ACS Appl. Mater. Interfaces.*, **2016**, *8*, 22953–22962.
- [10] Johnson, I.; Spence, M.; *Molecular Probes Handbook*, Life Technologies Corporation, Carlsbad, 11<sup>th</sup> Ed., **2010**.
- [11] Sindy, H. A.; *Dyes Pigm.*, **2017**, *145*, 505–513.
- [12] Niu, S.; Ulrich, G.; Retailleau, P.; Ziessel, R.; *Tetrahedron Letters*, **2011**, *52*, 4848–4853.
- [13] Wu, X.; Zhang, Y.; Takle, K.; Bilsel, O.; Li, Z.; Lee, H.; Zhang, Z.; Li, D.; Fan, W.; Duan, C.; Chan, E. M.; Lois, C.; Xiang, Y.; Han, G.; *ACS Nano*, **2016**, *10*, 1060–1066.
- [14] Bañuelos, J.; *Chem. Rec.*, **2016**, *16*, 335–348.
- [15] Heyer, E.; Retailleau, P.; Ziessel, R.; *Org. Lett.*, **2014**, *16*, 2330–2333.
- [16] Ni, Y.; Wu, J.; *Org. Biomol. Chem.*, **2014**, *12*, 3774–3791.
- [17] Hall, M. J.; McDonnell, S. O.; Killoran, J.; O'Shea, D. F.; *J. Org. Chem.*, **2005**, *70*, 5571–5578.
- [18] Ge, Y.; O'Shea, D. F.; *Chem. Soc. Rev.*, **2016**, *45*, 3846–3864.
- [19] Freyer, W.; Mueller, S.; Teuchner, K.; *J. Photochem. Photobio.*, **2004**, *163*, 231–240.
- [20] Kee, H. L.; Kirmaier, C.; Yu, L.; Thamyongkit, P.; Youngblood, W. J.; Calder, M. E.; Ramos, L.; Noll, B. C.; Bocian, D. F.; Scheidt, W.; Birge, R. R.; Lindsey, J. S.; Holten, D.; *J. Phys. Chem. B.*, **2005**, *109*, 20433–20443.
- [21] Gómez-Durán, C. F. A.; Esnal, I.; Valois-Escamilla, I.; Urías-Benavides, A.; Bañuelos, J.; López-Arbeloa, I.; García-Moreno, I.; Peña-Cabrera, E.; *Chem. Eur. J.*, **2016**, *22*, 1048–1061.
- [22] Durán-Sampedro, G.; Agarrabeitia, A. R.; Cerdán, L.; Pérez-Ojeda, M. E.; Costela, A.; García-Moreno, I.; Esnal, I.; Bañuelos, J.; López-Arbeloa, I.; Ortiz, M. J.; *Adv. Funct. Mater.*, **2013**, *23*, 4195–4205.
- [23] Masilamani, V.; Aldwayyan, A. S.; *Acta, Part A.*, **2004**, *60*, 2099–2106.
- [24] Cerdán, L.; Martínez-Martínez, V.; García-Moreno, I.; Costela, A.; Pérez-Ojeda, M. E.; López-Arbeloa, I.; Wu, L.; Burgess, K.; *Adv. Opt. Mater.*, **2013**, *1*, 984–990.
- [25] Durán-Sampedro, G.; Agarrabeitia, A. R.; Arbeloa Lopez, T.; Bañuelos, J.; López-Arbeloa, I.; Chiara, J. L.; García-Moreno, I.; Ortiz, M. J.; *Laser Phys. Lett.*, **2014**, *11*, 115818.
- [26] García-Moreno, I.; Costela, A.; Martín, V.; Pintado-Sierra, M.; Sastre, R.; *Adv. Funct. Mater.*, **2009**, *19*, 2547–2552.
- [27] Jones, G.; Kumar, S.; Klueva, O.; Pacheco, D.; *J. Phys. Chem. A.*, **2003**, *107*, 8429–8434.
- [28] Bixon, M.; Jortner, J.; Cortes, J.; Heitele, H.; Michel-Beyerle, M. E.; *J. Phys. Chem.*, **1994**, *98*, 7289–7299.
- [29] Shushkevich, I. K.; Pershukevich, P. P.; Stupak, A. P.; Solov'ev, K. N.; *J. Appl. Spectrosc.*, **2005**, *72*, 737–770.
- [30] Antina, E. V.; Bumagina, N.A.; *Chem. Heterocycl. Compd.*, **2017**, *53*, 39–41.
- [31] Prlj, A.; Vannay, L.; Corminboeuf, C.; *Helv. Chim. Acta.*, **2017**, *100*, e1700093.
- [32] Gut, A.; Lapok, I.; Jamróz, D.; Gorski, A.; Solariski, J.; Nowakowska, M.; *New J. Chem.*, **2017**, *41*, 12110–12122.

[33] Gómez-Durán, C. F. A.; Esnal, I.; Agarrabeitia, A. R.; Bañuelos, J.; Cerdán, L.; García-Moreno, I.; Costela, A.; López-Arbeloa, I.; Ortiz, M. J.; *Chem. Eur. J.*, **2014**, *20*, 2646–2653.

[34] Cerdán, L.; Costela, A.; García-Moreno, I.; Bañuelos, J.; López-Arbeloa, I.; *Laser Phys. Lett.*, **2012**, *9*, 426–433.



## CHAPTER 3

---

# Fluorescent Probes, Sensors and Photosensitizers for Bioimaging and Therapy

---

It is widely accepted that what you see is more credible than what you hear, which may be the basis of the well known proverb “Seeing is believing”. Methods to “see what happens in the body” are crucial if we want to treat illnesses, as well as for diagnosis purposes. On this subject, fluorescence is a very simple and straightforward tool to gather such information<sup>[1]</sup>. In comparison to other technologies such as X-ray radiography or magnetic resonance imaging (MRI)<sup>[2]</sup>, fluorescence imaging for the monitoring of biochemical processes and the real-time positioning of biomolecules in living systems is undergoing a great boom<sup>[3]</sup> assisted by the continuous development of the state-of-the-art-microscopy. This technique reveals great sensitivity (enabling detection at the single molecule level), high spatial resolution (down to the tens-of-nanometers) and is non-invasive, obtaining such information in situ, easily and intuitively<sup>[4-6]</sup>. What is more, the fluorescence signal can be modulated, relying on activation rather than just accumulation<sup>[7]</sup>. As a consequence, bioimaging is developing as one of the most effective techniques for the evolution of advanced biophotonic applications and biomedicine<sup>[8,9]</sup>. Indeed, nowadays fluorescence probes based on biocompatible small organic molecules are in the forefront in modern biology, since they contribute to the localization and

quantification of the molecules of interest but without manipulating the genetics of the sample<sup>[7]</sup>.

To this aim, the fluorophores should fulfill several characteristics to play the role of molecular probes, including specific absorption/emission wavelength, reasonable brightness and both bio- and photostability<sup>[2]</sup>. Fluorophores require excitation light to emit light. Exciting the dye in the ultraviolet can damage the tissue<sup>[10]</sup>. Blue or green excitation does not penetrate very much in the skin, being appropriate only for superficial imaging (Figure 3.1). When the excitation of the fluorophores is in the orange range of the electromagnetic spectra the autofluorescence process appears<sup>[11]</sup>. However, such setbacks can be avoided by the design of fluorophores displaying its excitation wavelength in the deep red-edge (Figure 3.1), as pointed in the preceding Chapter 2. Brightness is another crucial factor to be considered, since a high signal-to-noise ratio is key to ensure high sensitivity detection. Therefore, the fluorophore must have high quantum yield values<sup>[12]</sup> placed deep in the red-edge. Another worth mentioning characteristic is the stability, they must be stable after intracellular internalization and under long and strong pumping conditions<sup>[13]</sup>. Furthermore, a great chemical versatility is necessary for postfunctionalization purposes to enhance biocompatibility and promote the recognition of targeted sites<sup>[14]</sup>.

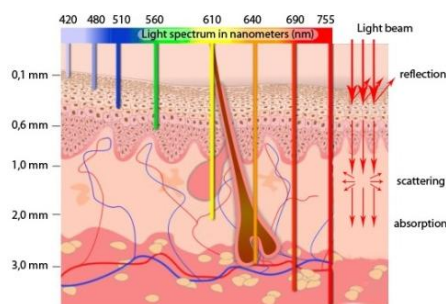


**Figure 3.1.** Light penetration capability through tissues depending on the excitation wavelength<sup>[15]</sup>.

Considering these requirements BODIPY thrives as a prevalent candidate for biological applications. We can join to the BODIPY biomolecules of interest or even induce different photophysical processes by linking specific receptors for biomolecules being its impact on the fluorescence dependence on the presence/absence of the latter in the media<sup>[16]</sup>. That is to say, it is possible to modify the structure of the BODIPY to monitor different biochemical processes and to detect them (probes/sensors). Taking that into account, on the one hand we have developed BODIPY-labeled carbohydrates (Section 3.1) as fluorescent glycoprobes for many biological processes<sup>[17]</sup>. On the other hand, sensors

for amino acids (AA) bearing thiol (Section 3.2) have also been synthesized since these biomolecules apart from being the main component of proteins, present also quantity levels related with many illnesses from Alzheimer to cardiovascular sicknesses<sup>[18]</sup>.

And that is not all, diagnosis of detrimental diseases like cancer and their solution by means of therapy would be feasible when BODIPYs are used as PS in PDT<sup>[19]</sup>. To this aim, the production of  $^1\text{O}_2$  through photosensitization is essential and requires three main components: the aforementioned photosensitizer, a light source and oxygen<sup>[20]</sup>. In our particular case the photosensitizer is going to be a dye, in particular a BODIPY dye (Section 3.3), and after its activation via light excitation the population of the triplet excited state ( $T_1$ ) of the dye is going to be promoted, owing to an allowed intersystem crossing (ISC) process from its  $S_1$ <sup>[21]</sup>, and if there is oxygen in the surrounding, cytotoxic reactive  $^1\text{O}_2$  is going to be generated. This cytotoxic specie is, in turn, the responsible for the destruction of tumor cells. To this aim, in Section 3.3 we describe a PS based on an orthogonal and symmetric BODIPY dimer directly linked. More information can be found in **Chemistry - A European Journal** (Section 3.1) and in **Organic Letters** (Section 3.2 and 3.3) attached to the annex III.

### 3.1. WATER-SOLUBLE BODIPY-LABELED CARBOHYDRATES

For most biological applications chromophores should present good water solubility so as to internalize in living cells thorough the membrane permeability<sup>[22]</sup>. Unfortunately BODIPY itself is not soluble in water despite the fact that its solubility in many organic solvents is inimitable<sup>[23]</sup>, both in polar and non-polar solvents. This hydrophobic nature of BODIPYs can be ameliorated by introducing water soluble groups on the molecular framework. Phosphonates, sulfonates and oligoethylenglycol chains have been linked covalently until today<sup>[24]</sup>. However, these dyes are still subject to significant aggregation phenomena (formation of non-fluorescent dimers and aggregates of higher dimensions)<sup>[25,26]</sup>. What is more, when water-solubilizing groups are introduced, synthetic routes have to be masked in order to avoid cross reactivity and consequent tedious purifications<sup>[27]</sup>. Taking advantage of the potential of BODIPY dye, we have combined this dye with carbohydrates generating at the same time fluorescence glycoprobes with enhanced properties (Figure 3.2). The new battery of compounds present two benefits: first, we have incorporated them at the beginning of the process

with the purpose of working as fluorescent glycosyl tags, so they are going to facilitate the detection and the aforementioned purification of the desired glycosidic compounds, and secondly, fluorescently labeled oligosaccharides have been obtained. This fluorescent probe is of great relevance as carbohydrate-receptor interactions take part in a lot of number of biological processes<sup>[28]</sup>. Moreover, this moiety linked to the BODIPY plays a significant role as a targeting agent<sup>[29]</sup> and facilitates the internalization<sup>[30]</sup>, being less cytotoxic<sup>[31]</sup>.

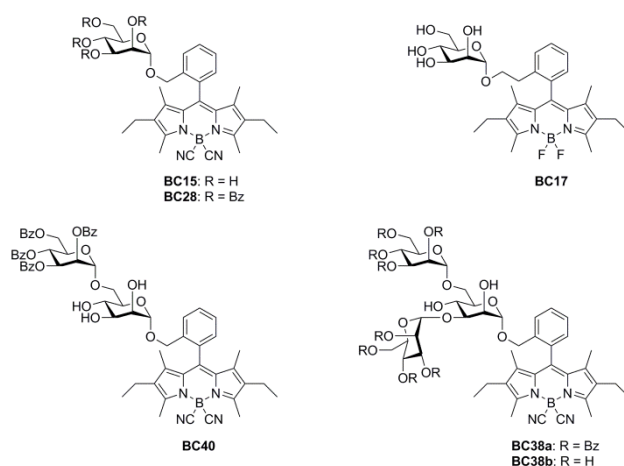


**Figure 3.2.** Molecular structures of fluorescently labeled protected and unprotected mono-, di-, and tri-saccharides (Bz = benzoyl).

When we desire to synthesize oligosaccharides, glycosylation protocols<sup>[32]</sup> must be employed where protecting group strategies are involved<sup>[33]</sup>. In that regard, “temporary” protecting groups (Bz) can be used (**BC28**, **BC40** and **BC38a**), which can be removed at the end resulting in unprotected (H) water-soluble compounds (**BC15**, **BC17** and **BC38b**). In addition, in the herein project, following a similar protocol to that explained in Chapter 1 (for the *N*-BODIPYs) to ameliorate the photonic performance, the fluorine atoms at the boron center (**BC17**) were substituted by cyano groups leading to the corresponding *C*-BODIPYs (**BC15**, **BC28**, **BC40** and **BC38a-b**) and the study of different numbers of inserted saccharides in the final dye was also included (monosaccharides **BC15**, **BC28** and **BC17**; disaccharide **BC40**; and trisaccharides **BC38a-b**).

### 3.1.1. Photophysical properties

In general terms, all of these compounds show similar trends in comparison with the reference PM567, in relation with the spectral bands positions as well as their probability. In fact, in most cases the fluorescence ability is higher than 0.80 (Table 3.1), the



same as PM567. Therefore, the inclusion of carbohydrates at the *ortho* position of C-8-benzyl is an adequate strategy to develop fluorescent labeled saccharides, since the presence of 8-aryl substituent is known to stabilize the fluorophore<sup>[34]</sup> due to the steric hindrance imposed by the bulky saccharides which ensures a compact molecular structure with low probability of non-radiative deactivation funnels.

**Table 3.1.** Photophysical properties of BODIPY-labeled carbohydrates dissolved in different solvents. The solvents are arranged from the less polar (cyclohexane) to the most polar (water). For comparison purposes, photophysical data of commercial PM567 in methanol are also included.

Dye	$\lambda_{ab}$ [nm]	$\epsilon_{max}$ [10 <sup>4</sup> M <sup>-1</sup> .cm <sup>-1</sup> ]	$\lambda_{fl}$ [nm]	$\phi$	$\tau$ [ns]	$k_{fl}^{a)}$ [10 <sup>8</sup> s <sup>-1</sup> ]	$k_{nr}^{b)}$ [10 <sup>8</sup> s <sup>-1</sup> ]
<b>PM567</b>	516.0	6.9	534.0	0.81	6.10	1.33	0.31
<b>BC15</b>							
Ethyl acetate	523.5	7.9	534.0	0.85	6.73	1.26	0.22
Methanol	523.5	7.7	535.0	0.87	7.21	1.20	0.18
Water	524.0	5.1	535.5	0.82	7.28	1.12	0.25
<b>BC17</b>							
Ethyl acetate	523.5	7.0	536.0	0.66	6.29	1.05	0.54
Methanol	523.0	5.4	536.0	0.74	6.67	1.11	0.39
Water	523.0	3.0	533.5	0.60	6.86	0.88	0.58
<b>BC28</b>							
c-hexane	528.0	7.0	536.5	0.82	6.22	1.32	0.29
Ethyl acetate	525.0	6.9	535.0	0.81	6.74	1.20	0.28
Methanol	525.0	6.7	535.5	0.81	7.24	1.12	0.26
<b>BC40</b>							
c-hexane	527.0	5.1	534.0	0.77	6.21	1.24	0.37
Ethyl acetate	524.5	6.0	534.0	0.87	7.16	1.21	0.18
Methanol	524.5	6.2	534.0	0.82	6.71	1.22	0.27
<b>BC38a</b>							
c-hexane	527.5	5.8	536.5	0.75	6.14	1.22	0.41
Ethyl acetate	524.0	6.6	534.5	0.85	6.59	1.29	0.23
Methanol	525.0	6.6	533.5	0.83	6.97	1.19	0.24
<b>BC38b</b>							
Ethyl acetate	524.5	4.7	534.0	0.66	6.61	1.00	0.51
Methanol	524.0	6.9	535.0	0.81	7.18	1.12	0.27
Water	525.0	5.2	537.0	0.77	7.29	1.05	0.32

<sup>a)</sup> Radiative decay rate; <sup>b)</sup> Non-radiative decay rate.

Moreover, the theoretical calculations (B3LYP/6-311G\*) predict that C-8-benzyl residue remains nearly orthogonal to the chromophoric core (dihedral angle around 85-90° in ground state of analogues **BC15** and **BC17**, see Figure 3.3) diminishing the probability of the non-radiative deactivation channels (internal conversion) involved in its free motion (see  $k_{nr}$  values in Table 3.1). Besides, this orthogonal disposition explains the low impact of the grafted functionalization on the photophysical properties (Table 3.1). Therefore, the number of saccharide units, protecting groups and chain-length between the saccharide and the 8-aryl unit is irrelevant. The chemical modification at the boron

bridge replacing the fluorine atoms by cyano groups entails a slight improvement in the fluorescence emission and an extension of the lifetime (reaching up to 7 ns values). Thus, C-BODIPY compounds present higher quantum yield values (higher than 0.80) in comparison to their parent F-BODIPY, where the majority of the values are in the range of 0.75 and below. These results are consistent with previously reported ones with similar functionalization pattern at the boron center<sup>[35]</sup>.

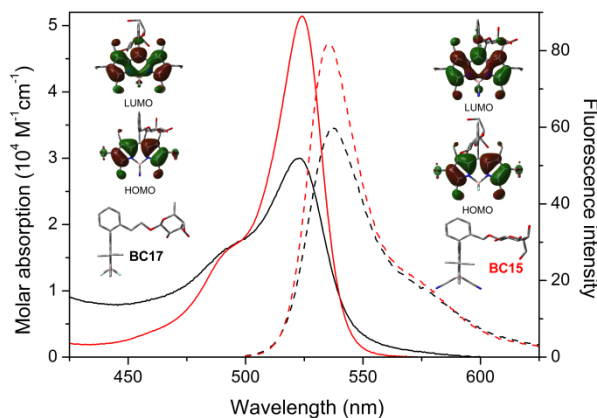


**Figure 3.3.** Theoretically predicted (B3LYP/6-311G\*) frontier molecular orbitals involved in the main absorption (solid lines) and fluorescence transitions (scaled by their fluorescence efficiency, dashed lines) in water for the BODIPY-labeled monosaccharide **BC17** (black) and its analogue **BC15** (red). The optimized ground state geometries are also included.

As expected, those BODIPYs bearing unprotected saccharides (**BC15**, **BC17** and **BC38b**) are water-soluble and show strong fluorescence emission (Table 3.1), being ideal fluorescence probes for carbohydrates. In contrast, these compounds are not soluble in cyclohexane and those bearing protected saccharides are so, but they are not water-soluble. That is to say, the more protected compounds we have, the more soluble are in polar media and less in non-polar one. However, when the concentration of the water-soluble compounds goes up they are prone to molecular aggregation. Dye **BC38b** for instance is water-soluble up to 2 mM, but at concentrations higher than 0.1 mM the dye starts to aggregate, as we can see in the increase of the absorbance detected at short-wavelengths (Figure 3.4). This finding is a distinctive feature of the formation of non-emissive H-aggregates, which diminishes both fluorescence emission and lasing efficiency. Indeed, these dyes do not lase in water. Nevertheless, taking into account that usually BODIPYs are not water-soluble and that in this case we have obtained more than one compound soluble in aqueous media and fluorescent up to 0.1 mM, it is sufficient to fulfill the requirements normally demanded in biological microscopy to display bright images.

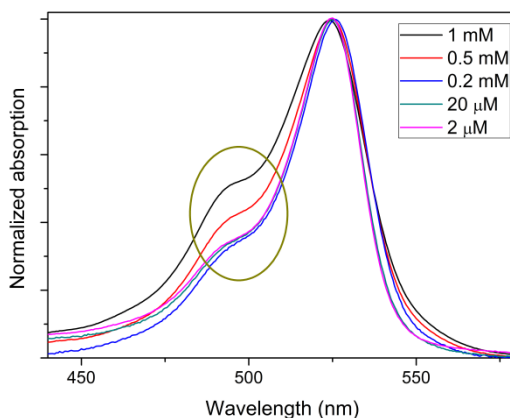


**Figure 3.4.** Normalized absorption spectra of **BC38b** at different concentrations in water. The growing absorption corresponding to the H-aggregate is highlighted.

### 3.1.2. Lasing properties

After the determination of the optimum dye concentration value (between 0.1 and 2 mM) the lasing efficiency and photostability were studied under pumping at 532 nm. All the dyes studied herein showed laser action in organic media peaked at 570 nm and the lasing efficiencies follow the same trend compared to the photophysical behavior. That is to say, the dyes with higher quantum yield present also the higher lasing efficiency (Figure 3.5). Moreover, when the fluorine atoms at the boron center are replaced by cyano groups, the lasing efficiency increases significantly (from 48% in the case of **BC17** to 68% in **BC15**). As happened for the photophysical properties, the lasing efficiencies are independent of the type of saccharide inserted in the final dye, making no difference between protected or unprotected saccharides and between mono-, di-, and tri-saccharides.

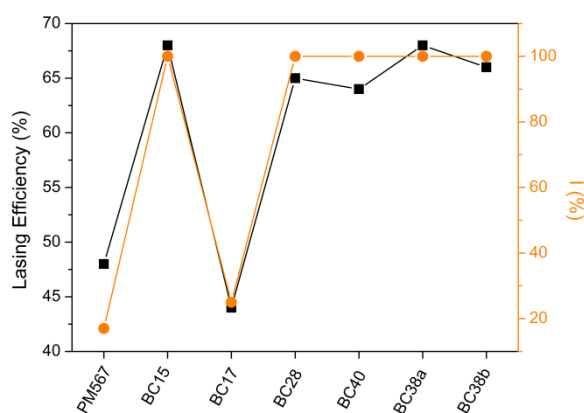


**Figure 3.5.** Lasing efficiency and photostability values (intensity of the laser output after 100000 pump pulses with respect to its initial intensity,  $I$  (%) =  $(I/I_0) \times 100$ ) of the new BODIPY-saccharides.

In this case, in order to study their lasing photostability under hard irradiation conditions and long operation times, the relation between the laser-induced fluorescence intensity at the beginning and after 100000 pump pulses was measured under transversal excitation at 532 nm. Over again, these compounds which present the lower non-radiative constants (see Table 3.1) are the strongest ones under long pumping conditions regardless of the nature of the carbohydrate linked to the dyes. According to the lasing properties, C-BODIPYs are by far more efficient and photostable than F-BODIPYs, since its laser emission intensity remains unchanged after 100000 pump pulses, being even more stable than the commercially available dye PM567, whose laser emission fell more than 80% in the same conditions.

Thus, we have designed fluorescent labeled carbohydrates soluble in the physiological media with high fluorescence response and substantial photostability to be monitored by bioimaging. Once demonstrated that the protocol to label saccharides with BODIPYs succeeded, current work is in progress to tag carbohydrates with  $\pi$ -extended BODIPYs, as those described in Chapter 2, with the aim of increasing biological tissue transparency and fulfill all the demands for improved bioimaging.

### **3.2. SENSING OF AMINO ACIDS BEARING THIOL**

The detection of biomolecules in the physiological media is actually a hot topic research, since they are the key role in many biochemical events and diseases<sup>[36,37]</sup>. On this subject, the detection of amino acids is in the spotlight, cysteine (CVS), homocysteine (HCYS) and glutathione (GSH), in particular<sup>[38]</sup>. These thiol-containing AA are involved in the growth of cells and tissues and in the cellular defense against toxins as well. Moreover, alterations in the local concentration of these AA are related to different diseases, from cancer to Alzheimer and a wide assortment of cardiovascular illnesses<sup>[18]</sup>. So, their monitoring and quantification is highly relevant and one of the best options nowadays to fulfill this is the molecular design of fluorescent sensors able to detect them in an effective and sensitive manner. In this way, an early diagnosis of these diseases is going to be feasible and thorough the knowledge of their biochemical mechanism patients receive the appropriate treatment as soon as possible.

There is a wide range of strategies for sensing available, but, as mentioned before, among them fluorescent chemosensors are one of the best choices<sup>[39,40]</sup>. There are two main approaches to design sensors and report the binding of the analyte via the fluorescence signal, i) the on-off switches and ii) the ratiometric sensors: i) The receptor (fluorophore) of the analyte experiences a drastic quenching of the emission (usually via activation of photoinduced electron transfer processes) (off state). Upon binding of the analyte to the receptor, such quenching pathway is suppressed and the fluorescence signal is suddenly recovered (on state). These switches are usually applied in the detection of ions as it has been demonstrated in Chapter 1. ii) The receptor induces a drastic change in the spectral signatures (for instance spectral shifts) of the fluorophore. Once the analyte interacts with the recognition site of the chromophore the above mentioned alteration is modulated, leading to the growing and/or decrease of the absorption and/or emission band. Thus, different spectral windows can be used to monitor and quantify the presence of the analyte.

In the herein section we have designed the ratiometric sensor **BAA5** for the detection of the aforementioned thiolated AA (Figure 3.6). To this aim, and taking advantage of the synthesized 3,5-diformylBODIPYs, which are ideal precursors for postfunctionalization purposes, unsaturated esters at those chromophoric positions were attached (Figure 3.6). This functionalization has a dual purpose. On the one hand, it induces a pronounced bathochromic shift of the spectral bands towards the red-edge of the visible, which enhances the penetration of the light into tissues avoiding interference from the surrounding bioenvironment<sup>[18]</sup> as it has been explained before. On the other hand, it acts as the recognition site for CYS, HCYS and GSH, since the double bond and the carbonyl groups are able to react with the nucleophilic amine or thiol group of these AA.

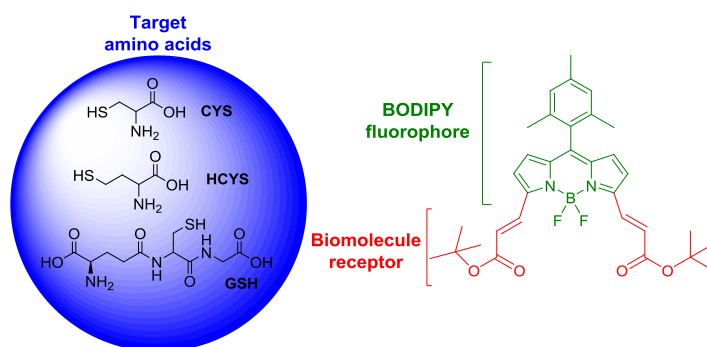


**Figure 3.6.** Molecular structure of the BODIPY-based fluorescent chemosensor **BAA5** for thiol-bearing AA.

The theoretical simulations (B3LYP/6-311G\*) predict that the localized  $\pi$ -system of the chromophore is extended through the whole aromatic structure owing to the resonant interaction between the unsaturated ester and the dipyrin core (Figure 3.7). As a result, the main absorption band is placed at the orange region reaching up to 590 nm with a molar coefficient of  $59000 \text{ M}^{-1}\cdot\text{cm}^{-1}$  whereas the fluorescence emission is red-shifted (600 nm), with a remarkable fluorescence efficiency of 0.62 and a lifetime of 5.42 ns.

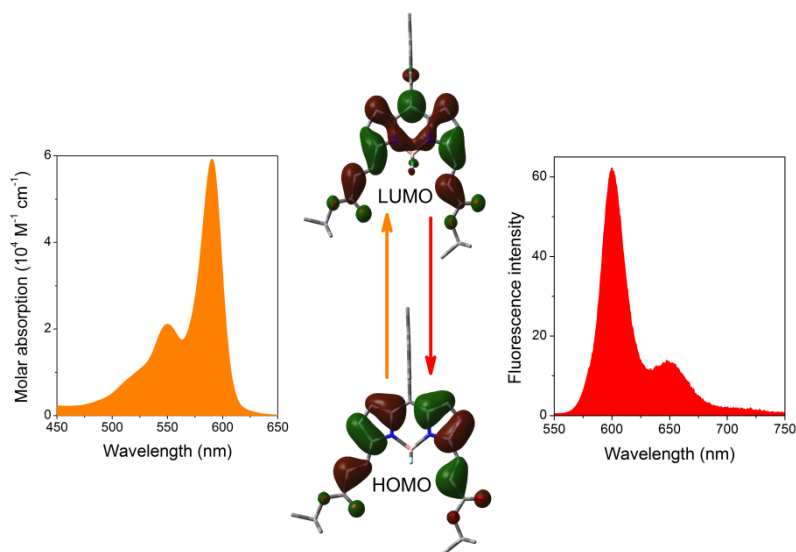


**Figure 3.7.** Absorption and fluorescence spectra of the chemosensor **BAA5** (dye concentration  $2 \mu\text{M}$ ) in ethanol, together with the computed frontier orbitals (HOMO and LUMO) involved in such electronic transitions (B3LYP/6-311G\*).

However, both absorption and fluorescence spectral profiles change when there are AA in the surrounding area (Figure 3.8 and 3.9, respectively). In effect, the spectral bands split clearly into three bands, whose relative intensity markedly depends on the concentration of AA in the media. The increase of concentration of AA provokes a loss of intensity of the longest wavelength absorption peak (590 nm) together with an increase of the two shorter-wavelengths absorptions (550 nm and 515 nm). Following this trend, similar changes, but even more marked, are observed in the fluorescence spectra (Figure 3.19); the emission at 600 nm progressively decrease while the new emissions at 560 nm and 525 nm increase. It is worth mentioning that even at low concentration (down to micromolar) an outstanding rise of the fluorescence signal centered at 560 nm is recorded. Thus, this chemosensor is quite sensitive and easy to track AA. On the contrary, higher AA concentrations are required to clearly see the growing of the emission at 525 nm. Although these spectral evolutions are the same regardless of the tested AA, the chemosensor **BAA5** is less sensitive to GSH than to CYS and HCYS mainly at the shortest

wavelength, likely owing to the larger size of the former which hinders its access to the reaction site.

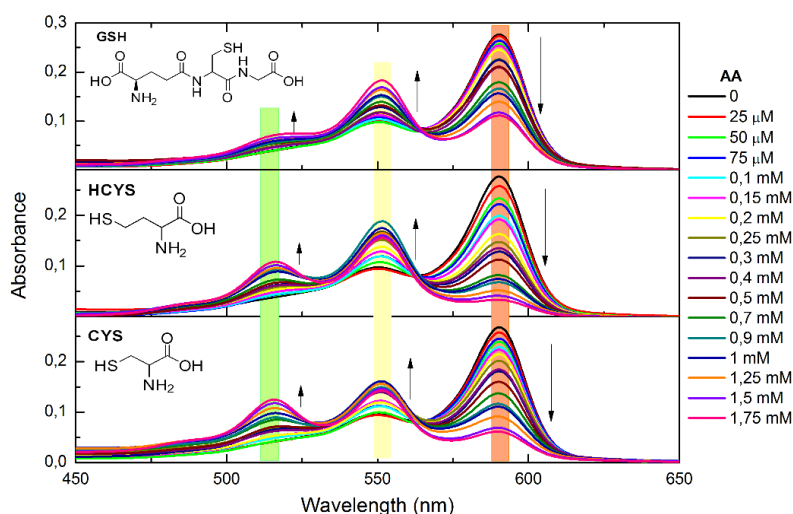


**Figure 3.8.** Absorption spectra of the chemosensor **BAA5** (dye concentration  $2\ \mu\text{M}$ ) at different concentrations of **CYS**, **HCYS** and **GSH** in ethanol/HEPES (1:1) mixtures to mimic the physiological media.

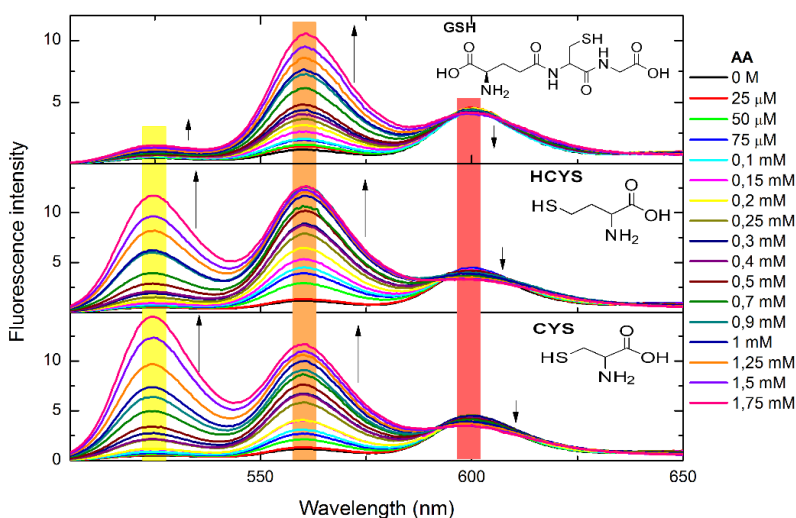


**Figure 3.9.** Fluorescence spectra of the chemosensor **BAA5** (dye concentration  $2\ \mu\text{M}$ ) at different concentrations of **CYS**, **HCYS** and **GSH** in ethanol/HEPES (1:1) mixtures to mimic the physiological media.

The quantification of these AA in the media can be performed due to the growing/decrease of the emission intensity. In fact, up to three detection channels are available, making this BODIPY-based sensor highly sensitive as a ratiometric indicator. This versatility to visualize different AA can be seen in Figure 3.10. In this image, it can be seen the evolution of the fluorescence intensity at the selected wavelengths of each channel, and it is noticeable that the increase of the fluorescence intensity at 560 nm (orange emission) and at 525 nm (yellow emission) are the most effective channels. What is more,

apart from the quantitative way, such detection can be easily done qualitatively just by naked eye owing to the discernible change of the emission color, since the emission color of the solution changes from red to orange at low AA concentration, and from orange to yellow at higher concentrations. Therefore, in addition to its ratiometric behavior, it can be said that we have also designed a colorimetric sensor.

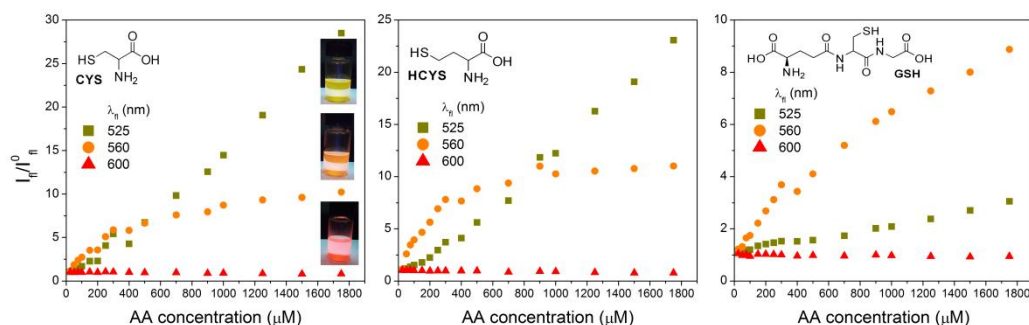


**Figure 3.10.** Ratio between the fluorescence intensity with AA in the media and without it at different concentrations of CYS, HCYS and GSH and at the three selected detection channels; 525 nm, 560 nm and 600 nm.

With view to explain the underlying mechanism in the sensing, we hypothesize that there is a chemical reaction between the nucleophilic thiol groups of the AA and the unsaturated ester of the chromophore (through the vinyl and carbonyl as reactive sites). After this interaction the extension of the conjugated  $\pi$ -system is decreased, leading to a shorter wavelength signal. That is to say, the selective interaction of the AA with the carbonyl would reduce the extension of the  $\pi$ -system of the BODIPY core just to both vinyls, leading to the absorption and fluorescence band at 550 nm and 560 nm, respectively. Further interaction with such vinyls limits the  $\pi$ -system even more to the dipyrin core, being this the responsible of the absorption and emission at 515 nm and 525 nm, respectively. The latter assignment coincides with the typical absorption and emission signals of the simplest BODIPY and the bathochromic shift of 35 nm by the attachment of  $\alpha$ -pyrrolic vinyls is also consistent to explain the absorption and fluorescence bands at 550 nm and 560 nm, respectively.

As a conclusion, we have designed a ratiometric AA chemosensor based on BODIPY able to detect sensitively and straightforwardly CYS, HCYS and GSH, allowing their quantification thanks to three detection channels, since the emission color switches from red to orange and to yellow as the concentration of AA increases. Further work is in progress to enhance the specificity between the thiolated AA in order to detect selectively one of them in spite of the presence of related AA in the surroundings.



### 3.3. HALOGEN-FREE SINGLET OXYGEN PHOTSENSITIZER

As mentioned before, in order to generate singlet oxygen ISC process must be boosted. BODIPY dyes are normally highly fluorescent and do not exhibit the necessary efficiency to populate the triplet state. The most known strategy to surpass this setback is linking heavy atoms like halogens<sup>[20]</sup> to the chromophoric moiety. Unfortunately, heavy atoms provoke fast  $T_1 \rightarrow S_0$  ISC, leading to short-lived triplet states and limiting their purpose in PDT<sup>[41]</sup>. In addition, heavy atoms usually increase the toxicity of the agent in the absence of light irradiation, lessening their biocompatibility<sup>[42]</sup>.

Although usually the dye which is able to populate the triplet state presents low fluorescence signal, it is important to highlight that it is extremely necessary to balance both properties properly with the required dual photonic action<sup>[19,43]</sup>. In this way, both diagnosis and therapy could be reached simultaneously. Theragnosis, promoted by a single biocompatible chemical system, is of great interest since it increases the success of cancer treatment by the assistance of the in situ visualization of the lesion to be healed<sup>[44]</sup>. Nowadays this practice seems to be one of the most promising pathway to deal with different types of cancer<sup>[45]</sup>. Because of that, in the herein section we have designed and synthesized successfully the halogen-free dimer BODIPY **BPS4**, assisted by the aforementioned formulated BODIPY precursors (3,5-diformylBODIPYs, section 3.2), which thanks to its geometry<sup>[46]</sup> is able to populate the triplet state by ICT and generate  $^1O_2$  from the same chromophore (Figure 3.11).

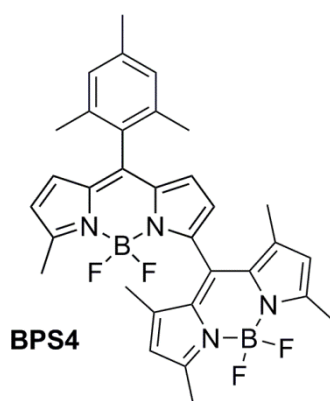


**Figure 3.11.** Molecular structure of the halogen-free photosensitizer **BPS4** for PDT.

The absorption spectra of this symmetric and constrained dimer consists of one single band centered at similar wavelengths of the monomer (dye PM546, whose absorption band places at around 490-500 nm) (Figure 3.12). This fact indicates that there is neither resonant nor excitonic interaction between BODIPY units. Indeed, the steric

hindrance exerted by the adjacent methyl groups at linking positions 3-8 places both chromophoric subunits orthogonal (Figure 3.12). However, the two BODIPYs do not contribute additively to the global absorption as the absorption molar coefficient is much lower than the related absorption for two chromophoric BODIPY units in the same structure (around  $9 \cdot 10^4 \text{ M}^{-1} \text{ cm}^{-1}$  whereas the single dye PM546 presents  $8 \cdot 10^4 \text{ M}^{-1} \text{ cm}^{-1}$  of the value). This reduction of the absorption probability together with the lack of another spectral band or shift explains that in spite the fact that there is not electronic coupling the electronic transitions are somehow affected. One of the most doable hypothesis relies on an electron transfer occurring from one BODIPY unit to the adjacent after the excitation, that is to say, the electronic transition acquires some charge transfer character and the absorption ability decreases.

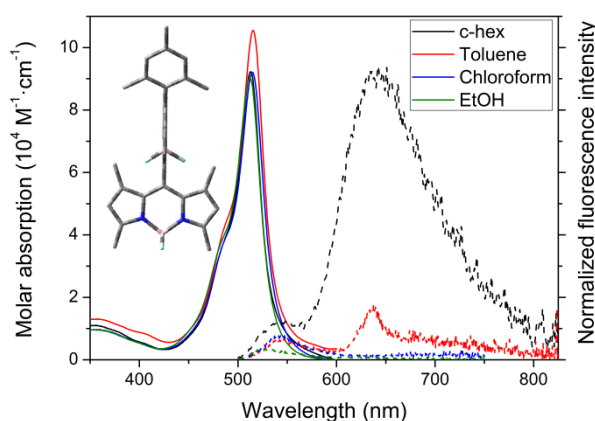


**Figure 3.12.** Absorption (solid lines) and normalized fluorescence (dashed lines) spectra of dye **BPS4** ( $2 \mu\text{M}$ ) in different solvents. A view of the theoretically calculated ( $\omega\text{B97XD/6-311G}^*$ ) optimized ground state geometry is also included.

The fluorescence signal is quite weak and the spectra displays a dual emission consisting on a weak emission at around 540 nm (matching the fluorescence peak of the monomers) followed by a dominating long-wavelength band at around 640 nm (Figure 3.12). Moreover, as the solvent polarity increases such long-wavelength emission becomes weaker, until it vanishes in the most polar media, where the short-wavelength emission prevails but strongly quenched (Figure 3.12). Although its fluorescence response is low, it is not negligible and the values are higher in non-polar solvents (Table 3.2). As a matter of fact, a bi-exponential fitting is required for the proper adjustment of the fluorescence decay curve of the compound **PBS4**, where the statistical weight of the largest lifetime (around 5 ns) progressively decreases in favor of a fast lifetimes (lower than 1 ns) as the solvent polarity increases. All these features suggest that the excited state dynamics of this dimer is ruled by an ongoing ICT process between both BODIPY subunits. Thus, the

short-wavelength emission is ascribed to the LE, whereas the long-wavelength one, and very sensitive to the solvent polarity, to the ICT.

**Table 3.2.** Photophysical properties of **BPS4** dissolved in different solvents. The solvents are arranged from the less polar (cyclohexane) to the most polar (ethanol).

Solvent	$\lambda_{ab}$ [nm]	$\epsilon_{max}$ [10 <sup>4</sup> M <sup>-1</sup> ·cm <sup>-1</sup> ]	$\lambda_{fl}$ [nm]	$\phi$	$\tau$ [ns]	$\phi_{\Delta}^{a)}$
c-hexane	513.0	9.2	642.5	0.046	2.58 (19%)–5.35 (81%)	-
toluene	515.0	10.5	537.5 637.5 546.5	0.020	2.68 (25%)–4.95 (75%)	0.54
chloroform	514.5	9.2	540.5	0.008	2.08 (20%)–5.07 (80%)	0.30
ethanol	512.0	9.0	527.5	0.003	0.61 (62%)–5.82 (38%)	-

<sup>a)</sup> <sup>1</sup>O<sub>2</sub>-generation quantum yield.

In the bibliography there is an active discussion about the ICT population and how it evolves into the triplet state. The mechanism to access to the ICT is a symmetry-breaking charge transfer (SBCT)<sup>[47-49]</sup>, where the driven force is the orthogonal geometrical disposition of the involved moieties, rather than the typical push-pull in dyes bearing electron-donor and acceptor entities. In directly linked dimers, the charge transfer recombination probability (CR) is feasible allowing the detection of its own fluorescence and even is able to populate the triplet state. This is why some author calls this ICT as spin-orbit coupling charge transfer (SOCT). As the ICT state is stabilized by the solvent polarity the CR is less effective and the charge separation (CS) is favored, enhancing the non-radiative deactivation and provoking the consequence loss of both fluorescence signal and population of the triplet manifold. Therefore in this dimer, the generation of the singlet oxygen is determined by an ICT-mediated ISC. As a result, the dimer **PBS4** is able to generate <sup>1</sup>O<sub>2</sub> with an efficiency of around 54% and 30% in toluene and chloroform, respectively. Such decrease in polar media reinforces the aforementioned balance between CR and CS in the ICT. In other words, an ICT process is needed to reach the triplet state via CR and promote singlet oxygen generation, but if the ICT is too favored, the singlet generation is lower because the excitation energy is dissipated through non-radiative relaxation channels related to CS.

Therefore, this dyad behaves as a halogen-free singlet oxygen photosensitizer with potential for light-driven therapeutic purposes in cancer illnesses.

We are currently working in the design of dimers and even trimers with different geometries and linkage positions to counterbalance the fluorescence response and the

singlet oxygen generation providing access to a battery of compounds with enhanced performance as PS or retaining enough fluorescent signal as theragnostic agents.

Besides, we are settling the basis of future collaborations to perform biological essays and test the viability of the herein described probes, sensors and photosensitizers in biological media.

## Bibliography

- [1] Guo, Z.; Park, S.; Yoon, J.; Shin, I.; *Chem. Soc. Rev.*, **2014**, 43, 16-29.
- [2] Kobayashi, H.; Ogawa, M.; Alford, R.; Choyke, P. L.; Urano, Y.; *Chem. Rev.*, **2010**, 110, 2620-2640.
- [3] Kowada, T.; Maeda, H.; Kikuchi, K.; *Chem. Soc. Rev.*, **2015**, 44, 4953-4972.
- [4] Weissleder, R.; Pittet, M. J.; *Nature*, **2008**, 452, 580-589.
- [5] Beliu, G.; Sauer, M.; *Light: Science & Applications*, **2020**, 9, 1-2.
- [6] Wen, G.; Vanheusden, M.; Acke, A.; Valli, D.; Neely, R. K.; Leen, V.; Hofkens, J.; *ACS Nano*, **2020**, 14, 7860-7867.
- [7] Teria, T.; Nagano, T.; *Current Opinion in Chemical Biology*, **2008**, 12, 515-521.
- [8] Abrahamse, H.; Hamblin, M. R.; *Biochem. J.*, **2016**, 473, 347-364.
- [9] Platnich, C. M.; Rizzuto, F. J.; Cosa, G.; Sleiman, H. F.; *Chem. Soc. Rev.*, **2020**, 49, 4220-4233.
- [10] Janssen, Y. M.; Van Houten, B.; Borm, P. J.; Mossman, B. T.; *Lab Invest.* **1993**, 69, 261-274.
- [11] Geddes, C. D.; Lakowicz, J. R.; *Reviews in Fluorescence, Organized assemblies probed by fluorescence spectroscopy*, Springer, Baltimore, Volume 2, 1-23, **2005**.
- [12] Lu, H.; Mack, J.; Yang, Y.; Shen, Z.; *Chem. Soc. Rev.*, **2014**, 43, 4778-4823.
- [13] Hama, Y.; Urano, Y.; Koyama, Y.; Bernardo, M.; Choyke, P. L.; Kobayashi, H.; *Bioconjugate Chem.*, **2006**, 17, 1426-1431.
- [14] Yuan, L.; Lin, W.; Zheng, K.; He, L.; Huang, W.; *Chem. Soc. Rev.*, **2013**, 42, 622-661.
- [15] <https://www.bronzedbodyspraytan.com/led-light-therapy.html>
- [16] Kaur, P.; Singh, K.; *J. Mater. Chem. C.*, **2019**, 7, 11361-11405.
- [17] Yan, H.; Yalagala, R. S.; Yan, F.; *Glyconconj. J.*, **2015**, 32, 559-574.
- [18] Geddes, C. D.; *Reviews in Fluorescence, Organized assemblies probed by fluorescence spectroscopy*, Springer, Berlin, 1<sup>st</sup> Ed., **2017**.
- [19] Kamkaew, A.; Lim, S. H.; Lee, H. B.; Kiew, L. V.; Chung, L. Y.; Burgess, K.; *Chem. Soc. Rev.*, **2013**, 42, 77-88.
- [20] Epelde-Elezcano, N.; Prieto-Montero, R.; Martínez-Martínez, V.; Ortiz, M. J.; Prieto-Castañeda, A.; Peña-Cabrera, E.; Belmonte-Vázquez, J. L.; López-Arbeloa, I.; Brown, R.; Lacombe, S.; *Phys. Chem. Chem. Phys.*, **2017**, 19, 13746-13755.
- [21] Zhao, J.; Xu, K.; Yang, K.; Wang, Z.; Zhong, F.; *Chem. Soc. Rev.*, **2015**, 44, 8904-8939.
- [22] Vegesna, G. K.; Sripathi, S. R.; Zhang, J.; Zhu, S.; He, W.; Luo, F. T.; Jhang, W. J.; Frost, M.; Liu, H.; *ACS Appl. Mater. Interfaces*, **2013**, 5, 4107-4112.
- [23] Bañuelos, J.; *Chem. Rec.*, **2016**, 16, 335-348.
- [24] Kesavan, P. E.; Pandey, V.; Raza, M. K.; Mori, S.; Gupta, I.; *Bioorganic Chemistry*, **2019**, 91, 103139.
- [25] Pliquet, J.; Dubois, A.; Racœur, C.; Mabrouk, N.; Amor, S.; Lescure, R.; Bettaieb, A.; Collin, B.; Bernhard, C.; Denat, F.; Bellaye, P. S.; Paul, C.; Bodio, E.; Goze, C.; *Bioconjugate Chem.*, **2019**, 30, 1061-1066.
- [26] Florès, O.; Pliquet, J.; Galan, L. A.; Lescure, R.; Denat, F.; Maury, O.; Pallier, A.; Bellaye, P. S.; Collin, B.; Mème, S.; Bonnet, C. S.; Bodio, E.; Goze, C.; *Inorg. Chem.*, **2020**, 59, 1306-1314.
- [27] Niu, S. L.; Ulrich, G.; Ziessel, R.; Kiss, A.; Renard, P. Y.; Romieu, A.; *Org. Lett.*, **2009**, 11, 2048-2052.
- [28] Yang, Y.; Jia, T. W.; Xu, F.; Li, W.; Tao, S.; Chu, L. Q.; He, Y.; Li, Y.; Iyer, Y. S. S.; Yu, P.; *ACS Appl. Nano Mater.*, **2018**, 1, 1058-1065.
- [29] Dou, W. T.; Zeng, Y. L.; Lv, Y.; Wu, J.; He, X. P.; Chen, G. R.; Tan, C.; *ACS Appl. Mater. Interfaces*, **2016**, 8, 13601-13606.
- [30] Nguyen, A. L.; Griffin, K. E.; Zhou, Z.; Fronczek, F. R.; Smith, K. M.; Vicente, M. G. H.; *New J. Chem.*, **2018**, 42, 8241-8246.
- [31] Liu, F.; Tang, P.; Ding, R.; Liao, L.; Wang, L.; Wang, M.; Wang, J.; *Dalton Trans.*, **2017**, 46, 7515-7522.
- [32] Nielsen, M. M.; Pedersen, C. M. M.; *Chem. Rev.*, **2018**, 118, 8285-8358.

- [33] Lipták, A.; Borbás, A.; Bajza, I.; *Protecting Group Manipulations in Carbohydrate Synthesis in Comprehensive Glycoscience. From Chemistry to Systems Biology*, Elsevier, Amsterdam, **2007**.
- [34] Mula, S.; Ray, A. K.; Banerjee, M.; Chaudhuri, T.; Dasgupta, K.; Chattopadhyay, S.; *J. Org. Chem.*, **2008**, *73*, 2146-2154.
- [35] Duran-Sampedro, G.; Esnal, I.; Agarrabeitia, A. R.; Bañuelos, J.; Cerdán, L.; García-Moreno, I.; Costela, A.; López-Arbeloa, I.; Ortiz, M. J.; *Chem. Eur. J.*, **2014**, *20*, 2646-2653.
- [36] Biju, V.; *Chem. Soc. Rev.*, **2014**, *43*, 744-764.
- [37] Ulrich, S.; Dumy, P.; Boturyn, D.; Renaudet, O.; *J. Drug Deliv. Sci. Technol.*, **2013**, *23*, 5-15.
- [38] Chen, X.; Zhou, Y.; Peng, X.; Yoon, J.; *Chem. Soc. Rev.*, **2010**, *39*, 2120-2135.
- [39] Cao, D.; Liu, Z.; Verwilst, P.; Koo, S.; Jangili, P.; Kim, J. S.; Lin, W.; *Chem. Rev.*, **2019**, *119*, 10403-10519.
- [40] Wu, D.; Sedgwick, A.C.; Gunnlaugsson, T.; Akkaya, E.U.; Yoon, J.; James, T.D.; *Chem. Soc. Rev.*, **2017**, *46*, 7105-7123.
- [41] Azenha, E. G.; Serra, A. C.; Pineiro, M.; Pereira, M. M.; Seixas de Melo, J.; Arnaut, L. G.; Formosinho, S. J.; d'A Rocha Gonsalves, A. M.; *Chem. Phys.*, **2002**, *280*, 177-190.
- [42] Zou, J.; Yin, Z.; Ding, K.; Tang, Q.; Li, J.; Si, W.; Shao, J.; Zhang, Q.; Huang, W.; Dong, X.; *ACS Appl. Mater. Interfaces*, **2017**, *9*, 32475-32481.
- [43] Ogilby, P. R.; *Chem. Soc. Rev.*, **2010**, *39*, 3181-3209.
- [44] Yordanova, A.; Eppard, E.; Kerpig, S.; Bundschuh, R. A.; Schçnberger, S.; Gonzalez-Carmona, M.; Feldmann, G.; Ahmadzadehfar, H.; Essler, M.; *Onco. Targets Ther.*, **2017**, *10*, 4821-4828.
- [45] Van Straten, D.; Mashayekhi, V.; De Bruijn, H. S.; Oliveira, S.; Robinson, D. J.; *Cancers*, **2017**, *9*, 19.
- [46] Jiménez, J.; Prieto-Montero, R.; Maroto, B. L.; Moreno, F.; Ortiz, M. J.; Oliden-Sánchez, A.; López-Arbeloa, I.; Martínez-Martínez, V.; de la Moya, S.; *Chem. Eur. J.*, **2020**, *26*, 601-505.
- [47] Golden, J. H.; Estergreen, L.; Porter, T.; Tadler, A. C.; Sylvinson, D.; Facendola, J. W.; Kubiak, C. P.; Bradforth, S. E.; Thompson, M. E.; *ACS Appl. Energy Mater.*, **2018**, *1*, 1083-1095.
- [48] Liu, Y.; Zhao, J.; Iagatti, A.; Bussotti, L.; Foggi, P.; Castellucci, E.; Di Donato, M.; Han, K. L.; *J. Phys. Chem. C.*, **2018**, *122*, 2502-2511.
- [49] Kellog, M.; Akil, A.; Sylvinson, D.; Ravinson, M.; Estergreen, L.; Bradforth, S. E.; Thompson, M. E.; *Faraday Discuss.*, **2019**, *216*, 379-394.

## CHAPTER 4

---

# Bis-BODIPY Laser Dyes with Chiroptical Response

---

Chirality has witnessed a renewed interest in the last years, being actually a hot topic of research in biotechnology<sup>[1]</sup>. The development of systems able to propagate visible light with a particular direction (left or right) is of great interest, since there are a lot of macroscopic structures in the nature (like human DNA or sea shells, for instance) which possess such distinctive feature<sup>[2]</sup>. Most of the biomolecules are chiral and the interaction between drugs and molecules markedly depends on the involved enantiomers. In fact, chirality derives from the dissymmetry of the environment and the progress in such technology allows us to obtain chiral information<sup>[3]</sup> from biomolecular components, especially in living organisms. The role of chirality, an inherent characteristic of many biochemical events, has boosted the enantioselective synthesis of chemical compounds and materials as well as the design of novel approaches to induce optical activity. Against this background, nanoscience and dye chemistry tools are being applied in synergy to develop molecular systems able to display CD. This spectroscopy measures the difference in absorption between the left- and right-handed circularly polarized light and is quantified by the dissymmetry factor ( $g_{\text{abs}}$ ), providing optical information about chiral structures at their ground states<sup>[4]</sup>. Moreover, particular interest is devoted to the

development of systems able to additionally display emission with preferred sign of circular polarization. Indeed, CPL<sup>[3,5]</sup>, quantified by the luminescence dissymmetry factor ( $g_{lum}$ ), is a powerful tool to extract valuable information such as stereochemical, conformational, and three-dimensional structural information on these significant systems. Furthermore, due to its excellent resolution to recognize chiral activity CPL endows high potential for the improvement of smart photonic materials in future optical technologies<sup>[6]</sup>, such as 3D displaying<sup>[7]</sup>, information storage and processing<sup>[8]</sup>, including high-security chiroptical cryptography<sup>[9]</sup>, biological probes and signatures<sup>[10]</sup>, CPL lasers<sup>[11]</sup>, or enantioselective CPL sensors<sup>[12]</sup>.

Therefore, it is undeniable that the CPL-based technology is a promising challenge in Biology that still needs some technological progress. Thus, the need to track molecular events while observing their spatial localization still requires further development of the state-of-the-art circularly polarized microscopy. To date, lanthanide complexes have shown the best CPL performance and they have been employed as potential molecular probes<sup>[13-15]</sup>, especially in solution trying to determine the enantiomeric excess by optical measurements. But their low fluorescence quantum yields and low  $g_{lum}$  values (lower than  $10^{-3}$ ) limit their potential applications. Hence, to implement and boost the workability of CPL, a battery of fluorescent and efficient CPL organic dyes compatible with the biological media must be developed. Once again BODIPY appears as an excellent choice to reach this goal since, as it has been demonstrated, this fluorophore is highly fluorescent. Although the BODIPY chromophore does not show chiroptical properties intrinsically, two main approaches can be used to induce it<sup>[16]</sup> thanks to its claimed excellent chemical versatility; the promotion of symmetry axis or, alternatively, the decoration of the core with chiral appendages. In the first one helical conformations as stereogenic center have been induced via the linkage of BODIPYs through conformational restricted spacers<sup>[17]</sup>. Alternatively, the optically active molecule 1,1-binaphthol (BINOL), previously applied for enantioselective recognition and asymmetric catalysis systems<sup>[18-19]</sup>, has been mostly selected for the second approach, leading to the corresponding *O*-BODIPYs<sup>[20-21]</sup>.

Taking inspiration from the second approach, we have synthesized a series of conformationally restricted and covalently linked bis-BODIPYs (Figure 4.1) using tartaric acid (indicated in blue in Figure 4.1) as an optical active spacer<sup>[22-23]</sup> between the boron atoms of both dyes. Such acid possesses three stereoisomeric forms, a pair of enantiomers (R,R and S,S) and an achiral *meso* isomer (R,S). In this way, the attached fluorophores will be positioned in different relative spatial orientations and the resulting



bichromophoric systems will present high conformational rigidity, thanks to the restricted rotation of aryl substituents at the *meso* position and the spiranic rings at the boron center. Moreover, alkyl substituents have been introduced on the chromophore skeleton (TBDP2b compounds) to infer a tunable steric hindrance and subsequent control on the conformational equilibrium, enabling the modulation of their chiroptical and photophysical properties. In the following sections the impact of bridge chirality (L-tartaric (R,R enantiomer) or *meso* (R,S diastereomer)) into the photophysical behavior and, especially, the excitonic interactions, is studied in detail. The comparison with their corresponding monomeric analogues (compounds TBDP3 and TBDP4 in Figure 4.1) is going to be accomplished as well. More information can be found in **Chemistry - A European Journal** attached to the annex IV.

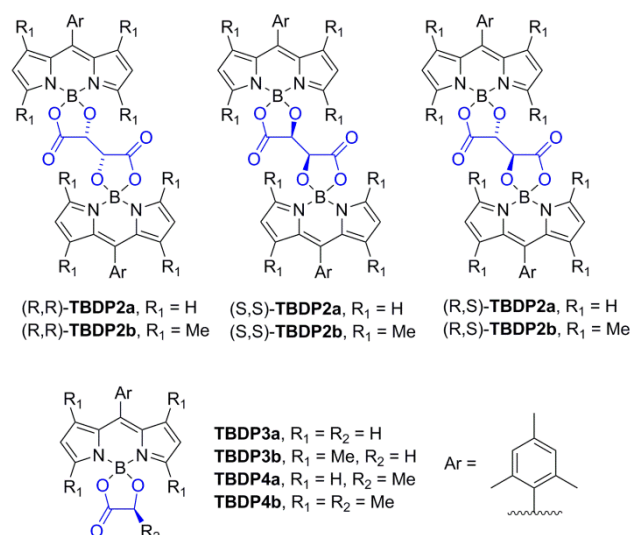


**Figure 4.1.** Molecular structure of new stereoisomeric bis-BODIPYs TBDP2 and monomeric analogues TBDP3 and TBDP4.

#### 4.1. STRUCTURE AND CONFORMATION

The molecular geometry of the single precursors features a planar dipyrin chromophore and an orthogonal *meso* aryl ring owing to the exerted hindrance by the substitution pattern at the *ortho* positions of such ring and additionally in the chromophoric neighboring positions. Moreover, the spiranic ring sharing the boron atom adds more rigidity to the whole molecule. In the bis-BODIPY the adopted geometry depends on the fundamental conformational characteristic of the tartaric acids; extended (*trans*, *T*) or bent (*gauche*, *G*) orientation. In most of the cases the theoretical simulations

done by DFT ( $\omega$ B97XD/6-31G<sup>\*</sup>) agree with the experimental results determined by X-ray crystallography. Both chiral compounds (R,R)-TBDP2a,b adopt the *T* conformation according to both experimental and theoretical results (Figure 4.2). The *meso* derivative (R,S)-TBDP2a, however, has a marked preference for the *G* conformer.

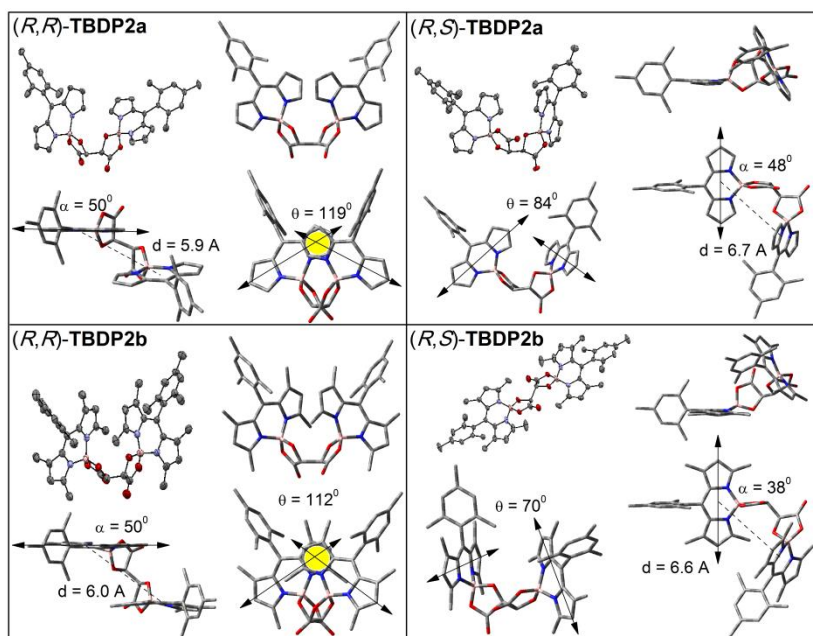


**Figure 4.2.** X-ray crystal structures (ball and sticks) and optimized ground-state geometries (capped sticks) in different views of the bis-O-BODIPYs. Theoretically calculated geometrical parameters such as center-of-mass to center-of-mass distance ( $d$  [Å]), dihedral angle ( $\theta$ ) between the transition dipole moments (double arrow along the chromophoric longitudinal axis), and the slip angle ( $\alpha$ ) between the transition moment and the line connecting the center of mass of the two BODIPY units (dotted line) are also depicted.

However, when its analogue is tetramethylated, dye (R,S)-TBDP2b, there is a contradiction. Whereas X-ray results show that compound (R,S)-TBDP2b crystallizes as the *T* conformation, DFT calculations conclude that the same dye converges exclusively (regardless of the starting input geometry) to the *G* conformer. In this case, the theoretical calculations predict that the extended *T* conformer is less stable ( $\Delta E = 9.7$  kcal/mol) than the bent conformer (Figure 4.3). Likely, the lower stability of the *T* conformer of dye (R,S)-TBDP2b is compensated by its expected more favorable crystal packing resulting from the extended coplanar geometrical arrangement to explain its presence in the crystal.

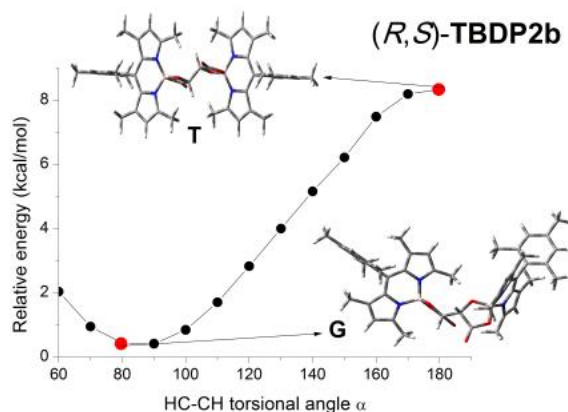


**Figure 4.3.** Conformational search performed by DFT ( $\omega$ B97XD/6-31G<sup>\*</sup>) along the central bond of the tartaric acid spacer (HC-CH torsional angle  $\alpha$ ) of (R,S)-**TBDP2b**. The corresponding geometries of the T and G conformers are also enclosed.

## 4.2. PHOTOPHYSICAL PROPERTIES

As explained in the initial chapters (Chapter 1-2), when the fluorine atoms at the boron center are replaced with other atoms like oxygen the spectral signatures are hardly unaltered. Indeed, all the monomeric BODIPYs **TBDP3a-3b** and **TBDP4a-4b** present similar properties when compared to their fluorinated parent analogues and other related O-BODIPYs<sup>[24]</sup> (Table 4.1). The aforementioned conformationally restricted molecular geometry both around the *meso* position and the boron center, reflected in the short Stokes shifts, avoids non-radiative deactivation channels ensuring highly efficient fluorescence signals (Table 4.1). The alkylation of the chromophore enhances both the molar absorption and the radiative deactivation processes probability, owing to its inductive electron donor effect. Thus, the fluorescence quantum yields increase slightly (being up to 100%) and the lifetimes decrease (Table 4.1). Therefore, the inclusion of the spiranic ring at the boron atom does not alter but preserves and even improves slightly the photophysical properties of the monomeric precursors, being an ideal scaffold for the development of the stereoisomeric O-BODIPY dimers using conformationally restricted tartaric acids.

**Table 4.1.** Photophysical properties of newly synthesized single *O*-BODIPY precursors and their corresponding bis-*O*-BODIPYs dissolved in ethyl acetate. The corresponding photophysical properties of the enantiomers (*S,S*) are not included as they are the same.

TBDP	$\lambda_{ab}$ [nm]	$\epsilon_{max}$ [10 <sup>4</sup> M <sup>-1</sup> ·cm <sup>-1</sup> ]	$\lambda_{fl}$ [nm]	$\Delta\nu_{St}$ [cm <sup>-1</sup> ]	$\phi$	$\tau$ [ns]
<b>3a</b>	504.5	5.7	516.0	440	0.96	7.71
<b>4a</b>	504.5	6.3	516.5	460	0.94	7.84
<b>3b</b>	504.0	8.4	613.0	350	1.00	6.44
<b>4b</b>	503.0	8.2	512.5	370	1.00	6.39
<b>(R,S)-2a</b>	506.0	11.4	518.5	475	0.90	6.39
<b>(R,S)-2b</b>	504.5	13.2	517.0	480	0.91	7.23
<b>(R,R)-2a</b>	518.0	8.6	560.5	1465	0.33	2.19 (97%) - 6.41 (3%)
<b>(R,R)-2b</b>	518.0	9.0	540.0	790	0.85	5.85

When these monomers are linked via the achiral *meso*-tartaric group, leading to (R,S)-TBDP2a and tetramethylated analogue (R,S)-TBDP2b, each chromophoric unit contributes additively to the absorption profile (Figure 4.4), featuring a single band whose extinction coefficients are nearly double to those recorded for the corresponding mono-BODIPY precursors TBDP3a-4b (Table 4.1). So, there is no intramolecular electronic interaction between the covalently anchored BODIPY units (at least in the ground state), retaining their identity and photophysical properties. Theoretical calculations also reinforce these results, since the frontier molecular orbitals involved in the lowest electronic transitions place their electronic density alternatively on one of the BODIPY units and with almost energetically degenerated occupied and unoccupied molecular orbitals (Figure 4.5). Hence, both chromophores are electronically decoupled in the ground state and each unit acts as an independent dye contributing to the total absorption of the dimer. Accordingly, both *meso*-derivatives (R,S)-TBDP2a and (R,S)-TBDP2b present high fluorescent quantum yields of around 0.90 together with mono-exponential fluorescence decay curves with long lifetime values (6 ns and 7 ns, respectively).

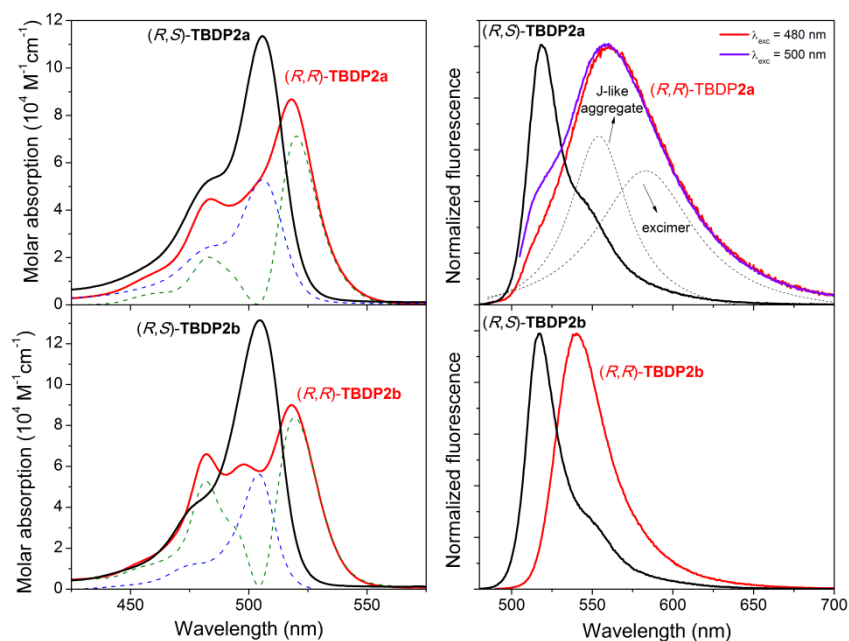


**Figure 4.4.** Absorption (left) and normalized fluorescence (right) spectra of chiral isomers  $(R,R)$ -**TBDP2a,b** and their corresponding meso diastereomers  $(R,S)$ -**TBDP2a,b** in ethyl acetate. The absorption spectra of the chiral compounds are deconvoluted (dotted lines) to show splitting resulting from the J-like intramolecular exciton-coupled BODIPYs. The fluorescence spectra of  $(R,R)$ -**TBDP2a** is also deconvoluted (dotted lines) to estimate the contribution of the J-like aggregate and the excimer to the whole emission profile.

However, when the non-methylated BODIPY units are covalently anchored via an optically active *L*-tartaric acid (compound  $(R,R)$ -**TBDP2a**) the photophysical features are totally different in comparison to its precursor **TBDP3a** and its meso-diastereomer  $(R,S)$ -**TBDP2a** (Table 4.1). The most striking change resides in the absorption spectra (Figure 4.4) where its main band becomes broadened and its maximum is red-shifted (around 15 nm). Furthermore, in Figure 4.4 a prominent shoulder appears at 480 nm and the absorption coefficient is not double. In fact, it is only just a little higher than that of its mono-BODIPY analogue **TBDP3a** (Table 4.1). Following the same trend, its fluorescence spectra is significantly broader and bathochromically shifted ( $\Delta\lambda = 45$  nm) in comparison to its precursor **TBDP3a**, increasing the Stokes shift from  $475$   $\text{cm}^{-1}$  to  $1460$   $\text{cm}^{-1}$  and distancing itself from the typical Stokes values of related BODIPY dimers<sup>[25]</sup>. So, in dye  $(R,R)$ -**TBDP2a** there are evident signals of a strong geometrical rearrangement upon excitation, facilitating the non-radiative deactivation channels and lessening both quantum yield (up to 0.33) and lifetime value. In fact, the fluorescence decay curve acquires a bi-exponential character with a main short lifetime component (2.19 ns vs 6.41 ns, see Table 4.1).

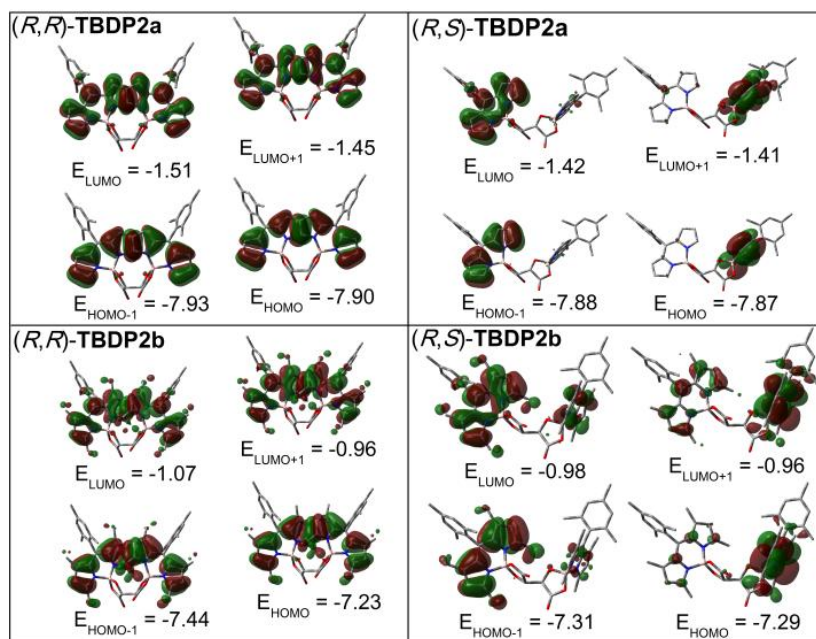


**Figure 4.5.** Theoretically predicted ( $\omega$ B97XD/6-31G<sup>\*</sup>) contour maps of the frontier molecular orbitals involved in the main electronic transitions of the bis-O-BODIPYs.

Taking into account the aforementioned results, it is undeniable that in compound (R,R)-TBDP2a occurs an intramolecular excitonic interaction which provokes the creation of a new emissive entity missed in the corresponding diastereomer (R,S)-TBDP2a. The contour maps of its frontier molecular orbitals support this as well, since the electronic density is simultaneously located over the two BODIPY units (Figure 4.5). The deconvolution of its absorption profile reveals the presence of two bands placed at 480 nm and 520 nm, flanking that of the mono-BODIPY placed at 500 nm (Figure 4.4). Moreover, the optimized ground state geometry of compound (R,R)-TBDP2a places the BODIPY units closer, as the center-of-mass to center-of-mass distance ( $d_{\text{CM}}$ ) is 5.9 Å, compared to that of the diastereomer (R,S)-TBDP2a where the  $d_{\text{CM}}$  value is 6.7 Å, in agreement with the X-ray diffraction data (Figure 4.2). Furthermore, in the latter compound the BODIPY units are located in different planes and show an orthogonal arrangement where the dihedral angle between the longitudinal transition dipole moments is 84°, remaining these BODIPY units sufficiently isolated to interact. On the contrary, in compound (R,R)-TBDP2a the transition dipole moments are tilted in a V-shape orientation forming a dihedral angle of 119°. This oblique disposition of the dipole moments facilitates “head-to-tail” excitonic intramolecular interactions through their overlapped lateral pyrroles. As a consequence, it seems that the long wavelength absorption correspond to an oblique J-like intramolecular aggregate, as it has been

recorded for similar weakly coupled electronic systems<sup>[26]</sup> according to the excitation theory of Kasha (Figure 4.2), modifying both absorption and fluorescence spectra.

Another evidence of the ongoing J-like intramolecular excitonic interaction is the aforementioned bathochromic shift observed in fluorescence. As a matter of fact, the angle between the vector connecting the centers of mass of the two BODIPY units and the transition moment is  $50^\circ$  (Figure 4.2). According to Kasha's rule, this corresponds to a J-type interaction, since the formed angle is lower than  $54.7^\circ$ , being able to display its own emission red-shifted with regard to the monomeric emission. BODIPYs with similar geometrical arrangements forming J-type dipolar couplings have been previously reported<sup>[27-28]</sup>.

Apart from these intramolecular J-type aggregates, small conformational changes upon excitation can alter the excitonic coupling<sup>[29]</sup> boosting the formation of stronger aggregates, more commonly renowned as excimers<sup>[30]</sup>, which can coexist with the previous ones leading to even more complex excited-state dynamics. The deconvolution of the fluorescence spectra yields two emission signals, one located at 560 nm, likely due to the J-type aggregate, and the second one placed at 580 nm, ascribed to the excimer (see compound (R,R)-TBDP2a in Figure 4.4). Besides and, as mentioned before, the fluorescence decay curve needed a bi-exponential fitting where the main lifetime component was the shortest one (around 2 ns). If this deactivation curve is monitored upon different emission wavelengths, the short-lived component becomes the main lifetime at longer wavelengths, supporting the presence of an excimer<sup>[30]</sup>. Meanwhile, the long-lived one (around 6-8 ns) increases markedly and it can be assigned to the intramolecular J-aggregate (Table 4.2). The recorded diminution in the quantum yield also supports the coexistence of excimers and intramolecular J-type aggregates, since the former usually shows lower emission efficiencies than the latter which shows higher radiative deactivation rate constants<sup>[31,32]</sup>. However, it should be pointed out that the study of these species is quite tough and further excited-state calculations would favor the better understanding of the process, but the required computationally demanding calculation level and the large size of these molecules make them unaffordable.

**Table 4.2.** Evolution of the fluorescence decay deconvolution with the excitation and emission wavelength for bis-O-BODIPY (R,R)-**TBDP2a**.

$\lambda_{\text{exc}}$ [nm]	$\lambda_{\text{em}}$ [nm]	$\tau$ [ns]
480	515	2.09 (50%)–8.12 (49%)
480	560	2.19 (97%)–6.41 (3%)
500	515	2.24 (35%)–8.19 (65%)
500	560	2.23 (97%)–8.09 (3%)
520	560	2.29

One option to acquire more knowledge on that field resides in the study of the other chiral tetramethylated derivative (R,R)-**TBDP2b**. Such methylation process affects the aforementioned intramolecular interaction/aggregation and provokes the splitting of the absorption spectra into three bands with stronger contribution of the J-like intramolecular aggregates, since the intensity ratio of the 480 nm and 520 nm bands is higher in comparison to that of (R,R)-**TBDP2a** (Figure 4.4). As the geometry of (R,R)-**TBDP2b** is more compact, the geometrical rearrangement upon excitation is more restricted and the emission band is blue-shifted with regard to compound (R,R)-**TBDP2a**. In this case, the fluorescence emission is constituted by one single and narrow band, which is more intense than that of its non-alkylated analogue (R,R)-**TBDP2a** and which belongs to the low-lying excited state of the intramolecular J-type exciton-coupled BODIPYs. The shape of this band does not change with respect to the excitation wavelength and the fluorescence quantum yield is recovered (up to 85%). Moreover, the fluorescence decay curve recovers a mono-exponential character commonly recorded for diastereomers and mono-BODIPYs (Table 4.1). Therefore, in dye (R,R)-**TBDP2b** the excimer generation probability is lower than in the case of the counterpart (R,R)-**TBDP2a**.

The theoretical simulations predict that the distance between the BODIPY units in (R,R)-**TBDP2b** is almost the same to that predicted for its non-alkylated analogue (R,R)-**TBDP2a** (6.0 Å vs 5.9 Å). The V-shape arrangement of the transition moments is also maintained, but the dihedral angle formed by them is even closer (112°), locating the “internal” pyrroles in a more cofacial disposition (Figure 4.2). This more constrained structure enhances intramolecular exciton coupling between the side pyrroles being responsible for the higher splitting of its absorption spectra and of a brighter emission (Table 4.1).



The formation of these intramolecular exciton-coupled BODIPYs occurs in the ground state regardless of the solvent polarity, but the fluorescence intensity decreases drastically when the solvent polarity is increased. As a result, only a weak fluorescence signal at high energies was recorded for (R,R)-**TBDP2a** related to the non-aggregated BODIPY in acetonitrile, being the emission from the intramolecular exciton-coupled BODIPYs completely lost (Figure 4.6). Therefore, the fluorescence ability of the intramolecular aggregate depends on the solvent polarity reaching almost negligible quantum yield value in acetonitrile (from 0.65 in cyclohexane to 0.02 in acetonitrile). However, such aggregated emission still prevailed in (R,R)-**TBDP2b**, although it was strongly quenched, accompanied by a very weak contribution of the non-aggregated BODIPY at lower wavelengths. Furthermore, the emission signal at higher energies (ascribed to *O*-BODIPY) is favored when the excitation wavelength is increased (see inset spectra at Figure 4.6). So, there is an additional non-radiative deactivation channel induced by solvent polarity, quenching the emission from the intramolecular exciton-coupled BODIPYs. This dependence of the fluorescence emission on the solvent polarity can be caused by an ICT process which is preferentially stabilized in high polarity environments, as it has been published for other closely spaced dyads<sup>[27]</sup>. As explained in Chapter 3, SBCT process has been reported as the ongoing ICT mechanism between symmetrical pair of chromophores<sup>[33]</sup>. This SBCT in bridged bis-BODIPYs efficiently quenches the emission in polar media because it stabilizes the CS but does not populate the triplet state as occurred in the directly linked orthogonal dimers of the preceding Chapter 3<sup>[34]</sup>. Indeed, we did not notice phosphorescence emission from singlet oxygen in the bis-BODIPYs undergoing ICT.

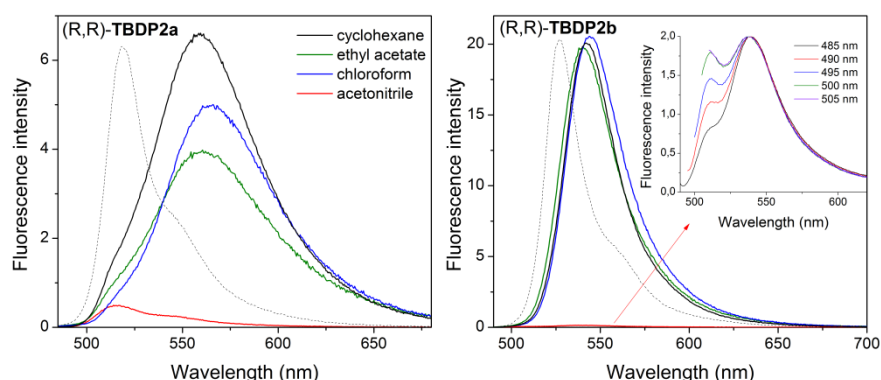


**Figure 4.6.** Evolution of the fluorescence spectra of chiral isomers (R,R)-**TBDP2a** (left) and (R,R)-**TBDP2b** (right) with the solvent polarity. The corresponding spectra of their meso-diastereomers ((R,S)-**TBDP2a** and (R,S)-**TBDP2b**, dashed line) are also added for comparison. The fluorescence spectra of (R,R)-**TBDP2b** in acetonitrile at different excitation wavelengths is also included.

### 4.3. CHIROPTICAL PROPERTIES

The photophysical properties of the enantiomeric pairs (R,R)-**TBDP2a**/(S,S)-**TBDP2a** and (R,R)-**TBDP2b**/(S,S)-**TBDP2b** are identical, however their ECD spectrums are not. In fact, their ECD signals are mirror-images (Figure 4.7). The (S,S) enantiomers show a negative Cotton effect, whereas the (R,R) enantiomers present a positive effect with maximum signals matching the maximum absorption of the BODIPY fluorophore at the visible (520 nm and 518 nm for dimers **TBDP2a** and **TBDP2b**, respectively). Moreover, theoretical simulations, albeit failed in the prediction of the band position as expected in TD methods<sup>[35]</sup>, agree with the experimental results on the signs of the Cotton effect, being the most intense signal the one of the non-methylated compound. So, the control over the stereochemistry and conformational rigidity appears to be crucial to tune both the photophysical and chiroptical properties in these bichromophoric systems.

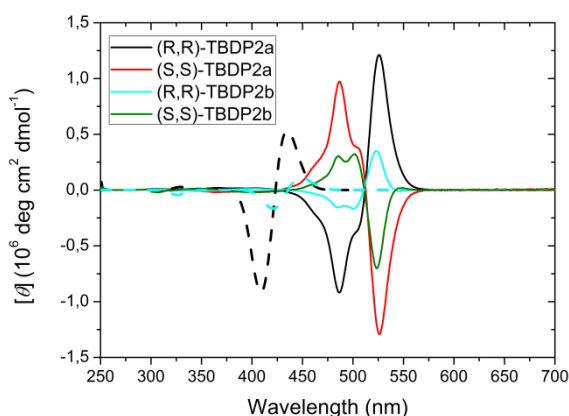


**Figure 4.7.** ECD spectra of chiral isomers (R,R)-**TBDP2a** and (R,R)-**TBDP2b** and their corresponding enantiomers (S,S) in ethyl acetate ( $1 \cdot 10^{-6}$  M). The theoretical (PCM/TD  $\omega$ B97XD/6-311G\*\*) normalized ECD spectra (dashed lines) for chiral bis-BODIPYs (R,R)-**TBDP2a** and (R,R)-**TBDP2b** are also included.

### 4.4. LASING PROPERTIES

The non-alkylated mono-BODIPYs **TBDP3a** and **TBDP4a** present similar laser properties to those previously reported O-BODIPYs with similar structures<sup>[24]</sup>. The highest laser efficiency (48% and 38%, respectively) is achieved at concentrations around 2 mM showing a single laser signal peaked at 528 nm. Nevertheless, an increase of the dye concentration (up to 8 mM) results in a significant decrease of the lasing efficiency (to 20%) due to re-absorption/re-emission processes. On the other hand, tetramethylated mono-BODIPYs **TBDP3b** and **TBDP4b** follow a similar trend and the lasing efficiencies correlated well with the photophysical properties, since these monomers show higher

laser efficiencies (51% and 48%, respectively at 3 mM) than those exhibited by the non-alkylated ones. Following the same trend, this efficiency diminishes when the dye concentration is increased, but presenting a less pronounced reduction since they maintained the value as high as 39% at 8 mM.

The covalent bonding of these mono-BODIPYs through a *meso*-tartaric linker had a significant effect on the laser signatures. The optimum concentration for the best laser performance of the dimers (R,S)-**TBDP2a** and (R,S)-**TBDP2b** is 1 mM and their corresponding laser efficiencies are 29% and 33%, respectively. Once again, the most fluorescent dyes show also the higher laser efficiencies, correlating well both properties; since these achiral dimers present lower values with respect to those exhibited by the corresponding monomers (see Table 4.1) at the same wavelength.

When the BODIPY subunits are covalently anchored via the optically active *L*-tartaric acid (compounds (R,R)-**TBDP2a,b**) the laser signals are redshifted to 575 nm and 555 nm respectively, following the photophysical trend. Accordingly, (R,R)-**TBDP2a** exhibits lower laser efficiency than (R,R)-**TBDP2b** (24% vs 45%). In this case, the laser emission from both chiral dimers presents single bands, enabling a tuning range of  $\Delta\lambda = 30$  nm, which is the usual tunability span of laser dyes.

However, after doing a polarimetric study<sup>[36]</sup> on the laser emission of optically active dye (R,R)-**TBDP2b** under vertically polarized pumping, this dye showed the same behavior than other simple organic molecules (*O*-BODIPYs bearing BINOL) enabling CPL with respect to the pump energy<sup>[11]</sup>. As a matter of fact, its laser emission was extremely polarized showing a degree of polarization around 1 in the vertical direction.

Therefore, we have demonstrated that the stereochemical and steric control of photophysical and chiroptical properties of these bichromophoric *O*-BODIPY systems is feasible. Thus, the employment of the optically active tartaric acid as a linker is an effective strategy to fine-tune their photonic behavior, since it presents a wide range of stereoisomeric forms which enables the modulation of specific excitonic interactions. Further modulation of such intramolecular interactions is achieved by alkylation of the chromophore. This structural control of the photonic performance paves the way to develop advanced photonic materials which can be applied as fluorescent biomarkers, where the stereochemical and steric control of their properties is extremely important to reduce the signal/noise ratio and improve the contrast in optical microscopy.

## Bibliography

- [1] Ma, J. L.; Peng, Q.; Zhao, C. H.; *Chem. Eur. J.*, **2019**, *25*, 15441-15454.
- [2] Addadi, L.; Weiner, S.; *Nature*, **2001**, *411*, 753-755.
- [3] Kumar, J.; Nakashima, T.; Kawai, T.; *J. Phys. Chem. Lett.*, **2015**, *6*, 3445-3452.
- [4] Hembury, G. A.; Borockov, V. V.; Inoue, Y.; *Chem. Rev.*, **2008**, *108*, 1-73.
- [5] Sánchez-Carnero, E. M.; Agarrabeitia, A. R.; Moreno, F.; Maroto, B. L.; Muller, G.; Ortiz, M. J.; de la Moya, S.; *Chem. Eur. J.*, **2015**, *21*, 13488-13500.
- [6] Nitti, A.; Pasini, D.; *Adv. Mater.*, **2020**, 1908021.
- [7] Wu, Z. G.; Han, H. B.; Yan, Z. P.; Luo, X. F.; Wang, Y.; Zheng, Y. X.; Zuo, J. L.; Pan, Y.; *Adv. Mater.*, **2019**, *31*, 1900524.
- [8] Zheng, H.; Li, W.; Li, W.; Wang, X.; Tang, Z.; Zhang, S. X. A.; Xu, Y.; *Adv. Mater.*, **2018**, *30*, 1705948.
- [9] Amako, T.; Nakabayashi, K.; Suzuki, N.; Guo, S.; Abdul-Rahim, N. A.; Harada, T.; Fujiki, M.; Imai, Y.; *Chem. Commun.*, **2015**, *51*, 8237-8240.
- [10] Yuasa, J.; Ohno, T.; Tsumatori, H.; Shiba, R.; Kamikubo, H.; Kataoka, M.; Hasegawa, Y.; Kawai, T.; *Chem. Commun.*, **2013**, *49*, 4604-4606.
- [11] Jiménez, J.; Cerdán, L.; Moreno, F.; Maroto, B. L.; García-Moreno, I.; Lunkley, J. L.; Muller, G.; de la Moya, S.; *J. Phys. Chem. C.*, **2017**, *121*, 5287-5292.
- [12] Gong, J.; Yu, M.; Wang, C.; Tan, J.; Wang, S.; Zhao, S.; Zhao, Z.; Qin, A.; Tang, B.; Zhang, X.; *Chem. Commun.*, **2019**, *55*, 10768-10771.
- [13] Muller, G.; *Dalton Trans.*, **2009**, 9692-9707.
- [14] Carr, R.; Evans, N. H.; Parker, D.; *Chem. Soc. Rev.*, **2012**, *41*, 7673-7686.
- [15] Seitz, M.; Moore, E. G.; Ingram, A. J.; Muller, G.; Raymond, K. N.; *J. Am. Chem. Soc.*, **2007**, *129*, 15468-15470.
- [16] Lu, H.; Mack, J.; Nyokong, T.; Kobayashi, N.; Shen, Z.; *Coordination Chemistry Reviews*, **2016**, *318*, 1-15.
- [17] Sánchez-Carnero, E. M.; Moreno, F.; Maroto, B. L.; Agarrabeitia, A. R.; Bañuelos, J.; Arbeloa, T.; López-Arbeloa, I.; Ortiz, M. J.; de la Moya, S.; *Chem. Commun.*, **2013**, *49*, 11641-11643.
- [18] Pu, L.; *Acc. Chem. Res.*, **2014**, *47*, 1523-1535.
- [19] Wang, C.; Wu, E.; Xu, X.; Zhang, G.; Pu, L.; *J. Am. Chem. Soc.*, **2015**, *137*, 3747-3750.
- [20] Sánchez-Carnero, E. M.; Moreno, F.; Maroto, B. L.; Agarrabeitia, A. R.; Ortiz, M. J.; Vo, B. G.; Muller, G.; de la Moya, S.; *J. Am. Chem. Soc.*, **2014**, *136*, 3346-3349.
- [21] Zhang, S.; Wang, Y.; Meng, F.; Dai, C.; Cheng, Y.; Zhu, C.; *Chem. Commun.*, **2015**, *51*, 9014-9017.
- [22] Grajewski, J.; Madry, T.; Kwit, M.; Warzajtis, B.; Rychlewska, U.; Gaeronski, J.; *Chem. Phys. Chem.*, **2017**, *18*, 2197-2207.
- [23] Liu, B.; Novikova, N.; Simpson, M. C.; Timmer, M. S.; Stocker, B. L.; Söhnel, T.; Wrae, D. C.; Brothers, P. J.; *Org. Biomol. Chem.*, **2016**, *14*, 5205-5209.
- [24] Manzano, H.; Esnal, I.; Marqués-Matesanz, T.; Bañuelos, J.; López-Arbeloa, I.; Ortiz, M. J.; Cerdán, L.; Costela, A.; García-Moreno, I.; Chiara, J. L.; *Adv. Funct. Mater.*, **2016**, *26*, 2756-2769.
- [25] Zinna, F.; Bruhn, T.; Guido, C. A.; Ahrens, J.; Bröring, M.; Di Bari, L.; Pescitelli, G.; *Chem. Eur. J.*, **2016**, *22*, 16089-16098.
- [26] Benniston, A. C.; Copley, G.; Harriman, A.; Howgego, D.; Harrington, R. W.; Clegg, W.; *J. Org. Chem.*, **2010**, *75*, 2018-2027.
- [27] Whited, M. T.; Patel, N. M.; Roberts, S. T.; Allen, K.; Djurovich, P. I.; Bradforth, S. E.; Thompson, M. E.; *Chem. Commun.*, **2012**, *48*, 284-286.
- [28] Patalag, J. L.; Ho, L. P.; Jones, P. G.; Werz, D. B.; *J. Am. Chem. Soc.*, **2017**, *139*, 15104-15113.
- [29] Ahrens, J.; Scheja, A.; Wicht, R.; Bröring, M.; *Eur. J. Org. Chem.*, **2016**, 2864-2870.
- [30] Alamiry, M. A. H.; Benniston, A. C.; Copley, G.; Harriman, A.; Howgego, D.; *J. Phys. Chem. A*, **2011**, *115*, 12111-12119.
- [31] Gierschner, J.; Park, S. Y.; *J. Mater. Chem. C.*, **2013**, *1*, 5818-5832.

- [32] Musser, A. J.; Rajendran, S. K.; Georgiou, K.; Gai, L.; Grant, R. T.; Shen, Z.; Cavazzini, M.; Ruseckas, A.; Turnbull, G. A.; Samuel, I. D. W.; Clark, J.; Lidzey, D. G.; *J. Mater. Chem. C*, **2017**, *5*, 8380-8389.
- [33] Kellog, M.; Akil, A.; Sylvinson, D.; Ravinson, M.; Estergreen, L.; Bradforth, S. E.; Thompson, M. E.; *Faraday Discuss.*, **2019**, *216*, 379-394.
- [34] Liu, Y.; Zhao, J.; Iagatti, A.; Bussotti, L.; Foggi, P.; Castellucci, E.; Di Donato, M.; Han, K. L.; *J. Phys. Chem. C*, **2018**, *122*, 2502-2511.
- [35] Momeni, M. R.; Brown, A.; *J. Chem. Theory Comput.*, **2015**, *11*, 2619-2632.
- [36] Cerdán, L.; García-Moreno, S.; Costela, A.; García-Moreno, I.; de la Moya, S.; *Sci. Rep.*, **2016**, *6*, 28740.



## CHAPTER 5

---

# Multichromophoric Energy Transfer Antennae

---

So far we have disclosed highly functionalized simple BODIPY dyes with a wide range of applications, such as, imaging, sensing, therapy and lasers. Although they possess rigid structures, their small Stokes shifts involve a higher probability for reabsorption/reemission processes and limited detection sensitivity, owing to the proximity of the excitation and monitoring regions, which infers background interferences. Apart from that, their limited photostability, intrinsic to the organic nature of the dye, under hard pumping conditions and low absorption probability over a broad spectral region are additional drawbacks. To offset such shortcomings, the exploration of multichromophores as artificial antenna systems emerges as one of the most suitable alternatives<sup>[1-3]</sup>. These energy donor-acceptor-based and covalently linked molecular architectures are able to harvest and transport the light with the desired energy, mimicking some of the more essential features of the natural process of photosynthesis<sup>[4,5]</sup>.

The key photophysical phenomenon in these covalently linked donor-acceptor systems is excitation energy transfer (EET)<sup>[6,7]</sup>. To boost its probability, a rational molecular design is mandatory. In fact, some parameters affecting its efficiency must be taken into account, such as a proper spectral overlap between the donor and acceptor emission and absorption bands, suitable interchromophoric distances (via an adequate spacer) and fine

control over their relative orientation. Besides, steric effects can be employed to retain the molecular identity of each of the units after the linkage and therefore enable a selective excitation of each moiety<sup>[8]</sup>, (chromophoric  $\pi$  systems of each building block electronically decoupled) and a broadband absorption over a wide spectral window. If the design is adequate, highly efficient intramolecular EET processes can take place, owing to the imposed short donor-acceptor distances by the covalent linkage, successively between the donor subunits (energy migration or homo-EET) and obtain the final emission from the acceptor subunit (hetero-EET), generally in the target red-region. When there is a substantial overlap of the donor emission spectrum with the acceptor absorption spectrum and a dipole-dipole coupling between the involved transition dipole moments is enabled (long-range interaction)<sup>[9]</sup>, the Förster resonance energy transfer (FRET) is promoted<sup>[10]</sup>. Normally, in FRET-mediated cassettes processes the chromophoric subunits are linked by a non-conjugated spacer and the energy transfer occurs through space (Figure 5.1a). Alternatively, if the spacer allows a direct linkage of the fragments (short-range interaction) or, alternatively, if it is a conjugated bridge (superexchange mechanism)<sup>[11]</sup>, the energy transfer process occurs through-bond (TBET)<sup>[12]</sup> (Figure 5.1b). Indeed, this last mechanism is driven by an electronic exchange through an orbital overlap<sup>[13]</sup>. In most of the molecular antennae both mechanisms are extremely efficient and take place at the same time, but depending on the donor-acceptor orientation and the spacer, one of them can prevail<sup>[14]</sup>.

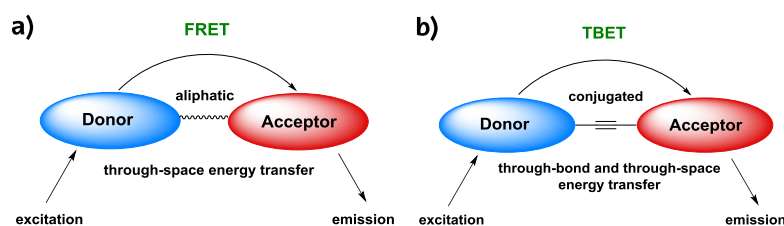


**Figure 5.1.** Through-space energy transfer (a) and through-bond energy transfer (b) cassettes.

The fine control of all these factors opens the door to develop competitive artificial photonic antennae with a huge number of applications: analysis of DNA structures, nucleic acid regulation, protein structure, function analysis, and immunoassays<sup>[15,16]</sup>, dye-sensitized solar cells<sup>[17]</sup>, luminescent solar concentrators<sup>[18]</sup>, tunable dye lasers<sup>[19]</sup> and light modulators in white-light emitting systems<sup>[20]</sup>. Regarding the dye laser application, this strategy is very appealing since the cassettes allow a more versatile selection of the pumping source and photodegradation is further reduced, since the final emitting chromophoric unit can be indirectly excited through EET from the donor<sup>[21,22]</sup>. Therefore, the design of multichromophoric systems nowadays focuses on shifting bathochromically



their bands to the reddest region of the electromagnetic spectrum (see Chapter 2 for the advantages of this kind of radiation) in order to improve bioimaging<sup>[23]</sup>. What is more, these systems possess large pseudo-Stokes shifts (the emission of the acceptor is far away from the absorption of the donor), which reduces the background interferences in bioimaging and sensing applications<sup>[24,25]</sup>.

Hence, thanks to the accessible molecular engineering in BODIPYs, in the herein Chapter we present a wide range of dye-combinations to obtain a selection of red emissive multichromophoric systems applied as energy transfer lasers. Furthermore, we analyze the impact of the spacer, linkage position and the number and type of donor and acceptor moieties in the final energy transfer efficiency of the cassettes. Firstly, in Section 5.1 simple BODIPYs and aza-BODIPYs (described in Chapter 2) have been combined through conjugated phenyl spacers leading to energy and charge transfer cassettes. Alternatively, in Section 5.2 different types of fluorophores (coumarin, BODIPY and perylene red) have been linked through flexible and/or rigid spacers obtaining panchromatic cassettes. Finally, in Section 5.3 all-BODIPY based pentad and hexads have been synthesized and thoroughly characterized. More information can be found in **Chemistry - A European Journal** (Section 5.1 and Section 5.3) and in **Physical Chemistry Chemical Physics** (Section 5.2) attached to the annex V.

## 5.1. RED/NIR AZA-BODIPY-BODIPY CASSETTES

The performance of aza-BODIPY dyes as bright and stable red/NIR emitters was supported in Chapter 2 (Section 2.2). As a matter of fact, the polyarylated aza-BODIPY **NIR2** displayed efficient and stable long-wavelength emission. Because of that, compound **NIR2-F** is an ideal energy and electron acceptor and scaffold to covalently anchor green-emitting BODIPY moieties acting as energy or electron donors (Figure 5.2). In this way, thanks to the claimed chemical versatility of the boron-azadipyrrin core, diverse aza-BODIPY-BODIPY cassettes have been synthesized where the number of BODIPY units acting as donors has been increased (compounds **ABB1**, **ABB2b** and **ABB4b**) and the same donor units have been tethered at the dipyrin backbone or at the boron atom of the acceptor unit (dyes **ABB1** and **ABB2** vs **ABB3** and **ABB4**). With this set of cassettes we aim

to modulate the light harvesting and the balance between energy and electron transfer, as a key factor governing the final efficiency of the red emission.

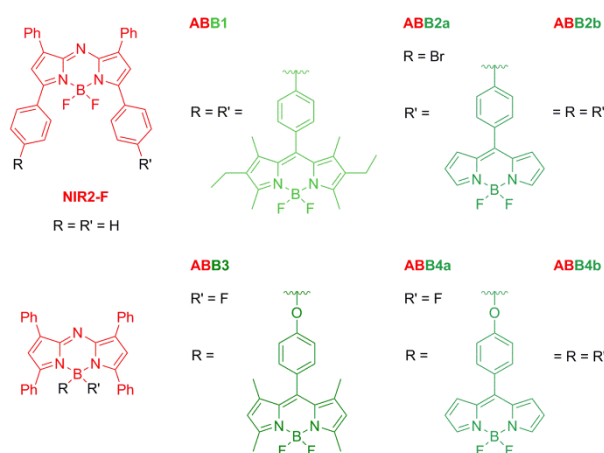


**Figure 5.2.** Structure of cassettes aza-BODIPY-BODIPYs. The structure of the precursor **NIR2-F** is also included.

### 5.1.1. Photophysical properties

The absorption spectra of these dyes feature two clearly discernible absorption bands, one localized at higher energies and ascribed to the pendant BODIPY chromophores (between 495 nm and 525 nm) and the other one at lower energies belonging to the  $\pi$ -extended aza-BODIPY (between 650 nm and 680 nm). The intensity of the former is proportional to the number of donor units attached to the acceptor (dyes **ABB2a** vs **ABB2b** or **ABB4a** vs **ABB4b** in Figure 5.3) and tends to red-shift when the alkylation degree is increased (compounds **ABB1** vs **ABB2a**). Hence, this absorption profile means that each chromophoric subunit retains its molecular identity after the linkage. This is supported by the molecular orbitals simulations, since the MOs involved in each electronic transition are exclusively located at one specific chromophoric moiety (Figure 5.4). Fluorescence spectra, however, are dominated by a single band located at the red-edge (peaked up to 720 nm in **ABB2b**) regardless of the excitation wavelength thanks to an efficient EET process from the BODIPY energy donor to the energy acceptor aza-BODIPY (Figure 5.3).

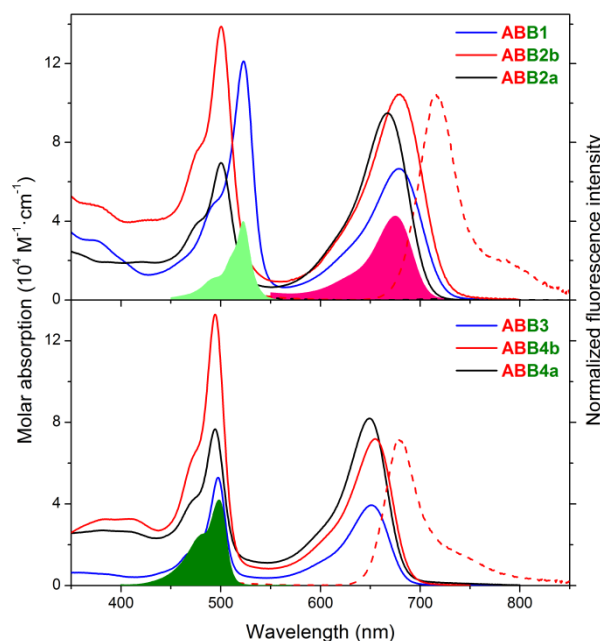


**Figure 5.3.** Absorption (solid lines) and fluorescence (dashed lines, after selective excitation of the BODIPY donor) spectra of cassettes **ABB1**, **ABB2b**, **ABB3** and **ABB4b** in ethyl acetate. To highlight the effect of the number of appended BODIPY donors, the absorption spectra of the dyads **ABB2a** and **ABB4a** are also included (lines in black). The absorption spectra (filled bands) of the isolated building blocks of the cassettes are also added to evidence the maintenance of the integrity of the chromophores after its covalent linkage.

Despite the high efficiency of the EET process (close to 100%) mainly due to the short donor-acceptor distances and their optimal geometrical disposition, the fluorescence quantum yield of these cassettes depends strongly on the alkylation degree of the donor. In fact, cassettes **ABB1** (diethylated) and **ABB3** (tetramethylated) become almost non-fluorescent (Table 5.1). Theoretical calculations supported these results, since they predicted that the HOMO is located in the peripheral BODIPY and energetically placed between the MOs responsible of the aza-BODIPY transition, thereby enabling a reductive PET process upon excitation<sup>[26]</sup> and avoiding fluorescence from the aza-BODIPY (Figure 5.4). Therefore, the alkylated BODIPYs were able to act as effective electron donors as well as energy donors. Nevertheless, the dealkylation of the donors suppressed this PET pathway and the fluorescence response was restored together with a substantial lengthening of the lifetime (Table 5.1)<sup>[27]</sup>. This structural change rearranged the MOs energetically lowering the energy of the HOMO of the donor BODIPY (from -5.27 eV in **ABB1** to -5.93 eV in **ABB2b**) to become HOMO-1 in the cassette (Figure 5.4) and making PET process thermodynamically unviable. Thus, the functionalization of the BODIPY donor played an important role triggering the PET and hence the effectiveness of the final emission of these cassettes.

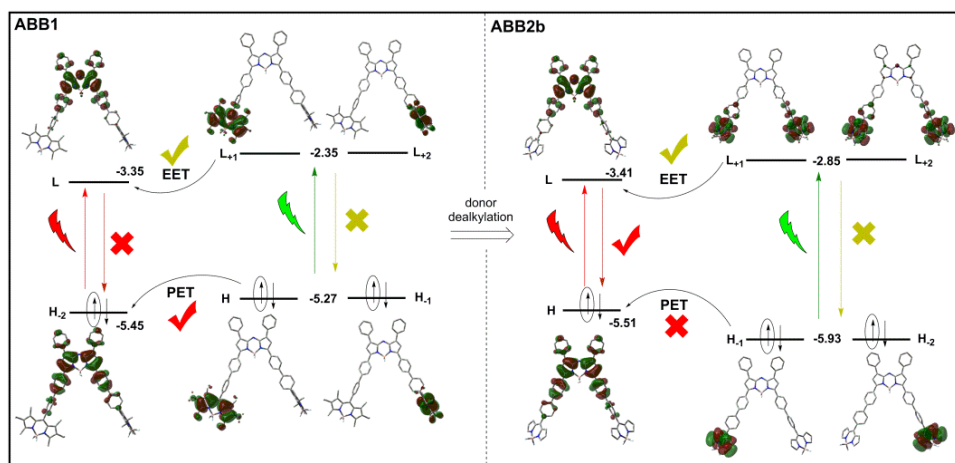


**Figure 5.4.** Theoretical molecular orbitals (B3LYP/6-31G<sup>\*</sup>) and energies (in eV) from the analogs **ABB1** and **ABB2b** differing in the alkylation degree at the dipyrin core of the BODIPY donor. The probability of the competing fluorescence, EET and PET processes is depicted.

Moreover, the grafted position at the aza-BODIPY core has a clear influence on the final fluorescence response of these antenna systems (Table 5.1). Thus, the linkage through the 3,5-biphenyl groups lead to brighter NIR emission than those linked directly to the boron bridge (30% vs 8% for triads **ABB2b** and **ABB4b**, respectively). This decrease in both quantum yield and lifetime values can be attributed to the higher conformational freedom after tethering the donor BODIPYs at the boron bridge of the aza-BODIPYs. Thus, the feasible rotation of such unconstrained BODIPY moieties increases the non-radiative internal conversion deactivation processes.

**Table 5.1.** Photophysical and lasing properties (pumped at 532 nm) and photostability of all the aza-BODIPY-BODIPY cassettes in ethyl acetate. The corresponding data of the isolated energy acceptor aza-BODIPY **NIR2-F** under identical experimental conditions are also included for comparison purposes.

ABB	$\lambda_{ab}$ [nm]	$\epsilon_{max}$ [10 <sup>4</sup> M <sup>-1</sup> ·cm <sup>-1</sup> ]	$\lambda_{fl}$ [nm]	$\phi$	$\tau$ [ns]	$\lambda_{la}$ (355 nm) [nm]	%Eff (355 nm)	$E_{dose}^a$ (355 nm) [GJ/mol]
<b>1</b>	678.5 523.0	6.7 12.1	711.5	0.006	NR	729.0*	-#	160#
<b>2a</b>	667.5 500.5	7.7 5.7	701.0	0.24	1.83	712.0(709.0)	22 (19)	76 (62)
<b>2b</b>	680.0 500.5	10.4 13.9	718.5	0.30	2.28	730.0(725.0)	25 (21)	142 (123)
<b>3</b>	651.5 497.5	3.9 5.3	672.5	0.007	NR	720.0*	-#	81#
<b>4a</b>	694.5 494.5	8.2 7.7	675.0	0.08	0.84	696.0(694.0)	21 (15)	64
<b>4b</b>	655.0 494.5	7.2 13.3	678.5	0.08	1.03	693.0(690.0)	23 (16)	145 (135)
<b>NIR2-F</b>	646.0	8.6	668.0	0.12	0.81	689.0(685.0)	6 (4)	22

<sup>a)</sup> photostability, defined as the amount of pumping energy absorbed by the dye to retain 90% of its initial emission at 532 nm; NR : non-recorded because they were below 50 ps, the time resolution of the photon counter; \* LIF; # the PET process induced by the molecular structure of these compounds was able to turn the laser action off but did not extinguish LIF emission.

Among the cassettes with biphenyl spacer, the best fluorescence response is recorded for the triad **ABB2b**, which shows even two-fold higher fluorescence efficiency than its monomeric precursor **NIR2-F** (Table 5.1, see Section 2.2. in Chapter 2 and its corresponding annex for more details). It seems that the presence of the biphenyl groups in positions 3 and 5 not only extends the  $\pi$ -system delocalization more than a single phenyl group, leading to a more pronounced bathochromic shift (Figure 5.3), but also restricts the conformational freedom, since the simple bonds between the phenyl groups adopt double bond character. Moreover, such extended delocalization puts further away the electronic density from the central BODIPY, decreasing the negative effect of the free rotation of the 1,7-phenyl groups. Therefore, the design of a cassette based on aza-BODIPY-BODIPY architecture is an appropriate pathway to obtain dyads and triads with high EET efficiencies and tunable emission capability emitting in the red-NIR edge of the electromagnetic spectrum.

### 5.1.2. Lasing properties

After transversal pumping at 532 nm (absorption region of the donor BODIPYs), all these cassettes, except those undergoing PET process, lase efficiently in the red spectral region (from 690 nm to 730 nm) after efficient EET, in good correlation with the fluorescence emission bands (see Table 5.1 and Figure 5.5). It is noteworthy that the same cassettes lase also when they are pumped at 355 nm showing similar laser performance thus. The low absorption of the isolated aza-BODIPY at this pumping wavelength demanded high concentrations. In contrast, the higher absorption of the cassettes reduces the required gain-media concentration (up to 75%) preventing dye solubility problems and aggregation processes, being very appealing in terms of laser action. So the ideal dye concentration in ethyl acetate for the best laser efficiency ranges from 0.2 mM to 0.9 mM depending on the given dye. As a consequence, these aza-BODIPY-BODIPY cassettes present high laser efficiencies (up to 25%), surpassing by far that exhibited by its monomeric precursor **NIR2-F** (Table 5.1).

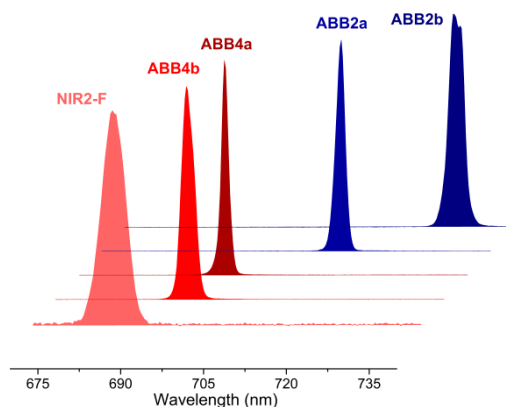


**Figure 5.5.** Normalized laser spectra of dyes **ABB2a-2b** and **ABB4a-4b** in ethyl acetate (0.5 mM) pumped at 532 nm. The corresponding laser signal of its monomeric precursor **NIR2-F** is also included.

Regarding the photostability, high energy doses (up to 160 GJ/mol) are required to decrease their LIF intensity at least 10% (Table 5.1). Once again the effectiveness of the EET process is the responsible for these outstanding results, considering that it reduces the photodegradation thanks to the indirect excitation of the acceptor. In other words, the photostable donor BODIPY receives the laser pumping and its damage, keeping the aza-BODIPY emitter unharmed. As a result, all aza-BODIPY-BODIPY cassettes herein developed are more photostable than the own monomeric precursor **NIR2-F** as well as other monomeric commercially available laser dyes emitting in the same spectral region ( $E_{\text{dose}}$  value of NB was 10 GJ/mol under same pumping conditions, see Chapter 2). Furthermore, the laser performance improves proportionally with the number of donor units independently of their linkage length and/or position, being the cassettes with higher number of donor the most efficient and photostable ones.

Nevertheless, the most striking feature of these new synthesized cassettes is the exhibited delayed fluorescence emission from 680 nm to 800 nm at delay times longer than 100  $\mu\text{s}$  after exposure to intense laser pulses at both 355 nm and 532 nm. It is noteworthy that this delayed emission was only recorded under laser excitation and was not detected under the mild conditions employed for the registration of the photophysical signatures. This delayed emission shows similar spectral profile in comparison to that of the prompt laser-induced fluorescence (Figure 5.6). Taking into account that the prompt fluorescence presents lifetime values shorter than 2 ns, this delayed fluorescence emission must unequivocally imply long-lived triplet excited states via thermally activated delayed fluorescence (TADF)<sup>[28]</sup> mechanism, which is able to convert the excited  $T_1$  state to emissive  $S_1$  state by absorbing environmental thermal energy through an efficient reverse intersystem crossing (RISC)<sup>[29,30]</sup>.

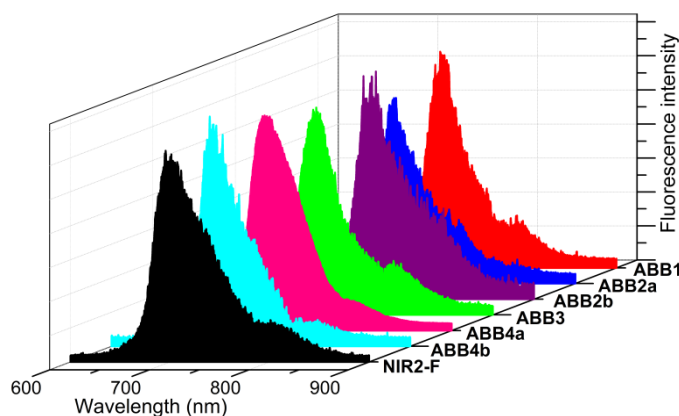


**Figure 5.6.** Delayed fluorescence spectra of the aza-BODIPY-BODIPY cassettes **ABB1-4** in aerated ethyl acetate solutions (0.1 mM) at room temperature recorded with a delay of 50  $\mu$ s with respect to the incoming laser radiation (532 nm and 20 mJ/cm<sup>2</sup> fluence). The delayed fluorescence spectrum of the precursor **NIR2-F** is also included for comparison.

It is widely known that the ISC probability in BODIPYs is extremely low (1%)<sup>[31]</sup> and advanced excited state calculations recently done for the simplest BODIPY revealed that the most feasible channel is through the conical intersection between  $S_1$  and the high-lying  $T_2$  state<sup>[32]</sup>. Likely, the presence of the aza group at the *meso* position increases the  $n-\pi^*$  character of the transition, reducing the  $S_1-T_2$  energy gap. Therefore, upon strong pumping, an electron in the excited state could reach the conical intersection to access a high-lying triplet state. Nevertheless, once there, the same electron could come back to the  $S_1$  state through a thermodynamically feasible RISC enabling the recording delayed fluorescence signal in a time-scale of hundreds of microseconds. This phenomenon is of great interest, since over the last few years an intense research effort has been made to develop TADF materials<sup>[33,34]</sup> and although a wealth of highly efficient blue, green, yellow and orange TADF emitters are available<sup>[35-38]</sup>, there is a lack of them in the red part of the visible. Indeed, this is the first time to the best of our knowledge that delayed emission is recorded from fluorophores based on aza-BODIPY scaffold maintaining a long-lived fluorescence emission in the red/near IR spectral region.

Summarizing, the herein designed cassettes are efficient light-harvesters across the UV-Vis region, displaying strong and long-lasting fluorescence and laser emission in the red region (beyond 700 nm), thanks to the effectiveness of the EET process. In addition, the delayed fluorescence emission property in the strategic red/NIR spectral region points out the rational design of these cassettes as a promising starting point from developing novel long-lived TADF materials with boosted medical and optoelectronic applications.

## 5.2. PANCHROMATIC CASSETTES WITH RED EMISSION

Another alternative to build the molecular antennae is to combine different family of laser dyes, with optimal photophysical properties in different spectral regions into a unique molecular structure (Figure 5.7). In this line of reasoning, perylene red (Per-Red), from the perylendiimide family (PDIs)<sup>[39,40]</sup>, was selected as the final emitting acceptor in the red-edge of the visible spectrum owing to its high photostability and outstanding fluorescent capacity. In order to complement the absorption profile, coumarins<sup>[41]</sup> (7-hydroxicoumarin, compounds **PC1** and **PC2**), with absorption/emission bands in the UV-blue regions, and BODIPYs (PM567, compound **PB1**), with absorption/emission bands in the green-yellow region, were selected as energy donors to decorate the Per-Red dye since they presented the required spectral overlap to switch on FRET processes. Moreover, these three dyes were also covalently linked to each other to design the tryad **PBC**. Alternatively, we also considered another blue BODIPY derivative with 8-amine group (compounds **PB2**, **PB3** and **PB4**) as energy donor appended to the perylene backbone.

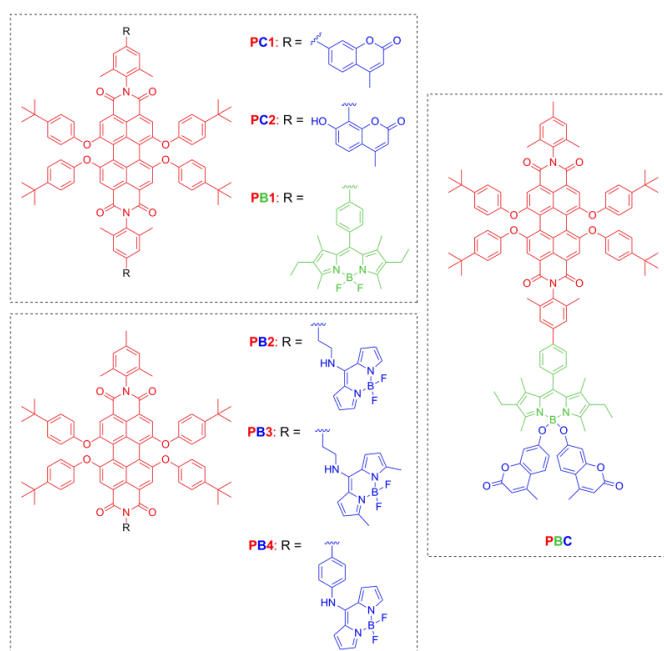


Figure 5.7. Structures of panchromatic molecular antennae based on Per-Red dye.

### 5.2.1. Photophysical properties

Before explaining the photophysical properties of these molecular antennae it is noteworthy to mention that all energy donors were anchored to the Per-Red through its *peri* position, since it did not modify its photophysics. This is logic if we pay attention to its



HOMO and LUMO MOs involved in the electronic transition (Figure 5.8). The corresponding contour maps showed that the electronic density is principally centered in the perylene core and slightly extended through the oxygen atoms of the phenoxy group and the carbonyls of the imides. However, the *N*-phenyl group at the *peri* position is twisted with respect to the perylene plane and does not take part in the delocalized system, having little impact on the photophysical properties of the dye. Therefore, the functionalization at the *peri* position becomes suitable to customize these cassettes.

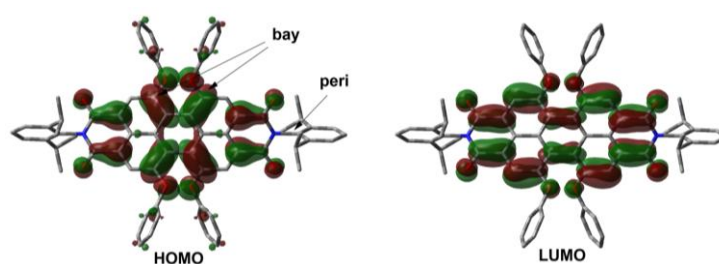


**Figure 5.8.** Theoretically calculated (B3LYP/6-31G) molecular orbitals of perylene red.

Such electronic isolation defines certainly the absorption profile of the cassettes as the sum of the electronic transition of each chromophoric unit regardless of the structure. As a result, dyads based on coumarin-peryene **PC1** and **PC2** show two main bands placed at 570 nm and around 325 nm corresponding to the Per-Red and coumarin units, respectively (Table 5.2). The latter is slightly masked by the more energetic transition ( $S_0-S_2$ ) of the perylene (Figure 5.9). Nevertheless, when two BODIPY units are anchored at both edges of the perylene core (dye **PB1**), a strong absorption band at 523 nm ( $165000 \text{ M}^{-1} \cdot \text{cm}^{-1}$ ) is recorded together with the aforementioned perylene one.

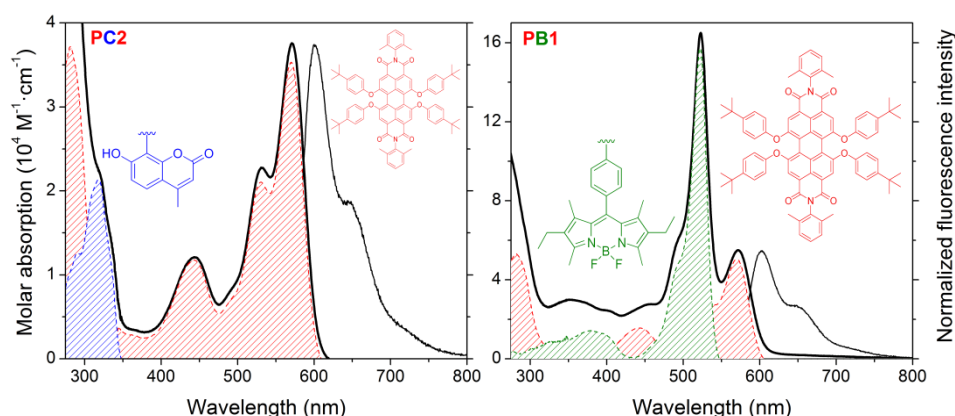


**Figure 5.9.** Absorption (black bold line) and fluorescence spectra (black thin line) of compounds **PC2** and **PB1**, upon selective excitation of the coumarin ( $\lambda_{\text{exc}} = 325 \text{ nm}$ ) and BODIPY ( $\lambda_{\text{exc}} = 490 \text{ nm}$ ) in ethyl acetate, respectively. The corresponding absorption bands of its chromophoric fragments (filled bands, hydroxycoumarin in blue, BODIPY in green and Per-Red in red) together with their molecular structure are also depicted. The corresponding spectra of **PC1** are not included because they are very similar to the structurally related **PC2**.

In the three cases the fluorescence spectra are mainly composed of one single band peaked at 600 nm corresponding to the Per-Red emission regardless of the excitation wavelength (Table 5.2 and Figure 5.9). Such independence of the fluorescence profile from the excitation wavelength as well as the lack of the donor emission supports the effectiveness of the EET process. Upon any excitation wavelength, the cassettes **PC1** and **PC2** show fluorescence efficiencies close to 1.00, but in dye **PB1** this quantum yield decreases slightly owing to the appearance of an extra internal conversion process driven by the higher flexibility of the biphenyl spacer (Table 5.2). However, such influence should be quite low, since the free motion is hampered by the methyl groups grafted at the *ortho* position of the *N*-phenyl ring of Per-Red. Indeed, a high fluorescence quantum yield value ( $\phi = 0.80$ ) is recorded. Moreover, the lifetime values monitored at the perylene region are very similar regardless of the excitation wavelength, even when the excitation is carried out where the BODIPY absorbed more than the perylene (5.26 ns and 5.30 ns, respectively), supporting the effectiveness of the intramolecular EET.

**Table 5.2.** Photophysical properties and lasing efficiencies of all the coumarin-erylene (**PC1-2**) and BODIPY-erylene (**PB1-4**) cassettes as well as **PBC** in ethyl acetate. The corresponding data of the isolated energy acceptor Per-Red under identical experimental conditions are also included for comparison purposes.

dye	$\lambda_{ab}$ [nm]	$\epsilon_{max}$ [10 <sup>4</sup> M <sup>-1</sup> .cm <sup>-1</sup> ]	$\lambda_{fl}$ [nm]	$\phi$ <sup>a)</sup>	$\tau$ [ns]	$k_{fl}$ [10 <sup>8</sup> s <sup>-1</sup> ]	$k_{nr}$ [10 <sup>8</sup> s <sup>-1</sup> ]	%Eff (355 nm)
Per-Red	568.0	4.9	597.5	1.00	6.16	1.62	0.00	22.0*
<b>PC1</b>	573.0	3.4	602.0	0.97	6.07	1.60	0.05	26.0
<b>PC2</b>	571.0	3.8	600.0	1.00	5.98	1.67	0.00	27.0
<b>PB1</b>	572.0	5.5	603.0	0.80	5.30	1.51	0.37	27.0*
	523.0	16.5			5.26 <sup>b)</sup>			
<b>PBC</b>	572.0	4.5	600.0	0.82	5.87	1.40	0.30	35.0
	525.0	8.3			5.84 <sup>b)</sup>			
<b>PB2</b>	574.0	4.5	609.0	0.87	6.21	1.40	0.21	24.0
	403.0	3.1						
<b>PB3</b>	574.0	4.6	604.5	0.51	6.53 (3%)	-	-	22.0
	422.5	4.1			2.17 (32%)			
<b>PB4</b>	569.0	4.5	602.5	0.97	6.08	1.59	0.06	30.0
	415.0	3.1						

<sup>a)</sup> similar values were attained (just 2% lower than the herein listed values upon direct excitation of the acceptor) upon selective excitation of the donors; <sup>b)</sup> recorded upon excitation at 470 nm (BODIPY region), instead of at 570 nm (direct excitation of perylene) as in the other data, and monitored at 600 nm (perylene region); \* pumped at 532 nm.

In view of the results obtained when coumarin-erylene and BODIPY-erylene were combined, the three chromophores were linked in one single molecular structure leading to the cassette **PBC**. Such molecular antenna presents an absorption profile composed by three main bands at 325 nm, 525 nm and 572 nm, corresponding to each fragment (Figure

5.10). Therefore, upon excitation at any wavelength there is a single fluorescence band around 600 nm corresponding to the Per-Red emission owing to the efficient EET process through a cascade-like mechanism from coumarin to BODIPY and from here to the final perylene acceptor which quenches efficiently the fluorescence emission from the donors. Moreover, the excitation spectrum fully matches the absorption spectrum. Once again, the quantum yield value is slightly lower ( $\phi = 0.82$ ) than that of Per-Red and compounds **PC1-2**, and very similar to that of the dye **PB1** due to aforementioned flexibility which slightly increases the non-radiative (internal conversion) rate constant (Table 5.2).

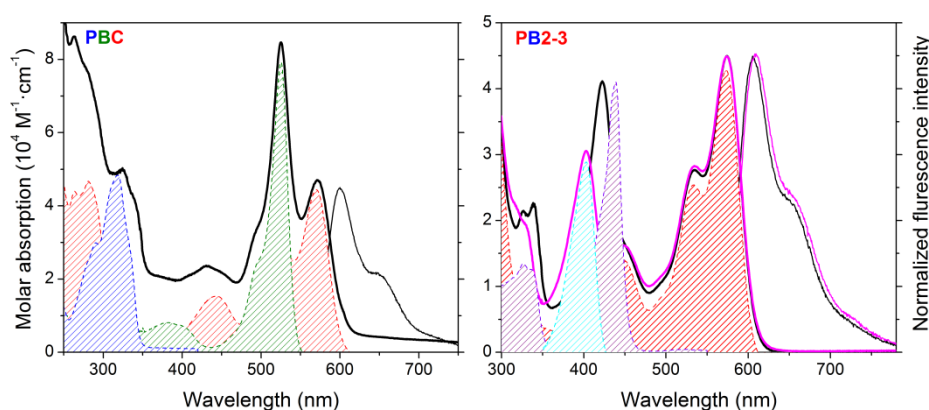


**Figure 5.10.** Absorption (bold line) and fluorescence spectra (thin line) of compounds **PBC**, **PB2** (black line) and **PB3** (pink line), upon selective excitation of the coumarin ( $\lambda_{exc} = 325$  nm) and 8-aminoBODIPY ( $\lambda_{exc} = 390$  nm) in ethyl acetate, respectively. The corresponding absorption bands of its chromophoric fragments (filled bands, hydroxycoumarin in blue, BODIPY in green, 8-aminoBODIPY in cyan, its alkylated counterpart in purple and Per-Red in red) are also depicted.

All the cassettes presented up to now show enhanced absorption profiles in the visible region, but the absorption of the BODIPY overlaps with the perylene one in the green region and the absorption of the coumarin is masked by the perylene. As a result, although the BODIPY increases the light absorption ability, it does not span as much as requested the absorption spectral window. Thus, to achieve a panchromatic absorption over the whole visible region, the 8-aminoBODIPY moiety was selected to complement the Per-Red dye (compounds **PB2-4**). It is well known that the amino substitution at the *meso* position of the BODIPY core provokes a blue-shift. Furthermore, the methylation at positions 3 and 5 ameliorates its fluorescence response (from 0.42 to 0.90 in ethyl acetate)<sup>[42]</sup>.

In compounds **PB2** and **PB3** such 8-aminoBODIPY moiety and its 3,5-dimethylated counterpart are linked through an aliphatic chain. Two clearly distinct bands in the visible region comprise the absorption profile (Figure 5.10). The alkylation of the donor in dye **PB3**

shifts the higher energy absorption maximum around 20 nm to lower energies increasing, at the same time, its absorption ability due to inductive donor effect of the alkyls (Table 5.2). In both systems the fluorescence spectra are composed by a single band placed at around 605 nm, and corresponding to the emission of the final acceptor via the EET process. However, whereas **PB2** shows high fluorescence ability ( $\phi = 0.82$  and  $\tau = 6.21$  ns) in the red-edge, **PB3** presents lower quantum yield value ( $\phi = 0.51$ ) and the decay curve needs a multiexponential fitting where the short-lifetime components prevail (Table 5.2). Theoretical calculations predict that the simple methylation process increases the HOMO energy of compound **PB3** (from -5.79 eV to -5.46 eV), locating it between the MOs responsible of the red emission from the perylene. That is to say, in cassette **PB3** the HOMO is placed at the BODIPY instead of at the perylene (like in compound **PB2**), enabling a reductive PET from the BODIPY to the perylene upon selective excitation of the latter (Figure 5.11), as an extra non-radiative pathway quenching the emission.

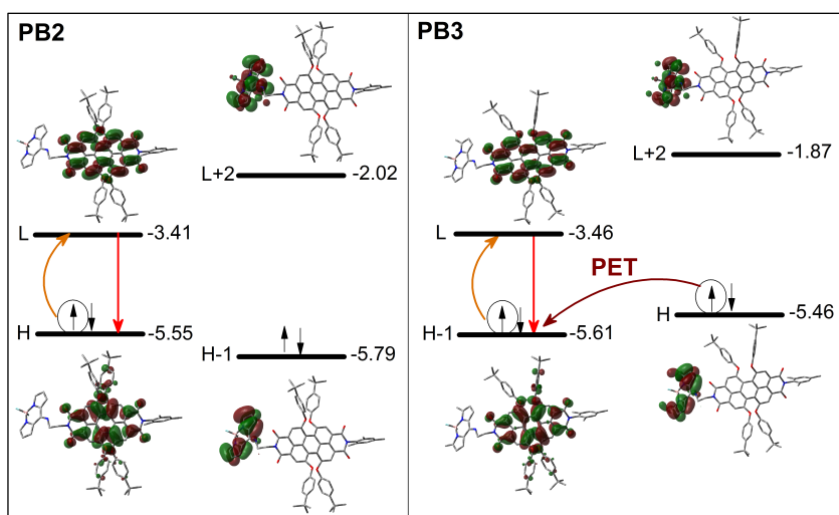


**Figure 5.11.** Theoretically predicted (B3LYP/6-31G) energy diagrams (in eV) of the molecular orbitals involved in the main electronic transition as well as in the fluorescence quenching PET of **PB2** and **PB3**.

When the flexible aliphatic spacer of **PB2** is replaced by a more rigid and conjugated one (phenyl linker in dye **PB4**), the fluorescence response is improved (Table 5.2). Although this structural modification does not change neither the shape nor the position of the spectral bands, the more constrained spacer decreases the non-radiative pathways and increases the fluorescence ability (from 0.87 in **PB2** to 0.97 in **PB4**). These results bring to light the key role of a rigid structure into the fluorescence response of these molecular assemblies. Moreover, the fluorescence response reaches almost identical values than that shown by Per-Red (Table 5.2). Therefore, **PB4** becomes the best

dye as a light-harvesting molecular antenna among all of the cassettes herein studied owing to its broadband absorption in the visible, but providing exclusive emission in the red region approaching the 100%.

### 5.2.2. Lasing properties

As these molecular antennae increase the absorbance of Per-Red at key pumping wavelengths (Nd:YAG second and third harmonic, 532 and 355 nm, respectively), thus improved laser action is expected. In this regard, all the cassettes presented herein were pumped at 355 nm, except Per-Red and PB1, which were pumped at 532 nm, displaying a unique laser signal at around 625 nm due to the high effectiveness of the EET process. In general terms, the laser behavior correlates well with their photophysical features, being the most fluorescent cassettes the ones with the highest lasing efficiencies. Furthermore, dyes presenting the higher Stokes shifts and the lower non-radiative rate constants are the most photostable ones under hard pumping conditions (see Table 5.2 and Figure 5.12).

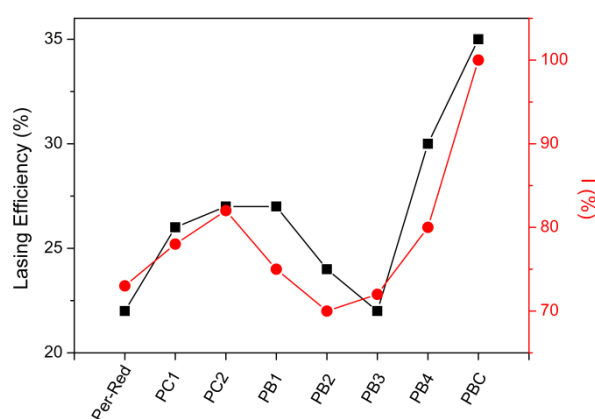


**Figure 5.12.** Lasing efficiency and photostability values (intensity of the laser output after 100000 pump pulses with respect to its initial intensity,  $I$  (%) =  $(I/I_0) \times 100$ ) of the new panchromatic cassettes as well as the isolated energy acceptor Per-Red in ethyl acetate.

The aforementioned increase of the absorbance ability at the pumping wavelengths enables a drastic decrease of the dye concentration in the active medium (from 9 mM in Per-Red to 1-3 mM in the new synthesized cassettes), reducing at the same time reabsorption/reemission effects and aggregation processes. The dyads based on coumarin (PC1 and PC2) and the one based on BODIPY unit (PB1) display similar photostability values in comparison to Per-Red, but slightly higher lasing efficiencies under identical experimental conditions (Figure 5.12). Nevertheless, the cassettes based on 8-aminoBODIPY show similar lasing efficiency values (24% and 22% for PB2 and PB3,

respectively) to Per-Red despite the fact that they present the worst photophysical properties (albeit they are notable) owing to their flexible spacer. When such connector between donor-acceptor units are replaced by a more rigid one (**PB4**), the lasing efficiency increases up to 30% following the same trend as in photophysics.

Although the triad **PBC** does not show the best photophysical performance, it is still good enough. Indeed, it presents the highest lasing efficiency and photostability values (Figure 5.12), improving the laser action of Per-Red with lasing efficiency up to 35% and no sign of photodegradation after a prolonged exposure of intense laser irradiation. The latter feature is of great interest since the photostability of **PBC** is significantly higher than those exhibited by the rest of the compounds, surpassing by far the value of Per-Red. This clearly demonstrates the benefits of embedding the three individual components into a proper single molecular architecture.

In brief, the herein applied strategy based on energy transfer dye lasers boost the performance of perylene dyes as active media for red-emitting lasers. The new molecular antennae improve noticeably both photophysical and laser performance of the unmodified and commercial Per-Red. Moreover, the ameliorated key optical factors, such as higher absorption coefficients at standard pumping wavelengths, wider spectral window for light-harvesting and higher efficient emission in the red-edge regardless of the excitation wavelength, expand their photonic applicability.

### 5.3. ALL-BODIPY BASED PENTAD AND HEXAD LASER DYES

In the previous sections the final acceptor in the red-edge was the aza-BODIPY (Section 5.1) or the Per-Red dye (Section 5.2) and the donor units were either coumarin or modified BODIPYs. In the herein section, and based on the tunable spectral region afforded by the BODIPYs (thanks to their great chemical versatility), we have linked covalently BODIPYs with absorption/emission bands in the green/yellow regions (**PM567**) and BODIPYs in the red-edge thanks to their  $\pi$ -extended systems mainly through styryl substituents at positions 3 and 5, leading to all-BODIPY based cassettes (Figure 5.13). The main novelty resides in the number of donors and acceptors linked in the cassette. Thus, the linkage of the BODIPY donors was done through the *ortho* position of its 8-phenyl to ensure a conformationally restricted geometry, but, whereas in triads **ALLB6a-b** and

**ALLB7** the two peripheral donors were connected at the 3,5-styryls of the acceptor BODIPY, in triad **ALLB8** they were anchored at the 2,6-triazoles of the acceptor BODIPY. The combination of these last two approaches led to pentad **ALLB9**, where up to four donors were linked simultaneously to the central acceptor. Finally, compound **ALLB6a** was dimerized through 8-benzylic ureas to render the complex hexad **ALLB10**, bearing up to six donor and two acceptors in the same molecular architecture. This set of cassettes enables us to ascertain the role of the number of donors and acceptors in the photonic properties of multichromophoric dyes.

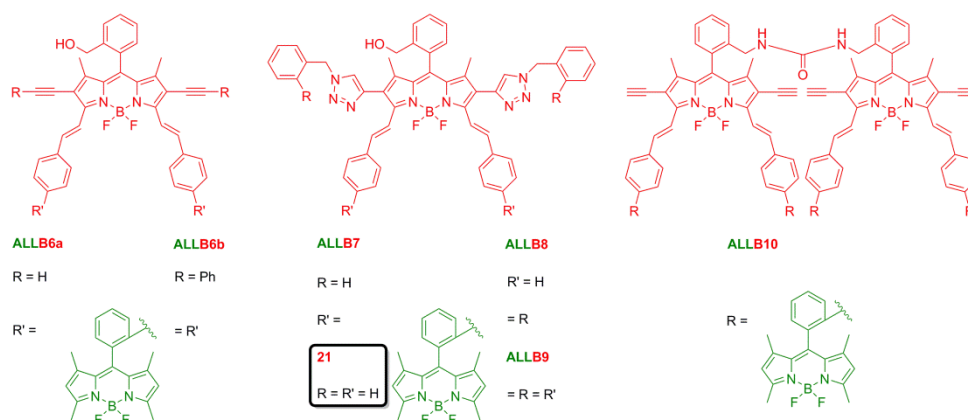


**Figure 5.13.** Structure of all-BODIPY based cassettes. The corresponding structure of the isolated red-emitting dye **21** is also included.

### 5.3.1. Photophysical properties

The absorption spectra of cassettes **ALLB6-10** is composed by three well defined bands, since, as consequence of the rational design, each chromophoric unit maintains its molecular identity after the covalent linkage contributing additively to the whole absorption profile (Figure 5.14). The band at the lowest energies (around 630 nm) belongs to the  $\pi$ -extended central subunit matching the spectrum registered for the isolated dye **21**. The same band is bathochromically shifted up to 655 nm when the triazol group at positions 2 and 6 was replaced by acetylene or by acetylenphenyl. The hexad **ALLB10** bearing two  $\pi$ -extended central BODIPYs presents the highest molar absorption coefficient in this region (up to  $170000 \text{ M}^{-1}\cdot\text{cm}^{-1}$ ). However, the most intense absorption band in each cassette is recorded at around 505 nm and is assigned to the peripheral tetramethylated BODIPYs (Figure 5.14). Its molar absorption coefficient is directly proportional to the number of BODIPY donors. As a result, dyes bearing four pendant peripheral BODIPYs (compounds **ALLB9** and **ALLB10**) show extinction coefficients higher

than  $200000 \text{ M}^{-1}\cdot\text{cm}^{-1}$  in the green region. Finally, the band with the lowest molar absorption probability and at the lowest wavelength is attributed to the interaction between the styryl groups at positions 3 and 5 and the pyrrole groups of the central BODIPY<sup>[43]</sup>. It is noteworthy that this band matches with the most energetic transitions of the BODIPY and therefore these peripheral BODIPYs contribute to increase the absorption in this spectral region.

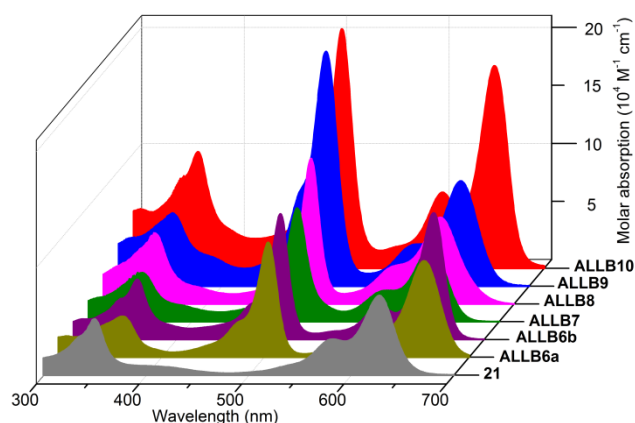


**Figure 5.14.** Absorption spectra of the all-BODIPY-based cassettes in diethyl ether ( $2 \mu\text{M}$ ). The corresponding spectrum of the isolated red-emitting dye **21** is also included.

All these assignments are reinforced by the theoretical simulations which predict that the molecular orbitals involved in the long-wavelength transition (HOMO  $\rightarrow$  LUMO) are placed exclusively in the central BODIPY (Figure 5.15). Moreover, the MOs responsible of the absorption in the green region are energetically close and located just at each peripheral BODIPY. The geometrical arrangement supports also the electronic isolation of the building blocks in the ground state and the broadband absorption, since the steric hindrance around the acceptor and donor connection (involving the *ortho* position of the *meso* aryl substituent with the adjacent positions 1 and 7 methylated) ensures an orthogonal fixed orientation between the aromatic fragment and the BODIPY core avoiding excitonic couplings.



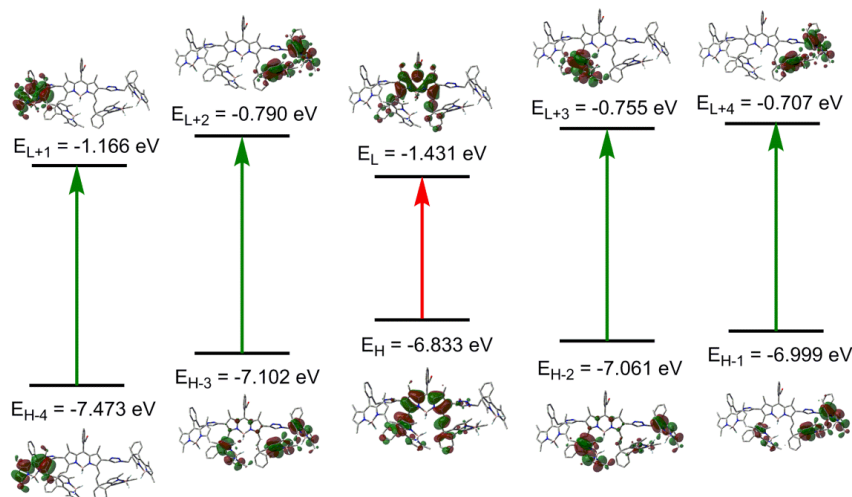


**Figure 5.15.** Theoretically predicted ( $\omega$ B97XD/6-31G<sup>\*</sup>) energy diagrams (in eV) of the molecular orbitals involved in the main visible transitions of the pentad **ALLB9**. The UV transition centered at 355 nm involves several configurations of molecular orbitals and it is not included for the sake of simplicity of the scheme.

In agreement with the aforementioned issues the fluorescence spectra of these cassettes, are composed by a single band in the red-edge at around 650-680 nm depending on the aromatic group grafted at positions 2 and 6, but regardless of the excitation wavelength. Indeed, the emission from the donors is almost residual with a fluorescence quantum yield lower than 1%. So, once again there is an efficient intramolecular EET (> 98% in all media and cassettes) from the peripheral BODIPY donors to the central  $\pi$ -extended BODIPY.

The fluorescence quantum yields are high (up to 0.69) at least in apolar media. Nevertheless, in compounds bearing the donor grafted at the styryl groups (all of them except **ALLB8**) this value decreases strongly when the solvent polarity increases (Table 5.3). Whereas the fluorescent efficiency ranges from 0.55 to 0.69 and the lifetime is around 4.5 ns in diethyl ether, the emission is almost negligible in the most polar media (Figure 5.16) and the fluorescence decay curves acquires a bi-exponential character with a main and fast component of few hundred picoseconds (Table 5.3). These results reveal that there is an effective non-radiative deactivation channel which can be ascribed to ICT. In fact, in Figure 5.15 it can observe that the transition between HOMO and LUMO implies certain charge transfer character, since there is an electronic density transfer from the aromatic substituents to the BODIPY upon excitation.

**Table 5.3.** Photophysical properties of all-BODIPY-based cassettes in diluted solutions (2  $\mu$ M) of apolar (diethyl ether, Et<sub>2</sub>O) and polar (methanol, MeOH) solvents.

ALLB	$\lambda_{ab}$ [nm]	$\epsilon_{max}$ [10 <sup>4</sup> M <sup>-1</sup> ·cm <sup>-1</sup> ]	$\lambda_{fl}$ [nm]	$\phi$	$\tau$ [ns]	
<b>6a</b>	Et <sub>2</sub> O	652.0	10.4	662.5	0.65	4.72
		501.5	10.6			
		361.5	5.3			
	MeOH	649.5	8.4	660.5	0.016	0.14 (97%)–0.47 (3%)
		500.5	9.3			
		360.5	4.9			
<b>6b</b>	Et <sub>2</sub> O	655.0	8.8	676.5	0.65	4.50
		604.0	10.2			
		361.5	4.0			
	MeOH	657.5	8.1	682.0	0.030	0.26 (99%)–1.81 (1%)
		503.5	9.7			
		361.5	4.0			
<b>7</b>	Et <sub>2</sub> O	632.5	7.2	654.5	0.54	4.39
		503.0	10.2			
		350.5	5.4			
	MeOH	629.0	7.0	651.0	0.024	0.22 (90%)–0.92 (10%)
		502.5	10.2			
		350.5	6.1			
<b>8</b>	Et <sub>2</sub> O	627.0	8.6	652.0	0.68	4.32
		502.5	13.6			
		349.5	6.8			
	MeOH	624.5	8.7	649.5	0.45	2.78
		502.0	12.8			
		347.5	7.2			
<b>9</b>	Et <sub>2</sub> O	633.5	9.0	657.5	0.69	4.25
		502.0	20.2			
		352.0	6.2			
	MeOH	631.0	9.5	655.5	0.042	0.44 (91%)–1.13 (9%)
		501.0	19.6			
		349.0	7.1			
<b>10</b>	Et <sub>2</sub> O	651.5	17.4	664.5	0.65	4.56
		503.0	20.6			
		362.0	10.0			
	MeOH	650.5	15.4	666.0	0.018	0.12 (77%)–0.48 (23%)
		501.5	20.0			
		362.0	8.8			

However, triad **ALLB8** shows lower dependence on the solvent polarity, as its fluorescence efficiency remains as high as 0.45 in polar methanol and, despite the fact that the lifetime decreases up to 2.78 ns in polar media, the decay curve maintains its mono-exponential character (see Figure 5.16 and Table 5.3). In this case the difference resides in the grafted position of the BODIPY donor units, since trimer **ALLB8** is the unique compound where the tetramethylated BODIPYs are linked at positions 2 and 6 (instead of at the 3,5-styryl groups like in the rest of the cases) of the central acceptor BODIPY. This finding supported that the functionalization of the styryl groups at positions 3 and 5 with BODIPY stabilizes the ICT process, since the isolated  $\pi$ -extended BODIPY with the same groups (isolated dye **21**) at these positions shows high fluorescence response in both polar

and apolar media<sup>[44]</sup>. Moreover, in compound **ALLB10** the urea spacer between acceptor units is also able to induce the ICT process due to its electron donor ability, as reported previously for similar symmetric bis-BODIPYs<sup>[45]</sup>. Therefore, both functional groups contribute to switch on ICT processes, becoming compound **ALLB10** the less fluorescent in polar media among all the cassettes herein studied (Figure 5.16 and Table 5.3).

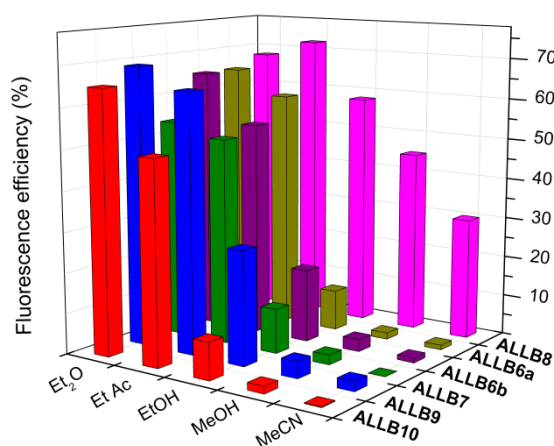


**Figure 5.16.** Fluorescence quantum yields of all the cassettes according to the solvent polarity.

As a consequence, the best choice to fulfill all the desirable features of an optimal photonic cassette is to extend the  $\pi$ -system through the positions 3 and 5 using styryl groups but without functionalizing them in order to ensure high fluorescence response in all media, regardless of its polarity. Therefore, grafting the BODIPY donor units at positions 2 and 6 appears as a suitable strategy to ensure broad and efficient light harvesting together with competitive EET to the final acceptor which emits bright light in all tested media regardless of the excitation spectral region.

### 5.3.2. Lasing properties

Taking into account the absorption properties of all-BODIPY-based compounds their lasing properties were studied under transversal pumping at 355 nm and 532 nm exhibiting similar results (Table 5.4). It is noteworthy that in this case the pumping conditions (8 mJ per pulse and 15 Hz, as pumping energy and repetition rate, respectively) were more drastic than those usually selected for the laser characterization of BODIPY dyes (5 mJ per pulse and 10 Hz)<sup>[46]</sup>. Owing to the high number of energy donors with strong absorption at the pumping wavelengths, the optimal concentration for the highest laser efficiency ranges from 0.09 to 2 mM, reducing the gain-media concentrations in

comparison to the isolated dye (**21**) and avoiding the aforementioned emission quenching due to aggregation processes.

**Table 5.4.** Lasing properties of all-BODIPY based cassettes in ethyl acetate pumped at 355 nm and 532 nm (shaded data). The corresponding data of the isolated red-emitting dye **21** under identical experimental conditions are also included for comparison purposes.

ALLB	$\lambda_{la}$ [nm]	%Eff	$E_{dose}^a)$ [GJ/mol]	$\lambda_{la}$ [nm]	%Eff	$E_{dose}$ [GJ/mol]
<b>21</b> <sup>b)</sup>	690.0	30	55			
<b>6a</b>	716.0	49	265	720.0	52	308
<b>6b</b>	704.0	50	294	710.0	47	342
<b>7</b>	700.0	53	327	703.0	51	388
<b>8</b>	699.0	58	445	705.0	62	524
<b>9</b>	710.0	65	843	715.0	68	993
<b>10</b>	722.0	56	938	730.0	57	1137

<sup>a)</sup> photostability, defined as the amount of pumping energy absorbed by the dye to retain 50% of its initial emission;

<sup>b)</sup> only pumped at 355 nm due to its low absorption at 532 nm.

As expected, their lasing emission signal is located in the red-edge (ranging from 700 nm to 730 nm) with high efficiency (up to 68%) and extremely ameliorated photostability values (up to 1150 GJ/mol). It is clear that the laser behavior of these antennae is improved compared to that exhibited by the corresponding acceptor component owing to the increased absorption ability at both pumping wavelengths. Moreover, the higher the number of BODIPY donor units, the higher the lasing efficiency and specially the photostability. In fact, pentad **ALLB9** and hexad **ALLB10**, each one comprising four BODIPY donor units, show an efficiency and photostability up to two- and 20-fold higher, respectively, than those recorded from the isolated red-emitting dye **21**, presenting the best laser behavior among all the cassettes herein tested (see Table 5.4 and Figure 5.17).

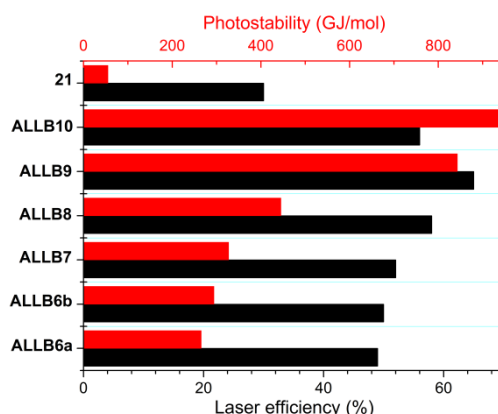


**Figure 5.17.** Lasing efficiency and photostability of all-BODIPY-based cassettes under pumping at 355 nm with respect to the isolated energy acceptor **21**.

All these outstanding lasing properties are achieved thanks to the increase absorption at the pumping wavelengths and the ulterior effective EET process which reduced the required energy doses to surpass the losses in the gain media. Besides, the not direct excitation of the final red-emitting energy acceptor further contributes to decrease the rate of the photodegradation processes. Thus, the rational design of these challenging multichromophoric BODIPY cassettes and the deep understanding of the structural factors ruling the complex relationship between the molecular structure and the photophysical properties allow the development of smart photonic materials as optimized molecular antennae or tunable dye lasers.

## Bibliography

- [1] Hewavitharanage, P.; Warshawsky, R.; Rosokha, S. V.; Vaal, J.; Stickler, K.; Bachynsky, D.; Jairath, N.; *Tetrahedron*, **2020**, *76*, 131515.
- [2] Azarias, C.; Russo, R.; Cupellini, L.; Mennucci, Jacquemin, D.; *Phys. Chem. Phys. Chem.*, **2017**, *19*, 6443-6453.
- [3] Balsukuri, N.; Manav, N.; Lone, M. Y.; Mori, S.; Das, A.; Sen, P.; Gupta, I.; *Dyes Pigm.*, **2020**, *176*, 108249.
- [4] Mirkovic, T.; Ostroumov, E. E.; Anna, J. M.; van Grondelle, R.; Govindjee, G.; Scholes, G. D.; *Chem. Rev.*, **2017**, *117*, 249-293.
- [5] Chenu, A.; Scholes, G. D.; *Annu. Rev. Phys. Chem.*, **2015**, *66*, 69-96.
- [6] Speiser, S.; *Chem. Rev.*, **1996**, *96*, 1953-1976.
- [7] Fan, J.; Hu, M.; Zhan, P.; Peng, X.; *Chem. Soc. Rev.*, **2013**, *42*, 29-43.
- [8] Albinsson, B.; Mårtensson, J.; *J. Photochem. Photobiol. C.*, **2008**, *9*, 138-155.
- [9] Dos Remedios, C. G.; Moens, P. D. J.; *J. Struct. Biol.*, **1995**, *115*, 175-185.
- [10] Medintz, I.; Hildebrandt, N.; *FRET-Förster Resonance Energy Transfer*, Wiley-VCH, Weinheim, 1<sup>st</sup> Ed., **2014**.
- [11] Curutchet, C.; Feist, F. A.; Van Aeverbeke, V.; Mennucci, B.; Jacob, J.; Müllen, K.; Basché, T.; Beljonne, D.; *Phys. Chem. Phys. Chem.*, **2010**, *12*, 7378-7385.
- [12] Cao, D.; Zhu, L.; Liu, Z.; Lin, W.; *J. Photochem. Photobiol. C.*, **2020**, *44*, 100371.
- [13] Benniston, A. C.; Harriman, A.; *Coord. Chem. Rev.*, **2008**, *252*, 2528-2539.
- [14] Bai, D.; Benniston, A. C.; Hagon, J.; Lemmetyinen, H.; Tkachenko, N. V.; Clegg, W.; Harrington, R. W.; *Phys. Chem. Phys. Chem.*, **2012**, *14*, 4447-4456.
- [15] Dutta, P. K.; Varghese, R.; Nangreave, J.; Lin, S.; Yan, H.; Liu, Y.; *J. Am. Chem. Soc.*, **2011**, *133*, 11985-11993.
- [16] Goryacheva, O. A.; Beloglazova, N. V.; Vostrikova, A. M.; Pozharov, M. V.; Sobolev, A. M.; Goryacheva, I. Y.; *Talanta*, **2017**, *164*, 377-385.
- [17] Saravanan, V.; Ganesan, S.; Rajakumar, P.; *RSC Adv.*, **2020**, *10*, 18390-18399.
- [18] Davis, J. L. K.; MacQueen, R. W.; Jones, S. T. E.; Orofino-Pena, C.; Cortizo-Lacalle, D.; Taylor, R. G. D.; Credgington, D.; Skabara, P. J.; Greenham, N. C.; *J. Mater. Chem. C.*, **2017**, *5*, 1952-1962.
- [19] Esnal, I.; Durán-Sampedro, G.; Agarrabeitia, A. R.; Bañuelos, J.; Gracia-Moreno, I.; Macías, M. A.; Peña-Cabrera, E.; López-Arbeloa, I.; de la Moya, S.; Ortiz, M. J.; *Phys. Chem. Phys. Chem.*, **2015**, *17*, 8239-8247.
- [20] Vohra, V.; Calzaferri, G.; Destri, S.; Pasini, M.; Porzio, W.; Botta, C.; *ACS Nano*, **2010**, *4*, 1409-1416.
- [21] Cerdán, L.; Enciso, E.; Martín, V.; Bañuelos, J.; López-Arbeloa, I.; Costela, A.; García-Moreno, I.; *Nat. Photonics*, **2012**, *6*, 621-626.
- [22] Durán-Sampedro, G.; Agarrabeitia, A. R.; García-Moreno, I.; Gartzia-Rivero, L.; de la Moya, S.; Bañuelos, J.; López-Arbeloa, I.; Ortiz, M. J.; *Chem. Commun.*, **2015**, *51*, 11382-11285.
- [23] Berlien, H. P.; Müller, G. J.; Breuer, H.; Krasner, N.; Okunata, T.; Sliney, D.; *Applied Laser Medicine*, Springer-Verlag, Berlin, 1<sup>st</sup> Ed., **2003**.
- [24] Zhao, Y.; Zhang, Y.; Lv, X.; Liu, Y.; Chen, M.; Wang, P.; Liu, J.; Guo, W.; *J. Mater. Chem.*, **2011**, *21*, 13168-13171.
- [25] Lin, W.; Yuan, L.; Cao, Z.; Feng, Y.; Song, J.; *Angew. Chem. Int. Ed.*, **2010**, *49*, 375-379.
- [26] El-Khouly, M. E.; Amin, A. N.; Zandler, M. E.; Fukuzumi, S.; D'Souza, F.; *Chem. Eur. J.*, **2012**, *18*, 5239-5247.
- [27] Kumar, S.; Thorat, K. G.; Ravikanth, M.; *J. Org. Chem.*, **2017**, *82*, 6568-6577.
- [28] Yonemoto, D. T.; Papa, C. M.; Mongin, C.; Castellano, F. G.; *J. Am. Chem. Soc.*, **2020**, *142*, 10883-10893.
- [29] Zhou, Z.; Qiao, C.; Wang, K.; Wang, L.; Liang, J.; Peng, Q.; Wei, Z.; Dong, H.; Zhang, C.; Shuai, Z.; Yan, Y.; Zhao, Y. S.; *Angew. Chem. Int. Ed.*, **2020**, *59*, 2-8.
- [30] Chen, X. K.; Kim, D.; Brédas, J. L.; *Acc. Chem. Res.*, **2018**, *51*, 2215-2224.

- [31] Zhao, J.; Xu, K.; Yang, W.; Zhong, F.; *Chem. Soc. Rev.*, **2015**, 44, 8904-8939.
- [32] de Vetta, M.; González, L.; Corral, I.; *ChemPhotoChem.*, **2019**, 3, 727-738.
- [33] Liang, X.; Tu, Z. L.; Zheng, Y. X.; *Chem. Eur. J.*, **2019**, 25, 5623-5642.
- [34] Nguyen, V. N.; Kumar, A.; Lee, M. H.; Yoon, J.; *Coord. Chem. Rev.*, **2020**, 425, 213545.
- [35] Oh, C. S.; Sa Pereira, D.; Han, H.; Park, H. J.; Higginbotham, H. F.; Monkman A. P.; Lee, J. Y.; *ACS Appl. Mater. Interfaces*, **2018**, 10, 35420-35429.
- [36] Deng, C.; Zheng, S.; Wang, D.; Yang, J.; Yue, Y.; Li, M.; Zhou, Y.; Niu, S.; Tao, L.; Tsuboi, T.; Zahng, Q.; *J. Phys. Chem. C.*, **2019**, 49, 29875-29883.
- [37] Chen, D.; Rajamalli, P.; Tenopala-Carmona, F.; Carpenter-Warren, C. L.; Cordes, D. B.; Keum, C. M.; Slawin, A. M. Z.; Gather, M. C.; Zysman-Colman, E.; *Adv. Opt. Mater.*, **2020**, 8, 1901283.
- [38] Chen, J. X.; Tao, W. W.; Xiao, Y. F.; Wang, K.; Zhang, M.; Fna, X. C.; Chen, W. C.; Yu, J.; Li, S.; Geng, F. X.; Zhang, X. H.; Lee, C. S.; *ACS Appl. Mater Interfaces*, **2019**, 32, 29086-29093.
- [39] Castiglioni, F.; Lanzani, G.; Mele, A.; Monguzzi, A.; Passarello, M.; Ruggirello, A.; Scotognella, F.; Liveri, V. T.; *J. Mater. Sci.*, **2011**, 46, 6402-6407.
- [40] Zhang, B.; Soleimaninejad, H.; Jones, D. J.; White, J. M.; Ghiggino, K. P.; Smith, T. A.; Wong, W. W. H.; *Chem. Mater.*, **2017**, 29, 8395-8403.
- [41] López-Arbeloa, F.; López-Arbeloa, T.; López-Arbeloa, I.; *Handbook of Advanced Electronic and Photonic Materials and Devices*, Academic, New York, Ed. Nalwa, H. S., 7, 209-245, **2001**.
- [42] Esnal, I.; Valois-Escamilla, I.; Gómez-Durán, C. F. A.; Urías-Benavides, A.; Betancourt-Mendiola, M. L.; López-Arbeloa, I.; Bañuelos, J.; García-Moreno, I.; Costela, A.; Peña-Cabrera, E.; *ChemPhysChem.*, **2013**, 14, 4134-4142.
- [43] Gómez-Durán, C. F. A.; Esnal, I.; Valois-Escamilla, A.; Urías-Benavides, A.; Bañuelos, J.; López-Arbeloa, I.; García-Moreno, I.; Peña-Cabrera, E.; *Chem. Eur. J.*, **2016**, 22, 1048-1061.
- [44] Rohand, T.; Qin, W.; Boens, N.; Dehaen, W.; *Eur. J. Org. Chem.*, **2006**, 4658-4663.
- [45] López, J. C.; del Rio, M.; Oliden, A.; Bañuelos, J.; López-Arbeloa, I.; García-Moreno, I.; Gómez, A. M.; *Chem. Eur. J.*, **2017**, 23, 17511-17520.
- [46] Cerdán, L.; Costela, A.; Gracia-Moreno, I.; Bañuelos, J.; López-Arbeloa, I.; *Laser Phys. Lett.*, **2012**, 9, 426-433.





---

## Conclusions

---

We have demonstrated that BODIPYs are suitable scaffolds to develop modern, versatile and applied fluorophores. In this regard the rational design of the molecular structure is a key factor to successfully cover a wide assortment of different applications ranging from lasers, chiroptics and light harvesters to fluorescent probes and sensors, as well as photosensitizers for biophotonics. In each case, it is essential to understand the photophysical phenomena (energy and electron transfer, electronic coupling, excitonic interactions) induced by the molecular pattern which opens the door to improve their performance and supply the required application.

Hereafter, we briefly detail the main conclusions derived from this thesis:

- *N*-BODIPYs are an appealing approach not only by their high chemical versatility for post-functionalization, but also owing to their notable laser performance. Moreover, those compounds bearing spiranic cycles are able to improve the laser performance and emit in the solid state. In contrast, electron rich moieties at the boron center are able to induce electron transfer processes that quench efficiently the emission output, but enable their use as on-off fluorescent switches for the sensing of cations.

- Benzofuran-fused BODIPYs and polyarylated aza-BODIPYs are suitable strategies to achieve red and NIR dye lasers, endowed with improved efficiency and more long-lasting emission than the commercially available ones in each spectral window. In contrast to *F*-BODIPYs, the chemical modification around the boron atom of aza-BODIPYs is detrimental for the photostability.
- The labeling of carbohydrates with BODIPY is an effective way to achieve fluorescent probes for bioimaging with improved water solubility (up to concentrations around 0.1 mM, without no sign of aggregation), one of the main drawbacks of these dyes, while keeping the characteristic high fluorescence response of the dye.
- The linkage of unsaturated esters to the BODIPY leads to ratiometric and colorimetric sensor to monitor and visualize the presence of thiolated amino acids, providing up to three detection channels for their quantitative sensing even at low concentrations (down to micromolar).
- The covalent dimerization of BODIPYs involving their *meso* position is an effective alternative to design halogen-free photosensitizers to generate singlet oxygen for therapy, thanks to the triplet state population mediated by the induced charge transfer between the chromophoric subunits.
- The stereochemical properties of the tartaric bridge and the alkylation degree of the BODIPY fragments allow fine-tuning the intramolecular excitonic interactions in bis-BODIPYs. Thus, an enantiomeric spacer provides chiroptical response and emission from J-aggregates and excimers, whereas the diastereoisomeric one suppresses such coupling yielding efficient laser signal.
- The molecular assembly of suitable dyes improves the photonic properties of single dyes in terms of broadband absorption and improved photostability mediated by efficient energy transfer processes. Therefore, light harvesting arrays with long-wavelength and long-lasting bright laser emission are recorded from these multichromophoric dyes. It is noteworthy the remarkable increase on both the laser efficiency and especially photostability as the number of energy donors in the assembly increases.

---

## Outlook

---

Albeit one can think that the chemistry of the BODIPY is fully exploited in view of the huge number of publications dealing with this dye, much work is still pending to fully explore the potential of these modern and chameleonic dyes for advanced photonic applications. Hereafter, we briefly describe some of the challenges related with the thesis that we are currently exploring.

- The chemical modification at the boron atom with amino (*N*-BODIPYs) and carboxylic acids (*COO*-BODIPYs) adds further versatility to the BODIPY, since it increases the attachable amounts of functional groups. For instance, specific groups for the selective recognition of biomolecules or organelles can be attached for bioimaging and therapy. Furthermore, even chromophores can be easily appended to access multichromophoric architectures ongoing energy or electron transfer processes.
- The red and NIR emitting BODIPYs are ideal tags for fluorescent labeling of carbohydrates. Related with the chemistry of carbohydrates we are working to further increase the water solubility of BODIPYs keeping their fluorescence response in the red-edge. Moreover, we are testing crystalline nanocellulose as scaffold to modulate the photonic performance of some commercial dyes such as Nile Blue, Rhodamine 6G and LDS 722. In fact, some of these preliminary results have been recently published in the journal "Advanced Photonics Research", during the redaction of the thesis. This scaffold allows a fine control of the photophysics of the dye depending on the electrostatic interaction between them.

- Regarding the photosensitizers we are designing new dimers and trimers directly linked but testing different linkage positions with the aim of modulating the balance between fluorescence and triplet state populations. The purpose is to know which structural factors favor the singlet oxygen generation and which ones allow to attain dual response for theragnosis. This would allow to gather deeper insight about the challenging and complex mechanism allowing the population of the triplet manifold from the ongoing charge transfer process.
- Multichromophoric dyes can be considered as a new generation of fluorophores which improve the performance of the corresponding single dyes and where new and exotic intramolecular photophysical processes can be switched on. Besides, there is a plethora of chromophoric building blocks that can be combined through different spacers and at different linkage positions. Thus, further work is in progress to design new molecular assemblies to improve the laser performance of commercially available dyes. In fact, some of these preliminary results have been recently published, during the redaction of the thesis, in the journal "Chemical Communications" where the aforementioned COO-BODIPYs are used as platform to easily access multichromophoric assemblies ongoing energy transfer processes.
- The recently observed delayed fluorescence in aza-BODIPY-BODIPY under hard irradiation regimes opens the door to the study of new excited state dynamics almost unexplored hitherto. We are in close collaboration with a research group of CSIC to implement advanced time resolved techniques to study such complex light-induced photophysical processes.
- Finally, we are setting the basis of future collaborations with research groups specialized in biology and biochemistry for the in vitro and in vivo evaluation of the fluorescent probes, sensors and photosensitizers for diagnosis, therapy and theragnosis in biomedicine. To this aim we are currently working with a research group from Universidad de Alcalá. Indeed, we have recently submitted a manuscript to "Chemical Communications" dealing with the ability of formylated BODIPYs (in particular the precursors of the BODIPYs tested in Chapter 3 for biophotonics) as neutral fluorescent probes for selective tracking of mitochondria by bioimaging under the confocal fluorescence microscope.

# List of Publications

---

## ANNEXES / ERANSKINAK

### Annex I (Chapter 1) / I. Eranskina (1go Kapituluua)

Article 1 / 1go Artikulua: *Chem. Eur. J.*, **2017**, 23, 9383-9390

### Annex II (Chapter 2) / II. Eranskina (2. Kapituluua)

Article 2 / 2. Artikulua: *J. Org. Chem.*, **2019**, 84, 2523-2541

Article 3 / 3. Artikulua: *ChemPhotoChem*, **2019**, 3, 75-85  
and its corresponding front cover (2/2019)

### Annex III (Chapter 3) / III. Eranskina (3. Kapituluua)

Article 4 / 4. Artikulua: *Chem. Eur. J.*, **2020**, 26, 5388-5399  
and its corresponding front cover (24/2020)

Article 5 / 5. Artikulua: *Org. Lett.*, **2019**, 21, 4563-4566

### Annex IV (Chapter 4) / IV. Eranskina (4. Kapituluua)

Article 6 / 6. Artikulua: *Chem. Eur. J.*, **2018**, 24, 3802-3815

### Annex V (Chapter 5) / V. Eranskina (5. Kapituluua)

Article 7 / 7. Artikulua: *Chem. Eur. J.*, **2020**

Article 8 / 8. Artikulua: *Phys. Chem. Chem. Phys.*, **2017**, 19, 13210-13218

Article 9 / 9. Artikulua: *Chem. Eur. J.*, **2019**, 25, 14959-14971

Apart from the published articles presented in the annex and included in the thesis report, the work carried out during the period of the thesis has also yielded other publications.

**Articles not included in the thesis report:**

1. Sola-Llano, R.; Jiménez, J.; Avellanal-Zaballa, E.; Johnson, M.; Cabrerros, T. A.; Moreno, F.; Maroto, B. L.; Muller, G.; Bañuelos, J.; Cerdán, L.; García-Moreno, I.; de la Moya, S.; "BOPHYs versus BODIPYs: A comparison of their performance as effective multi-function organic dyes", *Dyes Pigm.*, **2019**, 170, 107662.
2. Ray, C.; Schad, C.; Avellanal-Zaballa, E.; Moreno, F.; Maroto, B. L.; Bañuelos, J.; García-Moreno, I.; de la Moya, S.; "Multichromophoric COO-BODIPYs: an advantageous design for the development of energy transfer and electron transfer systems", *Chem. Commun.*, **2020**, 56, 13025-13028.
3. Avellanal-Zaballa, E.; Gartzia-Rivero, L.; Bañuelos, J.; García-Moreno, I.; Agarrabeitia, A. R.; Peña-Cabrera, E.; Ortiz, M. J.; "A Palette of Efficient and Stable Far-Red and NIR Dye Lasers", *Appl. Sci.*, **2020**, 20, 6206.
4. Avellanal-Zaballa, E.; Bañuelos, J.; Manzano, H.; Chiara, J. L.; Cerdán, L.; García-Moreno, I.; "Taming the photonic behavior of laser dyes through specific and dynamic self-assembly onto cellulose nanocrystals", accepted in *Adv. Photonics Res.*, doi: 10.1002/adpr.202000107.

**Chapter in a book:**

1. Sola-Llano, R.; Avellanal-Zaballa, E.; Bañuelos, J.; Gómez-Durán, C. F. A.; Belmonte-Vázquez, J. L.; Peña-Cabrera, E.; "Dyes: Towards Fluorescence Standards across the Visible Spectral Region", in *Photochemistry and Photophysics: Fundamentals to Applications*, edited by S. Saha and S. Mondal, IntechOpen, London, **2018**.

**Publications in Basque as scientific dissemination articles:**

1. Avellanal-Zaballa, E.; Esnal, I.; Bañuelos, J.; "Ikusgai-eremu elektromagnetiko osoan zehar igorpen sintonizagarria duten BODIPY laser-koloratzaileak", *EKAIA*, **2018**, 33, 97-114.
2. Avellanal-Zaballa, E.; Bañuelos, J.; "Koloratzaile-laserra, ezinbesteko argi iturria eguneroko bizitzan", *EKAIA*, **2018**, 34, 243-260.
3. Avellanal-Zaballa, E.; Bañuelos, J.; "Luminiszentzia, baliabide aproposa ioien eta biomolekulen presentzia agerian jartzeko", *EKAIA*, **2020**, 38, 215-230.





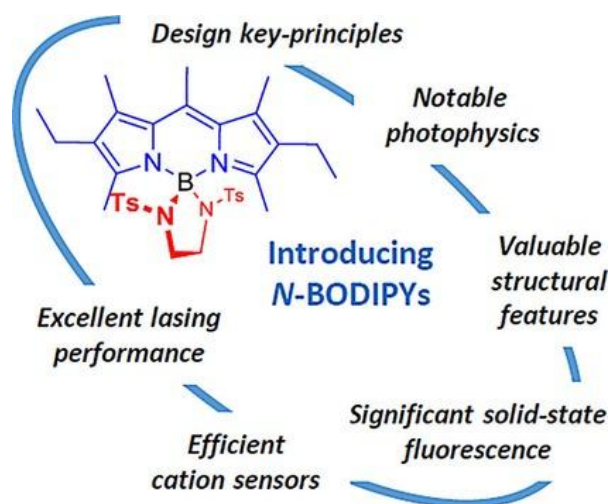
# Annex I (Chapter 1) / I. Eranskina (1go Kapituluua)

---

## Article 1 / 1go Artikuluua

N-BODIPYs Come into Play: Smart Dyes for Photonic Materials

*Chemistry - A European Journal*, 2017, 23, 9383-9390





## Dyes/Pigments

## N-BODIPYs Come into Play: Smart Dyes for Photonic Materials

César Ray,<sup>[a]</sup> Laura Díaz-Casado,<sup>[a]</sup> Edurne Avellanal-Zaballa,<sup>[b]</sup> Jorge Bañuelos,<sup>[b]</sup>  
Luis Cerdán,<sup>[a, c]</sup> Inmaculada García-Moreno,<sup>[c]</sup> Florencio Moreno,<sup>[a]</sup> Beatriz L. Maroto,<sup>[a]</sup>  
Íñigo López-Arbeloa,<sup>[b]</sup> and Santiago de la Moya<sup>\*[a]</sup>

**Abstract:** *N*-BODIPYs (diaminoboron dipyrromethenes) are unveiled as a new family of BODIPY dyes with huge technological potential. Synthetic access to these systems has been gained through a judicious design focused on stabilizing the involved diaminoboron chelate. Once stabilized, the obtained *N*-BODIPYs retain the effective photophysical behavior exhibited by other boron-substituted BODIPYs, such as *O*-BODIPYs. However, key bonding features of nitrogen compared to those of oxygen (enhanced bond valence and different bond directionality) open up new possibilities for functionalizing BODIPYs, allowing an increase in the number of pendant moieties (from two in *O*-BODIPYs, up to four in *N*-BODIPYs) near the chromophore and, therefore, greater control of the photophysics. As a proof of concept, the fol-

lowing findings are discussed: (1) the low-cost and straightforward synthesis of a selected series of *N*-BODIPYs; (2) their outstanding photophysical properties compared to those of related effective dyes (excellent emission signatures, including fluorescence in the solid state; notable lasing capacities in the liquid phase and when doped into polymers; improved laser performance compared to the parent *F*-BODIPYs); (3) the versatility of the diaminoboron moiety in allowing the generation of multifunctionalized BODIPYs, permitting access to both symmetric and asymmetric dyes; (4) the capability of such versatility to finely modulate the dye photophysics towards different photonic applications, from lasing to chemosensing.

## Introduction

BODIPYs (boron dipyrromethenes; 4-bora-3a,4a-diaza-s-indacenes) constitute one of the most valuable families of technological dyes.<sup>[1–10]</sup> Nowadays, there is a plethora of available synthetic procedures for their direct functionalization, focused on appropriate modulation of key physical (mainly photophysical) properties.<sup>[6,8,11–15]</sup> These transformations usually involve the BODIPY dipyrin moiety and well-established chemical reactions, such as nucleophilic and electrophilic aromatic substitutions, metal-catalyzed cross-couplings or enol-like condensations, among others (blue in Figure 1).<sup>[16–20]</sup> This ample reactivi-

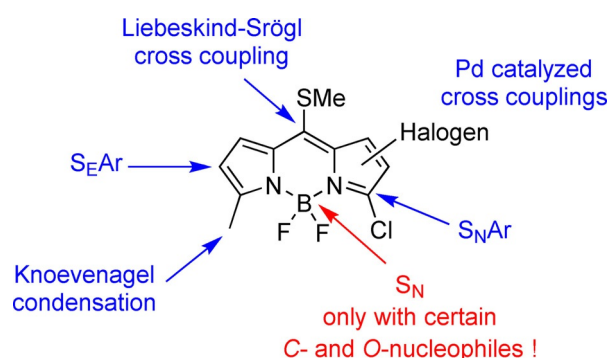


**Figure 1.** Some useful chemical transformations in BODIPY dyes. In red, functionalizations at boron reported to date.

ty allows the derivatization of BODIPYs at their dipyrin moieties with a great variety of pendant functional groups. However, less synthetic diversity is found when directly functionalizing BODIPYs at boron<sup>[21–36]</sup> (red in Figure 1), although such functionalization allows the facile preparation of dyes with enhanced photostability for lasing,<sup>[21–24]</sup> with improved water solubility for biological applications,<sup>[25–27]</sup> with boosted energy-transfer processes for efficient light collection,<sup>[19,28–31,33]</sup> or with enhanced chiral perturbation enabling circularly polarized luminescence,<sup>[32–36]</sup> among other valuable properties.

Remarkably, all reported protocols to directly functionalize BODIPYs at boron with key pendant functionalities have hitherto been based only on nucleophilic substitutions with certain

[a] C. Ray, L. Díaz-Casado, Dr. L. Cerdán, Prof. Dr. F. Moreno, Prof. Dr. B. L. Maroto, Prof. Dr. S. de la Moya  
Departamento de Química Orgánica I, Facultad de CC. Químicas  
Universidad Complutense de Madrid  
Ciudad Universitaria s/n, 28040 Madrid (Spain)  
E-mail: santmoya@ucm.es

[b] E. Avellanal-Zaballa, Prof. Dr. J. Bañuelos, Prof. Dr. Í. López-Arbeloa  
Departamento de Química Física  
Universidad del País Vasco-EHU  
Apartado 644, 48080 Bilbao (Spain)

[c] Dr. L. Cerdán, Prof. Dr. I. García-Moreno  
Departamento de Sistemas de Baja Dimensionalidad, Superficies y Materia  
Condensada, Instituto de Química-Física Rocasolano  
CSIC Serrano 119, 28006 Madrid (Spain)

Supporting information, which includes full experimental details, and the ORCID identification number for the author of this article can be found under <https://doi.org/10.1002/chem.201701350>.

C- and O-moieties under specific reaction conditions,<sup>[21–36]</sup> yielding the corresponding respective C- and O-BODIPYs (i.e., BODIPYs having boron–carbon or boron–oxygen bonds). Such a low variety of BODIPYs functionalized at boron (only *halogen*-, *O*-, and C-BODIPYs are currently available) can be explained by a key factor, namely the decrease in stability of the dyes that stems from substitution of the highly electronegative fluorine atoms in the parent *F*-BODIPY frameworks. Thus, the absence of fluorine atoms significantly increases the electron density at the boron center, lowering its Lewis acidity and diminishing its capability to be chelated by the dipyrin moiety. This drawback has been solved in stabilized C- and O-BODIPYs by using sufficiently electron-poor C- and O-moieties, such as aryl,<sup>[23]</sup> alkenyl,<sup>[23]</sup> alkynyl,<sup>[21,23,25–28]</sup> aryloxy,<sup>[29,32–36]</sup> or acyloxy<sup>[22,24]</sup> units, even bearing additional electron-withdrawing groups in some cases.<sup>[21,25–27,36]</sup>

To expand the applicability of BODIPY dyes, efforts should be made to increase the range of boron-substituted BODIPYs. In this sense, the specific structural and electronic features of nitrogen, intermediate between those of carbon and oxygen, make access to hitherto unknown diaminoboron dipyrromethenes (*N*-BODIPYs) particularly interesting. Thus, the photophysical properties of stabilized *N*-BODIPYs should be similar to those of related *O*-BODIPYs (e.g., significant fluorescence would be expected). However, the distinct key bonding features of nitrogen compared with those of oxygen (enhanced bond valence and different bond directionality) should open up new possibilities for functionalizing BODIPY dyes, allowing an increase in the number of pendant moieties near the BODIPY chromophore (from two in *O*-BODIPYs, up to four different residues in *N*-BODIPYs). Such versatile and multiple functionalization is of great interest for achieving a smarter modulation of the BODIPY photophysics, which should increase the applicability of these dyes as advanced photonic platforms.

In view of their technological relevance, as well as the relative ease with which *O*- and C-BODIPYs may be synthesized by means of straightforward nucleophilic substitutions, there is a striking lack of reported *N*-BODIPY dyes. We hypothesize that this unavailability must be attributed to the lack of specific protocols/designs to properly stabilize the diaminoboron chelate. In this sense, simply compensating the charge redistribution by means of modulating key electronic effects in the boron moiety may not be enough to achieve chemical stability, and specific steric and/or reactive factors imposed by the nitrogen-based pendant functionalities must also be taken into account (note the structural and reactive differences between related moieties based on carbon, nitrogen, or oxygen, for example, C=C–B versus C=N–B, the latter expected to be highly reactive towards nucleophiles).

To support this hypothesis, we report here the synthesis, structural features, photophysics, lasing behavior, and workability as sensors of an unprecedented library of *N*-BODIPYs. Through its deep analysis, the impact of the key versatile *N*-substitution pattern (symmetric vs. asymmetric, rigid and closed vs. more flexible open structures) on the stabilization of the resulting BODIPY dyes and, consequently, on their photonic behavior, has been rigorously delineated.

## Results and Discussion

### Synthesis of *N*-BODIPYs

An *N,N'*-ditosylated diamine moiety based on ethylenediamine (in red in Figure 2) was chosen to confirm the hypothesis of obtaining the first *N*-BODIPY by stabilizing the corresponding diaminoboron complex. Thus, the reduced electron-donating

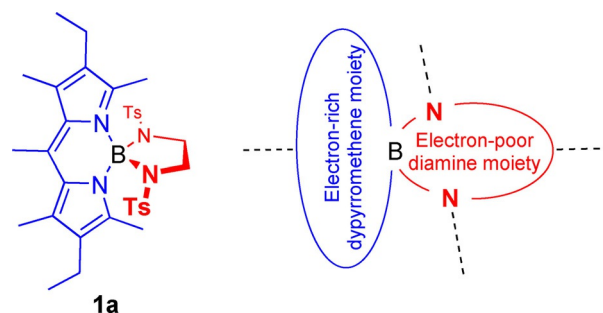


Figure 2. Electronically stabilized spiranic design for achieving *N*-BODIPYs.

ability of the relevant nitrogen atoms caused by the tosyl substitution was expected to generate a diaminoboron moiety (in red in Figure 2) with sufficient Lewis acidity as to be efficiently chelated by the dipyrin ligand (in blue in Figure 2). With the same purpose, a dipyrromethene electronically enriched with alkyl groups (in blue in Figure 2) was selected as the chelating ligand. Besides, the orthogonal spiranic design of **1 a**, based on ethylenediamine, should also improve the stability of the final boron complex by minimizing steric hindrances, as well as its fluorescence by diminishing conformational flexibility, as shown below. Finally, the selection of an amine-based diaminoboron moiety (C–N–B) instead of an imine-based one (C=N–B) is crucial, not only to allow *N*-tosyl functionalization, but also to improve the chemical robustness of the diaminoboron moiety.

On the basis of the above design, *N*-BODIPY **1 a** could be straightforwardly prepared (75% isolated yield) from the parent *F*-BODIPY (the commercially available PM567 dye) and commercial *N,N'*-ditosylethylenediamine by a simple one-pot nucleophilic *F*-substitution promoted by boron trichloride (Figure 3).<sup>[37]</sup>

Based on **1 a**, a selected library of stabilized *N*-BODIPYs (**1** in Figure 4) could be straightforwardly obtained following the

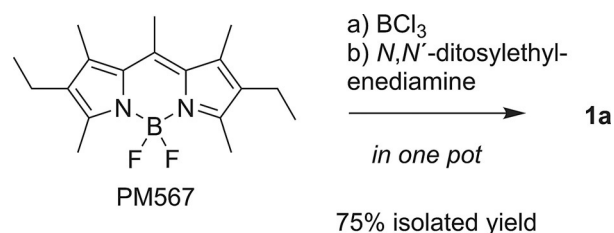
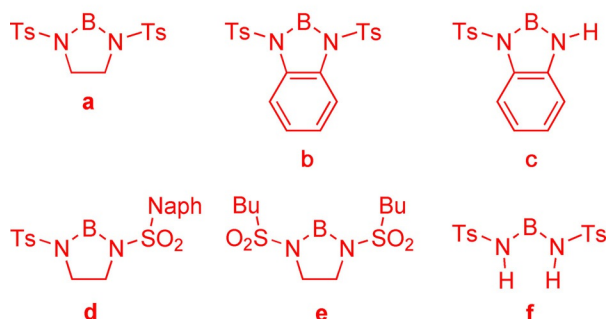
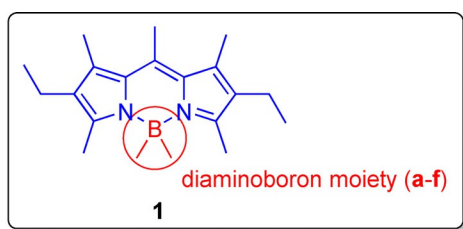


Figure 3. Synthesis of *N*-BODIPYs from commercially available starting materials (exemplified for **1 a**). See the Supporting Information for experimental details.



**Figure 4.** Developed library of *N*-BODIPYs (Ts = *p*-toluenesulfonyl (tosyl), Naph = 2-naphthyl, Bu = butyl).

same procedure (Figure 4). This series was judiciously chosen to corroborate the stabilization strategy and to test the amenability of the new BODIPY design to fine modulation of its photophysics through different functionalization of the diaminoboron nitrogen atoms. Thus, different *N,N'*-difunctionalized (**1 f**), *N,N,N'*-trifunctionalized (**1 c**), and *N,N,N',N'*-tetrafunctionalized (**1 a**, **1 b**, **1 d**, and **1 e**) *N*-BODIPYs, having different structural designs (symmetric vs. asymmetric, spiranic vs. more flexible open structures, etc.), were obtained. A consistent feature is sulfonamide units attached to the boron atom, so that the electron-donor character of the nitrogen atoms is minimized, stabilizing the final *N*-BODIPY (diaminoboron chelate). Indeed, we have confirmed that analogous *N*-BODIPYs based on electron-rich diamines (e.g., simple ethylenediamine) cannot be prepared under the same conditions. It should be noted here that both aryl sulfonamide and alkyl sulfonamide moieties can be used for this stabilizing purpose (see, for example, **1 a** and **1 e**, respectively), which broadens the range of possibilities for BODIPY functionalization. Benzo-fused derivatives (**1 b** and **1 c**) can also be efficiently obtained. On the other hand, the open (non-spiranic) *N*-BODIPY **1 f** proved to be less stable than its

spiranic analogue **1 a** (although it could nevertheless be prepared and isolated; see the Supporting Information). This fact highlights the importance of the initially proposed spiranic design to properly stabilize the involved diaminoboron chelate. These results confirmed our starting hypothesis: simply compensating the charge redistribution by means of modulating electronic factors (inductive effects of the involved dipyrin and boron moieties) is not sufficient to achieve chemical stability in *N*-BODIPYs, and specific steric or/and reactive factors imposed by the nitrogen centers must also be taken into account.

### Photophysical properties

A comprehensive computationally-aided photophysical study based on conventional steady-state and time-resolved UV/Vis spectroscopies was performed on the newly synthesized *N*-BODIPYs (Table 1; Table S1 and Figure S1 in the Supporting Information). Compounds **1 a**, **1 d**, **1 e**, and **1 f** maintain the excellent photophysical signatures of the parent PM567,<sup>[16]</sup> which are also almost independent of the solvent used (polarity and protic character; Table S1). Replacement of the strongly electronegative fluorine atoms by sulfonated amine groups results in a slight bathochromic shift of the spectral bands (by around 10 nm) and a modest reduction of the absorption probability. This correlates with the decrease in the radiative rate constant, as reflected in longer lifetimes (Table 1). In this sense, the spiranic design of **1 a**, **1 d**, and **1 e** restricts the conformational flexibility of the molecules, lowering the probability of non-radiative relaxation channels from the excited state. In contrast, one may expect a higher flexibility and, in turn, a lower fluorescent capability, in the non-spiranic compound **1 f**.<sup>[29]</sup> However, the size of the tosyl groups and the steric hindrance exerted by the methyl groups at BODIPY positions 3 and 5 suffice to hamper the conformational freedom of this compound. In fact, the geometries optimized on the basis of density functional theory (DFT) for **1 a**, **1 d**, **1 e**, and **1 f** (not shown) reveal an orthogonal arrangement between the diaminoboron and dipyrin moieties (especially if they are grafted spiranically), leaving the tosyl groups held apart from the dipyrin backbone. This disposition is in good agreement with the solid-state geometry determined experimentally by X-ray

**Table 1.** Photophysical properties of *N*-BODIPYs dissolved in ethyl acetate. Full photophysical data in different solvents are listed in Table S1. For comparison purposes, photophysical data of commercial PM567 are also included.

Dye	$\lambda_{ab}^{[a]}$ [nm]	$\epsilon_{max}^{[b]}$ [ $M^{-1} cm^{-1}$ ]	$\lambda_{fl}^{[c]}$ [nm]	$\phi^{[d]}$	$\tau^{[e]}$ [ns]	$k_r^{[f]}$ [ $10^8 s^{-1}$ ]	$k_{nr}^{[g]}$ [ $10^8 s^{-1}$ ]
PM567	517.0	76 000	533.0	0.84	5.78	1.45	0.28
<b>1 a</b>	526.5	65 000	543.5	0.83	7.65	1.08	0.22
<b>1 b</b>	529.0	43 000	546.5	0.009	0.011 (99%) 5.84 (1%)	–	–
<b>1 c</b>	524.5	25 000	540.5	0.004	–	–	–
<b>1 d</b>	527.0	63 000	544.5	0.80	7.70	1.03	0.27
<b>1 e</b>	523.5	50 000	540.5	0.80	7.19	1.11	0.28
<b>1 f</b>	528.0	59 000	547.0	0.76	7.64	1.00	0.31

[a] Absorption maximum wavelength. [b] Molar extinction coefficient at maximum. [c] Fluorescence maximum wavelength. [d] Fluorescence quantum yield. [e] Fluorescence lifetime. [f] Radiative decay rate. [g] Non-radiative decay rate.

diffraction analysis for **1a** (see Figures S2 and S3 and Table S2 in the Supporting Information).

Notably, *N*-BODIPYs **1a**, **1d**, **1e**, and **1f** also display significant fluorescence in the solid state (Figure 5; Figure S4). In particular, **1a** in the crystalline state shows an absolute quantum yield of around 3% (see the Supporting Information for experimental details). The corresponding fluorescence peaks are

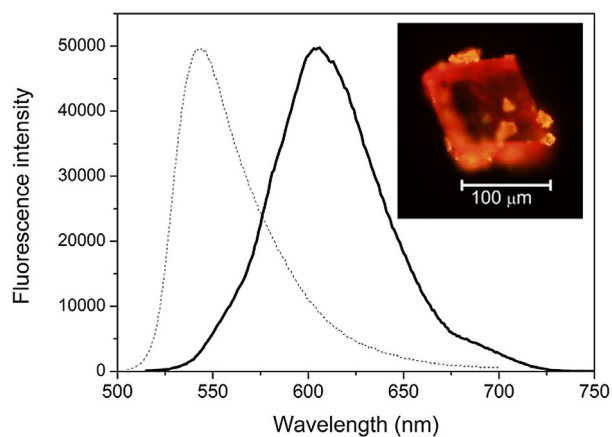


**Figure 5.** Fluorescence image of a representative crystal of **1a** and its fluorescence spectrum in the solid state (bold line) upon irradiation at 470 nm. The corresponding spectrum recorded from a diluted solution of **1a** in ethyl acetate (dashed line) is included to account for the influence of the solid environment and the role of the re-absorption/re-emission phenomena (very important due to the large size of the crystal), as well as to rule out chromophoric aggregation within the crystal. See the Supporting Information for experimental details.

bathochromically shifted by 50–60 nm with respect to those in solution. The absence of new spectral features suggests that these shifts are not due to aggregate formation, but to the presence of strong re-absorption/re-emission effects, owing to their short Stokes shifts (around  $600\text{ cm}^{-1}$ ; similar to those exhibited by common BODIPYs; see Table S1). The valuable fluorescent ability of these compounds in the solid state may also be explained in terms of their exceptional structures. Thus, the X-ray crystal structure of **1a** (Figures S2 and S3 in the Supporting Information) shows the tosyl groups disposed in a cross-like arrangement, one in front of the dipyrromethene moiety and the other one behind, depending on the orientation of the ethyl groups present. Such a disposition of the bulky tosyl groups leads to a crystalline packing in which the dipyrin chromophores are far away from one another (Figure S3), avoiding chromophoric interactions and aggregations, and causing **1a** to display a significant fluorescence response in the solid state.

Unlike the opening of the spiranic ring, which proved to have negligible effect on the photophysics, the fusion of a benzene ring to the spiranic diazaboracycle (see compounds **1b** and **1c**) led to a reduction in the absorption probability and an almost complete quenching of the emission, which was more noticeable for asymmetric **1c** (Table 1). Besides, the fluorescence decay curve of **1b** acquires a bi-exponential character, with the main contribution from the short-lifetime compo-

nent (around 100 ps; the weak fluorescence of **1c** hinders full analysis of the decay curve). The origin of this drastic reduction in fluorescence might be the electron-donor capability of the amine group grafted to the boron atom, which should be stronger upon its arylation and even more so after removal of one tosyl unit. A similar fluorescence quenching has been reported in a related, catechol-based *O*-BODIPY.<sup>[38]</sup> Indeed, theoretical calculations based on DFT point to a photoinduced electron transfer (PET) process as being responsible for the fluorescence quenching. As can be appreciated in Figure 6, the

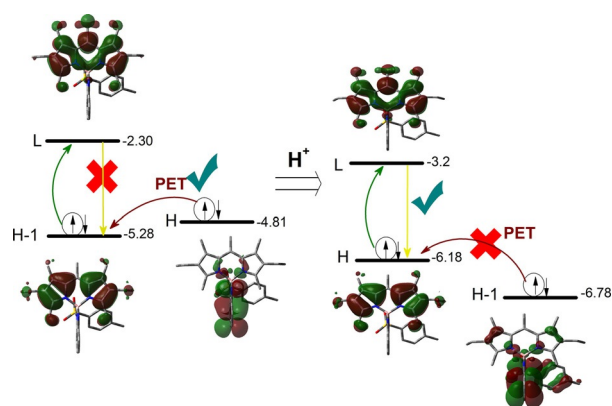


**Figure 6.** Computationally aided energy diagram (in eV) of the molecular orbitals involved in the absorption/fluorescence electronic transitions, as well as in the quenching PET pathway, for **1c** and its amino-protonated form.

HOMO–1 and LUMO of compound **1c**, responsible for the absorption and emission transitions under visible excitation, are located entirely on the BODIPY core, whereas the HOMO is centered almost entirely on the diamino fragment anchored to the boron atom.

Thus, upon photoinduced promotion of an electron from the HOMO–1 to the LUMO, an electron transfer (PET) from the HOMO to the semi-vacant low-lying HOMO–1 is thermodynamically feasible. Such a reductive PET from the monotosylated amines to the BODIPY core avoids radiative deactivation from the LUMO back to the HOMO–1, explaining the almost negligible fluorescence response of **1c**. However, in symmetric **1b** the localizations of the HOMO and HOMO–1 are interchanged compared with those in the asymmetrically substituted **1c** (Figure S5). This is because the amine moieties of the former are both tosylated and, therefore, less electron-donating than the mono-tosylated diamine moiety of the latter. Nevertheless, despite the PET process becoming thermodynamically less favorable in **1b**, the frontier orbitals HOMO and HOMO–1 are so energetically close (within ca. 0.1 eV) that the PET process can effectively compete (i.e., under thermal activation) with the fluorescence emission, thus reducing the overall quantum yield. The improvement of the fluorescent quantum yield in polar and protic solvents, such as 2,2,2-trifluoroethanol (Table S1), with an ability to interact with the amine lone pairs to reduce its electron-donor character, supports PET as the quenching mechanism operating in these *N*-BODIPYs.

As we have shown, two distinct photophysical behaviors may be observed for the new derivatives depending on the substituents. Compounds **1a**, **1d**, **1e**, and **1f** show a highly efficient fluorescence that could be useful in applications in which light extraction efficiency is of central importance, such as in biophotonics or laser devices. In contrast, compounds **1b** and **1c** are barely fluorescent in common neat solvents, but owing to the operation of PET and its dependency on the electron-donor ability of the amines, they could be useful as cation sensors. The prospects for using the newly designed *N*-BODIPYs for lasing and sensing applications are assessed below.

### *N*-BODIPYs as laser media

*N*-BODIPYs **1a**, **1d**, **1e**, and **1f** were expected to exhibit technologically valuable lasing behavior in solution (see the Supporting Information for experimental details). Thus, under transversal pumping at 532 nm (second harmonic of Nd:YAG laser), the new fluorescent derivatives **1a**, **1d**, **1e**, and **1f** exhibit a highly efficient laser emission centered at 569 nm (lasing efficiencies of 65, 60, 57, and 55%, respectively). These efficiencies are much higher than that recorded for PM567, which does not exceed 48% when pumped under identical experimental conditions. This fact could be related to the significant increase in the molar absorption at 532 nm of the *N*-BODIPYs ( $\epsilon \approx 5\text{--}6 \times 10^4 \text{ M}^{-1} \text{ cm}^{-1}$ ) compared to the *F*-BODIPY ( $\epsilon \approx 1.8 \times 10^4 \text{ M}^{-1} \text{ cm}^{-1}$ ). Consequently, the dye concentration required to achieve optimal pumping conditions is much lower for **1a**, **1d**, **1e**, and **1f** than for PM567 (0.35 vs. 1.00 mM), which is also an important obvious advantage when developing dye lasers.

As a proof of concept on the technological potential of *N*-BODIPYs in lasing, we assessed the laser properties of **1a** operated as an integrated device,<sup>[39]</sup> and compared them to those observed for parent dye PM567. To explore this new application field, we doped each laser dye, **1a** and PM567, in poly(methyl methacrylate) (PMMA) films of thickness 635 nm, implemented as distributed feedback (DFB) lasers.<sup>[40]</sup> The concentrations were chosen so as to give absorbance of around 0.1 at the pump wavelength (532 nm). Full details on the DFB laser operation, sample preparation, and evaluation are given in the Supporting Information. Figure 7 shows the differential lasing behavior obtained.

Thus, by pumping the devices based on **1a** and PM567 at well above the threshold, DFB laser emission with a line width of about 0.2 nm centered at around 567 nm was obtained (Figure 7), consistent with the Bragg resonant wavelength expected for the chosen corrugated substrate and film thickness. Notably, the dependence of the laser emission intensity (DFB output intensity) on the pump (input) intensity was significantly different in the respective cases (see the corresponding light–light curves in Figure 7). Thus, *N*-BODIPY **1a** not only has a lower DFB laser threshold than that of parent dye PM567 (17 vs. 28  $\text{kW cm}^{-2}$ ), but also shows a two-fold enhancement in output intensity when pumped at well above the said thresholds (Figure 7). These results show the potential of the herein

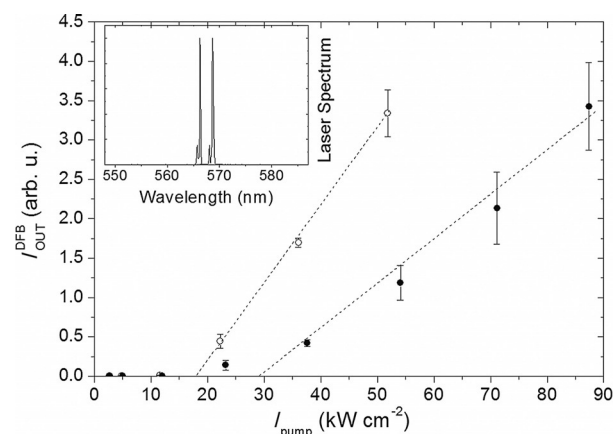


**Figure 7.** Light–light curves for the solid-state DFB laser emission of **1a** (hollow circles) and PM567 (filled circles). A dye-doped 635 nm-thick PMMA film (giving an absorbance of 0.1) deposited on a corrugated substrate was used as an integrated lasing device (see the Supporting Information for experimental details). Error bars account for the standard deviation in three acquisitions. Inset: DFB laser spectra at  $I_{\text{pump}} = 50 \text{ kW cm}^{-2}$ . The change in the curve slope shows the DFB laser threshold.

reported new BODIPY structure in the development of valuable solid-state lasing devices.

### *N*-BODIPYs as cation sensors

With regard to the use of non-fluorescent *N*-BODIPY **1c** as a cation sensor, theoretical calculations revealed that the induced PET process is no longer workable upon protonation of the non-tosylated amine. In fact, the HOMO becomes localized along the BODIPY core and lies well above the HOMO–1 (by around 0.6 eV), which is now centered on the pendant group grafted to the boron atom (see Figure 6). As a consequence of this energy separation, the said PET process from the mono-tosylated amine is thermodynamically inaccessible. Therefore, blocking the availability of the electronic lone pair on the amine (e.g., by interaction with protons as shown above) should preclude the non-radiative PET channel and the bright fluorescence should be recovered, providing the basis of a potential off/on switch for the detection of cations.<sup>[4]</sup> To confirm this hypothesis, we firstly conducted a screening of the fluorescence response of this compound with an excess of different cations, including protons (Figure S6 in the Supporting Information, around 25 equivalents of cation per dye molecule).

The presence of the assayed monovalent metal cations ( $\text{Li}^+$ ,  $\text{Na}^+$ , or  $\text{K}^+$ ) in the surrounding environment of **1c** and some of the assayed divalent cations ( $\text{Ca}^{2+}$ ,  $\text{Mg}^{2+}$ ,  $\text{Ni}^{2+}$ , and  $\text{Zn}^{2+}$ ) elicited the opposite behavior to what was expected, leading to a decrease in the fluorescence signal. This fluorescence quenching was most likely due to the promotion of non-radiative deactivation channels (i.e., intersystem crossing by the intermolecular heavy atom effect, charge-transfer phenomena, or collisional effects) because of the excess of such cations. Such ion sensing (based on a cation-induced loss of fluorescence) is not recommended because the detection may be masked by photobleaching. However, the addition of protons,

as well as of metal ions such as  $\text{Co}^{2+}$  and  $\text{Fe}^{2+}$  or the more electrophilic trivalent cations  $\text{Fe}^{3+}$  and  $\text{Cr}^{3+}$ , induced a marked increase in fluorescence intensity (Figure S6), whereas the absorption probability remained unaltered (or even decreased slightly; data not shown). Such results not only support that **1c** undergoes a PET process, as predicted theoretically, but also suggest that this fluorophore is valuable for the detection of the latter set of cations. Indeed, complexation of cations by the amine groups at the boron bridge hinders the PET process, leading to an enhancement of the fluorescence response. This distinct behavior caused by the cations added to **1c** can be explained in terms of the lyotropic series (Figure S6). The required electrostatic interaction for the sensing process should be driven by the cation charge density, which is defined as the ratio between the charge and the solvation volume. Thus, each ion carries its solvation shell, which decreases the electrostatic interaction. Consequently, in the first set of cations (monovalent, with the exception of the proton, and the divalent ones with the lowest charge density), such solvation hampers their interaction with the amine groups. However, the high charge density in the second set of cations (the remaining divalent and trivalent ones, and the proton) allows interaction with the electron lone pair on the amine, suppressing the PET process (mainly the proton, which is placed first in the lyotropic series) and making the off/on fluorescence sensing feasible.

To gain a deeper insight into this sensing behavior, we performed titration measurements on the cations having a greater impact on the fluorescence response of **1c**; that is, the proton,

divalent  $\text{Co}^{2+}$ , and trivalent  $\text{Cr}^{3+}$ . The high sensitivity of the dye to the presence of protons and  $\text{Cr}^{3+}$  should be noted, with up to 90- and 70-fold increases, respectively, in the fluorescence intensity under the same experimental conditions (Figure 8). Accordingly, the minimum detection level for these cations was well below  $10^{-5}$  M. In all cases, the fluorescence intensity increased progressively with the cation concentration until it reached a maximum response (between 1 and  $4 \times 10^{-4}$  M, depending on the cation). Beyond this point, the fluorescence decreased, presumably due to the huge excess of metal ions, which activates competitive non-radiative relaxation pathways suchlike those mentioned above. Therefore, these results show that this dye behaves like an off (absence of cation, PET allowed)/on (presence of cation; forbidden PET) fluorescence switch for the detection of certain cations, and even as a proton sensor.

Finally, it must be highlighted that the maximum fluorescence response attained for moderately acidic  $\text{Cr}^{3+}$  ( $I_{\text{on}}/I_{\text{off}} \approx 70$  in Figure 8) was reached at a cation concentration of  $8 \times 10^{-5}$  M, whereas a higher proton concentration (ca.  $16 \times 10^{-5}$  M in Figure 8) was required to reach the same response level. On the other hand,  $\text{Ni}^{2+}$  and  $\text{Zn}^{2+}$ , aqueous complexes of which are as acidic as those formed from  $\text{Co}^{2+}$  and  $\text{Fe}^{2+}$ , respectively,<sup>[41]</sup> were not detected under the same experimental conditions. These results discard significant effects caused by protons from possible acidic cation–water complexes formed in the measuring media.

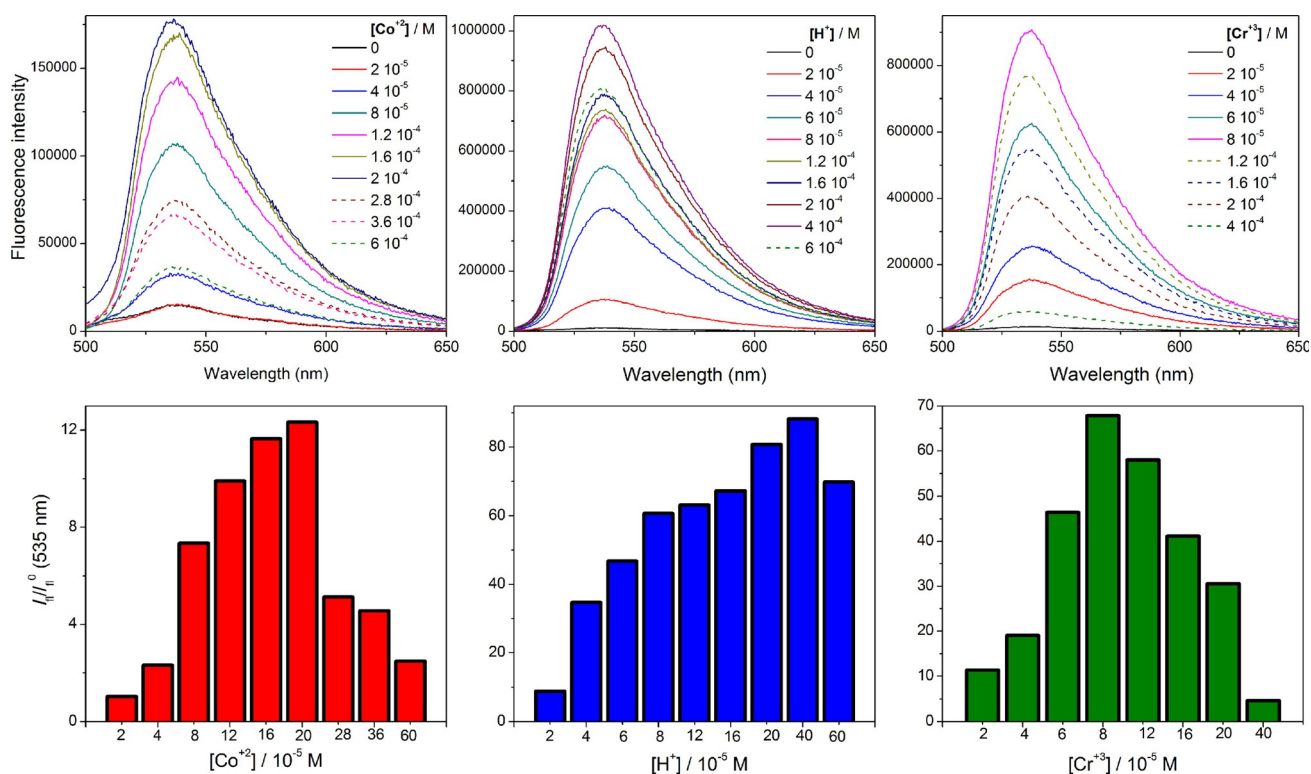


**Figure 8.** Fluorescence spectra corresponding to the titration of dilute ethanolic solutions of **1c** (dye concentration  $4 \times 10^{-6}$  M) with representative cations ( $\text{Co}^{2+}$ ,  $\text{H}^+$ , and  $\text{Cr}^{3+}$  from concentrated aqueous solutions). The spectra in dashed lines are those in which the fluorescence intensity starts to decay with the cation concentration. Beneath each spectral plot, the ratio between the fluorescence intensity (at 535 nm) with ( $I_{\text{on}}$ ) and without ( $I_{\text{off}}$ ) cation has been plotted as a function of cation concentration.



## Conclusion

In summary, we have reported the key design principles for stabilizing *N*-BODIPY dyes, allowing their straightforward synthetic access: (1) use of electron-poor amine moieties based on sulfonylated amines with both low flexibility and low steric hindrance, and (2) use of electron-rich BODIPY cores. The workability of such principles has been evidenced by the synthesis of the first library of *N*-BODIPYs, which were easily prepared in a single step from a commercial *F*-BODIPY precursor. The key diamino boron group of the *N*-BODIPYs opens up interesting possibilities for multifunctionalization of the technologically valuable BODIPY dyes at boron, allowing a smarter modulation of the dye photophysics directed to different specific applications, from lasing to chemosensing. Indeed, we have shown that the photophysical signatures of these novel compounds depend markedly on chemical modifications around the nitrogen atoms of their diamino boron moieties. Thus, stabilized *N*-BODIPYs based on tosylated amines (and even those in which the arylsulfonyl group is replaced by an alkylsulfonyl group), spiranic or not, give rise to bright fluorophores even in the solid crystalline state, with notable lasing capacities in the liquid phase (surpassing 60% laser efficiencies) and when doped into polymers, improving the laser performance of their commercial counterpart PM567. In contrast, sole arylation of the spiranic diamino boron moiety (benzene fusion) activates a PET process that effectively quenches the fluorescence response of the dye. The reliability of such a pathway has been predicted theoretically, and supported experimentally by the recorded increase in fluorescence emission upon the addition of cations with high charge density. This fluorescence sensitivity makes the described benzo-fused spiranic *N*-BODIPYs quite useful as cation sensors, especially for protons and Cr<sup>3+</sup> ions.

In conclusion, the ability to finely modulate the photophysical properties of stabilized *N*-BODIPYs by properly selecting the substitution pattern around the nitrogen atoms, together with the multiple possibilities for such patterns and straightforward synthetic access from accessible *F*-BODIPYs, make these new dyes highly interesting scaffolds to expand the applications of BODIPY dyes towards the development of improved photonic materials.

## Acknowledgements

Financial support from the Spanish MICINN (grant nos. MAT2014-51937-C3-1-P, MAT2014-51937-C3-2-P, MAT2014-51937-C3-3-P, and MAT2015-68837-REDT) and the Gobierno Vasco (IT912-16) is gratefully acknowledged. E.A.Z. thanks the Gobierno Vasco for a predoctoral fellowship. The authors thank Profs. Drs. M. J. Ortiz and A. R. Agarrabeitia, from UCM, for generous help and valuable comments related to this work.

## Conflict of interest

The authors declare no conflict of interest.

**Keywords:** BODIPYs • fluorescence • lasers • photophysics • sensors

- [1] A. Costela, I. García-Moreno, R. Sastre, *Phys. Chem. Chem. Phys.* **2003**, *5*, 4745–4763.
- [2] A. C. Benniston, G. Copley, *Phys. Chem. Chem. Phys.* **2009**, *11*, 4124–4131.
- [3] M. Benstead, G. H. Mehl, R. W. Boyle, *Tetrahedron* **2011**, *67*, 3573–3601.
- [4] N. Boens, V. Leen, W. Dehaen, *Chem. Soc. Rev.* **2012**, *41*, 1130–1172.
- [5] A. Kamkaew, S. H. Lim, H. B. Lee, L. V. Kiew, L. Y. Chung, K. Burgess, *Chem. Soc. Rev.* **2013**, *42*, 77–88.
- [6] J. Fan, M. Hu, P. Zhan, X. Peng, *Chem. Soc. Rev.* **2013**, *42*, 29–43.
- [7] S. P. Singh, T. Gayathri, *Eur. J. Org. Chem.* **2014**, 4689–4707.
- [8] Y. Ni, J. Wu, *Org. Biomol. Chem.* **2014**, *12*, 3774–3791.
- [9] T. Kowada, H. Maeda, K. Kikuchi, *Chem. Soc. Rev.* **2015**, *44*, 4953–4972.
- [10] J. Bañuelos, *Chem. Rec.* **2016**, *16*, 335–348.
- [11] A. Bessette, G. S. Hanan, *Chem. Soc. Rev.* **2014**, *43*, 3342–3405.
- [12] H. Lu, Y. Mack, J. Yang, Z. Shen, *Chem. Soc. Rev.* **2014**, *43*, 4778–4823.
- [13] J. Zhao, K. Xu, W. Yang, Z. Wang, F. Zhong, *Chem. Soc. Rev.* **2015**, *44*, 8904–8939.
- [14] C. Ray, E. M. Sánchez-Carnerero, F. Moreno, B. L. Maroto, A. R. Agarrabeitia, M. J. Ortiz, Í. López-Arbelo, J. Bañuelos, K. D. Cohovi, J. L. Lunkley, G. Muller, S. de la Moya, *Chem. Eur. J.* **2016**, *22*, 8805–8808.
- [15] C. Ray, J. Bañuelos, T. Arbeloa, B. L. Maroto, F. Moreno, A. R. Agarrabeitia, M. J. Ortiz, Í. López-Arbelo, S. de la Moya, *Dalton Trans.* **2016**, *45*, 11839–11848.
- [16] F. López Arbeloa, J. Bañuelos, V. Martínez, T. Arbeloa, Í. López Arbeloa, *Int. Rev. Phys. Chem.* **2005**, *24*, 339–374.
- [17] A. Loudet, K. Burgess, *Chem. Rev.* **2007**, *107*, 4891–4932.
- [18] R. Ziessel, G. Ulrich, A. Harriman, *New J. Chem.* **2007**, *31*, 496–501.
- [19] G. Ulrich, R. Ziessel, R. A. Harriman, *Angew. Chem. Int. Ed.* **2008**, *47*, 1184–1201; *Angew. Chem.* **2008**, *120*, 1202–1219.
- [20] N. Boens, B. Verbelen, W. Dehaen, *Eur. J. Org. Chem.* **2015**, 6577–6595.
- [21] K. K. Jagtap, N. Shivran, S. Mula, D. B. Naik, S. K. Sarkar, *Chem. Eur. J.* **2013**, *19*, 702–708.
- [22] G. Durán-Sampedro, A. R. Agarrabeitia, L. Cerdán, M. E. Pérez-Ojeda, A. Costela, I. García-Moreno, I. Esnal, J. Bañuelos, Í. López-Arbelo, M. J. Ortiz, *Adv. Funct. Mater.* **2013**, *23*, 4195–4205.
- [23] G. Durán-Sampedro, I. Esnal, A. R. Agarrabeitia, J. Bañuelos, L. Cerdán, I. García-Moreno, A. Costela, Í. López-Arbelo, M. J. Ortiz, *Chem. Eur. J.* **2014**, *20*, 2646–2653.
- [24] H. Manzano, I. Esnal, T. Marques-Matesanz, J. Bañuelos, Í. López-Arbelo, M. J. Ortiz, L. Cerdán, A. Costela, I. García-Moreno, J. L. Chiara, *Adv. Funct. Mater.* **2016**, *26*, 2756–2769.
- [25] G. Fan, L. Yang, Z. Chen, *Front. Chem. Sci. Eng.* **2014**, *8*, 405–417.
- [26] A. Poiré, P. Retailleau, A. De Nicola, R. Ziessel, *Chem. Eur. J.* **2014**, *20*, 1252–1257.
- [27] L. Yang, G. Fan, X. Ren, L. Zhao, J. Wang, Z. Chen, *Phys. Chem. Chem. Phys.* **2015**, *17*, 9167–9172.
- [28] R. Ziessel, G. Ulrich, A. Haeefe, A. Harriman, *J. Am. Chem. Soc.* **2013**, *135*, 11330–11344.
- [29] E. M. Sánchez-Carnerero, L. Gartzia-Rivero, F. Moreno, B. L. Maroto, A. R. Agarrabeitia, M. J. Ortiz, J. Bañuelos, Í. López-Arbelo, S. de la Moya, *Chem. Commun.* **2014**, *50*, 12765–12767.
- [30] V. Bandi, S. K. Das, S. G. Awuah, Y. You, F. D'Souza, *J. Am. Chem. Soc.* **2014**, *136*, 7571–7574.
- [31] I. Esnal, G. Durán-Sampedro, A. R. Agarrabeitia, J. Bañuelos, I. García-Moreno, M. A. Macías, E. Peña-Cabrera, Í. López-Arbelo, S. de la Moya, M. J. Ortiz, *Phys. Chem. Chem. Phys.* **2015**, *17*, 8239–8247.
- [32] E. M. Sánchez-Carnerero, F. Moreno, B. L. Maroto, A. R. Agarrabeitia, M. J. Ortiz, B. G. Vo, G. Muller, S. de la Moya, *J. Am. Chem. Soc.* **2014**, *136*, 3346–3349.
- [33] S. Zhang, Y. Wang, F. Meng, C. Dai, Y. Cheng, C. Zhu, *Chem. Commun.* **2015**, *51*, 9014–9017.
- [34] R. B. Alnoman, S. Rihn, D. C. O'Connor, F. A. Black, B. Costello, P. G. Waddell, W. Clegg, R. D. Peacock, W. Herrebut, J. G. Knight, M. J. Hall, *Chem. Eur. J.* **2016**, *22*, 93–96.
- [35] H. Lu, J. Mack, T. Nyokong, N. Kobayashi, Z. Shen, *Coord. Chem. Rev.* **2016**, *318*, 1–15.

- [36] J. Jiménez, L. Cerdán, F. Moreno, B. L. Maroto, I. García-Moreno, J. L. Lunkley, G. Muller, S. de la Moya, *J. Phys. Chem. C* **2017**, *121*, 5287–5292.
- [37] Formation of the corresponding *Cl*-BODIPY as a synthetic intermediate was not observed in the conducted BODIPY fluorine substitutions activated by boron chloride. For these intermediates relating to BODIPYs with different substitution patterns, see: T. Lundrigan, A. Thompson, *J. Org. Chem.* **2013**, *78*, 757–761.
- [38] S. Shaban Ragab, S. Swaminathan, E. Deniz, B. Captain, F. M. Raymo, *Org. Lett.* **2013**, *15*, 3154–3157.
- [39] C. Grivas, M. Pollnau, *Laser Photonics Rev.* **2012**, *6*, 419–462.
- [40] I. D. W. Samuel, G. A. Turnbull, *Chem. Rev.* **2007**, *107*, 1272–1295.
- [41] V. E. Jackson, A. R. Felmy, D. A. Dixon, *J. Phys. Chem. A* **2015**, *119*, 2926–2939.

---

Manuscript received: March 24, 2017

Accepted manuscript online: May 3, 2017

Version of record online: June 12, 2017

## Annex II (Chapter 2) / II. Eranskina (2. Kapituluua)

### Article 2 / 2. Artikuluua

Synthetic Approach to Readily Accessible Benzofuran-Fused Borondipyrromethenes as Red-Emitting Laser Dyes

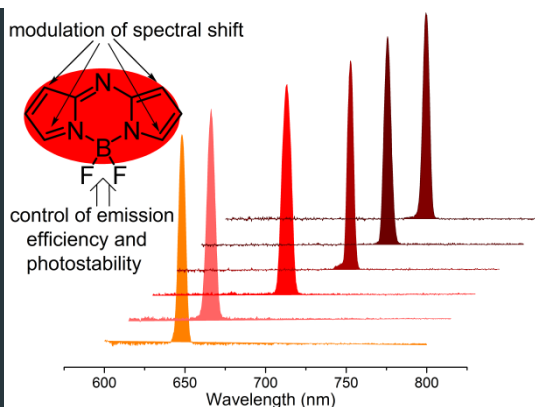
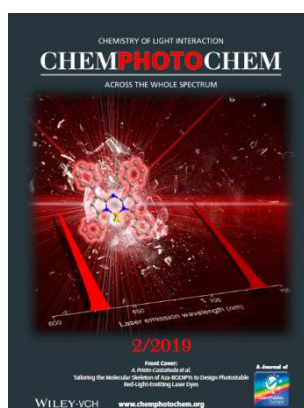
*The Journal of Organic Chemistry*, 2019, 84, 2523-2541



### Article 3 / 3. Artikuluua

Synthetic Approach to Readily Accessible Benzofuran-Fused Borondipyrromethenes as Red-Emitting Laser Dyes

*The Journal of Organic Chemistry*, 2019, 84, 2523-2541





# Synthetic Approach to Readily Accessible Benzofuran-Fused Borondipyrromethenes as Red-Emitting Laser Dyes

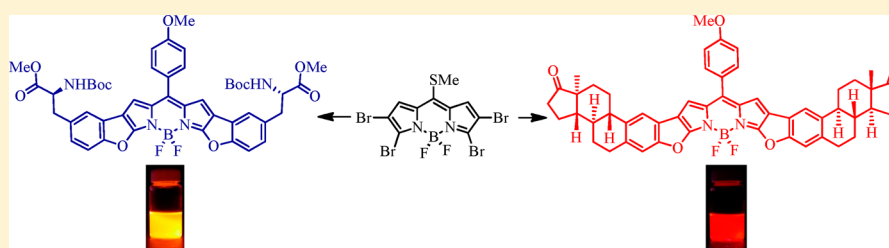
José L. Belmonte-Vázquez,<sup>†</sup> Edurne Avellanal-Zaballa,<sup>‡</sup> Ernesto Enríquez-Palacios,<sup>†</sup> Luis Cerdán,<sup>§</sup> Ixone Esnal,<sup>‡</sup> Jorge Bañuelos,<sup>\*,‡</sup> Clarisa Villegas-Gómez,<sup>†</sup> Iñigo López Arbeloa,<sup>‡</sup> and Eduardo Peña-Cabrera<sup>\*,†</sup>

<sup>†</sup>Departamento de Química, Universidad de Guanajuato, Noria Alta S/N, Guanajuato, Guanajuato, Mexico 36050

<sup>‡</sup>Departamento de Química Física, Universidad del País Vasco-EHU, Apartado 644, 48080 Bilbao, Spain

<sup>§</sup>Instituto de Química-Física “Rocasolano”, CSIC, Serrano 119, 28006 Madrid, Spain

## Supporting Information



**ABSTRACT:** We took advantage of the chemoselective *meso*-functionalization of 2,3,5,6-tetrabromo-8-methylthioBODIPY **6** to prepare a series of 2,3,5,6-tetrabromo-8-arylBODIPY derivatives suitable for  $S_NAr$  substitution reactions with phenols exclusively at positions 3 and 5. Pd(0)-catalyzed intramolecular arylation reaction ensued on the remaining brominated positions 2 and 6 to give a new family of benzofuran-fused BODIPY dyes. This method utilizes readily available starting materials and allows for the preparation of the title compounds with excellent functional group tolerance. Moreover, it was demonstrated that the methodology described herein is amenable for the incorporation of biomolecules. The photophysical and lasing properties of the benzofuran-fused BODIPY dyes were thoroughly analyzed with the aid of electrochemical measurements and quantum mechanical simulations. These dyes show bright and intriguing emission (both fluorescence and laser) toward the red edge of the visible spectrum with remarkable tolerance under strong and continuous irradiation.

## INTRODUCTION

Borondipyrromethenes (BODIPYs) **1** (Figure 1) are arguably some of the most versatile fluorophores.<sup>2</sup> Plenty has been written about their synthesis,<sup>3</sup> postfunctionalization,<sup>4</sup> water solubility,<sup>5</sup> and halogenated derivatives.<sup>6</sup> Similarly, there is vast

amount of information regarding their applications: in organic photovoltaic devices,<sup>7</sup> as components of novel light active materials,<sup>8</sup> as fluorescent tools,<sup>9</sup> as sensitizers for dye-sensitized solar cells,<sup>10</sup> as sensors for reactive oxygen species,<sup>11</sup> and in photodynamic therapy,<sup>12</sup> just to mention a few.

There are well-established fluorophores with a marked diversity of structures that emit at specific wavelengths.<sup>13</sup> However, the core structure of BODIPYs is one of the few capable of fluorescing over the whole visible and near-infrared (NIR) regions of the electromagnetic spectrum, if properly functionalized (Figure 1).<sup>2,14</sup>

The possibility of inducing a bathochromic shift in the optical properties of these dyes is highly desirable. Many imaginative attempts to design red-emitting BODIPYs have been tested.<sup>15</sup> The reason for this search rests in the serious drawbacks of most of the available fluorophores in that spectral region for their optimal practical application.<sup>16</sup> In fact, cyanine dyes can provide spectral bands deep in the red edge, even reaching the near infrared (NIR), but with low fluorescence

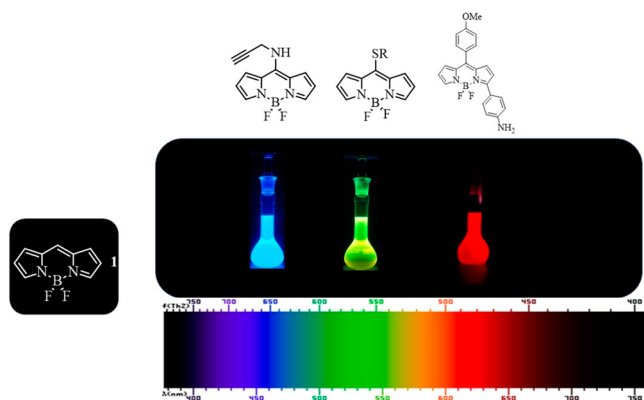


Figure 1. Panchromatic properties of BODIPY dyes.

Received: November 17, 2018

Published: January 31, 2019

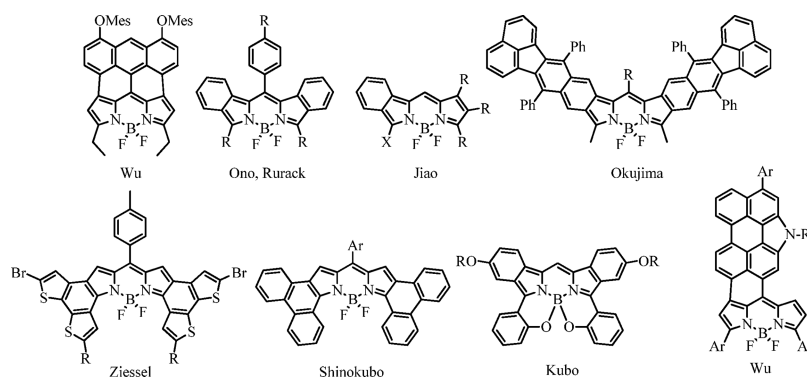


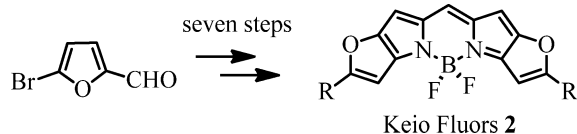
Figure 2. Representative examples of BODIPYs with extended conjugation.

efficiencies because of their push–pull and conformationally flexible chromophores.<sup>17</sup> On the other hand, oxazine dyes render bright emission but are easily photobleached.<sup>18</sup> One way to circumvent such limitations is by shifting the spectral bands of BODIPYs, characterized by their excellent photophysics and robustness,<sup>2</sup> to the red edge thanks to the chemical versatility of its dipyrin core.<sup>4</sup> These red-emitting BODIPYs are used as building blocks to prepare polymers that can be used in photovoltaics, solar cells, photodetectors, etc.<sup>19</sup> Such compounds find numerous applications in biomedicine and related areas. Thus, NIR-emitting BODIPYs have been used as pH probes and in bioimaging,<sup>20</sup> in photodynamic therapy,<sup>21</sup> and as molecular probes for reactive oxygen species (ROS).<sup>22</sup>

A well-known approach to red-shift both the absorption and the emission of BODIPY dyes is to reduce their HOMO–LUMO gap by extending their conjugated system. Thus, the groups of Wu,<sup>23</sup> Rurack,<sup>24</sup> Jiao,<sup>25</sup> Okujima,<sup>26</sup> Ziessel,<sup>27</sup> Shinokubo,<sup>28</sup> and Kubo,<sup>29</sup> among others, have reported a variety of different BODIPY structures featuring extended conjugated systems (Figure 2). Moreover, Wu and Ni have published a review with additional conjugated BODIPY structures.<sup>30</sup>

The so-called Keio Fluors **2** are BODIPY dyes with extension of the conjugation, including heterocycles, specifically, furan. These features result in dyes with improved properties, such as color tunability, sharp spectral bands, high extinction coefficients, and fluorescence quantum yields. Additionally, their brightness depends little on solvent polarity. A significant disadvantage is that each derivative must be prepared by a linear synthesis comprising seven steps, leaving little or no room for further modifications of the final products (Scheme 1).<sup>31</sup>

#### Scheme 1. Linear Synthesis of Keio Fluors



The synthesis of a single regioisomer **3** was described in 2010, using an alternative methodology (Scheme 2).<sup>32</sup>

After analyzing the synthetic sequence, one realizes that it becomes quite an undertaking to prepare different analogues for each of them because that would require repeating the whole process to vary the *meso*-substituent. Moreover, the

introduction of additional functional groups into the benzofuran system would need a substituted *o*-bromophenol.

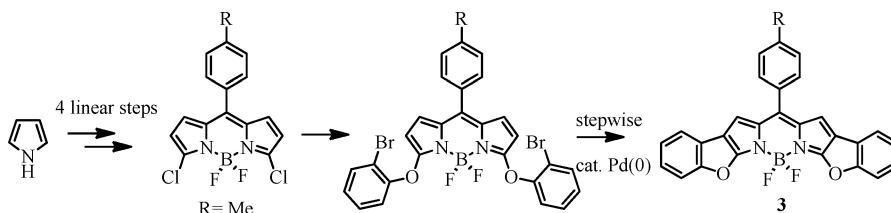
Herein, we disclose a fully flexible method that allows the preparation of a novel family of benzofuran-fused BODIPY dyes. Easy modifications in the synthesis permit variations both at the *meso*-position and in the benzofuran substitution pattern because the latter requires only substituted phenols. This method also features the use of an advanced, commercially available BODIPY starting material **4**, complete chemoselective control over three reaction sites, and the preparation of BODIPY dyes with unique architectures and important photophysical and laser properties. In 2016,<sup>33</sup> we reported the synthesis of multifunctional BODIPY **5** and demonstrated that it displayed orthogonal reactivity; i.e., the C–S bond was activated under Liebeskind–Srogl cross-coupling reaction (LSCC)<sup>34</sup> conditions, leaving the C–Br bond intact. This chemoselectivity allowed us to introduce a variety of functional groups in a programmed fashion on the periphery of the BODIPY core. Now we decided to challenge even further the chemoselectivity of novel BODIPY building block **6** and apply it this time to the preparation of a new family of benzofuran-fused BODIPY dyes (Figure 3).

The types of benzofuran-fused BODIPYs readily available by this novel approach display quite red-shifted absorption and emission bands. Hereafter, we describe the photophysical and lasing properties of the benzofuran-fused BODIPYs and demonstrate their viability as laser dyes endowed with high laser and fluorescence efficiencies and high photostability under strong and prolonged pumping. To the best of our knowledge, the laser capabilities of the red-emitting benzofuran-fused BODIPYs overall are almost hitherto unexploited (just early conference proceedings from SPIE).<sup>35</sup>

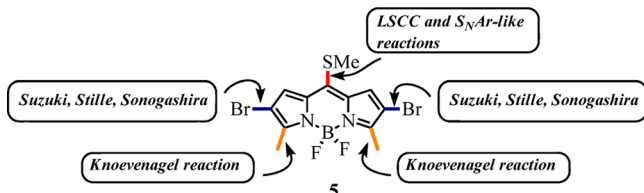
## RESULTS AND DISCUSSION

**Retrosynthetic Analysis.** The retrosynthetic analysis is shown in Scheme 3. The final products **9** will be formed after a Pd-catalyzed arylation reaction of **8**.<sup>36</sup> Bis-phenoxy-containing intermediate **8** would be formed after a double  $S_NAr$  of **7** with substituted phenols under basic conditions, at exclusively positions 3 and 5 because only those C–Br bonds are activated toward the addition–elimination process.<sup>37</sup> *Meso*-Aryl-substituted BODIPY **7** would be prepared from the chemoselective LSCC under neutral conditions leaving intact the four brominated positions.<sup>33</sup> This selectivity would allow for the introduction of varied aryl groups at the *meso*-position, a key step of our synthetic plan. Finally, tetrabrominated intermediate **6** would be produced from commercially available **4**.

Scheme 2. Synthesis of BODIPY 3



Previous work:



This work:

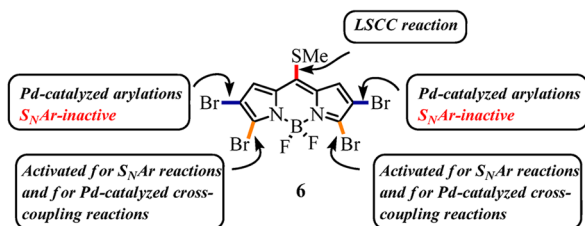
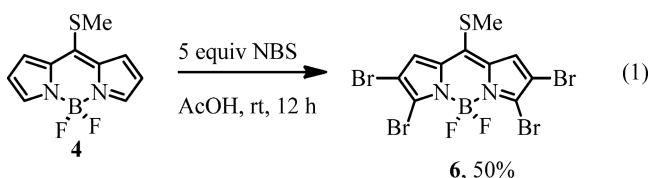


Figure 3. BODIPY dyes with orthogonal reactivity.

**Synthesis.** Tetrabromination of commercially available 8-methylthioBODIPY **4** was carried out according to eq 1. Next, the key step of our synthetic plan followed, i.e., the chemoselective LSCC in the presence of other reactive sites (Table 1).



The typical Cu(I) sources for the LSCC reaction were tested. All of them, except CuI, yielded the desired product (entry 5); however, the best results were observed with CuTC (entry 1). A further increase in the yield was observed when 3

equiv of the boronic acid was used (entry 2). Notably, under these reaction conditions, only BODIPY **10** was produced along with trace amounts of other colored compounds in quantities too small to be characterized. This key result allowed the selective functionalization of the *meso*-position leaving the other brominated positions available to be manipulated at will.

Once the best conditions were determined, we set out to react **6** with several arylboronic acids (Table 2) to study the scope of the LSCC reaction.

The LSCC took place smoothly in the set of phenols that we studied to give the *meso*-aryl-substituted products in modest to good yields in relatively short reaction times. Electron-rich boronic acids gave the highest yields (entries 4 and 6). No detrimental effect due to sterics was observed when *o*-tolylboronic acid was employed (entry 2). Once derivatives **10–15** were obtained, the nucleophilic substitution of phenol at position 3 was explored. The results are listed in Table 3.

Phenol was added to BODIPYs **10–15** under basic conditions in acetonitrile at 110 °C.<sup>32</sup> The 2-fold substitution reaction took place uneventfully to give 3,5-diphenoxy-substituted BODIPY dyes in good yields (entries 1–5). However, when we attempted to add phenol to BODIPY **15**, decomposition of this compound was observed.

Next, the polyfunctionalized BODIPYs so prepared were subjected to the Pd-catalyzed intramolecular arylation (Chart 1).

In sharp contrast to the reaction conditions that gave rise to isomer **3**,<sup>38</sup> 2-fold arylation reaction of dyes **16–20** was achieved under mild conditions to furnish the cyclized products in yields that ranged from 48 to 72%. The electronic properties of the *meso*-aryl ring did not seem to have any significant influence on either the reaction time or the resulting isolated yield.

We then decided to study the scope and limitations of the overall process using various substituted phenols (Table 4). Compound **11** was chosen to start the sequence because it has hindered rotation around the *C*<sub>meso</sub>-aryl bond. This feature

Scheme 3. Retrosynthetic Analysis of the Preparation of Benzofuran-Fused BODIPY Dyes

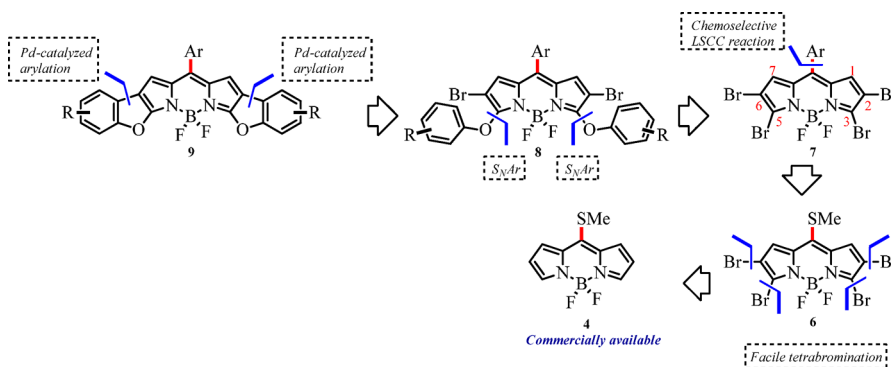
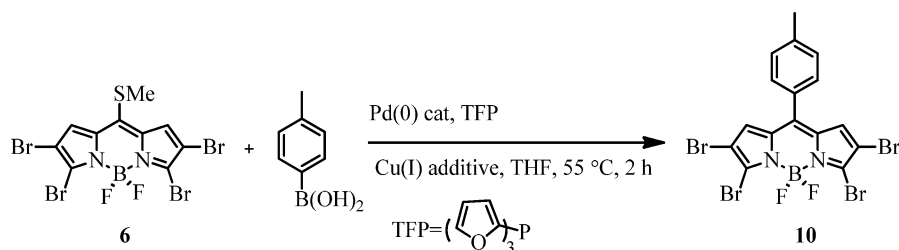
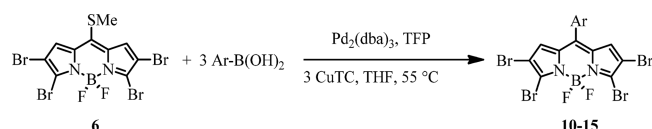


Table 1. Optimization of the LSCC Reaction on 6<sup>a</sup>

entry	boronic acid (equiv)	Cu source	Pd source	% of conversion <sup>b</sup>
1	1	CuTC <sup>c</sup>	Pd <sub>2</sub> (dba) <sub>3</sub>	72
2	3	CuTC	Pd <sub>2</sub> (dba) <sub>3</sub>	80
3	3	CuMeSal <sup>d</sup>	Pd <sub>2</sub> (dba) <sub>3</sub>	24
4	3	CuO <sub>2</sub> PPh <sub>2</sub> <sup>e</sup>	Pd <sub>2</sub> (dba) <sub>3</sub>	65
5	3	CuI	Pd <sub>2</sub> (dba) <sub>3</sub>	— <sup>f</sup>
6	3	CuTC	Pd(PPh <sub>3</sub> ) <sub>4</sub> <sup>g</sup>	10

<sup>a</sup>Conditions: 6 (1 equiv), Pd(0) (2.5 mol %), TFP (2.5 mol %), Cu(I) source (equimolar with respect to the boronic acid). <sup>b</sup>Determined by HPLC. <sup>c</sup>Copper(I) thiophene-2-carboxylate. <sup>d</sup>Copper(I) 3-methylsalicylate. <sup>e</sup>Copper(I) diphenylphosphinate. <sup>f</sup>No product was formed. <sup>g</sup>No TFP was used.

Table 2. LSCC Reaction on BODIPY 6<sup>a</sup>

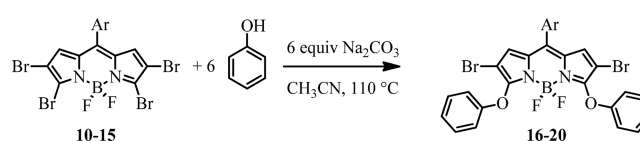
Entry	Ar-	Reaction time	% Yield <sup>b</sup>	Compound
1		2 h	50	10
2		1 h	76	11
3		1 h	38	12
4		40 min	63	13
5		2h	18	14
6		1 h	83	15

<sup>a</sup>Conditions: 6 (1 equiv), boronic acid (3 equiv), Pd<sub>2</sub>(dba)<sub>3</sub> (2.5 mol %), TFP (2.5%), CuTC (3 equiv), in THF at 55 °C. <sup>b</sup>Isolated yield.

increases the probability of observing a high fluorescent quantum yield ( $\Phi_f$ ) in the final products due to restricted rotation of said bond, thereby inhibiting nonradiative relaxation pathways.<sup>39</sup>

Addition of substituted phenols took place as expected. All of the products were obtained, except when 4-hydroxyphenylboronic acid and 1-hydroxypyrene were used, for decomposition was observed in both cases (entries 6 and 7, respectively). Addition of the rest of the substituted phenols and naphthol was carried out under mild reaction conditions and short reaction times (1–2 h) to yield the highly colored products in good to excellent yields (entries 1–5).

With derivatives 27–31 in hand, we proceeded to study their Pd(0)-catalyzed ring closure to yield the corresponding benzofuran-fused products. The results are illustrated in Chart 2.

Table 3. Nucleophilic Substitution of Phenol on Derivatives 10–15<sup>a</sup>

Entry	Ar	Reaction time (h)	% Yield <sup>b</sup>	Compound
1		6	80	16
2		3	77	17
3		3	57	18
4		5	72	19
5		3	60	20
6		-	- <sup>c</sup>	21

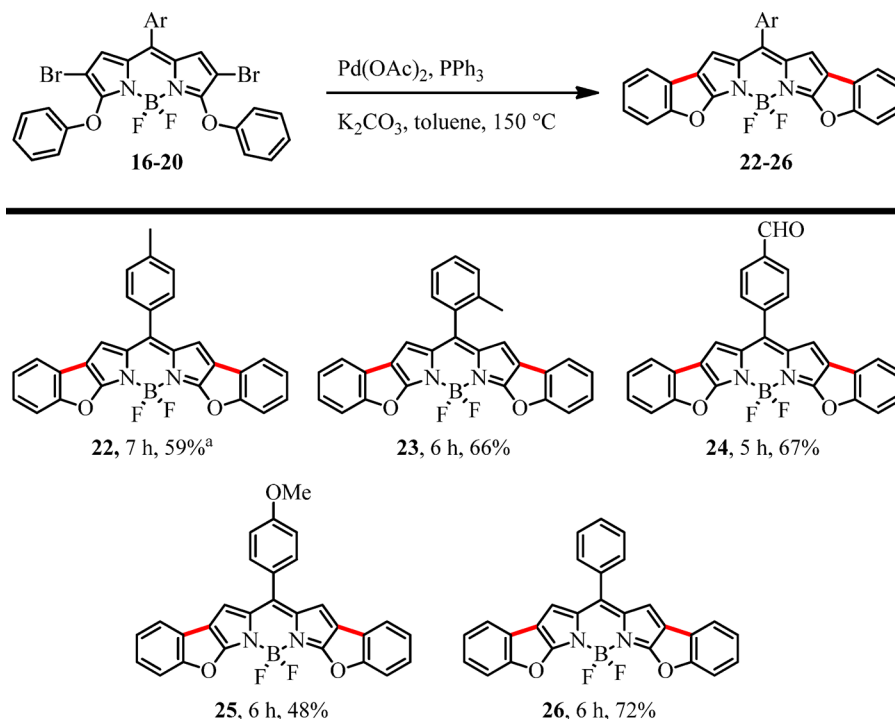
<sup>a</sup>Conditions: BODIPYs (1 equiv), phenol (6 equiv), Na<sub>2</sub>CO<sub>3</sub> (6 equiv), sealed tube. <sup>b</sup>Isolated yields. <sup>c</sup>Decomposition of the BODIPY was observed.

Satisfyingly, the cyclization reaction took place to produce the final products in moderate to good yields. Iodine-containing derivative 38 was not formed because quick decomposition of the starting material was observed within the first 30 min. Presumably, the more reactive iodide participated in undesired reaction in the presence of Pd.

**Incorporation of Two Biomolecules.** To demonstrate the applicability of the methodology described herein, two phenolic biomolecules were chosen to be incorporated into the BODIPY core: estrone and *N*-BOC-*L*-tyrosine methyl ester. TetrabromoBODIPY 13 was chosen as the starting material because the *o*-tolyl analogue 11 would give rise to diastereoisomeric final products due to its hindered rotation around the *meso*- $\sigma$  bond. To this end, both biomolecules were reacted with 13 under the reaction conditions described in Tables 3 and 4 (Scheme 4), producing the expected products in good yields and short reaction times.

We then proceeded to carry out the arylation reaction on both 39 and 40 that would produce the final products



Chart 1. Pd-Catalyzed Arylation of BODIPYs 16–20<sup>a,b</sup>

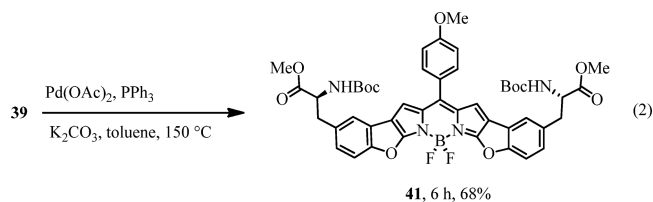
<sup>a</sup>Conditions: BODIPY (1 equiv), Pd(OAc)<sub>2</sub> (0.05 equiv), PPh<sub>3</sub> (0.1 equiv), K<sub>2</sub>CO<sub>3</sub> (3 equiv), in toluene at 150 °C in a sealed tube. <sup>b</sup>Isolated yield.

Table 4. Addition–Elimination Reaction of Substituted Phenols on TetrabromoBODIPY 11<sup>a</sup>

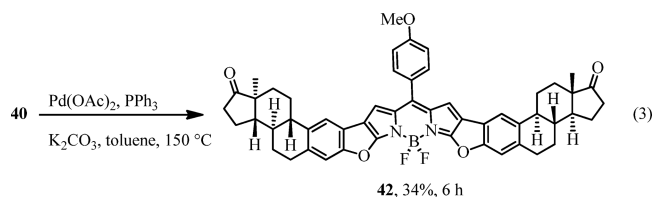
Entry	Phenol derivative	Reaction time	% Yield <sup>b</sup>	Compound
1		2 h	79	27
2		2 h	90	28
3		1 h	90	29
4		1 h	81	30
5		2 h	58	31
6		2.5 h	- <sup>c</sup>	32
7		15 min	- <sup>d</sup>	33

<sup>a</sup>Conditions: BODIPY (1 equiv), phenol (6 equiv), Na<sub>2</sub>CO<sub>3</sub> (6 equiv), in MeCN at 110 °C in a sealed tube. <sup>b</sup>Isolated yields. <sup>c</sup>The product decomposed on chromatography (SiO<sub>2</sub> gel) purification. <sup>d</sup>Decomposition was observed.

according to the conditions depicted in Charts 1 and 2. Cyclization of 39 gave fused derivative 41 in 68% yield after 6 h (eq 2). Cyclization of 40 posed an interesting regiochemistry issue because the estrone fragment has two nonequivalent reaction sites (Figure 4).



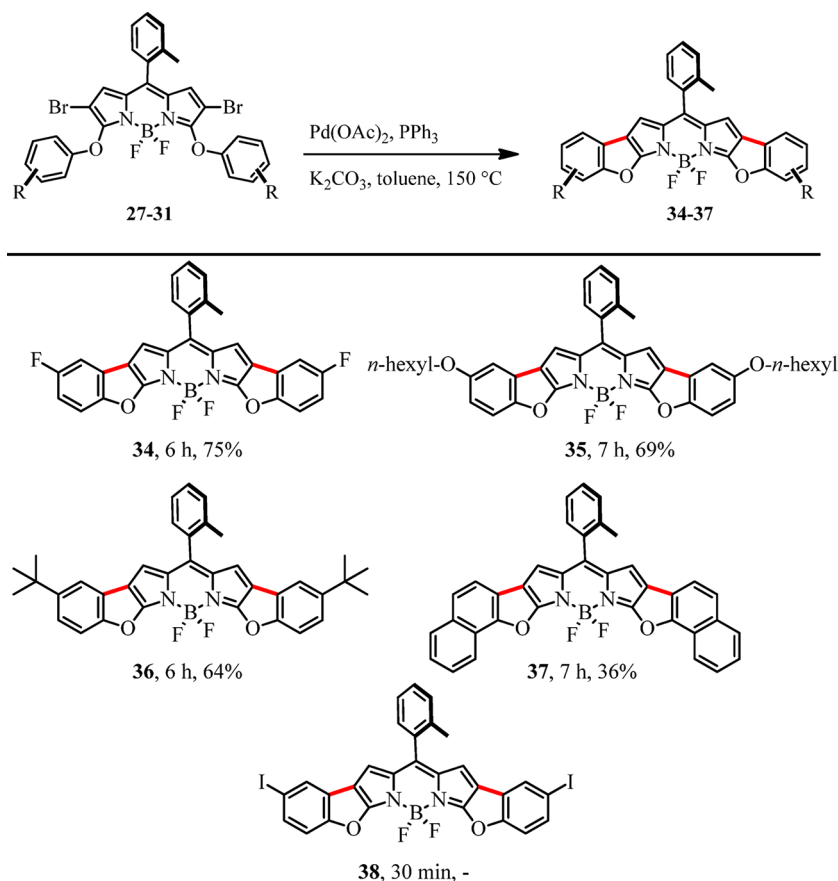
With these aspects in mind, the Pd-catalyzed arylation reaction on BODIPY 40 was carried out (eq 3). Even though



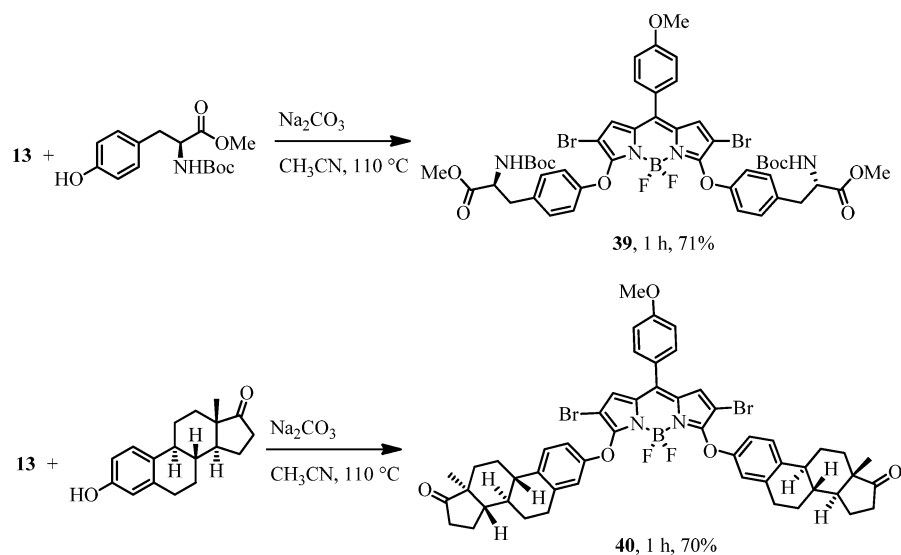
the overall isolated yield was low (34%), only regioisomer 42 was obtained after 6 h. Inspection of the NMR data led us to this conclusion. If isomer 43 had been formed, in addition to the characteristic AA'XX' coupling pattern of the 8-(*p*-MeOphenyl) fragment, and a singlet of the pyrrole moiety, two doublets should appear in the aromatic region due to the *cis*-hydrogens from the estrone fragment (red protons in Figure 5). On the other hand, if 42 were formed, the two aromatic protons of estrone would be *para* to each other (blue protons in Figure 5) and therefore uncoupled. Indeed, the latter is the pattern we observe.

The actual COSY spectrum of 42 is illustrated in Figure 6, showing no cross-peaks between aromatic protons d and e.

**X-ray Structure of 25.** BODIPY 25 was crystallized by diffusion from petroleum ether/CH<sub>2</sub>Cl<sub>2</sub> (Figure 7). The heterocyclic fragment of 25 is almost planar, displaying a

Chart 2. Pd-Catalyzed Arylation of BODIPYs 27–31<sup>a,b</sup>

<sup>a</sup>Conditions: BODIPY (1 equiv), Pd(OAc)<sub>2</sub> (0.05 equiv), PPh<sub>3</sub> (0.1 equiv), K<sub>2</sub>CO<sub>3</sub> (3 equiv), in toluene at 150 °C in a sealed tube. <sup>b</sup>Isolated yields.

Scheme 4. Reaction of Estrone and *N*-BOC-*L*-Tyrosine Methyl Ester with BODIPY 13

very slight concavity at the center. On the other hand, the B atom has a tetrahedral geometry (the F–B–F angle is 110°, and the N–B–N angle is 104°) and lies off the plane by 10°. The 8-aryl ring is at a 55° angle with respect to the BODIPY plane because of the steric hindrance between the hydrogens placed at the *ortho*-position of the ring and those at chromophoric positions 1 and 7. The X-ray structure of tolyl

analogue **22** was already reported and displays very similar features.<sup>32</sup>

**Photophysical Properties.** The fusion of benzofuran rings to the  $\alpha$ – $\beta$  positions of the dipyrin core extends the  $\pi$ -system and, in turn, entails a pronounced bathochromic spectral shift that pushes the spectral band toward the red spectral window (Figure 8 and Figures S1–S3). In contrast, the *meso*-aryl group

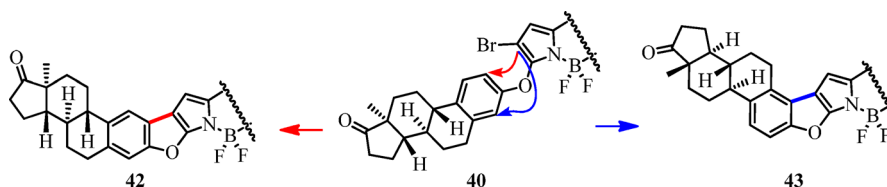


Figure 4. Two possible regioisomers that could be produced from the cyclization reaction of 40.

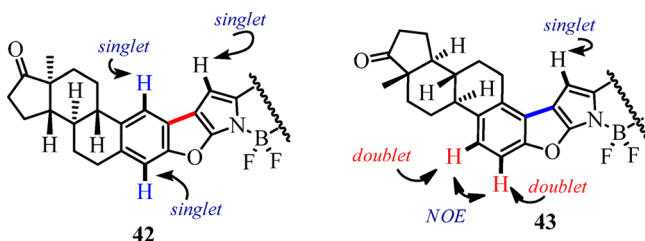


Figure 5. Expected  $^1\text{H}$  NMR signals of isomers 42 and 43.

has no effect in the spectral band positions. In fact, in the compounds bearing methyl at the *ortho* position of the 8-phenyl, the sterical hindrance places this ring almost orthogonal to the dipyrin plane (dye 23), but even in absence of such alkylation (dye 22 or 26 for example in Chart 1), the 8-phenyl is also twisted (around  $60^\circ$ ), because of steric hindrance with the hydrogens at chromophoric positions 1 and 7 and, hence, it is not electronically coupled to the chromophoric core. Such a red-shift is strengthened by the addition of larger and more conjugated aryl groups to the chromophoric core. For instance, in dye 37, with an aromatic framework comprising up to seven aromatic rings, the spectral bands are located well above 600 nm (Figure 8). The electrochemistry measurements reveal that all of the dyes have a similar cyclic voltammogram featuring two well-resolved and reversible anodic (around 1.25 V) and cathodic (around  $-0.75$  V) waves (Figure 9 and Figure S4). The extension of the chromophoric framework (dye 37) implies a reduction of both redox potential [with regard to its analogue, 23 (Figure 9)], in agreement with the calculated lower-energy gap between the frontier molecular orbitals (from 5.80 eV in 23 to 5.73 eV in 37) and the recorded bathochromic shift (Figure 8).

Despite the number of rings fused to the dipyrin core and the ensuing structural stress, the whole chromophore remains planar (for instance, deviations of  $<2^\circ$  in compound 26, even in the excited state). As a result of this planar and rigid molecular structure, reflected in a small Stokes shift [overall  $<500\text{ cm}^{-1}$  (Table S1)], the aromaticity is high (as shown by a bond length

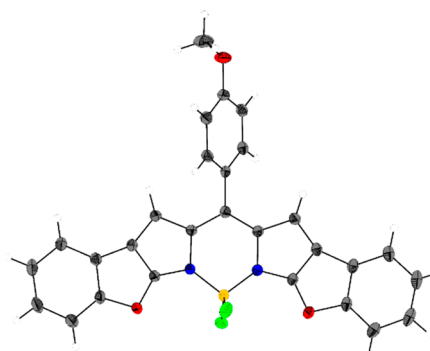


Figure 7. X-ray structure of 25 (ORTEP drawing, 50% probability). The corresponding crystallographic data are listed in Table S3.

alternation, BLA, parameter of  $\sim 0.02$  in the ground and excited states). These features explain the remarkably high absorption probability [reaching values of  $>2 \times 10^5\text{ M}^{-1}\text{ cm}^{-1}$  (Table 5)], the notable radiative rate constant [ $k_{\text{fl}} > 2 \times 10^8\text{ s}^{-1}$  (Table 5)], and the low internal conversion probability (Table 5). Therefore, these conformationally restricted and symmetrical red-emitting dyes display a bright fluorescence response, approaching 100% in apolar media (Table 5). It should be highlighted that the presence of unconstrained 8-aryl fragments with conformational freedom efficiently quenches the fluorescence response in simpler and more compact BODIPYs.<sup>40</sup> In contrast, in the dyes tested herein, the extension of the  $\pi$ -system through the aryls fused to the pyrroles shifts the electronic density away from the key *meso* position, avoiding, or at least hampering, the quenching pathway associated with the 8-aryl motion.<sup>33</sup> In fact, those dyes sharing the same chromophoric unit (dipyrin fused with benzofurans), but differing in their *meso*-substitution, show similar and high fluorescence quantum yields (Table 5) regardless of the conformational mobility of the 8-aryl (unconstrained, twisting angle of the phenyl of  $\sim 65^\circ$  in dyes 22 and 26, or constrained, orthogonal *o*-tolyl in 23) or its functionalization (electron donor *p*-methoxy in 25). The only exception to the rule is 24 with a *para*-formylated 8-aryl, which shows an unexpected weak

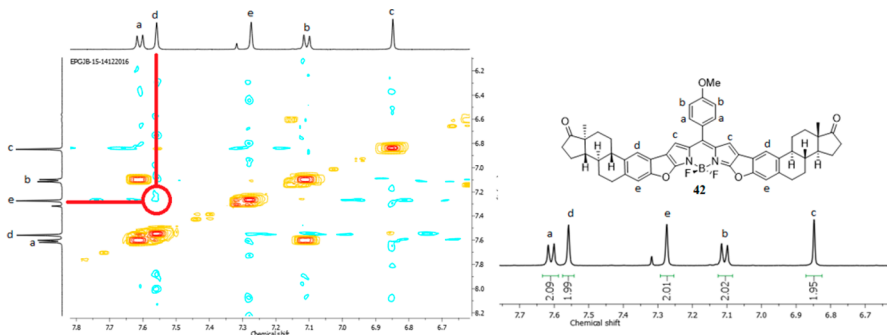
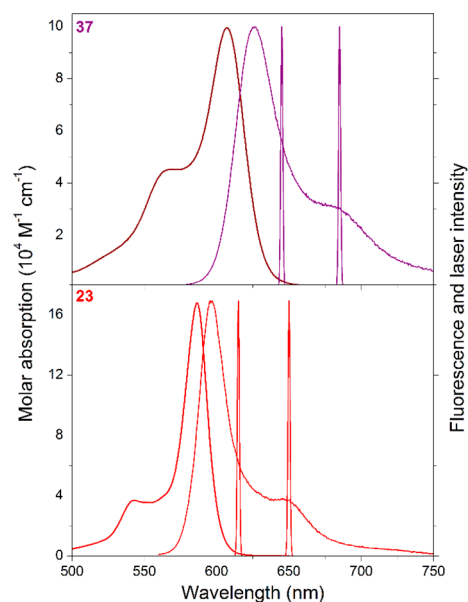
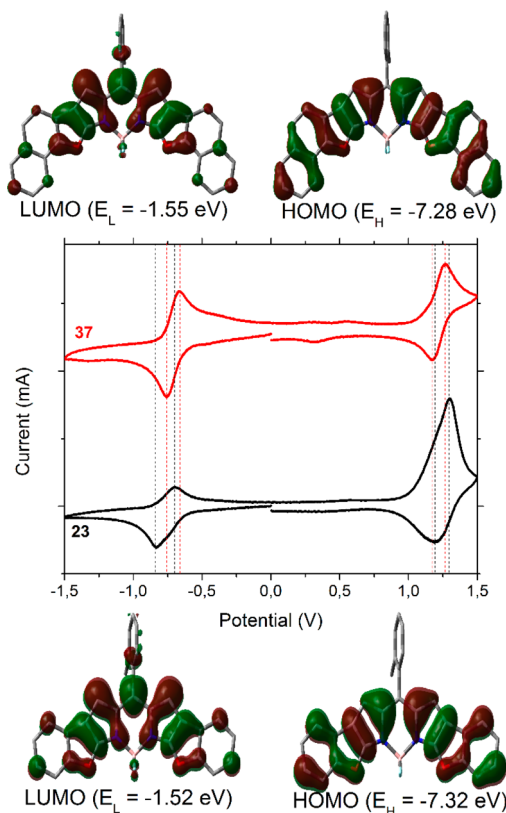


Figure 6. Aromatic region of the COSY spectrum of estrone-fused BODIPY 42.



**Figure 8.** Absorption, normalized fluorescence, and laser (dual emission depending on the dye concentration) spectra of dye 23 and its analogue, 37, with additional fused phenyl rings, in ethyl acetate. The spectra of the rest of the compounds are included in Figures S1–S3.



**Figure 9.** Cyclic voltammograms and calculated contour maps and energies of the frontier orbitals for compounds 23 and 37. Additional voltammograms of representative compounds are collected in Figure S4.

fluorescence response (Table 5). This exception will be rationalized below.

The evolution of the fluorescence efficiency with the solvent depends both on the type of functional groups decorating the chromophoric backbone and on the number of fused rings (Figure 10 and Table S1). Thus, the presence of heteroatoms, like fluorine 34, or alkyl groups (bulky *tert*-butyl in 36) or a functionalized aliphatic chain (tyrosine biomolecule in 41) in the fused benzofuran renders highly fluorescent dyes in all of the considered solvents. In contrast, the addition of alkoxy chains (35) induces a progressive decrease in both the fluorescence efficiency and the fluorescence lifetime with solvent polarity [down to 29% and 1.67 ns, respectively, in methanol (Table S1)]. Such a tendency is consistent with the activation of an intramolecular charge transfer (ICT) state in polar media. Thus, the benzofuran itself could act as an electron donor because of its oxygen heteroatom at the  $\alpha$ -pyrrolic position. The additional presence of alkoxy groups in the periphery increases such electron donor character, thereby being high enough to switch on the nonfluorescence ICT. Indeed, in the contour maps depicted in Figure 9, some electron transfer from the benzofuran to the dipyrin upon excitation can be visualized (from HOMO to LUMO). Likely, such charge separation is enlarged with fused benzofuran bearing alkoxy moieties, further favoring the nonradiative energy loss through the claimed ICT. Moreover, similar red-emitting dyes have been reported in the literature but with nitrogen instead of oxygen (fusion of indole).<sup>41</sup> The stronger electron donor ability of the aza group induced a more pronounced spectral red-shift but lower fluorescence efficiencies compared to those of analogue 26 tested herein, likely related to a higher charge transfer probability. In this line of reasoning, the presence of electron-withdrawing groups at the 8-aryl moiety, albeit moderately weak like the formyl group in dye 24, could reinforce the formation of ICT processes, because of the induced push–pull character (from the alkoxy-containing benzofuran to the formylated 8-phenyl group), explaining the unexpected quenching of this dye in polar media mentioned above (Figure 10 and Table 5). To unambiguously back up the idea that the ongoing ICT is the key process that rules the fluorescence response in these last dyes (24 and 35), we have measured the photophysical properties of the structurally related analogues 22 (bearing a nonformylated 8-phenyl ring) and 24 (with the said formylated ring) in a battery of solvents with different physicochemical properties (Table S2). Whereas in the former dye 22 the fluorescence quantum yield remains high [always >0.84 (Table S2 and Figure S5)] regardless of the solvent properties [described by the normalized  $E_T(30)$  solvent scale<sup>42</sup>], in the last dye 24 the fluorescence quantum yields are lower and the values show a marked dependency on solvent polarity [from 0.63 in cyclohexane to 0.37 in acetonitrile (Table S2 and Figure S5)]. Such a decrease in fluorescence efficiency with solvent polarity is a fingerprint of an ongoing dark ICT, which quenches the emission from the locally excited (LE) state, mainly in polar media where the low-lying ICT is further stabilized. Indeed, the recorded fluorescence quantum yield for dye 24 in a polar/protic solvent (methanol) does not follow the expected trend (Figure S5), and the value is higher [0.44 (Table S2)]. Such an exception is likely due to a specific interaction with the electron donor (oxygen atom of the benzofuran), which hampers the population of the photo-induced ICT state.

On the other hand, compounds 37 and 42, bearing the most fused aryl fragments, show low fluorescence efficiencies in polar

Table 5. Photophysical pProperties of Red-Emitting Benzofuran-Fused BODIPYs in Cyclohexane<sup>a</sup>

	$\lambda_{ab}$ (nm)	$\epsilon_{max}$ ( $\times 10^4$ M <sup>-1</sup> cm <sup>-1</sup> )	$\lambda_{fl}$ (nm)	$\Delta\nu_{St}$ (cm <sup>-1</sup> )	$\phi$	$\tau$ (ns)	$k_{fl}$ ( $\times 10^8$ s <sup>-1</sup> )	$k_{nr}$ ( $\times 10^8$ s <sup>-1</sup> )
22	548.5	21.5	596.5	345	0.88	4.09	2.15	0.29
23	586.5	21.5	595.5	260	0.88	4.21	2.09	0.29
24	592.5	13.7	612.0	540	0.63	2.47	2.55	1.49
25	583.5	20.0	593.5	290	0.88	4.10	2.14	0.29
26	586.0	15.6	597.5	330	0.84	3.99	2.10	0.40
34	581.5	17.3	590.0	250	0.95	4.02	2.35	0.14
35	592.0	19.0	603.0	310	0.96	4.12	2.33	0.09
36	591.5	23.2	602.0	295	0.89	4.11	2.16	0.27
37	613.0	12.9	625.0	315	0.81	4.31	1.89	0.43
41	586.5	18.0	596.5	285	0.81	3.94	2.07	0.47
42 <sup>b</sup>	596.5	17.9	611.5	410	0.88	4.04	2.18	0.30

<sup>a</sup>All of the photophysical data in additional solvents are listed in Table S1. <sup>b</sup>42 was insoluble in cyclohexane; thus, the reported data were recorded in diethyl ether.

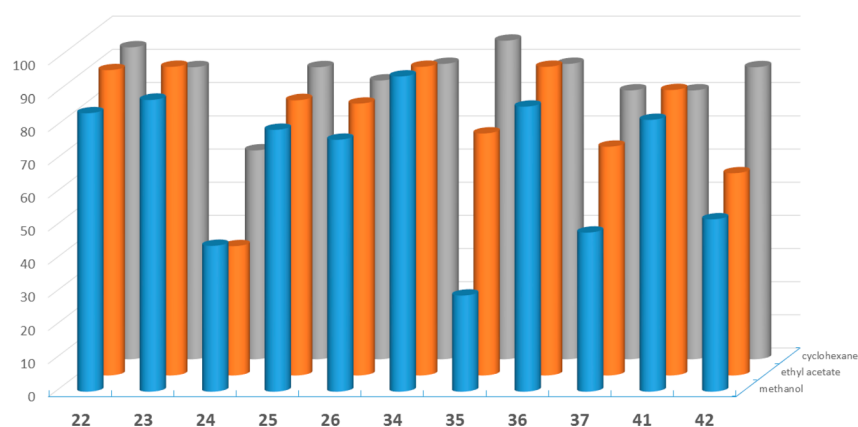


Figure 10. Evolution of the fluorescence quantum yield of the novel red-emitting BODIPYs reported herein with the tested media (from apolar cyclohexane in gray to polar methanol in blue).

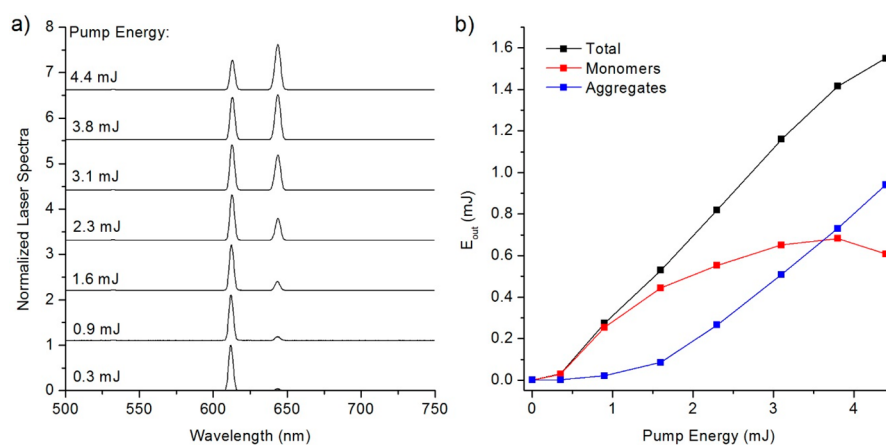


Figure 11. Normalized laser spectra (left) and output energy (right) as a function of pump energy for dye 25 at 0.38 mM in ethyl acetate.

media [down to 50% in methanol (Figure 10)], but the fluorescence lifetimes remain similar ( $\sim 3$  ns) (Table 5). In these highly extended derivatives, the structural stress to keep the whole chromophore planar should be high, although theoretical calculations predict that the chromophore remains quite planar. However, in the more polar media, where the interactions are stronger, such planarity could be slightly distorted, likely increasing the level of internal conversion relaxation with a consequent reduction in the fluorescence ability. Alternatively, a further addition of aromatic rings to the chromophoric core could increase the charge separation,

enhancing the nonradiative deactivation pathways in polar media.

**Laser Properties.** In view of the high fluorescence efficiency of these red-emitting dyes, we tested their performance as active media for tunable lasers (see the [Methods in the Supporting Information](#)). Because of the limited solubility of some of the dyes in apolar media, we chose ethyl acetate as the right solvent to measure the laser properties. In addition, this solvent allows assessment of the prospects of doping these dyes into solid state dye lasers (SSDL), as it mimics the chemical structure of methyl methacrylic polymers.<sup>43</sup> Hence, the laser

characterization and optimization in ethyl acetate could be directly extrapolated to these polymers. Even so, in the most functionalized and largest dyes, the solubility was restricted to 0.5 mM (37 and 41) or the required concentration to attain laser emission could not be reached (42).

The laser properties correlate, *grosso modo*, with the photophysical signatures (Table 5 and Table S1). At high concentrations, all of the dyes (with the aforementioned exception of 42 owing to solubility reasons) display a laser emission line far from the absorption and fluorescence band (around 70 and 50 nm, respectively), much stronger than what is usually recorded for BODIPY dyes (around 40 and 20 nm, respectively).<sup>44</sup> In particular, dye 37 presents the redder laser band, which is centered at 685 nm because of its larger number of aromatic rings fused to the chromophoric core (Figure 8). In contrast, at low concentrations or low pump energies, the laser emission band appears in the expected position for BODIPYs (Figure 8), leading, in some cases, to bichromatic emission (Figure 11 and Table S3). Such dual laser emission has been previously ascribed to the formation of excited state aggregates (excimers or superexciplexes) under strong laser pumping conditions of high-optical density active media;<sup>45</sup> hence, it is absent from the photophysical measurements. In this sense, the laser band recorded for these dyes at high concentrations in ethyl acetate corresponds to an aggregated form of the dyes, whereas the blue-shifted laser band at low concentrations corresponds to the dye in monomeric form (Figure 11). The presence of this kind of aggregate also enables widening of the tuning range.<sup>45b</sup>

With regard to the laser efficiencies, those dyes that showed a high fluorescence efficiency regardless of the surrounding medium (22, 23, 25, 26, 34, 36, and 41) display high laser efficiencies (surpassing 40% at the optimal concentration). On the other hand, those dyes that exhibited the lowest fluorescence efficiencies (24 and 37) show accordingly the worst laser efficiency (<30%). The only exception to such a good correlation is dye 35, which underwent an ICT process. Indeed, in spite of its weak fluorescence response, the recorded laser efficiency for 35 places this compound among the best in this study. Such an apparent mismatch can be rationalized considering the shorter excited state lifetime of such a dye, which favors the stimulated radiative deactivation and compensates for the low spontaneous emission probability. An analogous behavior was reported previously for LDS722, a hemicyanine dye with a quantum yield as low as 14% but a 43% laser efficiency owing to a lifetime of ~500 ps.<sup>46</sup> Most of the dyes show a good tolerance to a prolonged and intense laser pumping, with the exception of the dyes bearing methoxy (25 and 41) or formyl (24) functional groups at the *para*-position of the 8-phenyl ring. Indeed, >3 GJ/mol is required to decrease the laser output energy to 90% of its initial value, with the exception of fluorinated dye 34, which is able to tolerate up to 7.4 GJ/mol before the same energy loss is recorded (Table 6). These results are consistent with a previously reported strategy based on the fluorination of organic dyes, which enabled the achievement of long-lasting active media even under a drastic pumping regime.<sup>47</sup>

To put these results into perspective, we compared the laser performance of these red-emitting laser dyes with that of the commercially available BODIPY PM650, consisting of a methylated dipyrin core with a cyano group at the *meso*-position, that emits in the same spectral region.<sup>43</sup> This dye is very photostable (tolerance of ≤6.3 GJ/mol) because of the

**Table 6. Laser Properties of Red-Emitting Benzofuran-Fused BODIPYs in Ethyl Acetate at the Optimum Dye Concentration<sup>a</sup>**

dye	[dye] (mM)	Eff <sup>b</sup> (%)	$\lambda_{\text{peak}}$ (nm)	$E_{\text{dose}}^{90\%}$ (GJ/mol)
22	0.75	44	646.5	2.14
23	0.50	48	648.8	3.30
24	0.50	28	636.0	1.07
25	1.00	45	645.2	0.96
26	0.75	44	647.2	1.94
34	1.25	43	642.0	7.39
35	1.25	43	657.6	5.26
36	0.75	43	656.2	4.24
37	0.50	27	685.0	4.46
41	0.50	40	650.0	1.96
PM650	1.00	31	656.5	6.29

<sup>a</sup>The full set of laser data as a function of dye concentration appears in Table S3. The data corresponding to the commercially available red-emitting BODIPY laser dye (PM650) are included for comparison. <sup>b</sup>Abbreviations: Eff, laser efficiency or ratio of output/input energy;  $\lambda_{\text{peak}}$ , laser peak wavelength;  $E_{\text{dose}}^{90\%}$ , molar energy dose needed to reduce LIF to 90% of its initial value (see the Experimental Section for a detailed description).

electron withdrawing character of the said cyano group, which reduces the reactivity against the oxidizing ambient oxygen, involved in the photodegradation mechanism.<sup>48</sup> At the same time, such functionalization enables the population of ICT states. Such a nonradiative deactivation channel shortens the lifetime, supporting the recorded moderately high laser efficiencies [30% (Table 6)] in spite of its reduced fluorescence efficiency. The photostabilities of most of the dyes tested herein are lower than that of PM650, but some of them reach close values, with the exception of dye 34 whose photostability surpasses even that of the reference PM650. On the other hand, the recorded laser efficiencies of most of the dyes tested herein (mainly, 22, 23, 25, 26, 34, 36, and 41) are better than that displayed by PM650. Therefore, the benzofuran-fused BODIPYs reported herein are suitable candidates for the development of efficient red-emitting lasers with a reasonable photostability.

## CONCLUSIONS

We have described a novel synthetic methodology for preparing benzofuran-fused BODIPY dyes in four steps starting from commercially available 8-methylthioBODIPY 4. Careful selection of the reaction conditions permitted the chemoselective functionalization of the *meso*-position of multiply functionalized BODIPY 6. The  $S_{\text{N}}\text{Ar}$ -like reaction of phenolates exclusively at positions 3 and 5 allows the positioning of such a moiety for the final intramolecular Pd(0)-catalyzed arylation at positions 2 and 6 of the BODIPY nucleus. The synthetic avenue reported herein not only allows easy access to benzofuran-fused BODIPYs with different substitution patterns but also enables incorporation of relevant biomolecules into the BODIPYs core. Once these biomolecules are endowed with new fluorescent properties, they may find very interesting biology-related applications such as use as sensors, cell imaging, protein labeling, etc. The extended aromatic framework of these conformationally restricted BODIPYs renders strong absorption, fluorescence, and laser bands shifted to the red edge of the visible spectrum. Indeed, the fluorescence and laser efficiencies almost reach 100% and

are >40%, respectively, in the best cases. It is worth noting that the laser emission is rather intriguing, displaying a deep shift toward the red edge because of the promotion of excited state aggregates at high concentrations and under intense laser pumping. Therefore, these  $\pi$ -extended BODIPYs show good behavior as red laser dyes in terms of efficiency and photostability, because  $\leq 7.3$  GJ/mol of dye is required to induce a decrease in the output laser emission of just 10%, overcoming the limitations of most of the commercially available dyes (such as cyanines or oxazines) in this spectral region. This method is amenable to grafting other heterocycles such as indoles and benzothiophenes by adding either anilines or thiophenols. We are currently exploring these possibilities as well as the cell imaging properties of both **41** and **42**. The results will be reported in due course.

## ■ EXPERIMENTAL SECTION

**Photophysical Properties.** Spectroscopic properties were registered in diluted solutions ( $\sim 2 \times 10^{-6}$  M), prepared by adding the corresponding solvent (spectroscopic grade) to the residue from the adequate amount of a concentrated stock solution in acetone, after vacuum evaporation of this solvent. UV-vis absorption and fluorescence spectra and decay curves were recorded on a Varian model CARY 4E spectrophotometer and an Edinburgh Instruments spectrofluorimeter (model FLSP 920), respectively. Fluorescence quantum yields ( $\phi$ ) were obtained using as a reference commercial cresyl violet ( $\phi^r = 0.54$  in methanol). The values were corrected by the refractive index of the solvent. Radiative decay curves were registered with the time-correlated single-photon counting technique using a multichannel plate detector with picosecond time resolution. The fluorescence emission was monitored at the maximum emission wavelength after excitation by means of a wavelength-tunable Fianium Supercontinuum laser. The fluorescence lifetime ( $\tau$ ) was obtained after the deconvolution of the instrumental response signal from the recorded decay curves by means of an iterative method. The goodness of the exponential fit was controlled by statistical parameters ( $\chi^2$  and the analysis of the residuals). The radiative ( $k_{\text{r}}$ ) and nonradiative ( $k_{\text{nr}}$ ) rate constants were calculated from the fluorescence quantum yield and lifetime;  $k_{\text{r}} = \phi/\tau$ , and  $k_{\text{nr}} = (1 - \phi)/\tau$ .

**Quantum Mechanical Calculations.** Ground state geometries were optimized with density functional theory (DFT) using the range-separated hybrid wB97XD method, whereas the first singlet excited state was optimized by the time-dependent (TD) method and the same functional. In both cases, the triple valence basis set with two polarization functions (6-311g\*\*) was used. The geometries were considered as energy minima when the corresponding frequency analysis did not give any negative value. The solvent effect (ethyl acetate) was considered in the conducted theoretical simulations by means of the polarizable continuum model (PCM). All of the calculations were performed using Gaussian 16 as implemented in the computational cluster "arina" of the UPV/EHU.

**Electrochemistry.** Cyclic voltammograms (Metrohm Autolab) were recorded using a three-electrode setup with a platinum layer (surface of 8 mm  $\times$  7.5 mm) working electrode, a platinum wire counter electrode, and a Ag/AgCl reference electrode. A 0.1 M solution of tetrabutylammonium hexafluorophosphate (TBAPF<sub>6</sub>) in dry acetonitrile was used as the electrolyte solvent in which the compounds were dissolved to achieve a concentration of  $\sim 1$  mM. All redox potentials were reported versus ferrocene as the internal standard. The solutions were purged with argon, and all of the measurements were performed under an inert atmosphere.

**Laser Measurement Setup.** Liquid solutions of dyes in ethyl acetate were contained in 1 cm optical path length rectangular quartz cells carefully sealed to avoid solvent evaporation during experiments. The liquid solutions were transversely pumped with 20 ns full width at half-maximum (fwhm) pulses from a frequency-doubled (532 nm) Q-switched Nd:YAG laser (Lotis TII SL-2132) at a repetition rate of 1 Hz. The exciting pulses were line-focused onto the cell using a

combination of positive and negative cylindrical lenses ( $f = 15$  cm and  $f = -15$  cm, respectively) perpendicularly arranged. The plane parallel oscillation cavity (2 cm length) consisted of a 90% reflectivity aluminum mirror acting as a back reflector and with the lateral face of the cell acting as an output coupler (4% reflectivity). The pump and output energies were detected by a calibrated laser energy meter (QE 12LP-S-MB-DO, Gentec). The output laser emission was directed toward a fiber bundle and detected with a spectrograph/monochromator (Spectrapro-300i Acton Research) equipped with a thermoelectrically cooled CCD detector (SpectruMM:GS 128B). A shortwave cutoff filter (OptoSigma, cutoff at 540 nm) was placed before the fiber bundle to prevent any scattered pump light from entering the spectrograph. Neutral density filters were used to avoid CCD detector saturation.

The photostability of the dyes in an ethyl acetate solution was evaluated by using a pumping energy and geometry exactly equal to those of the laser experiments. We used spectroscopic quartz cuvettes with 1 cm optical path lengths and depths ( $L$ ) of 0.1 cm to allow the minimum solution volume ( $V_s = 60 \mu\text{L}$ ) to be excited. The lateral facets were grounded, whereupon no laser oscillation was obtained. Nevertheless, information about photostabilities can be obtained by monitoring the decrease in laser-induced fluorescence (LIF) intensity. To facilitate comparisons in a manner independent of the experimental conditions and sample, the photostability figure of merit was defined as the accumulated pump energy absorbed by the system ( $E_{\text{dose}}$ ), per mole of dye, before the output energy falls to 90% of its initial value. In terms of experimental parameters, this energy dose, in units of gigajoules per mole, can be expressed as

$$E_{\text{dos}}^{90\%} = \frac{E_{\text{pump}}(1 - 10^{-\epsilon CL}) \sum_{\# \text{ pulses}} f}{CV_s} \quad (4)$$

where  $E_{\text{pump}}$  is the energy per pulse in gigajoules,  $C$  is the molar concentration,  $\epsilon$  is the molar absorption coefficient in units of  $\text{M}^{-1} \text{cm}^{-1}$ ,  $L$  is the depth of the cuvette in centimeters,  $V_s$  is the solution volume, in liters, within the cuvette, and  $f$  is the ratio of the LIF intensity after  $\#$  pulses to the LIF intensity in the first pulse. It can be shown that  $\sum f$  accounts for the reduction in pump absorption due to species photodegradation. To accelerate the experiment, the pump repetition rate was increased to 15 Hz. The fluorescence emission was monitored perpendicular to the exciting beam, collected by an optical fiber, and acquired using the previously described spectrograph/monochromator system.

**X-ray Crystal Structure Determination.** Intensity data were collected on an Agilent Technologies Super-Nova diffractometer, which was equipped with monochromated Cu  $K\alpha$  radiation ( $\lambda = 1.54184 \text{ \AA}$ ) and an Atlas CCD detector. Measurement was carried out at 99.99(10) K with the help of an Oxford Cryostream 700 PLUS temperature device. Data frames were processed (unit cell determination, analytical absorption correction with face indexing, intensity data integration, and correction for Lorentz and polarization effects) using the CrysAlis software package. The structure was determined using Olex2 and refined by full-matrix least squares with SHELXL-97. Final geometrical calculations were carried out with Mercury and PLATON as integrated in WinGX. Crystallographic data (excluding structure factors) for the structure(s) reported in this paper have been deposited with the Cambridge Crystallographic Data Centre as supplementary publication CCDC-1877155. Copies of the data can be obtained free of charge from [www.ccdc.cam.ac.uk/conts/retrieving.html](http://www.ccdc.cam.ac.uk/conts/retrieving.html).

**Synthesis and Characterization.**  $^1\text{H}$  and  $^{13}\text{C}$  NMR spectra were recorded in deuteriochloroform ( $\text{CDCl}_3$ ), with either tetramethylsilane (TMS) (0.00 ppm for  $^1\text{H}$ , 0.00 ppm for  $^{13}\text{C}$ ) or chloroform (7.26 ppm for  $^1\text{H}$ , 77.00 ppm for  $^{13}\text{C}$ ). Data are reported in the following order: chemical shift in parts per million, multiplicities [br (broadened), s (singlet), d (doublet), t (triplet), q (quartet), m (multiplet), exch (exchangeable), and app (apparent)], coupling constants,  $J$  (hertz), and integration. Infrared spectra were recorded on a FTIR spectrophotometer. Peaks are reported ( $\text{cm}^{-1}$ ) with the following relative intensities: s (strong, 67–100%), m (medium, 40–

67%), and *w* (weak, 20–40%). Melting points are not corrected. TLC was conducted in silica gel on TLC Al foils. Detection was achieved with UV light (254 or 365 nm). HRMS samples were ionized by ESI+ and recorded via the TOF method.

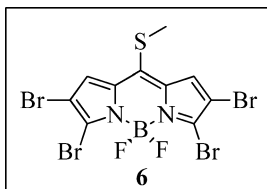
**Materials.** Starting 8-methylthioBODIPY, CuTC, tri(2-furyl)-phosphine, and boronic acids are commercially available. Solvents were dried and distilled before use.

**General Procedure for the L–S Cross-Coupling Reaction (GP1).** A Schlenk tube equipped with a stir bar was charged with **6** (1.0 equiv), the corresponding boronic acid (3.0 equiv), and dry THF (0.03 M). The mixture was sparged with N<sub>2</sub> for 3 min, whereupon Pd<sub>2</sub>(dba)<sub>3</sub> (2.5 mol %), trifurylphosphine (7.5%), and CuTC (3.0 equiv) were added under N<sub>2</sub>. The Schlenk tube was then immersed in a preheated oil bath at 55 °C. The oil bath was removed after the starting material **6** BODIPY was consumed (TLC, AcOEt/hexanes). After the mixture reached rt, the solvent was removed and the crude material was adsorbed in SiO<sub>2</sub> gel, dried under reduced pressure, and purified by flash chromatography on SiO<sub>2</sub> gel using AcOEt/hexanes as eluent.

**General Procedure for the Nucleophilic Substitution with Phenols and Phenol Derivatives (GP2).** A sealed tube with a stir bar was charged with the corresponding BODIPYs (**10–15**) (1.0 equiv), phenol or phenol derivatives (4 or 6 equiv), Na<sub>2</sub>CO<sub>3</sub> (5 or 6 equiv), and acetonitrile (0.02 M), and then the mixture was sparged with N<sub>2</sub> for 5 min. The tube was sealed, and the solution was stirred at 110 °C until competition ensued (TLC monitoring, AcOEt/hexanes, THF/hexane, or acetone/hexane as indicated). The oil bath was removed after the starting BODIPY was consumed. After the mixture reached rt, the solvent was removed under reduced pressure, and the crude material was adsorbed in SiO<sub>2</sub> gel, dried under vacuum, and purified by flash chromatography on SiO<sub>2</sub> gel using THF/hexanes, acetone/hexanes, CHCl<sub>3</sub>/hexanes, or AcOEt/hexanes as indicated.

**General Procedure for the Cyclization Reaction (GP3).** A sealed tube with a stir bar was charged with the corresponding BODIPY (**16–21** and **27–33**) (1.0 equiv), Pd(OAc)<sub>2</sub> (0.05 equiv), PPh<sub>3</sub> (0.1 equiv), K<sub>2</sub>CO<sub>3</sub> (3 equiv), and toluene, and then the mixture was sparged with N<sub>2</sub> for 5 min. The tube was sealed, and the solution was stirred at 150 °C until the reaction reached completion (TLC monitoring, AcOEt/hexanes, THF/hexane, or CHCl<sub>3</sub>/hexane as indicated). The oil bath was removed after the starting BODIPY was consumed. After the mixture reached rt, the solvent was removed under reduced pressure, and the crude material was adsorbed in SiO<sub>2</sub> gel, dried under vacuum, and purified by flash chromatography on SiO<sub>2</sub> gel using acetone/hexanes or CHCl<sub>3</sub>/hexanes as indicated.

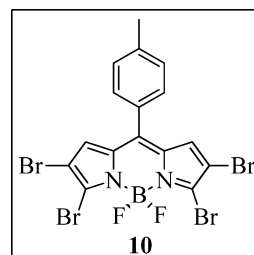
#### Synthesis of **6**.



A round-bottom flask under N<sub>2</sub> was charged with **4** (30 mg, 0.126 mmol, 1 equiv), *N*-bromosuccinimide (112.1 mg, 0.63 mmol, 5.0 equiv), and acetic acid (4.2 mL). The reaction mixture was stirred at room temperature overnight whereupon water (30 mL) was added and the pH was adjusted using saturated Na<sub>2</sub>CO<sub>3</sub> to pH 7. The product was extracted with ethyl acetate, washed with brine (5 × 20 mL), dried with anhydrous MgSO<sub>4</sub>, and filtered. The solvent was removed under reduced pressure, and the crude product was adsorbed in SiO<sub>2</sub> gel, dried under vacuum, and purified by flash chromatography using 10% EtOAc/hexanes. The desired product (20 mg, 0.036 mmol, 70%) was obtained as a dark red solid: TLC (15% EtOAc/hexanes; *R*<sub>f</sub> = 0.25); mp 212–214 °C; IR (KBr, cm<sup>-1</sup>) 2669 (w), 1516 (s), 1441 (m), 1364 (s), 1335 (s), 1303 (m), 1237 (s), 1161 (s), 1097 (s), 979 (m), 966 (m), 916 (s), 819 (w), 808 (w), 744 (w), 632 (w), 587 (w), 502 (w); <sup>1</sup>H NMR (500 MHz, CDCl<sub>3</sub>) δ 7.44 (s, 2H), 2.83 (s, 3H); <sup>13</sup>C{<sup>1</sup>H} NMR (126 MHz, CDCl<sub>3</sub>) δ 147.7, 134.9, 133.5, 128.7, 111.8,

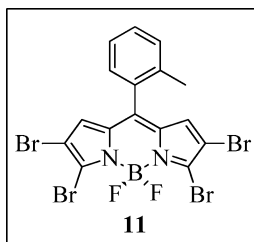
21.5; HRMS (ESI+) *m/z* calcd for C<sub>10</sub>H<sub>5</sub>BBr<sub>4</sub>F<sub>2</sub>N<sub>2</sub>SK [M + K]<sup>+</sup> 592.6560, found 592.6547.

#### Synthesis of **10**.<sup>49</sup>



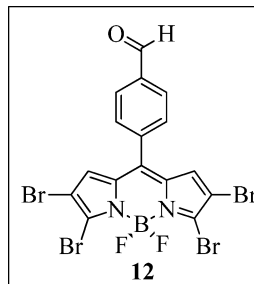
According to GP1. **6** (25 mg, 0.045 mmol), *p*-tolylboronic acid (18.4 mg, 0.135 mmol), Pd<sub>2</sub>(dba)<sub>3</sub> (1.0 mg, 1.1 × 10<sup>-3</sup> mmol), TFP (0.79 mg, 3.4 × 10<sup>-3</sup> mmol), and CuTC (25.8 mg, 0.135 mmol) were used. After 2 h, the crude was purified using 0.2% AcOEt/hexanes. The desired product (13 mg, 0.022 mmol, 48%) was obtained as a dark red solid: TLC (20% THF/hexanes; *R*<sub>f</sub> = 0.79); mp >260 °C dec; <sup>1</sup>H NMR (500 MHz, CDCl<sub>3</sub>) δ 7.38 (d, *J* = 8.1 Hz, 2H), 7.35 (d, *J* = 8.2 Hz, 2H), 6.93 (s, 2H), 2.47 (s, 3H); HRMS (ESI+) *m/z* calcd for C<sub>17</sub>H<sub>10</sub>BBr<sub>4</sub>F<sub>2</sub>N<sub>2</sub> [M + H]<sup>+</sup> 598.7596, found 598.7619.

#### Synthesis of **11**.



According to GP1. **6** (20 mg, 0.036 mmol), *o*-tolylboronic acid (14.7 mg, 0.108 mmol), Pd<sub>2</sub>(dba)<sub>3</sub> (0.82 mg, 9.0 × 10<sup>-4</sup> mmol), TFP (0.63 mg, 2.7 × 10<sup>-3</sup> mmol), and CuTC (20.7 mg, 0.108 mmol) were used. After 2 h, the crude material was purified using 3% AcOEt/hexanes. The desired product (16.5 mg, 0.027 mmol, 76% yield) was obtained as dark red crystals: TLC (20% AcOEt/hexanes; *R*<sub>f</sub> = 0.57); mp >260 °C dec; IR (KBr, cm<sup>-1</sup>) 3679 (w), 2921 (w), 2661 (w), 1554 (s), 1539 (s), 1488 (m), 1452 (w), 1354 (s), 1312 (s), 1247 (s), 1225 (s), 1179 (s), 1141 (s), 1083 (s), 1014 (m), 999 (m), 905 (m), 839 (m), 819 (m), 737 (s), 701 (m), 651 (w), 597 (w), 543 (w), 488 (w); <sup>1</sup>H NMR (500 MHz, CDCl<sub>3</sub>) δ 7.45 (t, *J* = 7.1 Hz, 2H), 7.35–7.28 (m, 2H), 7.21 (d, *J* = 7.4 Hz, 2H), 6.68 (s, 2H), 2.23 (s, 3H); <sup>13</sup>C{<sup>1</sup>H} NMR (126 MHz, CDCl<sub>3</sub>) δ 142.5, 136.6, 135.7, 135.4, 131.0, 131.0, 130.9, 130.6, 129.9, 125.9, 112.3, 20.2; HRMS (ESI+) *m/z* calcd for C<sub>16</sub>H<sub>10</sub>BBr<sub>4</sub>F<sub>2</sub>N<sub>2</sub> [M + H]<sup>+</sup> 598.7596, found 598.7620.

#### Synthesis of **12**.

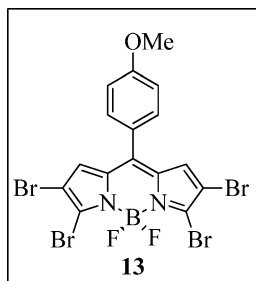


According to GP1. **6** (10 mg, 0.02 mmol), *p*-formylphenyl boronic acid (5.4 mg, 0.04 mmol), Pd<sub>2</sub>(dba)<sub>3</sub> (0.4 mg, 5.0 × 10<sup>-4</sup> mmol), TFP (0.3 mg, 1.4 × 10<sup>-3</sup> mmol), and CuTC (10.3 mg, 0.05 mmol) were used. After 1 h, the crude material was purified using 5% AcOEt/hexanes. The desired product (4.2 mg, 0.007 mmol, 38% yield) was obtained as green crystals: TLC (15% AcOEt/hexanes; *R*<sub>f</sub> = 0.46); mp 271–272 °C; IR (KBr, cm<sup>-1</sup>) 3679 (w), 3120 (w), 1701 (s), 1573 (s), 1551 (s), 1447 (w), 1357 (s), 1314 (m), 1287 (w), 1238 (s), 1207 (w), 1179 (w), 1097 (s), 1018 (w), 995 (m), 833 (m), 753 (m), 705 (m), 652 (w), 486 (w); <sup>1</sup>H NMR (500 MHz, CDCl<sub>3</sub>) δ 10.15 (s, 1H),



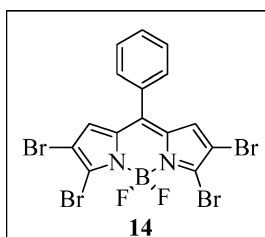
8.07 (d,  $J = 8.0$  Hz, 2H), 7.67 (d,  $J = 8.0$  Hz, 2H), 6.85 (s, 3H);  $^{13}\text{C}\{^1\text{H}\}$  NMR (126 MHz,  $\text{CDCl}_3$ )  $\delta$  191.0, 140.5, 138.2, 137.3, 136.6, 134.7, 131.3, 131.0, 130.0, 112.8; HRMS (ESI+)  $m/z$  calcd for  $\text{C}_{16}\text{H}_7\text{BBr}_4\text{F}_2\text{N}_2\text{O}_2\text{Na}$  [ $M + \text{Na}$ ] $^+$  634.7208, found 634.7212.

#### Synthesis of 13.



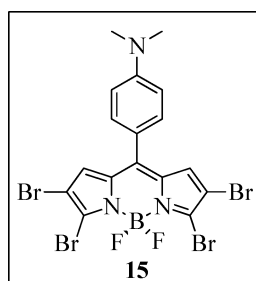
According to GP1. **6** (20 mg, 0.036 mmol), *p*-methoxyphenyl boronic acid (16.5 mg, 0.108 mmol),  $\text{Pd}_2(\text{dba})_3$  (0.83 mg,  $9.0 \times 10^{-4}$  mmol), TFP (0.63 mg,  $2.7 \times 10^{-3}$  mmol), and CuTC (20.7 mg, 0.11 mmol) were used. After 3 h, the crude was purified using 15% AcOEt/hexanes. The desired product (14 mg, 0.023 mmol, 63% yield) was obtained as a dark red solid: TLC (20% AcOEt/hexanes;  $R_f = 0.5$ ); mp 238–239 °C;  $^1\text{H}$  NMR (500 MHz,  $\text{CDCl}_3$ )  $\delta$  7.46 (d,  $J = 8.7$  Hz, 2H), 7.06 (d,  $J = 8.7$  Hz, 2H), 6.95 (s, 2H), 3.92 (s, 3H); HRMS (ESI+)  $m/z$  calcd for  $\text{C}_{16}\text{H}_9\text{BBr}_4\text{F}_2\text{N}_2\text{O}_2\text{Na}$  [ $M + \text{Na}$ ] $^+$  636.7366, found 636.7364.

#### Synthesis of 14.



According to GP1. **6** (50 mg, 0.090 mmol), phenylboronic acid (40.0 mg, 0.072 mmol),  $\text{Pd}_2(\text{dba})_3$  (1.7 mg,  $1.8 \times 10^{-3}$  mmol), TFP (1.3 mg,  $5.4 \times 10^{-3}$  mmol), and CuTC (41.3 mg, 0.260 mmol) were used. After 2 h, the crude was purified using 1% AcOEt/hexane. The desired product (9.5 mg, 0.016 mmol, 18%) was obtained as a purple solid: TLC (10% AcOEt/hexanes;  $R_f = 0.48$ ); mp >200 °C dec;  $^1\text{H}$  NMR (500 MHz,  $\text{CDCl}_3$ )  $\delta$  7.63 (t,  $J = 7.4$  Hz, 1H), 7.55 (t,  $J = 7.6$  Hz, 2H), 7.48 (d,  $J = 7.2$  Hz, 2H), 6.90 (s, 1H); HRMS (ESI+)  $m/z$  calcd for  $\text{C}_{15}\text{H}_7\text{BBr}_4\text{F}_2\text{N}_2\text{Na}$  [ $M + \text{Na}$ ] $^+$  606.7259, found 606.7278.

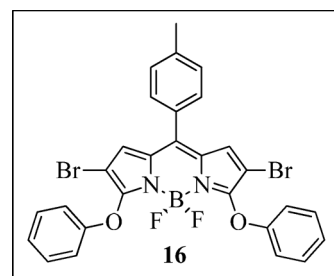
#### Synthesis of 15.



According to GP1. **6** (50 mg, 0.09 mmol), 4-(dimethylamino)phenyl boronic acid (44.7 mg, 0.27 mmol),  $\text{Pd}_2(\text{dba})_3$  (2.07 mg,  $2.3 \times 10^{-3}$  mmol), TFP (1.6 mg,  $6.8 \times 10^{-3}$  mmol), and CuTC (51.7 mg, 0.27 mmol) were used. After 50 min, the crude material was purified using 30% AcOEt/hexanes. The desired product (30 mg, 0.048 mmol, 53% yield) was obtained as a dark blue solid: TLC (20% AcOEt/hexanes;  $R_f = 0.2$ ); mp 221–223 °C; IR (KBr,  $\text{cm}^{-1}$ ) 2918 (w), 1602 (s), 1542 (w), 1512 (m), 1493 (m), 1431 (w), 1403 (w), 1361 (s), 1328 (m), 1283 (m), 1254 (m), 1195 (m), 1106 (m), 1004 (w), 984 (m), 976 (m), 826 (w), 751 (w), 647 (w), 537 (w);  $^1\text{H}$  NMR (500 MHz,  $\text{CDCl}_3$ )  $\delta$  7.45 (d,  $J = 8.8$  Hz, 2H), 7.01 (s, 2H), 6.79 (d,  $J = 8.8$  Hz, 2H), 3.13 (s, 3H);  $^{13}\text{C}\{^1\text{H}\}$  NMR (126 MHz,  $\text{CDCl}_3$ )  $\delta$  153.3, 144.4,

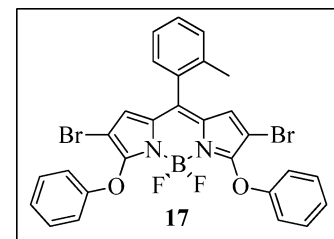
134.3, 133.4, 131.6, 131.0, 119.9, 112.0, 110.8, 40.3; HRMS (ESI+)  $m/z$  calcd for  $\text{C}_{17}\text{H}_{13}\text{BBr}_4\text{F}_2\text{N}_3$  [ $M + \text{H}$ ] $^+$  627.7862, found 627.7854.

#### Synthesis of 16.



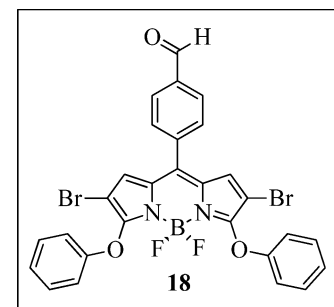
According to GP2. **10** (46.0 mg, 0.08 mmol), phenol (36.2 mg, 0.39 mmol),  $\text{Na}_2\text{CO}_3$  (40.8 mg, 0.39 mmol), and acetonitrile (4 mL) were used. The reaction mixture was stirred at 110 °C for 6 h. The crude was purified using 1% AcOEt/hexanes. The desired product (19.4 mg, 0.032 mmol, 80% yield) was obtained as red crystals: TLC (10% AcOEt/hexanes;  $R_f = 0.26$ ); mp 197–199 °C; IR (KBr,  $\text{cm}^{-1}$ ) 3679 (w), 2971 (w), 1571 (m), 1553 (m), 1546 (m), 1501 (m), 1485 (m), 1448 (s), 1333 (w), 1253 (s), 1204 (w), 1181 (m), 1128 (s), 1038 (s), 1003 (w), 988 (w), 840 (m), 711 (w);  $^1\text{H}$  NMR (500 MHz,  $\text{CDCl}_3$ )  $\delta$  7.44 (d,  $J = 8.0$  Hz, 2H), 7.38–7.30 (m, 6H), 7.16–7.09 (m, 6H), 6.94 (s, 2H), 2.48 (s, 2H);  $^{13}\text{C}\{^1\text{H}\}$  NMR (126 MHz,  $\text{CDCl}_3$ )  $\delta$  157.9, 155.8, 142.6, 141.6, 132.1, 130.5, 129.8, 129.6, 129.5, 127.7, 124.6, 117.9, 96.1, 21.6; HRMS (ESI+)  $m/z$  calcd for  $\text{C}_{28}\text{H}_{19}\text{BBr}_2\text{F}_2\text{N}_2\text{O}_2\text{Na}$  [ $M + \text{Na}$ ] $^+$  646.9753, found 646.9743.

#### Synthesis of 17.



According to GP2. **11** (43.0 mg, 0.07 mmol), phenol (33.8 mg, 0.36 mmol),  $\text{Na}_2\text{CO}_3$  (38.1 mg, 0.36 mmol), and acetonitrile (4 mL) were used. The reaction mixture was stirred at 110 °C for 3 h. The crude was purified using 1% AcOEt/hexanes. The desired product (34.6 mg, 0.055 mmol, 77% yield) was obtained as red crystals: TLC (10% AcOEt/hexanes;  $R_f = 0.30$ ); mp 202–203 °C; IR (KBr,  $\text{cm}^{-1}$ ) 3672 (w), 2972 (w), 2917 (w), 1563 (m), 1485 (m), 1450 (s), 1352 (w), 1337 (w), 1251 (s), 1197 (m), 1182 (m), 1118 (s), 1034 (s), 1003 (w), 912 (w), 839 (m), 741 (m), 706 (w), 685 (w);  $^1\text{H}$  NMR (500 MHz,  $\text{CDCl}_3$ )  $\delta$  7.46–7.41 (m, 1H), 7.37–7.27 (m, 7H), 7.17–7.10 (m, 6H), 6.69 (s, 2H), 2.31 (s, 3H);  $^{13}\text{C}\{^1\text{H}\}$  NMR (126 MHz,  $\text{CDCl}_3$ )  $\delta$  158.1, 155.7, 141.7, 136.9, 131.5, 131.4, 130.8, 130.3, 130.1, 129.8, 128.1, 125.7, 124.7, 118.0, 96.2, 20.2; HRMS (ESI+)  $m/z$  calcd for  $\text{C}_{28}\text{H}_{20}\text{BBr}_2\text{F}_2\text{N}_2\text{O}_2$  [ $M$ ] $^+$  624.9933, found 624.9934.

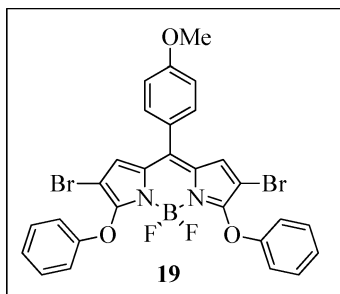
#### Synthesis of 18.



According to GP2. **12** (20.0 mg, 0.03 mmol), phenol (18.5 mg, 0.20 mmol),  $\text{Na}_2\text{CO}_3$  (20.8 mg, 0.20 mmol), and acetonitrile (2 mL) were used. The reaction mixture was stirred at 110 °C for 3 h. The crude material was purified using 10% AcOEt/hexanes. The desired product

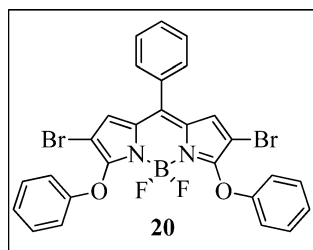
(12.0 mg, 0.019 mmol, 57% yield) was obtained as red crystals: TLC (20% AcOEt/hexanes;  $R_f = 0.30$ ); mp 112–113 °C; IR (KBr,  $\text{cm}^{-1}$ ) 3694 (w), 2973 (w), 1704 (m), 1574 (m), 1556 (m), 1500 (m), 1450 (s), 1350 (w), 1253 (s), 1201 (m), 1182 (m), 1123 (s), 1037 (s), 1003 (m), 833 (m), 757 (w), 686 (w);  $^1\text{H NMR}$  (500 MHz,  $\text{CDCl}_3$ )  $\delta$  10.15 (s, 1H), 8.07 (d,  $J = 8.2$  Hz, 2H), 7.72 (d,  $J = 8.1$  Hz, 2H) 7.37–7.30 (m, 4H), 7.16 (t,  $J = 7.4$  Hz, 2H), 7.13–7.10 (m, 4H), 6.86 (s, 2H);  $^{13}\text{C}\{^1\text{H}\}$  NMR (126 MHz,  $\text{CDCl}_3$ )  $\delta$  191.3, 158.6, 155.6, 139.8, 138.0, 137.8, 131.8, 131.1, 129.9, 129.9, 127.4, 124.9, 118.0, 96.7; HRMS (ESI+)  $m/z$  calcd for  $\text{C}_{28}\text{H}_{18}\text{BBr}_2\text{F}_2\text{N}_2\text{O}_3$   $[\text{M} + \text{H}]^+$  638.9726, found 638.9730.

#### Synthesis of 19.



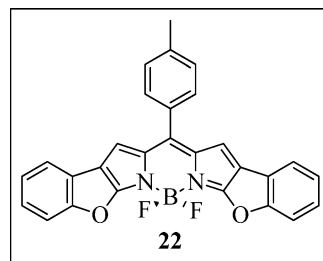
According to GP2. **13** (34.5 mg, 0.06 mmol), phenol (26.4 mg, 0.29 mmol),  $\text{Na}_2\text{CO}_3$  (29.8 mg, 0.28 mmol), and acetonitrile (3 mL) were used. The reaction mixture was stirred at 110 °C for 5.5 h. The crude material was purified using 2% AcOEt/hexanes. The desired product (25.9 mg, 0.040 mmol, 72% yield) was obtained as orange crystals: TLC (10% AcOEt/hexanes;  $R_f = 0.08$ ); mp 237–238 °C; IR (KBr,  $\text{cm}^{-1}$ ) 3694 (w), 2972 (w), 2917 (w), 2845 (w), 1605 (w), 1575 (m), 1551 (s), 1500 (m), 1485 (m), 1452 (s), 1444 (s), 1351 (w), 1333 (w), 1297 (w), 1256 (s), 1182 (s), 1130 (s), 1108 (s), 1039 (s), 1020 (m), 838 (s), 716 (m), 684 (w), 606 (w), 575 (w);  $^1\text{H NMR}$  (500 MHz,  $\text{CDCl}_3$ )  $\delta$  7.50 (d,  $J = 8.7$  Hz, 2H), 7.35–7.30 (m, 4H), 7.17–7.05 (m, 8H), 6.96 (s, 2H), 3.92 (s, 3H);  $^{13}\text{C}\{^1\text{H}\}$  NMR (126 MHz,  $\text{CDCl}_3$ )  $\delta$  162.2, 157.7, 155.9, 142.4, 132.3, 132.0, 129.8, 127.6, 124.7, 124.6, 117.9, 114.5, 96.0, 55.73; HRMS (ESI+)  $m/z$  calcd for  $\text{C}_{28}\text{H}_{20}\text{BBr}_2\text{F}_2\text{N}_2\text{O}_3$   $[\text{M} + \text{H}]^+$  640.9883, found 640.9867.

#### Synthesis of 20.



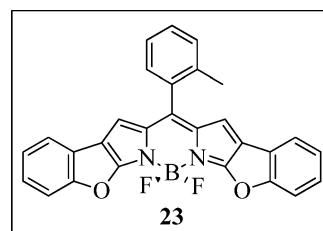
According to GP2. **14** (31 mg, 0.05 mmol), phenol (25 mg, 0.27 mmol),  $\text{Na}_2\text{CO}_3$  (28.1 mg, 0.27 mmol), and acetonitrile (2.5 mL) were used. The reaction mixture was stirred at 110 °C for 3 h. The crude material was purified using 2% AcOEt/hexanes. The desired product (38.4 mg, 0.062 mmol, 60% yield) was obtained as red crystals: TLC (10% AcOEt/hexanes;  $R_f = 0.30$ ); mp 213–214 °C; IR (KBr,  $\text{cm}^{-1}$ ) 3368 (w), 2972 (w), 1578 (w), 1551 (s), 1502 (m), 1485 (m), 1451 (s), 1440 (s), 1333 (w), 1289 (w), 1253 (s), 1206 (w), 1182 (m), 1123 (s), 1038 (s), 1003 (w), 988 (w), 840 (m), 731 (w), 718 (w), 605 (w);  $^1\text{H NMR}$  (500 MHz,  $\text{CDCl}_3$ )  $\delta$  7.62–7.58 (m, 1H), 7.35–7.31 (m, 4H), 7.16–7.09 (m, 6H), 6.92 (s, 2H);  $^{13}\text{C}\{^1\text{H}\}$  NMR (126 MHz,  $\text{CDCl}_3$ )  $\delta$  158.1, 155.8, 142.2, 132.3, 132.1, 130.9, 130.5, 129.8, 128.9, 127.7, 124.7, 117.9, 96.2; HRMS (ESI+)  $m/z$  calcd for  $\text{C}_{27}\text{H}_{18}\text{BBr}_2\text{F}_2\text{N}_2\text{O}_2$   $[\text{M} + \text{H}]^+$  610.9777, found 610.9767.

#### Synthesis of 22.



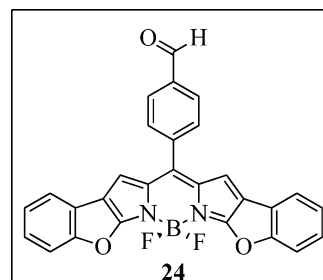
According to GP3. **16** (30.0 mg, 0.05 mmol),  $\text{Pd}(\text{OAc})_2$  (0.54 mg,  $2.4 \times 10^{-3}$  mmol, 0.05 equiv),  $\text{PPh}_3$  (1.3 mg,  $4.8 \times 10^{-3}$  mmol, 0.1 equiv),  $\text{K}_2\text{CO}_3$  (19.9 mg, 0.14 mmol, 3 equiv), and toluene (4 mL) were used. The reaction mixture was stirred at 150 °C for 7 h. The crude material was purified using 80%  $\text{CHCl}_3$ /hexanes. The desired product (13.0 mg, 0.04 mmol, 59% yield) was obtained as a golden solid: TLC (20% THF/hexanes;  $R_f = 0.3$ ); mp 263–265 °C; IR (KBr,  $\text{cm}^{-1}$ ) 2921 (w), 1628 (w), 1577 (s), 1478 (m), 1449 (s), 1442 (s), 1408 (s), 1367 (s), 1348 (s), 1323 (s), 1291 (m), 1277 (m), 1186 (w), 1159 (m), 1143 (s), 1113 (s), 1012 (w), 987 (s), 926 (w), 818 (m), 808 (m), 760 (w), 743 (m), 714 (w), 696 (w), 555 (m), 467 (w);  $^1\text{H NMR}$  (500 MHz,  $\text{CDCl}_3$ )  $\delta$  7.60–7.50 (m, 6H), 7.38 (d,  $J = 7.7$  Hz, 2H), 7.33 (t,  $J = 7.3$  Hz, 2H), 7.29–7.24 (m, 3H), 6.87 (s, 2H), 2.51 (s, 3H);  $^{13}\text{C}\{^1\text{H}\}$  NMR (126 MHz,  $\text{CDCl}_3$ )  $\delta$  167.4, 161.0, 145.9, 140.8, 134.6, 130.9, 130.5, 129.3, 126.6, 124.7, 121.6, 121.6, 118.7, 118.1, 113.2, 21.6; HRMS (ESI+)  $m/z$  calcd for  $\text{C}_{28}\text{H}_{18}\text{BF}_2\text{N}_2\text{O}_2$   $[\text{M} + \text{H}]^+$  463.1429, found 463.1419.

#### Synthesis of 23.



According to GP3. **17** (30.0 mg, 0.05 mmol),  $\text{Pd}(\text{OAc})_2$  (0.54 mg,  $2.4 \times 10^{-3}$  mmol, 0.05 equiv),  $\text{PPh}_3$  (1.3 mg,  $4.8 \times 10^{-3}$  mmol, 0.1 equiv),  $\text{K}_2\text{CO}_3$  (19.9, 0.14 mmol, 3 equiv), and toluene (4 mL) were used. The reaction mixture was stirred at 150 °C for 6 h. The crude was purified using 60%  $\text{CHCl}_3$ /hexanes. The desired product (14.7 mg, 0.04 mmol, 66% yield) was obtained as a golden solid: TLC (60%  $\text{CHCl}_3$ /hexanes;  $R_f = 0.3$ ); mp >300 °C dec; IR (KBr,  $\text{cm}^{-1}$ ) 3352 (w), 3066 (w), 2972 (w), 1627 (m), 1578 (s), 1477 (m), 1448 (s), 1441 (s), 1344 (s), 1319 (s), 1292 (s), 1185 (w), 1158 (s), 1140 (s), 1107 (s), 1012 (m), 985 (s), 818 (s), 762 (m), 745 (m), 737 (m), 702 (m), 554 (m), 529 (m), 476 (w);  $^1\text{H NMR}$  (500 MHz,  $\text{CDCl}_3$ )  $\delta$  7.56–7.52 (m, 4H), 7.47 (t,  $J = 8.2$  Hz, 1H), 7.41–7.30 (m, 5H), 7.28–7.23 (m, 3H), 6.63 (s, 2H), 2.33 (s, 3H);  $^{13}\text{C}\{^1\text{H}\}$  NMR (126 MHz,  $\text{CDCl}_3$ )  $\delta$  167.6, 161.1, 144.9, 137.3, 134.8, 132.5, 130.6, 130.6, 129.8, 126.7, 125.6, 124.7, 121.7, 121.5, 118.4, 118.0, 113.2, 20.1; HRMS (ESI+)  $m/z$  calcd for  $\text{C}_{28}\text{H}_{18}\text{BF}_2\text{N}_2\text{O}_2$   $[\text{M} + \text{H}]^+$  463.1429, found 463.1438.

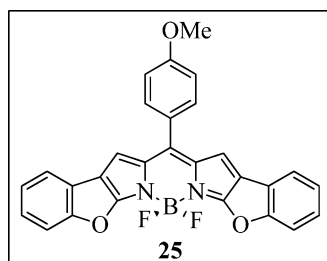
#### Synthesis of 24.



According to GP3. **18** (25.0 mg, 0.04 mmol),  $\text{Pd}(\text{OAc})_2$  (0.44 mg,  $1.9 \times 10^{-3}$  mmol, 0.05 equiv),  $\text{PPh}_3$  (1.0 mg,  $3.9 \times 10^{-3}$  mmol, 0.1 equiv),

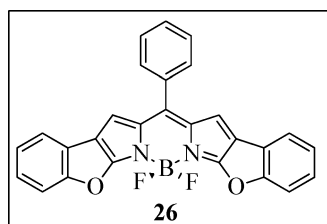
K<sub>2</sub>CO<sub>3</sub> (16.2 mg, 0.12 mmol, 3 equiv), and toluene (4 mL) were used. The reaction mixture was stirred at 150 °C for 5 h. The crude was purified using 30% CHCl<sub>3</sub>/hexanes. The desired product (12.5 mg, 0.03 mmol, 67% yield) was obtained as a golden solid: TLC (30% CHCl<sub>3</sub>/hexanes; *R<sub>f</sub>* = 0.1); mp >300 °C dec; IR (KBr, cm<sup>-1</sup>) 3116 (w), 3063 (w), 2971 (w), 2732 (w), 1705 (s), 1627 (s), 1557 (s), 1479 (s), 1450 (s), 1442 (s), 1415 (m), 1377 (s), 1355 (s), 1324 (m), 1292 (w), 1191 (w), 1161 (m), 1144 (s), 1118 (s), 1110 (s), 1013 (s), 992 (s), 820 (s), 810 (w), 751 (m), 697 (m), 557 (m); <sup>1</sup>H NMR (500 MHz, CDCl<sub>3</sub>) δ 10.19 (s, 1H), 8.10 (d, *J* = 8.1 Hz, 2H), 7.83 (d, *J* = 8.0 Hz, 2H), 7.56 (t, *J* = 8.9 Hz, 4H), 7.35 (t, *J* = 8.5 Hz, 2H), 7.30–7.26 (m, 2H), 6.77 (s, 2H); <sup>13</sup>C{<sup>1</sup>H} NMR (126 MHz, CDCl<sub>3</sub>) δ 191.5, 167.9, 161.2, 143.3, 139.2, 137.6, 134.2, 131.5, 129.8, 127.1, 124.9, 121.8, 121.3, 118.9, 118.2, 113.3; HRMS (ESI<sup>+</sup>) *m/z* calcd for C<sub>28</sub>H<sub>15</sub>BF<sub>2</sub>N<sub>2</sub>O<sub>3</sub> [M]<sup>+</sup> 476.1143, found 476.1154.

#### Synthesis of 25.



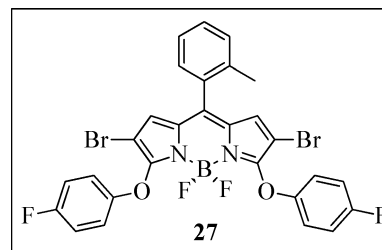
According to GP3. **19** (20.0 mg, 0.03 mmol), Pd(OAc)<sub>2</sub> (0.35 mg, 1.6 × 10<sup>-3</sup> mmol, 0.05 equiv), PPh<sub>3</sub> (0.82 mg, 3.1 × 10<sup>-3</sup> mmol, 0.1 equiv), K<sub>2</sub>CO<sub>3</sub> (12.9 mg, 0.094 mmol, 3 equiv), and toluene (4 mL) were used. The reaction mixture was stirred at 150 °C for 6 h. The crude material was purified using 80% CHCl<sub>3</sub>/hexanes. The desired product (7.2 mg, 0.02 mmol, 48% yield) was obtained as a golden solid: TLC (20% THF/hexanes; *R<sub>f</sub>* = 0.4); mp 297–299 °C; IR (KBr, cm<sup>-1</sup>) 2970 (w), 2926 (w), 2854 (w), 1735 (w), 1627 (w), 1605 (w), 1577 (s), 1478 (m), 1449 (s), 1442 (s), 1371 (s), 1356 (s), 1292 (m), 1252 (m), 1180 (w), 1159 (s), 1144 (s), 1114 (s), 1012 (m), 989 (s), 818 (m), 761 (w), 746 (w), 697 (w), 556 (w); <sup>1</sup>H NMR (500 MHz, CDCl<sub>3</sub>) δ 7.61–7.53 (m, 6H), 7.33 (t, *J* = 8.5 Hz, 2H), 7.29–7.26 (m, 2H), 7.10 (d, *J* = 8.6 Hz, 2H), 6.89 (s, 2H), 3.94 (s, 3H); <sup>13</sup>C{<sup>1</sup>H} NMR (126 MHz, CDCl<sub>3</sub>) δ 167.2, 161.7, 161.0, 145.7, 134.5, 132.4, 126.6, 125.8, 124.7, 121.7, 121.6, 118.6, 118.1, 114.2, 113.2, 55.7; HRMS (ESI<sup>+</sup>) *m/z* calcd for C<sub>28</sub>H<sub>17</sub>BF<sub>2</sub>N<sub>2</sub>O<sub>3</sub> [M]<sup>+</sup> 478.1300, found 478.1322.

#### Synthesis of 26.



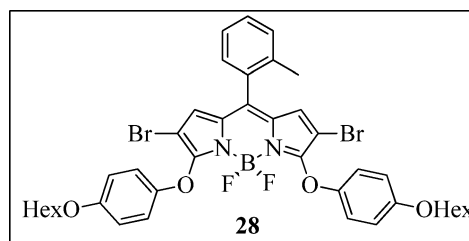
According to GP3. **20** (30.0 mg, 0.05 mmol), Pd(OAc)<sub>2</sub> (0.55 mg, 2.4 × 10<sup>-3</sup> mmol, 0.05 equiv), PPh<sub>3</sub> (1.3 mg, 4.9 × 10<sup>-3</sup> mmol, 0.1 equiv), K<sub>2</sub>CO<sub>3</sub> (20.4 mg, 0.15 mmol, 3 equiv), and toluene (4 mL) were used. The reaction mixture was stirred at 150 °C for 6 h. The crude material was purified using 60% CHCl<sub>3</sub>/hexanes. The desired product (15.9 mg, 0.03 mmol, 72% yield) was obtained as a golden solid: TLC (20% THF/hexanes; *R<sub>f</sub>* = 0.4); mp >290 °C dec; IR (KBr, cm<sup>-1</sup>) 2972 (w), 1628 (w), 1578 (s), 1478 (m), 1448 (s), 1345 (s), 1324 (s), 1292 (m), 1185 (w), 1159 (s), 1143 (s), 1108 (s), 1012 (w), 983 (s), 926 (w), 819 (s), 762 (w), 747 (w), 721 (m), 554 (m), 519 (w); <sup>1</sup>H NMR (500 MHz, CDCl<sub>3</sub>) δ 7.66–7.54 (m, 9H), 7.34 (t, *J* = 8.5 Hz, 2H), 7.29–7.24 (m, 2H), 6.85 (s, 2H); <sup>13</sup>C{<sup>1</sup>H} NMR (126 MHz, CDCl<sub>3</sub>) δ 167.5, 161.1, 145.6, 134.6, 133.4, 130.8, 130.4, 128.6, 126.7, 124.7, 121.7, 121.6, 118.7, 118.3, 113.2; HRMS (ESI<sup>+</sup>) *m/z* calcd for C<sub>27</sub>H<sub>16</sub>BF<sub>2</sub>N<sub>2</sub>O<sub>2</sub> [M + H]<sup>+</sup> 449.1272, found 449.1271.

#### Synthesis of 27.



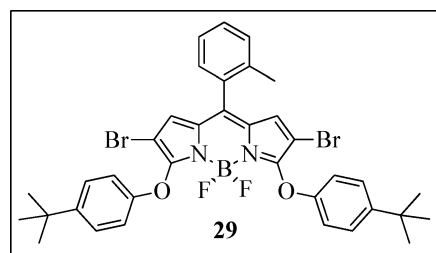
According to GP2. **11** (30.0 mg, 0.05 mmol), *p*-fluorophenol (33.8 mg, 0.30 mmol), Na<sub>2</sub>CO<sub>3</sub> (31.9 mg, 0.30 mmol), and acetonitrile (2.5 mL) were used. The reaction mixture was stirred at 110 °C for 2 h. The crude material was purified using 15% AcOEt/hexanes. The desired product (26.1 mg, 0.039 mmol, 79% yield) was obtained as red crystals: TLC (20% THF/hexanes; *R<sub>f</sub>* = 0.55); mp 89–91 °C; IR (KBr, cm<sup>-1</sup>) 3121 (w), 2922 (w), 1564 (s), 1504 (s), 1491 (s), 1449 (s), 1351 (w), 1337 (w), 1252 (s), 1190 (s), 1175 (s), 1119 (s), 1033 (s), 1010 (s), 994 (s), 911 (m), 860 (m), 835 (m), 791 (m), 741 (m), 704 (m), 573 (w), 514 (w); <sup>1</sup>H NMR (500 MHz, CDCl<sub>3</sub>) δ 7.46–7.42 (m, 1H), 7.36–7.27 (m, 3H), 7.13–7.07 (m, 4H), 7.05–7.00 (m, 4H), 6.69 (s, 2H), 2.29 (s, 3H); <sup>13</sup>C{<sup>1</sup>H} NMR (126 MHz, CDCl<sub>3</sub>) δ 160.7, 158.7, 158.1, 151.6, 151.5, 136.8, 131.8, 131.2, 130.8, 130.3, 130.2, 125.8, 119.6, 119.5, 116.5, 116.3, 95.9, 20.2; HRMS (ESI<sup>+</sup>) *m/z* calcd for C<sub>28</sub>H<sub>18</sub>BBr<sub>2</sub>F<sub>4</sub>N<sub>2</sub>O<sub>2</sub> [M + H]<sup>+</sup> 660.9745, found 660.9772.

#### Synthesis of 28.



According to GP2. **11** (30.0 mg, 0.05 mmol), 4-(hexyloxy)phenol (58.5 mg, 0.30 mmol), Na<sub>2</sub>CO<sub>3</sub> (31.9 mg, 0.30 mmol), and acetonitrile (2.5 mL) were used. The reaction mixture was stirred at 110 °C for 2 h. The crude material was purified using 60% CHCl<sub>3</sub>/hexanes. The desired product (37.2 mg, 0.045 mmol, 90% yield) was obtained as a red oil: TLC (15% DCM/hexanes; *R<sub>f</sub>* = 0.90); IR (KBr, cm<sup>-1</sup>) 3694 (w), 2952 (s), 2929 (s), 2870 (s), 2858 (s), 1565 (s), 1493 (s), 1450 (s), 1350 (w), 1337 (w), 1295 (w), 1251 (s), 1213 (s), 1193 (s), 1178 (s), 1118 (s), 1033 (s), 1007 (m), 994 (m), 831 (m), 793 (w), 740 (m), 706 (m), 610 (w), 515 (w); <sup>1</sup>H NMR (500 MHz, CDCl<sub>3</sub>) δ 7.42 (t, *J* = 8.8 Hz, 1H), 7.35–7.25 (m, 3H), 7.06 (d, *J* = 9.1 Hz, 4H), 6.83 (d, *J* = 9.1 Hz, 4H), 6.63 (s, 2H), 3.91 (t, *J* = 6.6 Hz, 4H), 2.28 (s, 3H), 1.79–1.71 (m, 4H), 1.50–1.40 (m, 4H), 1.37–1.27 (m, 8H), 0.90 (t, *J* = 6.9 Hz, 6H); <sup>13</sup>C{<sup>1</sup>H} NMR (126 MHz, CDCl<sub>3</sub>) δ 158.4, 156.3, 149.3, 140.9, 136.9, 131.5, 131.5, 130.7, 130.3, 130.0, 127.8, 125.7, 119.3, 115.3, 95.5, 68.6, 31.7, 29.4, 25.8, 22.7, 20.2, 14.2; HRMS (ESI<sup>+</sup>) *m/z* calcd for C<sub>40</sub>H<sub>44</sub>BBBr<sub>2</sub>F<sub>2</sub>N<sub>2</sub>O<sub>4</sub> [M + H]<sup>+</sup> 825.1714, found 825.1730.

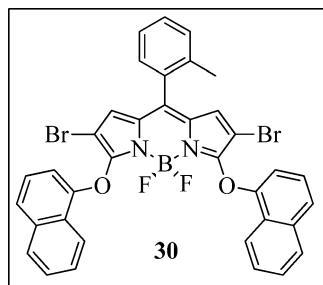
#### Synthesis of 29.



According to GP2. **11** (30.0 mg, 0.05 mmol), 4-*tert*-butylphenol (45.2 mg, 0.30 mmol), Na<sub>2</sub>CO<sub>3</sub> (31.9 mg, 0.30 mmol), and acetonitrile (2.5 mL) were used. The reaction mixture was stirred at 110 °C for 1 h. The crude was purified using 15% THF/hexanes. The desired product

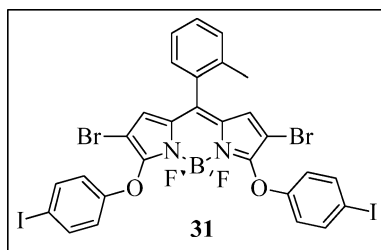
(33.3 mg, 0.045 mmol, 90% yield) was obtained as a red solid: TLC (20% THF/hexanes;  $R_f = 0.68$ ); mp 108–110 °C; IR (KBr,  $\text{cm}^{-1}$ ) 3681 (w), 2962 (m), 2864 (w), 1564 (m), 1494 (m), 1451 (s), 1364 (w), 1351 (w), 1334 (w), 1252 (s), 1215 (m), 1194 (m), 1120 (s), 1033 (s), 1013 (w), 830 (w), 741 (w), 699 (w), 549 (w);  $^1\text{H}$  NMR (500 MHz,  $\text{CDCl}_3$ )  $\delta$  7.43 (t,  $J = 8.1$  Hz, 1H), 7.36–7.27 (m, 7H), 7.02 (d,  $J = 8.8$  Hz, 4H), 6.67 (s, 2H), 2.30 (s, 3H), 1.29 (s, 18H);  $^{13}\text{C}\{^1\text{H}\}$  NMR (126 MHz,  $\text{CDCl}_3$ )  $\delta$  158.2, 153.5, 147.5, 141.3, 136.9, 131.4, 131.3, 130.7, 130.3, 130.1, 128.0, 126.6, 125.7, 117.2, 96.3, 34.5, 31.6, 20.2; HRMS (ESI+)  $m/z$  calcd for  $\text{C}_{36}\text{H}_{36}\text{BBr}_2\text{F}_2\text{N}_2\text{O}_2$  [ $\text{M} + \text{H}$ ] $^+$  737.1188, found 737.1203.

#### Synthesis of 30.



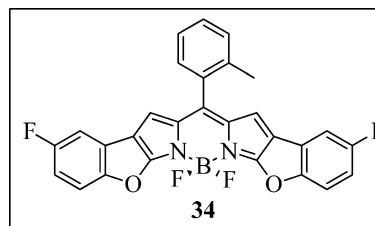
According to GP2. 11 (30.0 mg, 0.05 mmol), 1-naphthol (28.9 mg, 0.20 mmol),  $\text{Na}_2\text{CO}_3$  (21.3 mg, 0.20 mmol), and acetonitrile (2.5 mL) were used. The reaction mixture was stirred at 110 °C for 1 h. The crude material was purified using 20% THF/hexanes. The desired product (29.3 mg, 0.040 mmol, 81% yield) was obtained as a purple solid: TLC (20% THF/hexanes;  $R_f = 0.3$ ); mp 223–225 °C; IR (KBr,  $\text{cm}^{-1}$ ) 3673 (w), 3113 (w), 3055 (w), 1599 (w), 1560 (s), 1492 (s), 1455 (s), 1389 (s), 1349 (w), 1248 (s), 1223 (s), 1178 (m), 1132 (s), 1072 (s), 1044 (s), 1013 (s), 878 (m), 791 (w), 771 (m), 742 (m), 703 (m), 541 (w);  $^1\text{H}$  NMR (500 MHz,  $\text{CDCl}_3$ )  $\delta$  8.33–8.31 (m, 2H), 7.86–7.82 (m, 2H), 7.65 (d,  $J = 8.3$  Hz, 2H), 7.57–7.49 (m, 4H), 7.48–7.42 (m, 1H), 7.40–7.31 (m, 5H), 7.04 (d,  $J = 7.6$  Hz, 2H), 6.72 (s, 2H), 2.36 (s, 3H);  $^{13}\text{C}\{^1\text{H}\}$  NMR (126 MHz,  $\text{CDCl}_3$ )  $\delta$  158.4, 151.4, 141.3, 136.8, 134.6, 131.4, 131.3, 130.7, 130.2, 130.0, 128.0, 127.5, 126.9, 126.4, 125.6, 125.5, 125.2, 124.7, 121.9, 112.2, 95.7, 20.1; HRMS (ESI+)  $m/z$  calcd for  $\text{C}_{36}\text{H}_{24}\text{BBr}_2\text{F}_2\text{N}_2\text{O}_2$  [ $\text{M} + \text{H}$ ] $^+$  725.0249, found 725.0267.

#### Synthesis of 31.



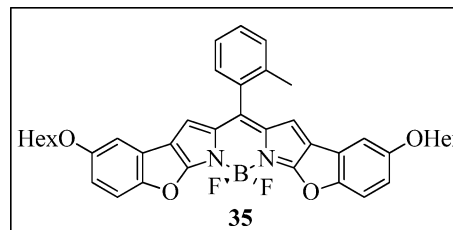
According to GP2. 11 (30.0 mg, 0.05 mmol), 4-iodophenol (66.3 mg, 0.30 mmol, 6 equiv),  $\text{Na}_2\text{CO}_3$  (31.9 mg, 0.30 mmol, 6 equiv), and acetonitrile (2.5 mL) were used. The reaction mixture was stirred at 110 °C for 2 h. The crude material was purified using 10% THF/hexanes. The desired product (25.6 mg, 0.03 mmol, 58% yield) was obtained as a red solid: TLC (20% THF/hexanes;  $R_f = 0.6$ ); mp 106–107 °C; IR (KBr,  $\text{cm}^{-1}$ ) 3680 (w), 2972 (w), 1561 (s), 1496 (m), 1477 (s), 1448 (s), 1351 (w), 1336 (w), 1252 (s), 1216 (s), 1202 (s), 1186 (m), 1120 (s), 1033 (s), 1006 (s), 911 (w), 839 (w), 823 (w), 741 (w), 707 (w), 687 (w), 541 (w), 488 (w);  $^1\text{H}$  NMR (500 MHz,  $\text{CDCl}_3$ )  $\delta$  7.63 (d,  $J = 8.9$  Hz, 4H), 7.44 (t,  $J = 8.2$  Hz, 1H), 7.37–7.26 (m, 3H), 6.87 (d,  $J = 8.9$  Hz, 4H), 6.70 (s, 2H), 2.29 (s, 3H).  $^{13}\text{C}\{^1\text{H}\}$  NMR (126 MHz,  $\text{CDCl}_3$ )  $\delta$  157.6, 155.6, 142.5, 138.8, 136.8, 131.7, 131.1, 130.9, 130.3, 130.3, 128.2, 125.8, 120.0, 96.4, 88.1, 20.3; HRMS (ESI+)  $m/z$  calcd for  $\text{C}_{28}\text{H}_{18}\text{BBr}_2\text{F}_2\text{I}_2\text{N}_2\text{O}_2$  [ $\text{M} + \text{H}$ ] $^+$  876.7866, found 876.7868.

#### Synthesis of 34.



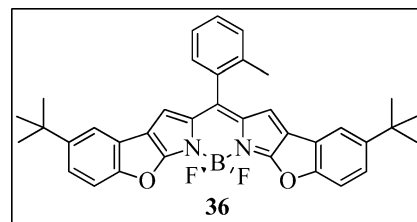
According to GP3. 27 (23.0 mg, 0.04 mmol),  $\text{Pd}(\text{OAc})_2$  (0.39 mg,  $1.7 \times 10^{-3}$  mmol, 0.05 equiv),  $\text{PPh}_3$  (0.91 mg,  $3.5 \times 10^{-3}$  mmol, 0.1 equiv),  $\text{K}_2\text{CO}_3$  (14.4 mg, 0.104 mmol, 3 equiv), and toluene (4 mL) were used. The reaction mixture was stirred at 150 °C for 6 h. The crude material was purified using 60%  $\text{CHCl}_3$ /hexanes. The desired product (13.3 mg, 0.03 mmol, 75%) was obtained as a golden solid: TLC (20% THF/hexanes;  $R_f = 0.6$ ); mp >300 °C; IR (KBr,  $\text{cm}^{-1}$ ) 3401 (w), 2972 (w), 1635 (m), 1579 (s), 1474 (w), 1459 (m), 1374 (s), 1312 (s), 1265 (w), 1168 (w), 1137 (s), 1101 (s), 1072 (w), 993 (s), 966 (m), 860 (w), 804 (w), 771 (w), 740 (w), 699 (w), 601 (w), 563 (w), 507 (w);  $^1\text{H}$  NMR (500 MHz,  $\text{CDCl}_3$ )  $\delta$  7.50–7.45 (m, 3H), 7.41–7.33 (m, 3H), 7.22 (dd,  $J = 8.0, 2.7$  Hz, 2H), 7.03 (td,  $J = 8.9, 2.7$  Hz, 2H), 6.66 (s, 2H), 2.32 (s, 3H);  $^{13}\text{C}\{^1\text{H}\}$  NMR (126 MHz,  $\text{CDCl}_3$ )  $\delta$  168.2, 161.0, 159.1, 156.9, 156.9, 145.9, 137.2, 135.0, 132.1, 130.7, 130.5, 130.0, 125.7, 122.5, 122.4, 118.8, 118.1, 113.8, 113.8, 113.7, 113.5, 108.5, 108.3, 20.1; HRMS (ESI+)  $m/z$  calcd for  $\text{C}_{28}\text{H}_{16}\text{BF}_4\text{N}_2\text{O}_2$  [ $\text{M} + \text{H}$ ] $^+$  499.1240, found 499.1238.

#### Synthesis of 35.



According to GP3. 28 (40.0 mg, 0.05 mmol),  $\text{Pd}(\text{OAc})_2$  (0.54 mg,  $2.4 \times 10^{-3}$  mmol, 0.05 equiv),  $\text{PPh}_3$  (1.3 mg,  $4.8 \times 10^{-3}$  mmol, 0.1 equiv),  $\text{K}_2\text{CO}_3$  (20.1 mg, 0.15 mmol, 3 equiv), and toluene (4 mL) were used. The reaction mixture was stirred at 150 °C for 7 h. The crude material was purified using 40%  $\text{CHCl}_3$ /hexanes. The desired product (22.3 mg, 0.03 mmol, 69%) was obtained as a golden solid: TLC (20% THF/hexanes;  $R_f = 0.7$ ); mp 205–206 °C; IR (KBr,  $\text{cm}^{-1}$ ) 3066 (w), 2934 (m), 2868 (m), 1635 (m), 1577 (s), 1465 (s), 1460 (s), 1452 (s), 1415 (m), 1350 (s), 1316 (s), 1275 (s), 1207 (s), 1150 (s), 1106 (s), 993 (s), 965 (s), 945 (m), 871 (w), 858 (w), 828 (w), 778 (m), 742 (m), 701 (m), 691 (m), 580 (m), 494 (m);  $^1\text{H}$  NMR (500 MHz,  $\text{CDCl}_3$ )  $\delta$  7.45 (t,  $J = 8.2$  Hz, 1H), 7.42–7.31 (m, 5H), 7.03 (d,  $J = 2.0$  Hz, 2H), 6.85 (dd,  $J = 9.0, 2.6$  Hz, 2H), 6.58 (s, 2H), 3.94 (t,  $J = 6.6$  Hz, 4H), 2.32 (s, 3H), 1.85–1.71 (m, 4H), 1.49–1.41 (m, 4H), 1.39–1.25 (m, 8H), 0.9 (t,  $J = 7.0$  Hz, 6H);  $^{13}\text{C}\{^1\text{H}\}$  NMR (126 MHz,  $\text{CDCl}_3$ )  $\delta$  168.1, 156.6, 155.5, 144.6, 137.2, 134.7, 132.5, 130.6, 130.5, 129.7, 125.5, 122.0, 118.7, 117.8, 113.7, 113.4, 106.9, 69.0, 31.7, 29.4, 25.8, 22.7, 20.1, 14.2; HRMS (ESI+)  $m/z$  calcd for  $\text{C}_{40}\text{H}_{42}\text{BF}_2\text{N}_2\text{O}_4$  [ $\text{M} + \text{H}$ ] $^+$  663.3207, found 663.3194.

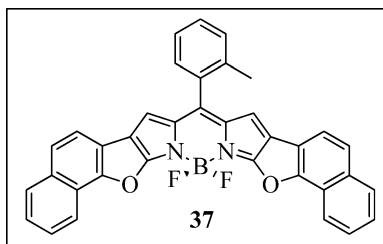
#### Synthesis of 36.



According to GP3. 29 (26.0 mg, 0.04 mmol),  $\text{Pd}(\text{OAc})_2$  (0.4 mg,  $1.8 \times 10^{-3}$  mmol, 0.05 equiv),  $\text{PPh}_3$  (0.9 mg,  $3.5 \times 10^{-3}$  mmol, 0.1 equiv),  $\text{K}_2\text{CO}_3$  (14.6 mg, 0.11 mmol, 3 equiv), and toluene (4 mL) were

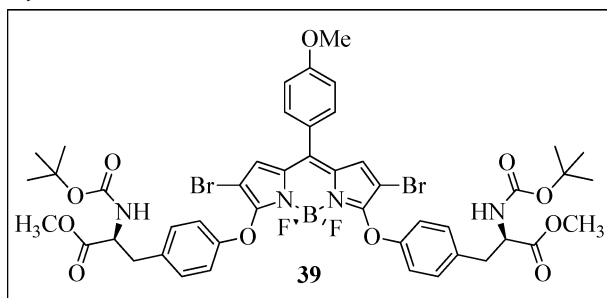
added. The reaction mixture was stirred at 150 °C for 6 h. The crude material was purified using 60% CHCl<sub>3</sub>/hexanes. The desired product (13.0 mg, 0.02 mmol, 64% yield) was obtained as a golden solid: TLC (15% AcOEt/hexanes; *R<sub>f</sub>* = 0.5); mp 250–252 °C; IR (KBr, cm<sup>-1</sup>) 3684 (w), 2960 (m), 2906 (m), 2868 (m), 1632 (m), 1575 (s), 1460 (s), 1404 (m), 1356 (s), 1342 (s), 1311 (m), 1291 (m), 1168 (s), 1124 (s), 1099 (s), 993 (s), 962 (m), 857 (w), 816 (s), 742 (w), 697 (m), 596 (w), 562 (w), 517 (w), 461 (w); <sup>1</sup>H NMR (500 MHz, CDCl<sub>3</sub>) δ 7.55 (d, *J* = 2.0 Hz, 2H), 7.46–7.42 (m, 3H), 7.41–7.30 (m, 5H), 6.61 (s, 2H), 2.33 (s, 3H), 1.34 (s, 18H); <sup>13</sup>C{<sup>1</sup>H} NMR (126 MHz, CDCl<sub>3</sub>) δ 167.9, 159.2, 147.9, 144.3, 137.3, 134.7, 132.6, 130.6, 130.5, 129.7, 125.5, 124.1, 121.1, 118.7, 118.5, 117.6, 112.3, 35.0, 31.8, 20.1; HRMS (ESI+) *m/z* calcd for C<sub>36</sub>H<sub>34</sub>BF<sub>2</sub>N<sub>2</sub>O<sub>2</sub> [M + H]<sup>+</sup> 575.2683, found 575.2675.

#### Synthesis of 37.



According to GP3. **30** (30.0 mg, 0.04 mmol), Pd(OAc)<sub>2</sub> (0.5 mg, 2.07 × 10<sup>-3</sup> mmol, 0.05 equiv), PPh<sub>3</sub> (1.1 mg, 4.1 × 10<sup>-3</sup> mmol, 0.1 equiv), K<sub>2</sub>CO<sub>3</sub> (17.2 mg, 0.12 mmol, 3 equiv), and toluene (4 mL) were used. The reaction mixture was stirred at 150 °C for 7 h. The crude material was purified using 30% CHCl<sub>3</sub>/hexanes. The desired product (8.4 mg, 0.01 mmol, 36% yield) was obtained as golden crystals: TLC (60% CHCl<sub>3</sub>/hexanes; *R<sub>f</sub>* = 0.4); mp >300 °C; IR (KBr, cm<sup>-1</sup>) 3058 (w), 2970 (w), 1639 (w), 1606 (m), 1580 (s), 1558 (m), 1461 (m), 1438 (m), 1390 (s), 1373 (s), 1357 (s), 1335 (s), 1279 (m), 1262 (m), 1144 (s), 1131 (s), 1026 (s), 1005 (s), 965 (s), 847 (m), 803 (m), 736 (m), 696 (m), 671 (w), 602 (w), 582 (w), 560 (w), 503 (w), 457 (w); <sup>1</sup>H NMR (500 MHz, CDCl<sub>3</sub>) δ 8.42 (d, *J* = 8.3 Hz, 2H), 7.92 (d, *J* = 8.2 Hz, 2H), 7.72 (d, *J* = 8.4 Hz, 2H), 7.68–7.60 (m, 4H), 7.54 (t, *J* = 8.0 Hz, 2H), 7.49 (t, *J* = 8.2 Hz, 1H), 7.45 (d, *J* = 6.6 Hz, 1H), 7.43–7.34 (m, 2H), 6.67 (s, 2H), 2.37 (s, 3H); <sup>13</sup>C{<sup>1</sup>H} NMR (126 MHz, CDCl<sub>3</sub>) δ 167.5, 156.6, 145.3, 137.3, 135.1, 132.8, 132.6, 130.7, 130.6, 129.8, 128.5, 127.3, 126.4, 125.6, 125.1, 121.8, 120.9, 119.5, 119.1, 117.3, 116.9, 20.2; HRMS (ESI+) *m/z* calcd for C<sub>36</sub>H<sub>21</sub>BF<sub>2</sub>N<sub>2</sub>O<sub>2</sub>K [M + K]<sup>+</sup> 601.1302, found 601.1288.

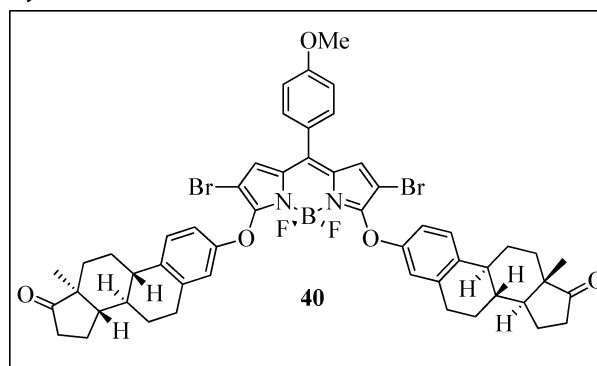
#### Synthesis of 39.



According to GP2. **13** (30.0 mg, 0.05 mmol), *N*-(*tert*-butoxycarbonyl)-*L*-tyrosine methyl ester (86.6 mg, 0.29 mmol, 6 equiv), Na<sub>2</sub>CO<sub>3</sub> (31.1 mg, 0.29 mmol, 6 equiv), and acetonitrile (2.5 mL) were used. The reaction mixture was stirred at 110 °C for 1 h. The crude material was purified using 20% acetone/hexanes. The desired product (36.0 mg, 0.034 mmol, 71% yield) was obtained as a red solid: TLC (20% acetone/hexanes; *R<sub>f</sub>* = 0.9); mp 106–108 °C; IR (KBr, cm<sup>-1</sup>) 3666 (w), 2975 (w), 1743 (m), 1713 (s), 1605 (w), 1575 (m), 1555 (m), 1510 (m), 1492 (s), 1450 (s), 1366 (w), 1350 (w), 1255 (s), 1209 (m), 1179 (m), 1164 (m), 1127 (s), 1037 (m), 1016 (m), 993 (w), 854 (w), 835 (w), 760 (w), 706 (w); <sup>1</sup>H NMR (500 MHz, CDCl<sub>3</sub>) δ 7.49 (d, *J* = 8.7 Hz, 2H), 7.10–7.00 (m, 10H), 6.94 (s, 2H), 4.94 (d, *J* = 8.1 Hz, 2H), 4.54 (dd, *J* = 13.7, 6.1 Hz, 2H), 3.91 (s, 3H), 3.65 (s,

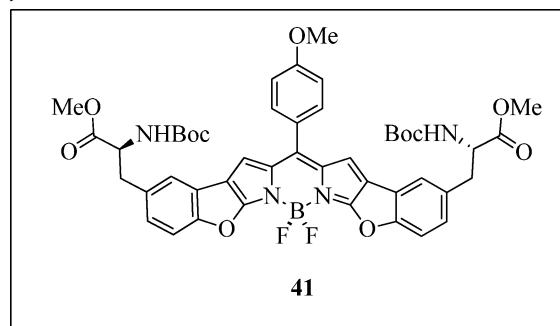
6H), 3.10–2.99 (m, 4H), 1.41 (s, 18H); <sup>13</sup>C{<sup>1</sup>H} NMR (126 MHz, CDCl<sub>3</sub>) δ 172.3, 162.2, 157.6, 155.2, 154.9, 142.4, 132.4, 132.2, 132.0, 130.6, 127.5, 124.6, 118.0, 114.5, 95.8, 80.1, 55.7, 54.6, 52.3, 37.8, 28.4; HRMS (ESI+) *m/z* calcd for C<sub>46</sub>H<sub>50</sub>BBr<sub>2</sub>F<sub>2</sub>N<sub>4</sub>O<sub>11</sub> [M + H]<sup>+</sup> 1043.1891, found 1043.1884.

#### Synthesis of 40.



According to GP2. **13** (30.0 mg, 0.05 mmol), estrone (79.3 mg, 0.29 mmol, 6 equiv), Na<sub>2</sub>CO<sub>3</sub> (31.1 mg, 0.29 mmol, 6 equiv), and acetonitrile (2.5 mL) were used. The reaction mixture was stirred at 110 °C for 1 h. The crude material was purified using 40% AcOEt/hexanes. The desired product (34.0 mg, 0.034 mmol, 70% yield) was obtained as a red solid: TLC (40% acetone/hexanes; *R<sub>f</sub>* = 0.2); mp 180–182 °C; IR (KBr, cm<sup>-1</sup>) 2929 (s), 2862 (s), 1738 (s), 1605 (s), 1576 (s), 1554 (s), 1487 (s), 1450 (s), 1349 (m), 1297 (w), 1252 (s), 1225 (s), 1202 (s), 1179 (s), 1123 (s), 1036 (s), 993 (m), 928 (m), 913 (s), 837 (w), 819 (w), 792 (w), 763 (w), 732 (w), 707 (w), 634 (w), 548 (w); <sup>1</sup>H NMR (500 MHz, CDCl<sub>3</sub>) δ 7.50 (d, *J* = 7.8 Hz, 2H), 7.20 (d, *J* = 8.5 Hz, 2H), 7.06 (d, *J* = 7.8 Hz, 2H), 6.95 (s, 2H), 6.85–6.79 (m, 4H), 3.92 (s, 3H), 2.86 (d, *J* = 5.2 Hz, 4H), 2.50 (dd, *J* = 19.1, 8.7 Hz, 2H), 2.40–2.33 (m, 2H), 2.29–2.22 (m, 2H), 2.18–2.09 (m, 2H), 2.07–1.91 (m, 6H), 1.69–1.37 (m, 15H), 0.91 (s, 6H); <sup>13</sup>C{<sup>1</sup>H} NMR (126 MHz, CDCl<sub>3</sub>) δ 220.9, 162.1, 157.6, 153.9, 142.2, 138.3, 135.8, 132.2, 131.8, 127.6, 126.6, 124.8, 117.4, 114.7, 114.4, 96.2, 55.7, 50.6, 48.1, 44.2, 38.2, 36.0, 31.7, 29.6, 26.5, 25.9, 21.7, 14.0; HRMS (ESI+) *m/z* calcd for C<sub>52</sub>H<sub>52</sub>BBr<sub>2</sub>F<sub>2</sub>N<sub>2</sub>O<sub>5</sub> [M + H]<sup>+</sup> 993.2293, found 993.2271.

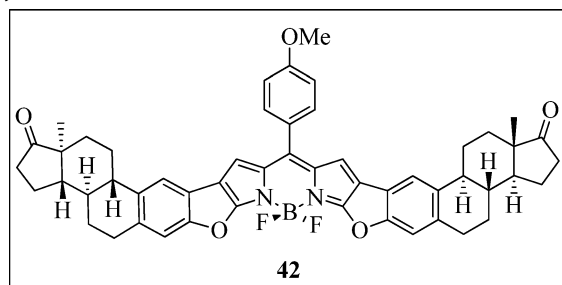
#### Synthesis of 41.



According to GP3. **39** (35.0 mg, 0.03 mmol), Pd(OAc)<sub>2</sub> (0.4 mg, 1.68 × 10<sup>-3</sup> mmol, 0.05 equiv), PPh<sub>3</sub> (0.9 mg, 3.4 × 10<sup>-3</sup> mmol, 0.1 equiv), K<sub>2</sub>CO<sub>3</sub> (24.0 mg, 0.10 mmol, 3 equiv), and toluene (4 mL) were used. The reaction mixture was stirred at 150 °C for 6 h. The crude material was purified using 35% acetone/hexanes. The desired product (20.0 mg, 0.02 mmol, 68% yield) was obtained as a dark blue solid: TLC (40% acetone/hexanes; *R<sub>f</sub>* = 0.5); mp 144–146 °C; IR (KBr, cm<sup>-1</sup>) 3351 (w), 2975 (w), 1739 (m), 1715 (m), 1694 (m), 1605 (m), 1577 (s), 1525 (w), 1510 (w), 1497 (w), 1468 (m), 1459 (m), 1416 (w), 1360 (s), 1293 (m), 1255 (m), 1159 (s), 1111 (s), 1001 (s), 860 (w), 814 (w), 801 (w), 754 (w), 721 (w), 699 (w), 558 (w), 528 (w); <sup>1</sup>H NMR (500 MHz, CDCl<sub>3</sub>) δ 7.59 (d, *J* = 8.7 Hz, 2H), 7.46 (d, *J* = 8.4 Hz, 2H), 7.37 (d, *J* = 1.6 Hz, 2H), 7.13–7.06 (m, 4H), 6.87 (s, 2H), 5.01 (d, *J* = 8.0 Hz, 2H), 4.60 (dd, *J* = 12.3, 5.6 Hz, 2H), 3.95 (s, 3H), 3.69 (s, 6H), 3.22–3.06 (m, 4H), 1.40 (s, 18H); <sup>13</sup>C{<sup>1</sup>H} NMR (126

MHz, CDCl<sub>3</sub>)  $\delta$  172.4, 167.4, 161.8, 160.1, 155.2, 145.8, 134.5, 132.8, 132.5, 127.6, 125.7, 122.2, 121.9, 118.7, 117.9, 114.2, 113.0, 80.2, 55.7, 54.8, 52.5, 38.6, 28.4; HRMS (ESI+)  $m/z$  calcd for C<sub>46</sub>H<sub>48</sub>BF<sub>2</sub>N<sub>4</sub>O<sub>11</sub> [M + H]<sup>+</sup> 881.3383, found 881.3378.

#### Synthesis of 42.



According to GP3. **40** (32.0 mg, 0.03 mmol), Pd(OAc)<sub>2</sub> (0.4 mg, 1.61 × 10<sup>-3</sup> mmol, 0.05 equiv), PPh<sub>3</sub> (0.8 mg, 3.2 × 10<sup>-3</sup> mmol, 0.1 equiv), K<sub>2</sub>CO<sub>3</sub> (13.4 mg, 0.10 mmol, 3 equiv), and toluene (4 mL) were used. The reaction mixture was stirred at 150 °C for 6 h. The crude material was purified using 60% CHCl<sub>3</sub>/hexanes. The desired product (9.1 mg, 0.01 mmol, 34% yield) was obtained as a blue solid: TLC (50% acetone/hexanes; R<sub>f</sub> = 0.6); mp >300 °C dec; IR (KBr, cm<sup>-1</sup>) 2930 (w), 2864 (w), 1738 (m), 1606 (w), 1574 (m), 1454 (m), 1417 (w), 1362 (s), 1338 (s), 1289 (m), 1254 (w), 1183 (m), 1114 (s), 996 (m), 983 (s), 974 (s), 906 (w), 892 (w), 877 (w), 758 (w), 737 (w), 702 (w), 666 (w), 583 (w); <sup>1</sup>H NMR (500 MHz, CD<sub>2</sub>Cl<sub>2</sub>/CDCl<sub>3</sub>)  $\delta$  7.61 (d, J = 8.4 Hz, 2H), 7.56 (s, 2H), 7.27 (s, 2H), 7.11 (d, J = 8.4 Hz, 2H), 6.85 (s, 2H), 3.94 (s, 3H), 3.07–3.01 (m, 4H), 2.52–2.32 (m, 6H), 2.18–2.02 (m, 7H), 2.02–1.88 (m, 3H), 1.69–1.57 (m, 6H), 1.56–1.39 (m, 6H), 0.91 (s, 6H); <sup>13</sup>C{<sup>1</sup>H} NMR (126 MHz, CD<sub>2</sub>Cl<sub>2</sub>/CDCl<sub>3</sub>)  $\delta$  221.0, 167.9, 162.2, 160.0, 145.4, 137.4, 136.9, 134.8, 133.0, 126.3, 119.8, 118.9, 118.7, 118.3, 114.6, 113.1, 56.2, 51.2, 48.5, 45.0, 38.7, 36.5, 32.3, 30.9, 27.0, 26.8, 22.2, 14.4; HRMS (ESI+)  $m/z$  calcd for C<sub>52</sub>H<sub>50</sub>BF<sub>2</sub>N<sub>2</sub>O<sub>5</sub> [M + H]<sup>+</sup> 831.3784, found 831.3773.

## ■ ASSOCIATED CONTENT

### Supporting Information

The Supporting Information is available free of charge on the ACS Publications website at DOI: 10.1021/acs.joc.8b02933.

Crystallographic data determined by X-ray diffraction (CIF)

<sup>1</sup>H and <sup>13</sup>C NMR spectra of the compounds prepared, absorption and fluorescence spectra, cyclic voltammograms, correlation of the fluorescence efficiency with solvent scales, photophysical and laser data, and XYZ coordinates and energies of the simulated geometries (PDF)

## ■ AUTHOR INFORMATION

### Corresponding Authors

\*E-mail: jorge.banuelos@ehu.eus.

\*E-mail: eduardop@ugto.mx.

### ORCID

Luis Cerdán: 0000-0002-7174-2453

Jorge Bañuelos: 0000-0002-8444-4383

Eduardo Peña-Cabrera: 0000-0002-2069-6178

### Notes

The authors declare no competing financial interest.

## ■ ACKNOWLEDGMENTS

The authors gratefully acknowledge the Spanish Ministerio de Economía y Competitividad (MAT2017-83856-C3-3-P) and Gobierno Vasco (Project IT912-16) for financial support. E.A.-

Z. thanks also Gobierno Vasco for a predoctoral fellowship. The authors thank SGiker of UPV/EHU for technical and human support with the X-ray diffraction measurements and computational calculations, which were carried out in the “arina” informatic cluster. J.L.B.-V. and E.E.-P. thank CONACyT for scholarships. CONACyT (Grants 253623 and 123732) is acknowledged. The donation of 8-methylthioBODIPY by Cuantico de Mexico is appreciated.

## ■ REFERENCES

- (1) (a) Molecular Probes Inc., Eugene, OR. (b) Haugland, R. P. *The Handbook. A Guide to Fluorescent Probes and Labeling Technologies*, 10th ed.; Molecular Probes Inc.: Eugene, OR, 2011.
- (2) Bañuelos, J. BODIPY Dye, the Most Versatile Fluorophore Ever? *Chem. Rev.* **2016**, *16*, 335–348.
- (3) (a) Loudet, A.; Burgess, K. BODIPY Dyes and Their Derivatives: Syntheses and Spectroscopic Properties. *Chem. Rev.* **2007**, *107*, 4891–4932. (b) Wood, T. E.; Thompson, A. Advances in the Chemistry of Dipyrins and Their Complexes. *Chem. Rev.* **2007**, *107*, 1831–1861.
- (4) (a) Ulrich, G.; Ziessel, R.; Harriman, A. The Chemistry of Fluorescent Bodipy Dyes: Versatility Unsurpassed. *Angew. Chem., Int. Ed.* **2008**, *47*, 1184–1201. (b) Boens, N.; Verbelen, B.; Dehaen, W. Postfunctionalization of the BODIPY Core: Synthesis and Spectroscopy. *Eur. J. Org. Chem.* **2015**, *2015*, 6577–6595. (c) Vellanki, L.; Sharma, R.; M. Ravikanth, M. Functionalized Boron-Dipyrromethenes and Their Applications. *Rep. Org. Chem.* **2016**, *6*, 1–24.
- (5) (a) Li, L.; Han, J.; Nguyen, B.; Burgess, K. Syntheses and Spectral Properties of Functionalized, Water-Soluble BODIPY Derivatives. *J. Org. Chem.* **2008**, *73*, 1963–1970. (b) Poirel, A.; Retailleau, P.; De Nicola, A.; Ziessel, R. Synthesis of Water Soluble Red Emitting Thiényl-BODIPYs and Bovine Serum Albumin Labeling. *Chem. - Eur. J.* **2014**, *20*, 1252–1257. (c) Brellier, M.; Duportail, G.; Baati, R. Convenient Synthesis of Water-Soluble Nitrotriacetic Acid (NTA) BODIPY Dyes. *Tetrahedron Lett.* **2010**, *51*, 1269–1272.
- (6) Lakshmi, V.; Rajeswara Rao, M.; Ravikanth, M. Halogenated Boron-Dipyrromethenes: Synthesis, Properties and Applications. *Org. Biomol. Chem.* **2015**, *13*, 2501–2517.
- (7) Bessette, A.; Hanan, G. S. Design, Synthesis and Photophysical Studies of Dipyrromethene-Based Materials: Insights into Their Applications in Organic Photovoltaic Devices. *Chem. Soc. Rev.* **2014**, *43*, 3342–3405.
- (8) Benstead, M.; Mehl, G. H.; Boyle, R. W. 4,4'-Difluoro-4-Bora-3a,4a-Diaza-S-Indacenes (BODIPYs) as Components of Novel Light Active Materials. *Tetrahedron* **2011**, *67*, 3573–3601.
- (9) Ziessel, R.; Ulrich, G.; Harriman, A. The Chemistry of Bodipy: A New El Dorado for Fluorescence Tools. *New J. Chem.* **2007**, *31*, 496–501.
- (10) Singh, S. P.; Gayathri, T. Evolution of BODIPY Dyes as Potential Sensitizers for Dye Sensitized Solar Cells. *Eur. J. Org. Chem.* **2014**, *2014*, 4689–4707.
- (11) Benniston, A. C.; Copley, G. Lighting the Way Ahead with Boron Dipyrromethene (Bodipy) Dyes. *Phys. Chem. Chem. Phys.* **2009**, *11*, 4124–4131.
- (12) (a) Kamkaew, A.; Lim, S. H.; Lee, H. B.; Kiew, L. V.; Chung, L. Y.; Burgess, K. BODIPY Dyes in Photodynamic Therapy. *Chem. Soc. Rev.* **2013**, *42*, 77–88. (b) Awuah, S. G.; You, Y. Boron Dipyrromethene (BODIPY)-Based Photosensitizers for Photodynamic Therapy. *RSC Adv.* **2012**, *2*, 11169–11183.
- (13) Lavis, L. D.; Raines, R. T. Bright Ideas for Chemical Biology. *ACS Chem. Biol.* **2008**, *3*, 142–155.
- (14) Husen Alamudi, S.; Satapathy, R.; Kim, J.; Su, D.; Ren, H.; Das, R.; Hu, L.; Alvarado-Martínez, E.; Lee, J. Y.; Hoppmann, C.; Peña-Cabrera, E.; Ha, H.-H.; Park, H.-S.; Wang, L.; Chang, Y.-T. Development of background-free “Tame” fluorescent probes for intracellular live cell imaging. *Nat. Commun.* **2016**, *7*, 11964.
- (15) Lu, H.; Mack, J.; Yang, Y.; Shen, Z. Structural Modification Strategies for the Rational Design of Red/NIR Region BODIPYs. *Chem. Soc. Rev.* **2014**, *43*, 4778–4823.

- (16) Fayed, T. A. Extension of Fluorescence Response to the Near-IR Region. In *Reviews in Fluorescence*; Geddes, C. D., Ed.; Springer, 2009; pp 75–111.
- (17) Shindy, H. A. Fundamentals in the Chemistry of Cyanine Dyes: A Review. *Dyes Pigm.* **2017**, *145*, 505–513.
- (18) Sauer, M.; Hofkens, J.; Enderlein, J. *Handbook of Fluorescence Spectroscopy and Imaging*; Wiley-VCH: Weinheim, Germany, 2010.
- (19) Dou, L.; Liu, Y.; Hong, Z.; Li, G.; Yang, Y. Low-Bandgap Near-IR Conjugated Polymers/Molecules for Organic Electronics. *Chem. Rev.* **2015**, *115*, 12633–12665.
- (20) Ni, Y.; Wu, J. Far-Red and Near Infrared BODIPY Dyes: Synthesis and Applications for Fluorescent pH Probes and Bio-Imaging. *Org. Biomol. Chem.* **2014**, *12*, 3774–3791.
- (21) Awuah, S. G.; You, Y. Boron Dipyrromethene (BODIPY)-Based Photosensitizers for Photodynamic Therapy. *RSC Adv.* **2012**, *2*, 11169–11183.
- (22) You, Y.; Nam, W. Designing Photoluminescent Molecular Probes for Singlet Oxygen, Hydroxyl Radical, and Iron–oxygen Species. *Chem. Sci.* **2014**, *5*, 4123–4135.
- (23) (a) Zeng, L.; Jiao, C.; Huang, X.; Huang, K.-W.; Chin, W.-S.; Wu, J. Anthracene-Fused BODIPYs as Near-Infrared Dyes with High Photostability. *Org. Lett.* **2011**, *13*, 6026–6029. (b) Jiao, C.; Huang, K.-W.; Wu, J. Perylene-Fused BODIPY Dye with Near-IR Absorption/Emission and High Photostability. *Org. Lett.* **2011**, *13*, 632–635.
- (24) Shen, Z.; Röhr, H.; Rurack, K.; Uno, H.; Spieles, M.; Schulz, B.; Reck, G.; Ono, N. Boron–Diindomethene (BDI) Dyes and Their Tetrahydrobicyclo Precursors-en Route to a New Class of Highly Emissive Fluorophores for the Red Spectral Range. *Chem. - Eur. J.* **2004**, *10*, 4853–4871.
- (25) Jiao, L.; Yu, C.; Liu, M.; Wu, Y.; Cong, K.; Meng, T.; Wang, Y.; Hao, E. Synthesis and Functionalization of Asymmetrical Benzo-Fused BODIPY Dyes. *J. Org. Chem.* **2010**, *75*, 6035–6038.
- (26) Okujima, T.; Tomimori, Y.; Nakamura, J.; Yamada, H.; Uno, H.; Ono, N. Synthesis of  $\pi$ -Expanded BODIPYs and Their Fluorescent Properties in the Visible-near-infrared Region. *Tetrahedron* **2010**, *66*, 6895–6900.
- (27) Heyer, E.; Retailleau, P.; Ziessel, R.  $\alpha$ -Fused Dithienyl BODIPYs Synthesized by Oxidative Ring Closure. *Org. Lett.* **2014**, *16*, 2330–2333.
- (28) Hayashi, Y.; Obata, N.; Tamaru, M.; Yamaguchi, S.; Matsuo, Y.; Saeki, A.; Seki, S.; Kureishi, Y.; Saito, S.; Yamaguchi, S.; Shinokubo, H. Facile Synthesis of Biphenyl-Fused BODIPY and Its Property. *Org. Lett.* **2012**, *14*, 866–869.
- (29) Kubo, Y.; Minowa, Y.; Shoda, T.; Takeshita, K. Synthesis of a New Type of Dibenzopyrromethene-boron Complex with Near-Infrared Absorption Property. *Tetrahedron Lett.* **2010**, *51*, 1600–1602.
- (30) Ni, Y.; Wu, J. Far-Red and near Infrared BODIPY Dyes: Synthesis and Applications for Fluorescent pH Probes and Bio-Imaging. *Org. Biomol. Chem.* **2014**, *12*, 3774–3791.
- (31) (a) Umezawa, K.; Nakamura, Y.; Makino, H.; Citterio, D.; Suzuki, K. Bright, Color-Tunable Fluorescent Dyes in the Visible-Near-Infrared Region. *J. Am. Chem. Soc.* **2008**, *130*, 1550–1551. (b) Umezawa, K.; Matsui, A.; Nakamura, Y.; Citterio, D.; Suzuki, K. Bright, Color-Tunable Fluorescent Dyes in the Vis/NIR Region: Establishment of New “Tailor-Made” Multicolor Fluorophores Based on Borondipyrromethene. *Chem. - Eur. J.* **2009**, *15*, 1096–1106.
- (32) Leen, V.; Qin, W.; Yang, W.; Cui, J.; Xu, C.; Tang, X.; Liu, W.; Robeyns, K.; Van Meervelt, L.; Beljonne, D.; Lazzaroni, R.; Tonnelé, C.; Boens, N.; Dehaen, W. Synthesis, Spectroscopy, Crystal Structure Determination, and Quantum Chemical Calculations of BODIPY Dyes with Increasing Conformational Restriction and Concomitant Red-Shifted Visible Absorption and Fluorescence Spectra. *Chem. - Asian J.* **2010**, *5*, 2016–2026.
- (33) Gómez-Durán, C. F. A.; Esnal, I.; Valois-Escamilla, I.; Urías-Benavides, A.; Bañuelos, J.; López Arbeloa, I.; García-Moreno, I.; Peña-Cabrera, E. Near-IR BODIPY Dyes á la Carte-Programmed Orthogonal Functionalization of Rationally Designed Building Blocks. *Chem. - Eur. J.* **2016**, *22*, 1048–1061.
- (34) (a) Prokopcová, H.; Kappe, C. O. The Liebeskind–Srogl C-C Cross Coupling Reaction. *Angew. Chem., Int. Ed.* **2009**, *48*, 2276–2286. (b) Cheng, H.-G.; Chen, H.; Liu, Y.; Zhou, Q. The Liebeskind–Srogl Cross-Coupling Reaction and its Synthetic Applications. *Asian J. Org. Chem.* **2018**, *7*, 490–508.
- (35) (a) Jones, G., II; Huang, Z.; Kumar, S.; Pacheco, D. Fluorescence and Lasing Properties of Benzo-Fused Pyrromethene Dyes in Poly(methyl methacrylate) Solid Host Media. *Proc. SPIE* **2002**, *4630*, 72–81. (b) Jones, G., II; Huang, Z.; Pacheco, D. Fluorescence and Lasing Properties of Meso-Substituted Benzo-Fused Pyrromethene Dyes in Solid Media. *Proc. SPIE* **2003**, *4968*, 24–34.
- (36) Zeni, G.; Larock, R. C. Synthesis of Heterocycles via Palladium-Catalyzed Oxidative-Addition. *Chem. Rev.* **2006**, *106*, 4644–4680.
- (37) Jiang, T.; Zhang, P.; Yu, C.; Yin, J.; Jiao, L.; Dai, E.; Wang, J.; Wei, Y.; Mu, X.; Hao, E. Straightforward Synthesis of Oligopyrroles through a Regioselective  $S_NAr$  Reaction of Pyrroles and Halogenated Boron Dipyrins. *Org. Lett.* **2014**, *16*, 1952–1955.
- (38) Isomer **3** was prepared in two steps; the first arylation reaction took place in refluxing dioxane for 96 h, while the second arylation took place in refluxing toluene for 48 h (see ref 32).
- (39) Chen, J.; Burghart, A.; Derecskei-Kovacs, A.; Burgess, K. 4,4-Difluoro-4-bora-3a,4a-diaza-s-indacene (BODIPY) Dyes Modified for Extended Conjugation and Restricted Bond Rotations. *J. Org. Chem.* **2000**, *65*, 2900–2906.
- (40) Kee, H. L.; Kirmaier, C.; Yu, L.; Thamyongkit, P.; Youngblood, W. J.; Calder, M. E.; Ramos, L.; Noll, B. C.; Bocian, D. F.; Scheidt, W. R.; Birge, R. R.; Lindsey, J. S.; Holten, D. Structural Control of the Photodynamics of Boron-Dipyrin Complexes. *J. Phys. Chem. B* **2005**, *109*, 20433–20443.
- (41) Luo, L.; Wu, D.; Li, W.; Zhang, S.; Ma, Y.; Yan, S.; You, J. Regioselective Decarboxylative Direct C–H Arylation of Boron Dipyrromethenes (BODIPYs) at 2,6-Positions: A Facile Access to a Diversity-Oriented BODIPY Library. *Org. Lett.* **2014**, *16*, 6080–6083.
- (42) Reichardt, C. Solvatochromic Dyes as Solvent Polarity Indicators. *Chem. Rev.* **1994**, *94*, 2319–2358.
- (43) García-Moreno, I.; Costela, A.; Martín, V.; Pintado-Sierra, M.; Sastre, R. Materials for a Reliable Solid-state Dye Laser at the Red Spectral Edge. *Adv. Funct. Mater.* **2009**, *19*, 2547–2552.
- (44) Durán-Sampedro, G.; Agarrabeitia, A. R.; Cerdán, L.; Pérez-Ojeda, M. E.; Costela, A.; García-Moreno, I.; Esnal, I.; Bañuelos, J.; López-Arbeloa, I.; Ortiz, M. J. Carboxylates vs Fluorines: Boosting the Emission Properties of Commercial BODIPYs in Liquid and Solid Media. *Adv. Funct. Mater.* **2013**, *23*, 4195–4205.
- (45) (a) Masilamani, V.; Aldwayyan, A. S. Structural and Solvent Dependence of Superexciplex. *Spectrochim. Acta, Part A* **2004**, *60*, 2099–2106. (b) Cerdán, L.; Martínez-Martínez, V.; García-Moreno, I.; Costela, A.; Pérez-Ojeda, M. E.; López-Arbeloa, I.; Wu, L.; Burgess, K. Naturally Assembled Excimers in Xanthenes as Singular and Highly Efficient Laser Dyes in Liquid and Solid Media. *Adv. Opt. Mater.* **2013**, *1*, 984–990.
- (46) Cerdán, L.; Costela, A.; García-Moreno, I.; Bañuelos, J.; López-Arbeloa, I. Singular Laser Behaviour of Hemicyanine Dyes: Unsurpassed Efficiency and Finely Structured Spectrum in the Near-IR Region. *Laser Phys. Lett.* **2012**, *9*, 426–433.
- (47) Durán-Sampedro, G.; Agarrabeitia, A. R.; Arbeloa Lopez, T.; Bañuelos, J.; López-Arbeloa, I.; Chiara, J. L.; Garcia-Moreno, I.; Ortiz, M. J. Increased Laser Action in Commercial Dyes from Fluorination Regardless of their Skeleton. *Laser Phys. Lett.* **2014**, *11*, 115818.
- (48) Jones, G., II; Kumar, S.; Klueva, O.; Pacheco, D. Photoinduced Electron Transfer for Pyrromethene Dyes. *J. Phys. Chem. A* **2003**, *107*, 8429–8434.
- (49) Lakshmi, V.; Ravikanth, M. Synthesis of Hexasubstituted Boron Dipyrromethenes Having a Different Combination of Substituents. *Eur. J. Org. Chem.* **2014**, *2014*, 5757–5766.
- (50) Jiao, L.; Pang, W.; Zhou, J.; Wei, Y.; Mu, X.; Bai, G.; Hao, E. Regioselective Stepwise Bromination of Boron Dipyrromethene (BODIPY) Dyes. *J. Org. Chem.* **2011**, *76*, 9988–9996.







# Tailoring the Molecular Skeleton of Aza-BODIPYs to Design Photostable Red-Light-Emitting Laser Dyes

Alejandro Prieto-Castañeda,<sup>[a]</sup> Edurne Avellanal-Zaballa,<sup>[b]</sup> Leire Gartzia-Rivero,<sup>[b]</sup> Luis Cerdán,<sup>\*[c]</sup> Antonia R. Agarrabeitia,<sup>[a, d]</sup> Inmaculada García-Moreno,<sup>[c]</sup> Jorge Bañuelos,<sup>\*[b]</sup> and María J. Ortiz<sup>[a]</sup>

In this article the design and characterization of a set of novel red-light-emitting laser aza-BODIPY dyes is reported. The applied synthetic method allows an exhaustive and versatile functionalization of both the dipyrin core and the boron bridge. From the analysis of the photophysical and laser signatures, we determine the suitable modifications of the chromophoric backbone necessary to modulate the emission spectral region, efficiency and photostability under a strong irradiation regime. These dyes are endowed with efficient

fluorescence and laser emission, and are particularly outstanding in terms of their high photostability, a key parameter to guarantee long-lasting emission in any (bio)technological application. The herein-reported results support, for the first time, the viability of aza-BODIPYs as tunable red laser dyes. In fact, the laser performances of some of the tested aza-BODIPYs surpass those of commercially available laser dyes in the same spectral region.

## 1. Introduction

The search for organic fluorophores with specific functionalities is the cornerstone of many ongoing challenging researches. The careful selection of the groups decorating the chromophoric core rules the photophysical properties and defines the target application field in which the luminophore might be applied. In this regard, modern synthetic avenues enable an exhaustive structural modification of previously existing dyes or the design of new families of organic molecules with tailor made functionalities.<sup>[1]</sup> Such chemical versatility supports the success and spread of organic dyes in many application fields ranging from lasers<sup>[2]</sup> to labeling or photosensing,<sup>[3]</sup> thereby, covering most of the demands from photonics or biomedicine, including super resolution optical detection techniques.<sup>[4]</sup> To this aim, it is not only desirable to use fluorophores with bright

fluorescence response, biocompatibility or recognition of specific binding sites, but it is fundamental that they also display high resistance to photodegradation under prolonged and intense irradiation. Otherwise, the fluorophore can be easily photobleached, hampering the visualization and monitoring of the molecular event in real time.

Accordingly, one of the most active topics in dye chemistry deals with the development of highly efficient and stable fluorophores but with emission deeply shifted towards the red edge of the visible spectral region, even reaching the near-infrared (NIR).<sup>[5]</sup> Both its lower spectral overlap with tissues auto-fluorescence background and its deeper penetration into them (if the energy falls within the so-called biological window, 650–900 nm) provide additional advantages for higher resolution sensing.<sup>[6]</sup> Hitherto, dyes based mainly on cyanine (including squaraine and aza-derivatives)<sup>[7]</sup> or oxazines cores have been usually tested as red-emitting fluorochromes.<sup>[8]</sup> However, they present some important drawbacks: low emission efficiencies and/or poor photostability under intense irradiation, and limited chemical versatility for postfunctionalization to enhance biocompatibility and promote the recognition of targeted sites. In the last years, fluorophores based on the difluoroboron dipyrromethene (BODIPY)<sup>[9]</sup> chromophore have arisen as an alternative, since they can be designed to meet all the above pointed requirements. Originally, the spectral bands of this dye are placed in the middle part of the visible (green-yellow region).<sup>[10]</sup> Nevertheless, the chemical versatility of its dipyrin core, readily amenable to a wide pool of chemical reactions, enables an exhaustive functionalization of the chromophoric core.<sup>[11]</sup> In fact, many red-emitting BODIPYs have been already reported in the literature.<sup>[12]</sup> Different synthetic strategies have been tested to this aim: (i) extension of the  $\pi$ -system through peripheral aromatic substituents,<sup>[9,10,11a,13]</sup> (ii) fusion of aromatic rings<sup>[14]</sup> and (iii) replacement of the central *meso*-carbon by a

[a] A. Prieto-Castañeda, Prof. Dr. A. R. Agarrabeitia, Prof. Dr. M. J. Ortiz  
Departamento de Química Orgánica

Facultad de Ciencias Químicas  
Ciudad Universitaria s/n, 28040 Madrid (Spain)

[b] E. Avellanal-Zaballa, Dr. L. Gartzia-Rivero, Prof. Dr. J. Bañuelos

Departamento de Química-Física  
Universidad del País-Vasco-EHU Apartado 644  
48080 Bilbao (Spain)  
E-mail: jorge.banuelos@ehu.es

[c] Dr. L. Cerdán, Dr. I. García-Moreno  
Departamento de Sistemas de Baja Dimensionalidad

Superficies y Materia Condensada  
Instituto de Química-Física "Rocasolano" (CSIC)  
Serrano 119, 28006 Madrid (Spain)  
E-mail: lcerdan@iqfr.csic.es

[d] Prof. Dr. A. R. Agarrabeitia  
Departamento de Química Orgánica

Facultad de Óptica y Optometría  
c/ Arcos de Jalón 118, 28037, Madrid (Spain)

Supporting information for this article is available on the WWW under  
<https://doi.org/10.1002/cptc.201800225>

nitrogen leading to aza-BODIPYs.<sup>[15]</sup> This last approach is very appealing since such simple structural change entails a pronounced red shift of the spectral bands.<sup>[16]</sup> Thus, nowadays, bright long-wavelength emitting dyes have been designed based on aza-BODIPYs in combination with the aforementioned strategies, that is,  $\pi$ -extended aza-BODIPYs<sup>[17]</sup> or benzo-fused aza-BODIPYs.<sup>[18]</sup> These fluorochromes have been successfully applied as near-infrared fluorophores<sup>[17,18]</sup> or polymers,<sup>[19]</sup> fluorescent sensors<sup>[20]</sup> and labels for bioimaging,<sup>[21]</sup> subunits in molecular antennae,<sup>[22]</sup> photosensitizers for solar cells,<sup>[23]</sup> and light-driven therapeutic purposes in biomedicine.<sup>[24]</sup>

To the best of our knowledge, the evaluation of the performance of aza-BODIPYs under strong irradiation regime has not been yet reported, despite photostability playing a key role for a useful operative lifetime. Therefore, in the present work we have designed and synthesized a battery of aza-BODIPYs with peripheral aromatic groups ( $\pi$ -extended aza-BODIPYs) to push their emission deeper into the red-edge (Figure 1). The conducted chemical modifications are not

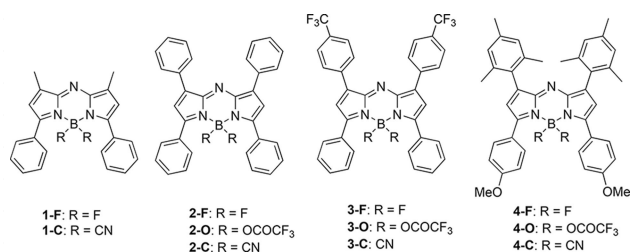


Figure 1. Studied aza-BODIPY molecules.

limited to the dipyrin backbone, since the boron atom has been functionalized as well to yield both *O*-aza-BODIPYs and *C*-aza-BODIPYs, from the corresponding *F*-aza-BODIPYs. In the literature some pioneer reports can be found dealing with the displacement of fluorine by *O*- and *C*- nucleophiles, respectively.<sup>[20a,25,26]</sup>

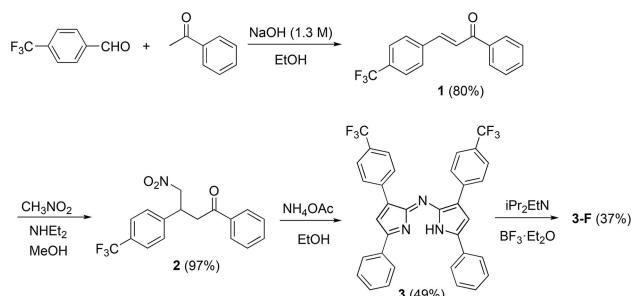
Apart from the comprehensive analysis of the photophysical signatures, aided by computational simulations, we focus mainly on the photostability of the dyes under laser pumping to offset this lack of information. Moreover, we report for the first time to the best of our knowledge the laser performance of these red-emitting aza-BODIPYs under suitable pumping conditions. To put the laser performance of the aza-BODIPYs into perspective we compare their lasing signatures with representative commercially available laser dyes working in the same spectral region.

## 2. Results and Discussion

### 2.1. Synthesis

The known aza-BODIPYs **1-F**,<sup>[27]</sup> **2-F**<sup>[15a,24a]</sup> and **4-F**<sup>[28]</sup> were prepared according to the previously described procedure, from an aldol condensation between aldehydes and ketones, a

subsequent Michael addition of nitromethane, and a final condensation with ammonium acetate and  $\text{BF}_3$  complexation reactions. We used the same methodology to synthesize **3-F** in a four step route from 4-(trifluoromethyl)benzaldehyde and benzophenone (Scheme 1). Condensation of aldehyde with



Scheme 1. Synthesis of aza-BODIPY **3-F**.

ketone gave  $\alpha,\beta$ -unsaturated ketone **1**.<sup>[29]</sup> Conjugate addition of nitromethane to **1** in MeOH with diethylamine (DEA) gave the nitroketone **2** in excellent yield. This nitroketone has been previously described but through a different procedure.<sup>[30]</sup> Subsequently, the aza-dipyrromethene **3** was obtained in 49% yield by refluxing compound **2** with ammonium acetate in ethanol. This intermediate was used for the synthesis of compound **3-F** (37%) by reaction with  $\text{BF}_3\cdot\text{Et}_2\text{O}$  and *N,N*-diisopropylamine in dichloromethane (Scheme 1).

Replacement of the fluorine atoms of the boron bridge by trifluoroacetoxy (**2-O**, **3-O** and **4-O**) or cyano (**1-C**, **2-C**, **3-C** and **4-C**) groups was carried out by the reaction of *F*-aza-BODIPY with trimethylsilyl trifluoroacetate ( $\text{TMSOCOCF}_3$ ) or trimethylsilyl cyanide ( $\text{TMSCN}$ ), respectively, in the presence of  $\text{AlCl}_3$  as Lewis acid in 18 to 79% yield (see Experimental Section), according to the experimental procedure previously describe by our research group.<sup>[31]</sup>

### 2.2. Photophysical Properties

The periphery of the dipyrin core of the aza-BODIPY, as well as its boron bridge (*C*- and *O*-aza-BODIPYs from the corresponding *F*-aza-BODIPYs), have been systematically functionalized to gain a deeper insight into the complex impact of the molecular structure onto the photophysical and laser signatures.

#### 2.2.1. *F*-aza-BODIPYs

The sole replacement of the central *meso* carbon by an aza group entails a pronounced bathochromic shift of the spectral bands. The electronegative character of the nitrogen stabilizes the LUMO state (around 0.58 eV), whose electronic density is concentrated in such key *meso* position, lowering the energy gap (Figure 2).<sup>[32]</sup> To push this shift even further towards the red edge of the visible region, the chromophoric backbone has been decorated with aromatic frameworks, bearing also

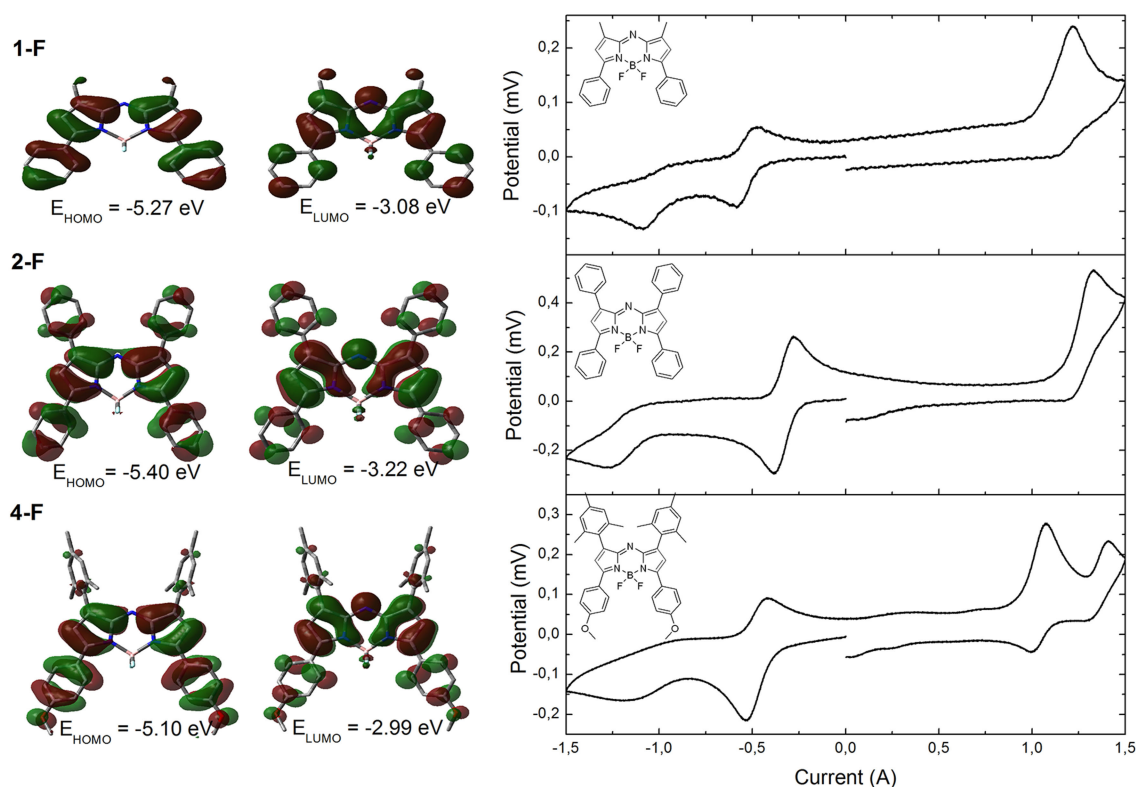


**Figure 2.** Calculated frontier orbitals from the ground state optimized geometries (B3LYP/6-311G\*) and cyclic voltammograms (in acetonitrile 0.1 M TBAPF<sub>6</sub>) of the *F*-aza-BODIPYs 1-F, 2-F and 4-F. The corresponding maps and scans of 3-F are closely related to those of 2-F, owing to their structural similarity, and are not including for the sake of simplicity.

electronic rich moieties (such as electron donor methoxy and electron acceptor trifluoromethyl), at positions 3 and 5, and 1 and 7 respectively. The addition of phenyl rings at the  $\alpha$ -pyrrolic positions (1-F) places the spectral bands in the red part of the visible (Figure 3), as consequence of a more extended  $\pi$ -system (Figure 2). Further bathochromic shift (around 30–40 nm) can be achieved by the additional insertion of phenyls at the opposite 1 and 7 positions (2-F), being slightly higher (around

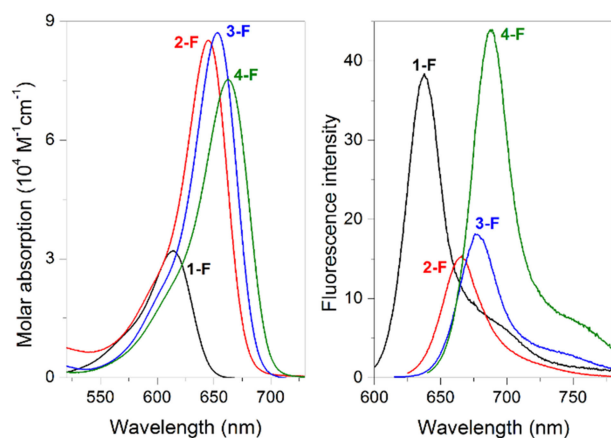


**Figure 3.** Absorption (scaled by their molar absorption) and fluorescence (scaled by their fluorescence efficiency) of the *F*-aza-BODIPYs (1-F to 4-F) in diluted solutions (2  $\mu$ M) of cyclohexane.

10 nm) upon functionalization with *para*-trifluoromethyl groups (3-F) (Figure 3). It should be noticed that the presence of aromatic rings at positions 1 and 7 has typically a limited impact on the spectroscopic properties of BODIPYs, since they adopt an almost orthogonal disposition owing to steric reasons.<sup>[33]</sup> However, the replacement of the *meso*-methine by an aza group, vanishes such geometrical constraint and now the 1,7-aryls can promote resonant interactions. Indeed, the twisting angle of such phenyls is just 24° with respect to the dipyrin plane in the ground state (Figure 2). Therefore, the delocalized  $\pi$ -system comprises the whole molecule, including the four peripheral aryl rings. Nevertheless, the strongest spectral shift towards the red-edge is achieved acting at positions 3 and 5. In fact, their functionalization with anisoles (4-F) pushes the absorption and emission bands more deeply into the red region (670 nm and 710 nm, respectively, Figure 3), even though the 1,7-mesityl groups do not interact by resonance with the dipyrin owing to steric reasons (*ortho*-methyl groups force them to be orthogonally oriented). Therefore, the designed strategy to develop red-emitting BODIPYs is successful owing to the synergetic contribution of the replacement by the aza group and the anchoring of peripheral aromatic moieties.

The electrochemistry measurements reveal that the herein tested *F*-aza-BODIPYs are easier to reduce (around -0.5 V), owing to the presence of cathodic waves at low potentials, while the anodic waves remain at high potentials (1.2–1.3 V), in

agreement with the theoretically predicted LUMO stabilization by the replacement of the central methine by an aza group (Figure 2). Moreover, the extension of the chromophoric  $\pi$ -system lowers the reduction potential (from  $-0.53$  V in **1-F** to  $-0.32$  V in **2-F**). In contrast, the further addition of electron donor methoxy groups entails a decrease of the oxidation potential down to  $1.0$  V, matching the theoretically predicted increase of the HOMO energy (Figure 2).

Dye **1-F** displays a moderate absorption probability (molar absorption around  $30000\text{ M}^{-1}\text{ cm}^{-1}$ ) but reasonable bright fluorescence signal (almost 40% with a lifetime of 2.6 ns in non-polar cyclohexane) at around 640 nm (Table 1). A further increase of the solvent polarity implies a concomitant and

parallel decrease of both parameters (down to 18% and 1.44 ns, respectively in polar methanol, Table 1). Usually BODIPYs are characterized by higher fluorescence efficiencies and longer lifetimes,<sup>[9,10,11a]</sup> but a red-shift of the spectral bands implies that the ground and excited state are closer, hence, enhancing the internal conversion (energy gap law).<sup>[34]</sup> Besides, Kuznetsova *et al.* pointed out to a higher  $n\text{-}\pi^*$  character of the transition upon replacement of the central methine unit by an aza group.<sup>[35]</sup> Such trend could increase the intersystem crossing probability, further enhancing the non-radiative rate constant (Table 1 and S1). However, Harriman *et al.* suggested that, albeit the replacement of the methine carbon by an aza group affects the  $S_1\text{-}T_1$  energy gap, the intersystem crossing is

**Table 1.** Photophysical properties of the polyarylated aza-BODIPYs in diluted solutions of non-polar (cyclohexane, c-hex) and polar/protic (methanol, MeOH) solvents. Photophysical data in additional solvents are collected in Table S1.<sup>[a]</sup>

Compound Solvent	$\lambda_{\text{ab}}$ [nm]	$\epsilon_{\text{max}}$ [ $10^4\text{ M}^{-1}\text{ cm}^{-1}$ ]	$\lambda_{\text{fl}}$ [nm]	$\Delta\nu_{\text{St}}$ [ $\text{cm}^{-1}$ ]	$\phi$	$\tau$ [ns]	$k_{\text{fl}}$ [ $10^8\text{ s}^{-1}$ ]	$k_{\text{nr}}$ [ $10^8\text{ s}^{-1}$ ]
<b>1-F</b>								
c-hex	614.0	3.2	637.5	600	0.39	2.64	1.51	2.28
MeOH	613.0	3.0	638.0	640	0.18	1.44	1.25	5.69
<b>1-C</b>								
c-hex	599.5	5.6	636.5	970	0.34	2.53	1.33	2.61
MeOH	600.5	5.3	636.0	930	0.12	1.14	1.05	7.72
<b>2-F</b>								
c-hex	645.0	8.5	666.0	490	0.15	0.90	1.65	9.39
MeOH	644.0	8.4	665.5	500	0.09	0.60	1.50	15.20
<b>2-O</b>								
c-hex	643.5	5.7	675.5	735	0.42	3.70	1.13	1.57
MeOH	641.5	4.8	665.5	560	0.09	0.95	0.95	9.58
<b>2-C</b>								
c-hex	653.0	7.8	669.5	380	0.51	4.49	1.14	1.09
MeOH	650.0	6.6	667.0	390	0.38	3.92	0.98	1.57
<b>3-F</b>								
c-hex	653.0	8.7	676.0	520	0.19	1.51	1.26	5.36
MeOH	652.0	8.5	676.0	545	0.12	1.16	1.03	7.58
<b>3-O</b>								
c-hex	651.0	6.9	683.5	730	0.43	4.05	1.06	1.40
MeOH	649.0	5.7	679.0	680	0.10	1.43	0.70	6.29
<b>3-C</b>								
c-hex	648.5	6.3	676.0	870	0.11	1.03	1.07	8.64
MeOH	650.0	7.3	679.0	655	0.13	1.48	0.88	5.88
<b>4-F</b>								
c-hex	662.5	7.5	688.5	570	0.46	3.26	1.41	1.65
MeOH	668.0	7.5	699.0	665	0.28	2.32	1.20	3.10
<b>4-O</b>								
c-hex	672.5	8.0	699.5	575	0.54	3.98	1.35	1.15
MeOH	666.5	5.0	709.5	830	0.18	1.80	1.00	4.55
<b>4-C</b>								
c-hex	662.5	5.3	693.0	665	0.24	2.00	1.20	3.80
MeOH	666.0	5.6	705.0	830	0.15	1.73	0.87	4.91

[a] Absorption ( $\lambda_{\text{ab}}$ ) and fluorescence ( $\lambda_{\text{fl}}$ ) wavelengths; molar absorption at the maximum absorbance ( $\epsilon_{\text{max}}$ ); Stokes shift ( $\Delta\nu_{\text{St}}$ ); fluorescence quantum yield ( $\phi$ ) and lifetime ( $\tau$ ); radiative ( $k_{\text{fl}}$ ) and non-radiative ( $k_{\text{nr}}$ ) rate constants.

ineffective in aza-BODIPYs.<sup>[32]</sup> They pinpoint that the sensitivity of the fluorescence deactivation with the solvent could be related to a specific interaction between hydrogen bonding solvents (i.e., alcohols) and the chromophoric aza group. Thus, the lone pair would be located at the nitrogen rather than delocalized, decreasing the aromaticity and the radiative rate constant. The key role of hydrogen bonding on the fluorescence efficiency has been verified for other dyes.<sup>[36]</sup> Furthermore, such specific interaction entails that the nitrogen can interconvert from a planar  $sp^2$  hybridization to a tetrahedral  $sp^3$ , which tends to be out of plane. This umbrella like motion (ULM model)<sup>[37]</sup> could have a meaningful impact in aza-BODIPYs since the typical butterfly-like bending of the dipyrin core takes place along the transversal axis. Indeed, the aza atom carries the highest negative charge in the whole molecule (i.e., for dye **1-F** is  $-0.52$ , even larger than in the fluorine atoms, Figure S1). Therefore, the *meso* nitrogen is readily available to H-bonding with the solvent, supporting the recorded fluorescence quenching in alcohols.

Further arylation of the aza-BODIPY (**2-F**) provides a more extended and aromatic  $\pi$ -system, as reflected in a higher absorption probability (up to  $85000\text{ M}^{-1}\text{ cm}^{-1}$ , Table 1). However, the red shift of the emission goes hand in hand with a decline in the fluorescence response (efficiencies lower than 15% and lifetime shorter than 1 ns, Table 1). The photophysical properties of **2-F** have been analysed in detail in the bibliography.<sup>[38]</sup> The published fluorescence quantum yields are quite different depending on the consulted bibliographic source. Our results are in better agreement with those recently published by Antina *et al.*<sup>[38c]</sup> Such fluorescence quenching should be related to the free motion of the aryls at positions 1 and 7, in analogy to the detected high internal conversion probability in unconstrained 8-arylBODIPYs.<sup>[39]</sup> In this line of reasoning, the corresponding analogue bearing *para*-trifluoromethyl groups at such rings (**3-F**) displays also low fluorescence response (Table 1), albeit slightly higher than in **2-F** owing to the electron withdrawing character of such functionalization which seems to slightly counterbalance the deleterious effect of the phenyl motion. Low fluorescence efficiencies have been also reported for aza-BODIPYs decorated with electron withdrawing groups in the peripheral aryl groups.<sup>[40]</sup> It should be mentioned that the sensitivity of the fluorescence quantum yield and lifetime of compounds **2-F** and **3-F** with the solvent is lower than in **1-F** (Table 1). This could be related to the presence of the adjacent twisted phenyls, which makes the aza-group less accessible to the H-bonding in alcohols.

In view of these results, and to unambiguously check the role of the flexibility/rigidity around positions 1 and 7, we designed an aza-BODIPY (**4-F**) bearing bulky mesityls at such positions, and with anisoles at positions 3 and 5 to reinforce the pursued red-shift (Figure 3). As a result, we achieve a strong absorption (almost  $80000\text{ M}^{-1}\text{ cm}^{-1}$  at around 670 nm) and bright emission at 700 nm with an efficiency approaching the 50% and a lifetime of around 3 ns (Table 1), being the higher among the herein tested *F*-aza-BODIPYs. In fact, high fluorescence responses have been reported for conformation-

ally restricted aza-BODIPYs.<sup>[28,41]</sup> Again the fluorescence response is lower in alcohols (down to 28% and 2.3 ns, respectively in methanol, Table 1), supporting an ongoing H-bonding as an additional non-radiative pathway in these media. Indeed in this dye the negative charge at the aza group increases up to  $-0.64$  (see dye **4** in Figure S1), likely related to the electron donor ability of the methoxy groups. Besides, the perpendicular disposition of the adjacent phenyl rings makes the aza group more accessible to the solvent.

### 2.2.2. Chemical Modifications at the Boron Centre: C- and O-aza-BODIPYs

In previous publications dealing with BODIPYs, we reported that their fluorescence response could be ameliorated by substituting the fluorine atoms at the boron bridge with electron withdrawing moieties like cyano and, especially, trifluoroacetoxy.<sup>[31]</sup> Against this background, we tested this strategy in the above described *F*-aza-BODIPYs and designed the corresponding C- and O-aza-BODIPYs to further optimize the fluorescence performance of the red-emitting dyes. The corresponding O-aza-BODIPY from compound **1-F** could not be attained, since the product was chemically unstable and decomposed quickly.

On first consideration, the replacement of the fluorine atoms of the boron bridge should faintly affect the spectral bands positions, however the recorded photophysics show that it matters and depends on the substitution pattern at the dipyrin core (Table 1). Indeed, the spectral bands shift moderately but randomly upon functionalization at the boron bridge and no common trend can be drawn out. Albeit the boron does not take part in the delocalized  $\pi$ -system, the replacement of a highly electronegative fluorine by electron withdrawing moieties with different strength could rearrange the electronic density at the chromophore, swaying its aromaticity.<sup>[28,41]</sup>

Figure 4 shows a comparison of the fluorescence quantum yield of each set of dyes, after modification at the boron atom, in two opposite solvents. It should be highlighted the nice correlation with the fluorescence lifetime (Table 1), since an increase/decrease of the fluorescence efficiency is correlated with a lengthening/shortening of the lifetime.

In all cases, the fluorescence response in low polarity solvents is ameliorated with regard to their parent *F*-aza-BODIPYs (Figure 4). Such improvement is modest in compound **4-O**, but very pronounced in the dyes bearing the unconstrained 1,7-aryls (**2-O** and **3-O**). Indeed, in these last dyes the increase of the fluorescence efficiency is around 2–3 fold (Figure 4) and the lengthening of the lifetime around 2–3 ns (Table 1 and S1) with regard to compounds **2-F** and **3-F**, respectively. Therefore, this straightforward molecular design at the boron centre is strongly suitable (fluorescence efficiency up to 45% with a lifetime of around 4 ns, Table 1). However, the fluorescence response in alcohols is again limited, likely by the claimed hydrogen bond, reaching values similar to those recorded for *F*-aza-BODIPYs (Figure 4). Indeed, overall the fluorescence efficiency of the O-aza-BODIPYs is more sensitive

to the solvent effect than their *F*-aza-BODIPYs counterparts. The corresponding charge distribution suggests that the replacement of the fluorine by trifluoroacetoxy at the boron implies an increase of the negative charge at the *meso* nitrogen (up to  $-0.69$  in dye **4-O**, the highest among the herein tested dyes). Therefore, in *O*-aza-BODIPYs the lone pair of the aza group is more available to interact with surrounding hydrogens, even in presence of sterically hindered adjacent phenyl groups.

The impact of the cyano group at the boron centre on the fluorescence signatures was rather intriguing. The *C*-aza-BODIPYs **1-C**, **3-C** and **4-C** do not ameliorate the fluorescence signatures of their corresponding *F*-aza-BODIPYs (Figure 5 and Table 1). However, dye **2-C**, bearing unconstrained 1,7-aryl groups, shows a notable increase of the fluorescence response. A similar trend was attained for the corresponding *O*-aza-BODIPY analogue (**2-O**). However, in the *C*-aza-BODIPY **2-C** the fluorescence efficiency and lifetime remain strikingly high regardless of the surrounding environment, even in alcohols (Table 1 and S1), being one of the herein developed aza-BODIPYs with the best fluorescence performance. The rearrangement of the electronic charge distribution induced by the cyano group decreases the negative charge at the aza-group ( $-0.37$  for **2-C**, among the lowest of the herein tested dyes). Thus, its aza group is less prone to undergo hydrogen bonding, avoiding this fluorescence quenching pathway in alcohols. In this line of reasoning, it is rather unexpected the fluorescence performance of the **3-C** analogue, bearing also 1,7-phenyls with conformational freedom but *para*-functionalized with electron acceptor trifluoromethyl groups (Figure 5 and Table 1). The fluorescence parameters are rather insensitive to the solvent effect, in agreement with a lower negative charge at the aza atom ( $-0.38$ ) and steric hindrance induced by the neighbouring twisted 1,7-phenyls. However, the recorded fluorescence quantum yield and lifetime are rather low. Perhaps, the presence of the electron withdrawing trifluoromethyls and cyano groups at

opposite positions could increase the charge separation upon excitation, adding an unexpected additional non-radiative pathway in **3-C**.

Summing up, whereas all the *O*-aza-BODIPYs ameliorate the fluorescence response of *F*-aza-BODIPYs in less polar media, specific *C*-aza-BODIPYs are more suitable to overcome the fluorescence quenching in alcohols (Figure 5). These results point out that the chemical modification around the boron atom is a successful approach to enhance the fluorescence response, however there is not a common trend and the more suitable functionalization of the boron should be adjusted depending on the substitution pattern of the dipyrin core.

### 2.3. Laser Properties

Once adjusted the chemical modification at the dipyrin core and at the boron bridge, some of the developed aza-BODIPYs might be suitable candidates as laser dyes in the red-edge. In the bibliography, just a short mention of laser emission from a tetra-arylated aza-BODIPYs has been reported.<sup>[42]</sup> However, the authors recognize that the low recorded efficiency (4%) could be underestimated owing to the low absorbance of this dye at the pumping wavelength (532 nm, second harmonic of Nd:YAG). Hence, to test unambiguously the laser performance (tunability range, efficiency and photostability) of the aza-BODIPYs, they were transversally pumped by a wavelength-tunable Optical Parametric Oscillator (OPO), which allows irradiation of each dye at its maximum absorption wavelength (see Experimental Section). The registered results of the laser performance are collected in Table 2. The concentration which optimizes the laser efficiency, understood as the ratio of the output and input (pump) energies, depends on the given dye (around 0.75–0.5 mM). In this sense, the laser output efficiency

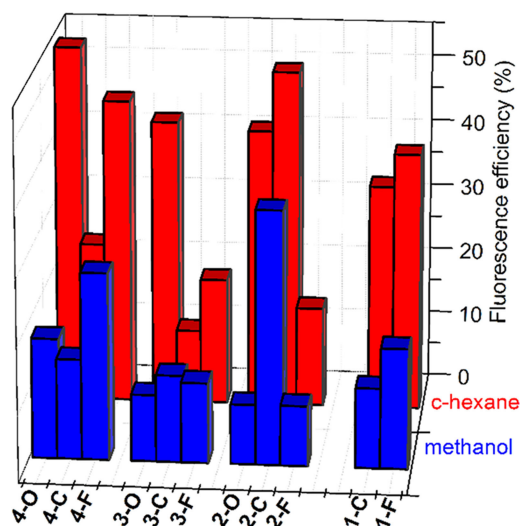


**Figure 4.** Evolution of the fluorescence efficiency of the novel *O*-aza-BODIPYs (**2-O** to **4-O**) and *C*-aza-BODIPYs (**1-C** to **4-C**) with regard to their parent *F*-aza-BODIPY (**1-F** to **4-F**) in non-polar (cyclohexane) and polar/protic (methanol) solvents.

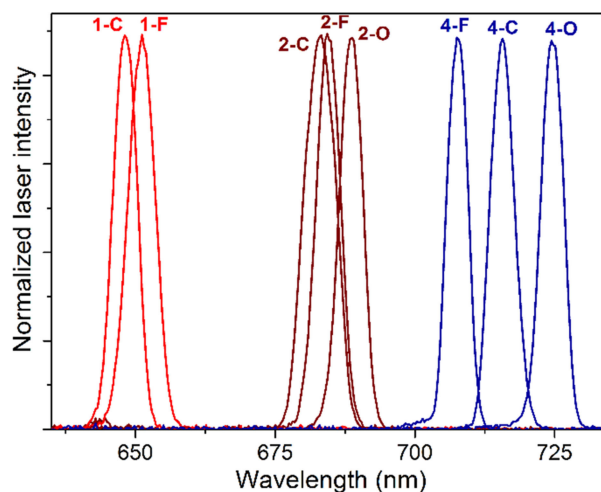


**Figure 5.** Normalized laser spectra of **1-F**, **2-F** and **4-F**, and their corresponding *O*- (**1-O**, **2-O** and **4-O**) and *C*-aza-BODIPYs (**1-C**, **2-C** and **4-C**) in ethyl acetate at 0.5 mM. The corresponding spectra of the dyes derived from **3-F** (**3-O** and **3-C**) are not included because they are similar (around 690–700 nm) to those recorded for those derived from **2-F**, **2-O** and **2-C**, respectively.

**Table 2.** Lasing wavelength ( $\lambda_{\text{la}}$ ), efficiency (%Eff) and photostability ( $E_{\text{dose}}^{90\%}$ ) of the aza-BODIPYs in ethyl acetate at different concentrations. The amount of pumping energy absorbed by the dye to retain 90% of the emission has been calculated for the concentration which optimizes the laser efficiency in each dye.

		Dye concentration [mM]					$E_{\text{dose}}^{90\%}$ [GJ/mol]
		1	0.75	0.5	0.25	0.1	
1-F	%Eff	10	10	12	13	10	44.3
	$\lambda_{\text{la}}$ [nm]	656	653	651	647	643	
1-C	%Eff	7	10	12	13	3	13.5
	$\lambda_{\text{la}}$ [nm]	653	651	648	644	641	
2-F	%Eff	11	13	15	16	5	47.2
	$\lambda_{\text{la}}$ [nm]	689	687	684	681	676	
2-O	%Eff	13	16	19	17	10	21.2
	$\lambda_{\text{la}}$ [nm]	693	691	689	684	681	
2-C	%Eff	11	12	11	8	0	21.1
	$\lambda_{\text{la}}$ [nm]	688	686	683	679	–	
3-F	%Eff	12	16	19	20	13	24.9
	$\lambda_{\text{la}}$ [nm]	696	695	694	690	687	
3-O	%Eff	15	14	15	16	11	9.91
	$\lambda_{\text{la}}$ [nm]	702	700	699	696	691	
3-C	%Eff	14	15	16	14	11	14.3
	$\lambda_{\text{la}}$ [nm]	695	694	692	688	684	
4-F	%Eff	16	19	23	22	18	16.8
	$\lambda_{\text{la}}$ [nm]	711	710	708	704	700	
4-O	%Eff	15	20	30	33	32	4.75
	$\lambda_{\text{la}}$ [nm]	725	724	723	720	716	
4-C	%Eff	27	29	24	21	12	11.8
	$\lambda_{\text{la}}$ [nm]	719	717	715	712	706	

increases with the concentration up to a maximum plateau, from which it decreases owing to reabsorption/reemission phenomena, whose probability is high owing to the low Stokes shift (mostly between 500–700  $\text{cm}^{-1}$ , Table 1). The shift of the emission peak to longer wavelengths with the concentration increase backs up this interpretation (Table 2).

All the tested dyes show laser emission in the red-edge of the visible, ranging from 640 nm to 730 nm, depending mainly on the anchored peripheral aromatic groups and to a lesser

extent on the chemical modification around the boron atom (Figure 5). In general terms, the evolution of the laser wavelength correlates well with the fluorescence one. Thus, the dyes non-arylated at positions 1 and 7 lase at higher energies (around 650 nm), followed by those arylated at such positions (around 690–700 nm), and finally the dyes with the laser emission deeper in the red (up to 725 nm) are those bearing anisole at positions 3 and 5.

The *F*-aza-BOIPYs bearing unrestricted 1,7-phenyl groups (**2-F** and **3-F**) show an unexpected high laser efficiency (Table 2), even higher than that of dye **1-F**, although this last one was characterized by a higher fluorescence efficiency (Table 1). This apparent mismatch can be rationalized taking into account the short lifetime of the former dyes. Such fast decay ameliorates the population inversion and enhances the stimulated emission probability, counterbalancing their low probability of spontaneous emission. Indeed, styryldyes, which are also characterized by low fluorescence efficiency and short lifetimes, show unusual high laser efficiencies also in the red-edge of the visible.<sup>[43]</sup> On the other hand, the conformationally restricted dye **4-F** shows the higher laser efficiency (23%) among the tested *F*-aza-BODIPYs, being also the one with the highest fluorescence quantum yield (Table 2 vs 1).

The chemical modification around the boron atom has low impact in the laser efficiency of the corresponding derivatives from **1-F**, **2-F** and **3-F**. The recorded increase of the fluorescence efficiency upon replacement of the fluorine, mainly by trifluoroacetoxy in the last two dyes (**2-O** and **3-O**, Table 1), is not so noticeable in the laser efficiency providing similar values (*C*-aza-BODIPYs) or slightly higher (*O*-aza-BODIPYs, Table 2). However, in the conformationally restricted aza-BODIPYs bearing anisole the structural modification at the boron atom is effective. In fact, the *O*-aza-BODIPY **4-O** display laser efficiency up to 33% (Table 2), being the highest (and the reddest) one among all the tested dyes, in good agreement with the photophysical results since this dye is also the one with the highest fluorescence response (Table 1).

Regarding the photostability, described as the required energy to decrease the laser induced fluorescence (LIF) in a 10% (see Experimental Section), an opposite trend is observed, and the more photostable dyes are those with the lower efficiencies (Table 2). In any case, most of the dyes retain 90% of the laser output after receiving more than 10 GJ/mol. Moreover, the *F*-aza-BODIPYs are the most stable ones under strong laser irradiation, requiring up to 47 GJ/mol for a 10% decrease of the LIF (see dye **2-F** in Table 2). The free motion of the 1,7-phenyl is likely dissipating the excess energy during the pumping process. It is noticeable that the chemical modification at the boron implies a decrease of the photostability. In fact, we realized that the stored solutions of *O*- and *C*-aza-BODIPYs were bleached (loss of colour) in just a few days. Probably, such lower chemical stability could be related with their reduced photostability.

To put these results into perspective and settle the performance of aza-BODIPYs as laser dyes, we compare them with Nile Blue, a commercially available oxazine with emission in a similar spectral region (around 690 nm) (Figure 6). Nile Blue is a bright

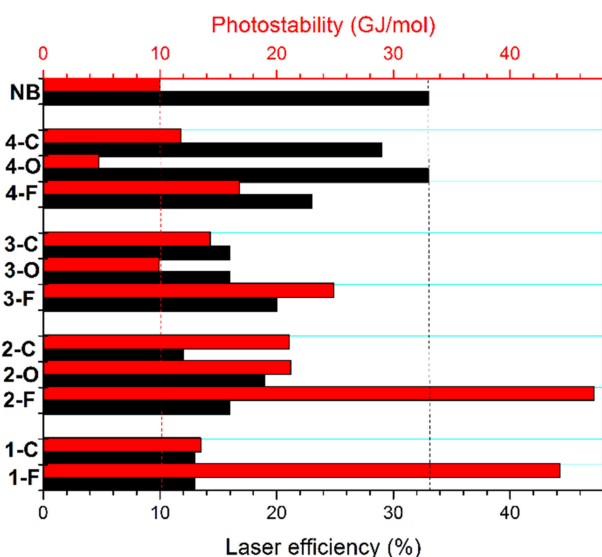


**Figure 6.** Comparison of the laser efficiency and photostability under prolonged and continuously pulsed irradiation of the herein-tested aza-BODIPYs with respect to Nile Blue (NB). Vertical lines are plotted for a better comparison of the laser efficiency and photostability.

fluorophore with remarkable high laser efficiency (33%) but limited photostability (10 GJ/mol for a 10% loss of the LIF output). Most of the tested aza-BODIPYs show lower laser efficiencies than Nile Blue, but some of them (dyes **4-F**, **4-O** and **4-C**, Figure 6) reach similar laser efficiencies. Therefore, they can be considered as efficient laser dyes able to compete with the standard ones in this red spectral region. Nonetheless, the most noteworthy improvement of aza-BODIPYs relies on the photostability, since most of the herein tested aza-BODIPYs are able to tolerate higher energies for a given loss of laser output (Figure 6). Moreover, some of these dyes are by far more photostable. In fact, the *F*-aza-BODIPYs **1-F** and **2-F** show a four times higher tolerance under strong pumping (Figure 6). These results support the viability of the aza-BODIPYs as bright and long lasting active media for laser and bioimaging purposes.

## 4. Conclusions

Hitherto the laser performance and resistance under intense irradiation of the aza-BODIPY was unreported, or at least not well documented due to technical reasons. We have shown that, thanks to the chemical versatility of the chromophoric core, suitable structural modifications can improve the photonic behavior of these dyes affording bright and stable red-emitting luminophores.

The extension of the delocalized  $\pi$ -system of aza-BODIPYs through functionalized aromatic peripheral groups is a suitable strategy to shift the emission deep into the red-edge of the visible. There are some key structural guidelines to consider in the molecular design not only to modulate the spectral shift but also to adjust mainly the fluorescence signatures. Rigidized substituents should be anchored to the 1 and 7 positions to ensure high fluorescence efficiencies. Alternatively, the fluorescence response can be further ameliorated acting at the boron atom. In fact, *O*-aza-BODIPYs display the higher fluorescence efficiency, whereas *C*-aza-BODIPYs are recommended to avoid H-bonding and ameliorate the fluorescence response in polar/protic media.

All the tested aza-BODIPYs display a bright laser emission at the red region, with good tolerance to strong and prolonged pumping. To improve the laser efficiency, conformationally restricted and boron functionalized aza-BODIPYs are recommended, whereas to enhance the photostability *F*-aza-BODIPYs are more suitable, being up to 4 times stronger than the reference Nile Blue. In other words, we have designed aza-BODIPYs with better laser efficiency and photostability than those commercially available in the red-edge of the visible spectrum. It must be highlighted the improved photostability since it is a key parameter to take into account for any application dealing with labeling, sensing and photonics since it guarantees long-lasting photoactive media.

## Experimental Section

### General Synthesis Details

Anhydrous solvents were prepared by distillation over standard drying agents according to common methods. All other solvents were of HPLC grade and were used as provided. Starting chemical substrates and reagents were used as commercially provided unless otherwise indicated. Thin-layer chromatography (TLC) was performed with silica gel plates, and the chromatograms were visualized by using UV light ( $\lambda = 254$  or 365 nm). Flash column chromatography was performed using silica gel (230–400 mesh).  $^1\text{H}$ - and  $^{13}\text{C}$ -NMR spectra were recorded in  $\text{CDCl}_3$  solution at 20 °C. NMR chemical shifts are expressed in parts per million ( $\delta$  scale) downfield from tetramethylsilane and are referenced to the residual signals of  $\text{CDCl}_3$  ( $\delta = 7.260$  and 77.03 ppm, respectively). Data are presented as follows: chemical shift, multiplicity (*s* = singlet, *d* = doublet, *t* = triplet, *m* = multiplet and/or multiple resonances, *b* = broad), coupling constants in hertz (Hz), integration and assignment. Assignments were based on signal multiplicity and DEPT-135 NMR experiments for  $^1\text{H}$ - and  $^{13}\text{C}$ -NMR signals, respectively. FTIR spectra were obtained from neat samples using the attenuated total reflection (ATR) technique. High-resolution mass spectrometry (HRMS) was performed using the EI and MALDI-TOF techniques.

### Photophysical, Electrochemical and Quantum Mechanical Properties

The photophysical properties were registered in diluted solutions (around  $2 \times 10^{-6}$  M), prepared by adding the corresponding solvent to the residue from the adequate amount of a concentrated stock solution in acetone, after vacuum evaporation of this solvent. UV-Vis absorption and fluorescence spectra were recorded on a Varian model CARY 4E spectrophotometer and an Edinburgh Instruments spectrofluorimeter (model FLSP 920), respectively. Fluorescence quantum yields ( $\phi$ ) were obtained using a zinc phthalocyanine ( $\phi = 0.30$  in toluene with 1% of pyridine) as reference, from corrected spectra (detector sensibility to the wavelength). The values were corrected by the refractive index of the solvent. Radiative decay curves were registered with the time correlated single-photon counting technique as implemented in the aforementioned spectrofluorimeter. Fluorescence emission was monitored at the maximum emission wavelength after excitation by means of a Fianium pulsed laser (time resolution of picoseconds) with tunable wavelength. The fluorescence lifetime ( $\tau$ ) was obtained after the deconvolution of the instrumental response signal from the recorded decay curves by means of an iterative method. The goodness of the exponential fit was controlled by statistical parameters (chi-square, Durbin-Watson and the analysis of the residuals). The radiative ( $k_{\text{r}}$ ) and non-radiative ( $k_{\text{nr}}$ ) rate constants were calculated from the fluorescence quantum yield and lifetime;  $k_{\text{r}} = \phi/\tau$  and  $k_{\text{nr}} = (1-\phi)/\tau$ .

Electrochemical experiments (Metrohm Autolab) were done using a three-electrode set up with a platinum layer (surface 8 mm  $\times$  7.5 mm) working electrode, platinum wire as counter electrode and Ag/AgCl as reference electrode. A 0.1 M solution of tetrabutylammonium hexafluorophosphate (TBAPF<sub>6</sub>) in dry acetonitrile was used as the electrolyte solvent in which the compounds were dissolved to achieve a concentration of around 1 mM. All redox potentials were reported vs ferrocene as internal standard. The solutions were purged with argon and all the measurements were performed under an inert atmosphere.

Ground state geometries were optimized with the B3LYP hybrid functional, within the Density Functional Theory (DFT), using the triple valence basis set with a polarization function (6-311G\*), as



implemented in the Gaussian 16. The geometries were considered as energy minimum when the corresponding frequency analysis did not give any negative value. The charge density was simulated by the CHelpG method, which fits the charge of each atom to the molecular electrostatic potential. All the calculations were carried out considering the solvent effect (ethyl acetate) by means of the Polarizable Continuum Model (PCM).

## Laser Experiments

Liquid solutions of dyes in ethyl acetate were contained in 1 cm optical-path rectangular quartz cells carefully sealed to avoid solvent evaporation during experiments. The liquid solutions were transversely pumped with a wavelength tunable OPO coupled to the third harmonic (355 nm) of a Q-switched Nd:YAG laser (Lotis TII 2134) at a repetition rate of 1 Hz. The exciting pulses were line-focused onto the cell using a combination of positive and negative cylindrical lenses ( $f=15$  cm and  $f=-15$  cm, respectively) perpendicularly arranged. The plane parallel oscillation cavity (2 cm length) consisted of a 90% reflectivity aluminium mirror acting as back reflector, and the lateral face of the cell acting as output coupler (4% reflectivity). The pump and output energies were detected by an Ophir powermeter.

The photostability of the dyes in ethyl acetate solution was evaluated by using a pumping energy and geometry exactly equal to that of the laser experiments. We used spectroscopic quartz cuvettes with 1 cm optical paths and depths  $L=0.1$  cm to allow for the minimum solution volume ( $V_S=40$   $\mu$ L) to be excited. The lateral faces were grounded, whereupon no laser oscillation was obtained. Nevertheless, information about photostabilities can be obtained by monitoring the decrease in laser-induced fluorescence (LIF) intensity. In order to facilitate comparisons independently of the experimental conditions and sample, the photostability figure of merit was defined as the accumulated pump energy absorbed by the system ( $E_{\text{dose}}$ ), per mole of dye, before the output energy falls to a 90% its initial value. In terms of experimental parameters, this energy dose, in units of  $\text{GJ}\cdot\text{mol}^{-1}$ , can be expressed as Equation (1):

$$E_{\text{dose}}^{90\%}(\text{GJ}\cdot\text{mol}^{-1}) = \frac{E_{\text{pump}}(\text{GJ}) \cdot (1 - 10^{-\epsilon CL}) \cdot \sum_{\text{\#pulses}} f}{CV_S} \quad (1)$$

where  $E_{\text{pump}}$  is the energy per pulse,  $C$  is the molar concentration,  $\epsilon$  is the molar absorption coefficient in units of  $\text{M}^{-1}\text{cm}^{-1}$ ,  $L$  is the depth of the cuvette expressed in cm,  $V_S$  is the solution volume, in litres, within the cuvette, and  $f$  is the ratio between the LIF intensity after #pulses and the LIF intensity in the first pulse. It can be shown that  $\sum f$  accounts for the reduction in pump absorption due to species photodegradation. To speed up the experiment the pump repetition rate was increased up to 10 Hz. The fluorescence emission was monitored perpendicular to the exciting beam, collected by an optical fibre, and imaged onto a spectrometer (USB2000+ from Ocean Optics).

## Synthesis and Characterization

Aza-BODIPYs **1-F**,<sup>[27]</sup> **2-F**<sup>[15a,24a]</sup> and **4-F**<sup>[28]</sup> and compound **1**<sup>[29]</sup> were synthesized by the corresponding described method.

**Compound 2:** This nitroketone was obtained through a method different from that previously described in the literature.<sup>[30]</sup> To a

solution of **1**<sup>[29]</sup> (1.76 g, 6.4 mmol) in MeOH (25 mL) were added, under an argon atmosphere, diethylamine (3.3 mL, 32 mmol) and nitromethane (1.7 mL, 32 mmol). The mixture was refluxed for 24 h, then cooled to r.t. and removed the solvent at reduced pressure. The residue was dissolved in  $\text{CH}_2\text{Cl}_2$  (50 mL) and washed with a solution of HCl (10% m/v) (50 mL) and then with  $\text{H}_2\text{O}$  ( $2\times 50$  mL). The organic layer was dried over anhydrous  $\text{Na}_2\text{SO}_4$ , filtered and evaporated the solvent to dryness under vacuum. The obtained residue was submitted to purification by flash chromatography on silica gel using hexane/EtOAc (9:1) as eluent to give **2** (2.09 g, 97%) as a yellow oil. The spectroscopic data are in agreement with the literature.<sup>[30]</sup>

**Compound 3:** A mixture of **2** (2.09 g, 6.2 mmol) and ammonium acetate (7.17 g, 93 mmol) in EtOH (50 mL) was refluxed for 24 h, under an argon atmosphere. Then, the reaction was cooled to r.t. and removed the solvent at reduced pressure. The residue was dissolved in  $\text{CH}_2\text{Cl}_2$  (50 mL) and washed with  $\text{H}_2\text{O}$  ( $2\times 50$  mL). The organic layer was dried over anhydrous  $\text{Na}_2\text{SO}_4$ , filtered and evaporated the solvent to dryness under vacuum. The obtained residue was submitted to purification by flash chromatography on silica gel using hexane/ $\text{CH}_2\text{Cl}_2$  (9:1) as eluent to give **3** (889 mg, 49%) as a blue solid.  $^1\text{H}$  NMR (700 MHz,  $\text{CDCl}_3/\text{TFA}$ )  $\delta$  8.02 (d,  $J=7.0$  Hz, 4H), 7.68 (d,  $J=8.4$  Hz, 4H), 7.64–7.59 (m, 6H), 7.56 (d,  $J=7.7$  Hz, 4H), 7.40 (s, 2H) ppm;  $^{13}\text{C}$  NMR (176 MHz,  $\text{CDCl}_3/\text{TFA}$ )  $\delta$  156.8 (C), 147.2 (C), 136.3 (C), 135.0 (C), 133.8 (CH), 131.5 (q,  $^2J_{\text{CF}}=32.9$  Hz), 130.6 (CH), 129.9 (CH), 128.2 (CH), 127.5 (C), 125.4 (s, CH), 123.8 (q,  $^1J_{\text{CF}}=272.6$  Hz), 116.8 (CH) ppm; FTIR  $\nu$  2923, 2853, 1537, 1461, 1378, 1328, 1128, 1070, 1039, 991  $\text{cm}^{-1}$ ; HRMS (EI)  $m/z$  585.1630 (585.1640 calcd for  $\text{C}_{34}\text{H}_{21}\text{F}_6\text{N}_3$ ).

**Compound 3-F:** To a solution of **3** (1.80 g, 3.07 mmol) in anhydrous  $\text{CH}_2\text{Cl}_2$  (15 mL) were added, under an argon atmosphere, ethyldiisopropylamine (2.7 mL, 15.4 mmol) and  $\text{BF}_3\cdot\text{Et}_2\text{O}$  (7.9 mL, 30.7 mmol), and the reacting mixture was stirred at r.t. for 4 h. Then, the mixture was treated with a solution of HCl (10% m/v) (50 mL) and  $\text{H}_2\text{O}$  ( $2\times 50$  mL). The organic layer was separated by decantation and dried over anhydrous  $\text{Na}_2\text{SO}_4$ , filtered and evaporated the solvent to dryness under vacuum. The obtained residue was submitted to purification by flash chromatography on silica gel using hexane/ $\text{CH}_2\text{Cl}_2$  (8:2) as eluent to give **3-F** (719 mg, 37%) as a red solid.  $^1\text{H}$  NMR (300 MHz,  $\text{CDCl}_3$ )  $\delta$  8.12 (d,  $J=8.1$  Hz, 4H), 8.07–8.03 (m, 4H), 7.71 (d,  $J=8.1$  Hz, 4H), 7.53–7.48 (m, 6H), 7.11 (s, 2H) ppm;  $^{13}\text{C}$  NMR (75 MHz,  $\text{CDCl}_3$ )  $\delta$  160.2 (C), 145.6 (C), 142.4 (C), 135.4 (C), 131.4 (CH), 131.13 (q,  $^2J_{\text{CF}}=32.2$  Hz), 131.10 (C), 129.7 (t,  $J_{\text{CF}}=4.5$  Hz, CH), 129.4 (CH), 128.8 (CH), 125.6 (q,  $^3J_{\text{CF}}=3.7$  Hz, CH), 124.0 (q,  $^1J_{\text{CF}}=270.7$  Hz), 120.4 (CH) ppm;  $^{19}\text{F}$  NMR (282 MHz,  $\text{CDCl}_3$ )  $\delta$  -62.7 (s,  $\text{CF}_3\text{Ar}$ ), -131.7 (q,  $J=31.0$  Hz,  $\text{BF}_2$ ) ppm; FTIR  $\nu$  2926, 2855, 1523, 1482, 1457, 1326, 1128, 1069, 1033  $\text{cm}^{-1}$ ; HRMS (EI)  $m/z$  633.1628 (633.1623 calcd for  $\text{C}_{34}\text{H}_{20}\text{BF}_8\text{N}_3$ ).

**General synthetic procedure for nucleophilic substitution reaction in the boron atom:** To a solution of aza-BODIPY (1 equiv) in dry  $\text{CH}_2\text{Cl}_2$  was added  $\text{AlCl}_3$  (3 equiv) under an argon atmosphere and the mixture resulting was stirred at 60 °C for 15 min. Then, trimethylsilyl trifluoroacetate ( $\text{TMSOCOCF}_3$ ) or trimethylsilyl cyanide ( $\text{TMSCN}$ ) (20 equiv.) was added and the mixture was stirred at 60 °C until the complete consumption of the starting material (observed by TLC). Water was added, and the solution was extracted with  $\text{CH}_2\text{Cl}_2$ . The organic layer was dried over  $\text{Na}_2\text{SO}_4$ , filtered and concentrated to dryness. The compounds were purified by flash chromatography on silica gel.

**Compound 1-C:** According to the above mentioned general procedure, **1-F** (50 mg, 0.13 mmol) in  $\text{CH}_2\text{Cl}_2$  (10 mL),  $\text{AlCl}_3$  (53.3 mg, 0.40 mmol) and  $\text{TMSCN}$  (0.33 mL, 2.6 mmol) were reacted for 1 h. Flash chromatography using hexane/ $\text{CH}_2\text{Cl}_2$  (5:5) afforded **1-C** (29.5 mg, 57%) as a metallic blue solid.  $^1\text{H}$  RMN (700 MHz,

CDCl<sub>3</sub>) δ 7.85 (d, *J* = 7.0 Hz, 4H), 7.52–7.51 (m, 6H), 6.62 (s, 2H), 2.43 (s, 6H) ppm; <sup>13</sup>C RMN (176 MHz, CDCl<sub>3</sub>) δ 160.9 (C), 145.7 (C), 143.8 (C), 131.4 (CH), 130.4 (C), 129.4 (CH), 128.8 (CH), 123.3 (CH), 11.4 (CH<sub>3</sub>) ppm, CN not observed; FTIR ν 2924, 2855, 2340, 1538, 1514, 1487, 1452, 1394, 1133, 1097, 966 cm<sup>-1</sup>; HRMS (EI) *m/z* 387.1651 (387.1655 calcd. for C<sub>24</sub>H<sub>18</sub>BN<sub>5</sub>).

**Compound 2-O:** According to the above mentioned general procedure, **2-F** (60 mg, 0.12 mmol) in CH<sub>2</sub>Cl<sub>2</sub> (10 mL), AlCl<sub>3</sub> (48 mg, 0.36 mmol) and TMSOCOFC<sub>3</sub> (0.41 mL, 2.4 mmol) were reacted for 1 h. Flash chromatography using hexane/CH<sub>2</sub>Cl<sub>2</sub> (7:3) afforded the corresponding aza-dipyrrromethene<sup>[44]</sup> (31 mg, 57%) as a blue solid, and **2-O** (15 mg, 18%) as a blue solid. <sup>1</sup>H RMN (700 MHz, CDCl<sub>3</sub>) δ 8.11 (d, *J* = 7.0 Hz, 4H), 7.74 (d, *J* = 7.0 Hz, 4H), 7.48 (broad s, 12H), 6.99 (s, 2H) ppm; <sup>13</sup>C RMN (176 MHz, CDCl<sub>3</sub>) δ 159.1 (C), 156.1 (q, <sup>2</sup>*J*<sub>CF</sub> = 42.2 Hz, COO), 146.0 (C), 145.6 (C), 131.8 (C), 131.2 (CH), 130.5 (C), 130.2 (CH), 129.7 (CH), 129.1 (CH), 128.72 (CH), 128.70 (CH), 119.7 (CH), 114.2 (q, <sup>1</sup>*J*<sub>CF</sub> = 286.9 Hz, CF<sub>3</sub>) ppm; <sup>19</sup>F NMR (282 MHz, CDCl<sub>3</sub>) δ -76.1 (s, CF<sub>3</sub>CO) ppm; FTIR ν 2925, 2854, 2337, 1767, 1515, 1475, 1220, 1163, 1120, 1163, 1121, 1039 cm<sup>-1</sup>; HRMS (MALDI-TOF) *m/z* 685.1600 (685.1608 calcd. for C<sub>36</sub>H<sub>22</sub>BF<sub>6</sub>N<sub>3</sub>O<sub>4</sub>).

**Compound 2-C:** According to the above mentioned general procedure, **2-F** (50 mg, 0.1 mmol) in CH<sub>2</sub>Cl<sub>2</sub> (10 mL), AlCl<sub>3</sub> (40 mg, 0.3 mmol) and TMSOCSN (0.25 mL, 2.0 mmol) were reacted for 1 h. Flash chromatography using hexane/EtOAc (8:2) afforded **2-C** (41 mg, 79%) as a blue solid. <sup>1</sup>H RMN (700 MHz, CDCl<sub>3</sub>) δ 8.49 (d, *J* = 7.7 Hz, 4H), 8.12 (d, *J* = 7.7 Hz, 4H), 7.51–7.40 (m, 12H), 7.17 (s, 2H) ppm; <sup>13</sup>C RMN (176 MHz, CDCl<sub>3</sub>) δ 158.2 (C), 145.3 (C), 142.5 (C), 132.9 (C), 132.2 (C), 131.2 (CH), 130.3 (CH), 129.3 (CH), 128.9 (CH), 128.5 (CH), 128.3 (CH), 119.1 (CH) ppm, CN not observed; FTIR ν 2925, 2854, 2338, 1518, 1479, 1131, 1013, 896 cm<sup>-1</sup>; HRMS (EI) *m/z* 511.1958 (511.1968 calcd. for C<sub>34</sub>H<sub>22</sub>BN<sub>3</sub>O<sub>2</sub>).

**Compound 3-O:** According to the above mentioned general procedure, **3-F** (30 mg, 0.047 mmol) in CH<sub>2</sub>Cl<sub>2</sub> (10 mL), AlCl<sub>3</sub> (19 mg, 0.14 mmol) and TMSOCOFC<sub>3</sub> (0.16 mL, 0.94 mmol) were reacted for 1.5 h. Flash chromatography using hexane/CH<sub>2</sub>Cl<sub>2</sub> (9:1) afforded **3-O** (10 mg, 26%) as a purple solid, and aza-dipyrrromethene **3** (12.5 mg, 45%) <sup>1</sup>H NMR (700 MHz, CDCl<sub>3</sub>) δ 8.16 (d, *J* = 7.7 Hz, 4H), 7.76–7.74 (m, 8H), 7.53–7.49 (m, 6H), 7.07 (s, 2H) ppm; <sup>13</sup>C NMR (176 MHz, CDCl<sub>3</sub>) δ 159.8 (C), 156.2 (q, <sup>2</sup>*J*<sub>CF</sub> = 42.2 Hz, COO), 146.1 (C), 143.8 (C), 134.9 (C), 131.8 (CH), 131.7 (q, <sup>2</sup>*J*<sub>CF</sub> = 31.7 Hz, C), 130.0 (C), 129.7 (CH), 129.2 (CH), 128.9 (CH), 125.6 (q, <sup>3</sup>*J*<sub>CF</sub> = 3.2 Hz, CH), 123.9 (q, <sup>1</sup>*J*<sub>CF</sub> = 272.8 Hz, CF<sub>3</sub>Ar), 121.0 (CH), 114.2 (q, <sup>1</sup>*J*<sub>CF</sub> = 286.9 Hz, CF<sub>3</sub>CO) ppm; <sup>19</sup>F NMR (282 MHz, CDCl<sub>3</sub>) δ -62.7 (s, CF<sub>3</sub>Ar), -76.7 (s, CF<sub>3</sub>CO) ppm; FTIR ν 2926, 2855, 1769, 1521, 1480, 1325, 1162 cm<sup>-1</sup>; HRMS (MALDI-TOF) *m/z* 821.1367 (821.1355 calcd for C<sub>38</sub>H<sub>20</sub>BF<sub>12</sub>N<sub>3</sub>O<sub>4</sub>).

**Compound 3-C:** According to the above mentioned general procedure, **3-F** (40 mg, 0.063 mmol) in CH<sub>2</sub>Cl<sub>2</sub> (10 mL), AlCl<sub>3</sub> (25.4 mg, 0.19 mmol) and TMSOCSN (0.16 mL, 1.26 mmol) were reacted for 1 h. Flash chromatography using hexane/CH<sub>2</sub>Cl<sub>2</sub> (7:3) afforded **3-C** (30 mg, 73%) as a red solid. <sup>1</sup>H NMR (300 MHz, CDCl<sub>3</sub>) δ 8.12 (d, *J* = 8.1 Hz, 4H), 7.96–7.95 (m, 4H), 7.76 (d, *J* = 8.1 Hz, 4H), 7.60–7.58 (m, 6H), 7.13 (s, 2H) ppm; <sup>13</sup>C NMR (75 MHz, CDCl<sub>3</sub>) δ 161.6 (C), 143.6 (C), 143.0 (C), 134.6 (C), 132.1 (CH), 131.9 (q, <sup>2</sup>*J*<sub>CF</sub> = 30.7 Hz, C), 129.9 (C), 129.6 (CH), 129.5 (CH), 129.1 (CH), 125.8 (q, <sup>3</sup>*J*<sub>CF</sub> = 3.7 Hz, CH), 123.9 (q, <sup>1</sup>*J*<sub>CF</sub> = 270.0 Hz, C), 121.6 (CH) ppm, CN not observed; <sup>19</sup>F NMR (282 MHz, CDCl<sub>3</sub>) δ -62.8 (s, CF<sub>3</sub>Ar) ppm; FTIR ν 2926, 2854, 2250, 1516, 1479, 1325, 1126, 1101, 1068, 1034 cm<sup>-1</sup>; HRMS (EI) *m/z* 647.1707 (647.1716 calcd for C<sub>36</sub>H<sub>20</sub>BF<sub>6</sub>N<sub>3</sub>).

**Compound 4-O:** According to the above mentioned general procedure, **4-F** (27 mg, 0.042 mmol) in CH<sub>2</sub>Cl<sub>2</sub> (10 mL), AlCl<sub>3</sub> (17.3 mg, 0.13 mmol) and TMSOCOFC<sub>3</sub> (0.14 mL, 0.84 mmol) were

reacted for 1 h. Flash chromatography using hexane/CH<sub>2</sub>Cl<sub>2</sub> (9:1) afforded **4-O** (9 mg, 26%) as a red solid, and the corresponding aza-dipyrrromethene<sup>[45]</sup> (14.6 mg, 58%) as a blue solid. <sup>1</sup>H RMN (700 MHz, CDCl<sub>3</sub>) δ 7.84 (d, *J* = 8.4 Hz, 4H), 6.99 (d, *J* = 8.4 Hz, 4H), 6.86 (s, 4H), 6.64 (s, 2H), 3.88 (s, 6H), 2.27 (s, 6H), 2.16 (s, 12H) ppm; <sup>13</sup>C RMN (176 MHz, CDCl<sub>3</sub>) δ 162.2 (C), 157.5 (C), 155.9 (q, <sup>2</sup>*J*<sub>CF</sub> = 42.2 Hz, COO), 147.0 (C), 146.3 (C), 137.7 (C), 137.0 (C), 131.5 (CH), 129.1 (C), 128.1 (CH), 124.0 (CH), 122.8 (C), 114.4 (q, <sup>1</sup>*J*<sub>CF</sub> = 286.9 Hz, CF<sub>3</sub>), 114.3 (CH), 55.6 (CH<sub>3</sub>O), 21.1 (CH<sub>3</sub>), 20.9 (CH<sub>3</sub>) ppm, CN not observed; <sup>19</sup>F NMR (282 MHz, CDCl<sub>3</sub>) δ -76.5 (s, CF<sub>3</sub>CO) ppm; FTIR ν 2925, 2855, 1770, 1604, 1495, 1466, 1435, 1266, 1220, 1154, 1097, 1034 cm<sup>-1</sup>; HRMS (MALDI-TOF) *m/z* 829.2785 (829.2758 calcd. for C<sub>44</sub>H<sub>38</sub>BF<sub>6</sub>N<sub>3</sub>O<sub>6</sub>).

**Compound 4-C:** According to the above mentioned general procedure, **4-F** (20 mg, 0.03 mmol) in CH<sub>2</sub>Cl<sub>2</sub> (10 mL), AlCl<sub>3</sub> (12.0 mg, 0.09 mmol) and TMSOCSN (0.075 mL, 0.60 mmol) were reacted for 1 h. Flash chromatography using hexane/CH<sub>2</sub>Cl<sub>2</sub> (5:5) afforded **4-C** (13 mg, 64%) as a green solid. <sup>1</sup>H RMN (700 MHz, CDCl<sub>3</sub>) δ 8.00 (d, *J* = 8.4 Hz, 4H), 7.09 (d, *J* = 8.4 Hz, 4H), 6.87 (s, 4H), 6.69 (s, 2H), 3.90 (s, 6H), 2.28 (s, 6H), 2.13 (s, 12H) ppm; <sup>13</sup>C RMN (176 MHz, CDCl<sub>3</sub>) δ 162.4 (C), 159.3 (C), 146.6 (C), 143.0 (C), 138.0 (C), 136.8 (C), 131.9 (CH), 128.7, 128.3 (CH), 124.9 (CH), 122.8 (C), 114.5 (CH), 55.5 (CH<sub>3</sub>O), 21.11 (CH<sub>3</sub>), 21.07 (CH<sub>3</sub>) ppm, CN not observed; FTIR ν 2925, 2854, 2340, 1603, 1468, 1434, 1263, 1181, 1095, 1028 cm<sup>-1</sup>; HRMS (EI) *m/z* 655.3113 (655.3119 calcd. for C<sub>42</sub>H<sub>38</sub>BN<sub>2</sub>O<sub>2</sub>).

## Acknowledgements

We gratefully acknowledge the Spanish Ministerio de Economía y Competitividad for financial support (projects MAT2017-83856-C3-1-P, 2-P and 3-P, and MAT2015-68837-REDT). We also acknowledge the Gobierno Vasco for financial support (project IT912-16), and for a predoctoral fellowship to E.A.-Z and a postdoctoral fellowship to L.G.-R. In addition, A.P.-C. wishes to thank Consejería de Educación, Juventud y Deporte de la Comunidad de Madrid and Fondo Social Europeo for a research assistant contract (CT2/17/CT3/17/ PEJ16/MED/AI-1598). The authors thank SGlker of UPV/EHU for technical support with the computational calculations, which were carried out in the "arina" informatic cluster.

## Conflict of Interest

The authors declare no conflict of interest.

**Keywords:** azaBODIPYs • dyes and pigments • organic laser chemistry • photophysics • photostability

- [1] a) D. M. DSouza, T. J. J. Muller, *Chem. Soc. Rev.* **2007**, *36*, 1095–1108; b) R. N. D'Souza, U. Pischel, W. M. Nau, *Chem. Rev.* **2011**, *111*, 7941–7980; c) F. De Moliner, N. Kiehlend, R. Lavilla, M. Vendrell, *Angew. Chem. Int. Ed.* **2017**, *56*, 3758–3769; *Angew. Chem.* **2017**, *129*, 3812–3823.
- [2] a) S. Chénais, S. Forget, *Polym. Int.* **2012**, *61*, 390–406; b) L. Cerdán, E. Enciso, V. Martín, J. Bañuelos, I. López-Arbeloa, A. Costela, I. García-Moreno, *Nat. Photonics* **2012**, *6*, 621–626; c) A. J. C. Kuehne, M. C. Gather, *Chem. Rev.* **2016**, *116*, 12823–12864.
- [3] a) R. W. Sinkeldam, N. J. Greco, Y. Tor, *Chem. Rev.* **2010**, *110*, 2579–2619; b) O. S. Wolfbeis, *Chem. Soc. Rev.* **2015**, *44*, 4743–4768; c) T. Kowada, H. Maeda, K. Kikuchi, *Chem. Soc. Rev.* **2015**, *44*, 4953–4972; d) H.

- Abrahamse, M. R. Hamblin, *Biochem. J.* **2016**, *473*, 347–364; e) D. Wu, A. C. Sedgwick, T. Gunnlaugsson, E. U. Akkaya, J. Yoon, T. D. James, *Chem. Soc. Rev.* **2017**, *46*, 7105–7123.
- [4] a) E. Betzig, *Angew. Chem. Int. Ed.* **2015**, *54*, 8034–8053; *Angew. Chem.* **2015**, *127*, 8146–8166; b) S. W. Hell, *Angew. Chem. Int. Ed.* **2015**, *54*, 8054–8066; *Angew. Chem.* **2015**, *127*, 8167–8181; c) W. E. Moerner, *Angew. Chem. Int. Ed.* **2015**, *54*, 8067–8093; *Angew. Chem.* **2015**, *127*, 8182–8210.
- [5] a) S. A. Hilderbrand, R. Weissleder, *Curr. Opin. Chem. Biol.* **2010**, *14*, 71–79; b) L. Yuan, W. Lin, K. Zheng, L. He, W. Huang, *Chem. Soc. Rev.* **2013**, *42*, 622–661.
- [6] a) J. V. Frangioni, *Curr. Opin. Chem. Biol.* **2003**, *7*, 626–634; b) J. T. Marques, B. R. G. Williams, *Nat. Biotechnol.* **2005**, *23*, 1399–1405.
- [7] H. A. Sindy, *Dyes Pigm.* **2017**, *145*, 505–513.
- [8] T. A. Fayed, in *Rev. Fluoresc.*, **2009**, ED. C. D. Geddes, pp. 75–111, Springer Science + Business Media.
- [9] A. Loudet, K. Burgess, *Chem. Rev.* **2007**, *107*, 4891–4932.
- [10] J. Bañuelos, *Chem. Rec.* **2016**, *16*, 355–348.
- [11] a) G. Ulrich, R. Ziessel, A. Harriman, *Angew. Chem. Int. Ed.* **2008**, *47*, 1184–1201; *Angew. Chem.* **2008**, *120*, 1202–1219; b) V. Lakshmi, R. Sharma, M. Ravikanth, *Rep. Org. Chem.* **2016**, *6*, 1–24.
- [12] H. Lu, J. Mack, Y. Yang, Z. Shen, *Chem. Soc. Rev.* **2014**, *43*, 4778–4823.
- [13] a) O. Buyukcakir, O. A. Bozdemir, S. Kolemen, S. Erbas, E. U. Akkaya, *Org. Lett.* **2009**, *11*, 4644–4647; b) C. F. A. Gómez-Durán, I. Esnal, I. Valois-Escamilla, A. Urias-Benavides, J. Bañuelos, I. López-Arbeloa, I. García-Moreno, E. Peña-Cabrera, *Chem. Eur. J.* **2016**, *22*, 1048–1061.
- [14] K. Umezawa, A. Matsui, Y. Nakamura, D. Citterio, K. Suzuki, *Chem. Eur. J.* **2009**, *15*, 1096–1106.
- [15] a) G. Sathyamoorthi, M.-L. Soong, T. W. Ross, J. H. Boyer, *Heteroat. Chem.* **1993**, *4*, 603–608; b) M. J. Hall, S. O. McDonell, J. Killoran, D. F. O'Shea, *J. Org. Chem.* **2005**, *70*, 5571–5578.
- [16] Y. Ge, D. F. O'Shea, *Chem. Soc. Rev.* **2016**, *45*, 3846–3864.
- [17] a) X.-D. Jiang, D. Xi, J. Zhao, H. Yu, G.-T. Sun, L.-J. Xiao, *RSC Adv.* **2014**, *4*, 60970–60973; b) C. M. Dadario, Q. Han, M. Zeller, G. Sauvé, *Eur. J. Inorg. Chem.* **2015**, 3649–3657; c) A. Koch, S. Kumar, M. Ravikanth, *Tetrahedron* **2017**, *73*, 1459–1465; d) W.-J. Shi, P.-C. Lo, D. K. P. Ng, *Dyes Pigm.* **2018**, *154*, 314–319.
- [18] a) W. Zhao, E. M. Carreira, *Angew. Chem. Int. Ed.* **2005**, *44*, 1677–1679; *Angew. Chem.* **2005**, *117*, 1705–1707; b) S. Shimizu, T. Iino, Y. Araki, N. Kobayashi, *Chem. Commun.* **2013**, 49, 1621–1623; c) J. Wang, J. Li, N. Chen, E. Hao, Y. Wei, X. Mu, L. Jiao, *New J. Chem.* **2016**, *40*, 5966–5975; d) L. Zhang, L. Zhao, K. Wang, J. Jiang, *Dyes Pigm.* **2016**, *134*, 427–433; e) J. Cui, W. Sheng, Q. Wu, C. Yu, E. Hao, P. Bobadova-Parvanova, M. Storer, A. M. Asiri, H. M. Marwani, L. Jiao, *Chem. Asian J.* **2017**, *12*, 2486–2493.
- [19] a) X. Ma, X. Mao, S. Zhang, X. Huang, Y. Cheng, C. Zhu, *Polym. Chem.* **2013**, *4*, 520–527; b) H. Yamane, K. Tanaka, Y. Chujo, *Polym. J.* **2018**, *50*, 271–275; c) C. Tian, J. Wei, Y. Xu, L. Zhang, Z. Cheng, X. Zhu, *Nanoscale* **2018**, *10*, 10277–10287.
- [20] a) A. Palma, M. Tasiar, D. O. Frimannsson, T. T. Vu, R. Méallet-Renault, D. F. O'Shea, *Org. Lett.* **2009**, *11*, 3638–3641; b) A. Dvivedi, S. Kumar, M. Ravikanth, *Sens. Actuators B* **2016**, *224*, 364–371; c) Y. Gao, Y. Pan, Y. He, H. Chen, V. N. Nemykin, *Sens. Actuators B* **2018**, *269*, 151–157.
- [21] a) Y. Ni, J. Wu, *Org. Biomol. Chem.* **2014**, *12*, 3774–3791; b) Y. Tachapermon, S. Thavornpradit, A. Charoenpanich, J. Sirirak, K. Burgess, N. Wanichacheva, *Dalton Trans.* **2017**, 46, 16251–16256; c) L. Zhu, W. Xie, L. Zhao, Y. Zhang, Z. Chen, *RSC Adv.* **2017**, *7*, 55839–55845; d) X. Lu, M. Zhao, P. Chen, Q. Fan, W. Wang, W. Huang, *J. Mater. Chem. B* **2018**, *6*, 4531–4538.
- [22] a) S. Kumar, K. G. Thorat, M. Ravikanth, *J. Org. Chem.* **2017**, *82*, 6568–6577; b) N. Balsukuri, N. J. Boruah, P. E. Kesavan, I. Gupta, *New J. Chem.* **2018**, *42*, 5875–5888.
- [23] a) T. Mueller, R. Gresser, K. Leo, M. Riede, *Sol. Energy Mater. Sol. Cells* **2012**, *99*, 176–181; b) W. Senevirathna, J.-Y. Liao, Z. Mao, J. Gu, M. Porter, C. Wang, R. Fernando, G. Sauvé, *J. Mater. Chem. A* **2014**, *3*, 4203–4214; c) T. Y. Li, T. Meyer, R. Meerheim, M. Höppner, C. Körner, K. Vandewal, O. Zeika, K. Leo, *J. Mater. Chem. A* **2017**, *5*, 10696–10703.
- [24] a) A. Gorman, J. Killoran, C. O'Shea, T. Kenna, W. M. Gallagher, D. F. O'Shea, *J. Am. Chem. Soc.* **2004**, *126*, 10619–10631; b) D. Chen, Q. Tang, J. Zou, X. Yang, W. Huang, Q. Zhang, J. Shao, X. Dong, *Adv. Healthcare Mater.* **2018**, 1701272; c) Q. Wang, D. K. P. Ng, P.-C. Lo, *J. Mater. Chem. B* **2018**, *6*, 3285–3296; d) D. Chen, J. Zhang, Y. Tang, X. Huang, J. Shao, W. Si, J. Ji, Q. Zhang, W. Huang, X. Dong, *J. Mater. Chem. B* **2018**, *6*, 4522–4530; e) W. Xiao, P. Wang, C. Ou, X. Huang, Y. Tang, M. Wu, W. Si, J. Shao, W. Huang, X. Dong, *Biomaterials* **2018**, *183*, 1–9.
- [25] a) A. N. Amin, M. E. El-Khouly, N. K. Subbaiyan, M. E. Zandler, S. Fukuzumi, F. D'Souza, *Chem. Commun.* **2012**, 48, 206–208; b) V. Bandi, H. B. Gobeze, V. N. Nesterov, P. A. Karr, F. D'Souza, *Phys. Chem. Chem. Phys.* **2014**, *16*, 25537–25547.
- [26] E. Bodio, C. Goze, *Dyes Pigm.* **2018**, DOI: 10.1016/j.dyepig.2018.08.062, and references cited therein.
- [27] D. Wu, D. F. O'Shea, *Org. Lett.* **2013**, *15*, 3392–3395.
- [28] L. Jiao, Y. Wu, Y. Ding, S. Wang, P. Zhang, C. Yu, Y. Wei, X. Mu, E. Hao, *Chem. Asian J.* **2014**, *9*, 805–810.
- [29] S.-J. Chen, G.-P. Lu, C. Cai, *RSC Adv.* **2015**, *5*, 13208–13211.
- [30] a) Z.-W. Sun, F.-Z. Peng, Z.-Q. Li, L.-W. Zou, S.-X. Zhang, X. Li, Z. H. Shao, *J. Org. Chem.* **2012**, *77*, 4103–4110; b) J. Flores-Ferrándiz, A. Stiven, L. Sotorrios, E. Gómez-Bengoa, R. Chinchilla, *Tetrahedron: Asymmetry* **2015**, *26*, 970–979.
- [31] a) G. Durán-Sampedro, A. R. Agarrabeitia, L. Cerdán, M. E. Pérez-Ojeda, A. Costela, I. García-Moreno, I. Esnal, J. Bañuelos, I. López-Arbeloa, M. J. Ortiz, *Adv. Funct. Mater.* **2013**, *23*, 4195–4205; b) G. Durán-Sampedro, I. Esnal, A. R. Agarrabeitia, J. Bañuelos, L. Cerdán, I. García-Moreno, A. Costela, I. López-Arbeloa, M. J. Ortiz, *Chem. Eur. J.* **2014**, *20*, 2646–2653.
- [32] J. K. G. Karlsson, A. Harriman, *J. Phys. Chem. A* **2016**, *120*, 2537–2546.
- [33] a) J. Li, B. Hu, G. Hu, X. Li, P. Lu, Y. Wang, *Org. Biomol. Chem.* **2012**, *10*, 8848–8859; b) V. Lakshmi, M. Ravikanth, *Eur. J. Org. Chem.* **2014**, 5757–5766.
- [34] M. Bixon, J. Jortner, J. Cortes, H. Heitele, M. E. Michel-Beyerle, *J. Phys. Chem.* **1994**, *98*, 7289–7299.
- [35] R. T. Kuznetsova, Y. V. Aksenova, D. E. Bashkirtsev, A. A. Prokopenko, E. N. Tel'minov, G. V. Mayer, N. A. Dudina, E. V. Antina, A. Y. Nikonova, M. B. Berezin, A. S. Semeikin, *High Energy Chem.* **2015**, *49*, 16–23.
- [36] a) L. Biczók, T. Bérces, H. Inoue, *J. Phys. Chem. A* **1999**, *103*, 3837–3842; b) I. K. Shushkevich, P. P. Pershukovich, A. P. Stupak, K. N. Solov'ev, *J. Appl. Spectrosc.* **2005**, *72*, 737–770.
- [37] F. López Arbeloa, T. López Arbeloa, I. López Arbeloa, *Trends Photochem. Photobiol.* **1994**, *3*, 145–155.
- [38] a) A. Loudet, R. Bandichhor, L. Wu, K. Burgess, *Tetrahedron* **2008**, *64*, 3642–3654; b) X.-D. Jiang, S. Li, J. Guan, T. Fang, X. Liu, L.-J. Xiao, *Curr. Org. Chem.* **2016**, *20*, 1736–1744; c) E. V. Antina, N. A. Bumagina, *Chem. Heterocycl. Compd.* **2017**, *53*, 39–41.
- [39] A. Prlj, L. Vannay, C. Corminboeuf, *Helv. Chim. Acta* **2017**, *100*, e1700093.
- [40] A. Gut, L. Lapok, D. Jamróz, A. Gorski, J. Solariski, M. Nowakowska, *New J. Chem.* **2017**, *41*, 12110–12122.
- [41] W. Zhao, E. M. Carreira, *Chem. Eur. J.* **2006**, *12*, 7254–7263.
- [42] a) T. H. Allik, R. E. Hermes, G. Sathyamoorthi, J. H. Boyer, *SPIE* **1994**, *2115*, 239–248; b) R. T. Kuznesova, I. V. Aksenova, D. E. Bashkirtsev, A. S. Shulev, E. V. Antina, M. B. Berezin, N. A. Bumagina, *High Energy Chem.* **2017**, *51*, 175–181.
- [43] L. Cerdán, A. Costela, I. García-Moreno, J. Bañuelos, I. López-Arbeloa, *Laser Phys. Lett.* **2012**, *9*, 426–433.
- [44] J. Killoran, L. Allen, J. F. Gallagher, W. M. Gallaher, D. F. O'Shea, *Chem. Commun.* **2002**, 1862–1863.
- [45] L. Jiao, Y. Ding, N. Gao, P. Zhang, Patent CN 103183696A 20130703, **2013**.

Manuscript received: November 8, 2018

Accepted manuscript online: November 28, 2018

Version of record online: December 13, 2018

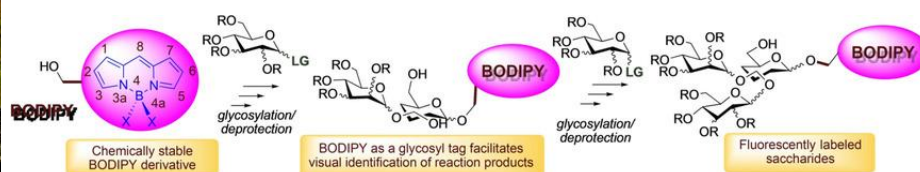


# Annex III (Chapter 3) / III. Eranskina (3. Kapitulu)

## Article 4 / 4. Artikulu

BODIPYs as Chemically Stable Fluorescent Tags for Synthetic Glycosylation Strategies towards Fluorescently Labeled Saccharides

*Chemistry - A European Journal*, 2020, 26, 5388-5399



## Article 5 / 5. Artikulu

FormylBODIPYs by PCC-Promoted Selective Oxidation of  $\alpha$ -MethylBODIPYs. Synthetic Versatility and Applications

*Organic Letters*, 2019, 21, 4563-4566





## Labeled Saccharides

## BODIPYs as Chemically Stable Fluorescent Tags for Synthetic Glycosylation Strategies towards Fluorescently Labeled Saccharides

Clara Uriel,<sup>[a]</sup> Caterina Permingeat,<sup>[a]</sup> Juan Ventura,<sup>[a]</sup> Edurne Avellanal-Zaballa,<sup>[b]</sup> Jorge Bañuelos,<sup>\*[b]</sup> Inmaculada García-Moreno,<sup>[c]</sup> Ana M. Gómez,<sup>\*[a]</sup> and J. Cristobal Lopez<sup>\*[a]</sup>

**Abstract:** A series of fluorescent boron-dipyrromethene (BODIPY, 4,4-difluoro-4-bora-3a,4a-diaza-s-indacene) dyes have been designed to participate, as aglycons, in synthetic oligosaccharide protocols. As such, they served a dual purpose: first, by being incorporated at the beginning of the process (at the reducing-end of the growing saccharide moiety), they can function as fluorescent glycosyl tags, facilitating the detection and purification of the desired glycosidic intermediates, and secondly, the presence of these chromophores on the ensuing compounds grants access to fluorescently labeled saccharides. In this context, a sought-after

feature of the fluorescent dyes has been their chemical robustness. Accordingly, some BODIPY derivatives described in this work can withstand the reaction conditions commonly employed in the chemical synthesis of saccharides; namely, glycosylation and protecting-group manipulations. Regarding their photophysical properties, the BODIPY-labeled saccharides obtained in this work display remarkable fluorescence efficiency in water, reaching quantum yield values up to 82%, as well as notable lasing efficiencies and photostabilities.

## Introduction

The chemical synthesis of oligosaccharides<sup>[1]</sup> and the development of fluorescent probes<sup>[2]</sup> are two well-recognized research areas with increasing relevance. In addition, the combination of fluorescent labels and carbohydrates for the generation of fluorescent glycoprobes has become an active topic of research in recent years.<sup>[3]</sup> Remarkably, the interest in these assemblies could arise from at least two different research fields. Focusing on the carbohydrate partner, the fluorescent labeling of glycans allows investigations on glycoconjugates and their interactions in biological systems at high sensitivity.<sup>[4,5,6]</sup> Alternatively, from the fluorescent-probe standpoint, owing to the relevance that carbohydrate–receptor interactions have on a

number of biological processes,<sup>[7]</sup> a glycosyl moiety linked to a fluorophore could play a significant role as a targeting<sup>[8]</sup> and internalizing<sup>[9]</sup> agent for the probe, sometimes providing less cytotoxic entities.<sup>[10]</sup>

On the other hand, borondipyrromethene (BODIPY) dyes, for example, **A** (Scheme 1),<sup>[11]</sup> have emerged as remarkable fluorophores owing to their outstanding properties that include strong UV/Vis absorption profiles, high fluorescence quantum yields ( $\varphi$ ) and excellent photochemical and thermal stabilities, which has led to their use in biomaterials labeling,<sup>[12]</sup> among others.<sup>[13]</sup>

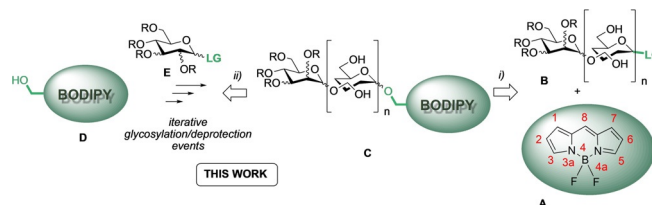
Of particular interest to us was that the ligation step of the fluorophore, for example, **A**, and the glycoligand, for example, **B**, leading to glycoprobes, for example, **C** (Scheme 1, approach *i*), is generally carried out as the last synthetic event, sometimes in situ, prior to their submission to the different vis-

[a] Dr. C. Uriel, C. Permingeat, Dr. J. Ventura, Dr. A. M. Gómez, Prof. J. C. Lopez  
Instituto de Química Orgánica General (IQOG-CSIC)  
Juan de la Cierva 3, 28006 Madrid (Spain)  
E-mail: ana.gomez@csic.es  
jc.lopez@csic.es

[b] E. Avellanal-Zaballa, Dr. J. Bañuelos  
Dpto. Química Física  
Universidad del País Vasco (UPV/EHU)  
Apto. 644, 48080 Bilbao (Spain)  
E-mail: jorge.banuelos@ehu.es

[c] Prof. I. García-Moreno  
Instituto Química-Física "Rocasolano" (IQFR-CSIC)  
Serrano 119, 28006 Madrid (Spain)

Supporting information and the ORCID identification numbers for the authors of this article can be found under:  
<https://doi.org/10.1002/chem.201905780>



**Scheme 1.** *i*) General synthetic approach to glycoprobe **C** by ligation of a given saccharide **B** to a generic BODIPY dye (**A**, IUPAC numbering); and *ii*) proposed sequential glycosylation/deprotection/glycosylation strategy from hydroxymethyl-BODIPY **D** and glycosyl donors **E**, leading to BODIPY-saccharide structures **C**.

ualization or detection techniques.<sup>[14]</sup> Based on these precedents, we decided to investigate the feasibility of a synthetic approach to fluorescently labeled oligosaccharides in which the fluorescent probe, installed at the reducing end of the growing saccharide from the beginning of the process, could additionally function as a tagging element, facilitating the visualization and detection of the synthetic saccharide intermediates (Scheme 1, approach *ii*).

Accordingly, in this manuscript, we disclose our investigations on an alternative approach to BODIPY-saccharide derivatives, that is, **C** (Scheme 1), based on sequential glycosylation/deprotection/glycosylation events of a starting hydroxymethyl-BODIPY **D**, with different glycosyl donors, for example, **E** (Scheme 1, approach *ii*).

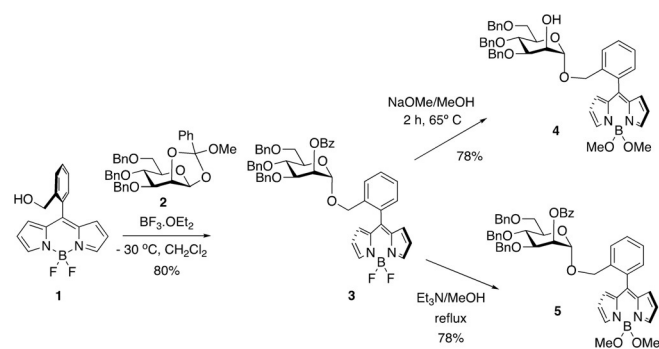
Consequently, our studies have focused on the search for BODIPY derivatives that can endure the reaction events commonly employed in oligosaccharide synthesis; namely, glycosylation protocols<sup>[15]</sup> and protecting-group manipulations.<sup>[16,17]</sup>

## Results and Discussion

The present studies on the potential of BODIPY-aglycons as glycosyl tags in synthetic oligosaccharide strategies originated from an ongoing project that required a reliable synthetic route to an appropriately protected 2-hydroxy-mannopyranoside bearing a fluorophore as aglycon, and able to undergo further glycosylation at *O*-2.

Accordingly, based on our experience with 1,2-methyl orthoesters<sup>[18,19]</sup> (MeOEs) in glycosylation,<sup>[20]</sup> and our recent method for the efficient, one-pot, access<sup>[21]</sup> to hydroxymethyl-BODIPY **1**,<sup>[22]</sup> we attempted the glycosylation of the latter with MeOE **2** (Scheme 2). The glycosyl coupling, mediated by  $\text{BF}_3 \cdot \text{OEt}_2$ , took place smoothly to provide BODIPY-mannopyranoside **3**, which, upon treatment with NaOMe in MeOH, produced 4,4'-methoxy-BODIPY **4**.<sup>[23,24]</sup> The latter was the result of an unwanted methoxy substitution at boron accompanying the desired de-*O*-benzoylation process. The use of milder saponification conditions ( $\text{Et}_3\text{N}/\text{MeOH}$ , reflux) also induced methoxy substitution at boron, but left the 2-*O*-Bz group in mannosyl-BODIPY **5**, unaffected.

Thus, even though compound **4** displayed good fluorophoric behavior, it was found to be of no use to us since further



**Scheme 2.** Glycosylation of BODIPY **1** with MeOE **2**. Attempted saponification of benzoate **3**, leading to *O*-BODIPYs **4** and **5**.

glycosylation attempts on **4** with MeOE donors, mediated by  $\text{BF}_3 \cdot \text{OEt}_2$ , resulted in partial or total methoxy—fluor replacement at boron, thus giving rise to complex product mixtures.

According to these results, and despite the fact that BODIPYs are typically described as “chemically robust” substrates,<sup>[24b,25,26]</sup> we considered that a comprehensive screening of the compatibility of the BODIPY core with the reaction conditions employed in standard glycosylation protocols (including protecting-group manipulations) will be necessary prior to their use as fluorophoric tags in oligosaccharide synthesis.

In this context, a general survey of the scientific literature on the chemical stability of BODIPYs allowed us to identify at least two structural aspects with an influence on their stability. Thus, the degree of peripheral alkyl-substitution on the BODIPY core<sup>[27]</sup> and the presence of an 8-aryl substituent,<sup>[28,29]</sup> have long been known to stabilize the fluorophore. On the other hand, substitution at boron has also been identified as a key factor determining the stability of BODIPYs.<sup>[30]</sup> In this context, Yan and co-workers recognized 4,4'-diphenyl BODIPY derivatives as more stable, under acidic and basic conditions, than the corresponding 4,4'-dimethyl, 4,4'-dimethoxy, or 4,4'-difluoro derivatives.<sup>[31]</sup> More recently, reports from Vicente's and Bobadova-Parvanova's laboratories have identified 4,4'-dicyano-BODIPYs<sup>[32]</sup> as the most stable derivatives, under acidic conditions, from a series of 4,4'-disubstituted BODIPYs (including -F, -CN, -Ph, -Me and -OMe derivatives).<sup>[33]</sup>

According to these literature precedents, we selected readily available BODIPYs **6–10**<sup>[21]</sup> to conduct our stability studies (Figure 1). Thus, derivatives **6** and **7**, and **8** and **9** differed in the substitution at boron (F vs. CN). Compounds **8** and **9** possessed ethyl substituents at C-2 and C-6 (when compared to **6** and **7**) aimed at shielding the BODIPY core towards the electrophilic reagents<sup>[34]</sup> required in the activation of some of the glycosyl donors evaluated in this work. Additionally, since our planned studies also include the stability of these BODIPYs under hydrogenolytic conditions (necessary to deprotect benzyl groups at the glycosyl units), the hydroxyethyl derivative **10**<sup>[35]</sup> was also considered as a non-benzylic analogue of **8**.

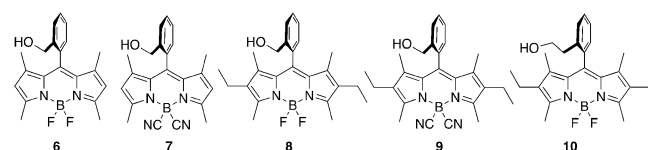


**Figure 1.** BODIPY derivatives **6–10** selected for our studies.

### BODIPYs and protecting group manipulations

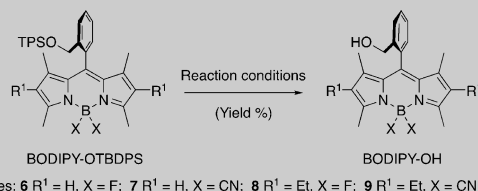
The polyhydroxylic nature of carbohydrates and the high reactivity of the hydroxyl groups in glycosylation reactions is the reason why, in most cases, only the hydroxyl group that is meant to be glycosylated can remain unprotected during the glycosylation reaction. Therefore, protecting group manipulations have become a key issue in oligosaccharide synthesis.<sup>[17]</sup> In this context, most of the synthetic strategies towards oligosaccharides require the handling of at least three types of or-



thogonal<sup>[16,17]</sup> protecting groups: acyl derivatives, silyl ethers and benzyl ethers. Among them, the first two are considered “temporary” protecting groups, since they can be placed and removed several times during the synthesis, whereas benzyl ethers are regarded as “permanent” protecting groups, since they are: 1) only to be removed at the very end of the saccharide preparation, 2) stable to all reaction conditions used, and 3) removable under reaction conditions that do not tamper with the integrity of the target (oligo)saccharide.<sup>[36]</sup> For these reasons, we have evaluated the compatibility of the reaction conditions used for the deprotection of benzoyl esters, and silyl and benzyl ethers with the structural integrity of some of the BODIPYs displayed in Figure 1.

Thus, to find appropriate reaction conditions for the removal of the protecting groups, we carried out our initial model studies with *tert*-butyldiphenylsilyl BODIPYs (BODIPY-OTBDPS), and benzoyl BODIPYs (BODIPY-OBz) (Table 1 and Table 2, respectively).

**Table 1.** De-O-silylation of BODIPY-*tert*-butyldiphenylsilyl ethers (BODIPY-OTBDPS) to regenerate the starting BODIPY-OHs (6–9).

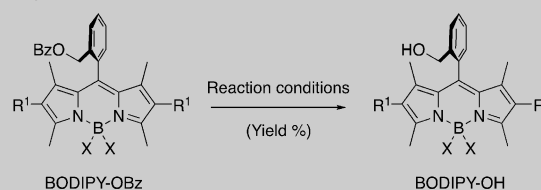


Entry	BODIPY-OTBDPS	Reaction conditions	BODIPY-OH	Yield [%] <sup>[c]</sup>
1	6-OTBDPS	TBAF <sup>[a]</sup>	<b>6</b>	48
2	7-OTBDPS	TBAF <sup>[a]</sup>	<b>7</b>	41
3	8-OTBDPS	TBAF <sup>[a]</sup>	<b>8</b>	38
4	9-OTBDPS	TBAF <sup>[a]</sup>	<b>9</b>	–
5	6-OTBDPS	HF/pyridine <sup>[b]</sup>	<b>6</b>	52 <sup>[d]</sup>
6	7-OTBDPS	HF/pyridine <sup>[b]</sup>	<b>7</b>	64 <sup>[e]</sup>
7	8-OTBDPS	HF/pyridine <sup>[b]</sup>	<b>8</b>	78 <sup>[f]</sup>
8	9-OTBDPS	HF/pyridine <sup>[b]</sup>	<b>9</b>	94
9	6-OTBDPS	HCl/MeOH <sup>[c]</sup>	<b>6</b>	47 <sup>[g]</sup>
10	7-OTBDPS	HCl/MeOH <sup>[c]</sup>	<b>7</b>	93
11	8-OTBDPS	HCl/MeOH <sup>[c]</sup>	<b>8</b>	–
12	9-OTBDPS	HCl/MeOH <sup>[c]</sup>	<b>9</b>	94

[a] Tetra-*n*-butylammonium fluoride (TBAF; 1.5 equiv), CH<sub>2</sub>Cl<sub>2</sub>, 0 °C → RT. [b] HF-pyridine (40 equiv), THF, RT. [c] HCl/MeOH (1.25 M), THF, microwave irradiation, 60 °C. [d] 88% corrected yield, based on recovered starting material. [e] 87% corrected yield, based on recovered starting material. [f] 92% corrected yield, based on recovered starting material. [g] Yield obtained after treatment of the crude reaction mixture with Et<sub>3</sub>N, BF<sub>3</sub>·OEt<sub>2</sub>.

As representative methods for de-O-silylation, we selected three sets of reaction conditions: 1) tetra-*n*-butyl ammonium fluoride (TBAF); 2) HF-pyridine in THF; and 3) HCl/methanol in THF, under microwave irradiation (Table 1). The best results in terms of deprotection yields and substrate stabilities were obtained with 4,4'-dicyano BODIPYs (7-OTBDPS and 9-OTBDPS) upon treatment with HCl/methanol under microwave irradiation (entries 5 and 7, respectively). Treatment with HF/pyridine furnished an excellent yield of 4,4'-dicyano-2,6-diethyl BODIPY-

**Table 2.** Saponification of BODIPY benzoates (BODIPY-OBz) to regenerate the starting BODIPY-OHs (6–9).



Entry	BODIPY-OBz	Reaction conditions	BODIPY-OH	Yield [%] <sup>[c]</sup>
1	6-OBz	NaOMe/MeOH <sup>[a]</sup>	<b>6</b>	92
2	7-OBz	NaOMe/MeOH <sup>[a]</sup>	<b>7</b>	47
3	8-OBz	NaOMe/MeOH <sup>[a]</sup>	<b>8</b>	92
4	9-OBz	NaOMe/MeOH <sup>[a]</sup>	<b>9</b>	95
5	6-OBz	Et <sub>3</sub> N/MeOH <sup>[b]</sup>	<b>6</b>	43 <sup>[c]</sup>
6	7-OBz	Et <sub>3</sub> N/MeOH <sup>[b]</sup>	<b>7</b>	– <sup>[d]</sup>
7	8-OBz	Et <sub>3</sub> N/MeOH <sup>[b]</sup>	<b>8</b>	65 <sup>[e]</sup>
8	9-OBz	Et <sub>3</sub> N/MeOH <sup>[b]</sup>	<b>9</b>	– <sup>[f]</sup>

[a] Sodium methoxide (4.4 equiv) in methanol, RT, 1–2 h. [b] Triethylamine in methanol, reflux, overnight. [c] An additional 23% of the starting benzoate was recovered. [d] Complex reaction mixture containing at least five different compounds including B(F,OMe) and B(OMe)<sub>2</sub>-BODIPYs, with or without the C-8-*ortho* benzoyl substituent. [e] 86% corrected yield, based on recovered starting material. [f] The reaction mixture consisted of the corresponding B(F,OMe) and B(OMe)<sub>2</sub>-BODIPYs, with and without the C-8-*ortho*-benzoyl substituent.

OH (**9**) (entry 8), and reasonable yields of BODIPYs **7** and **8** (entries 6 and 7, respectively).

From the results in Table 1, we concluded that desilylation could be successfully carried out with HCl/methanol in derivatives arising from 4,4'-dicyano-BODIPYs **7** and **9**, and with HF/pyridine in 4,4'-dicyano-2,6-diethyl BODIPY-OH (**9**). In the case of silyl BODIPYs **6** and **8**, treatment with HCl/methanol (entries 9 and 11, respectively) caused desilylation accompanied by nitrogen–boron cleavage on the BODIPY core leading to the corresponding, non-fluorescent, dipyrromethenes.<sup>[37]</sup> This could be confirmed in the case of 6-OTBDPS, for which treatment of the crude desilylation mixture with BF<sub>3</sub>·OEt<sub>2</sub> produced BODIPY **6** (entry 9; 47% yield).<sup>[37]</sup>

Finally, in keeping with literature precedents,<sup>[38]</sup> TBAF caused considerable decomposition of the BODIPY-core in all the derivatives (Table 1, entries 1–4).

Analogously, de-O-benzylation of the corresponding BODIPY-OBz **6–9** derivatives was attempted under two sets of reaction conditions: 1) NaOMe/MeOH and 2) Et<sub>3</sub>N in methanol (reflux) (Table 2).

The best outcome in terms of reaction yields and substrate stabilities, was observed in the case of 4,4'-difluoro BODIPYs **6**-OBz and **8**-OBz, and 4,4'-dicyano-BODIPY **9**-OBz derivatives, upon treatment with NaOMe in MeOH (Table 2, entries 1, 3, and 4, respectively). Contrariwise, the treatment of B(CN)<sub>2</sub>-BODIPY with Et<sub>3</sub>N in MeOH produced complex mixtures containing B(OMe,CN)- and B(OMe)<sub>2</sub>-BODIPYs, with or without the *ortho*-8-benzoyl group (entries 5–8).

In these debenzylation studies in basic media, regardless of the reaction conditions employed, BF<sub>2</sub>-BODIPYs, i.e., **6** and **8**,

were found to be more stable than the corresponding  $B(CN)_2$ -BODIPYs (compare Table 2 entry 1 vs. entry 2, and entries 5 and 7 vs. entries 6 and 8). Nevertheless, de-*O*-benzylation of peralkylated  $B(CN)_2$ -BODIPY **9**-OBz proved to be successful when short reaction times and stoichiometric amounts of NaOMe were used.

### BODIPYs and glycosylation reactions

We next set up to study the behavior of our hydroxymethyl-BODIPYs in glycosylation reactions. Accordingly, we have validated five types of commonly employed glycosyl donors: trichloroacetimidates (TCA),<sup>[39]</sup> thioglycosides,<sup>[40]</sup> glycosyl bromides,<sup>[41]</sup> *n*-pentenyl orthoesters (NPOEs),<sup>[42]</sup> and MeOEs.<sup>[18,20]</sup>

The results obtained are collected in Scheme 3 and Scheme 4. Accordingly, trichloroacetimidate **11**, reacted smoothly with 4,4'-dicyano BODIPYs **7** and **9**, upon activation with  $BF_3 \cdot OEt_2$  at low temperature, to give tetra-*O*-benzoyl manno- and galactopyranosides **12** and **14**, respectively, in moderate yields (Scheme 3A and B). These benzoyl glycosides yielded, upon saponification with NaOMe/MeOH, tetraols **13** and **15**, respectively (Scheme 3A and B). Likewise, glycosylation of 4,4'-difluoro-BODIPY **10** with TCA **11** at higher temperature yielded

mannopyranoside **16**, which, upon saponification, produced tetraol glycoside **17** (Scheme 3C).

Next, the glycosylation of BODIPY **9** with phenyl thioglycosides **18**, **19**, **22** and **25**, was examined. Thus, armed and disarmed<sup>[43]</sup> thioglycosides could be activated by treatment with NIS in the presence of  $Yb(OTf)_3$ ,<sup>[44]</sup> to yield BODIPY-glycosides **14**, **20** and **23** in moderate to good yields (Scheme 3D, E, and F, respectively), the latter being isolated as a (2:1)  $\alpha/\beta$  anomeric mixture. The use of the *N*-iodosuccinimide (NIS)/ $BF_3 \cdot OEt_2$  system,<sup>[45]</sup> as the promotor in the activation of the thioglycosides, caused partial replacement of -CN by fluoride at boron, thus yielding mixtures of the corresponding 4,4-difluoro- and 4-fluor-4'-cyano-BODIPY glycosides. The use of electrophilic NIS as promotor precluded the use of BODIPYs **6** and **7** as acceptors, owing to the nucleophilicity of the BODIPYs at positions C-2 and C-6.<sup>[34]</sup> On the other hand, desilylation of BODIPY-glycosides **20** and **23**, leading to the hydroxyl derivatives **21** and **24** (Scheme 3E and F, respectively), could be efficiently effected by treatment with HCl/methanol, as seen before (Table 1, entry 12). Finally, activation of phenyl thioglycoside **25** with the thiophilic promotor system  $Ph_2SO/Tf_2O$ ,<sup>[46]</sup> in the presence of 4-*tert*-butyl-2,6-dimethylpyridine (TBMP), was also possible and yielded glucoside **26** in 68% yield, as an (8:1)  $\alpha/\beta$  anomeric mixture with the  $\alpha$ -anomer prevailing.

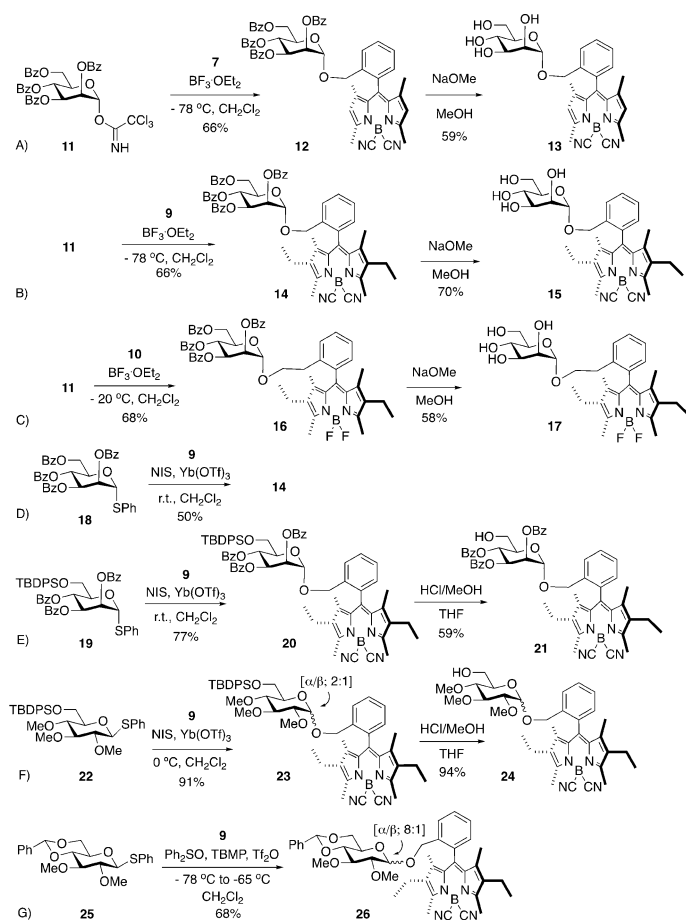
In keeping with these studies, the system NIS/ $BF_3 \cdot OEt_2$  was found to successfully activate NPOE **27** in the glycosylation of BODIPY **9**, to furnish manno- and galactopyranosyl BODIPY **28** in 85% yield (Scheme 4A). In this case, no -CN replacement by fluoride at boron was observed, probably due to the short reaction time required for the reaction to be completed (15 min).

As seen earlier (Scheme 2), MeOEs could be efficiently activated by the action of  $BF_3 \cdot OEt_2$  at low temperature, and, accordingly, glycosyl BODIPYs **28**, **14**, **12** and **20** were uneventfully obtained from MeOEs **2**, **29** and **30**, (Scheme 4B–E). The use of AgOTf to activate glycosyl bromide **31**, was also compatible with BODIPY **9**, and manno- and galactopyranosyl BODIPY **32** could be obtained in 36% yield (45% yield based on recovered starting material, Scheme 4F). In this case, the low yield of **32** was explained by a competing acetylation of the BODIPY aglycon (24% of BODIPY-OAc **9** could be isolated).

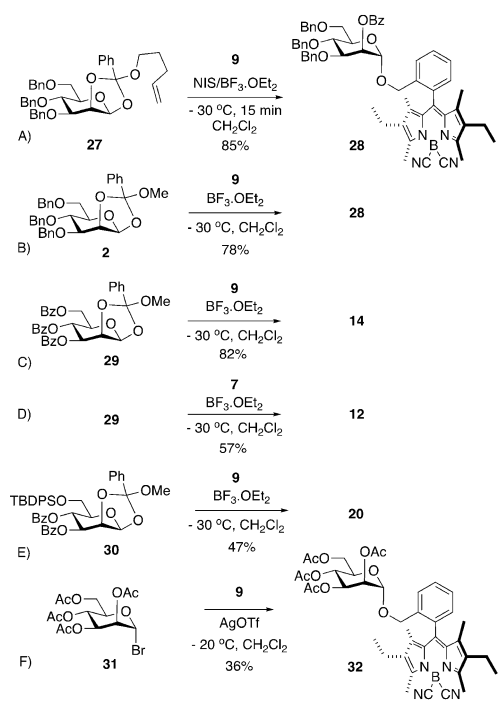
### Glycosyl BODIPYs and benzyl protecting groups

As noted earlier, benzyl groups play a key role in the synthesis of saccharides, since they are visualized as permanent protecting groups to be usually removed at one of the last steps of the synthetic sequence.<sup>[47]</sup> Thus, the question of the stability of our BODIPYs, and their benzylic BODIPY-glycoside bonds under hydrogenolytic conditions became worthy of study.

In this context, previous studies had shown that alkylated BODIPYs were stable under hydrogenolytic conditions.<sup>[48]</sup> With these precedents in mind, we

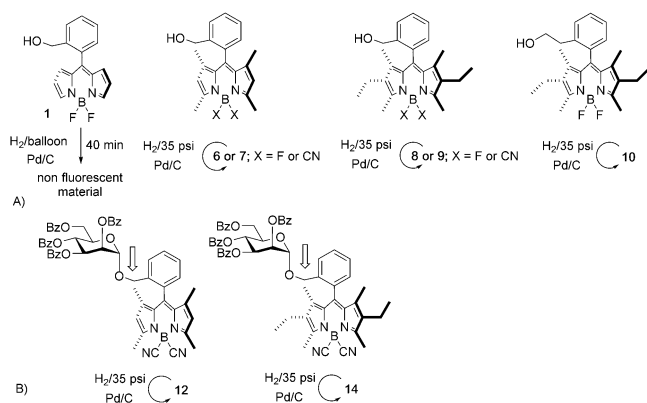


**Scheme 3.** Glycosylation of BODIPYs **7**, **9**, and **10** with glycosyl trichloroacetimidate **11**, and glycosylation of BODIPY **9** with thioglycosyl donors **18**, **19**, **22**, and **25**.



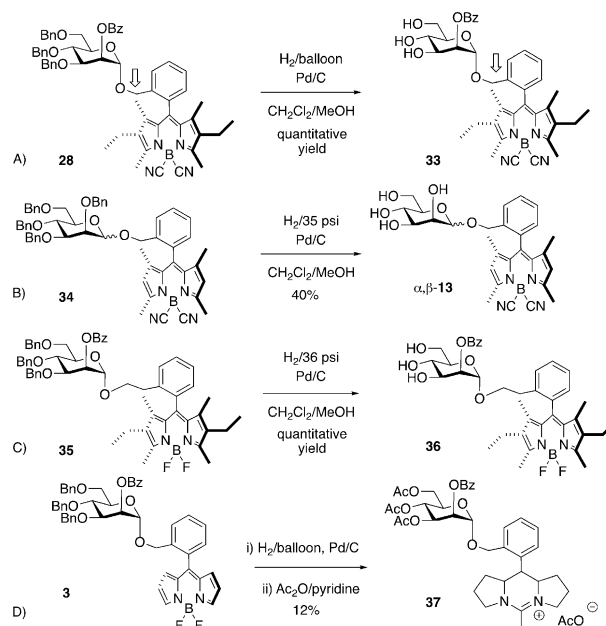
**Scheme 4.** NPOE **27**, MeOEs **2**, **29**, and **30** and glycosyl bromide **31**, in the glycosylation of BODIPYs **7** and **9**.

checked the stability of substituted BODIPYs **6–10**, compared to that of non-alkylated BODIPY **1** (Scheme 5A). Thus, whereas the former derivatives were recovered unmodified after prolonged treatment with H<sub>2</sub> [(35 psi), 7 h, Pd/C, MeOH/CH<sub>2</sub>Cl<sub>2</sub>], treatment of fluorescent BODIPY **1** with H<sub>2</sub> (balloon, Pd/C, MeOH/CH<sub>2</sub>Cl<sub>2</sub>, 40 min) caused complete disappearance of its fluorescence, thereby indicating that cleavage of the BODIPY core might have taken place (Scheme 5A). Next, we tested the stability of the benzylic-BODIPY bond in our BODIPY-glycosides by submitting perbenzoylated derivatives **12** and **14**, to hydrogenolytic conditions (Scheme 5B). Accordingly, treatment of glycosides **12** and **14** with H<sub>2</sub> [(35 psi), 7 h, Pd/C, MeOH/CH<sub>2</sub>Cl<sub>2</sub>], left the substrates unchanged, proving the stability of the benzylic BODIPY bond (Scheme 5B).



**Scheme 5.** Hydrogenolysis studies on BODIPYs **1**, **6**, **7**, **8**, and **10** and BODIPY glycosides **12** and **14**.

Based on these preliminary results, the hydrogenation of tri-*O*-benzyl-mannopyranoside **28**, and tetrabenzyl mannopyranoside **34** took place uneventfully, leading to triol **33** and tetraol  $\alpha,\beta$ -**13**, respectively, in excellent yields (Scheme 6A and B).



**Scheme 6.** Hydrogenolysis of BODIPY-glycosides **28**, **34**, **35**, and **3**.

Likewise, hydrogenation of tri-*O*-benzyl mannopyranoside **35** gave access to triol **36** in almost quantitative yield (Scheme 6C). Finally, to gain further knowledge on the behavior of “non-substituted” BODIPY **1** towards hydrogenation, a green fluorescent solution of mannopyranosyl BODIPY **3** was treated with H<sub>2</sub> [(balloon), Pd/C, MeOH/CH<sub>2</sub>Cl<sub>2</sub>]. After 40 min, and in line with our previous observation (Scheme 5A), the fluorescence as well as the green color of the solution had completely disappeared. Then, acetylation of the ensuing crude reaction mixture led to the isolation of a nonfluorescent glycoside, for which we tentatively propose the structure **37**, based on its NMR and mass spectra (Scheme 6D).

From these studies, it appeared that benzyl ethers in the saccharide portion of these BODIPY glycosides could be removed chemoselectively, leaving the (benzyl)BODIPY aglycon intact (e.g., Scheme 6A and B).

From these studies, it also seemed that the benzyl BODIPY bond between the BODIPY and the carbohydrate is more resistant to hydrogenolysis than the “standard” benzyl protecting groups, probably owing to the steric hindrance of its “*ortho*-BODIPY” substituent. Finally, alkylation around the BODIPY core in these derivatives played an important role in determining their stability towards hydrogenation, especially when compared to that of non-alkylated BODIPY **1**.

Accordingly, benzyl ethers could be used as protecting groups in combination with our BODIPY derivatives; the former being able to be chemoselectively removed without tampering with the BODIPY aglycon.

From the collection of results summarized above, it became clear that some BODIPY derivatives could tolerate, without decomposition, the protection and deprotection events commonly employed in oligosaccharide synthesis.

### Synthesis of BODIPY trisaccharides

As proof of concept, and to illustrate the potential of BODIPY aglycons for the synthesis of oligosaccharides, we embarked on the synthesis of one branched and one linear BODIPY-labeled mannose trisaccharides **38** and **39**, respectively (Scheme 7A and B). Thus, unprotected mannopyranoside **15** (Scheme 3B) was glycosylated with perbenzoylated thioglycoside **18** to give disaccharide **40**, which was then regioselectively glycosylated at *O*-3 with NPOE **41**,<sup>[49]</sup> to yield branched trimannan **38a**. Saponification of the latter (NaOMe/MeOH) yielded unprotected trisaccharide **38b** (Scheme 7A). On the other hand, the route to linear trimannan derivative **39**, started from 6-hydroxy mannopyranoside **21** (Scheme 3E), which, upon glycosylation with thioglycoside donor **19**, mediated by NIS/Yb(OTf)<sub>3</sub>, produced disaccharide **42a**. De-*O*-silylation of the latter (HCl/MeOH, MW irradiation) yielded disaccharide **42b**, in fairly good yield. Finally, glycosylation of disaccharide **42b** with phenyl thioglycoside **18** generated trisaccharide **39a**, which, upon de-*O*-benzoylation, yielded linear BODIPY-labeled trimannan **39b** (Scheme 7B).

### Photophysical studies

To impel the advanced applications of the new glycoprobes we have analyzed the photonic behavior under low (photophysical properties) and high (laser properties) irradiation regimes of some representative BODIPY-labeled saccharides. The *ortho*-glycosylation of the chromophoric C-8-benzyl group led to a rigid and compact molecular structure because of a higher steric hindrance imposed by the bulky saccharides (up

to three units in **38a** and **38b**). In fact, the structural arrangement of the C-8-benzyl residue was nearly orthogonal (twisting dihedral angle computed in the ground state of 85–90° in analogues **15** and **17**, Figure 2) reducing the internal conversion pathways associated with its free motion. Such geometrical disposition explained the low impact of the grafted functionalization (number of saccharide units, sugar protecting groups, and chain-length between the saccharide and the eight-aryl unit) on the photophysical signatures and the recorded high fluorescence efficiencies (Table 3). The replacement at the boron bridge of fluorine atoms (*F*-BODIPYs) by cyano groups (*CN*-BODIPYs) had a low impact on the spectral properties of the BODIPYs (Figure 2), but induced an increase in the emission efficiency (see for example **17** versus **15** in Table 3), reaching values higher than 80%, and approaching the value reported for the parent 1,3,5,7,8-pentamethyl-2,6-diethylpyromethene-difluoroborate (pyromethene PM567) dye (Table 3).<sup>[50]</sup> Such enhancement, upon chemical modification at the boron

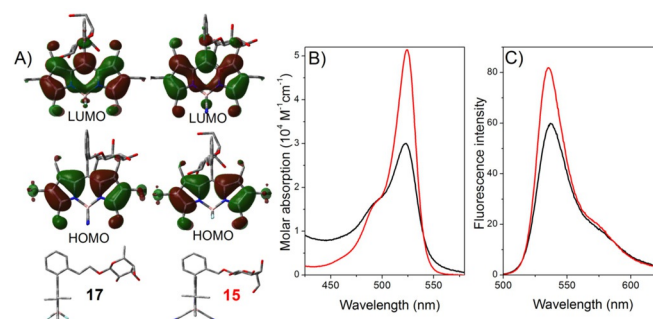


**Figure 2.** A) Computed frontier molecular orbitals (b3lyp/6-311g\*)<sup>[52]</sup> involved in B) the recorded absorption, and C) fluorescence (scaled by their efficiency) transitions in water for the BODIPY-labeled monosaccharide **17** (in black) and its analogue **15** (in red), where the 4,4'-fluorine atoms are replaced with cyano groups. The ground-state optimized geometries in side-view (A) are also shown to highlight the orthogonal arrangement of the 8-aryl moiety linked to the BODIPY scaffold.

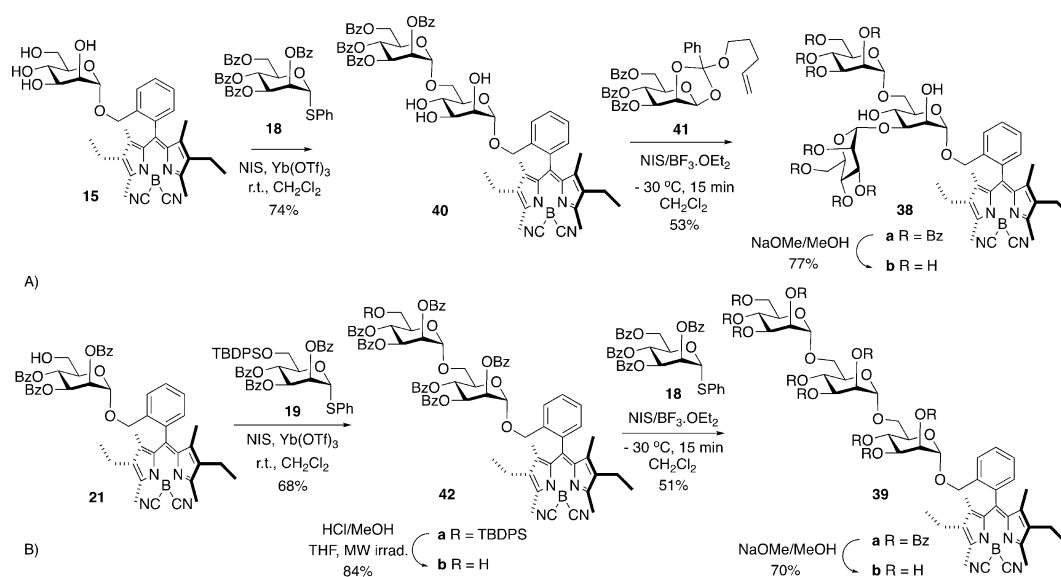


**Table 3.** Photophysical<sup>[a]</sup> and laser<sup>[b]</sup> properties of the synthesized glycoprobes in a common solvent (methanol). The corresponding data for the water-soluble compounds (in H<sub>2</sub>O) are also included (in italics). Additional photophysical data in other solvents are collected in Table S1 in the Supporting Information.

	$\lambda_{ab}$ [nm] <sup>[a]</sup>	$\epsilon_{max} \times 10^4$ [M <sup>-1</sup> cm <sup>-1</sup> ] <sup>[a]</sup>	$\lambda_{fl}$ [nm] <sup>[a]</sup>	$\Phi$ <sup>[a]</sup>	$\tau$ [ns] <sup>[a]</sup>	Eff [%] <sup>[b]</sup>	$I$ [%] <sup>[b]</sup>
<b>PM567</b>	516.0	6.9	534.0	0.81	6.10	48	17
<b>15</b>	523.5	7.7	535.0	0.87	7.21	68	100
	<i>524.0</i>	<i>5.1</i>	<i>535.5</i>	<i>0.82</i>	<i>7.28</i>		
<b>17</b>	523.0	5.4	536.0	0.74	6.67	44	25
	<i>523.0</i>	<i>3.0</i>	<i>533.5</i>	<i>0.60</i>	<i>6.86</i>		
<b>28</b>	525.0	6.7	535.5	0.81	7.24	65	100
<b>40</b>	524.5	6.2	534.0	0.82	6.71	64	100
<b>38 a</b>	525.0	6.6	533.5	0.83	6.97	68	100
<b>38 b</b>	524.0	6.9	535.0	0.81	7.18	66	100
	<i>525.0</i>	<i>5.2</i>	<i>537.0</i>	<i>0.77</i>	<i>7.29</i>		

[a] Dye concentration: 2  $\mu$ M. Absorption ( $\lambda_{ab}$ ) and fluorescence ( $\lambda_{fl}$ ) wavelength, molar absorption at the maximum ( $\epsilon_{max}$ ), fluorescence quantum yield ( $\Phi$ ) and lifetime ( $\tau$ ). [b] Dye concentration 0.8 mM. Laser efficiency (Eff [%]) and photostability ( $I$  [%]): intensity of the laser output after 100 000 pump pulses with respect to its initial intensity  $I_0$ ;  $I$  (%) =  $(I/I_0) \times 100$ , at 10 Hz repetition rate.

bridge with electron-withdrawing groups, is consistent with previously reported results with similar functionalization at the boron center.<sup>[32b]</sup>

It is worth mentioning that the glycoprobes based on fully unprotected saccharides, such as **17** and **15** (with a monosaccharide) and **38 b** (with a trisaccharide), displayed high water solubility. In fact, these derivatives, and particularly those based on 4,4'-dicyano BODIPYs, displayed a remarkable fluorescence efficiency in water, reaching quantum yield values up to 82% (Table 3). Nevertheless, they showed a slight trend toward molecular aggregation upon increasing the dye concentration in water. For example, **38 b**, which was soluble in water at concentrations as high as 2 mM, tended to aggregate at concentrations higher than 0.1 mM, as revealed by the increased absorbance observed at the short-wavelength vibronic shoulder (Figure S1 in the Supporting Information). Such change in the absorption spectrum profiles can be regarded as a fingerprint of non-emissive H-aggregates, which decreased the fluorescence response and impaired effective laser action. However, it is worth mentioning that a water-soluble and highly fluorescent BODIPY at concentrations up to 0.1 mM fulfilled the requirements normally demanded in biological microscopy studies. As a corollary, from a photophysical standpoint, the ensuing BODIPY-labeled saccharides could be used as stable and fluorescent water-soluble chromophores, thereby addressing one of the current challenges in molecular imaging.

### Lasing properties

According to their absorption properties, the lasing properties of the new dyes were studied under pumping at 532 nm. Under our experimental conditions (transversal excitation and strong focusing of the incoming pump radiation) the concentration of the dyes should be in the millimolar range, to ensure

total absorption of the pump radiation within the first millimeter at most of the solution, in order to obtain an emitted beam with near-circular cross-section and optimize the lasing efficiency (ratio between the energy of the dye laser output and the pump energy incident on the sample surface). To determine the dye concentration that optimizes the laser emission of the new dyes, first the dependence of their laser emission on the corresponding dye concentrations was analyzed in methanol by varying the concentration from 0.1 to 2 mM, while keeping all the other experimental parameters constant. In all cases, the dyes followed the typical behavior, with the lasing efficiency first increasing with dye concentration until a maximum value was reached. Increasing the dye concentration beyond this point resulted in a decrease of the lasing efficiency that can be related to reabsorption/reemission processes, which become increasingly important as the dye concentration rises. The optimum value of the dye concentration so determined was then used to analyze the effect of the molecular structure of the solvent on the laser properties of the different derivatives. The lasing data recorded under these experimental conditions are collected in Table 3.

All the new dyes exhibited laser action that peaked at ca. 570 nm, with a pump threshold energy of 0.8 mJ, a beam divergence of 0.5 mrad, and a pulse duration of 8 ns full-width at half-maximum (FWHM). The observed lasing efficiencies correlated well with their photophysical properties; 1) the higher the fluorescence quantum yield the higher became the lasing efficiency; 2) the replacement at the boron bridge of the fluorine atoms with cyano groups enhanced significantly the lasing efficiency; that is, from 48% recorded for **17** to an impressive 68% recorded for its similar cyano derivative **15**; and 3) the lasing efficiency of the glycoprobes built on *F*-BODIPY as well as on *CN*-BODIPY scaffold became independent of the structure of the saccharide inserted in the final dye (i.e., protected and unprotected mono-, di-, and tri-saccharides led to a lasing efficiency ca. 48% for *F*-BODIPYs and 68% for the corresponding *C*-BODIPYs).

An important parameter for any practical applications of these glycoprobes is their lasing photostability under hard radiation conditions and long operation times. A reasonable evaluation of the photostability of these dyes can be obtained by irradiating a small amount of solution with exactly the same pumping energy and geometry as used in the laser experiments, and monitoring the evolution of the laser-induced fluorescence intensity with respect to the number of pump pulses (see Experimental Section). In Table 3 are collected data on the decrease of the laser-induced fluorescence intensity under transversal excitation at 532 nm, with 5 mJ/pulse and 10 Hz repetition rate after 100 000 pump pulses, for the new glycoprobes herein synthesized. Once again, the lasing photostability of the new BODIPY-saccharides matched their photophysical properties since the lower the non-radiative rate constant, the higher became the resistance to pumping showed by the new dyes regardless of the saccharide inserted in its molecular structure. In this way, the glycoprobes derived from the *CN*-BODIPY skeleton behaved as highly efficient and photostable dyes since its laser emission remained at its initial

level after 100 000 pump pulses, enhancing that recorded with the corresponding *F*-BODIPY saccharides which lasing emission dropped more than 80% in the same pumping period.

## Conclusions

To validate the potential of BODIPY dyes as aglycons in synthetic sequences leading to saccharides, we have performed a comprehensive study of the compatibility of some BODIPY derivatives with the reaction conditions normally employed in these protocols, namely: 1) glycosylation and 2) protecting-group manipulations. Regarding the glycosylation phase, we have evaluated the endurance of BODIPY derivatives in glycosylations with glycosyl trichloroacetimidates, thioglycosides, *n*-pentenyl orthoesters (NPOEs), 1,2-methyl orthoesters (MeOEs), or glycosyl bromides, as glycosyl donors. From the standpoint of protecting-group manipulations, we have identified reaction conditions that do not tamper with the BODIPY core and allow the removal of silyl and benzoyl substituents, as representative of “temporary” protecting groups, and of benzyl substituents as protecting groups that are regarded as “permanent”.<sup>[36]</sup> In general, and in keeping with literature precedents,<sup>[33]</sup> we have found that B(CN)<sub>2</sub>-BODIPYs are more resistant to acidic conditions than the corresponding BF<sub>2</sub> derivatives. The latter, however, are more stable than the former under basic conditions. Also noteworthy, we have observed that the substitution pattern on the dipyrromethene core also plays a significant role in determining the stability of the dye. Thus, 1,3,5,7-tetramethyl-2,6-diethyl BODIPY derivatives, that is, **8** and **9**, proved to be more stable than their corresponding 2,6-*des*-ethyl analogues, that is, **6** and **7**, under either acidic or basic conditions.

Accordingly, it has become apparent from these studies that BODIPY derivatives **8** or **9** could be successfully employed as aglycons in synthetic oligosaccharide synthesis. As such, they could play a dual role, as glycosyl tags by facilitating the visualization and identification of reaction products, and as fluorescent labels in the target oligosaccharides.

Appealingly, from a synthetic standpoint, access to these BODIPYs could be carried out efficiently in gram-scale operations. Thus, BODIPY **8** is readily obtained by a one-step reaction from 2,4-dimethyl-3-ethyl pyrrole and phthalide,<sup>[21]</sup> and B(CN)<sub>2</sub>-BODIPY **9** is then easily available from BF<sub>2</sub>-BODIPY **7** by reaction with TMSCN mediated by BF<sub>3</sub>·OEt<sub>2</sub>.<sup>[32]</sup>

From the photophysical perspective, B(CN)<sub>2</sub>-BODIPYs displayed better photophysical properties than the corresponding BF<sub>2</sub> derivatives, possibly making B(CN)<sub>2</sub>-BODIPY **9** the aglycon of choice in BODIPY-assisted fluorescent saccharide synthesis. In addition, we have found that the carbohydrate subunits have a beneficial effect on the, already good, photophysical features of these BODIPY dyes.

In summary, the incorporation of a BODIPY tag at the reducing-end of the target saccharide could prove particularly useful in glycosylations when an excess of nonfluorescent glycosyl donors will be required, because it allows the easy visualization of the fluorescent final product and the unreacted glycosyl acceptor.

## Experimental Section

### Synthesis of fluorescently labeled branched trisaccharide **36 b**, using [B(CN)<sub>2</sub>] BODIPY **9** as the aglycone; Typical procedure

**Synthesis of B(CN)<sub>2</sub>-BODIPY **9** from BF<sub>2</sub>-BODIPY **8**:** A solution of BF<sub>2</sub>-BODIPY **8**<sup>[21]</sup> (1.3 g, 3.17 mmol) in anhydrous CH<sub>2</sub>Cl<sub>2</sub> (20 mL) was cooled to 0 °C and treated with BF<sub>3</sub>·OEt<sub>2</sub> (78 μL, 0.63 mmol). The mixture was stirred at r.t. for 5–10 min, then TMSCN (1.97 mL, 15.8 mmol) was added and the reaction mixture was kept under these conditions for 120 min. The mixture was neutralized with saturated aqueous NaHCO<sub>3</sub> solution, diluted with CH<sub>2</sub>Cl<sub>2</sub> and washed with water (2×). The organic phase was dried over MgSO<sub>4</sub>, concentrated and purified on a silica gel column (hexane/ethyl acetate; 9:1). Yield: 1.17 g (87%); <sup>1</sup>H NMR (400 MHz, CDCl<sub>3</sub>): δ = 7.70 (d, *J* = 7.7 Hz, 1H), 7.55 (d, *J* = 7.6 Hz, 1H), 7.44 (t, *J* = 7.5 Hz, 1H), 7.18 (d, *J* = 7.7 Hz, 1H), 4.56 (s, 2H), 2.69 (s, 6H), 2.34 (q, *J* = 7.6 Hz, 4H), 1.31 (s, 6H), 1.00 ppm (t, *J* = 7.6 Hz, 6H); <sup>13</sup>C NMR (100 MHz, CDCl<sub>3</sub>): δ = 154.4, 139.7, 139.2, 138.3, 134.5 (broad C), 132.6, 130.0, 128.8 (broad C), 128.6, 128.1, 62.3, 17.3, 14.6, 13.5, 11.5 ppm; <sup>19</sup>F NMR (376 MHz, CDCl<sub>3</sub>): no peaks; <sup>11</sup>B NMR (128 MHz, CDCl<sub>3</sub>): δ = −16.25 ppm; HRMS (ESI-TOF): *m/z* calcd for C<sub>26</sub>H<sub>30</sub>BN<sub>4</sub>O: 425.25118 [M+H]<sup>+</sup>; found: 425.25088.

**Mannopyranosyl BODIPY **14**:** To a solution of BODIPY-acceptor **9** (424 mg, 1 mmol) and TCA **11** (1 g, 1.36 mmol) in anhydrous CH<sub>2</sub>Cl<sub>2</sub> (15 mL) was added 4 Å molecular sieves (100% w/w). The mixture was stirred at r.t. for about 15 min under an Ar atmosphere, then cooled to −78 °C. Fresh BF<sub>3</sub>·OEt<sub>2</sub> (84 μL, 0.68 mmol) was then added and the reaction mixture was kept at this temperature. The mixture was stirred under these conditions for 30 min, and then neutralized by addition of Et<sub>3</sub>N (1 mL). The mixture was evaporated and purified by chromatography over silica gel flash column (hexane/ethyl acetate, 8:2) to give compound **14** (661 mg, 66%); red film-like solid; [α]<sub>D</sub><sup>21</sup> = +15.1 (c 0.4 in CHCl<sub>3</sub>); <sup>1</sup>H NMR (500 MHz, CDCl<sub>3</sub>): δ = 8.01–7.16 (m, 24H), 6.01 (t, *J* = 10.1 Hz, 1H), 5.63 (dd, *J* = 10.2, 3.3 Hz, 1H), 5.28 (dd, *J* = 3.3, 1.8 Hz, 1H), 4.91 (d, *J* = 1.8 Hz, 1H), 4.64 (d, *J* = 11.5 Hz, 1H), 4.57 (dd, *J* = 12.3, 2.7 Hz, 1H), 4.40 (d, *J* = 11.5 Hz, 1H), 4.34 (dd, *J* = 12.3, 3.4 Hz, 1H), 4.19 (dt, *J* = 10.1, 3.1 Hz, 1H), 2.60 (s, 6H), 2.38–2.19 (m, 4H), 1.36 (s, 3H), 1.25 (s, 3H), 0.91 (t, *J* = 7.5 Hz, 3H), 0.90 ppm (t, *J* = 7.5 Hz, 3H); <sup>13</sup>C NMR (126 MHz, CDCl<sub>3</sub>): δ = 166.2, 165.5, 165.1, 156.1, 153.9, 140.4, 139.0, 138.4, 135.3, 134.7, 134.4, 134.3, 133.5, 133.4, 133.3, 133.1, 130.3, 130.1, 130.0, 129.9, 129.8, 129.7, 129.5, 129.2, 128.8, 128.6, 128.5, 128.4 ppm; <sup>11</sup>B NMR (128 MHz, CDCl<sub>3</sub>): δ = −16.16 ppm; <sup>19</sup>F NMR (376 MHz, CDCl<sub>3</sub>): no peaks; HRMS (ESI-TOF): *m/z* calcd for C<sub>60</sub>H<sub>59</sub>BN<sub>5</sub>O<sub>10</sub>: 1020.43594 [M + NH<sub>4</sub>]<sup>+</sup>; found: 1020.43754; *m/z* calcd for C<sub>60</sub>H<sub>55</sub>BN<sub>4</sub>NaO<sub>10</sub>: 1025.39133 [M + Na]<sup>+</sup>; found: 1025.39126.

**Mannopyranosyl-tetraol BODIPY **15**:** A solution of BODIPY mannanopyranoside **14** (572 mg, 0.57 mmol) in MeOH (10 mL) was treated with NaOMe (184 mg, 3.42 mmol). After stirring at RT for 3 h, the solution was neutralized with ion-exchange resin (H<sup>+</sup>), then filtered and concentrated. The residue was purified by column chromatography on silica gel (MeOH/CH<sub>2</sub>Cl<sub>2</sub>; 9:1) to provide tetraol **15** (228 mg, 70%) as a red solid; m.p. 140.1 °C (decomposition); [α]<sub>D</sub><sup>21</sup> = +179.4 (c 0.07 in MeOH); <sup>1</sup>H NMR (500 MHz, CDCl<sub>3</sub>): δ = 7.61–7.44 (m, 3H), 7.21 (d, *J* = 7.2 Hz, 1H), 4.67 (s, 1H), 4.50 (d, *J* = 11.0 Hz, 1H), 4.22 (d, *J* = 11.4 Hz, 1H), 3.80–3.55 (m, 2H), 3.53–3.34 (m, 3H), 3.13–2.99 (m, 1H), 2.66 (m, 6H), 2.44–2.25 (m, 4H), 1.27 (s, 6H), 1.00 ppm (q, *J* = 7.5 Hz, 6H); <sup>13</sup>C NMR (126 MHz, CDCl<sub>3</sub>): δ = 154.5, 154.3, 140.0, 139.8, 139.1, 134.8, 134.7, 134.5, 133.8, 130.0, 129.9, 129.3, 129.0, 128.7, 128.3, 100.2, 72.4, 71.5, 70.6, 67.3, 65.8,

60.6, 17.3, 14.6, 14.5, 13.5, 11.6, 11.5 ppm;  $^{11}\text{B}$  NMR (128 MHz,  $\text{CDCl}_3$ ):  $\delta = -16.25$  ppm; HRMS (ESI-TOF):  $m/z$  calcd for  $\text{C}_{32}\text{H}_{43}\text{BN}_5\text{O}_6$ : 604.33066  $[\text{M}+\text{NH}_4]^+$ ; found: 604.33040;  $m/z$  calcd for  $\text{C}_{32}\text{H}_{39}\text{B N}_4\text{NaO}_6$ : 609.28605  $[\text{M}+\text{Na}]^+$ ; found: 609.28555.

**BODIPY-disaccharide 40:** To a stirred solution of tetraol **15** (50 mg, 0.087 mmol), and thioglycoside donor **18** (139 mg, 0.22 mmol) and *N*-iodosuccinimide (NIS) (49 mg, 0.22 mmol) in  $\text{CH}_2\text{Cl}_2$  (8 mL),  $\text{Yb}(\text{OTf})_3$  (136 mg, 0.22 mmol) was added at RT. The reaction mixture was stirred for 15 min and then partitioned between aqueous sodium thiosulfate/ $\text{NaHCO}_3$  and  $\text{CH}_2\text{Cl}_2$ . After washing with water and brine, the combined organic extracts were dried over anhydrous  $\text{Na}_2\text{SO}_4$  and evaporated. The residue was purified by chromatography over silica gel flash column (hexane/ethyl acetate, 6:4) to give disaccharide **40** (75 mg, 74%) as a red film-like solid;  $[\alpha]_D^{21} = +392.1$  (c 0.2 in  $\text{CHCl}_3$ );  $^1\text{H}$  NMR (500 MHz,  $\text{CDCl}_3$ ):  $\delta = 8.21$ –7.69 (m, 8H), 7.67–7.21 (m, 16H), 6.11 (t,  $J = 10.2$  Hz, 1H), 5.94 (dd,  $J = 10.2$ , 3.3 Hz, 1H), 5.69 (dd,  $J = 3.3$ , 1.8 Hz, 1H), 5.24 (d,  $J = 1.8$  Hz, 1H), 4.72–4.64 (m, 3H), 4.58–4.52 (m, 1H), 4.47 (dd,  $J = 12.2$ , 4.1 Hz, 1H), 4.35 (d,  $J = 11.3$  Hz, 1H), 3.97 (dd,  $J = 11.4$ , 5.5 Hz, 1H), 3.89 (dd,  $J = 11.4$ , 1.9 Hz, 1H), 3.70 (td,  $J = 9.6$ , 2.7 Hz, 1H), 3.59–3.52 (m, 1H), 3.31 (td,  $J = 9.1$ , 3.5 Hz, 1H), 3.28–3.21 (m, 1H), 2.70 (s, 3H), 2.68 (s, 3H), 2.39–2.31 (m, 4H), 1.35 (s, 3H), 1.30 (s, 3H), 1.04–0.97 ppm (m, 6H);  $^{13}\text{C}$  NMR (126 MHz,  $\text{CDCl}_3$ ):  $\delta = 166.3$ , 165.7, 165.6, 154.2, 154.1, 140.6, 140.1, 139.9, 134.7, 134.6, 133.6, 133.5, 133.3, 133.1, 131.0, 130.1, 130.0, 129.9, 129.6, 129.4, 129.2, 128.7, 128.6, 128.5, 128.4, 100.6, 97.6, 71.9, 71.5, 70.9, 70.1, 69.9, 69.2, 69.0, 68.1, 67.1, 66.9, 63.0, 17.4, 17.3, 14.6, 13.6, 11.9, 11.5 ppm; HRMS (ESI-TOF):  $m/z$  calcd for  $\text{C}_{66}\text{H}_{69}\text{BN}_5\text{O}_{15}$ : 1182.4885  $[\text{M}+\text{NH}_4]^+$ ; found: 1182.49303;  $m/z$  calcd for  $\text{C}_{66}\text{H}_{65}\text{BN}_4\text{NaO}_{15}$ : 1187.44424  $[\text{M}+\text{Na}]^+$ ; found: 1187.44934.

**BODIPY-trisaccharide 38a:** To a stirred solution of BODIPY-disaccharide **40** (41 mg, 0.035 mmol), NPOE donor **41** (70 mg, 0.105 mmol) and *N*-iodosuccinimide (23 mg, 0.105 mmol) in  $\text{CH}_2\text{Cl}_2$  (8 mL),  $\text{BF}_3\text{OEt}_2$  (5  $\mu\text{L}$ , 0.022 mmol) was added at  $-30^\circ\text{C}$ . The reaction mixture was stirred for 15 min and then partitioned between aqueous sodium thiosulfate/ $\text{NaHCO}_3$  and  $\text{CH}_2\text{Cl}_2$ . After washing with water and brine, the combined organic extracts were dried over anhydrous  $\text{Na}_2\text{SO}_4$  and evaporated. The residue was purified by chromatography over silica gel flash column (hexane/ethyl acetate, 6:4) to give compound **38a** as a noncrystalline red film-like solid product (76 mg, 53%);  $[\alpha]_D^{21} = -125.9$  (c 0.9 in  $\text{CHCl}_3$ );  $^1\text{H}$  NMR (500 MHz,  $\text{CDCl}_3$ ):  $\delta = 8.19$ –7.76 (m, 16H), 7.67–7.17 (m, 28H), 6.20 (t,  $J = 10.2$  Hz, 1H), 6.14 (t,  $J = 10.1$  Hz, 1H), 5.98 (dd,  $J = 4.5$ , 3.2 Hz, 1H), 5.96 (dd,  $J = 4.4$ , 3.3 Hz, 1H), 5.78 (dd,  $J = 3.2$ , 1.9 Hz, 1H), 5.73 (dd,  $J = 3.3$ , 1.8 Hz, 1H), 5.34 (d,  $J = 1.8$  Hz, 1H), 5.10 (d,  $J = 2.0$  Hz, 1H), 4.86 (dt,  $J = 10.3$ , 3.1 Hz, 1H), 4.73 (dd,  $J = 12.2$ , 2.5 Hz, 1H), 4.67 (d,  $J = 1.7$  Hz, 1H), 4.64 (dd,  $J = 12.3$ , 2.6 Hz, 1H), 4.62 (d,  $J = 11.2$  Hz, 1H), 4.60–4.53 (m, 2H), 4.50 (dd,  $J = 12.2$ , 3.9 Hz, 1H), 4.25 (d,  $J = 11.1$  Hz, 1H), 4.15 (t,  $J = 9.7$  Hz, 1H), 4.03 (dd,  $J = 11.8$ , 4.5 Hz, 1H), 3.89 (dd,  $J = 11.8$ , 1.8 Hz, 1H), 3.81 (s, 1H), 3.63 (dd,  $J = 9.4$ , 3.2 Hz, 1H), 3.52 (ddd,  $J = 9.9$ , 4.5, 1.8 Hz, 1H), 2.65 (s, 3H), 2.60 (s, 3H), 2.35–2.23 (m, 2H), 2.22–2.13 (m, 2H), 1.29 (s, 3H), 1.29 (s, 3H), 1.29 (s, 3H), 0.93 (t,  $J = 7.6$  Hz, 3H), 0.75 ppm (t,  $J = 7.6$  Hz, 3H);  $^{13}\text{C}$  NMR (126 MHz,  $\text{CDCl}_3$ ):  $\delta = 166.4$ , 166.3, 165.8, 165.6, 165.5, 154.6, 154.4, 140.0, 139.7, 139.4, 134.8, 134.6, 134.5, 133.7, 133.6, 133.5, 133.4, 133.3, 133.2, 133.1, 131.0, 130.2, 130.1, 130.0, 129.9, 129.5, 129.4, 129.3, 129.2, 129.1, 128.8, 128.7, 128.6, 128.5, 128.4, 100.7, 99.2, 97.8, 82.9, 72.1, 71.0, 70.8, 70.4, 70.1, 69.6, 69.4, 69.0, 68.5, 67.1, 66.6, 65.1, 63.0, 62.9, 17.4, 17.3, 14.6, 14.4, 13.6, 13.5, 11.8, 11.5 ppm;  $^{11}\text{B}$  NMR (128 MHz,  $\text{CDCl}_3$ ):  $\delta = -16.25$  ppm; HRMS (ESI-TOF):  $m/z$  calcd for  $\text{C}_{100}\text{H}_{95}\text{BN}_5\text{O}_{24}$ : 1760.64696  $[\text{M}+\text{NH}_4]^+$ ; found: 1760.64620;  $m/z$  calcd for  $\text{C}_{100}\text{H}_{91}\text{BN}_4\text{NaO}_{24}$ : 1765.60236  $[\text{M}+\text{Na}]^+$ ; found: 1765.61089.

**BODIPY-trimannan derivative 38b:** A solution of benzoylated trisaccharide **38a** (56 mg, 0.032 mmol) in  $\text{MeOH}/\text{CH}_2\text{Cl}_2$  (v/v 2:1, 4 mL) was treated with  $\text{NaOMe}$  (14 mg, 0.26 mmol). After stirring at RT for 4 h, the solution was neutralized with ion-exchange resin ( $\text{H}^+$ ), then filtered and concentrated. The residue was purified by column chromatography on silica gel (ethyl acetate/ $\text{MeOH}/\text{H}_2\text{O}$ ; 10:2:1) to give **38b** (22 mg, 77%) as a red film-like solid;  $[\alpha]_D^{21} = +960.9$  (c 0.3 in  $\text{CHCl}_3$ );  $^1\text{H}$  NMR (500 MHz,  $\text{CDCl}_3$ ):  $\delta = 7.70$  (dd,  $J = 7.7$ , 1.4 Hz, 1H), 7.63 (td,  $J = 7.6$ , 1.5 Hz, 1H), 7.58 (dt,  $J = 7.5$ , 1.4 Hz, 1H), 7.33 (dd,  $J = 7.5$ , 1.4 Hz, 1H), 4.94 (d,  $J = 1.8$  Hz, 1H), 4.78 (d,  $J = 1.7$  Hz, 1H), 4.71 (d,  $J = 1.7$  Hz, 1H), 4.60 (d,  $J = 10.8$  Hz, 1H), 4.27 (d,  $J = 10.9$  Hz, 1H), 3.94 (dd,  $J = 3.4$ , 1.8 Hz, 1H), 3.91 (dd,  $J = 3.4$ , 1.7 Hz, 1H), 3.83–3.74 (m, 6H), 3.73–3.65 (m, 3H), 3.64–3.57 (m, 4H), 3.45–3.40 (m, 2H), 3.14 (ddd,  $J = 10.1$ , 4.8, 1.9 Hz, 1H), 2.70 (s, 3H), 2.69 (s, 3H), 2.54–2.37 (m, 4H), 1.42 (s, 3H), 1.37 (s, 3H), 1.04 ppm (t,  $J = 7.5$  Hz, 67H);  $^{13}\text{C}$  NMR (126 MHz,  $\text{CDCl}_3$ ):  $\delta = 156.2$ , 155.0, 142.0, 141.4, 141.0, 136.5, 136.2, 136.1, 136.0, 135.5, 132.4, 131.2, 130.7, 130.5, 130.2, 129.7, 103.6, 101.9, 101.2, 81.2, 74.8, 74.0, 73.3, 72.6, 72.5, 72.1, 71.9, 71.0, 68.7, 68.6, 68.1, 66.5, 66.4, 62.8, 62.7, 18.2, 18.0, 14.9, 14.9, 13.8, 13.6, 12.1, 11.9 ppm; HRMS (ESI-TOF):  $m/z$  calcd for  $\text{C}_{44}\text{H}_{63}\text{BN}_5\text{O}_{16}$ : 928.43650  $[\text{M}+\text{NH}_4]^+$ ; found: 928.43253;  $m/z$  calcd for  $\text{C}_{44}\text{H}_{59}\text{BN}_4\text{NaO}_{16}$ : 933.39190  $[\text{M}+\text{Na}]^+$ ; found: 933.39046.

**Photophysical properties:** Spectroscopic properties were recorded in dilute solutions (ca.  $2 \times 10^{-6}$  M), prepared by adding the corresponding solvent (spectroscopic grade) to the residue from the required amount of a concentrated stock solution in acetone, after vacuum evaporation of this solvent. UV/Vis absorption spectra were recorded with a Varian model CARY 4E spectrophotometer; the fluorescence and excitation spectra, as well as the decay curves were recorded with an Edinburgh Instruments spectrofluorimeter (model FLSP 920). Fluorescence quantum yields ( $\phi$ ) were obtained using as reference commercial cresyl violet ( $\phi^f = 0.54$  in methanol), for the long-wavelength emission of the energy acceptor, and commercial PM546 ( $\phi^f = 0.81$  in methanol) to account for the green, and quenched emission owing to energy transfer of the energy donor subunit. The values were corrected for the refractive index of the solvent. Radiative decay curves were registered with the time correlated single-photon counting technique using a multichannel plate detector with picosecond time-resolution. Fluorescence emission was monitored at the maximum emission wavelength after excitation by means of a wavelength-tunable Fianium Supercontinuum laser. The fluorescence lifetime ( $\tau$ ) was obtained after the deconvolution of the instrumental response signal from the recorded decay curves by means of an iterative method. The decay curve was essentially the same regardless of the excited visible absorption band. The goodness of the exponential fit was controlled by statistical parameters (chi-square and the analysis of the residuals). The radiative ( $k_r$ ) and nonradiative ( $k_{nr}$ ) rate constants were calculated from the fluorescence quantum yield and lifetime;  $k_r = \phi/\tau$  and  $k_{nr} = (1 - \phi)/\tau$ .

**Quantum mechanical calculations:** Ground-state geometries were optimized at the density functional theory (DFT) level using range-separated hybrid wB97XD method. The vertical Franck–Condon electronic transition was predicted by the time-dependent (TD) method and the same functional. In both cases the double valence basis set with one polarization function (6–31g\*) was used because of the large size of the computed multichromophoric molecules. The geometries were considered as energy minimum when the corresponding frequency analysis did not give any negative value. The solvent effect (cyclohexane) was considered in the conducted theoretical simulations by applying the polarizable continuum model (PCM). All the calculations were performed using the Gaussi-

an 16 software<sup>[51]</sup> as implemented in the computational cluster “arina” of the UPV/EHU.

**Laser properties:** Laser efficiency was evaluated from concentrated solutions (millimolar) of dyes in ethyl acetate contained in 1-cm optical-path rectangular quartz cells carefully sealed to avoid solvent evaporation during experiments. The liquid solutions were transversely pumped with 8 mJ, 8 ns FWHM pulses from the third harmonic (355 nm) or the second harmonic (532 nm) of a Q-switched Nd:YAG laser (Lotis TII 2134) at a repetition rate of 1 Hz. The excitation pulses were line-focused onto the cell using a combination of positive and negative cylindrical lenses ( $f = 15$  cm and  $f = -15$  cm, respectively) arranged perpendicularly. The plane parallel oscillation cavity (2 cm length) consisted of a 90% reflectivity aluminum mirror acting as back reflector, and the lateral face of the cell acting as output coupler (4% reflectivity). The pump and output energies were detected with a GenTec power meter. The photostability of the dyes in ethyl acetate solution was evaluated by using a pumping energy and geometry exactly equal to that of the laser experiments. We used spectroscopic quartz cuvettes with 0.1 cm optical path to allow for the minimum solution volume ( $V_s = 40 \mu\text{L}$ ) to be excited. The lateral faces were ground, whereupon no laser oscillation was obtained. Information about photostability was obtained by monitoring the decrease in laser-induced fluorescence (LIF) intensity. To facilitate comparisons independently of the experimental conditions and sample, the photostability figure of merit was defined as the accumulated pump energy absorbed by the system ( $E_{\text{dose}}$ ), per mole of dye, before the output energy falls to 50% of its initial value. In terms of experimental parameters, this energy dose, in units of  $\text{GJ mol}^{-1}$ , can be expressed as Equation (1):

$$E_{\text{dose}}^{80\%} (\text{GJ mol}^{-1}) = \frac{E_{\text{pump}} (\text{GJ}) (1 - 10^{-\epsilon C L}) \sum_{\text{\#pulses}} f}{CV_s} \quad (1)$$

where  $E_{\text{pump}}$  is the energy per pulse,  $C$  is the molar concentration,  $\epsilon$  is the molar absorption coefficient in units of  $\text{M}^{-1} \text{cm}^{-1}$ ,  $L$  is the depth of the cuvette expressed in cm,  $V_s$  is the solution volume, in liters, within the cuvette, and  $f$  is the ratio between the LIF intensity after #pulses and the LIF intensity in the first pulse. To speed up the experiment, the pump repetition rate was increased to 15 Hz. The fluorescence emission and laser spectra were monitored perpendicular to the excitation beam, collected with an optical fiber, and imaged with a spectrometer (Acton Research corporation) and detected with a charge-coupled device (CCD) (SpectruMM:GS128B). The fluorescence emission was recorded by feeding the signal to the boxcar (Stanford Research, model 250) to be integrated before being digitized and processed by a computer. The estimated error in the energy and photostability measurements was 10%.

## Acknowledgements

We gratefully acknowledge the Spanish Ministerio de Economía y Competitividad for financial support (projects CTQ2015-66702-R, MAT2017-83856-C3-1-P and 3-P). We also thank the Ministerio de Ciencia Innovación y Universidades (project RTI2018-094862-B-I00) and the Gobierno Vasco for financial support (project IT912-16) and for a predoctoral fellowship to E. A.-Z. Additionally, C.P., on leave from the Universidad Nacional de Rosario (UNR), is grateful to the EVA mobility program (UNR) for partial financial support. The authors thank SGIker of

UPV/EHU for technical support with the computational calculations, which were carried out in the “arina” informatic cluster. We are very grateful to Ms. Marina Rodríguez (IQOG-CSIC) for skillful technical support.

## Conflict of interest

The authors declare no conflict of interest.

**Keywords:** dyes/pigments · carbohydrates · fluorescent probes · glycoconjugates · glycosylation

- [1] a) G.-J. Boons, *Tetrahedron* **1996**, *52*, 1095–1121; b) D. P. Galonić, D. Y. Gin, *Nature* **2007**, *446*, 1000–1007; c) X. Zhu, R. R. Schmidt, *Angew. Chem. Int. Ed.* **2009**, *48*, 1900–1934; *Angew. Chem.* **2009**, *121*, 1932–1967; d) *Handbook of Chemical Glycosylation: Advances in Stereoselectivity and Therapeutic Relevance* (Ed.: A. V. Demchenko), Wiley-VCH, Weinheim, **2008**; e) *Reactivity Tuning in Oligosaccharide Assembly, Vol. 301* (Eds.: B. Fraser-Reid, J. C. Lopez), Springer, Berlin, **2011**.
- [2] a) L. D. Davis, R. T. Raines, *ACS Chem. Biol.* **2008**, *3*, 142–155; b) H. Kobayashi, M. Ogawa, R. Alford, P. L. Choyke, Y. Urano, *Chem. Rev.* **2010**, *110*, 2620–2640; c) L. D. Davis, R. T. Raines, *ACS Chem. Biol.* **2014**, *9*, 2535.
- [3] a) M. Sawa, T.-L. Hsu, T. Itoh, M. Sugiyama, S. R. Hanson, P. K. Vogt, C.-H. Wong, *Proc. Natl. Acad. Sci. USA* **2006**, *103*, 12371–12376; b) L. Krishnamoorthy, L. K. Mahal, *ACS Chem. Biol.* **2009**, *4c*, 715–732; c) S. T. Laughlin, C. R. Bertozzi, *Proc. Natl. Acad. Sci. USA* **2009**, *106*, 12–17; d) H. Yan, R. S. Yalagala, F. Yan, *Glycoconjugate J.* **2015**, *32*, 559–574; e) B. Thomas, K.-C. Yan, X.-L. Hu, M. Donnier-Maréchal, G.-R. Chen, X.-P. He, S. Vidal, *Chem. Soc. Rev.* **2020**, *49*, 593–641.
- [4] Y. Mechref, M. V. Novotny, *Chem. Rev.* **2002**, *102*, 321–369.
- [5] a) B. Xia, Z. S. Kowar, T. Ju, R. A. Alvarez, G. P. Sachdev, R. D. Cummings, *Nat. Methods* **2005**, *2*, 845–850; b) A. Lohse, R. Martins, M. R. Jørgensen, O. Hindsgaul, *Angew. Chem. Int. Ed.* **2006**, *45*, 4167–4172; *Angew. Chem.* **2006**, *118*, 4273–4278; c) R. B. Keithley, A. S. Rosenthal, D. C. Essaka, H. Tanaka, Y. Yoshimura, M. M. Palcic, O. Hindsgaul, N. J. Dovichi, *Analyst* **2013**, *138*, 164–170.
- [6] a) A. K. Yadav, D. L. Shen, X. Shan, X. He, A. R. Kermode, D. J. Vocadlo, *J. Am. Chem. Soc.* **2015**, *137*, 1181–1189; b) I. M. Ivanova, S. A. Nepogodiev, G. Saalbach, E. C. O’Neill, M. D. Urbaniak, M. A. J. Ferguson, S. S. Gurucha, G. S. Besra, R. A. Field, *Carbohydr. Res.* **2017**, *438*, 26–38.
- [7] a) C. R. Bertozzi, L. L. Kiessling, *Science* **2001**, *291*, 2357–2364; b) T. Feizi, W. Chai, *Nat. Rev. Mol. Cell Biol.* **2004**, *5*, 582–588; c) F. T. Liu, G. A. Rabinovich, *Nat. Rev. Cancer* **2005**, *5*, 29–41; d) Y. Yang, T. W. Jia, F. Xu, W. Li, S. Tao, L.-Q. Chu, Y. He, Y. Li, Y. S. S. Iyer, P. Yu, *ACS Appl. Nano Mater.* **2018**, *1*, 1058–1065.
- [8] a) M. H. Lee, J. H. Han, P.-S. Kwon, S. Bhuniya, J. Y. Kim, J. L. Sessler, C. Kang, J. S. Kim, *J. Am. Chem. Soc.* **2012**, *134*, 1316–1322; b) W.-T. Dou, Y. Zhang, Y. Lv, J. Wu, Y. Zang, C. Tan, J. Li, G.-R. Chen, X. P. He, *Chem. Commun.* **2016**, *52*, 3821–3824; c) M. Wahiba, X. Q. Feng, Y. Zang, T. D. James, J. Li, G.-R. Chen, X. P. He, *Chem. Commun.* **2016**, *52*, 11689–11692; d) W.-T. Dou, Y. L. Zeng, Y. Lv, J. Wu, X.-P. He, G.-R. Chen, C. Tan, *ACS Appl. Mater. Interfaces* **2016**, *8*, 13601–13606; e) Q. Zhang, Y. Cai, X.-J. Wang, J.-L. Xu, Z. Ye, S. Wang, P. H. Seeberger, J. Yin, *ACS Appl. Mater. Interfaces* **2016**, *8*, 33405–33411; f) L. Liu, Z. Ruan, T. Li, P. Yuan, L. Yan, *Biomater. Sci.* **2016**, *4*, 1638–1645; g) N. Shivran, M. Tyagi, S. Mula, P. Gupta, B. Saha, B. S. Patro, S. Chattopadhyay, *Eur. J. Med. Chem.* **2016**, *122*, 352–365; h) H.-H. Han, C.-Z. Wang, Y. Zang, J. Li, T. D. James, X. P. He, *Chem. Commun.* **2017**, *53*, 9793–9796; i) Q. Zhang, Y. Cai, Q.-Y. Li, L.-N. Hao, Z. Ma, X.-J. Wang, J. Yin, *Chem. Eur. J.* **2017**, *23*, 14307–14311; j) P. Kesavan, V. Pandey, M. K. Raza, S. Mori, I. Gupta, *Bioorg. Chem.* **2019**, *91*, 103139; k) N. E. M. Kaufman, Q. Meng, K. E. Griffin, S. S. Singh, A. Dahal, Z. Zhou, F. R. Fronczek, J. M. Mathis, S. D. Jois, M. G. H. Vicente, *J. Med. Chem.* **2019**, *62*, 3323–3335.
- [9] a) K. Yin Zhang, K. K.-S. Tso, M.-W. Louie, H.-W. Liu, K. K.-W. Lo, *Organometallics* **2013**, *32*, 5098–5102; b) T. Papalia, G. Siracusano, I. Colao, A. Barattucci, M. C. Aversa, S. Serroni, G. Zappala, S. Campagna, M. T. Scior-



- tino, F. Puntoriero, P. Bonaccorsi, *Dyes Pigm.* **2014**, *110*, 67–71; c) D.-T. Shi, D. Zhou, Y. Zang, J. Li, G.-R. Chen, T. D. James, X. P. He, H. Tian, *Chem. Commun.* **2015**, *51*, 3653–3655; d) C. S. Wong, S. Hoogendoorn, G. A. van der Marel, H. S. Overkleeft, J. D. C. Codee, *ChemPlusChem* **2015**, *80*, 928–937; e) E. Calatrava-Pérez, S. A. Bright, S. Achermann, C. Moylan, M. O. Senge, E. B. Veale, D. C. Williams, T. Gunlaugsson, E. M. Scanlan, *Chem. Commun.* **2016**, *52*, 13086–13089; f) A. L. Nguyen, K. E. Griffin, Z. Zhou, F. R. Fronczek, K. M. Smith, M. G. H. Vicente, *New J. Chem.* **2018**, *42*, 8241–8246.
- [10] a) L. Dong, Y. Zang, D. Zhou, X.-P. He, G.-R. Chen, T. D. James, J. Li, *Chem. Commun.* **2015**, *51*, 11852–11855; b) F. Liu, P. Tang, R. Ding, L. Liao, L. Wang, M. Wang, J. Wang, *Dalton Trans.* **2017**, *46*, 7515–7522.
- [11] a) A. Louret, K. Burgess, *Chem. Rev.* **2007**, *107*, 4891–4932; b) R. Ziessel, G. Ulrich, A. Harriman, *New J. Chem.* **2007**, *31*, 496–501; c) G. Ulrich, R. Ziessel, A. Harriman, *Angew. Chem. Int. Ed.* **2008**, *47*, 1184–1201; *Angew. Chem.* **2008**, *120*, 1202–1219.
- [12] a) D. Fahy, M. N. M. E. Sanad, K. Duscha, M. Lyons, F. Liu, P. Bozhkov, H.-H. Kunz, J. Hu, H. E. Neuhaus, P. G. Steel, A. Smertenko, *Sci. Rep.* **2017**, *7*, 39069; b) S. C. Alexander, K. N. Busby, C. M. Cole, C. Y. Zhou, N. K. Devaraj, *J. Am. Chem. Soc.* **2015**, *137*, 12756–12759; c) J. Yang, J. Seckute, C. M. Cole, N. K. Devaraj, *Angew. Chem. Int. Ed.* **2012**, *51*, 7476–7479; *Angew. Chem.* **2012**, *124*, 7594–7597; d) N. K. Devaraj, S. Hilderband, R. Upadhyay, R. Mazitschek, R. Weissleder, *Angew. Chem. Int. Ed.* **2010**, *49*, 2869–2872; *Angew. Chem.* **2010**, *122*, 2931–2934.
- [13] a) M. L. Agazzi, M. B. Ballatore, A. M. Durantini, E. N. Durantini, A. C. Tomé, *J. Photochem. Photobiol. C* **2019**, *40*, 21–48; b) S. Kolemen, E. U. Akkaya, *Coord. Chem. Rev.* **2018**, *354*, 121–134; c) T. Kowada, H. Maeda, K. Kikuchi, *Chem. Soc. Rev.* **2015**, *44*, 4953–4972.
- [14] a) K. Villadsen, M. C. Martos-Maldonado, K. J. Jensen, M. B. Thygesen, *ChemBioChem* **2017**, *18*, 574–612; b) X.-P. He, Y.-L. Zeng, Y. Zang, J. Li, R. A. Field, G.-R. Chen, *Carbohydr. Res.* **2016**, *429*, 1–22.
- [15] M. M. Nielsen, C. M. M. Pedersen, *Chem. Rev.* **2018**, *118*, 8285–8358.
- [16] M. Schelhaas, H. Waldmann, *Angew. Chem. Int. Ed.* **1999**, *38*, 2056–2083; *Angew. Chem.* **1999**, *118*, 2192–2219.
- [17] a) A. M. Gómez, *Reaction at Oxygen Atoms in Glycoscience*, 2nd ed. (Eds.: B. Fraser-Reid, K. Tatsuta, J. Thiem), Springer, Berlin, **2008**, pp. 103–177; b) A. Lipták, A. Borbás, I. Bajza, *Protecting Group Manipulations in Carbohydrate Synthesis in Comprehensive Glycoscience. From Chemistry to Systems Biology* (Ed.: J. P. Kamerling), Elsevier, Amsterdam, **2007**, Chapter 1.06, pp. 203–259; c) S. Oscarson, *Protective Group Strategies in The Organic Chemistry of Sugars* (Eds.: D. E. Levy, P. Fügedi), Taylor & Francis, Boca Raton, **2006**, Chapter 3.
- [18] a) N. K. Kochetkov, *Tetrahedron* **1987**, *43*, 2389–2436; b) N. K. Kochetkov, A. J. Khorlin, A. F. Bochkov, *Tetrahedron Lett.* **1964**, *5*, 289–293.
- [19] 1,2-MeOEs are readily available by reaction of per-O-acylated pyranosyl bromides with methanol in the presence of anhydrous sodium bicarbonate, according to S. Wei, J. Zhao, H. Shao, *Can. J. Chem.* **2009**, *87*, 1733–1737.
- [20] a) C. Uriel, J. Ventura, A. M. Gómez, J. C. López, B. Fraser-Reid, *Eur. J. Org. Chem.* **2012**, 3122–3131; b) C. Uriel, J. Ventura, A. M. Gómez, J. C. López, B. Fraser-Reid, *J. Org. Chem.* **2012**, *77*, 795–800; c) C. Uriel, P. Rijo, A. S. Fernandes, A. M. Gómez, B. Fraser-Reid, J. C. López, *Chemistry-Select* **2016**, *1*, 6011–6015.
- [21] M. del Río, F. Lobo, J. C. López, A. Oliden, J. Bañuelos, I. López-Arbeloa, I. García-Moreno, A. M. Gómez, *J. Org. Chem.* **2017**, *82*, 1240–1247.
- [22] R. I. Roacho, A. J. Metta-Magaña, E. Peña-Cabrera, K. H. Pannell, *J. Phys. Org. Chem.* **2013**, *26*, 345–351.
- [23] Y. Gabe, T. Ueno, Y. Urano, H. Kojima, T. Nagano, *Anal. Bioanal. Chem.* **2006**, *386*, 621–626.
- [24] For related access to 4,4'-dialkoxy BODIPYs, see: a) A. L. Nguyen, P. Bobadova-Parvanova, M. Hopfinger, F. R. Fronczek, K. M. Smith, M. G. H. Vicente, *Inorg. Chem.* **2015**, *54*, 3228–3236; b) A. M. Courtis, S. A. Santos, Y. Guan, J. A. Hendricks, B. Ghosh, D. M. Szantai-Kis, S. A. Reis, J. V. Shah, R. Mazitschek, *Bioconjugate Chem.* **2014**, *25*, 1043–1051; c) B. Brizet, C. Bernhard, Y. Volkova, Y. Roussel, P. D. Harvey, C. Goze, F. Denat, *Org. Biomol. Chem.* **2013**, *11*, 7729–7737; d) C. Tahtaoui, C. Thomas, F. Rohmer, P. Klotz, G. Duportail, Y. Mely, D. Bonnet, M. Hibert, *J. Org. Chem.* **2007**, *72*, 269–272.
- [25] E. V. Rummyantsev, S. N. Alyoshin, Y. S. Marfi, *Inorg. Chim. Acta* **2013**, *408*, 181–185.
- [26] a) T. Zhang, C. Ma, T. Sun, Z. Xe, *Coord. Chem. Rev.* **2019**, *390*, 76–85; b) J. Ahrens, B. Cordes, R. Wicht, B. Wolfram, M. Bröring, *Chem. Eur. J.* **2016**, *22*, 10320–10325; c) L. G. Meimetis, E. Boros, J. C. Carlson, C. Ran, P. Caravan, R. Weissleder, *Bioconjugate Chem.* **2016**, *27*, 257–263.
- [27] In this context, owing to its highest reactivity, the “simplest” unsubstituted BODIPY dye could only be obtained years after the first BODIPY derivative was described by Treibs and Kreuzer, in 1968. See: a) A. Treibs, F.-H. Kreuzer, *Justus Liebigs Ann. Chem.* **1968**, *718*, 208–223; and b) I. J. Arroyo, R. Hu, G. Merino, B. Z. Tang, E. Peña-Cabrera, *J. Org. Chem.* **2009**, *74*, 5719–5722; c) A. Schmitt, B. Hinkeldey, M. Wild, G. Jung, *J. Fluoresc.* **2009**, *19*, 755–758; d) K. Tram, H. Yan, H. A. Jenkins, S. Vassiliv, D. Bruce, *Dyes Pigm.* **2009**, *82*, 392–395.
- [28] a) I. García-Moreno, A. Costela, L. Campo, R. Sastre, F. Amat-Guerri, M. Liras, F. López Arbeloa, J. Bañuelos Prieto, I. López Arbeloa, *J. Phys. Chem. A* **2004**, *108*, 3315–3323; b) S. Mula, A. K. Ray, M. Banerjee, T. Chaudhuri, K. Dasgupta, S. Chattopadhyay, *J. Org. Chem.* **2008**, *73*, 2146–2154.
- [29] I. V. Aksenova, R. T. Kuznetsova, E. N. Tel'minov, G. V. Mayer, E. V. Antina, M. B. Berezin, *Russ. J. Phys. Chem.* **2016**, *90*, 349–355.
- [30] E. Bodio, C. Goze, *Dyes Pigm.* **2019**, *160*, 700–710.
- [31] L. Yang, R. Simionescu, A. Lough, H. Yan, *Dyes Pigm.* **2011**, *91*, 264–267.
- [32] a) L. Li, B. Nguyen, K. Burgess, *Bioorg. Med. Chem. Lett.* **2008**, *18*, 3112–3116; b) G. Duran-Sampedro, I. Esnal, A. R. Agarrabeitia, J. Bañuelos Prieto, L. Cerdán, I. García-Moreno, A. Costela, I. Lopez-Arbeloa, M. J. Ortiz, *Chem. Eur. J.* **2014**, *20*, 2646–2653; c) A. L. Nguyen, F. R. Fronczek, K. M. Smith, M. G. H. Vicente, *Tetrahedron Lett.* **2015**, *56*, 6348–6351.
- [33] a) M. Wang, M. G. H. Vicene, D. Mason, P. Bobadova-Parvanova, *ACS Omega* **2018**, *3*, 5502–5510; b) A. L. Nguyen, M. Wang, P. Bobadova-Parvanova, Q. Do, Z. Zhou, F. R. Fronczek, K. M. Smith, M. G. H. Vicente, *J. Porphyrins Phthalocyanines* **2016**, *20*, 1409–1419.
- [34] For an overview of the reactivity of the BODIPY core, including its reactivity, at C-2 and C-6, toward electrophilic reagents, see: a) N. Boens, B. Verbelen, W. Dehaen, *Eur. J. Org. Chem.* **2015**, 6577–6595; b) N. Boens, B. Verbelen, M. J. Ortiz, L. Jiao, W. Dehaen, *Coord. Chem. Rev.* **2019**, *399*, 213024.
- [35] Compound **10**, was prepared according to our methodology (ref. [21]), in a one-pot procedure from isophthalide and 2,4-dimethyl-3-ethyl pyrrole. See also: A. Oliden, R. Sola-Llano, J. Bañuelos, I. García-Moreno, C. Uriel, J. C. Lopez, A. M. Gomez, *Front. Chem.* **2019**, *7*, 801.
- [36] *Protecting groups. Strategies and Applications in Carbohydrate Chemistry* (Ed.: S. Vidal), Wiley-VCH, Weinheim, **2019**.
- [37] M. Yu, J. K.-H. Wong, C. Tang, P. Turner, M. H. Todd, P. J. Rutledge, *Beilstein J. Org. Chem.* **2015**, *11*, 37–41.
- [38] a) J. O. Huh, Y. Do, M. H. Lee, *Organometallics* **2008**, *27*, 1022–1025; b) G. Meng, S. Velayudham, A. Smith, R. Luck, H. Liu, *Macromolecules* **2009**, *42*, 1995–2001; A. Koskun, E. U. Akkaya, *Tetrahedron Lett.* **2004**, *45*, 4947–4949.
- [39] a) R. R. Schmidt, K.-H. Jung, in *Preparative Carbohydrate Chemistry* (Ed.: S. Hanessian), Marcel-Dekker, New York, **1997**, pp. 283–312; b) R. R. Schmidt, W. Kinzy, *Adv. Carbohydr. Chem. Biochem.* **1994**, *50*, 21–123.
- [40] a) J. D. C. Codée, R. E. J. N. Litjens, L. J. van den Bos, H. S. Overkleeft, G. A. van der Marel, *Chem. Soc. Rev.* **2005**, *34*, 769–782; b) P. J. Garegg, *Adv. Carbohydr. Chem. Biochem.* **1997**, *52*, 179–266; c) P. Fügedi, P. J. Garegg, H. Loenn, T. Norberg, *Glycoconjugate J.* **1987**, *4*, 97–108.
- [41] H. Paulsen, *Angew. Chem. Int. Ed. Engl.* **1982**, *21*, 155–173; *Angew. Chem.* **1982**, *94*, 184–201.
- [42] a) M. Mach, U. Schlueter, F. Mathew, B. Fraser-Reid, K. C. Hazen, *Tetrahedron* **2002**, *58*, 7345–7354; b) B. Fraser-Reid, J. C. López, *Orthoesters and Related Derivatives in Handbook of Chemical Glycosylation* (Ed.: A. V. Demchenko), Wiley-VCH, Weinheim, **2008**; pp. 381–416.
- [43] a) B. Fraser-Reid, J. C. López in *Handbook of Chemical Glycosylation: Advances in Stereoselectivity and Therapeutic Relevance* (Ed.: A. V. Demchenko), Wiley-VCH, Weinheim, **2008**, pp. 1–29; b) D. R. Mootoo, P. Konradsson, U. Udodong, B. Fraser-Reid, *J. Am. Chem. Soc.* **1988**, *110*, 5583–5584.
- [44] K. N. Jayaprakash, B. Fraser-Reid, *Org. Lett.* **2004**, *6*, 4211–4214.
- [45] J. C. López, A. M. Gómez, C. Uriel, B. Fraser-Reid, *Tetrahedron Lett.* **2003**, *44*, 1417–1420.
- [46] J. D. C. Codée, R. E. J. N. Litjens, R. den Heeten, H. S. Overkleeft, J. H. van Boom, G. A. van der Marel, *Org. Lett.* **2003**, *5*, 1519–1522
- [47] F. Roussel, M. Takhi, R. R. Schmidt, *J. Org. Chem.* **2001**, *66*, 8540–8548.

- [48] There are literature examples on the stability of substituted BODIPYs under hydrogenation conditions, see: a) H. Sunahara, Y. Urano, H. Kojima, T. Nagano, *J. Am. Chem. Soc.* **2007**, *129*, 5597–5604; b) D. P. Kennedy, C. M. Kormos, S. C. Burdette, *J. Am. Chem. Soc.* **2009**, *131*, 8578–8586; c) T. Komatsu, Y. Urano, Y. Fujikawa, T. Kobayashi, H. Kojima, T. Terai, K. Hanaoka, T. Nagano, *Chem. Commun.* **2009**, 7015–7017.
- [49] a) J. C. López, A. Agocs, C. Uriel, A. M. Gómez, B. Fraser-Reid, *Chem. Commun.* **2005**, 5088–5090; b) C. Uriel, A. Agocs, A. M. Gómez, J. C. López, B. Fraser-Reid, *Org. Lett.* **2005**, *7*, 4899–4902; c) C. Uriel, A. M. Gómez, J. C. López, B. Fraser-Reid, *Org. Biomol. Chem.* **2012**, *10*, 8361–8370.
- [50] F. López Arbeloa, J. Bañuelos, V. Martínez, T. Arbeloa, I. López Arbeloa, *Int. Rev. Phys. Chem.* **2005**, *24*, 339–374.
- [51] Gaussian 16, Revision C.01, M. J. Frisch, G. W. Trucks, H. B. Schlegel, G. E. Scuseria, M. A. Robb, J. R. Cheeseman, G. Scalmani, V. Barone, G. A. Petersson, H. Nakatsuji, X. Li, M. Caricato, A. V. Marenich, J. Bloino, B. G. Janesko, R. Gomperts, B. Mennucci, H. P. Hratchian, J. V. Ortiz, A. F. Izmaylov, J. L. Sonnenberg, D. Williams-Young, F. Ding, F. Lipparini, F. Egidi, J. Goings, B. Peng, A. Petrone, T. Henderson, D. Ranasinghe, V. G. Zakrzewski, J. Gao, N. Rega, G. Zheng, W. Liang, M. Hada, M. Ehara, K. Toyota, R. Fukuda, J. Hasegawa, M. Ishida, T. Nakajima, Y. Honda, O. Kitao, H. Nakai, T. Vreven, K. Throssell, J. A. Montgomery, Jr., J. E. Peralta, F. Ogliaro, M. J. Bearpark, J. J. Heyd, E. N. Brothers, K. N. Kudin, V. N. Staroverov, T. A. Keith, R. Kobayashi, J. Normand, K. Raghavachari, A. P. Rendell, J. C. Burant, S. S. Iyengar, J. Tomasi, M. Cossi, J. M. Millam, M. Klene, C. Adamo, R. Cammi, J. W. Ochterski, R. L. Martin, K. Morokuma, O. Farkas, J. B. Foresman, D. J. Fox, Gaussian, Inc., Wallingford CT, **2016**.
- [52] F. Jensen, *J. Phys. Chem. A* **2017**, *121*, 6104–6107

---

Manuscript received: December 23, 2019

Accepted manuscript online: January 30, 2020

Version of record online: March 13, 2020

# FormylBODIPYs by PCC-Promoted Selective Oxidation of $\alpha$ -MethylBODIPYs. Synthetic Versatility and Applications

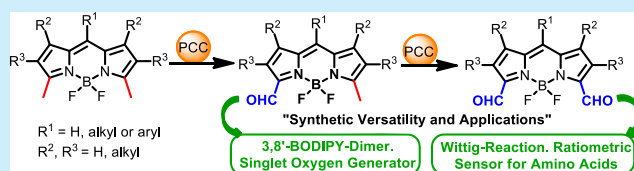
Ágata Ramos-Torres,<sup>†</sup> Edurne Avellanal-Zaballa,<sup>‡</sup> Alejandro Prieto-Castañeda,<sup>†</sup> Fernando García-Garrido,<sup>†</sup> Jorge Bañuelos,<sup>‡</sup> Antonia R. Agarrabeitia,<sup>\*,†</sup> and María J. Ortiz<sup>\*,†</sup>

<sup>†</sup>Departamento de Química Orgánica, Facultad de Ciencias Químicas, Universidad Complutense de Madrid, Ciudad Universitaria s/n, 28040 Madrid, Spain

<sup>‡</sup>Departamento de Química-Física, Universidad del País-Vasco-EHU, Apartado 644, 48080 Bilbao, Spain

**S** Supporting Information

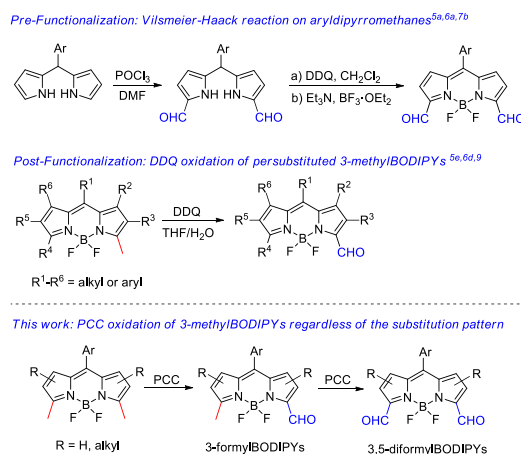
**ABSTRACT:** An efficient synthesis of formylBODIPYs has been established based on an oxidation with PCC of 3-methylBODIPYs. It has been demonstrated that this reagent can oxidize methyl groups at such position of the BODIPY core, regardless of its substitution pattern. Moreover, through this procedure it is possible to synthesize 8-aryl-3,5-diformylBODIPYs, which are otherwise difficult to obtain. These precursors have been functionalized to develop fluorescent sensors of amino acids or photosensitizers for singlet oxygen generation.



Fifty years ago, when Treibs and Kreuzer<sup>1</sup> accidentally discovered a small but very versatile molecule, 4,4-difluoro-4-bora-3a,4a-diaza-s-indacene (known as BODIPY), they could not imagine the importance of this discovery today. This fluorophore was not studied for 20 years, and it was not until the beginning of the 1990s when this type of dye began to be studied in depth.<sup>2</sup> Since then, development of these dyes has grown exponentially.<sup>3</sup> Currently, they are the cornerstone of many ongoing research projects around the world to modify their functionalization with one main objective: to obtain BODIPYs with improved properties for the different and important applications available with this smart and multi-functional chromophore.<sup>4</sup>

Within the research carried out in our group, we were interested in obtaining 3-formyl- and 3,5-diformylBODIPYs, since they are versatile precursors in various synthetic routes<sup>5</sup> and also show notable applications as sensors.<sup>6</sup> The data collected in the literature show that 2-formyl- and 2,6-diformylBODIPYs can be easily obtained by post-functionalization of the BODIPY core through the Vilsmeier–Haack reaction.<sup>7</sup> This same reaction can be used to obtain 3-formyl- and 3,5-diformylBODIPYs, although in this case, as far as we are aware, the reaction has been carried out in *meso*-aryldipyrromethanes, obtained only from the corresponding benzaldehyde and unsubstituted pyrroles (Scheme 1).<sup>5a,6a,7b</sup> Another method for obtaining 3-formylBODIPYs was described by Boyer et al. in 1994 by means of an oxidation reaction of the commercial BODIPY PM567 using 2,3-dichloro-5,6-dicyano-1,4-benzoquinone (DDQ) as an oxidizing agent.<sup>8</sup> The authors indicate that it is not possible to obtain the formyl derivative if there is any free position in the BODIPY skeleton. Thus, when they carried out the study with

## Scheme 1. Strategies for the Synthesis of 3-Formyl and 3,5-DiformylBODIPYs, and Our Observations



1,3,5,7,8-pentamethyl- and 1,2,3,5,6,7-hexamethylBODIPYs, they only observed complex mixtures of products.

Subsequently, other authors, following this same protocol, have obtained a few 8-aryl-3-formylBODIPYs with all positions of the BODIPY core substituted by alkyl or aryl groups (Scheme 1).<sup>5c,6d,9</sup>

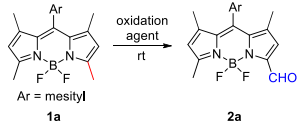
We were interested in the use of this last method since a post-functionalization of the BODIPY is highly attractive because it avoids the manipulation of unstable pyrroles and allows us to work with a larger variety of derivatives. Therefore, we wanted to check whether oxidation with DDQ was possible

Received: April 26, 2019

Published: June 10, 2019

in 8-arylBODIPYs with hydrogens in the 2,6-positions of the skeleton. First, we carried out the reaction of 8-mesityl-1,3,5,7-tetramethylBODIPY (**1a**) with this oxidizing agent, under the conditions described in the literature for referable compounds (THF/H<sub>2</sub>O, rt) for 24 h, not observing the desired product (Table 1, entry 1). By increasing the time to 48 h, it was possible to isolate 10% of the corresponding formyl derivative **2a**, recovering 30% of the starting compound (Table 1, entry 2).

Table 1. Optimization of Reaction Conditions

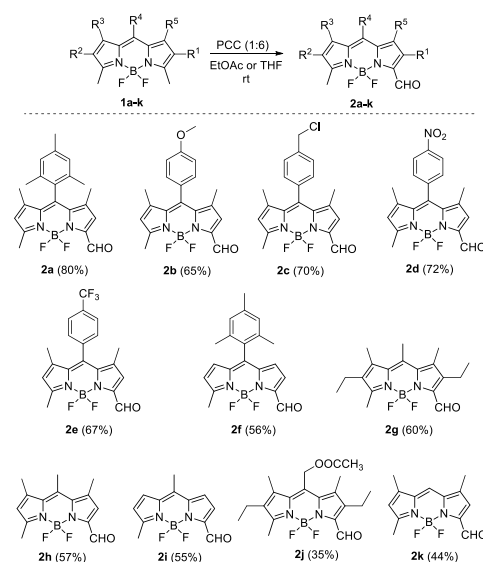


entry	oxidation agent (equiv)	solvent	time (h)	% yield
1	DDQ (1:4)	THF/H <sub>2</sub> O	24	traces
2	DDQ (1:4)	THF/H <sub>2</sub> O	48	10
3	PCC (1:4)	THF/H <sub>2</sub> O	48	traces
4	PCC (1:6)	THF	24	55
5	PCC (1:9)	THF	24	45
6	PCC (1:6)	DCM	24	25
7	PCC (1:6)	EtOAc	24	80
8	DDQ (1:6)	EtOAc	24	traces

However, during the course of this study, Kang et al.<sup>10</sup> reported the synthesis of 3-formyl-8-(*p*-methoxyphenyl)-1,5,7-trimethylBODIPY by oxidation with DDQ of the corresponding 1,3,5,7-tetramethylBODIPY, with a yield of 60%. This result contrasted with that observed by us for the BODIPY **1a** (Table 1, entries 1 and 2). In order to clarify this discrepancy, we reinvestigated the results under the same conditions indicated by the authors, and we isolated only traces of the 3-formyl derivative. A longer reaction time (72 h) allowed us to isolate the said derivative but with a 15% yield, similar to that obtained by us with **1a**. Considering the observed results, we set out to investigate the possibility of using another oxidizing agent that would allow the optimization of this type of reaction. Therefore, we chose to carry out the reaction in the presence of pyridinium chlorochromate (PCC) as an alternative oxidizing agent. The reaction of **1a** with PCC in the conditions above employed, for 48 h, did not lead to the expected product **2a** (Table 1, entry 3). However, when the reaction was carried out with PCC in a 1:6 ratio, using THF as solvent at rt, it allowed us to obtain **2a** with a 55% yield (Table 1, entry 4) and recover 20% of the starting compound. A larger amount of PCC (1:9) was also added, but no improvement was observed (Table 1, entry 5). Screening of the reaction solvent revealed that EtOAc afforded the best result (Table 1, entries 6 and 7). Then, DDQ was used under the optimal reaction conditions, and **2a** was obtained only in traces (Table 1, entry 8).

Next, we further investigated the scope of the reaction using a variety of 3,5-dimethylBODIPYs (**1**; see Figure S1) under optimized conditions, using EtOAc as solvent (Scheme 2). Thus, the reaction of 8-(*p*-methoxyphenyl)-1,3,5,7-tetramethylBODIPY (**1b**) with PCC during 24 h gave a 65% yield of the corresponding 3-formylBODIPY (**2b**), which indicates that, according to the results obtained by us, PCC is a better oxidizing agent than DDQ in this process. Similarly, 8-(*p*-chloromethylphenyl)-1,3,5,7-tetramethylBODIPY (**1c**), 8-(*p*-

Scheme 2. Scope of the Oxidation Reaction of 3-MethylBODIPYs

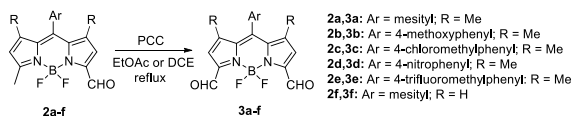


nitrophenyl)-1,3,5,7-tetramethylBODIPY (**1d**), and 8-(*p*-trifluoromethylphenyl)-1,3,5,7-tetramethylBODIPY (**1e**) were converted to the corresponding 3-formyl derivatives **2c–e** in good yields (ca. 70%). Considering these results, we carried out the reaction over a 3,5-dimethylBODIPY with hydrogens in the 1,2,6,7-positions. Thus, treatment of 8-mesityl-3,5-dimethylBODIPY (**1f**) under the same conditions allowed us to obtain **2f** in 56% yield (Scheme 2).

At this point, we were interested in checking the possibility of extending this reaction to aliphatic BODIPYs. Then, the reaction was carried out using alkylBODIPYs (**1g–k**) with different degrees and types of substitution, under the same conditions, but with THF or EtOAc as solvents (see the SI), obtaining in all cases the corresponding 3-formyl derivatives (**2g–k**) in 35–60% yields (Scheme 2). These additional examples add further support to the proposal that PCC is a versatile and general oxidant that allows aldehydes to be obtained in the 3-position of the BODIPY core, regardless of the degree and type of substitution, contrary to previous reports.<sup>8</sup>

Encouraged by these interesting results, we explored the possibility of obtaining 8-aryl-3,5-diformylBODIPYs. We chose to start our study with **1a** as a model substrate, but unfortunately, only traces of **3a**, together with a low yield of **2a** and a complex mixture of unidentifiable polar compounds, were observed when the reaction was carried out at reflux with different solvents and **1a**/PCC ratios (Table S1). In contrast, when 3-formylBODIPY **2a** was refluxed in EtOAc or DCE with PCC (1:6 ratio) the desired product **3a** was obtained with a yield about 40%. No transformation was observed by treatment of **2a** with DDQ under the above-mentioned conditions (Table S1). Next, we focus on the extent of the synthesis of 8-aryl-3,5-diformylBODIPYs using the corresponding 3-formylBODIPYs as starting material. The reactions of **2b–f** gave the corresponding products **3b–f** with yields of 30–40% (Scheme 3). These results are important since the 8-aryl-3,5-diformylBODIPYs, which are very useful synthetic intermediates, cannot be obtained by oxidation with DDQ. In addition, with exception of **3j**, synthesis by direct formylation of 8-

### Scheme 3. Synthesis of 8-Aryl-3,5-diformylBODIPYs by Oxidation with PCC of 3-FormylBODIPYs

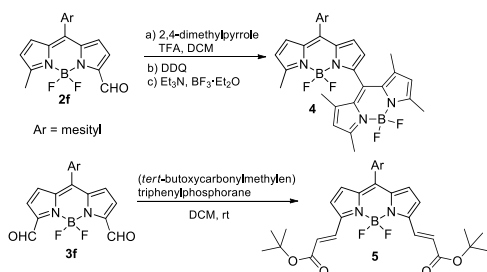


aryldiopyromethanes is not trivial either, since it requires using pyrrole precursors that are difficult to obtain.

The photophysical properties of the reference BODIPYs **1a–k** (Scheme 1) are ruled by the *meso*-substituent. As expected, alkylated BODIPYs (**1g–i** and **1k**) are highly fluorescent (higher than 80%, Table S2).<sup>4c</sup> Dye **1j** retains notable emission but is red-shifted (around 50 nm, Table S2) owing to the reduced energy gap provided by the electron acceptor 8-acetoxy methyl group.<sup>4c</sup> Arylation at the *meso* position (**1a–f**) has a minor impact in the spectral band positions but triggers the fluorescence response. Thus, the sterical hindrance provided by the adjacent 1,7-methyls avoids nonradiative pathways associated with the aryl-free motion,<sup>4c</sup> leading to notable emission (up to 100% in **1a** and around 40–50% in the rest, Table S2), regardless of the functionalization of the 8-phenyl group (**1a–c** and **1e–f**). The only exception is dye **1d**, where the attachment of the electron acceptor nitro at the constrained 8-phenyl drastically decreases the fluorescence efficiency (down to almost 0, Table S2), according to the quenching induced by the promoted intramolecular charge transfer (ICT) processes. The 3-monoformylation of these compounds (**2a–k**, Scheme 2) implies a slight bathochromic shift of the spectral bands and a reduction of the fluorescence efficiency together with faster lifetimes (Table S2). This last trend is strikingly stronger for the dyes featuring alkylated cores (**2h** and **2k** and mainly **2g** and **2j**).<sup>6c</sup> Such trend is strengthened upon further formylation (3,5-diformylBODIPYs **3a–f**, Scheme 3). The only clear exception to the rule are the nitro derivatives **2d** and **3d**, where formylation at the opposite positions to the nitro group seems to soften the ICT and ameliorates the fluorescence efficiency (Table S2).

At this point, taking advantage of the chemical versatility afforded by the formyl group, **2f** was easily converted to the 3–8' dimer **4** in 20% yield (Scheme 4). It should be noted that

### Scheme 4. Synthesis of 3,8'-BODIPY Dimer and 3,5-Bis(3-*tert*-butoxy-3-oxoprop-1-en-1-yl)BODIPY



only one similar dimer, albeit less constrained around the 3–8' linkage, has been previously described.<sup>11</sup> Such steric hindrance avoids electronic couplings, placing both chromophoric subunits orthogonal. This disposition favors ICT processes according to a symmetry-breaking mechanism (SBCT). Thus, the spectral band positions match those of the monomers and the fluorescence response is very low (almost 0, Table S3). Just

in apolar solvent the red-shifted and weak emission of the ICT (at 640 nm) can be hardly detected, together with the strongly quenched emission from the locally excited (LE) state at 540 nm. However, it is known that the photoinduced SBCT can populate the triplet state after charge recombination.<sup>4b</sup> Therefore, we measured the singlet oxygen generation as up to 54% in toluene (Table S3). Thus, this dyad behaves as a halogen-free singlet oxygen photosensitizer with potential for light-driven therapeutic purposes in cancer diseases.

On the other hand, in view of the reported viability of formylated dyes as sensors for amino acids (AA),<sup>6c,d,12</sup> we decided to test this possibility for the dyes listed in Schemes 2 and 3. Thus, we performed a screening of the sensibility of their photophysical signatures to the presence of a fixed amount of AA, like cysteine (CYS), homocysteine (HCYS), and glutathione (GSH) in buffered water–ethanol mixtures simulating the physiological environment (Figure S2). From such a systematic study we concluded that just the diformylated **3d** works as an AA sensor. Indeed, its fluorescence intensity decreases progressively with the content of AA in the media, being more prominent for HCYS and GSH (Figures S3–S6). We hypothesize that the nucleophilic attack of the amine or thiol groups to the formyls places electron-donor groups at the 3,5-methines,<sup>6d</sup> increasing the push–pull character and enhancing the fluorescence quenching by the nitro-enabling ICT. However, those sensors based a switch off of the fluorescence signal upon detection of the target analyte are not the best owing to the competing degradation of the dyes under prolonged irradiation.

Therefore, we decided to convert one of these 3,5-diformylBODIPYs into the corresponding  $\alpha,\beta$ -unsaturated diester, which could be used for specific sensing of thiols.<sup>13</sup> Thus, **3f** has been employed in a Wittig reaction, affording **5** in 56% yield (Scheme 4), and we carried out the study of this dye as sensor for AA. The resonance interaction of such a conjugated moiety increases the  $\pi$ -system delocalization in **5** and induces a pronounced bathochromic shift of the spectral bands (around 90 nm, Table S2). The addition of AA provokes noticeable changes in the profile of the spectral bands (HCYS in Figure 1, CYS in Figure S7, and GSH in Figure S8). Indeed, the main band, both in absorption (590 nm) and fluorescence (600 nm) spectra, decreases in favor of new growing hypsochromic bands (550 nm in absorption and 560 nm in

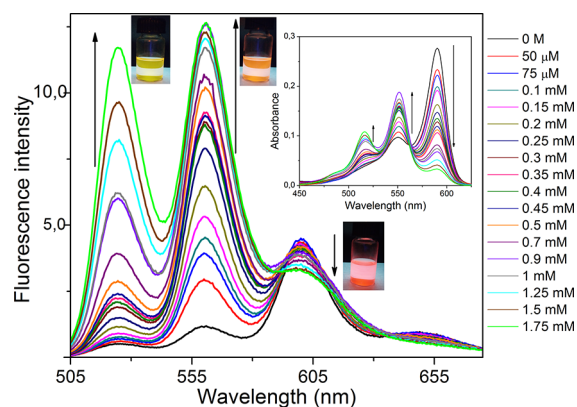


**Figure 1.** Fluorescence spectra of **5** ( $5 \mu\text{M}$ ) at different concentrations of HCYS in HEPES/ethanol (1:1). Photographs under UV lamp at representative amounts of HCYS for each emission band. Inset: corresponding absorption spectra.

fluorescence, and 515 and 525 nm, respectively, at high amounts, around mM, of AA), being especially notorious for CYS and HCYS (sensitivity down to micromolar level, Figure 1). It should be noted that this ratiometric sensor 5 provides up to three channels for detection of AA both by absorption and mainly fluorescence spectroscopy since the new hypsochromic bands induced by AA show higher fluorescence response. We believe that the nucleophilic attack of the AA at the vinyl group of compound 5 breaks the resonant interaction at the 3 and 5 positions, explaining the decline of the long-wavelength band and the growth of the short-wavelength ones. Indeed, the shorter wavelength absorption and emission match those expected for the 3,5-alkylated BODIPYs.

In summary, we have designed a straightforward route to obtain 3-mono- and 3,5-diformylated BODIPYs by oxidation with PCC of  $\alpha$ -methylBODIPYs regardless of the substitution pattern. These functionalizations pave the way for the design of multifunctional dyes for advanced photonic applications. Thus, the attachment of a second BODIPY unit leads to singlet oxygen photosensitizers suitable for photodynamic therapy. On the other hand, the insertion of unsaturated esters leads to a ratiometric and sensitive sensor for AA. Further work in this area is in progress.

## ■ ASSOCIATED CONTENT

### Supporting Information

The Supporting Information is available free of charge on the ACS Publications website at DOI: 10.1021/acs.orglett.9b01465.

Experimental procedures, characterization of products, photophysical data, AA sensing experiments, and  $^1\text{H}$  and  $^{13}\text{C}$  NMR (PDF)

## ■ AUTHOR INFORMATION

### Corresponding Authors

\*E-mail: agarrabe@ucm.es.

\*E-mail: mjortiz@quim.ucm.es.

### ORCID

Jorge Bañuelos: 0000-0002-8444-4383

María J. Ortiz: 0000-0002-0394-4045

### Notes

The authors declare no competing financial interest.

## ■ ACKNOWLEDGMENTS

We acknowledge the Spanish Ministerio de Economía y Competitividad (MAT2017-83856-C3-2-P and 3-P) and Gobierno Vasco (IT912-16) for financial support. A.R.-T., A.P.-C., F.G.-G., and E.A.-Z. thank Comunidad de Madrid and Gobierno Vasco for a postdoctoral contract, two research assistant contracts, and a predoctoral fellowship, respectively.

## ■ REFERENCES

- (1) Treibs, A.; Kreuzer, F.-H. *Liebigs Ann. Chem.* **1968**, *718*, 208–223.
- (2) (a) Shah, M.; Thangaraj, K.; Soong, M. L.; Wolford, L. T.; Boyer, J. H.; Politzer, I. R.; Pavlopoulos, T. G. *Heteroat. Chem.* **1990**, *1*, 389–399. (b) Boyer, J. H.; Haag, A. M.; Sathyamoorthi, G.; Soong, M. L.; Thangaraj, K. T.; Pavlopoulos, G. *Heteroat. Chem.* **1993**, *4*, 39–49.
- (3) Selected reviews: (a) Loudet, A.; Burgess, K. *Chem. Rev.* **2007**, *107*, 4891–4932. (b) Ulrich, G.; Ziessel, R.; Harriman, A. *Angew. Chem., Int. Ed.* **2008**, *47*, 1184–1201. (c) Boens, N.; Verbelen, B.; Dehaen, W. *Eur. J. Org. Chem.* **2015**, *2015*, 6577–6595.

(4) Selected reviews: (a) Boens, N.; Leen, V.; Dehaen, W. *Chem. Soc. Rev.* **2012**, *41*, 1130–1172. (b) Kamkaew, A.; Lim, S. H.; Lee, H. B.; Kiew, L. V.; Chung, L. Y.; Burgess, K. *Chem. Soc. Rev.* **2013**, *42*, 77–88. (c) Bañuelos, J. *Chem. Rec.* **2016**, *16*, 335–348. (d) Marfin, Y. S.; Solomonov, A. V.; Timin, A. S.; Rumyantsev, E. V. *Curr. Med. Chem.* **2017**, *24*, 2745–2772. (e) Kolemen, S.; Akkaya, E. U. *Coord. Chem. Rev.* **2018**, *354*, 121–134.

(5) (a) Pereira, N.; Serra, A. C.; Gonsalves, A. M. d'A. R.; Abrantes, M.; Laranjo, M.; Botelho, F. J. *Porphyryns Phthalocyanines* **2010**, *14*, 438–445. (b) Madhu, S.; Ravikanth, M. *Inorg. Chem.* **2012**, *51*, 4285–4292. (c) Lakshmi, V.; Ravikanth, M. *J. Org. Chem.* **2013**, *78*, 4993–5000. (d) Bill, N. L.; Lim, J. M.; Davis, C. M.; Bährin, S.; Jeppesen, J. O.; Kim, D.; Sessier, J. L. *Chem. Commun.* **2014**, *50*, 6758–6761. (e) Zhang, Y.; Swaminathan, S.; Tang, S.; García-Amorós, J.; Boulina, M.; Captain, B.; Baker, J. D.; Raymo, F. M. *J. Am. Chem. Soc.* **2015**, *137*, 4709–4719.

(6) (a) Madhu, S.; Rao, M. R.; Shaikh, M. S.; Ravikanth, M. *Inorg. Chem.* **2011**, *50*, 4392–4400. (b) Madhu, S.; Basu, S. K.; Jadhav, S.; Ravikanth, M. *Analyst* **2013**, *138*, 299–306. (c) Wu, Q.; Zhou, J.; Yu, C.; Hao, E.; Jiao, L. *New J. Chem.* **2016**, *40*, 1387–1395. (d) Wu, Q.; Wu, Y.; Zhang, M.; Yu, C.; Hao, E.; Jiao, L. *J. Porphyryns Phthalocyanines* **2016**, *20*, 444–455.

(7) (a) Jiao, L.; Yu, C.; Li, J.; Wang, Z.; Wu, M.; Hao, E. *J. Org. Chem.* **2009**, *74*, 7525–7528. (b) Yu, C.; Jiao, L.; Yin, H.; Zhou, J.; Pang, W.; Wu, Y.; Wang, Z.; Yang, G.; Hao, E. *Eur. J. Org. Chem.* **2011**, *2011*, 5460–5468.

(8) Sathyamoorthi, G.; Wolford, L. T.; Haag, A. M.; Boyer, J. H. *Heteroat. Chem.* **1994**, *5*, 245–249.

(9) (a) Haefele, A.; Zedde, C.; Retailleau, P.; Ulrich, G.; Ziessel, R. *Org. Lett.* **2010**, *12*, 1672–1675. (b) Zhao, N.; Vicente, M. G. H.; Fronczek, F. R.; Smith, K. M. *Chem. - Eur. J.* **2015**, *21*, 6181–6192.

(10) Kang, J.; Huo, F.; Zhang, Y.; Chao, J.; Glass, T. E.; Yin, C. *Spectrochim. Acta, Part A* **2019**, *209*, 95–99.

(11) Zhang, X.-F. *Dyes Pigm.* **2017**, *146*, 491–501.

(12) (a) Chen, X.; Zhou, Y.; Peng, X.; Yoon, J. *Chem. Soc. Rev.* **2010**, *39*, 2120–2135. (b) Poirel, A.; De Nicola, A.; Ziessel, R. *J. Org. Chem.* **2014**, *79*, 11463–11472.

(13) Lee, J.-J.; Lee, S.-C.; Zhai, D.; Ahn, Y.-H.; Yeo, H. Y.; Tan, Y. L.; Chang, Y.-T. *Chem. Commun.* **2011**, *47*, 4508–4510.

# Annex IV (Chapter 4) / IV. Eranskina (4. Kapituluu)

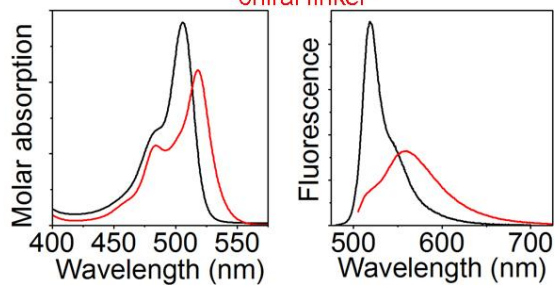
---

## Article 6 / 6. Artikuluu

Stereochemical and Steric Control of Photophysical and Chiroptical Properties in  
Bichromophoric Systems

*Chemistry - A European Journal*, 2018, 24, 3802-3815

STEREOCHEMICAL CONTROL OF  
BI-CHROMOPHORIC SYSTEMS PHOTOPHYSICS







## Bichromophoric Systems

## Stereochemical and Steric Control of Photophysical and Chiroptical Properties in Bichromophoric Systems

Alberto Blázquez-Moraleja,<sup>[a]</sup> Luis Cerdán,<sup>\*[b]</sup> Inmaculada García-Moreno,<sup>[b]</sup> Eurne Avellanal-Zaballa,<sup>[c]</sup> Jorge Bañuelos,<sup>\*[c]</sup> M. Luisa Jimeno,<sup>[d]</sup> Iñigo López-Arbeloa,<sup>[c]</sup> and Jose Luis Chiara<sup>\*[a]</sup>

**Abstract:** Stereochemical and steric control of the relative spatial arrangement of the chromophoric units in multichromophoric systems offers an interesting strategy for raising unusual and appealing light-induced emission states. To explore and exploit this strategy, a series of conformationally restricted boron-dipyrromethene (BODIPY) dimers were designed by using tartaric acid as a symmetrical connector between the boron atoms of the dyes. The variety of stereoisomeric forms available for this bis(hydroxy acid) allows the

relative spatial orientation of the chromophoric units in the dimer to be modified, which thus opens the door to modulation of the photophysical and chiroptical properties of the new bichromophoric systems. Chromophore alkylation introduces an additional level of control through distance-dependent steric interactions between the BODIPY units in the dimer, which also modulates their relative spatial disposition and properties.

## Introduction

Multichromophoric systems have been the object of intense research activity over the last decades in both natural<sup>[1]</sup> and artificial settings owing to their interesting potential applications as light-harvesting antenna<sup>[2]</sup> components for direct solar production of chemical fuels through artificial photosynthesis<sup>[3]</sup> and for the conversion of solar light into electricity in dye-sensitized solar cells.<sup>[4]</sup> In addition, multichromophores have been developed as heavy-atom-free singlet-oxygen generators for photodynamic therapy<sup>[5]</sup> and as luminescence sensors in biological research by exploiting either through-space (Förster resonance energy transfer, FRET)<sup>[6]</sup> and through-bond (through-bond energy transfer, TBET)<sup>[7]</sup> photoinduced energy transfer between the donor and acceptor chromophoric subunits or

the better wavelength separation between the exciting and the analyzing light signals (as in dark resonance energy transfer, DRET).<sup>[8]</sup>

Since their first synthesis in the late 1960s,<sup>[9]</sup> boron-complexed dipyrromethenes (BODIPYs, Figure 1) have emerged as a remarkable group of chromophores owing to their outstanding chemical, electronic, and physical properties.<sup>[10]</sup> Thus, BODI-

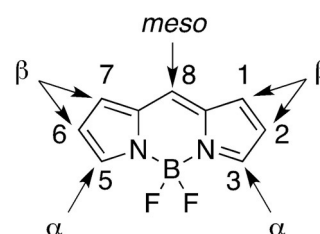


Figure 1. General structure of F-BODIPYs.

PYs exhibit exceptionally rich chemistry<sup>[11]</sup> that allows fine-tuning of their photophysical properties, including large molar absorption coefficients, sharp fluorescence emissions with high fluorescence quantum yields, good solubility in organic solvents, and excellent photostability. As a consequence, for the past three decades this family of chromophores has remained the focus of novel developments in photovoltaics, optoelectronics, nonlinear optics, bioimaging, sensing, photodynamic therapy, and theragnosis.<sup>[12]</sup> In recent years, a vast amount of work has been done on the preparation and study of multichromophoric systems based on BODIPYs, which display different phenomena and properties such as intercomponent energy transfer,<sup>[13]</sup> intramolecular charge transfer,<sup>[14]</sup> facile inter-

[a] A. Blázquez-Moraleja, Dr. J. L. Chiara  
Instituto de Química Orgánica General, IQOG-CSIC  
Juan de la Cierva 3, 28006 Madrid (Spain)  
E-mail: jl.chiara@csic.es

[b] Dr. L. Cerdán, Prof. Dr. I. García-Moreno  
Instituto Química-Física "Rocasolano", IQFR-CSIC  
Serrano 119, 28006 Madrid (Spain)  
E-mail: lcerdan@iqfr.csic.es

[c] E. Avellanal-Zaballa, Dr. J. Bañuelos, Prof. Dr. I. López-Arbeloa  
Departamento de Química Física  
Universidad del País Vasco-EHU, Facultad de Ciencias y Tecnología  
Apartado 644, 48080 Bilbao (Spain)  
E-mail: jorge.bañuelos@ehu.es

[d] M. L. Jimeno  
Centro Nacional de Química Orgánica "Manuel Lora Tamayo"  
CENQUIOR-CSIC, Juan de la Cierva 3, 28006 Madrid (Spain)

Supporting Information and the ORCID identification number(s) for the author(s) of this article can be found under <https://doi.org/10.1002/chem.201705698>.

system crossing,<sup>[14c,15]</sup> circularly polarized luminescence (CPL),<sup>[16]</sup> broadband light harvesting,<sup>[13c,g,17]</sup> redshifted emission,<sup>[14e,17c,18]</sup> and large (pseudo-)Stokes shifts.<sup>[8,19]</sup> A large variety of dimeric, oligomeric, and polymeric BODIPYs have been prepared by using different connection types between the chromophores and their properties have been studied: 1) with fused BODIPY structures,<sup>[18c,20]</sup> which show intense near infrared (NIR) absorption/emission owing to expanded  $\pi$  conjugation; 2) with direct *meso-meso*,<sup>[14f,15d]</sup>  $\beta$ - $\beta$ ,<sup>[16h,21]</sup> *meso*- $\beta$ ,<sup>[14c,15d]</sup> or  $\alpha$ - $\alpha$ <sup>[19a,22]</sup> carbon-carbon single-bond connections between the dipyrromethene systems, which behave as heavy-atom-free singlet-oxygen photosensitizers or CPL emitters; 3) with linear aliphatic carbon scaffolds linked through carbon-carbon or carbon-heteroatom single bonds, which show solvent- and spacer-switchable red emission,<sup>[14d,e,23]</sup> 4) with unsaturated (alkenyl, alkynyl, aryl, or heteroaryl) connectors linked through carbon-carbon or carbon-heteroatom single bonds,<sup>[7e,19b,24]</sup> which show redshifted emission maxima or interesting electrogenerated chemiluminescence (ECL) properties; and 5) with heteroatomic connectors (N=N,<sup>[25]</sup> S and S-S,<sup>[26]</sup> or Si<sup>[27]</sup>), displaying NIR light absorption and/or increased fluorescence quantum yields. In addition to these linear or two-dimensional systems, 3D assemblies of BODIPYs have also been described, including flexible dendrimers<sup>[13h,28]</sup> and systems with a 3D-shape-persistent structure based on fullerene,<sup>[29]</sup> cubic octasilsesquioxane,<sup>[30]</sup> or triptycene<sup>[31]</sup> central scaffolds, and they have provided information on the effect of appropriate alignment of transition dipole moment vectors on the efficiency of energy-transfer processes.

We herein report a series of conformationally restricted BODIPY dimers following a dynamic and versatile synthesis method based on the following:

- 1) High conformational rigidity of the bichromophoric system with orthogonal disposition of the substituents with respect to the mean plane of the boradiazaindacene unit, which has proven key to raise light-induced exotic emission states.<sup>[32]</sup>
- 2) Substitution on the boron atom of the BODIPYs, which has a negligible effect on the photophysical properties that, consequently, will only be affected by the geometry of the bichromophoric system.
- 3) The use of tartaric acid as a symmetrical connector between the boron atoms of both dyes.<sup>[33]</sup> Although tartaric acid has played a central role in the development of organic stereochemistry and optically active compounds, it has very scarcely been used for the preparation of bichromophoric systems.<sup>[34]</sup> Given that tartaric acid exists in three stereoisomeric forms, a pair of enantiomers (*R,R* and *S,S*) and an achiral *meso* isomer (*R,S*), the attached chromophores will be positioned in different relative spatial orientations, which will consequently affect their photophysical and chiroptical properties.
- 4) The introduction of alkyl substituents on the chromophore skeleton should have a significant influence on the conformational equilibrium of the dimers as a result of steric factors, which will thus modulate their photophysics accordingly.

We describe below the synthesis, conformational properties in solution, crystal structure, quantum-chemical simulations, and the photophysical, electrochemical, laser, and chiroptical properties of a series of *O*-BODIPY dimers with a tartaric acid connector and the effect of stereochemistry and chromophore alkylation on their photophysical properties in comparison with their corresponding monomeric analogues.

## Results and Discussion

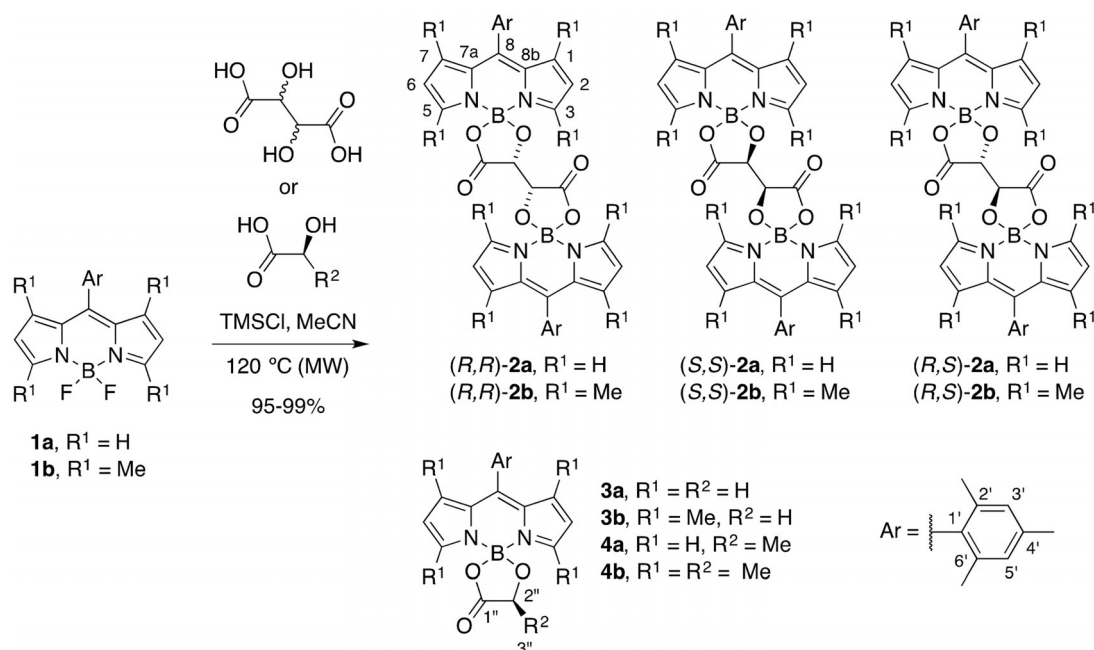
### Synthesis of compounds

The new *O*-BODIPYs included in this work were readily prepared by following our recently described protocol for the one-step synthesis of *O*-BODIPYs with a rigid *B*-spiranic 4,4-diacyloxy or 4-acyloxy-4-alkoxy substitution pattern from the corresponding *F*-BODIPY and a dicarboxylic acid or an  $\alpha/\beta$ -hydroxy acid, respectively.<sup>[32]</sup> Thus, a stoichiometric mixture of *F*-BODIPY **1** and the corresponding  $\alpha$ -hydroxy acid in anhydrous MeCN containing an excess amount of TMSCl (20–40 equiv.) was heated under microwave irradiation (120 °C, 0.5–8 h) to afford the targeted *O*-BODIPY in almost quantitative yield (95–99%) after solvent removal and chromatographic purification (Scheme 1). The three possible stereoisomeric L-(–)/(*R,R*)-, D-(+)/(*S,S*)-, and *meso*-(*R,S*)-tartaric acids were used for the preparation of bichromophoric systems **2**, whereas glycolic acid and L-(–)-lactic acid were selected to obtain model monomeric analogues **3** and **4**, respectively, for comparative purposes.

### Structure and conformation of the bichromophoric systems

We studied the conformational properties of bis-BODIPYs **2** both experimentally, in solution and in the solid state, as well as through theoretical calculations. The conformational preferences of tartaric acids and their derivatives have been the object of extensive previous studies.<sup>[34,35]</sup> The fundamental conformational characteristic of these molecules is the extended (*trans*) or bent (*gauche*) orientation of the four-carbon chain. In dimers **2**, covalent attachment of each  $\alpha$ -hydroxy acid moiety of tartaric acid to the boron atom of a BODIPY unit reduces the number of total attainable conformers of the molecule by fixing the carbonyl group in an orientation that is *anti* to its vicinal  $\alpha$ -C–O bond in the 1,3,2-dioxaborolane ring. Thus, only a single degree of freedom remains for the conformational equilibrium of **2** through rotation around the central carbon-carbon bond of the tartrate system. Figure 2 shows the Newman projections of the three possible staggered conformers of the *meso* isomer and one of the enantiomers of **2**, as defined by the torsion angle  $\alpha$ .

Conformational data were obtained in solvents of different polarity by using <sup>1</sup>H NMR spectroscopy (see the Supporting Information). For symmetry reasons, the <sup>3</sup>J<sub>H,H</sub> coupling constants of the tartrate hydrogen atoms could not be directly measured in compounds **2**, and thus, the <sup>13</sup>C satellite signals were employed.<sup>[36]</sup> The low <sup>3</sup>J<sub>H,H</sub> values measured for these protons in chiral derivatives (*R,R*)- and (*S,S*)-**2 a,b** (0.8–1.5 Hz, Table 1) are



**Scheme 1.** Synthesis and structure of new stereoisomeric *O*-BODIPY dimers **2** and monomeric analogues **3** and **4**.

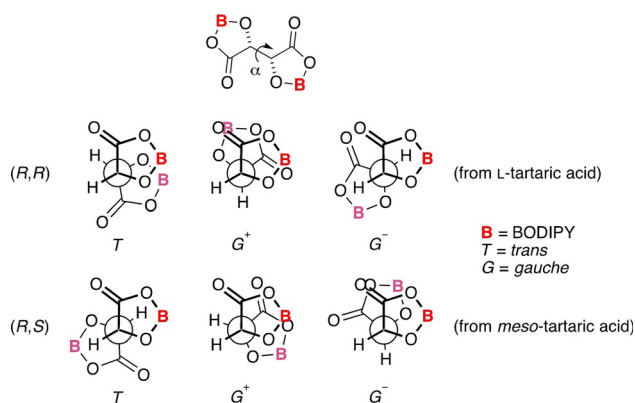


**Figure 2.** Newman projections of the possible staggered conformers of the chiral (*R,R*) and *meso* (*R,S*) series of bichromophoric systems **2**.

usually characteristic of a preferred extended (*T*) conformation of the tartrate carbon chain, as also observed for (*R,R*)-tartaric acid, its esters, and NH amide derivatives with either free or acylated hydroxy groups.<sup>[34,35]</sup> DFT calculations (see below) convincingly excluded the presence of the alternative, but unstable *G*<sup>+</sup> conformer, for which low <sup>3</sup>J<sub>H,H</sub> values may also be expected. Somewhat counterintuitively, small <sup>3</sup>J<sub>H,H</sub> were also measured for *meso* derivatives (*R,S*)-**2a,b** (1.7–3.2 Hz), which revealed in this case the predominance of the two enantiomeric *gauche* conformers (*G*<sup>+</sup>, *G*<sup>-</sup>). Solvent effects on <sup>3</sup>J<sub>H,H</sub> were small for both series of compounds, which indicated that the conformational equilibrium was only marginally affected by the polarity of the medium. To define and confirm further the conformational equilibrium of these compounds, <sup>1</sup>H–<sup>1</sup>H NOEs were also studied. The experimental NOEs (see the Supporting Information) could be readily interpreted on the basis of interproton distances determined for the DFT energy-minimized con-

**Table 1.** Experimental vicinal coupling constants between protons of the tartrate system of compounds **2** and the estimated values predicted by the Altona empirical equation<sup>[37]</sup> for the DFT energy-minimized conformers (see Figure 3).

Compound	Experimental <sup>3</sup> J <sub>H,H</sub> [Hz]			Calculated <sup>3</sup> J <sub>H,H</sub> [Hz] <sup>[a]</sup>
	Toluene	CDCl <sub>3</sub>	MeCN	
( <i>R,R</i> )- <b>2a</b>	0.9	0.8	1.1	0.40
( <i>R,R</i> )- <b>2b</b>	1.3	1.5	1.7	0.43
( <i>R,S</i> )- <b>2a</b>	1.7	2.2	2.1	1.30
( <i>R,S</i> )- <b>2b</b>	2.3	3.2	2.9	1.88

[a] DFT energy-minimized conformers and the corresponding optimized HC–CH torsional angles of the tartrate protons: (*R,R*)-**2a**, 67.18° (*T* conformer); (*R,R*)-**2b**, 66.59° (*T* conformer); (*R,S*)-**2a**, 71.93° (*G* conformer); (*R,S*)-**2b**, 65.86° (*G* conformer). In the Altona equation, the O–B groups were considered as OR.

formers (see below) in both series of diastereomers of **2a,b**. The interproton NOEs and low <sup>3</sup>J<sub>H,H</sub> values measured for all bichromophoric compounds **2a,b** are compatible with the exclusive presence of the *T* and *G* conformers in solutions of the chiral and *meso* stereoisomers, respectively.

We also determined the X-ray crystal structures of bichromophoric compounds (*R,R*)- and (*R,S*)-**2a,b** and model monomeric BODIPYs **3a** and **3b** (Figure 3).<sup>[38]</sup> As observed in solution, chiral compounds (*R,R*)-**2a,b** also exist exclusively in the *T* conformation in the solid state. The *meso* derivatives, however, differ in their solid-state conformation. Whereas (*R,S*)-**2a** crystallizes as the *G* conformer, tetramethylated analogue (*R,S*)-**2b** is in a perfectly staggered *trans* (*T*) conformation in the crystal.

The energy-minimized structures and conformational search performed by DFT (ωB97XD/6-31G\*) calculations, simulating the solvent as a continuum, fully confirmed the aforementioned NMR spectroscopy results in solution. Indeed, chiral ste-

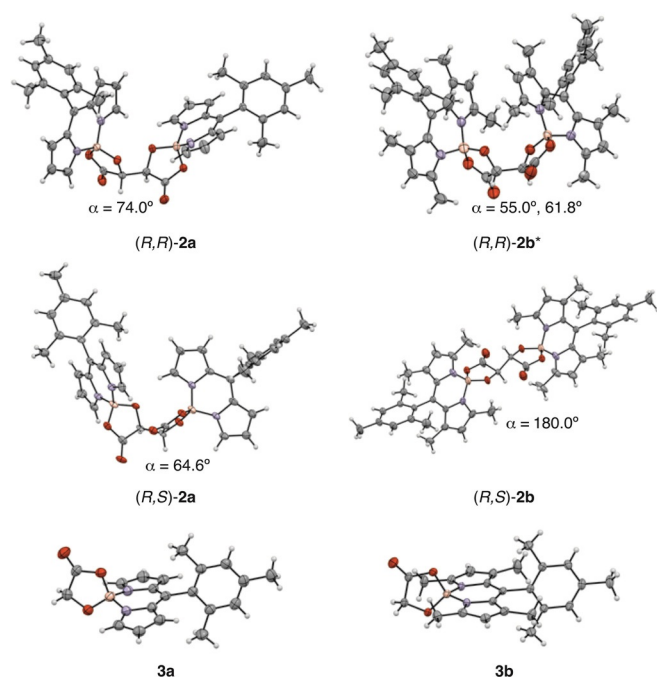


**Figure 3.** X-ray crystal structures of bichromophoric compounds  $(R,R)$ -**2a,b** and  $(R,S)$ -**2a,b** and model glycolic acid derived BODIPYs **3a,b**. The HC–CH torsional angle is also included for the dimers. For  $(R,R)$ -**2b**, the values for the two nonequivalent molecules present in the unit cell of the crystal of this compound are given.

reoisomers  $(R,R)$ -**2a,b** converged exclusively (regardless of the starting input geometry) to the *T* conformer observed by X-ray

diffraction in the solids, and this conformer is characterized by a folded arrangement of the dipyrromethene subunits (see Figure 4). Accordingly, the extended *G* conformer of  $(R,R)$ -**2a,b** is  $\Delta E \approx 20$  kcal mol<sup>-1</sup> higher in energy. Moreover, in corresponding achiral *meso*-diastereomers  $(R,S)$ -**2a,b**, the computed geometries showed a similar folded arrangement (*G* conformer in this case). Note that the X-ray crystal structures (Figure 3) showed a conformational change upon methylation that was not observed in the NMR spectroscopy studies in solution nor in the theoretical simulations that were performed. In fact, the different starting geometries used for energy minimization, without any geometrical constraints, all converged to the folded *G* conformer as the true global energy minimum for both compounds  $(R,S)$ -**2a,b**. Again, the DFT conformational search predicted that the extended *T* conformer was less stable [ $\Delta E = 17.5$  and  $9.7$  kcal mol<sup>-1</sup> for *meso* derivatives  $(R,S)$ -**2a** and  $(R,S)$ -**2b**, respectively], although the energy gap was lower than that in the corresponding chiral counterparts, particularly in methylated dyad  $(R,S)$ -**2b**. Likely, the lower stability of the *T* conformer of  $(R,S)$ -**2b** is compensated by its expected more favorable crystal packing resulting from the extended coplanar geometrical arrangement to explain its presence in the crystal.

### Photophysical properties

New mono-BODIPY dyes **3a** and **4a** exhibited typical spectral features of their fluorinated parent analogues and other structurally related *O*-BODIPYs (Table 2).<sup>[32,39]</sup> The absorption maxi-

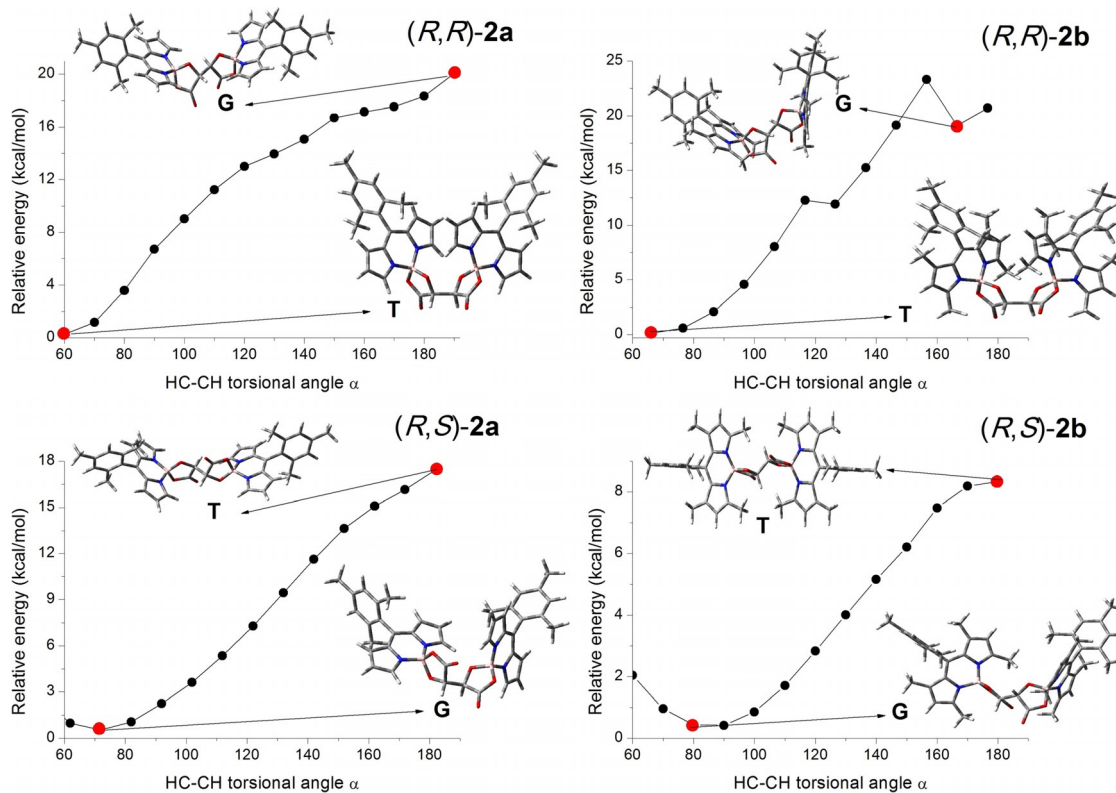


**Figure 4.** Conformational search performed by DFT ( $\omega$ B97XD/6-31G\*) along the central bond of the tartaric acid spacer (HC–CH torsional angle  $\alpha$ ). The corresponding geometries of the *T* and *G* conformers are also enclosed.

**Table 2.** Photophysical properties of micromolar ethyl acetate solutions of newly synthesized single *O*-BODIPYs precursors **3a,b** and **4a,b** and corresponding bis-*O*-BODIPYs **2a,b** by their linkage through a (*R,R*)- or (*R,S*)-tartaric acid connector. The data in other solvents for the bichromophoric compounds are listed in Table S1.

Compd	$\lambda_{ab}^{[a]}$ [nm]	$\epsilon_{max}^{[b]}$ [10 <sup>4</sup> M <sup>-1</sup> cm <sup>-1</sup> ]	$\lambda_{fl}^{[c]}$ [nm]	$\Delta\nu_{St}^{[d]}$ [cm <sup>-1</sup> ]	$\phi^{[e]}$	$\tau^{[f]}$ [ns]	$k_r^{[g]}$ [10 <sup>8</sup> s <sup>-1</sup> ]	$k_{nr}^{[h]}$ [10 <sup>8</sup> s <sup>-1</sup> ]
<b>3a</b>	504.5	5.7	516.0	440	0.96	7.71	1.25	0.05
<b>4a</b>	504.5	6.3	516.5	460	0.94	7.84	1.20	0.08
<b>3b</b>	504.0	8.4	513.0	350	1.00	6.44	1.55	0.00
<b>4b</b>	503.0	8.2	512.5	370	1.00	6.39	1.56	0.00
( <i>R,S</i> )- <b>2a</b>	506.0	11.4	518.5	475	0.90	6.39	1.41	0.15
( <i>R,S</i> )- <b>2b</b>	504.5	13.2	517.0	480	0.91	7.23	1.26	0.12
( <i>R,R</i> )- <b>2a</b>	518.0	8.6	560.5	1465	0.33 <sup>[i]</sup>	2.19 (97%) 6.41 (3%)	–	–
( <i>R,R</i> )- <b>2b</b>	518.0	9.0	540.0	790	0.85	5.85	1.45	0.26

[a] Absorption peak wavelength. [b] Molar extinction coefficient at peak. [c] Fluorescence peak wavelength, upon excitation at  $\lambda = 485$  nm. [d] Stokes shift. [e] Quantum yield. [f] Fluorescence lifetime. [g] Radiative decay rate. [h] Nonradiative decay rate. [i] This fluorescence quantum yield is only qualitative, owing to simultaneous contribution of the intramolecular *J*-like aggregate and the excimer to the whole emission profile.

mum is located at  $\lambda = 504$  nm, and the fluorescence emission spectrum centered at  $\lambda = 516$  nm is a mirror image of the absorption band. Theoretical simulations, in agreement with the crystalline structures provided by X-ray diffraction, predicted an orthogonal arrangement of both the 8-mesityl and 1,3,2-dioxaborolane rings of dyes **3a** and **4a** with respect to the boradiazaindacene system, which becomes even more constrained by methylation at the C1, C3, C5, and C7 positions (see Figure S1 in the Supporting Information). Consequently, the restriction of free motion and electronic coupling between the 8-mesityl group and the BODIPY core in dyes **3b** and **4b** led to both an enhanced molar absorption coefficient and a high fluorescence quantum yield, surpassing 0.95 (and even approaching 1).<sup>[32,39]</sup>

*meso*-Diastereomer (*R,S*)-**2a** and tetramethylated analogue (*R,S*)-**2b** exhibited similar spectral features, but the absorption coefficients were nearly double those recorded for the corresponding monomers, and this reflects the additive contribution of the locally excited states of each chromophoric unit (Table 2). Accordingly, they were highly fluorescent dyes, with quantum yields of approximately 0.9. This photophysical behavior indicates that the BODIPY units covalently anchored through a *meso*-tartaric group do not undergo intramolecular electronic interactions between them (at least in the ground state) and retain their identity and photophysical properties, which have additive contributions to the global transition. In agreement with the X-ray crystallographic data, ground-state DFT simulations of (*R,S*)-**2a** (Figures 4 and 5) predicted a nearly orthogonal arrangement of the BODIPY units (*G* conformer; dihedral angle between the longitudinal transition dipole moments  $\approx 84^\circ$ ), which remained fairly isolated, as the center-of-mass to center-of-mass distance ( $d_{CM}$ ) was 6.7 Å, which thus reduced the probability of exciton coupling. With respect to nonalkylated derivative (*R,S*)-**2a**, the methyl substituents of the BODIPY units in (*R,S*)-**2b** maintained the spatial configuration of the dimer (dihedral angle between the longitudinal transition dipole moments  $\approx 70^\circ$ ) and the distance between chromophores ( $d_{CM} = 6.6$  Å). As stated above, the theoretically predicted energy-minimized geometry of (*R,S*)-**2b** (Figure 5)

diverged from that observed in the crystal by X-ray crystallography (Figure 3), for which the chromophoric units are disposed in an extended coplanar arrangement (*T* conformer) that was not observed in our NMR spectroscopy studies in solution.

The frontier orbitals involved in the lowest electronic transitions for both *meso*-derivatives (*R,S*)-**2a** and (*R,S*)-**2b** allocated the electronic density preferentially on one of the chromophoric units (Figure S2). In fact, the energy gap between the HOMO and HOMO–1 was just 0.02 eV, which is very similar to that established between the empty LUMO and LUMO+1. Then, each BODIPY unit acts as an independent dye contributing with similar oscillator strength to the absorption of the dimer, which is double that of corresponding mono-BODIPY precursors **3/4b**. Indeed, electrochemistry measurements revealed that the oxidation–reduction properties of (*R,S*)-**2b** were comparable to those of its monomeric counterpart **4b** and, in turn, to those previously reported for the commercial dye PM546 (Figure S3 in the Supporting Information).<sup>[12h]</sup>

Covalently anchoring the non-methylated BODIPY units through an optically active *L*-tartaric linker had a drastic effect on the photophysical properties of derivative (*R,R*)-**2a** with respect to the behavior exhibited by both mono-BODIPY analogue **3a** and corresponding *meso*-diastereomer (*R,S*)-**2a** (Table 2). Regarding the absorption profile (Figure 6), the following can be noted: 1) the spectrum became broadened with a full width at half maximum (FWHM) value of approximately 1900 cm<sup>-1</sup>, which is approximately double the FWHM ( $\approx 940$  cm<sup>-1</sup>) of the mono-BODIPY absorption band; 2) the absorption maximum was bathochromically shifted by more than  $\Delta\lambda = 15$  nm; 3) a short-wavelength shoulder placed at  $\lambda = 480$  nm emerged; and 4) the absorption coefficient was not double, but only slightly higher than that of mono-BODIPY analogue **3a**. In addition, the fluorescence spectrum of (*R,R*)-**2a** (Figure 6) was no longer the mirror image of its absorption band and was significantly broadened and redshifted by more than  $\Delta\lambda = 45$  nm with respect to that of **3a**. This shift led to a significant increase in the Stokes shift, from  $\lambda = 475$  cm<sup>-1</sup> in **3a** [or diastereomer (*R,S*)-**2a**] to up to  $\lambda = 1460$  cm<sup>-1</sup> for chiral

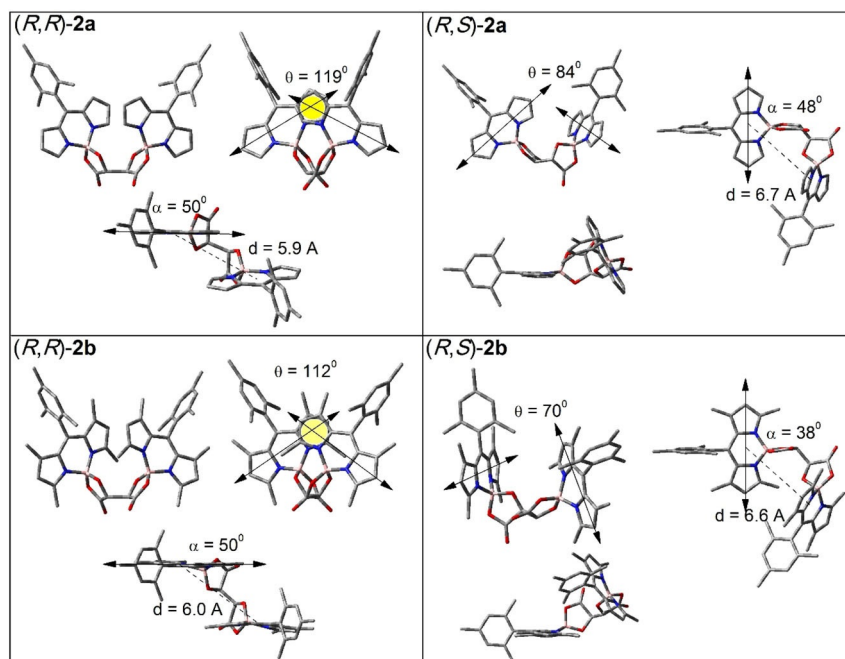


**Figure 5.** Optimized ground-state geometries in different views of the bis-*O*-BODIPYs with *L*-tartaric (left) and *meso*-tartaric (right) spacers. Geometrical parameters such as center-of-mass to center-of-mass distance ( $d$  [Å]), dihedral angle ( $\theta$ ) between the transition dipole moments (double arrow along the chromophoric longitudinal axis), and the slip angle ( $\alpha$ ) between the transition moment and the line connecting the center of mass of the two BODIPY units (dotted line) are also depicted. The shaded region highlights the head-to-tail exciton interaction through the side pyrroles leading to intramolecular oblique J-aggregation.

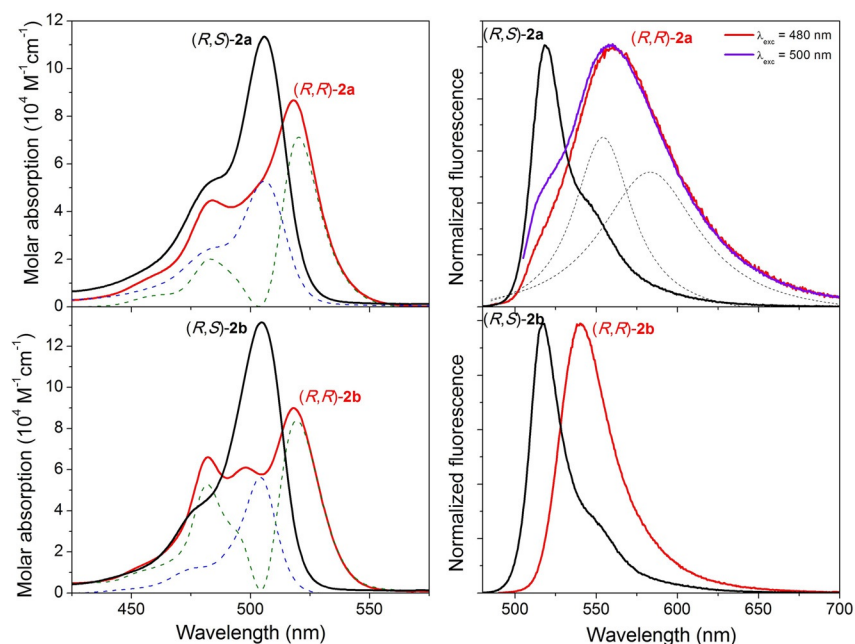


**Figure 6.** Absorption (left) and normalized fluorescence (right) spectra of chiral isomers  $(R,R)$ -**2a** and  $(R,R)$ -**2b** and their corresponding *meso* diastereomers  $(R,S)$ -**2a** and  $(R,S)$ -**2b**. The absorption spectra of the chiral compounds are deconvoluted (dotted lines) to show splitting resulting from the J-like intramolecular exciton-coupled BODIPYs. The fluorescence band of  $(R,R)$ -**2a** is also deconvoluted (dotted lines) to estimate the contribution of the J-like aggregate and the excimer to the whole emission profile.

dimer  $(R,R)$ -**2a**. This value even surpasses those observed for purposely designed energy-transfer cassettes<sup>[10]</sup> and reaches those of related BODIPY dimers.<sup>[40]</sup> These features are indicative of a geometrical rearrangement upon excitation, which boosts

energy-relaxation processes, and this leads to both a loss in fluorescence efficiency ( $\phi=0.33$ ) and a significant decrease in the fluorescence lifetime. In fact, the fluorescence decay curve of  $(R,R)$ -**2a** acquires biexponential character, with a main and

fast component ( $\tau=2$  ns) accompanied by a smaller contribution of a longer-lived ( $\tau=6$  ns) decay (Table 2).

All these trends provided solid arguments to conclude that in the ground state (*R,R*)-**2a** undergoes an intramolecular excitonic interaction [not observed in the corresponding diastereomer (*R,S*)-**2a**], which leads to a new emissive entity. Deconvolution of the absorption spectrum revealed that its profile actually involved two bands with maxima located at  $\lambda=480$  and 520 nm, which flank that of the single BODIPY unit peaked at  $\lambda=500$  nm (Figure 6). Time-dependent DFT (TD-DFT, TD  $\omega$ B97XD/6-311G\*\*) simulations also predicted a splitting of the absorption band with regard to its *meso* diastereomer, which does not undergo excitonic interaction (Figure S4). The absolute energies predicted for the electronic transition are not accurate, as expected for the TD DFT method,<sup>[41]</sup> but the method is able to describe the experimental findings properly and predicted an allowed excitonic coupled state at lower energies ( $475\text{ cm}^{-1}$ ) and a weakly allowed state at higher energies ( $345\text{ cm}^{-1}$ , Figure S4). Altogether, the corresponding orbital plots support the existence of these intramolecular interactions, as the electronic density of the frontier orbitals is simultaneously delocalized over the two BODIPY units for the same molecular orbital (Figure S2). Structure minimization, by using the same advanced DFT protocol, points out that the L-tartaric linker allocates the BODIPY units of (*R,R*)-**2a** in a more compact arrangement than in corresponding diastereomer (*R,S*)-**2a**, in agreement with the X-ray crystallographic data. As a consequence, the  $d_{\text{CM}}$  value is reduced to 5.9 Å, and the transition moments are slipped and tilted in a V-shape orientation with a dihedral angle of  $112^\circ$ , which allows "head-to-tail excitonic intramolecular interactions" (in term of the Kasha excitation model) through their overlapped lateral pyrroles (Figure 5). In terms of the Kasha exciton model, the geometrical arrangement of (*R,R*)-**2a** resembles an oblique J-like intramolecular aggregate in weakly coupled electronic systems.<sup>[42]</sup> Indeed, an oblique disposition of the transition dipole moments enables exciton splitting owing to "head-to-tail interactions", which modify significantly the absorption and fluorescence spectra. Thus, this excitonic intramolecular interaction led to two allowed absorption transitions located at higher and lower energies (the last one with higher probability) than those corresponding to the mono-BODIPY unit, in agreement with the experimental findings and the TD-DFT prediction of the absorption profile.

On the other hand, the redshifted fluorescence emission of (*R,R*)-**2a** provides further evidence of the ongoing J-like intramolecular excitonic interaction (Figure 6). In fact, the slip angle formed by the vector connecting the center of mass of two BODIPY units with the transition moment vector is lower than  $54.7^\circ$  (in particular  $50^\circ$ , Figure 5), which, in terms of the Kasha molecular exciton model, corresponds to a J-type interaction with low excitonic splitting, as theoretically predicted by TD-DFT methods (Figure S4). A similar twisted arrangement of the monomeric units was previously reported for other intermolecular J-aggregated BODIPY dyes.<sup>[14f, 43]</sup>

However, the broad fluorescence profile as well as the biexponential dynamics of the excited state of **2a** do not allow to

reject a priori the formation of a stronger aggregate, which could be described as an excimer.<sup>[44]</sup> Although excimer formation is not straightforward in view of the ground-state calculations, small conformational changes upon excitation can deeply alter the excitonic coupling<sup>[24j]</sup> assisting excimer formation, which can even coexist with intramolecular J-type aggregates, and this leads to complex excited-state dynamics. In fact, a closer inspection of the fluorescence spectrum reveals a shoulder at higher energies, the intensity of which depends on the excitation wavelength (Figure 6). Indeed, its deconvolution provides two clearly distinguishable emissions, one placed at  $\lambda \approx 560$  nm, which can be ascribed to the emission from the intramolecular J-type aggregates [see below the results for (*R,R*)-**2b** and Table 2], and another located at  $\lambda \approx 580$  nm, which can be ascribed to the emission from the excimer species. In addition, the fluorescence decay curves acquired biexponential character (Table S2) with a short-lived component ( $\approx 2$  ns), which became the main lifetime at longer emission wavelengths and can be associated to excimer emission, whereas the long-lived one ( $\approx 6-8$  ns) prevailed at shorter wavelengths and, hence, can be assigned to intramolecular J-type aggregates. Finally, the low fluorescence efficiency of (*R,R*)-**2a** (0.33) also supports the coexistence of excimers and intramolecular J-type aggregates upon excitation, as it is well established that excimers are usually characterized by emission efficiencies lower than those exhibited by J-aggregates.<sup>[45]</sup> To clarify the excimer/J-aggregation ratio in the (*R,R*)-**2a** dyad, excited-state calculations are required. However, the extended basis set needed and the rather large size of these bichromophoric molecules would require an extremely high computational cost.

To obtain deeper insight into this intramolecular excitonic interaction, we analyzed the photophysical features of tetramethylated chiral derivative (*R,R*)-**2b**. Once again, alkylation at the C1, C3, C5, and C7 positions of each BODIPY unit modified the spectral profile with respect to that of non-methylated analogue (*R,R*)-**2a**. In comparison, the absorption spectrum of (*R,R*)-**2b** also involved three absorption bands, but with a different intensity ratio, as the contribution of the above-claimed bands at  $\lambda=480$  and 520 nm, resulting from the J-like intramolecular exciton-coupled BODIPYs of the dyad, was higher than that of (*R,R*)-**2a** (Figure 6). In contrast with (*R,R*)-**2a**, the more constrained molecular structure of (*R,R*)-**2b** hindered geometrical distortions upon excitation, which led to a blueshifted and narrower fluorescence band, lower Stokes shift, higher fluorescence efficiency (up to 85%), and a monoexponential fluorescence decay curve with a longer lifetime (Table 2). These trends indicate that in this more compact dyad, excimer generation, if occurring, does so to a lesser extent and with lower probability than in the case of counterpart **2a**. Therefore, the fluorescence spectrum of (*R,R*)-**2b** is dominated solely by emission from the low-lying excited state of the intramolecular J-like exciton-coupled BODIPYs. As in (*R,R*)-**2a**, the frontier orbitals of (*R,R*)-**2b** are spread over the two chromophoric units, with orbital energies close to those predicted for diastereomer (*R,S*)-**2b** (Figure S2). In fact, the electrochemistry of (*R,R*)-**2b** was very similar to that of its *meso* diastereomer (*R,S*)-**2b** and that of its monomeric counterpart **3b** (Figure S3).

Regarding the molecular simulations, the methyl substituents in  $(R,R)$ -**2b** barely alter the distance between the BODIPY units ( $d_{cm} = 6.0 \text{ \AA}$ ), which retain the V-shape arrangement, closing the dihedral angle to  $112^\circ$  and locating the "internal" pyrroles in a more cofacial disposition than in non-alkylated analogue  $(R,R)$ -**2a** (Figure 5). The tighter and more compact geometrical disposition in  $(R,R)$ -**2b** enhances intramolecular exciton coupling between the side pyrroles, which accounts for a more evident splitting of its absorption profile and for a brighter emission (Table 2). Indeed, TD-DFT simulation predicted a stronger splitting energy for the low-lying coupled state (up to  $670 \text{ cm}^{-1}$ , Figure S4). These intramolecular exciton-coupled BODIPYs turned out to be rather stable species, as no sign of decoupling could be detected for  $(R,R)$ -**2a** or methylated derivative  $(R,R)$ -**2b** by heating up to  $70^\circ\text{C}$ .

Intramolecular exciton coupling in the ground states of  $(R,R)$ -**2a** and  $(R,R)$ -**2b** took place regardless of the solvent polarity (Figures S5 and S6, respectively), whereas their fluorescence efficiencies drastically decreased in polar media (Table S1). Thus, on the one hand, the emission from intramolecular exciton-coupled  $(R,R)$ -**2a** was completely lost in acetonitrile, and a very weak signal matching the position from the residual nonaggregated BODIPY was detected (Figure S4). On the other hand, the emission from the intramolecular exciton-coupled BODIPYs still prevailed in the fluorescence spectrum of  $(R,R)$ -**2b** in acetonitrile, although it was strongly quenched. Again, a very weak contribution of nonaggregated BODIPY emission could be detected at higher energies (Figure S5). Therefore, an increase in solvent polarity boosted a nonradiative deactivation channel, which quenched the emission from the intramolecular exciton-coupled BODIPYs. An intramolecular charge-transfer process was deemed responsible for this marked solvent sensitivity of the fluorescence efficiency in other closely spaced dyads, at least to some extent, among other possible nonradiative deactivation mechanisms.<sup>[14f]</sup>

### Chiroptical properties

Enantiomeric pairs  $(R,R)$ -**2a**/ $(S,S)$ -**2a** and  $(R,R)$ -**2b**/ $(S,S)$ -**2b** displayed identical absorption and emission spectra but with mirror-imaged electronic circular dichroism (ECD) spectra (Figure 7). The  $(R,R)$  enantiomers showed a positive Cotton effect with a maximum dichroic signal matching the maximum visible absorption of the BODIPY chromophore ( $\lambda \approx 520$  and  $518 \text{ nm}$  for chiral dimers **2a** and **2b**, respectively). The TD-DFT calculations conducted for such enantiomers nicely reproduced the positive Cotton effect observed in their ECD spectra and also the more intense signal of the non-methylated compound with respect to that of the tetramethylated one (Figure S7). The signs of the observed Cotton effects are also in agreement with those predicted by the exciton chirality method for the corresponding enantiomers of both compounds.<sup>[46]</sup> The maximum levels of visible ECD measured in terms of the absorption dissymmetric factor ( $g_{\text{abs}}$ )<sup>[47]</sup> values were  $+0.0040$  for  $(R,R)$ -**2a** and  $+0.0018$  for  $(R,R)$ -**2b**, as determined at the maximum absorption wavelength. Similar ECDs were also observed at higher concentrations ( $\approx 1 \times 10^{-5} \text{ M}$ ) for these compounds.

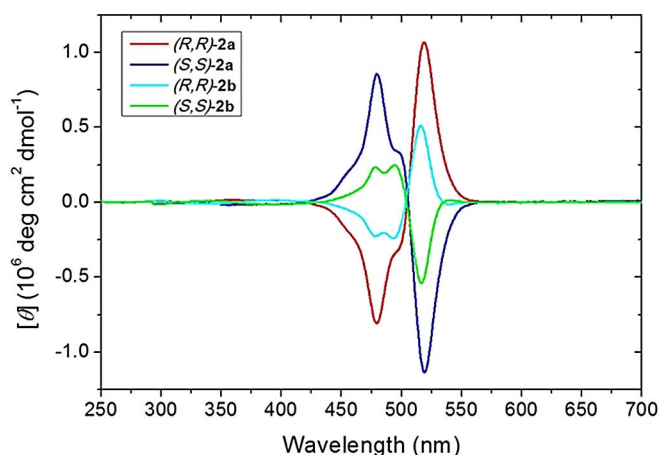


Figure 7. ECD spectra of compounds  $(R,R)$ -**2a**/ $(S,S)$ -**2a** and  $(R,R)$ -**2b**/ $(S,S)$ -**2b** in ethyl acetate ( $\approx 1 \times 10^{-6} \text{ M}$ ).

### Laser properties

The lasing properties of the new dyes were studied under pumping at the usual pump wavelengths of 355 and/or 532 nm, depending on their absorption properties. First, the dependence of the laser emission on dye concentration in ethyl acetate was analyzed by varying the optical density (for a 1 cm optical path length) from 2 to 40, while keeping all the other experimental parameters constant. Non-alkylated mono-BODIPYs **3a** and **4a** derived from glycolic acid and lactic acid, respectively, exhibited laser properties similar to those previously described for other *O*-BODIPYs with a *B*-spiranic 4,4-diacyloxy substitution pattern structurally related to the dyes herein synthesized.<sup>[32]</sup> Thus, **3a** and **4a** followed the expected behavior, with the lasing efficiency first increasing with dye concentration until a maximum value (48 and 39%, respectively, at  $\approx 2 \text{ mM}$ ) was reached. Increasing the dye concentration beyond this point (up to 8 mM) resulted in a significant decrease in the lasing efficiency (to 20%) that could be ascribed to activation of reabsorption/re-emission processes. Under these experimental conditions, the laser emission spectrum always arose as a single band peaked at  $\lambda = 528 \text{ nm}$ , which became slightly blueshifted as the concentration decreased.

On the contrary, the laser behavior of corresponding methylated mono-BODIPYs **3b** and **4b** deviated from the aforementioned dependence. In this case, the highest laser efficiency (51 and 48%, respectively) was recorded at a moderate concentration of approximately 3 mM. Furthermore, these lasing efficiencies exhibited a less pronounced reduction upon increasing the dye concentration. Thus, they maintained efficiencies as high as 39% at the highest concentration range (up to 8 mM), at which they were clearly operating under nonoptimal experimental conditions, as indicated by a cross section of the emitted beam not being near-circular (ideal conditions) but shaped as a narrow vertical ellipse. In addition, their laser spectra exhibited two distinct emission bands, at  $\lambda = 542$  and  $528 \text{ nm}$ , the relative strengths of which were strongly dependent on dye concentration (Figure 8). At the highest concentration, the spectrum was dominated by the long-wavelength



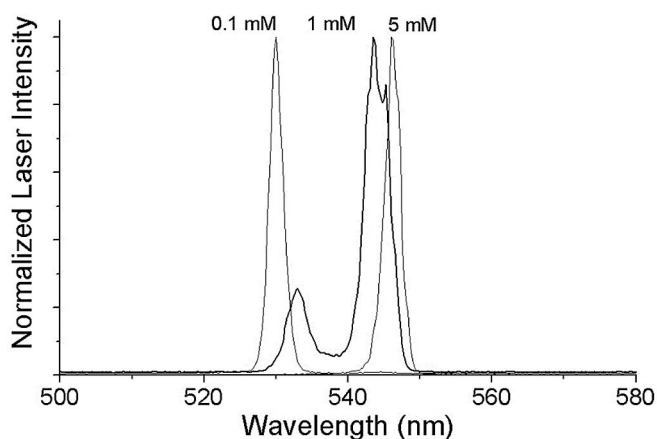


**Figure 8.** Laser spectra of methylated monomer **3b** in ethyl acetate as a function of the dye concentration.

emission band, whereas clear bichromatic emission was established at moderate concentrations ( $\approx 1$  mM). The short-wavelength band of this bichromatic emission kept on growing as the dye concentration decreased, and the laser spectrum eventually became a single-peak emission centered at  $\lambda = 526$  nm at the highest dilutions. As we unambiguously demonstrated in previous work, this behavior arises from self-assembly of the dyes into intermolecular J-aggregates, the emission of which is redshifted with respect to that of the nonaggregated units.<sup>[32]</sup> Thus, the high laser efficiencies recorded at high concentration, the low threshold energy for laser emission, and the dependence of the laser bichromatic emission on pump intensity, optical gain, and solvent polarity can only be explained by the super-radiance characteristic of intermolecular J-aggregates, which rules out the existence of any other type of aggregation, either in the ground state (dimers, trimers, or higher oligomers) or in the excited state (excimers or superexciplexes). Another distinctive property of laser emission from intermolecular J-aggregated dyes is its tuning capability over a very narrow spectral range. In the cases of monomers **3b** and **4b**, each of their laser bands featured dissimilar tuning capabilities. Placing the solution in a grazing-incidence grating tunable resonator, the short-wavelength band at  $\lambda = 528$  nm enabled a tuning range of approximately  $\Delta\lambda = 30$  nm ( $\lambda = 515$ – $540$  nm), which is the usual tunability span of laser dyes. In contrast, the long-wavelength laser band could only be tuned over a much narrower  $\Delta\lambda = 5$  nm range ( $\lambda = 540$ – $545$  nm), which is a “fingerprint” of intermolecular J-aggregates.

Covalent bonding of the BODIPY units through a *meso*-tartaric linker had a significant effect on the lasing action of resultant dimers (*R,S*)-**2a** and (*R,S*)-**2b**. At the optimum concentration (1 mM), these dyes exhibited lasing efficiencies of 29 and 33%, respectively. Lower and higher concentrations resulted in a significant decrease in these values, following the expected behavior. The lasing efficiencies correlated well with the photophysical properties: the lower the fluorescence quantum yield, the lower the lasing efficiency, which also accounted for the lower lasing efficiencies recorded from the (*R,S*)-dimeric BODIPYs with respect to those exhibited by the corresponding

monomeric dyes. Notably, the laser spectral profiles of (*R,S*)-**2a** and (*R,S*)-**2b** never became dual emission, even under extreme experimental conditions, such as high dye concentration, intense pumping radiation, and high optical gain. In fact, the laser spectrum exhibited a single band peaked at  $\lambda = 528$  nm, which was shifted to lower energies as the dye concentration increased, following the expected behavior as a consequence of the well-known reabsorption/re-emission processes.

Pumping at  $\lambda = 532$  nm (or at  $\lambda = 355$  nm), the laser spectra of non-methylated and methylated chiral dimers (*R,R*)-**2a** and (*R,R*)-**2b** also did not exhibit dual emission. With laser efficiencies of 24 and 45% and emission wavelengths at 575 and 555 nm, respectively, the laser signatures of (*R,R*)-**2a** and (*R,R*)-**2b** showed good correlation with their photophysical properties: the longer the fluorescence emission wavelength, the redder the laser emission; the higher the fluorescence quantum yield, the higher the lasing efficiency. Unlike methylated mono-BODIPYs **3b** and **4b**, the laser emission from both chiral dimers (*R,R*)-**2a** and (*R,R*)-**2b** enabled a tuning range of  $\Delta\lambda = 30$  nm, which is the usual tunability span of laser dyes. Therefore, covalent attachment of BODIPYs conforming both *meso* and chiral dimers prevents the laser-induced formation of intermolecular J-aggregates. Only methylated mono-BODIPYs **3b** and **4b** enabled fast and efficient intermolecular J-aggregation, which suppressed laser emission from single-dye molecules once the experimental laser conditions fulfilled the required pump fluence, dye concentration, and cavity configuration.

We also assessed the laser emission polarization state properties of the new chiral dimers (Figure S8). Thus, a complete polarimetric study<sup>[43b]</sup> was run on the laser emission of compound (*R,R*)-**2b** under vertically polarized pumping. Not surprisingly, this dye showed the same behavior with respect to the pump energy (Figure S9) than other simple organic molecules enabling circularly polarized luminescence.<sup>[48]</sup> In fact, the laser emission (see Figure S9 for notation) was highly polarized (degree of polarization,  $DOP \approx 1$ ) in the vertical direction ( $2\psi \approx 3.27$  rad), with ellipticity or circularly polarized laser emission (CPLE) levels approaching zero ( $|\chi| < 0.05$  rad) that came from the birefringence induced by the strong and polarized pump light.<sup>[43b,48]</sup>

## Conclusion

Herein, we demonstrated an effective strategy to fine-tune the photonic behavior of bichromophoric *O*-BODIPY systems through stereochemical and steric control of their structure and properties. The variety of stereoisomeric forms available for tartaric acid allowed modification of the relative spatial orientation of the chromophoric units in the dimer, which thus opened the door to the modulation of the photophysical and chiroptical properties of the new systems. Experimental characterization and theoretical calculations revealed that the chiral dimers have a preferred extended (*T*) conformation of the tartrate carbon chain, whereas a folded *G* conformation prevailed for the achiral *meso* diastereomers. The photophysical and laser properties of the latter fully resembled those of the corresponding mono-BODIPY analogues, but with twofold light ab-

sorption probability, thus revealing the independent and additive contributions of the two dipyrromethene subunits in the dyad. In contrast, the chiral bichromophores showed intramolecular exciton interaction with redshifted absorption and emission bands owing to more compact geometrical arrangement of the dipyrromethene subunits, which was in turn modulated by methylation of the chromophore. Thus, in methylated chiral dyad **2b** bright emission was achieved from a low-lying J-type intramolecular aggregate, whereas in more flexible counterpart **2a** the molecular dynamics were more complex, as excimer formation was also viable upon excitation. Covalent dimerization prevented laser-induced formation of the intermolecular J-aggregates observed in the corresponding monomeric *B*-spiranic *O*-BODIPY analogues, regardless of the stereochemistry and degree of alkylation. In conclusion, this novel strategy could open new avenues in the development of advanced photonic materials such as fluorescent biomarkers, for which stereochemical and steric control of their properties could substantially improve the contrast of fluorescent-based images by reducing background noise; this is a tight demand for the most sophisticated microscopy techniques.

## Experimental Section

### General methods

<sup>1</sup>H NMR and <sup>13</sup>C NMR spectra were recorded with a Bruker Avance III-400 (400 and 100 MHz, respectively) or a Varian System 500 (500 and 125 MHz, respectively) spectrometer. Chemical shifts are expressed in parts per million ( $\delta$  scale) downfield from tetramethylsilane and are referenced to residual signals of the deuterated NMR solvent used. Data are presented as follows: chemical shift, multiplicity (s = singlet, d = doublet, t = triplet, m = multiplet and/or multiple resonances, b = broad), coupling constants in hertz (Hz), integration, and assignment. Assignments are based on gCOSY, gHSQC, and gHMBC correlation experiments. Thin-layer chromatography (TLC) was performed with Merck Silica Gel 60 F254 plates. Chromatograms were visualized by using UV light ( $\lambda$  = 254 or 365 nm). Column chromatography was performed with a 971-FP Flash Purification System from Agilent Technologies by using SF Si35 silica cartridges. High-resolution mass spectrometry (HRMS) was performed with an Agilent 6520 Q-TOF instrument with an ESI source. Anhydrous solvents were prepared according to standard methods by distillation over drying agents or by elution through a PureSolv column drying system from Innovative Technology, Inc. All other solvents were of HPLC grade and were used as provided. Microwave irradiation experiments were performed under magnetic stirring with a single-mode Anton Parr Monowave 300 reactor by using standard Pyrex tubes (10 mL capacity) sealed with a polytetrafluoroethylene (PTFE)-lined rubber septum.

### Syntheses

**General procedure for the synthesis of *O*-BODIPYs by reaction of *F*-BODIPYs with hydroxy acids:** A solution of the starting *F*-BODIPY (0.074 mmol), the hydroxy acid (0.074 mmol), and chlorotrimethylsilane (1.49 mmol) in dry MeCN (2.5 mL) was heated under microwave irradiation at 120 °C between 30 min and 8 h, depending on the compound. The solvent and excess amounts of volatile reagents were removed under reduced pressure, and the

crude product was purified by flash column chromatography (hexane/EtOAc) or by crystallization.

**(*R,R*)-2a and (*S,S*)-2a:** Reaction of *F*-BODIPY **1a** (50 mg, 161.21  $\mu$ mol) with *L*- and *D*-tartaric acid (12.10 mg, 80.60  $\mu$ mol) following the general method for the synthesis of *O*-BODIPYs and heating for 6 h gave (*R,R*)-**2a** and (*S,S*)-**2a** (53 mg, 95%), respectively, as dark-red solids, after flash chromatography purification (hexane/EtOAc 100:0 to 40:60): <sup>1</sup>H NMR (500 MHz, CDCl<sub>3</sub>)  $\delta$  = 8.03 (brm, 1H, H3), 7.75 (brm, 1H, H5), 6.96 (s, 1H, H3'/H5'), 6.95 (s, 1H, H5'/H3'), 6.69 (d, *J* = 4.2 Hz, 1H, H7), 6.55 (d, *J* = 4.2 Hz, 1H, H1), 6.50 (dd, *J* = 4.2, 2.0 Hz, 1H, H6), 5.94 (dd, *J* = 4.2, 2.0 Hz, 1H, H2), 5.22 (s, 1H, H2''), 2.36 (s, 3H, CH<sub>3</sub>4'), 2.16 (s, 3H, CH<sub>3</sub>2'), 2.07 ppm (s, 3H, CH<sub>3</sub>6'); <sup>13</sup>C NMR (125 MHz, CDCl<sub>3</sub>)  $\delta$  = 176.15 (C1''), 147.95 (C3), 147.42 (C8), 144.32 (C5), 139.11 (C4'), 136.58 (C6'), 136.07 (C2'), 135.69 (C8b), 135.61 (C7a), 130.97 (C1), 130.56 (C7), 129.65 (C1'), 128.46 (C5'), 128.29 (C3'), 118.96 (C6), 118.90 (C2), 76.71 (C2''), 21.29 (CH<sub>3</sub>4'), 20.16 ppm (CH<sub>3</sub>2' and CH<sub>3</sub>6'); HRMS (API-ES<sup>+</sup>): *m/z* calcd for C<sub>40</sub>H<sub>37</sub>B<sub>2</sub>N<sub>4</sub>O<sub>6</sub>: 691.2907 [M+H]<sup>+</sup>; found: 691.2901.

**(*R,S*)-2a:** Reaction of *F*-BODIPY **1a** (50 mg, 161.21  $\mu$ mol) with *meso*-tartaric acid (12.10 mg, 80.60  $\mu$ mol) following the general method for the synthesis of *O*-BODIPYs and heating for 8 h gave (*R,S*)-**2a** (53 mg, 95%) as a dark-red solid, after flash chromatography purification (hexane/EtOAc 100:0 to 40:60): <sup>1</sup>H NMR (400 MHz, CDCl<sub>3</sub>)  $\delta$  = 8.36 (brm, 1H, H3), 7.70 (brm, 1H, H5), 6.96 (1H, H3'/H5'), 6.95 (s, 1H, H5'/H3'), 6.69 (d, *J* = 4.2 Hz, 1H, H1/H7), 6.68 (d, *J* = 4.2 Hz, 1H, H7/H1), 6.48 (dd, *J* = 4.2, 2.0 Hz, 1H, H6), 6.35 (dd, *J* = 4.2, 2.0 Hz, 1H, H2), 5.23 (s, 1H, H2''), 2.36 (s, 3H, CH<sub>3</sub>4'), 2.11 (s, 3H, CH<sub>3</sub>6'), 2.10 ppm (s, 3H, CH<sub>3</sub>2'); <sup>13</sup>C NMR (100 MHz, CDCl<sub>3</sub>)  $\delta$  = 174.68 (C1''), 148.27 (C3), 147.43 (C8), 143.58 (C5), 138.94 (C4'), 136.44 (C6'), 136.02 (C2'), 135.97 (C8b), 135.39 (C7a), 131.49 (C1), 130.18 (C7), 129.55 (C1'), 128.28 (C3'/C5'), 128.14 (C5'/C3'), 119.53 (C2), 118.59 (C6), 77.87 (C2''), 21.13 (CH<sub>3</sub>4'), 20.01 (CH<sub>3</sub>6'), 19.85 ppm (CH<sub>3</sub>2'); HRMS (API-ES<sup>+</sup>): *m/z* calcd for C<sub>40</sub>H<sub>37</sub>B<sub>2</sub>N<sub>4</sub>O<sub>6</sub>: 691.2907 [M+H]<sup>+</sup>; found: 691.2866.

**(*R,R*)-2b and (*S,S*)-2b:** Reaction of *F*-BODIPY **1b** (50 mg, 136.51  $\mu$ mol) with *L*- and *D*-tartaric acid (10.35 mg, 68.26  $\mu$ mol) following the general method for the synthesis of *O*-BODIPYs and heating for 6 h gave (*R,R*)-**2b** and (*S,S*)-**2b** (52 mg, 95%), respectively, as dark-red solids after flash chromatography purification (hexane/EtOAc 95:5 to 60:40): <sup>1</sup>H NMR (400 MHz, CDCl<sub>3</sub>)  $\delta$  = 6.98 (s, 1H, C5'H), 6.92 (s, 1H, C3'H), 5.93 (s, 1H, H2), 5.55 (s, 1H, H6), 4.90 (s, 1H, H2''), 2.42 (s, 3H, CH<sub>3</sub>3), 2.34 (s, 3H, CH<sub>3</sub>4'), 2.24 (s, 3H, CH<sub>3</sub>5), 2.21 (s, 3H, CH<sub>3</sub>2'), 1.99 (s, 3H, CH<sub>3</sub>6'), 1.37 (s, 3H, CH<sub>3</sub>7), 1.36 ppm (s, 3H, CH<sub>3</sub>1); <sup>13</sup>C NMR (100 MHz, CDCl<sub>3</sub>)  $\delta$  = 177.65 (C1''), 158.19 (C5), 154.13 (C3), 142.69 (C8b), 142.50 (C7a), 141.60 (C8), 138.78 (C4'), 135.05 (C2 and C6'), 131.50 (C1), 131.43 (C7), 131.21 (C1'), 129.15 (C5'), 129.14 (C3'), 122.95 (C6), 122.29 (C2), 77.28 (C2''), 21.35 (CH<sub>3</sub>4'), 19.83 (CH<sub>3</sub>2'), 19.52 (CH<sub>3</sub>6'), 15.85 (CH<sub>3</sub>3), 15.73 (CH<sub>3</sub>5), 13.63 (CH<sub>3</sub>1/CH<sub>3</sub>7), 13.62 ppm (CH<sub>3</sub>7/CH<sub>3</sub>1); HRMS (API-ES<sup>+</sup>): *m/z* calcd for C<sub>48</sub>H<sub>53</sub>B<sub>2</sub>N<sub>4</sub>O<sub>6</sub>: 803.4161 [M+H]<sup>+</sup>; found: 803.4131.

**(*R,S*)-2b:** Reaction of *F*-BODIPY **1b** (28.99 mg, 79.15  $\mu$ mol) with *meso*-tartaric acid (6 mg, 39.98  $\mu$ mol) following the general method for the synthesis of *O*-BODIPYs and heating for 4 h gave (*R,S*)-**2b** (30 mg, 95%) as a dark-red solid after flash chromatography purification (hexane/EtOAc 83:17 to 55:45): <sup>1</sup>H NMR (400 MHz, CDCl<sub>3</sub>)  $\delta$  = 6.96 (s, 1H, H5') 6.92 (s, 1H, H3'), 5.90 (s, 1H, H6), 5.87 (s, 1H, H2), 4.86 (s, 1H, H2''), 2.50 (s, 3H, CH<sub>3</sub>3), 2.43 (s, 3H, CH<sub>3</sub>5), 2.33 (s, 3H, CH<sub>3</sub>4'), 2.19 (s, 3H, CH<sub>3</sub>6'), 2.00 (s, 3H, CH<sub>3</sub>2'), 1.38 (s, 3H, CH<sub>3</sub>1), 1.35 ppm (s, 3H, CH<sub>3</sub>7); <sup>13</sup>C NMR (100 MHz, CDCl<sub>3</sub>)  $\delta$  = 175.85 (C1''), 158.56 (C3), 153.89 (C5), 143.88 (C8b), 142.70 (C7a), 141.83 (C8), 138.75 (C4'), 135.23 (C6'), 135.13 (C2'), 131.93 (C1), 131.61 (C7), 131.24 (C1'), 129.17 (C3'), 129.08 (C5'), 122.45 (C2), 122.06 (C6), 77.36 (C2''), 21.35 (CH<sub>3</sub>4'), 20.03 (CH<sub>3</sub>6'), 19.55 (CH<sub>3</sub>2'),

16.07 (CH<sub>3</sub>), 15.94 (CH<sub>3</sub>), 13.73 (CH<sub>3</sub>), 13.64 ppm (CH<sub>3</sub>); HRMS (API-ES<sup>+</sup>): *m/z* calcd for C<sub>48</sub>H<sub>53</sub>B<sub>2</sub>N<sub>4</sub>O<sub>6</sub>: 803.4161 [M+H]<sup>+</sup>; found: 803.4189.

**3a:** Reaction of *F*-BODIPY **1a** (27 mg, 87.05 μmol) with glycolic acid (6.06 mg, 78.89 μmol) following the general method for the synthesis of *O*-BODIPYs and heating for 2 h gave **3a** (30 mg, 85%) as a dark-red solid after flash chromatography purification (hexane/EtOAc 83:17 to 55:45): <sup>1</sup>H NMR (400 MHz, CDCl<sub>3</sub>) δ = 7.73 (brm, 2H, H3 and H5), 6.96 (s, 1H, H3'/H5'), 6.95 (s, 1H, H5'/H3'), 6.71 (d, *J* = 4.1 Hz, 2H, H1 and H7), 6.47 (dd, *J* = 4.1, 1.8 Hz, 2H, H2 and H6), 4.63 (s, 2H, H2''), 2.36 (s, 3H, CH<sub>3</sub>'), 2.12 (s, 3H, CH<sub>3</sub>2'/CH<sub>3</sub>6'), 2.08 ppm (s, 3H, CH<sub>3</sub>6'/CH<sub>3</sub>2'); <sup>13</sup>C NMR (100 MHz, CDCl<sub>3</sub>) δ = 176.80 (C1''), 148.33 (C8), 144.84 (C3 and C5), 139.18 (C4'), 136.60 (C2'/C6'), 136.30 (C6'/C2'), 135.93 (C7a and C8b), 131.20 (C1 and C7), 129.57 (C1'), 128.41 (C3'/C5'), 128.35 (C5'/C3'), 119.04 (C2 and C6), 66.58 (C2''), 21.28 (CH<sub>3</sub>4'), 20.19 (CH<sub>3</sub>2'/CH<sub>3</sub>6'), 20.11 ppm (CH<sub>3</sub>6'/CH<sub>3</sub>2'); HRMS (API-ES<sup>+</sup>): *m/z* calcd for C<sub>20</sub>H<sub>20</sub>BN<sub>2</sub>O<sub>3</sub>: 347.1565 [M+H]<sup>+</sup>; found: 347.15794.

**3b:** Reaction of *F*-BODIPY **1b** (28.90 mg, 78.89 μmol) with glycolic acid (6 mg, 78.11 μmol) following the general method for the synthesis of *O*-BODIPYs and heating for 30 min gave **3b** (30 mg, 95%) as a dark-red solid after flash chromatography purification (hexane/EtOAc 83:17 to 55:45): <sup>1</sup>H NMR (400 MHz, CDCl<sub>3</sub>) δ = 6.96 (s, 1H, H3'/H5'), 6.95 (s, 1H, H5'/H3'), 5.97 (s, 2H, H2 and H6), 4.50 (s, 2H, H2''), 2.40 (s, 6H, CH<sub>3</sub> and CH<sub>3</sub>5), 2.33 (s, 3H, CH<sub>3</sub>4'), 2.10 (s, 3H, CH<sub>3</sub>2'/CH<sub>3</sub>6'), 2.08 (s, 3H, CH<sub>3</sub>2'/CH<sub>3</sub>6'), 1.38 ppm (s, 6H, CH<sub>3</sub>1 and CH<sub>3</sub>7); <sup>13</sup>C NMR (100 MHz, CDCl<sub>3</sub>) δ = 177.46 (C1''), 155.32 (C3 and C5), 143.31 (C7a and C8b), 142.21 (C8), 138.76 (C4'), 134.93 (C2'/C6'), 134.73 (C6'/C2'), 131.75 (C1 and C7), 130.95 (C1'), 129.13 (C3'/C5'), 129.05 (C5'/C3'), 122.15 (C2 and C6), 66.95 (C2''), 21.20 (CH<sub>3</sub>4'), 19.50 (CH<sub>3</sub>2'/CH<sub>3</sub>6'), 19.48 (CH<sub>3</sub>6'/CH<sub>3</sub>2'), 15.09 (CH<sub>3</sub>-C5, CH<sub>3</sub>-C5), 13.58 ppm (CH<sub>3</sub>1 and CH<sub>3</sub>7); HRMS (API-ES<sup>+</sup>): *m/z* calcd for C<sub>24</sub>H<sub>28</sub>BN<sub>2</sub>O<sub>3</sub>: 403.2192 [M+H]<sup>+</sup>; found: 403.2210.

**4a:** Reaction of *F*-BODIPY **1a** (26.60 mg, 0.086 mmol) with L-(+)-lactic acid (6.10 mg, 0.088 mmol) following the general method for the synthesis of *O*-BODIPYs and heating for 7 h gave **4a** (30.80 mg, 99%) as a dark-red solid after flash chromatography purification (hexane/EtOAc 1:0 to 3:2): <sup>1</sup>H NMR (400 MHz, CDCl<sub>3</sub>): δ = 7.75 (brm, 1H, H3), 7.71 (brm, 1H, H5), 6.96 (s, 1H, H5'), 6.95 (s, 1H, H3'), 6.72–6.69 (m, 2H, H1 and H7), 6.47 (dd, *J* = 4.7, 1.9 Hz, 1H, H2/H6), 6.46 (dd, *J* = 4.7, 1.9 Hz, 1H, H6/H2) 4.78 (q, *J* = 6.8 Hz, 1H, H2''), 2.36 (s, 3H, CH<sub>3</sub>4'), 2.12 (s, 3H, CH<sub>3</sub>6'), 2.07 (s, 3H, CH<sub>3</sub>2'), 1.65 ppm (d, *J* = 6.8 Hz, 3H, H<sub>3</sub>3''); <sup>13</sup>C NMR (101 MHz, CDCl<sub>3</sub>): δ = 179.08 (C1''), 148.25 (C8), 144.99 (C3), 144.69 (C5), 139.13 (C4'), 136.59 (C6'), 136.30 (C2'), 135.93 (C7a and C8a), 131.31 (C1), 131.04 (C7), 129.61 (C1'), 128.39 (C5'), 128.32 (C3'), 119.01 (C2), 118.90 (C6), 72.49 (C2''), 21.27 (CH<sub>3</sub>4'), 20.60 (C3''), 20.17 (CH<sub>3</sub>6'), 20.07 ppm (CH<sub>3</sub>2'); HRMS (API-ES<sup>+</sup>): *m/z* calcd for C<sub>21</sub>H<sub>22</sub>BN<sub>2</sub>O<sub>3</sub>: 361.1723 [M+H]<sup>+</sup>; found: 361.1715.

**4b:** Reaction of *F*-BODIPY **1b** (27.20 mg, 0.074 mmol) with L-(+)-lactic acid (6.80 mg, 0.074 mmol) following the general method for the synthesis of *O*-BODIPYs and heating for 30 min gave **4b** (30.70 mg, 99%) as a dark-red solid after flash chromatography purification (hexane/EtOAc 1:0 to 7:3): <sup>1</sup>H NMR (400 MHz, CDCl<sub>3</sub>): δ = 6.95 (s, 1H, H5'), 6.94 (s, 1H, H3'), 5.97 (s, 1H, H2), 5.96 (s, 1H, H6), 4.68 (q, *J* = 6.9 Hz, 1H, H2''), 2.41 (s, 3H, CH<sub>3</sub>3), 2.42 (s, 3H, CH<sub>3</sub>5), 2.33 (s, 3H, CH<sub>3</sub>4'), 2.13 (s, 3H, CH<sub>3</sub>6'), 2.04 (s, 3H, CH<sub>3</sub>2'), 1.58 (d, *J* = 6.9 Hz, 3H, H<sub>3</sub>3''), 1.38 (s, 3H, CH<sub>3</sub>1), 1.37 ppm (s, 3H, CH<sub>3</sub>7); <sup>13</sup>C NMR (100 MHz, CDCl<sub>3</sub>): δ = 180.19 (C1''), 155.64 (C3), 154.91 (C5), 143.37 (C7a), 143.30 (C8a), 142.24 (C8), 138.86 (C4'), 135.02 (C1'), 131.92 (C1), 131.71 (C7), 131.17 (C2' and C6'), 129.22 (C3'), 129.16 (C5'), 122.55 (C2), 122.39 (C6), 72.83 (C2''), 21.32 (CH<sub>3</sub>4'), 19.75 (CH<sub>3</sub>6'), 19.55 (CH<sub>3</sub>2'), 18.66 (C3''), 16.37 (CH<sub>3</sub>3), 15.81 (CH<sub>3</sub>5),

13.74 ppm (CH<sub>3</sub>1 and CH<sub>3</sub>7); HRMS (API-ES<sup>+</sup>): *m/z* calcd for C<sub>25</sub>H<sub>30</sub>BN<sub>2</sub>O<sub>3</sub>: 417.2349 [M+H]<sup>+</sup>; found: 417.2338.

### Photophysical properties

Spectroscopic properties were registered in dilute solutions (≈ 2 × 10<sup>-6</sup> M) prepared by adding the corresponding solvent to the residue from an adequate amount of a concentrated stock solution in acetone after vacuum evaporation of this solvent. UV/Vis absorption and fluorescence spectra and decay curves were recorded with a Varian model CARY 4E spectrophotometer and an Edinburgh Instruments spectrofluorimeter (model FLSP 920), respectively. Fluorescence quantum yields (*φ*) were obtained by using commercial PM546 (*φ*' = 0.85 in ethanol) as a reference. The values were corrected by the refractive index of the solvent. Radiative decay curves were registered with the time-correlated single-photon counting technique by using a multichannel plate detector with picosecond time resolution. Fluorescence emission was monitored at different emission wavelengths (normally at the maximum) after tunable excitation (usually at λ = 485 nm) by means of a Fianium Supercontinuum laser. The fluorescence lifetime (*τ*) was obtained after deconvolution of the instrumental response signal from the recorded decay curves by means of an iterative method. The goodness of the exponential fit was controlled by statistical parameters (χ<sup>2</sup> and analysis of the residuals). The radiative (*k<sub>r</sub>*) [Eq. (1)] and nonradiative (*k<sub>nr</sub>*) [Eq. (2)] rate constants were calculated from the fluorescence quantum yield and lifetime:

$$k_r = \frac{\phi}{\tau} \quad (1)$$

$$k_{nr} = \frac{(1-\phi)}{\tau} \quad (2)$$

### Quantum-mechanical calculations

Ground-state geometries were optimized by density functional theory (DFT) by using the range-separated hybrid ωB97XD method and the triple valence basis set with two polarization functions (6-311G\*\*). The geometries were considered as energy minima if the corresponding frequency analysis did not give any negative value. The conformational search in the ground state was performed with a lower basis set (double valence with a polarization function 6-31G\*) than in the optimization step owing to the large size of the bis-BODIPYs, which demands an unavailable computational resource and an excessive calculation time. To this aim, relaxed scans (steps of 10°) were performed (in both directions, forward and backward) with regard to the torsional dihedral angle of the C–C bond connecting both rings of the tartaric acid spacer. The final minimum-energy geometries were further reoptimized by using the largest basis set (6-311G\*\*). The absorption spectrum and its exciton splitting in the chiral enantiomers as well as the ECD spectra were predicted by time-dependent (TD-DFT, in particular TD ωB97XD/6-311G\*\*) calculations. Solvent effects (ethyl acetate) were considered in the conducted theoretical simulations by means of the polarizable continuum model (PCM). All calculations were performed by using Gaussian 16 software, as implemented in the computational cluster "arina" of the UPV/EHU.

### Electrochemistry

Cyclic voltammograms (Metrohm Autolab) were obtained by using a three-electrode setup with a platinum layer (surface 8 × 7.5 mm) working electrode, platinum wire as the counter electrode, and

Ag/AgCl as reference electrode. A 0.1 M solution of tetrabutylammonium hexafluorophosphate (TBAPF<sub>6</sub>) in dry acetonitrile was used as the electrolyte solvent in which the compounds were dissolved to achieve a concentration of 0.5–1 mM. All redox potentials are reported versus ferrocene as an internal standard. The solutions were purged with argon, and all the measurements were performed under an inert atmosphere.

### Laser measurements

A sketch of the experimental setup used in this work is depicted in Figure S8. The dyes dissolved in organic solvents were placed in 1 cm optical path quartz cuvettes and were optically pumped at  $\lambda = 355$  and/or 532 nm with a frequency-doubled Q-switched Nd:YAG laser (Lotis TII SL-2132) emitting 20 ns full width at half maximum (FWHM) and operated at a 15 Hz repetition rate. Pump energy was measured with a calibrated pyroelectric energy meter (ED200, GenTec). The pump laser radiation was horizontally polarized, which allowed control of the pulse energy incident on the sample by insertion into the pump beam path of a half-wave plate (HWP) and a linear polarized (LP) set with its polarization axis horizontal or vertical, depending on the desired final pump polarization. By rotating the HWP, the linear polarization of the input beam was rotated out of the horizontal, and the pump beam was blocked more or less by the LP, depending on the rotation angle introduced by the HWP. In the transversal pumping configuration measurements, the light incident on the sample was perpendicular to the surface of the cuvette and was focused onto that surface in a stripe shape of approximately 300  $\mu\text{m}$  width by a combination of negative (NCL) and positive (PCL) cylindrical quartz lens ( $f = -15$  and  $+15$  cm, respectively) perpendicularly arranged. The oscillation cavity (2 cm length) consisted of a 90% reflectivity aluminum back mirror and the end face of the cuvette as output coupler. A beam splitter was used to send a reflection of the pump beam into a photodiode acting as the trigger. The trigger signal was fed to a boxcar (Stanford Research, model 250) to convert it into a delayed TTL pulse to trigger the digital oscilloscope (Yokogawa, model DL1620). The photodiode signal was also sent to the oscilloscope and was used as a reference signal to monitor and control the pump energy along the experiments. To analyze the degree of polarization and state of the dye laser emission, we tailored a polarimeter on the basis of a Fresnel rhomb, acting as a quarter-wave plate, combined to a linear polarized (Thorlabs LPVISB100-MP) and a pyroelectric energy meter, the signal of which was registered with the oscilloscope. The polarimetry formalism can be found elsewhere.<sup>[43b]</sup>

### Acknowledgements

We gratefully acknowledge the Spanish Ministerio de Economía y Competitividad for financial support (projects MAT2014-51937-C3-1-P, MAT2014-51937-C3-3-P, and MAT2015-68837-REDT) and for a FPI predoctoral contract to A.B.-M. We also acknowledge the Gobierno Vasco for financial support (project IT912-16) and for a predoctoral fellowship to E.A.-Z. The authors thank SGiker of UPV/EHU for technical and human support with the X-ray diffraction measurements and computational calculations, which were performed in the “arina” informatic cluster.

### Conflict of interest

The authors declare no conflict of interest.

**Keywords:** atomistic simulations · chromophores · dyes/pigments · fluorescence · lasers

- [1] T. Mirkovic, E. E. Ostroumov, J. M. Anna, R. van Grondelle, Govindjee, G. D. Scholes, *Chem. Rev.* **2017**, *117*, 249–293.
- [2] a) L. Gartzia-Rivero, J. Bañuelos, I. Lopez-Arbeloa, *Int. Rev. Phys. Chem.* **2015**, *34*, 515–556; b) P. Ensslen, H.-A. Wagenknecht, *Acc. Chem. Res.* **2015**, *48*, 2724–2733.
- [3] a) V. S. Vyas, V. W.-h. Lau, B. V. Lotsch, *Chem. Mater.* **2016**, *28*, 5191–5204; b) Y. Lin, X. Zhan, *Acc. Chem. Res.* **2016**, *49*, 175–183.
- [4] J. Warnan, Y. Pellegrin, E. Blart, F. Odobel, *Chem. Commun.* **2012**, *48*, 675–677.
- [5] B. Küçüköz, G. Sevinc, E. Yildiz, A. Karatay, F. Zhong, H. Yilmaz, Y. Tutel, M. Hayvali, J. Zhao, H. G. Yaglioglu, *Phys. Chem. Chem. Phys.* **2016**, *18*, 13546–13553.
- [6] H. Sahoo, *J. Photochem. Photobiol. C* **2011**, *12*, 20–30.
- [7] a) X. Zhang, Y. Xiao, L. He, Y. Zhang, *J. Org. Chem.* **2014**, *79*, 6315–6320; b) X. Qu, Q. Liu, X. Ji, H. Chen, Z. Zhou, Z. Shen, *Chem. Commun.* **2012**, *48*, 4600–4602; c) Y. Zhao, Y. Zhang, X. Lv, Y. Liu, M. Chen, P. Wang, J. Liu, W. Guo, *J. Mater. Chem.* **2011**, *21*, 13168–13171; d) Y. Xiao, D. Zhang, X. Qian, A. Costela, I. Garcia-Moreno, V. Martin, M. E. Perez-Ojeda, J. Bañuelos, L. Gartzia, I. L. Arbeloa, *Chem. Commun.* **2011**, *47*, 11513–11515; e) L. Wu, A. Loudet, R. Barhoumi, R. C. Burghardt, K. Burgess, *J. Am. Chem. Soc.* **2009**, *131*, 9156–9157; f) G.-S. Jiao, L. H. Thoresen, T. G. Kim, W. C. Haaland, F. Gao, M. R. Topp, R. M. Hochstrasser, M. L. Metzker, K. Burgess, *Chem. Eur. J.* **2006**, *12*, 7816–7826; g) J. Han, J. Jose, E. Mei, K. Burgess, *Angew. Chem. Int. Ed.* **2007**, *46*, 1684–1687; *Angew. Chem.* **2007**, *119*, 1714–1717; h) T. G. Kim, J. C. Castro, A. Loudet, J. G. S. Jiao, R. M. Hochstrasser, K. Burgess, M. R. Topp, *J. Phys. Chem. A* **2006**, *110*, 20–27; i) R. Bandichhor, A. D. Petrescu, A. Vespa, A. B. Kier, F. Schroeder, K. Burgess, *J. Am. Chem. Soc.* **2006**, *128*, 10688–10689; j) C.-W. Wan, A. Burghart, J. Chen, F. Bergstroem, L. B. A. Johansson, M. F. Wolford, T. G. Kim, M. R. Topp, R. M. Hochstrasser, K. Burgess, *Chem. Eur. J.* **2003**, *9*, 4430–4441; k) G.-S. Jiao, L. H. Thoresen, K. Burgess, *J. Am. Chem. Soc.* **2003**, *125*, 14668–14669.
- [8] a) D. Su, J. Oh, S.-C. Lee, J. M. Lim, S. Sahu, X. Yu, D. Kim, Y.-T. Chang, *Chem. Sci.* **2014**, *5*, 4812–4818; b) D. Su, C. L. Teoh, N.-Y. Kang, X. Yu, S. Sahu, Y.-T. Chang, *Chem. Asian J.* **2015**, *10*, 581–585.
- [9] A. Treibs, F. H. Kreuzer, *Justus Liebig's Ann. Chem.* **1968**, *718*, 208–223.
- [10] a) G. Ulrich, R. Ziessel, A. Harriman, *Angew. Chem. Int. Ed.* **2008**, *47*, 1184–1201; *Angew. Chem.* **2008**, *120*, 1202–1219; b) A. Loudet, K. Burgess, *Chem. Rev.* **2007**, *107*, 4891–4932; c) J. Bañuelos, *Chem. Rec.* **2016**, *16*, 335–348.
- [11] a) N. Boens, B. Verbelen, W. Dehaen, *Eur. J. Org. Chem.* **2015**, 6577–6595; b) V. Lakshmi, R. Sharma, M. Ravikanth, *Rep. Org. Chem.* **2016**, *6*, 1–24; c) V. Lakshmi, M. Rajeswara Rao, M. Ravikanth, *Org. Biomol. Chem.* **2015**, *13*, 2501–2517.
- [12] a) E. V. Antina, N. A. Bumagina, A. I. V'Yugin, A. V. Solomonov, *Dyes Pigm.* **2017**, *136*, 368–381; b) T. Kowada, H. Maeda, K. Kikuchi, *Chem. Soc. Rev.* **2015**, *44*, 4953–4972; c) S. P. Singh, T. Gayathri, *Eur. J. Org. Chem.* **2014**, 4689–4707; d) A. Kamkaew, S. H. Lim, H. B. Lee, L. V. Kiew, L. Y. Chung, K. Burgess, *Chem. Soc. Rev.* **2013**, *42*, 77–88; e) N. Boens, V. Leen, W. Dehaen, *Chem. Soc. Rev.* **2012**, *41*, 1130–1172; f) S. G. Awuah, Y. You, *RSC Adv.* **2012**, *2*, 11169–11183; g) A. Harriman, *Chem. Commun.* **2015**, *51*, 11745–11756; h) A. B. Nepomnyashchii, A. J. Bard, *Acc. Chem. Res.* **2012**, *45*, 1844–1853; i) J. Zhao, L. Huang, X. Cui, S. Li, H. Wu, *J. Mater. Chem. B* **2015**, *3*, 9194–9211.
- [13] a) Z. Mahmood, K. Xu, B. Kucukoz, X. Cui, J. Zhao, Z. Wang, A. Karatay, H. G. Yaglioglu, M. Hayvali, A. Elmali, *J. Org. Chem.* **2015**, *80*, 3036–3049; b) A. Harriman, P. Stachelek, A. Sutter, R. Ziessel, *Photochem. Photobiol. Sci.* **2015**, *14*, 1100–1109; c) G. Duran-Sampedro, A. R. Agarrabeitia, I. Garcia-Moreno, L. Gartzia-Rivero, S. de la Moya, J. Bañuelos, I. Lopez-Arbeloa, M. J. Ortiz, *Chem. Commun.* **2015**, *51*, 11382–11383; d) R. Ziessel, G. Ulrich, A. Haefele, A. Harriman, *J. Am. Chem. Soc.* **2013**,

- 135, 11330–11344; e) A. Harriman, M. A. H. Alamiry, J. P. Hagon, D. Hablot, R. Ziessel, *Angew. Chem. Int. Ed.* **2013**, *52*, 6611–6615; *Angew. Chem.* **2013**, *125*, 6743–6747; f) V. Engelhardt, S. Kuhri, J. Fleischhauer, M. Garcia-Iglesias, D. Gonzalez-Rodriguez, G. Bottari, T. Torres, D. M. Guldi, R. Faust, *Chem. Sci.* **2013**, *4*, 3888–3893; g) V. Bandi, K. Ohkubo, S. Fukuzumi, F. D'Souza, *Chem. Commun.* **2013**, *49*, 2867–2869; h) O. Altan Bozdemir, S. Erbas-Cakmak, O. O. Ekiz, A. Dana, E. U. Akkaya, *Angew. Chem. Int. Ed.* **2011**, *50*, 10907–10912; *Angew. Chem.* **2011**, *123*, 11099–11104.
- [14] a) A. Harriman, P. Stachelek, A. Sutter, R. Ziessel, *Phys. Chem. Chem. Phys.* **2015**, *17*, 26175–26182; b) J.-F. Lefebvre, X.-Z. Sun, J. A. Calladine, M. W. George, E. A. Gibson, *Chem. Commun.* **2014**, *50*, 5258–5260; c) N. Epelde-Elezcano, E. Palao, H. Manzano, A. Prieto-Castaneda, A. R. Agarrabeitia, A. Tabero, A. Villanueva, S. de la Moya, I. Lopez-Arbeloa, V. Martinez-Martinez, M. J. Ortiz, *Chem. Eur. J.* **2017**, *23*, 4837–4848; d) S. Thakare, P. Stachelek, S. Mula, A. B. More, S. Chattopadhyay, A. K. Ray, N. Sekar, R. Ziessel, A. Harriman, *Chem. Eur. J.* **2016**, *22*, 14356–14366; e) C. Ray, J. Bañuelos, T. Arbeloa, B. L. Maroto, F. Moreno, A. R. Agarrabeitia, M. J. Ortiz, I. Lopez-Arbeloa, S. de la Moya, *Dalton Trans.* **2016**, *45*, 11839–11848; f) M. T. Whited, N. M. Patel, S. T. Roberts, K. Allen, P. I. Djurovich, S. E. Bradforth, M. E. Thompson, *Chem. Commun.* **2012**, *48*, 284–286.
- [15] a) S. Kolemen, M. Isik, G. M. Kim, D. Kim, H. Geng, M. Buyuktemiz, T. Karatas, X.-F. Zhang, Y. Dede, J. Yoon, E. U. Akkaya, *Angew. Chem. Int. Ed.* **2015**, *54*, 5340–5344; *Angew. Chem.* **2015**, *127*, 5430–5434; b) J. Ma, X. Yuan, B. Kuecukoez, S. Li, C. Zhang, P. Majumdar, A. Karatay, X. Li, H. Gul Yaglioglu, A. Elmali, J. Zhao, M. Hayvali, *J. Mater. Chem. C* **2014**, *2*, 3900–3913; c) W. Wu, X. Cui, J. Zhao, *Chem. Commun.* **2013**, *49*, 9009–9011; d) S. Duman, Y. Cakmak, S. Kolemen, E. U. Akkaya, Y. Dede, *J. Org. Chem.* **2012**, *77*, 4516–4527; e) J. Zhao, K. Xu, W. Yang, Z. Wang, F. Zhong, *Chem. Soc. Rev.* **2015**, *44*, 8904–8939.
- [16] a) E. M. Sánchez-Carnerero, F. Moreno, B. L. Maroto, A. R. Agarrabeitia, M. J. Ortiz, B. G. Vo, G. Muller, S. de la Moya, *J. Am. Chem. Soc.* **2014**, *136*, 3346–3349; b) M. Saikawa, T. Nakamura, J. Uchida, M. Yamamura, T. Nabeshima, *Chem. Commun.* **2016**, *52*, 10727–10730; c) Y. Wang, Y. Li, S. Liu, F. Li, C. Zhu, S. Li, Y. Cheng, *Macromolecules* **2016**, *49*, 5444–5451; d) S. Zhang, Y. Wang, F. Meng, C. Dai, Y. Cheng, C. Zhu, *Chem. Commun.* **2015**, *51*, 9014–9017; e) F. Li, Y. Wang, Z. Wang, Y. Cheng, C. Zhu, *Polym. Chem.* **2015**, *6*, 6802–6805; f) X. Ma, E. Abdel Azeem, X. Liu, Y. Cheng, C. Zhu, *J. Mater. Chem. C* **2014**, *2*, 1076–1084; g) Y. Wu, X. Mao, X. Ma, X. Huang, Y. Cheng, C. Zhu, *Macromol. Chem. Phys.* **2012**, *213*, 2238–2245; h) T. Bruhn, G. Pescitelli, F. Witterauf, J. Ahrens, M. Funk, B. Wolfram, H. Schneider, U. Radius, M. Bröring, *Eur. J. Org. Chem.* **2016**, 4236–4243.
- [17] a) E. Avellanal-Zaballa, G. Duran-Sampedro, A. Prieto-Castaneda, A. R. Agarrabeitia, I. Garcia-Moreno, I. Lopez-Arbeloa, J. Bañuelos, M. J. Ortiz, *Phys. Chem. Chem. Phys.* **2017**, *19*, 13210–13218; b) L. Huang, X. Cui, B. Therrien, J. Zhao, *Chem. Eur. J.* **2013**, *19*, 17472–17482; c) R. Sharma, H. B. Gobeze, F. D'Souza, M. Ravikanth, *ChemPhysChem* **2016**, *17*, 2516–2524.
- [18] a) H. Lu, J. Mack, Y. Yang, Z. Shen, *Chem. Soc. Rev.* **2014**, *43*, 4778–4823; b) P. E. Kesavan, S. Das, M. Y. Lone, P. C. Jha, S. Mori, I. Gupta, *Dalton Trans.* **2015**, *44*, 17209–17221; c) J. Wang, Q. Wu, S. Wang, C. Yu, J. Li, E. Hao, Y. Wei, X. Mu, L. Jiao, *Org. Lett.* **2015**, *17*, 5360–5363.
- [19] a) M. Bröring, R. Krüger, S. Link, C. Kleeborg, S. Köhler, X. Xie, B. Ventura, L. Flamigni, *Chem. Eur. J.* **2008**, *14*, 2976–2983; b) O. A. Bozdemir, Y. Cakmak, F. Sozmen, T. Ozdemir, A. Siemiarzczuk, E. U. Akkaya, *Chem. Eur. J.* **2010**, *16*, 6346–6351; c) Y. Ueno, J. Jose, A. Loudet, C. Perez-Bolivar, P. Anzenbacher, K. Burgess, *J. Am. Chem. Soc.* **2011**, *133*, 51–55; d) E. Şen, K. Meral, S. Atilgan, *Chem. Eur. J.* **2016**, *22*, 736–745.
- [20] a) A. Wakamiya, T. Murakami, S. Yamaguchi, *Chem. Sci.* **2013**, *4*, 1002–1007; b) M. Nakamura, H. Tahara, K. Takahashi, T. Nagata, H. Uoyama, D. Kuzuhara, S. Mori, T. Okujima, H. Yamada, H. Uno, *Org. Biomol. Chem.* **2012**, *10*, 6840–6849; c) C. Yu, L. Jiao, T. Li, Q. Wu, W. Miao, J. Wang, Y. Wei, X. Mu, E. Hao, *Chem. Commun.* **2015**, *51*, 16852–16855.
- [21] a) L. Gai, H. Lu, B. Zou, G. Lai, Z. Shen, Z. Li, *RSC Adv.* **2012**, *2*, 8840–8846; b) A. B. Nepomnyashchii, M. Bröring, J. Ahrens, A. J. Bard, *J. Am. Chem. Soc.* **2011**, *133*, 8633–8645; c) Y. Hayashi, S. Yamaguchi, W. Y. Cha, D. Kim, H. Shinokubo, *Org. Lett.* **2011**, *13*, 2992–2995.
- [22] a) A. B. Nepomnyashchii, M. Bröring, J. Ahrens, A. J. Bard, *J. Am. Chem. Soc.* **2011**, *133*, 19498–19504; b) B. Ventura, G. Marconi, M. Bröring, R. Krüger, L. Flamigni, *New J. Chem.* **2009**, *33*, 428–438; c) M. Bröring, Y. Yuan, R. Krueger, C. Kleeborg, X. Xie, *Z. Anorg. Allg. Chem.* **2010**, *636*, 518–523.
- [23] a) D. Marushchak, S. Kalinin, I. Mikhalyov, N. Gretskeya, L. B. A. Johansson, *Spectrochim. Acta Part A* **2006**, *65*, 113–122; b) J. Ahrens, B. Cordes, R. Wicht, B. Wolfram, M. Bröring, *Chem. Eur. J.* **2016**, *22*, 10320–10325.
- [24] a) H. Qi, J. J. Teesdale, R. C. Pupillo, J. Rosenthal, A. J. Bard, *J. Am. Chem. Soc.* **2013**, *135*, 13558–13566; b) C. Dumas-Verdes, F. Miomandre, E. Lepicier, O. Galangau, T. T. Vu, G. Clavier, R. Meallet-Renault, P. Audebert, *Eur. J. Org. Chem.* **2010**, 2525–2535; c) S. Diring, F. Puntoriero, F. Nastasi, S. Campagna, R. Ziessel, *J. Am. Chem. Soc.* **2009**, *131*, 6108–6110; d) C. Goze, G. Ulrich, R. Ziessel, *Org. Lett.* **2006**, *8*, 4445–4448; e) F. Bergström, I. Mikhalyov, P. Haeggloef, R. Wortmann, T. Ny, L. B. A. Johansson, *J. Am. Chem. Soc.* **2002**, *124*, 196–204; f) S. J. Hendel, A. M. Poe, P. Khomein, Y. Bae, S. Thayumanavan, E. R. Young, *J. Phys. Chem. A* **2016**, *120*, 8794–8803; g) T. Kaur, V. Lakshmi, M. Ravikanth, *RSC Adv.* **2013**, *3*, 2736–2745; h) J. Ahrens, B. Haberlag, A. Scheja, M. Tamm, M. Bröring, *Chem. Eur. J.* **2014**, *20*, 2901–2912; i) W. Liu, A. Tang, J. Chen, Y. Wu, C. Zhan, J. Yao, *ACS Appl. Mater. Interfaces* **2014**, *6*, 22496–22505; j) J. Ahrens, A. Scheja, R. Wicht, M. Bröring, *Eur. J. Org. Chem.* **2016**, 2864–2870; k) T. Li, W. Gu, C. Yu, X. Lv, H. Wang, E. Hao, L. Jiao, *Chin. J. Chem.* **2016**, *34*, 989–996; l) C. Yu, Q. Wu, Z. Tian, T. Li, E. Hao, L. Jiao, *J. Porphyryns Phthalocyanines* **2016**, *20*, 475–489; m) T. Sakida, S. Yamaguchi, H. Shinokubo, *Angew. Chem. Int. Ed.* **2011**, *50*, 2280–2283; *Angew. Chem.* **2011**, *123*, 2328–2331; n) D. T. Chase, B. S. Young, M. M. Haley, *J. Org. Chem.* **2011**, *76*, 4043–4051.
- [25] H. Yokoi, S. Hiroto, H. Shinokubo, *Org. Lett.* **2014**, *16*, 3004–3007.
- [26] J. Ahrens, B. Boeker, K. Brandhorst, M. Funk, M. Bröring, *Chem. Eur. J.* **2013**, *19*, 11382–11395.
- [27] S. Wang, H. Lu, Y. Wu, X. Xiao, Z. Li, M. Kira, Z. Shen, *Chem. Asian J.* **2017**, *12*, 561–567.
- [28] a) S. Mula, S. Frein, V. Russo, G. Ulrich, R. Ziessel, J. Barbera, R. Descheunax, *Chem. Mater.* **2015**, *27*, 2332–2342; b) O. A. Bozdemir, M. D. Yilmaz, O. Buyukcakir, A. Siemiarzczuk, M. Tutas, E. U. Akkaya, *New J. Chem.* **2010**, *34*, 151–155; c) S. P. Upadhyay, K. M. Lupo, A. N. Marquard, J. D. Ng, D. M. Bates, R. H. Goldsmith, *J. Phys. Chem. C* **2015**, *119*, 19703–19714; d) E. T. Eçik, E. Senkuytu, Z. Cebesoy, G. Y. Ciftci, *RSC Adv.* **2016**, *6*, 47600–47606; e) M. Yuan, X. Yin, H. Zheng, C. Ouyang, Z. Zuo, H. Liu, Y. Li, *Chem. Asian J.* **2009**, *4*, 707–713.
- [29] J. Iehl, J.-F. Nierengarten, A. Harriman, T. Bura, R. Ziessel, *J. Am. Chem. Soc.* **2012**, *134*, 988–998.
- [30] a) M. E. Pérez-Ojeda, B. Trastoy, I. Lopez-Arbeloa, J. Bañuelos, A. Costela, I. Garcia-Moreno, J. L. Chiara, *Chem. Eur. J.* **2011**, *17*, 13258–13268; b) B. Trastoy, M. E. Perez-Ojeda, R. Sastre, J. L. Chiara, *Chem. Eur. J.* **2010**, *16*, 3833–3841.
- [31] T. Bura, F. Nastasi, F. Puntoriero, S. Campagna, R. Ziessel, *Chem. Eur. J.* **2013**, *19*, 8900–8912.
- [32] H. Manzano, I. Esnal, T. Marques-Matesanz, J. Bañuelos, I. Lopez-Arbeloa, M. J. Ortiz, L. Cerdan, A. Costela, I. Garcia-Moreno, J. L. Chiara, *Adv. Funct. Mater.* **2016**, *26*, 2756–2769.
- [33] a) A. Harriman, L. J. Mallon, K. J. Elliot, A. Haefele, G. Ulrich, R. Ziessel, *J. Am. Chem. Soc.* **2009**, *131*, 13375–13386; b) H. Maeda, Y. Nishimura, S. Hiroto, H. Shinokubo, *Dalton Trans.* **2013**, *42*, 15885–15888; c) A. Kaloudi-Chantzzea, E. Martinou, K. Seintis, N. Karakostas, P. Giastas, F. Pitterl, H. Oberacher, M. Fakis, G. Pistolis, *Chem. Commun.* **2016**, *52*, 3388–3391; d) A. Kaloudi-Chantzzea, N. Karakostas, F. Pitterl, C. P. Raptopoulou, N. Glezos, G. Pistolis, *Chem. Commun.* **2012**, *48*, 12213–12215; e) C. Ikeda, T. Nabeshima, *Chem. Commun.* **2008**, *721*–723; f) B. Liu, N. Novikova, M. C. Simpson, M. S. M. Timmer, B. L. Stocker, T. Sohnel, D. C. Ware, P. J. Brothers, *Org. Biomol. Chem.* **2016**, *14*, 5205–5209.
- [34] a) R. Cysewski, M. Kwit, B. Warzajtis, U. Rychlewska, J. Gawronski, *J. Org. Chem.* **2009**, *74*, 4573–4583; b) J. Grajewski, T. Madry, M. Kwit, B. Warzajtis, U. Rychlewska, J. Gawronski, *ChemPhysChem* **2017**, *18*, 2197–2207.
- [35] a) A. Janiak, U. Rychlewska, M. Kwit, U. Stępień, K. Gawrońska, J. Gawroński, *ChemPhysChem* **2012**, *13*, 1500–1506; b) J. Gawroński, K. Gawrońska, P. Skowronek, U. Rychlewska, B. Warzajtis, J. Rychlewski, M. Hoffmann, A. Szarecka, *Tetrahedron* **1997**, *53*, 6113–6144; c) J. Gawronski, A. Długokinska, J. Grajewski, A. Plutecka, U. Rychlewska, *Chirality* **2005**, *17*, 388–395.

- [36] J. W. Emsley, J. Feeney, L. H. Sutcliffe, In *High Resolution Nuclear Magnetic Resonance Spectroscopy*, Pergamon Press, Oxford, **1965**, p. 448.
- [37] a) C. A. G. Haasnoot, F. A. A. M. De Leeuw, C. Altona, *Tetrahedron* **1980**, *36*, 2783–2792; b) L. A. Donders, F. A. A. M. DeLeeuw, C. Altona, *Magn. Reson. Chem.* **1989**, *27*, 556–563.
- [38] CCDC 1550414, 1562200, 1562202, 1562204, 1562205, and 1562206 contain the supplementary crystallographic data for this paper. These data are provided free of charge by The Cambridge Crystallographic Data Centre.
- [39] a) F. López Arbeloa, J. Bañuelos, V. Martínez, T. Arbeloa, I. Lopez Arbeloa, *Int. Rev. Phys. Chem.* **2005**, *24*, 339–374; b) G. Durán-Sampedro, A. R. Agarrabeitia, L. Cerdan, M. E. Perez-Ojeda, A. Costela, I. Garcia-Moreno, I. Esnal, J. Bañuelos, I. L. Arbeloa, M. J. Ortiz, *Adv. Funct. Mater.* **2013**, *23*, 4195–4205.
- [40] F. Zinna, T. Bruhn, C. A. Guido, J. Ahrens, M. Bröring, L. Di Bari, G. Pescitelli, *Chem. Eur. J.* **2016**, *22*, 16089–16098.
- [41] a) A. D. Laurent, C. Adamo, D. Jacquemin, *Phys. Chem. Chem. Phys.* **2014**, *16*, 14334–14356; M. R. Momeni, A. Brown, *J. Chem. Theory Comput.* **2015**, *11*, 2619–2632.
- [42] A. C. Benniston, G. Copley, A. Harriman, D. Howgego, R. W. Harrington, W. Clegg, *J. Org. Chem.* **2010**, *75*, 2018–2027.
- [43] a) K. A. Kistler, C. M. Pochas, H. Yamagata, S. Matsika, F. C. Spano, *J. Phys. Chem. B* **2012**, *116*, 77–86; b) L. Cerdán, S. Garcia-Moreno, A. Costela, I. Garcia-Moreno, S. de la Moya, *Sci. Rep.* **2016**, *6*, 28740; c) X.-S. Ke, T. Kim, V. M. Lynch, D. Kim, J. L. Sessler, *J. Am. Chem. Soc.* **2017**, *139*, 13950–13956; d) L. J. Patalag, L. P. Ho, P. G. Jones, D. B. Werz, *J. Am. Chem. Soc.* **2017**, *139*, 15104–15113.
- [44] a) A. C. Benniston, A. Harriman, S. L. Howell, C. A. Sams, Y-G. Zhi, *Chem. Eur. J.* **2007**, *13*, 4665–4674; b) M. A. H. Alamiry, A. C. Benniston, G. Copley, A. Harriman, D. Howgego, *J. Phys. Chem. A* **2011**, *115*, 12111–12119.
- [45] a) J. Gierschner, S. Y. Park, *J. Mater. Chem. C* **2013**, *1*, 5818–5832; b) A. J. Musser, S. K. Rajendran, K. Georgiou, L. Gai, R. T. Grant, Z. Shen, M. Cavazzini, A. Ruseckas, G. A. Turnbull, I. D. W. Samuel, J. Clark, D. G. Lidzey, *J. Mater. Chem. C* **2017**, *5*, 8380–8389.
- [46] N. Harada, K. Nakanishi, N. Berona, in *Comprehensive Chiroptical Spectroscopy, Vol. 2* (Eds.: N. Berova, P. L. Polavarapu, K. Nakanishi, R. W. Woody), Wiley, Hoboken, **2012**, pp. 115–166.
- [47] The degree of dichroism is given by the absorbance dissymmetry ratio (Kuhn's dissymmetry ratio),  $g_{\text{abs}}(\lambda) = 2(\epsilon_L - \epsilon_R) / (\epsilon_L + \epsilon_R)$ , where  $\epsilon_L$  and  $\epsilon_R$  refer, respectively, to the molar absorptivity of left and right circularly polarized absorptions.
- [48] J. Jiménez, L. Cerdan, F. Moreno, B. L. Maroto, I. Garcia-Moreno, J. L. Lunkley, G. Muller, S. de la Moya, *J. Phys. Chem. C* **2017**, *121*, 5287–5292.

---

Manuscript received: December 1, 2017

Accepted manuscript online: January 3, 2018

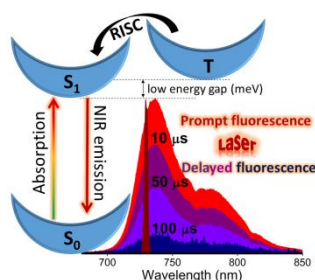
Version of record online: February 6, 2018

# Annex V (Chapter 5) / V. Eranskina (5. Kapituluua)

## Article 7 / 7. Artikulua

Red/NIR Thermally Activated Delayed Fluorescence from Aza-BODIPYs

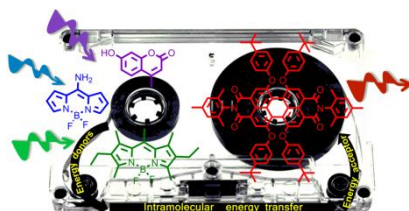
Accepted in *Chemistry - A European Journal*, 2020



## Article 8 / 8. Artikulua

Rational molecular design enhancing the photonic performance of red-emitting perylene bisimide dyes

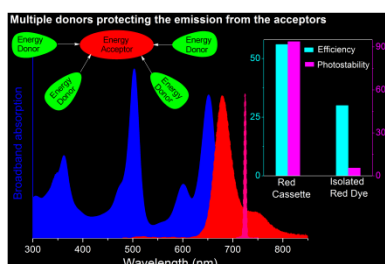
*Physical Chemistry Chemical Physics*, 2017, 19, 13210-13218



## Article 9 / 9. Artikulua

Towards Efficient and Photostable Red-Emitting Photonic Materials Based on Symmetric All-BODIPY-Triads, -Pentads, and -Hexads

*Chemistry - A European Journal*, 2019, 25, 14959-14971







## Dyes/Pigments

## Red/NIR Thermally Activated Delayed Fluorescence from Aza-BODIPYs

Edurne Avellanal-Zaballa,<sup>[a]</sup> Alejandro Prieto-Castañeda,<sup>[b]</sup> Fernando García-Garrido,<sup>[b]</sup> Antonia R. Agarrabeitia,<sup>[b]</sup> Esther Rebollar,<sup>[c]</sup> Jorge Bañuelos,<sup>\*,[a]</sup> Inmaculada García-Moreno,<sup>\*,[c]</sup> and María J. Ortiz<sup>[b]</sup>

**Abstract:** The search for long-lived red and NIR fluorescent dyes is challenging and hitherto scarcely reported. Herein, the viability of aza-BODIPY skeleton as a promising system for achieving thermal activated delayed fluorescent (TADF) probes emitting in this target region is demonstrated for the first time. The synthetic versatility of this scaffold allows the design of energy and charge transfer cassettes modulating the stereoelectronic properties of the energy donors, the spacer moieties and the linkage positions. Delayed emission from these architectures is recorded in the red spectral

region (695–735 nm) with lifetimes longer than 100  $\mu$ s in aerated solutions at room temperature. The computational-aided photophysical study under mild and hard irradiation regimes disclose the interplay between molecular structure and photonic performance to develop long-lived fluorescence red emitters through thermally activated reverse intersystem crossing. The efficient and long-lasting NIR emission of the newly synthesized aza-BODIPY systems provides a basis to develop advanced optical materials with exciting and appealing photonic response.

## Introduction

Over the last few years, an intense research effort has been focused on the design and synthesis of thermally activated delayed fluorescence (TADF) materials<sup>[1–5]</sup> liable of converting the excited  $T_1$  states to emissive  $S_1$  states by absorbing environmental thermal energy through an efficient reverse intersystem crossing (RISC).<sup>[6]</sup> Although a wealth of highly efficient blue<sup>[7–9]</sup> green,<sup>[10–12]</sup> yellow<sup>[13,14]</sup> and orange<sup>[15,16]</sup> TADF emitters are presently available, the progress on achieving long-lived fluorophores emitting in the deep red part of the visible spectrum has unfortunately been slowed because it requires the optimization of contrasting properties<sup>[17–20]</sup> The improved understanding of the processes ruling the effectiveness of RISC process has already revealed some basic design principles on develop-

ing highly-effective red TADF emitters<sup>[21–24]</sup> In this regard, the most effective strategy entails the synthesis of dyads with strong, rigid, chemically stable and sterically hindered donor and acceptor moieties spaced apart and twisted from each other through  $\pi$ -linker units<sup>[25–31]</sup> These integrated molecular platforms fulfil the photophysical and electronic key requirements to enhance TADF process, such as: 1) low singlet–triplet energy gap; 2) an electronic coupling between donor and acceptor neither too strong nor too weak to enable both forward and reverse ISC processes;<sup>[28]</sup> 3) a large fluorescence rate constant; and 4) a high chemical, photochemical, and photophysical stability of the molecular building blocks.


Among the chemical structures tested to design red TADF probes, long-wavelength emitting aza-BODIPY fluorophores has never being considered for this application despite dyes based on this aza-BODIPY scaffold stand out as bright, stable, and compact red/NIR emitters.<sup>[32–34]</sup> In fact, the simple replacement of the *meso*-methine group at the BODIPY core by an electronegative nitrogen atom induces a pronounced bathochromic shift of both the absorption and emission transitions as well as a drastic decrease of the energy gap between excited singlet and triplet states without promoting phosphorescence emission.<sup>[35]</sup> These effects can be enlarged through the peripheral arylation of the aza-BODIPY chromophoric core.<sup>[32–34]</sup> Recently, efficient and long-lasting fluorescent and laser emission in the target red/NIR spectral region have been recorded from polyarylated aza-BODIPYs under drastic pumping conditions.<sup>[36]</sup>

In this work, we report for the first time to the best of our knowledge red/NIR TADF emitters based on heavy-atom-free aza-BODIPY derivatives. The new dyes (1–4) were built up as

[a] E. Avellanal-Zaballa, Dr. J. Bañuelos  
Dpto. Química Física, Universidad del País Vasco (UPV/EHU)  
Apto 644, 48080 Bilbao (Spain)  
E-mail: jorge.banuelos@ehu.es

[b] A. Prieto-Castañeda, F. García-Garrido, Prof. A. R. Agarrabeitia,  
Prof. M. J. Ortiz  
Dpto. Química Orgánica, Universidad Complutense  
Ciudad Universitaria s/n, 28006 Madrid (Spain)

[c] Dr. E. Rebollar, Prof. I. García-Moreno  
Dpto. de Sistemas de Baja Dimensionalidad  
Superficies y Materia Condensada  
Instituto Química-Física "Rocasolano", IQFR-CSIC  
Serrano 119, 28006 Madrid (Spain)  
E-mail: i.garcia-moreno@iqfr.csic.es

 Supporting information and the ORCID identification number(s) for the author(s) of this article can be found under:  
<https://doi.org/10.1002/chem.202002916>

highly-effective energy and charge transfer cassettes based on a BODIPY moiety acting as donor and covalently linked to a polyarylated-aza-BODIPY group acting as acceptor and red/NIR emitting unit (Figure 1). The chemical versatility of this chromophoric core allowed synthesizing a library of structurally related dyads by: (i) increasing the number of donor BODIPY units to intensify the energy and charge transfer efficiency; (ii) tethering the donor units at the dipyrin backbone as well as at the boron bridge of the acceptor unit; (iii) modulating the link length between the donor-acceptor units through one or two phenyl rings acting as  $\pi$ -bridge ensuring no resonant interactions between the electronic clouds of the chromophoric subunits (via imposed steric hindrance and/or using the non-conjugated boron bridge as linkage position); and (iv) enhancing the photoinduced electron transfer (PET) capability of the donor unit as a new approach to increase intersystem crossing without relying on the phosphorescence emission.<sup>[37]</sup> This synthetic strategy has yielded the first aza-BODIPY/BODIPY architectures displaying red/NIR delayed emission even in aerated solutions at room temperature despite thermal activated delayed fluorescence was easily quenching by oxygen, reducing drastically its effectiveness, which becomes one of the major challenges for the applicability of TADF probes.<sup>[38,39]</sup> A comprehensive analysis, aided by computational simulations, of the photonic signatures of these new red-emitting materials under soft and drastic pumping conditions promoted an enhanced knowledge of the influence of the connecting modes between donor and acceptor units as well as of the underlying energy and charge transfer processes over the effectiveness of RISC mechanism. In this regard, the present work arises as the first proof-of-concept elucidating the interplay of molecular design, structural factors and photonic behavior in red-emitting cassettes to boost aza-BODIPY scaffold as a smart chromophoric platform in developing advanced red/NIR TADF materials.

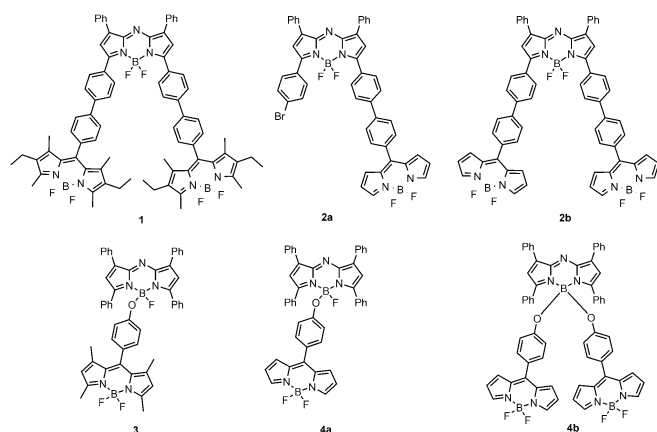


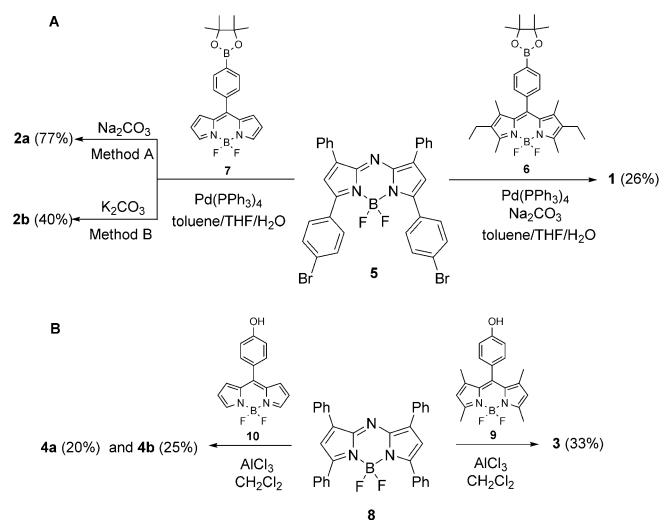
**Figure 1.** Structures of cassettes aza-BODIPY/BODIPY synthesized.

## Results and Discussion

### Synthesis and chemical characterization

Cassettes **1**, **2a** and **2b** were successfully obtained through Suzuki–Miyaura reactions from the halogenated aza-BODIPY **5**<sup>[40]</sup> and the corresponding pinacol boronate BODIPY **6**<sup>[41]</sup> and **7**<sup>[42]</sup> respectively (Scheme 1A). First, a mixture of the brominated aza-BODIPY **5** and pinacol boronate BODIPY **6** in presence of  $\text{Na}_2\text{CO}_3$  as base and  $\text{Pd}(\text{PPh}_3)_4$  as catalyst in a  $\text{H}_2\text{O}/\text{THF}/\text{toluene}$  mixture were heated at  $80^\circ\text{C}$  under argon atmosphere for 10 h, affording the cassette **1**, in 26% yield. Similarly, cassette **2a** was isolated, in 77% yield, by reaction of **5** with **7**, under the same conditions, for 20 h. Finally, cassette **2b** (40%) was obtained from **5** and **7** but using  $\text{K}_2\text{CO}_3$  as base and carrying out the reaction under microwave irradiation at  $120^\circ\text{C}$  for 1 h.

Subsequently, cassettes **3**, **4a** and **4b** were synthesized by replacement of one or two fluorine atoms at the boron bridge of the aza-BODIPY **8**<sup>[43,44]</sup> by reaction with the corresponding 8-(4-hydroxyphenyl)BODIPY **9**<sup>[45]</sup> or **10**<sup>[46]</sup> in the presence of  $\text{AlCl}_3$  as Lewis acid, according to the experimental procedure described in the literature<sup>[47]</sup> (Scheme 1B). All compounds were characterized using a combination of  $^1\text{H}$  NMR,  $^{13}\text{C}$  NMR, FTIR spectroscopy and high resolution mass spectrometry (HRMS). The synthesis and characterization of the new dyes are described in detail in the Supporting Information.



**Scheme 1.** Synthesis of cassettes aza-BODIPY/BODIPY 1–4.

### Photophysical properties: energy transfer vs. electron transfer

The absorption spectra of the new cassettes feature two strong and clearly distinguishable bands in the visible spectral region (Figures 2 and Figure S1 in the Supporting Information): the long wavelength absorption owed to the  $\pi$ -extended aza-BODIPY through the peripheral aryl groups linked at its dipyrin core (approaching 680 nm from the most arylated cassettes, **2a** and **2b**), whereas the short wavelength band was

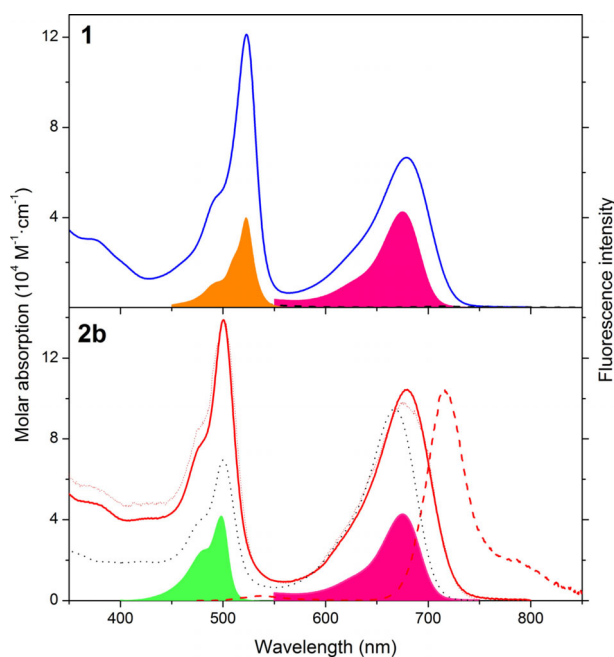


**Figure 2.** Absorption and fluorescence (dashed, after selective excitation of the BODIPY donor) and spectra of the triads linked through a biphenyl spacer (**1** and **2b**) in diluted solutions of ethyl acetate. The excitation spectrum (dotted, monitored at the aza-BODIPY emission) of **2b** is also included. To highlight the effect of the number of appended BODIPY donors, the absorption spectrum of the **2a** dyad is also included for comparison (dotted line in black). The absorption spectra (filled bands) of the isolated building blocks of the cassettes are also added to evidence the maintenance of the integrity of the chromophores after its covalent linkage. The corresponding spectra for the cassettes **3** and **4b**, linked at the boron atom, are collected in Figure S1 in the Supporting Information.

assigned to the pendant BODIPY moiety. In fact, the intensity of this last absorption band increased proportionally with the number of BODIPY subunits (**2a** vs. **2b** in Figure 2, or **4a** vs. **4b** in Figure S1 in the Supporting Information) and its spectral position was bathochromically shifted by increasing the alkylation degree at the dipyrin core of the BODIPY donor (**1** vs. **2b** in Figure 2, or **3** vs. **4a** in Figure S1 in the Supporting Information). Therefore, the broadband absorption exhibited by the new cassettes resulted from the additive contribution of the transitions of each chromophoric subunit, being each one electronically decoupled as supported by the computed molecular orbitals (Figures 3 and S2 in the Supporting Information). Indeed, the molecular orbitals (MOs) involved in each electronic transition were just located at the polyarylated aza-BODIPY moiety or alternatively at the BODIPY units. On the other hand, the fluorescence spectra of the new cassettes were dominated by a long-wavelength emission (peaked up to 720 nm in **2b**) regardless of the excited absorption band, as consequence of an efficient intramolecular excitation energy transfer (EET) from the BODIPY donor to the energy acceptor and NIR emitting aza-BODIPY unit (Figure 2 and Figure S1 in the Supporting Information). Actually, the emission from the donor BODIPY was almost negligible, yielding an EET efficiency close to the 100% in all media, as it was expected owing to the short donor–ac-

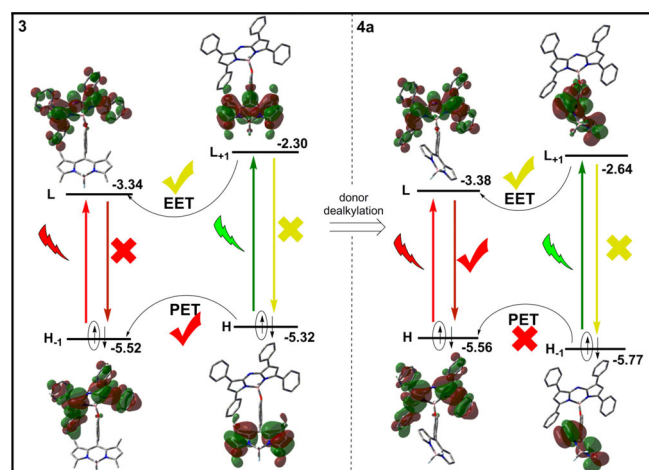


**Figure 3.** Computed molecular orbitals (b3lyp/6-31 g\*) and energies from the analogs **3** and **4a** differing just in the methylation of the energy donor BODIPY tethered at the boron of the aza-BODIPY. The probability of the competing fluorescence, EET and PET processes is depicted. The corresponding MOs diagram for the cassettes **1** and **2b**, linked at the 3,5-biphenyl group of the aza-BODIPY core, are collected in Figure S2 in the Supporting Information.

ceptor distance and geometrical disposition imposed by their mutual covalent linkage.

However, the fluorescence efficiency showed a marked dependence on the alkylation degree of the BODIPY acting as energy donor in all media; the cassettes bearing alkylated BODIPYs (tetramethylated in **3** or with further diethylation in **1**) became almost non-fluorescent (Table 1 and Table S1 in the Supporting Information). Quantum chemical calculations of the electronic density distribution based on DFT atomistic simulations (b3lyp/6-31G\*) predicted that the alkylated BODIPY, grafted at both the boron atom as well as the dipyrin core of the aza-BODIPY, was able to act as energy donor but also as effective electron donor. Indeed, the HOMO state of these cassettes was entirely located on the BODIPY unit and energetically placed above the HOMO-1 and therefore within the energy gap responsible of the aza-BODIPY transition (Figure 3 and Figure S2 in the Supporting Information). Such energetic distribution of MOs envisaged the ability of the alkylated BODIPY to effectively induce a reductive PET process upon excitation.<sup>[48]</sup> Thus, upon the photoinduced promotion of an electron from the HOMO to the LUMO+1 (under green excitation) or from HOMO-1 to LUMO (under red excitation), an electron transfer from the HOMO to the low-lying HOMO-1 was thermodynamically feasible. Such a reductive PET from the alkylated BODIPY grafted to the aza-BODIPY avoided radiative deactivation from LUMO back to the HOMO-1, thus explaining the almost negligible fluorescence emission recorded from **1** and **3**. Nevertheless, such undesirable PET pathway was totally suppressed just selecting fully non-alkylated BODIPY as energy donor units (**2a** and **2b**, or **4a** and **4b**). This substitution pattern lowered the energy of this HOMO state (i.e. from  $-5.32$  eV in **3** to  $-5.77$  eV in **4a**) to become HOMO-1 in these cassettes, being placed below the energy gap responsible of the aza-BODIPY electronic transitions (Figure 3 and Figure S2 in the Supporting Informa-

**Table 1.** Photophysical properties of all the cassettes in diluted solutions (2  $\mu\text{M}$ ) of ethyl acetate. The corresponding data of the isolated energy acceptor aza-BODIPY **8** are added for comparison.<sup>[36]</sup> The corresponding data in nonpolar and polar media are collected in Table S1 in the Supporting Information.

	$\lambda_{\text{ab}}^{[a]}$ [nm]	$\epsilon_{\text{max}}^{[b]}$ [ $10^4 \text{M}^{-1} \text{cm}^{-1}$ ]	$\lambda_{\text{fl}}^{[c]}$ [nm]	$\phi^{[d]}$	$\tau^{[e]}$ [ns]	$k_{\text{fl}}^{[f]}$ [ $10^8 \text{s}^{-1}$ ]	$k_{\text{nr}}^{[g]}$ [ $10^8 \text{s}^{-1}$ ]
<b>1</b>	678.5	6.7	711.5	0.006	NR	–	–
	523.0	12.1					
<b>2a</b>	667.5	7.7	701.0	0.24	1.83	1.31	4.15
	500.5	5.7					
<b>2b</b>	680.0	10.4	718.5	0.30	2.28	1.31	3.07
	500.5	13.9					
<b>3</b>	651.5	3.9	672.5	0.007	NR	–	–
	497.5	5.3					
<b>4a</b>	649.5	8.2	675.0	0.08	0.84	0.95	10.9
	494.5	7.7					
<b>4b</b>	655.0	7.2	678.5	0.08	1.03	0.77	8.93
	494.5	13.3					
<b>8</b>	646.0	8.6	668.0	0.12	0.81	1.48	9.64

[a] Absorption wavelengths. [b] Molar extinction coefficients at the absorption maxima. [c] Fluorescence wavelength. [d] Fluorescence quantum yield. [e] Fluorescence lifetime (independent of the excitation wavelength). [f] Radiative and [g] Non-radiative deactivation rate constants. NR: non-recorded because they are below 50 ps, the time resolution of the photon counter.

tion). This energetic rearrangement of the MOs hampered an effective PET process and, consequently, the fluorescence from the aza-BODIPY was restored, together with a substantial lengthening of the lifetime (Table 1 and Table S1 in the Supporting Information).<sup>[49,50]</sup> This result denoted that the BODIPY functionalization was mainly involved in the composition of the HOMO state of these cassettes controlling the effectiveness of its final emission. Theodore software was used to account for the probability upon excitation of the charge transfer underlying the PET process<sup>[51]</sup> (scaled from 0 to 1). The cassettes **2b** and **4b** bearing non-alkylated BODIPY as energy donor sustained a very low charge transfer probability (just 0.10 and 0.02 respectively). However, the sole alkylation of the BODIPY (structural-related **1** and **3**, respectively) drastically increased the probability of transferring an electron from the BODIPY subunit to the aza-BODIPY core (up to 0.78 and 0.72, respectively, in Table 1), supporting the viability of PET as the main non-radiative deactivation channel of the excited state in the cassettes featuring alkylated BODIPY as energy donors.

To support the viability of the predicted PET after anchoring alkylated energy donors to the aza-BODIPY, we conducted electrochemical measurements for the structural related pairs **1** vs. **2b**, and **3** vs. **4a** (Figure S3 in the Supporting Information). Whereas no changes were detected in the cathodic region with the first reduction potential peaked at the same potential (−0.27 V), as expected in view of the almost invariant LUMO energy (Figure 3 and Figure S2 in the Supporting Information), the anodic region showed variations upon alkylation of the energy donor. Thus, the alkylation of the energy donor BODIPY decreased the oxidation potential of the corresponding aza-BODIPY cassettes (1.1 V for **1** and 1.2 V for **3**, vs. 1.3 V for **2b** and 1.4 V for **4a**, respectively). Such difference of 0.2 eV nicely correlates with the predicted decrease of the HOMO energy in these cassettes upon removal of the alkyls in the BODIPY acting as energy donors (Figure 3 and Figure S2 in the Supporting Information). Therefore, it is again confirmed that the BODIPY alkylation enables a thermodynamically driven PET.

It is noteworthy that the fluorescence enhancement upon removing the alkyl groups of the BODIPY energy donor depended also on its grafted position at the aza-BODIPY core (Table 1 and Table S1 in Supporting Information). Thus, the linkage through the 3,5-biphenyl groups (**2a** or **2b**) led to bright NIR emission (up to 30% with a lifetime of 2.3 ns) but this efficiency was greatly reduced (8% with a lifetime of just 1 ns) by linking the donor unit at the boron bridge of the aza-BODIPY (**4a** and **4b**). This markedly different behavior could be attributed to the conformational freedom of each unit inside the cassette, which should be less restricted in the systems based on boron functionalization. With respect to **2b**, the feasible rotation of the BODIPY units linked at the boron bridge in **4b** increased the internal conversion deactivation process reducing consequently its fluorescence efficiency from 0.30 to a merely 0.08.

Therefore, cassette **2b**, which molecular design avoided deleterious effects (PET and internal conversion) on the emission quantum yield, stands out as NIR-emitter owing to both its more extended delocalized  $\pi$ -system and its high fluorescence efficiency, which became even 2-fold higher than that recorded from its isolated aza-BODIPY precursor **8** (Table 1).<sup>[36]</sup>

### Photonic behavior under hard pumping: laser and delayed fluorescence

With the exception of the multichromophoric systems (**1** and **3**) sustaining a PET process, the photophysical behavior of the new BODIPY-aza-BODIPY dyes as effective EET and ICT cassettes allowed them to lase efficiently in the red spectral region when they were transversally pumped at both 532 nm and 355 nm (second and third harmonic of a Nd:YAG laser, respectively). In fact, BODIPY-aza-BODIPY hybridation led to a drastic increase of the absorption at both pump lasing wavelengths with respect to that exhibited by the related monomeric aza-BODIPY **8**. This is a key factor from the point of view of the laser action, since it allowed reducing significantly the required

gain-media concentrations avoiding, consequently, dye-solubility problems, emission quenching and/or aggregation processes, all of them with detrimental effects on laser action. Under the selected experimental conditions (transversal excitation and hard focusing of the incoming pumping radiation) the concentration in ethyl acetate which optimized the laser efficiency, understood as the ratio of the output and input energies, depended on the given dye and were ranging from 0.2 mM to 0.9 mM. The lasing properties of the new systems recorded under the mentioned experimental conditions are reported in Table 2. The BODIPY-aza-BODIPY systems exhibited lasing emission peaked in the red-edge of the visible spectrum, from 696 nm (**4a**) to 730 nm (**2b**) (Table 2 and Figure 4). The dependence of the laser wavelength on the chemical structure of the cassettes showed good correlation with the photophysical properties: the longer the fluorescence wavelength, the “redder” became the lasing emission.

Despite its low fluorescence quantum yield, the new dyes showed an unexpected high laser efficiency (up to 25%), which was even higher than that exhibited by the monomeric aza-BODIPY **8** pumped at its maximum absorption wavelength.<sup>[36]</sup> This apparent mismatch can be rationalized taking into account the EET and ICT character of the emitting states in these cassettes leading to: (i) a high Stokes shift (up to 700 cm<sup>-1</sup>), which reduced the extension of re-absorption/re-emission processes and, thus, their deleterious effect in the laser action; (ii) a very short lifetime (below 0.6 ns), which ameliorated the population inversion and enhanced the stimulated emission probability, counterbalancing the low probability of spontaneous emission; and (iii) a high dipole moment (four- and six-fold higher than the isolated donor and acceptor fragments, respectively), allowing the molecular alignment with respect to the polarization of the exciting laser beam to enhance the emission efficiency of the media.<sup>[52]</sup> In this regard, the chemical modification around the boron atom had low impact in the laser efficiency of the corresponding derivatives (**4a** and

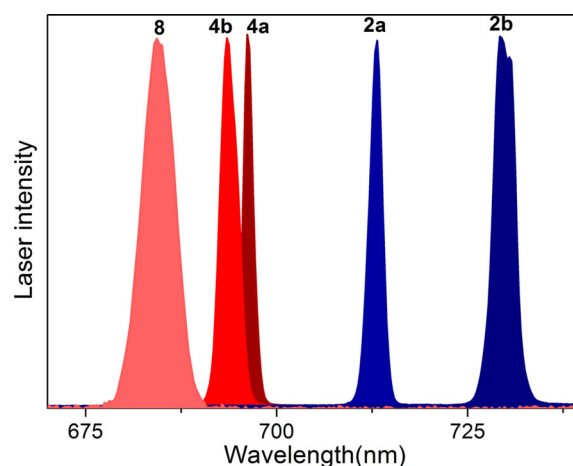


**Figure 4.** Normalized laser spectra of **2a**, **2b**, **4a** and **4b** in ethyl acetate solution at a concentration 0.5 mM pumped with laser pulses at 532 nm and 35 mJ cm<sup>-2</sup> fluence. The corresponding spectrum of its monomeric parent dye **8** was also included for comparison purposes.

**4b**) since the recorded decrease of the fluorescence efficiency upon replacement of the fluorine atom also entailed a drastic shortening of the corresponding lifetime (Table 1).

In terms of traceability and feasibility of red photonic materials, efficiency is not the only crucial variable to be considered. A further important parameter is the photostability of the emission over long operation times. Ideally, a high resistance to active medium photodegradation under repeated pumping is sought after. A reasonable evaluation of the photostability of laser materials can be obtained by irradiating a small amount of solution with exactly the same pumping energy and geometry as used in the laser experiments, and monitoring the evaluation of the laser-induced fluorescence (LIF) intensity with respect to the number of pump pulses (see Supporting Information). This experimental setup allowed us to analyze even the long-term photostability of the cassettes **1** and **3** since the PET process induced by its molecular structure was able to turn the laser action off but did not extinguish LIF emission. To properly compare the intrinsic photodegradation rate of the active media irrespective of the cavity configuration/parameters and sample concentrations used, we introduced a normalized photostability parameter such as the accumulated pump energy absorbed by the system, per mole of dye, before the output energy falls to a 10% of its initial value ( $E_{\text{dose}}$  in GJ mol<sup>-1</sup>). As it was expected, the new cassettes based on robust building blocks exhibited good photostability since up to 160 GJ mol<sup>-1</sup> were required for inducing a 10% decrease of its LIF emission (Table 2). Energy transfer from the peripheral BODIPYs to the central red-emitting aza-BODIPY reduced the rate and extension of the photodegradation processes and significantly enhanced the photostability of the multichromophoric systems with respect to the own monomeric aza-BODIPY **8**, as well as other monomeric commercial laser dyes with emission in the same spectral region.<sup>[36]</sup> This enhanced photostability was widespread to all the cassettes herein developed regardless of the acting EET, ICT and even PET mechanism sustained by its molecular design. Actually, the lasing

**Table 2.** Lasing properties and photostability of the new synthesized aza-BODIPY cassettes in ethyl acetate solution at the concentration, which optimizes the laser efficiency of each dye pumped at both wavelengths, 355 and 532 nm. The lasing behavior of the monomeric dye **8** pumped under identical experimental conditions are also included for comparison purposes.

[C] <sup>[a]</sup> [mM]	532 nm			355 nm				
	%Eff <sup>[b]</sup>	$\lambda_{\text{la}}$ <sup>[c]</sup> [nm]	$E_{\text{dose}}$ <sup>[d]</sup> [GJ mol <sup>-1</sup> ]	[C]	%Eff	$\lambda_{\text{la}}$ [nm]	$E_{\text{dose}}$ [GJ mol <sup>-1</sup> ]	
<b>1</b>		729 <sup>[e]</sup>	160					
<b>2a</b>	0.9	22	712	76	0.5	19	709	62
<b>2b</b>	0.5	25	730	142	0.3	21	725	123
<b>3</b>			720 <sup>[e]</sup>	81				
<b>4a</b>	0.8	21	696	64	0.4	15	694	
<b>4b</b>	0.9	23	693	145	0.4	16	690	135
<b>8</b>	2.0	6	689	22	1.6	4	685	

[a] Dye concentration. [b] Laser efficiency. [c] Laser wavelength. [d] Photostability defined as the amount of pumping energy absorbed by the dye to retain 90% of its initial emission at 532 nm. [e] Laser induced fluorescence.

action attending to both lasing efficiency and photostability depended on the number of donor units joined to the aza-BODIPY framework more than on its linkage length and/or position: the highest the number of peripheral BODIPYs acting as donor units the highest became the lasing efficiency and photostability (Table 2).

Other additional advantage of the light-harvesting molecular design of these cassettes is the excitation versatility enabling an efficient pumping also in the UV region of the visible spectrum. In fact, upon laser photoexcitation at 355 nm, the newly synthesized cassettes displayed a lasing behavior (attending to lasing wavelength, efficiency and photostability) similar to those recorded pumping at 532 nm (Table 2). Further enhancement of the photonic behavior on going from the monomeric dye **8** to the multichromophoric cassettes was recorded pumping **8** at 532 nm and 355 nm instead of at its maximum absorption wavelength.<sup>[36]</sup> To overcome the low absorption of **8** at these laser pump wavelengths highly concentrated solutions (up to 5-fold higher than those required for the cassettes) were needed. As it was mentioned above, this experimental issue had a deleterious effect on the laser action and, consequently, a 3-fold decrease in the lasing efficiency and photostability of **8** were recorded with respect to the values achieved pumping it at 654 nm.<sup>[36]</sup>

To get more inside on the photonic behavior of the newly synthesized aza-BODIPY cassettes time-gated emission related to its monomeric parent dye **8** was further investigated by irradiating the samples within the same optical configuration used in the laser characterization but under experimental conditions, attending to both dye concentration and pump laser fluence, well below the threshold for onset the laser action. To meet this requirement the analysis was carried out for dye concentrations and energy fluences lower than 0.2 mM and 32 mJ cm<sup>-2</sup>, respectively. Time-gated emission induced by laser pulses at 532 and 355 nm was detected with an intensified camera (iStar, Andor Technologies) coupled to a spectrograph (Kymera 193i-A, Andor Technologies). The camera enabled gate widths ranging from nanoseconds up to seconds and its opening can be delayed in a control way with respect to the incoming pump laser. It should be noted that neither long-pass-filters nor band-pass filters were used to remove the excitation laser since we verified that these filters (especially long pass filters) under drastic pump conditions exhibited its own fluorescence and/or phosphorescence emission, which could lead to misunderstanding the experimental results. This experimental set-up allowed carrying out the measurements even under adverse conditions, such as aerated solutions and at room temperature, in which the emission efficiency could become critically quenched.

Following exposure to intense laser pulses at both 355 nm and 532 nm all the new synthesized cassettes as well as the monomeric parent **8** exhibited delayed emission able to be registered at delay times longer than 100 μs with respect to the incoming laser pump radiation (Figure 5 and Figure S4 in the Supporting Information). Delayed emission appeared with similar spectral profile that the prompt laser-induced fluorescence and it did not change over time-exposure except for a

steady decrease of its intensity as the delay time was increased (Figure 5). This is the first time to the best of our knowledge that delayed emission was recorded from fluorophores based on aza-BODIPY scaffold, including both monomeric dyes and homo- and hetero-multichromophoric systems, although our experimental arrangement did not allow determining properly the efficiency of this delayed emission.

Considering that the prompt fluorescence had lifetimes as short as 2 ns, delayed emission with lifetimes longer than 100 μs must unequivocally imply long-lived triplet excited states. In this regard, it should be noted that neither solvents (i.e. iodoethane) nor triplet sensitizers were added to the dye solution trying to enhance the triplet quantum yield since at the same time the external heavy atom shortened the triplet lifetime. Two mechanisms can induce this delayed emission: thermally activated delayed fluorescence (TADF) or triplet-triplet annihilation (TTA). To distinguish between these two different processes the influence of different experimental and structural parameters on the delayed emission was systematically analyzed.

1) Small singlet-triplet energy gap is required to facilitate the RISC process in TADF probes. It is well known that the ISC probability in BODIPYs is extremely low (just a 1% of the excited electrons populate triplet excited states).<sup>[53,54]</sup> Advanced excited state calculations for the simplest BODIPY core revealed that the most feasible ISC funnel along the deactivation of the S<sub>1</sub> state took place through the conical intersection with the high-lying T<sub>2</sub> state.<sup>[55]</sup> Interestingly, and according to this study, the origin of an ineffective ISC in BODIPYs was not only the energy barrier to access to the S<sub>1</sub>-T<sub>2</sub> conical intersection (around 0.4–0.5 eV) but rather the very low spin-orbit coupling (1 cm<sup>-1</sup>).

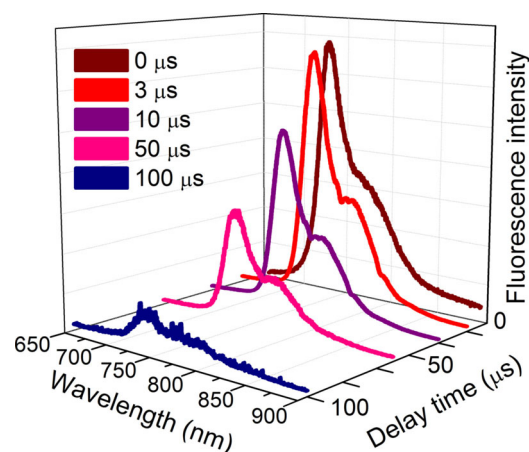


**Figure 5.** Delay time-dependent evolution of the fluorescence spectrum of **2b** in aerated ethyl acetate solution (0.1 mM) at room temperature upon excitation with laser pulses at 532 nm and 20 mJ cm<sup>-2</sup> fluence. The prompt laser-induced fluorescence spectrum recorded under otherwise identical experimental conditions is also included for comparison. It must be noted that the prompt fluorescence has been normalized to the intensity of the 3 μs delayed emission in order to demonstrate full spectral coincidence. However, its non-normalized intensity corresponds to a factor ×3, which does not apply because rescaling the delayed emissions for times longer than 50 μs would hardly be appreciated.

Trying to estimate the ISC probability in both the aza-BODIPY scaffold and the large-sized cassettes derived from it, we approached tentatively the S–T energy gap via Franck–Condon transitions (Figure S5 in the Supporting Information for details). In this regard, it should be noted that unlike the simplest BODIPY, the large molecular size of the herein synthesized cassettes hampered more advanced simulations and excited state calculations. In the monomeric **8** aza-BODIPY as well as in the newly synthesized dyads the excited state  $S_1$  and the closest triplet state ( $T_2$  in aza-BODIPYs or  $T_3$  in their corresponding cassettes) were almost energetically degenerate (energy gap < 20 meV). In this energetic picture, upon strong pumping, an electron in the excited state could reach the conical intersection to access a high-lying triplet state. However, once there, instead of relaxing down to the triplet states by internal conversion, it could come back to the  $S_1$  state via a thermodynamically feasible RISC allowing the recording of delayed fluorescence in a time-scale of hundreds of microseconds.

2) Strengthening the donor character of the final molecule on going from one donor to two donor units linked to the aza-BODIPY moiety (for instead **2a** and **2b**), some photophysical parameters critical for the effectiveness of TADF emission became enhanced. In fact, matching the optical density of **2a** and **2b** at the excitation wavelength (532 nm), an emission at delay time higher than 150  $\mu\text{s}$  could be recorded from **2b**, while **2a**, with only a donor BODIPY unit, showed considerably less and shorter delayed fluorescence, since no emission was registered beyond 100  $\mu\text{s}$ .

3) The replacement of the *meso*-methine group in the BODIPY core by an electronegative aza-N atom induced a marked change in the internal electronic properties due to the delocalization of the N electron lone pair along the dipyrin framework. Since the *meso* position greatly contributed to the LUMO state upon excitation,<sup>[36]</sup> the electronic transitions in the new dyads gained  $n\text{-}\pi^*$  character compared to the BODIPYs, which could enhance the spin-orbit coupling and the ensuing ISC.<sup>[56]</sup> In fact, according to the El-Sayed rule, the low-lying  $n\pi^*$  states significantly speed up the RISC transition compared to the TADF emitters where only  $\pi\pi^*$  excitons are energetically accessible.<sup>[57,58]</sup> Thus, as theoretically supported (Figure S5 in the Supporting Information) the qualitatively approached singlet-triplet energy gap should decrease but without promoting the triplet emission in aza-BODIPY.<sup>[35]</sup> As a result, either in the monomeric **8** aza-BODIPY or in the new 1–4 dyads we were unable to detect neither the phosphorescence emission nor the singlet oxygen emission sensitized from the corresponding triplet states.

4) Since the triplet concentration can be varied by dilution and/or by modulating the pump laser energy, the intensity of the emission delayed 10  $\mu\text{s}$  was recorded decreasing the dye concentration or the laser fluence. Under these experimental conditions the intensity of the delayed emission decreased linearly following therefore the expected dependence in one-photon process (Figures S6 and S7 in the Supporting Information.). Furthermore, we never observed the quadratic dependence of the emission intensity on dye concentration and/or

laser power required in a two-photon process such as triplet-triplet annihilation.

These results indicated that the delayed emission of the monomeric aza-BODIPY **8** and the herein synthesized multi-chromophoric cassettes should decay from the singlet excited state populated through RISC from the corresponding long-lived triplet excited states with no contribution of any other processes such as TTA. Hence, the aza-BODIPY moiety became an effective TADF probe maintaining a long-lived fluorescence emission in the red/near IR spectral region to boost its applicability in strategic research fields.

## Conclusions

Red/NIR thermally activated delayed fluorescence from dyes based on aza-BODIPY scaffolds was reported, to the best of our knowledge, for the first time. Thermally activated delayed fluorescence emission from 680 to 800 nm was registered even in aerated solutions at room temperature upon laser excitation at both 532 and 355 nm. Aza-BODIPYs due to the replacement of the central *meso*-carbon by an electronegative aza group became a better electron acceptor than the own BODIPY, thus being prone to electron transfer processes. A new series of cassettes based on grafting aza-BODIPY, acting as acceptor and red-emitting moiety, with one or two BODIPY donor units allowed to achieve a subtle balance between competing exciton energy and charge transfer processes to modulate properly the fluorescence response just adjusting the stereoelectronic properties of the energy donors, spacers and linkage positions.

The computational-assisted analysis of the photonic behavior of the herein synthesized energy and charge transfer cassettes revealed some key structural guidelines to enhance their prompt and delayed emission signatures with respect to that achieved from its monomeric aza-BODIPY. The new cassettes showed efficient light-harvesting properties across the UV-visible spectral region owing to the imposed steric hindrance to avoid both resonant electronic interactions as well as supramolecular aggregation by  $\pi\text{-}\pi$  stacking interactions, with deleterious effects on the emission efficiency. Thus, a judicious election of the BODIPY energy donors was crucial to avoid PET and to enable bright emission. Such modulation of the electron releasing ability of the energy donors can be straightforwardly done just adjusting the alkylation degree of the electron donors. In fact, non-alkylated BODIPY allowed suppressing PET and achieving bright NIR emission regardless of the excitation wavelength. Thereby, upon laser excitation at both 355 and 532 nm, these cassettes lasted beyond 700 nm, with efficiencies and photostabilities higher than those recorded from the monomeric aza-BODIPY as well as other commercially available dyes with emission in the red-edge of the visible spectrum and pumped under otherwise identical experimental conditions.

In addition, our synthetic approach fulfilled all the energetic and electronic requirements to achieve red/NIR emission delayed more than 100  $\mu\text{s}$  with respect to the incoming radiation, regardless on the laser pumping wavelength as well as on the excitation transfer mechanism sustained by the molecular

design. Through a systematic experimental and theoretical analysis of this surprising photonic behavior we unambiguously identified thermally activated reverse intersystem crossing from long-lived triplet excited states as the mechanism responsible for the observed delayed emission with no contribution of any other processes such could be triplet-triplet annihilation. These outstanding results pointed out the rational design of BODIPY-aza-BODIPY cassettes as a promising starting point from developing novel long-lived TADF materials with emission in the strategic red/NIR spectral region boosting their medical and optoelectronic applications.

## Acknowledgements

We gratefully acknowledge the Spanish Ministerio de Economía y Competitividad for financial support (projects MAT2017-83856-C3-1-P, 2-P and 3-P). We also thank the Gobierno Vasco for financial support (project IT912-16) and for a predoctoral fellowship to E.A.-Z. The authors thank SGiker of UPV/EHU for technical support with the computational calculations, which were carried out in the "ARINA" informatic cluster.

## Conflict of interest

The authors declare no conflict of interest.

**Keywords:** charge transfer · delayed fluorescence · dye chemistry · energy transfer · NIR emission

- T. Li, D. Yang, L. Zhai, S. Wang, B. Zhao, N. Fu, L. Wang, Y. Tao, W. Huang, *Adv. Sci.* **2017**, *4*, 1600166.
- Z. Yang, Z. Mao, Z. Xie, Y. Zhang, S. Liu, J. Zhao, J. Xu, Z. Chi, M. P. Aldred, *Chem. Soc. Rev.* **2017**, *46*, 915–1016.
- X.-K. Chen, D. Kim, J.-L. Brédas, *Acc. Chem. Res.* **2018**, *51*, 2215–2224.
- Y. Liu, Ch. Li, Z. Ren, S. Yan, M. R. Bryce, *Nat. Rev. Mater.* **2018**, *3*, 18020.
- X. Liang, Z.-L. Tu, Y.-X. Zheng, *Chem. Eur. J.* **2019**, *25*, 5623–5642.
- C. Baleizão, M. N. Berberan-Santos, *J. Chem. Phys.* **2007**, *126*, 204510.
- Q. Zhang, B. Li, S. Huang, H. Nomura, H. Tanaka, C. Adachi, *Nat. Photonics* **2014**, *8*, 326–332.
- S.-J. Woo, Y. Kim, M.-J. Kim, J. Y. Baek, S.-K. Know, Y.-H. Kim, J.-J. Kim, *Chem. Mater.* **2018**, *30*, 857–863.
- C.-S. Oh, D. Sa Pereira, S. H. Han, H.-J. Park, H. F. Higginbotham, A. P. Monkman, J. Y. Lee, *ACS Appl. Mater. Interfaces* **2018**, *10*, 35420–35429.
- C. W. Lee, J. Y. Lee, *ACS Appl. Mater. Interfaces* **2015**, *7*, 2899–2904.
- D. R. Lee, B. S. Kim, C. W. Lee, Y. Im, K. S. Yook, S.-H. Hwang, J. Y. Lee, *ACS Appl. Mater. Interfaces* **2015**, *7*, 9625–9629.
- C. Deng, S. Zheng, D. Wang, J. Yang, Y. Yue, M. Li, Y. Zhou, S. Niu, L. Tao, T. Tsuboi, Q. Zhang, *J. Phys. Chem. C* **2019**, *123*, 29875–29883.
- X.-L. Li, G. Xie, M. Liu, D. Chen, X. Cai, J. Peng, Y. Cao, S.-J. Su, *Adv. Mater.* **2016**, *28*, 4614–4619.
- D. Chen, P. Rajamalli, F. Tenopala-Carmona, C. L. Carpenter-Warren, D. B. Cordes, C.-M. Keum, A. M. Z. Slawin, M. C. Gather, E. Zysman-Colman, *Adv. Opt. Mater.* **2020**, *8*, 1901283.
- W. Zeng, H.-Y. Lai, W.-K. Lee, M. Jiao, Y.-J. Shiu, C. Zhong, S. Gong, T. Zhou, G. Xie, M. Sarma, K.-T. Wong, C.-C. Wu, C. Yang, *Adv. Mater.* **2018**, *30*, 1704961.
- J.-X. Chen, W.-W. Tao, Y.-F. Xiao, K. Wang, M. Zhang, X.-Ch. Fan, W.-C. Chen, J. Yu, S. Li, F.-X. Geng, X.-H. Zhang, C.-S. Lee, *ACS Appl. Mater. Interfaces* **2019**, *11*, 29086–29093.
- S. Wang, Z. Cheng, X. Song, X. Yan, K. Ye, Y. Lu, G. Yang, Y. Wang, *ACS Appl. Mater. Interfaces* **2017**, *9*, 9892–9901.
- J. H. Kim, J. H. Yun, J. Y. Lee, *Adv. Opt. Mater.* **2018**, *6*, 1800255.
- J.-X. Chen, W.-W. Tao, W.-C. Chen, Y.-F. Xiao, K. Wang, C. Cao, J. Yu, S. Li, F.-X. Geng, C. Adachi, C.-S. Lee, X.-H. Zhang, *Angew. Chem. Int. Ed.* **2019**, *58*, 14660–14665; *Angew. Chem.* **2019**, *131*, 14802–14807.
- X. Gong, P. Li, Y.-H. Huang, C. Y. Wang, C. H. Lu, W.-K. Lee, *Adv. Funct. Mater.* **2020**, *30*, 1908839.
- M. K. Etherington, J. Gibson, H. F. Higginbotham, T. J. Penfold, A. P. Monkman, *Nat. Commun.* **2016**, *7*, 13680.
- J. Gibson, T. J. Penfold, *Phys. Chem. Chem. Phys.* **2017**, *19*, 8428–8434.
- T. J. Penfold, F. B. Dias, P. Monkman, *Chem. Commun.* **2018**, *54*, 3926–3935.
- H. Wang, B. Zhao, P. Ma, Z. Li, X. Wang, C. Zhao, X. Fan, L. Tao, C. Duan, J. Zhang, C. Han, G. Chen, H. Xu, *J. Mater. Chem. C* **2019**, *7*, 7525–7530.
- Y. Im, M. Kim, Y.-J. Cho, J.-A. Seo, K. S. Yook, J. Y. Lee, *Chem. Mater.* **2017**, *29*, 1946–1963.
- Q. Zhang, H. Kuwabara, W. J. Potscavage, S. Huang, Y. Hatae, T. Shibata, C. Adachi, *J. Am. Chem. Soc.* **2014**, *136*, 18070–18081.
- G. A. Sommer, L. N. Mataranga-Popa, R. Czerwieniec, T. Hofbeck, H. H. Homeier, T. J. J. Müller, H. Yersin, *J. Phys. Chem. Lett.* **2018**, *9*, 3692–3697.
- G. Tang, A. A. Sukhanov, J. Zhao, W. Yang, Z. Wang, Q. Liu, V. K. Voronkova, M. Di Donato, D. Escudero, D. Jacquemin, *J. Phys. Chem. C* **2019**, *123*, 30171–30186.
- F. Gao, R. Du, C. Han, J. Zhang, Y. Wei, G. Lu, H. Xu, *Chem. Sci.* **2019**, *10*, 5556–5567.
- D. G. Congrave, B. H. Drummond, P. J. Conaghan, H. Francis, S. T. E. Jones, C. P. Grey, N. C. Greenham, D. Credgington, H. Bronstein, *J. Am. Chem. Soc.* **2019**, *141*, 18390–18394.
- S. Izumi, H. F. Higginbotham, A. Nyga, P. Stachek, N. Tohnai, P. de Silva, P. Data, Y. Takeda, S. Minakata, *J. Am. Chem. Soc.* **2020**, *142*, 1482–1491.
- Y. Ge, D. F. O'Shea, *Chem. Soc. Rev.* **2016**, *45*, 3846–3864.
- W. Mao, M. Zhu, C. Yan, Y. Ma, Z. Guo, W. Zhu, *ACS Appl. Bio Mater.* **2020**, *3*, 45–52.
- S. Shimizu, *Chem. Commun.* **2019**, *55*, 8722–8743.
- J. K. G. Karlsson, A. Harriman, *J. Phys. Chem. A* **2016**, *120*, 2537–2546.
- A. Prieto-Castañeda, E. Avellan-Zaballa, L. Garztia-Rivero, L. Cerdan, A. R. Agarrabaitia, I. García-Moreno, J. Bañuelos, M. J. Ortiz, *ChemPhotoChem* **2019**, *3*, 75–85.
- M. A. Filatov, S. Karthedath, P. M. Poletshuk, H. Savoie, K. J. Flanagan, C. Sy, E. Sitte, M. Telitchko, F. Laquai, R. W. Bpyle, M. O. Senge, *J. Am. Chem. Soc.* **2017**, *139*, 6282–6285.
- Q. Zhang, S. Xu, M. Li, Y. Wang, N. Zhang, Y. Guan, M. Chen, C.-F. Chen, H.-Y. Hu, *Chem. Commun.* **2019**, *55*, 5639–5642.
- Y. Wu, L. Jiao, F. Song, M. Chen, D. Liu, W. Yang, Y. Sun, G. Hong, L. Liu, X. Peng, *Chem. Commun.* **2019**, *55*, 14522–14525.
- P.-A. Bouit, K. Kamada, P. Feneyrou, G. Berginc, L. Toupet, O. Maury, C. Andraud, *Adv. Mater.* **2009**, *21*, 1151–1154.
- M. Koepf, M. Trabolzi, J. A. Wytoko, D. Paul, A. M. Albrecht-Gary, J. Weiss, *Org. Lett.* **2005**, *7*, 1279–1282.
- Z. Liu, S. G. Thacker, S. Fernandez-Castillejo, E. B. Neufeld, A. T. Remaley, R. Bittman, *ChemBioChem* **2014**, *15*, 2087–2096.
- G. Sathyamoorthi, M.-L. Soong, T. W. Ross, J. H. Boyer, *Heteroat. Chem.* **1993**, *4*, 603–608.
- A. Gorman, J. Killoran, C. O'Shea, T. Kenna, W. M. Gallagher, D. F. O'Shea, *J. Am. Chem. Soc.* **2004**, *126*, 10619–10631.
- A. Coskun, E. Deniz, E. U. Akkaya, *Org. Lett.* **2005**, *7*, 5187–5189.
- D. Prasannan, D. Raghav, S. Sujatha, H. Hareendrakrishna Kumar, K. Rathinasamy, C. Arunkumar, *RSC Adv.* **2016**, *6*, 80808–80824.
- G. Durán-Sampedro, A. R. Agarrabaitia, L. Cerdán, M. E. Pérez-Ojeda, A. Costela, I. García-Moreno, I. Esnal, J. Bañuelos, I. López Arbeloa, M. J. Ortiz, *Adv. Funct. Mater.* **2013**, *23*, 4195–4205.
- M. E. El-Khouly, A. N. Amin, M. E. Zandler, S. Fukuzumi, F. D'Souza, *Chem. Eur. J.* **2012**, *18*, 5239–5247.
- S. Kumar, H. B. Gobeze, T. Chatterjee, F. D'Souza, M. Ravikanth, *J. Phys. Chem. A* **2015**, *119*, 8338–8348.
- S. Kumar, K. G. Thorat, M. Ravikanth, *J. Org. Chem.* **2017**, *82*, 6568–6577.
- D. Escudero, *Acc. Chem. Res.* **2016**, *49*, 1816–1824.
- L. Cerdán, A. Costela, I. García-Moreno, J. Bañuelos, I. Lopez Arbeloa, *Laser Phys. Lett.* **2012**, *9*, 426–433.
- A. Schmitt, B. Hinkeldey, M. Wild, G. Jung, *J. Fluoresc.* **2009**, *19*, 755–758.



- [54] J. Zhao, K. Xu, W. Yang, Z. Wang, F. Zhong, *Chem. Soc. Rev.* **2015**, *44*, 8904–8939.
- [55] M. de Vetta, L. Gonzalez, I. Corral, *ChemPhotoChem* **2019**, *3*, 727–738.
- [56] R. T. Kuznetsova, Y. V. Aksenova, D. E. Bashkirtsev, A. A. Prokopenko, E. N. Tel'minov, G. V. Mayer, N. A. Dudina, E. V. Antina, A. Y. Nikonova, M. B. Berezin, A. S. Semeikin, *High Energy Chem.* **2015**, *49*, 16–23.
- [57] F. B. Dias, K. N. Bourdakos, V. Jankus, K. C. Moss, K. T. Kamtekar, V. Bhalla, J. Santos, M. R. Bryce, A. P. Monkman, *Adv. Mater.* **2013**, *25*, 3707–3714.
- [58] I. Lyskov, C. M. Marian, *J. Phys. Chem. C* **2017**, *121*, 21145–21153.

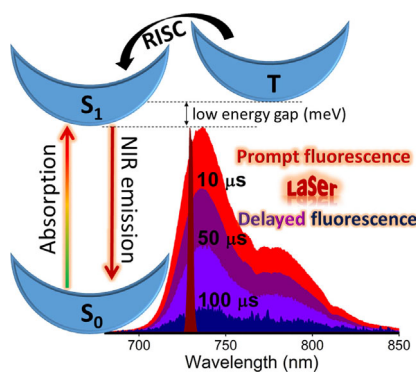
---

Manuscript received: June 17, 2020  
Revised manuscript received: July 19, 2020  
Accepted manuscript online: July 28, 2020  
Version of record online: ■ ■ ■ ■ 0000

## FULL PAPER

## ■ Dyes/Pigments

*E. Avellanal-Zaballa, A. Prieto-Castañeda,  
F. García-Garrido, A. R. Agarrabeitia,  
E. Rebollar, J. Bañuelos,\*  
I. García-Moreno,\* M. J. Ortiz*

**Red/NIR Thermally Activated Delayed  
Fluorescence from Aza-BODIPYs**

**Long-lived NIR fluorescence:** Aza-BODIPYs are attractive source of NIR fluorescence and laser emission. Herein, their ability to display delayed fluorescence via RISC under hard irradiation regimes is demonstrated for the first time. The designed cassettes are appealing materials endowed with efficient and long-lasting prompt NIR emission and with long-lived delayed emission (hundreds of microseconds) even in aerated solutions at room temperature.





Cite this: *Phys. Chem. Chem. Phys.*,  
2017, 19, 13210

Received 14th March 2017,  
Accepted 25th April 2017

DOI: 10.1039/c7cp01626c

rsc.li/pccp

## Rational molecular design enhancing the photonic performance of red-emitting perylene bisimide dyes†

E. Avellanal-Zaballa,<sup>a</sup> G. Durán-Sampedro,<sup>b</sup> A. Prieto-Castañeda,<sup>b</sup>  
A. R. Agarrabeitia,<sup>b</sup> I. García-Moreno,<sup>c</sup> I. López-Arbeloa,<sup>a</sup> J. Bañuelos <sup>\*a</sup> and  
M. J. Ortiz <sup>\*b</sup>

We report the synthesis of novel multichromophoric organic architectures, where perylene red is decorated with BODIPY and/or hydroxycoumarin dyes acting as light harvesters and energy donors. The computationally-aided photophysical study of these molecular assemblies reveals a broadband absorption which, regardless of the excitation wavelength, leads solely to a bright red-edge emission from perylene bisimide after efficient intramolecular energy transfer hops. The increase of the absorbance of these molecular antennas at key pumping wavelengths enhances the laser action of the commercial perylene red. The herein applied strategy based on energy transfer dye lasers should boost the use of perylene-based dyes as active media for red-emitting lasers.

### Introduction

Renewed interest has been focused on the design and synthesis of fluorophores with enhanced optical properties for new applications in medical, analytical, chemical, physics, biophysics science and technology fields.<sup>1</sup> Some of these advanced applications require highly fluorescent and photostable photonic materials under drastic irradiation conditions, such as hard radiation laser doses and/or prolonged times.<sup>2</sup> Although a wealth of organic dyes is known, most of the reported work on laser dyes has been focused on fluorophores derived from xanthenes<sup>3</sup> and boron dipyrromethene (BODIPY)<sup>4</sup> cores. Surprisingly, reports on the lasing behaviour of dyes derived from perylene bisimides (also known as perylene diimides, PDIs, Fig. 1) are scarce in spite of their particularly attractive optical properties.<sup>5</sup> In fact, these dyes exhibit exceptional chemical, thermal and photochemical stability with a fluorescence quantum yield close to unity.<sup>6</sup> In addition, PDI scaffolds enable straightforward functionalization at both the imide positions and the bay region allowing efficient modulation of their photonic behaviour.<sup>7</sup> However, several

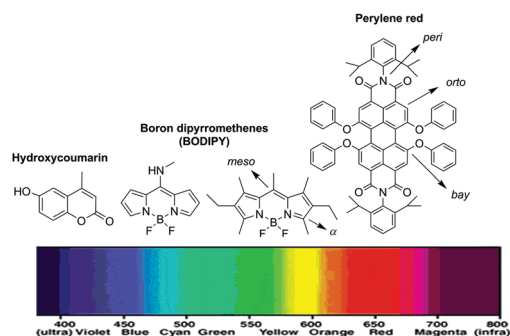


Fig. 1 Molecular structure of the dyes used to customize the molecular antennas ordered with regard to their emission profile along the visible spectral region.

reasons could justify the lack of lasers based on PDIs, mainly those related to a low solubility in common organic solvents and/or low absorption at standard laser excitation wavelengths, such as 532 nm and 355 nm (2th and 3th harmonics of an Nd:YAG laser).<sup>5–7</sup> To overcome this shortcoming, highly concentrated dye solutions are required to achieve laser gain. However, high dye concentrations ( $10^{-2}$  M) entail reabsorption/reemission and aggregation processes,<sup>8</sup> which reduce significantly the laser efficiency, thereby yielding much lower laser efficiencies than those recorded from other less fluorescent laser dyes. At lower dye concentrations (down to  $10^{-3}$  M), these deleterious effects are reduced but the absorption of the pump radiation is not enough to achieve net laser gain.

One approach to avoid these limitations is based on mixtures of dyes enabling Förster resonance energy transfer (FRET) where the excitation energy from an excited donor is non-radiatively

<sup>a</sup> Depto. de Química Física, Universidad del País Vasco-EHU, Apartado 644, 48080, Bilbao, Spain. E-mail: jorge.banuelos@ehu.es

<sup>b</sup> Depto. de Química Orgánica I, Facultad de CC. Químicas, Universidad Complutense de Madrid, Ciudad Universitaria s/n, 28040, Madrid, Spain. E-mail: mjortiz@ucm.es

<sup>c</sup> Depto. de Sistemas de Baja Dimensionalidad, Superficies y Materia Condensada, Instituto de Química-Física "Rocasolano", C.S.I.C., Serrano 119, 28006, Madrid, Spain

† Electronic supplementary information (ESI) available: Experimental, photophysical, computational and laser details, characterization data and NMR spectra of the new compounds, as well as Fig. S1–S7. See DOI: 10.1039/c7cp01626c

transferred “through space” to a proximal ground-state acceptor.<sup>9</sup> The effectiveness of this mechanism of excitation energy transfer (EET) depends strongly on the spectral overlap between donor emission and acceptor absorption bands, and the mutual orientation and distance between the donor and acceptor. As a matter of fact, the EET efficiency is greatly improved at short donor–acceptor distances. Consequently, the design of molecular cassettes with a rigid and short linker connecting donor and acceptor units should enhance significantly the efficiency of the FRET process with respect to the physical mixture of the chromophores.<sup>10</sup> Besides, and depending of the molecular assembly between the chromophores, an alternative EET mechanism to the aforementioned FRET can be switched on, in particular that known as “through-bond energy transfer” (TBET). Although this mechanism is not fully understood, it seems to be driven by an electronic exchange mediated *via* an orbital overlap.<sup>11</sup> Compared to the spectral overlap required for an effective FRET, TBET cassettes enable greater freedom for the selection of donor–acceptor pairs since they are apparently not constrained by the aforementioned requirements and just demand a direct linkage of the fragments or, alternatively, through a conjugated bridge (superexchange).

Molecular cassettes based on the PDI skeleton acting as the energy acceptor and BODIPY units as the donor have been developed as effective light-harvesting systems,<sup>12</sup> but never until now to boost the laser action of PDI dyes. To address this issue, we have synthesized a new library of EET cassettes to span the absorption spectra of the high red-emitting PDI dyes. As a result, high and broadband visible absorption, large pseudo-Stokes shifts and a sought-after improvement of the lasing efficiency and photostability are attained. In contrast to the previous large dendritic molecules based on BODIPY and PDI moieties connected by flexible and relatively long chains,<sup>12</sup> the herein reported multichromophoric systems feature compact integration of the donor–acceptor pair by a single C–C bond, shortening the intramolecular distance and impelling an ultra-fast and efficient EET process. As the final energy acceptor and red-emitting dye, we have chosen perylene red, (Per-Red, Fig. 1), whose molecular structure is based on a perylene bisimide backbone with aryloxy groups at the bay positions pushing the spectral bands towards the red edge of the visible region.<sup>13</sup> This fluorophore stands out by both its bright fluorescence, being among the best luminophores in the red region of the visible spectrum, and its chemical and photochemical robustness.<sup>6,13</sup> Thus, taking Per-Red as a scaffold, energy donor dyes working in the UV-blue region (coumarin) and the blue-yellow (BODIPY) part of the visible have been tethered to the side imide groups of the perylene core (Fig. 1). This synthetic versatility, attending to the structure and components, allows us to establish the dependence of the donor–acceptor combination and linkage positions on the photonic behavior of PDI laser dyes. The understanding of the composition–structure–property relationship should reorient the routes to design advanced materials with optimized properties for specific applications.

## Structural design

Prior to addressing the synthesis of the new molecular cassettes, several features, such as, the combined dyes, the linkage position or the kind of spacer connecting the building blocks, have to be judiciously selected. Indeed, to develop EET cassettes the molecular identity of each chromophoric fragment has to be maintained after covalent binding to afford a broadband absorption and selective excitation of each one to promote the intramolecular EET, whose mechanism depends on the molecular assembly.

Bearing all these facts in mind, and to ensure electronic isolation in the weak coupling limit regime<sup>14</sup> (no resonant interactions between the chromophores or with the spacers), we chose the *peri* position of the energy acceptor Per-Red as the target position to anchor the energy donors, since the *N*-imide does not take part in the delocalized system and should have little impact on the photophysical properties of the dye (see Fig. S1 in the ESI†). It should be mentioned that the basic structure of Per-Red was modified at the peripheral bisimide groups to favor its reactivity. As energy donors to be covalently linked at such a position we selected coumarin dyes<sup>15</sup> to reinforce the absorption in the UV/blue region, and BODIPY dyes<sup>16</sup> to increase the absorption probability at the green/yellow part of the visible spectral region. These dyes were selected since they are a benchmark for laser dyes in the respective spectral region. Besides, both fluorophores show the required spectral overlap with Per-Red to undergo effective FRET (Fig. S2 in ESI†). Firstly, the workability of the EET process in each coumarin (or BODIPY)–Per Red pair was assessed. To this aim, both nitrogen atoms at its *peri* positions were functionalized with two coumarin units (**PC-1** and **PC-2** in Fig. 2A) using a rigid *ortho*-methylated phenyl group as a spacer, which is placed at a different position in the benzopyrene core of coumarin. Alternatively, Per-Red was also linked through the same spacer to two BODIPY units (in particular PM567, **PB-1** in Fig. 2A) bearing an additional *para*-phenyl group at the *meso* position of the dipyrin core. Such an aryl group was sterically hindered by methyl moieties placed at the adjacent chromophoric positions to avoid its conformational freedom and consequently, the deleterious effect exerted on the emission efficiency.<sup>16</sup>

Taking advantage of the chemical versatility of BODIPYs and of their capacity to modulate their optical spectroscopic properties by the substitution pattern, we also built molecular dyads based on a 8-aminoBODIPY (characterized by blue-shifted spectral bands)<sup>17</sup> tethered to the said *peri* position of Per-Red *via* an alkyl chain (**PB-2** and **PB-3**) or a phenyl ring (**PB-4**) connecting the nitrogen atoms of both chromophores (Fig. 2B). Afterwards the next step, which was synthetically more challenging, was to span even more the absorption profile of Per-Red to cover a wider region of the visible spectrum by the combination of the said three dissimilar chromophores in a single molecular structure (**PBC** in Fig. 2C). To this aim, two hydroxycoumarin units were attached to a BODIPY–perylene dyad (similar to **PB-1** but bearing just one substituted *peri*-imide) through the boron bridge of the former, providing a molecular array where cascade-like EET should take place. The linkage of coumarin at the boron atom of the BODIPY unit was previously tested as an optimal design to

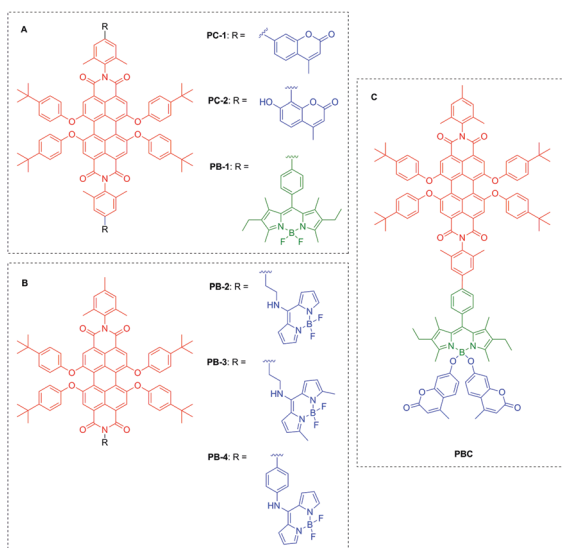


Fig. 2 Chemical structures of molecular cassettes.

render efficient FRET processes since this atom is not involved in the cyanine-like delocalized  $\pi$ -system.<sup>18</sup>

## Result and discussion

### Synthesis

PDI cassettes based on coumarin (**PC-1** and **PC-2**) or BODIPY (**PB-1**, **PB-2**, **PB-3** and **PB-4**) were readily prepared according to the convergent synthetic routes shown in Scheme 1 (for experimental details see the ESI<sup>†</sup>). The multichromophoric dye (**PBC**) based on BODIPY and coumarin dyes grafted to PDI was also synthesized following the same protocol.

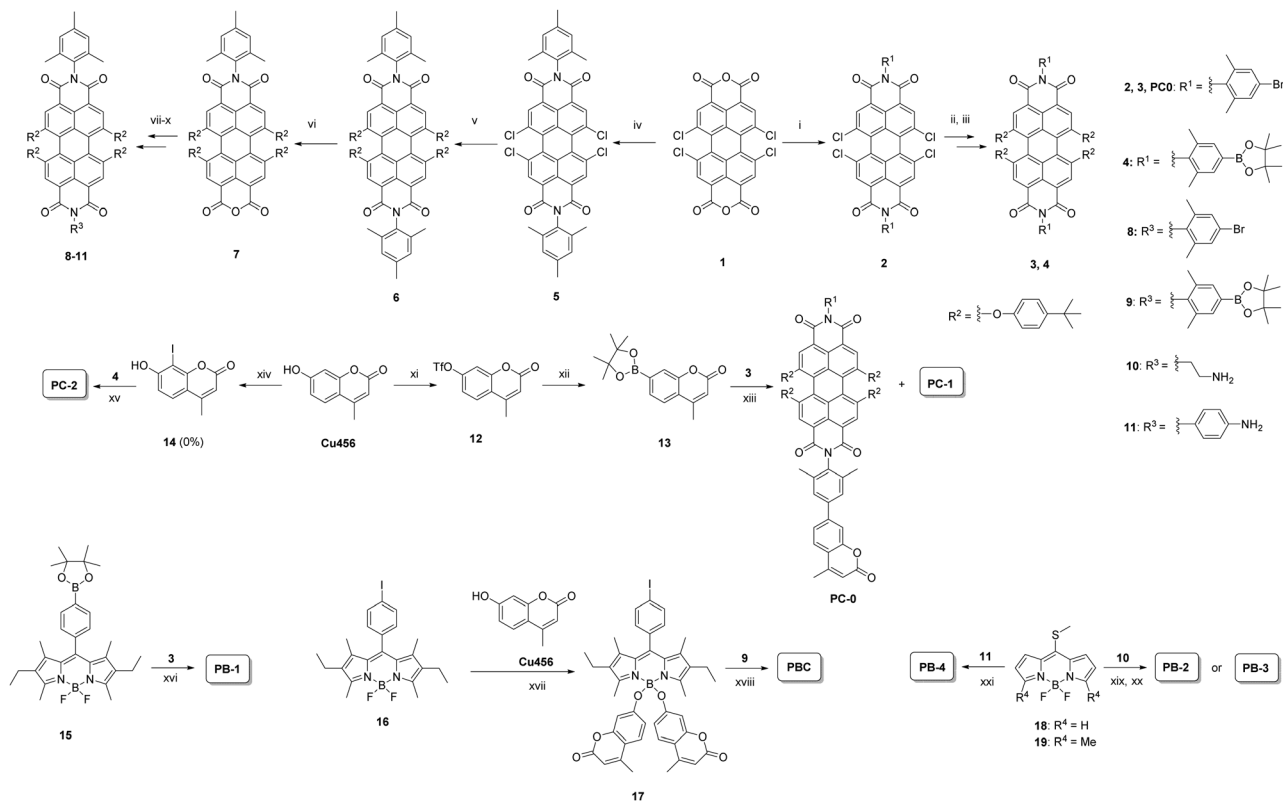
Key palladium-catalyzed Suzuki reactions were used to couple the PDI scaffolds to the corresponding BODIPY or/and coumarin moieties. Thus, Pd(PPh<sub>3</sub>)<sub>4</sub>, as a catalyst, was used to prepare cassettes **PC-1**, **PC-2** and **PB-1** from the appropriate boronate-ester and halogenated partners (steps xiii, xv and xvi, respectively, in Scheme 1). The same catalyst was used to prepare multichromophoric **PBC** from the corresponding boronate-ester PDI and coumarin-substituted (4-iodophenyl)BODIPY (step xviii in Scheme 1), with the latter obtained by nucleophilic substitution of fluorine atoms by coumarin in the corresponding *F*-BODIPY precursor (step xvii in Scheme 1). Finally, dyads **PB-2**, **PB-3** and **PB-4** were obtained from the corresponding 8-thiomethylBODIPY and amino-based PDI moieties (steps xix, xx and xxi, respectively, in Scheme 1), following the methodology described by E. Peña *et al.* for related compounds.<sup>19</sup>

### Photophysical properties

Initially, the photophysical behavior of the modified Per-Red was analyzed from diluted solutions in ethyl acetate (Table 1). Following the expected behavior, the conducted modifications around the *peri* position allow the coupling of energy donors and almost do not modify its photophysical behavior since the

*N*-phenyl group at the imide position almost does not contribute to the electronic density of the frontier orbitals involved in its visible spectral transition (Fig. S1 in ESI<sup>†</sup>). Proving our initial hypothesis, these perylene bisimides functionalized at the *N*-imide position (**3**, **6** and **8**, see Scheme 1) become suitable platforms to customize the searched molecular cassettes since they display fluorescence efficiency around 100%, even when heavy atoms (*i.e.* *p*-bromine units) are attached to their structure (Table 1). The electronic isolation provided by the phenyl group at the *peri* position of Per-Red defines the absorption profile of the new cassettes as the sum of the electronic transition of each chromophore, regardless of the chromophoric structure acting as a donor group. Thus, on one hand, in the coumarin–peryene cassettes (**PC-1** and **PC-2**) together with the red absorption of Per-Red (peaked at 570 nm), an UV band from coumarin (around 325 nm, slightly masked by the more energetic transitions of perylene) is recorded regardless of the coumarin structure side-linked to the perylene core (Table 2 and Fig. S3 in ESI<sup>†</sup>). On the other hand, the linkage of two BODIPY units at both edges of the perylene core (**PB-1**) gives rise to a strong absorption band at 523 nm ( $\epsilon_{\text{max}} = 165\,000\text{ M}^{-1}\text{ cm}^{-1}$ , Table 2 and Fig. S4 in ESI<sup>†</sup>), together with the perylene's own absorption.

With regard to the emission from these cassettes, the fluorescence band of Per-Red peaking at 600 nm prevails clearly in the spectral profile regardless of both the dye acting as a donor (coumarin or BODIPY) and the excitation wavelength (Table 2, Fig. S3 excitation at 325 nm and Fig. S4 excitation at 490 nm, respectively, in the ESI<sup>†</sup>). The quenching of the donor fluorescence, as well as the almost complete independence of the acceptor fluorescence quantum yield from the excitation wavelength (even in the donor region) highlights the effectiveness of the intra-EET process. Such an ongoing EET process should take place by a “through-space” (FRET) mechanism, since both systems fulfill the required spectral overlap to enhance the dipole–dipole coupling involved in this mechanism (Fig. S2 in ESI<sup>†</sup>), which is also improved by the short donor–acceptor distance imposed by the covalent linkage. However, considering the structure of these multichromophoric dyes, the contribution from the “through-bond” (TBET) mechanism cannot be ruled out, since the conjugated phenyl spacer enables the required electronic exchange.<sup>20</sup> It is noteworthy that it is quite difficult to account for the contribution of each pathway, and both could be additively contributing to the overall EET.<sup>20</sup> Upon excitation of the coumarin–peryene cassettes (**PC-1** and **PC-2**), the fluorescence efficiency is close to 100%, similar to that of the Per-Red dye (Table 1 *vs.* Table 2), and regardless of the excited absorption band. However, this efficiency decreases slightly in the cassette based on the BODIPY moiety (**PB-1**), probably due to the higher flexibility of the biphenyl spacer, which increases the non-radiative (internal conversion) rate constant. Nonetheless, the methyl groups grafted at the *ortho* position of the *N*-phenyl ring of Per-Red as well as at 1 and 7 positions of the BODIPY core hamper to some extent the free motion of the linker leading to a fluorescence quantum yield of 80% (Table 2).



**Scheme 1** Reagents, conditions and yields: (i) ClSO<sub>3</sub>H, I<sub>2</sub>, 70 °C, 5 h (62%); (ii) 4-*tert*-butylphenol (10 equiv.), K<sub>2</sub>CO<sub>3</sub> (5 equiv.), DMF, 90 °C, 24 h (**3**, 42%); (iii) PDI **3** (1 equiv.), bis(pinacolato)diboron (10 equiv.), KOAc (10 equiv.), Pd(dppf)Cl<sub>2</sub> (10%), DME, Δ, 16 h (**4**, 90%); (iv) 2,4,6-trimethylaniline (10 equiv.), propionic acid, Δ, 16 h (92%); (v) 4-*tert*-butylphenol (10 equiv.), K<sub>2</sub>CO<sub>3</sub> (5 equiv.), DMF, 90 °C, 16 h (78%); (vi) (a) KOH (3 equiv.), *tert*-butanol, Δ, 90 min; (b) acetic acid, Δ, 15 min (77%); (vii) 4-bromo-2,6-dimethylaniline (5 equiv.), propionic acid, Δ, 16 h (**8**, 77%); (viii) PDI **8** (1 equiv.), bis(pinacolato)diboron (3 equiv.), KOAc (3 equiv.), Pd(dppf)Cl<sub>2</sub> (10%), DME, Δ, 16 h (**9**, 87%); (ix) PDI **7** (1 equiv.), ethylenediamine (5 equiv.), toluene, 60 °C, 3 h (**10**, 83%); (x) PDI **7** (1 equiv.), 1,4-diaminobenzene (2.5 equiv.), toluene, 60 °C, 3 h (**11**, 36%); (xi) Tf<sub>2</sub>O (1.25 equiv.), *N,N*-diisopropylethylamine (1.5 equiv.), DCM, t.a., 8 h (61%); (xii) bis(pinacolato)diboron (2 equiv.), KOAc (2 equiv.), Pd(dppf)Cl<sub>2</sub> (10%), DME, Δ, 24 h (**13**, 81%); (xiii) PDI **3** (0.125 equiv.), K<sub>2</sub>CO<sub>3</sub> (1 equiv.), Pd(PPh<sub>3</sub>)<sub>4</sub> (10%), toluene/ethanol/water (2 : 2 : 1), Δ, 8 h (**PC-0**, 26%; **PC-1**, 47%); (xiv) I<sub>2</sub> (0.8 equiv.), periodic acid (0.2 equiv.), ethanol, r.t., 2 h (76%); (xv) BDP **4** (0.125 equiv.), K<sub>2</sub>CO<sub>3</sub> (1 equiv.), Pd(PPh<sub>3</sub>)<sub>4</sub> (10%), toluene/ethanol/water (2 : 2 : 1), Δ, 8 h (32%); (xvi) PDI **3** (0.34 equiv.), K<sub>2</sub>CO<sub>3</sub> (2 equiv.), Pd(PPh<sub>3</sub>)<sub>4</sub> (10%), toluene/ethanol/water (2 : 2 : 1), Δ, 1 h (83%); (xvii) (a) AlCl<sub>3</sub> (2 equiv.), 1,2-dichloroethane, Δ, 30 min; (b) **Cu456** (5 equiv.), Δ, 30 min (40%); (xviii) PDI **9** (0.33 equiv.), K<sub>2</sub>CO<sub>3</sub> (4 equiv.), Pd(PPh<sub>3</sub>)<sub>4</sub> (10%), toluene/ethanol/water (2 : 2 : 1), Δ, 1 h (20%); (xix) BODIPY **18** (1 equiv.), PDI **10** (0.5 equiv.), CH<sub>3</sub>CN, r.t., 3 h (**PB-2**, 52%); (xx) BODIPY **19** (1 equiv.), PDI **10** (0.5 equiv.), CH<sub>3</sub>CN, r.t., 3 h (**PB-3**, 42%); (xxi) BODIPY **18** (1 equiv.), PDI **11** (0.9 equiv.), copper(i) thiophene-2-carboxylate (1 equiv.), CH<sub>3</sub>CN, 70 °C, 24 h (45%).

**Table 1** Photophysical properties of the functionalized Per-Red compounds (**3**, **6** and **8**, see Scheme 1) in diluted solutions (2 μM) of ethyl acetate: absorption ( $\lambda_{ab}$ ) and fluorescence ( $\lambda_{fl}$ ) wavelengths, molar absorption ( $\epsilon_{max}$ ), Stokes shift ( $\Delta\nu_{st}$ ), fluorescence quantum yield ( $\phi$ ) and lifetime ( $\tau$ ), and radiative ( $k_{fl}$ ) and non-radiative ( $k_{nr}$ ) rate constants. The corresponding data for the commercial Per-Red (in *italic*) are added for comparison

	$\lambda_{ab}$ (nm)	$\epsilon_{max}$ (M <sup>-1</sup> cm <sup>-1</sup> )	$\lambda_{fl}$ (nm)	$\phi$	$\Delta\nu_{st}$ (cm <sup>-1</sup> )	$\tau$ (ns)	$k_{fl}$ (10 <sup>8</sup> s <sup>-1</sup> )	$k_{nr}$ (10 <sup>8</sup> s <sup>-1</sup> )
Per-Red	<i>568.0</i>	<i>49 000</i>	<i>597.5</i>	<i>1.00</i>	<i>865</i>	<i>6.16</i>	<i>1.62</i>	<i>0.00</i>
<b>3</b>	573.0	36 550	603.0	0.96	870	6.30	1.53	0.06
<b>6</b>	570.0	39 850	600.0	0.98	880	6.37	1.54	0.03
<b>8</b>	571.0	44 100	602.0	1.00	900	6.31	1.61	0.00

**Table 2** Photophysical properties of the coumarin–perylene (**PC-1** and **PC-2**) and BODIPY–perylene (**PB-1**) cassettes in diluted solutions of ethyl acetate

	$\lambda_{ab}$ (nm)	$\epsilon_{max}$ (M <sup>-1</sup> cm <sup>-1</sup> )	$\lambda_{fl}$ (nm)	$\phi^a$	$\Delta\nu_{st}$ (cm <sup>-1</sup> )	$\tau$ (ns)	$k_{fl}$ (10 <sup>8</sup> s <sup>-1</sup> )	$k_{nr}$ (10 <sup>8</sup> s <sup>-1</sup> )
<b>PC-1</b>	573.0	34 200	602.0	0.97	840	6.07	1.60	0.05
<b>PC-2</b>	571.0	37 600	600.0	1.00	845	5.98	1.67	0.00
<b>PB-1</b>	572.0	54 800	603.0	0.80	900	5.30	1.51	0.37
	523.0	165 000				5.26 <sup>b</sup>		

<sup>a</sup> Similar values were attained (just 2% lower than the herein listed values upon direct excitation of the acceptor) upon selective excitation of the donors or at the key lasing pumping wavelengths (355 and 532 nm). <sup>b</sup> Recorded upon excitation at 470 nm (BODIPY region), instead of at 570 nm (direct excitation of perylene) as in the other data, and monitored at 600 nm (perylene region).

With regard to the molecular antenna **PBC** based on the three linked chromophores, the absorption spectral profile shows the expected three main bands at 325 nm, 525 nm and 572 nm, corresponding to each fragment (hydroxycoumarin, BODIPY and Per-Red dyes, Fig. 3). The molecular frontier orbitals of **PBC** confirm the electronic isolation of each chromophoric unit in the antenna since the electron density is exclusively located on each chromophore, which retains its own absorption transition after the covalent linkage, and no electronic coupling between them is predicted (Fig. 4). Regardless of the selective excitation of each chromophore (in the UV, green/yellow or orange/red spectral region) the bright emission from the Per-Red dye (fluorescence efficiency 82% at 600 nm) is solely recorded as a consequence of the ongoing efficient intra-EET process. Moreover, the excitation spectrum, registered at the fluorescence wavelength of perylene dye, perfectly matches the absorption spectrum of **PBC** showing the three bands corresponding to each fragment (Fig. 3). Once again, these results support the viability of an effective EET process, which quenches efficiently the fluorescence emission from the coumarin and BODIPY fragments upon linkage to the perylene core (Fig. 3). Such an intra-EET process should take place through a cascade-like mechanism from coumarin to BODIPY, and from here to the final perylene acceptor. Nonetheless, we cannot rule out the possible contribution, albeit likely less feasible, of a direct FRET from coumarin to perylene, as observed in the corresponding donor-acceptor pairs (**PC-1** and **-2**).

The aforementioned cassettes enhance significantly the absorption of Per-Red in the green/yellow spectral region but less efficiently in the blue region. Thus, to achieve a panchromatic absorption of Per-Red over the whole visible region promoting its laser action, new molecular cassettes with strong absorption in the 350–450 nm range were synthesized by replacing the above energy donors by the 8-aminoBODIPY moiety, whose spectral bands properly complemented those of Per-Red. It is well established that the amino substitution at the *meso* position of the BODIPY core

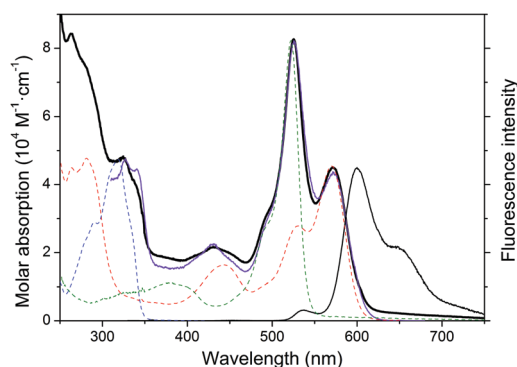


Fig. 3 Absorption (bold line) and fluorescence spectra (thin line), upon selective excitation of the coumarin fragment ( $\lambda_{\text{exc}} = 325$  nm), in ethyl acetate, of cassette **PBC** including hydroxycoumarin, BODIPY and Per-Red dyes in the same molecular structure. The corresponding absorption bands of these fragments (dashed lines, coumarin in blue, BODIPY in green and Per-Red in red) are also depicted. To emphasize the intra-EET the excitation spectrum (purple) monitored at 680 nm is also included.

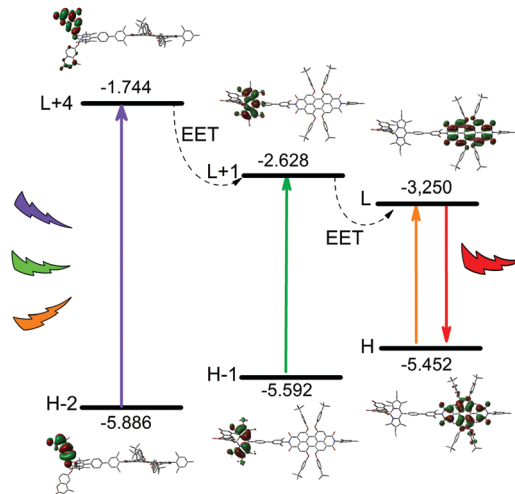


Fig. 4 Energy diagram (in eV) of the molecular orbitals involved in the main electronic transitions of the **PBC** cassette. The transition corresponding to the other coumarin fragment (H-3  $\rightarrow$  L+5) has not been included for simplicity, because it almost overlaps energetically with that herein depicted for coumarin (H-2  $\rightarrow$  L+4).

greatly shifts its spectral bands to higher energies owing to the formation of a hemicyanine mesomeric form (Fig. S5 in ESI $^\dagger$ ).<sup>17</sup> Therefore, 8-aminoBODIPY and its 3,5-dimethylated counterpart (such simple alkylation ameliorated the fluorescence response)<sup>17</sup> were linked to the *N*-imide of perylene through an aliphatic chain (**PB-2** and **PB-3**, respectively).

The absorption spectra of both dyads exhibit two main and distinct bands in the visible region, placed at 574 nm from perylene and at 403 nm from 8-aminoBODIPY (Fig. 5). The  $\alpha$ -methylation of the donor group in **PB-3** shifts the absorption maximum to 422 nm increasing, at the same time, the absorption probability due to the inductive donor effect of the alkyl moieties. In both cassettes, the selective excitation of 8-aminoBODIPY (at 390 nm) leads to a main fluorescence band corresponding to Per-Red (600 nm), suggesting that, once more, an intra-EET process takes place, but this time only through a FRET mechanism, since the polymethylene spacer avoids the electronic exchange required in the TBET process. Anyway, the EET process is still very efficient, as supported by the similarity of the excitation spectra monitored in the perylene emission region and the absorption spectra (Fig. 5).

Strikingly, the fluorescence response of both dyads is quite different (Table 3). While **PB-2** follows the expected behaviour, exhibiting a highly efficient fluorescence (around 87% and a monoexponential decay curve with a lifetime of 6.21 ns), the dimethylation of the BODIPY core (**PB-3**) modifies drastically the emission properties, decreasing the effectiveness to merely 51% and inducing a multiexponential decay curve where the short-lifetime components prevail (Fig. S6 in ESI $^\dagger$ ). Therefore, the solely alkylation of BODIPY seems to switch on a non-radiative pathway, which quenches the emission from the perylene dye.

To unravel the ongoing photophysical process, the molecular orbitals of these cassettes were simulated by DFT methods (Fig. 6). Thus, the energetic order of the molecular orbitals in **PB-2** is the expected one, with the less energetic transitions

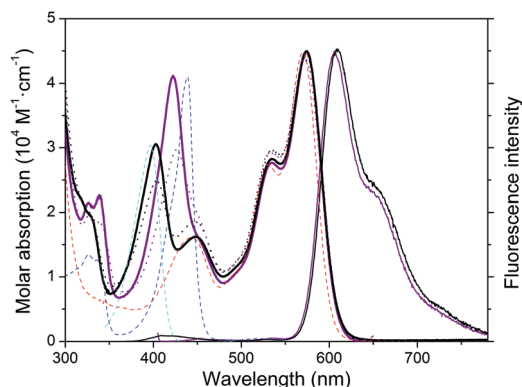


Fig. 5 Absorption (bold line) and fluorescence spectra (thin line) of the cassettes customized by the combination of Per-Red and 8-aminoBODIPY (**PB-2**, in black) or its 3,5-dimethylated derivative (**PB-3**, in purple) in ethyl acetate upon selective excitation at the BODIPY fragment ( $\lambda_{\text{exc}} = 390$  nm). The corresponding absorption bands of the building blocks (dashed lines, Per-Red in red, 8-aminoBODIPY in cyan and its alkylated counterpart in blue) are also depicted. To emphasize the ongoing EET the corresponding excitation spectra ( $\lambda_{\text{em}} = 580$  nm, dotted lines) are also depicted.

(HOMO  $\rightarrow$  LUMO) and (HOMO-1  $\rightarrow$  LUMO+2) being entirely located on the perylene and BODIPY cores, respectively. However, the simple methylation of BODIPY increases its HOMO energy (from  $-5.79$  eV to  $-5.46$  eV), locating it between the HOMO and LUMO energy gap of perylene. In other words, in cassette **PB-3**, the HOMO is placed on BODIPY, while the low-lying HOMO-1 is placed on perylene. This energetic disposition of the molecular orbitals enables, upon selective excitation of perylene, an electron transfer from BODIPY to perylene through a thermodynamically feasible reductive photoinduced electron transfer (PET), which quenches the fluorescence emission from perylene (Fig. 6). Nevertheless, it should be mentioned that it has been recently reported by computational simulations that the underlying quenching mechanism in some putative PET processes (mainly those involved in sensing) could be assigned to the population of “dark” states (such as ICT or  $n\pi^*$ ).<sup>21</sup> Unfortunately the excited state calculations (potential energy profile to unravel the conical intersections) required to unambiguously assign the involved mechanism are unaffordable due to the large size of the herein reported cassettes.

Trying to increase the emission efficiency of the cassettes based on 8-aminoBODIPY, the flexible aliphatic spacer in **PB-2** was replaced by a more rigid and conjugated phenyl linker in **PB-4**.

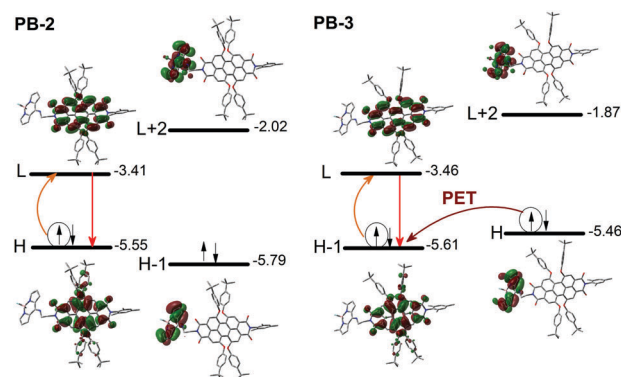


Fig. 6 Theoretically simulated energy (in eV) arrangement of the molecular orbitals of 8-aminoBODIPY-perylene dyads (**PB-2** and **PB-3**) to highlight the ongoing PET process upon alkylation of the former chromophore.

Such structural modification impacts neither the shape nor the position of the spectral bands, and also an effective intra-EET process takes place. Nonetheless, its more constrained geometry leads to an increase of the fluorescence efficiency up to 97% (Table 3), a value similar to that achieved for Per-Red (Table 1). Indeed, among all of the cassettes herein synthesized, **PB-4** displays the best performance as a light-harvesting molecular antenna, enabling panchromatic absorption in the visible spectral region and providing exclusively, and regardless of the excitation wavelength, a bright and red fluorescence emission from the perylene dye with an efficiency approaching 100%.

### Lasing properties

According to their absorption properties, the lasing behavior of the new dyes was analyzed under pumping at standard wavelengths of 355 nm and 532 nm. All the dyes studied in this work exhibit broad-line-width laser emission, with a pump threshold energy of  $\sim 0.8$  mJ, divergence of 5 mrad and pulse duration of 8 ns full-width at half maximum (FWHM) when placed in a simple plane-plane non-tunable resonator cavity. To optimize the laser action of the different dyes, we first analyzed the dependence of their lasing properties on dye concentration in ethyl acetate solutions, by varying the optical densities over an order of magnitude while keeping all other experimental parameters constant. The lasing wavelength, efficiency and photostability (see ESI<sup>†</sup>) of the new dyes at each optimal concentration are presented in Table 4. The lasing behavior

Table 3 Photophysical properties of the 8-aminoBODIPY-perylene cassettes (**PB-2** and **PB-3**) in diluted solutions of ethyl acetate

	$\lambda_{\text{ab}}$ (nm)	$\epsilon_{\text{max}}$ ( $\text{M}^{-1} \text{cm}^{-1}$ )	$\lambda_{\text{fl}}$ (nm)	$\phi^a$	$\Delta\nu_{\text{St}}$ ( $\text{cm}^{-1}$ )	$\tau$ (ns)	$k_{\text{fl}}$ ( $10^8 \text{ s}^{-1}$ )	$k_{\text{nr}}$ ( $10^8 \text{ s}^{-1}$ )
<b>PB-2</b>	574.0	44 900	609.0	0.87	1000	6.21	1.40	0.21
	403.0	30 600						
<b>PB-3</b>	574.0	46 100	604.5	0.51	880	6.53(3%)	—	—
	422.5	41 500				2.17(32%)		
<b>PB-4</b>	569.0	45 000	602.5	0.97	980	0.52(65%)	1.59	0.06
	415.0	31 000				6.08		

<sup>a</sup> Similar values were attained (just 2% lower than the herein listed values upon direct excitation of the acceptor) upon selective excitation of 8-aminoBODIPY or at the key lasing pumping wavelengths (355 and 532 nm).



**Table 4** Lasing properties of the new dyes reported at the dye concentration that optimizes the laser action in ethyl acetate solution. [c]: dye concentration;  $\lambda_{\text{pump}}$ : wavelength of pump laser radiation; Eff: lasing efficiency (ratio between the energy of the laser output and the pump energy incident on the sample surface);  $\lambda_{\text{la}}$ : peak wavelength of the laser emission;  $I$ : Intensity of the laser-induced emission after 100 000 pump pulses at 10 Hz repetition rate. The corresponding data for the commercial Per-Red are added for comparison

	[c] (mM)	$\lambda_{\text{pump}}$ (nm)	$\lambda_{\text{la}}$ (nm)	Eff (%)	$I^a$ (%)
Per-Red	9	532	625	22	73
<b>3</b>	9	532	632	19	73
<b>6</b>	9	532	628	20	70
<b>8</b>	9	532	630	21	73
<b>PC-1</b>	3	355	624	26	78
<b>PC-2</b>	3	355	623	27	82
<b>PB-1</b>	1	532	625	27	75
<b>PB-2</b>	2	355	623	24	70
<b>PB-3</b>	2	355	628	22	72
<b>PB-4</b>	2	355	625	30	80
<b>PBC</b>	1	355	628	35	100

<sup>a</sup>  $I(\%) = 100 (I/I_0)$ , with  $I_0$  being the initial intensity.

of the dyes shows a good correlation with their photophysical properties: the higher the fluorescence quantum yield, the higher the lasing efficiency; the higher the Stokes shift and the lower the non-radiative rate constant, the higher the lasing photostability. In addition, regardless of both the pumping wavelength and the structure of the multichromophoric systems, only the laser emission from Per-Red peaking at 625 nm appears since, due to the effectiveness of the intra-EET processes, laser emission from dyes acting as donor units was never recorded. Accordingly, the corresponding fluorescence spectra of the cassettes at these key pumping wavelengths (collected in Fig. S7 in the ESI†) show the expected predominant red emission from perylene, with almost no sign of emission from the donors.

Coumarin and BODIPY moieties grafted to Per-Red enhance the absorption of the molecular cassettes at the pumping wavelengths, allowing a drastic decrease of the dye concentration in the active medium and, consequently, a reduction of deleterious effects, such as reabsorption/reemission and aggregation processes, that becomes particularly important when highly concentrated solutions are required to induce efficient laser emission. So, the dyads based on coumarin dyes (**PC-1** and **PC-2**) pumped at 355 nm as well as that based on the BODIPY unit (**PB-1**) pumped at 532 nm lased at 624 nm with an efficiency around 27%, and a high photostability retaining 75% of their initial laser efficiency after 100 000 pump pulses at 10 Hz repetition rate. Note that the Per-Red pumped under identical experimental conditions exhibits a similar lasing lifetime but lower lasing efficiency (22%). The molecular cassettes based on 8-aminoBODIPY (**PB-2** and **PB-3**) pumped at 355 nm display similar lasing efficiency (23%) to Per-Red in spite of being the systems with the worst photophysical properties due to the flexible connector between donor-acceptor units. In fact, upon replacing it by a rigid spacer (**PB-4**) the lasing efficiency increases up to 30%.

Attending to the lasing efficiency and photostability, the molecular antenna **PBC** arises as a promising laser dye. When pumped

at 355 nm as well as at 532 nm, it improves the laser action of Per-Red, enabling an efficiency of 35% with high photostability since it retains its initial lasing efficiency without signs of degradation after the long-term pumping run. It is important to highlight that the photostability of **PBC** is noticeably higher than those exhibited individually by the corresponding chromophoric components. As an example, under identical pumping conditions, the key blue and green components of **PBC** lose completely the laser emission after just 40 000 and 75 000 pump pulses, respectively. The same takes place when the three individual components are physically mixed in a single solution, which clearly demonstrates the benefits of embedding them into a proper single molecular architecture.

## Conclusions

We have developed a straightforward and cost-effective synthetic approach to attain molecular cassettes enhancing significantly the already valuable photophysical and laser properties of perylene bisimide dyes. Compared to the “unmodified” and commercial Per-Red, the new multichromophoric systems span the absorption spectrum into a broad spectral region exhibiting, simultaneously, efficient fluorescence emission in the red-edge spectral region. The rational design of the new molecular systems ameliorates key optical factors to improve their photonic applicability: higher absorption coefficients at the standard pumping laser wavelengths; increased Stokes shifts, EET efficiency close to 100%; and lasing efficiency and photostability higher than that exhibited by the parent Per-Red, which is considered a bench-mark for red-emitting commercial dyes. In this sense, the synthetic versatility of these molecular cassettes together with a complete characterization of their photophysical signatures provides useful information for the understanding of the tangled composition–structure–property relationship, emerging as an effective tool to predict their lasing behavior and assisting in the rational design of new photonic systems with advanced applications.

## Acknowledgements

Financial support from the MICINN (MAT2014-51937-C3-1-P, MAT2014-51937-C3-2-P, MAT2014-51937-C3-3-P and MAT2015-68837-REDT) and Basque Government (IT912-16) is gratefully acknowledged. E. A.-Z. acknowledges the Basque Government for a predoctoral fellowship.

## References

- (a) H. Lu, J. Mack, Y. Yang and Z. Shen, *Chem. Soc. Rev.*, 2014, **43**, 4778–4823; (b) A. Bessette and G. S. Hanan, *Chem. Soc. Rev.*, 2014, **43**, 3342–3405; (c) K. Pei, Y. Wu, H. Li, Z. Geng, H. Tian and W.-H. Zhu, *ACS Appl. Mater. Interfaces*, 2015, **7**, 5296–5304; (d) G. Chen, H. Sasabe, T. Igarashi, Z. Hong and J. Kido, *J. Mater. Chem. A*, 2015, **3**, 14517–14534; (e) B. Xiao, X. Deng, W. Zhou and E.-K. In, *Front. Cell. Neurosci.*, 2016, **10**, 76; (f) S. M. Sharkar, S. M. Kim, S. H. Kim, I. In,

- H. Lee and S. Y. Park, *J. Mater. Chem. B*, 2015, **3**, 5833–5841; (g) L. Cerdan, J. Brabore, I. Garcia-Moreno, A. Costela and M. G. S. Londerborough, *Nat. Commun.*, 2015, **6**, 5958.
- 2 (a) M. Grossi, M. Morgunova, S. Cheung, D. Scholz, E. Conroy, M. Terrile, A. Panarella, J. C. Simpson, W. M. Gallagher and D. F. O'Shea, *Nat. Commun.*, 2016, **7**, 10855; (b) A. Kamkaew, S. H. Lim, H. B. Lee, L. V. Kiew, L. Y. Chung and K. Burgess, *Chem. Soc. Rev.*, 2013, **42**, 77–88; (c) X. Wu, Y. Zhang, K. Takle, O. Bilsel, Z. Li, H. Lee, Z. Zhang, D. Li, W. Fan, C. Duan, E. M. Chan, C. Lois, Y. Xiang and G. Han, *ACS Nano*, 2016, **10**, 1060–1066; (d) J. Liu, Y.-Q. Sun, H. Zhang, H. Shi, Y. Shi and W. Guo, *ACS Appl. Mater. Interfaces*, 2016, **8**, 22953–22962.
- 3 (a) H. N. Kim, M. H. Lee, H. J. Kim, J. S. Kim and J. Yoon, *Chem. Soc. Rev.*, 2008, **37**, 1465–1472; (b) M. Beija, C. A. M. Afonso and J. M. G. Martinho, *Chem. Soc. Rev.*, 2009, **38**, 2410–2433; (c) D. T. Quang and J. S. Kim, *Chem. Rev.*, 2010, **110**, 6280–6301; (d) X. Chen, T. Pradhan, F. Wang, J. S. Kim and J. Yoon, *Chem. Rev.*, 2012, **112**, 1910–1956; (e) Y.-Q. Sun, J. Liu, X. Lv, Y. Liu, Y. Zhao and W. Guo, *Angew. Chem., Int. Ed.*, 2012, **51**, 7634–7636.
- 4 (a) A. Loudet and K. Burgess, *Chem. Rev.*, 2007, **107**, 4891–4932; (b) G. Ulrich, R. Ziessel and A. Harriman, *Angew. Chem., Int. Ed.*, 2008, **47**, 1184–1201; (c) N. Boens, V. Leen and W. Dehaen, *Chem. Soc. Rev.*, 2012, **41**, 1130–1172; (d) T. Kowada, H. Maeda and K. Kikuchi, *Chem. Soc. Rev.*, 2015, **44**, 4953–4972; (e) A. J. C. Kuehne and M. C. Gather, *Chem. Rev.*, 2016, **116**, 12823–12864.
- 5 (a) Z. Lu, B. Jiang, X. Zhang, A. Tang, L. Chen, C. Zhan and J. Yao, *Chem. Mater.*, 2014, **26**, 2907–2914; (b) F. Würthner, C. R. Saha-Möller, B. Fimmel, S. Ogi, P. Leowanawat and D. Schmidt, *Chem. Rev.*, 2016, **116**, 962–1052.
- 6 (a) I. Garcia-Moreno, A. Costela, V. Martin, M. Pintado and R. Sastre, *Adv. Funct. Mater.*, 2009, **19**, 2547–2552; (b) L. Cerdan, A. Costela, G. Duran, I. Garcia-Moreno, M. Calle, M. Juan, J. de Abajo and G. A. Turnbull, *J. Mater. Chem.*, 2012, **22**, 8938–8947; (c) T. Ribeiro, S. Raja, A. S. Rodrigues, F. Fernandes, C. Baleizão and J. P. S. Farinha, *Dyes Pigm.*, 2014, **110**, 227–234; (d) M. G. Ramirez, M. Morales-Vidal, V. Navarro-Fuster, P. G. Boj, J. A. Quintana, J. M. Villalvilla, A. Retolaza, S. Merino and M. A. Diaz-Garcia, *J. Mater. Chem. C*, 2013, **1**, 1182–1191.
- 7 (a) Q. Yan, Y. Zhou, Y.-Q. Zheng, J. Pei and D. Zhao, *Chem. Sci.*, 2013, **4**, 4389–4394; (b) L. Chen, C. Li and K. Müllen, *J. Mater. Chem. C*, 2014, **2**, 1938–1956; (c) B. A. Llewellyn, E. S. Davies, C. R. Pfeiffer, M. Cooper, W. Lewis and N. R. Champness, *Chem. Commun.*, 2016, **52**, 2099–2102.
- 8 (a) R. O. Al-Kaysi, T. S. Ahn, A. M. Müller and C. J. Bardeen, *Phys. Chem. Chem. Phys.*, 2006, **8**, 3453–3459; (b) S. Ghosh, X.-Q. Li, V. Stepanenko and F. Würthner, *Chem. – Eur. J.*, 2008, **14**, 11343–11357; (c) T. E. Kaiser, V. Stepanenko and F. Würthner, *J. Am. Chem. Soc.*, 2009, **131**, 6719–6732; (d) H. Lin, R. Camacho, Y. Tian, T. E. Kaiser, F. Würthner and I. G. Scheblykin, *Nano Lett.*, 2010, **10**, 620–626.
- 9 (a) L. Cerdán, E. Enciso, V. Martín, J. Bañuelos, I. López-Arbeloa, A. Costela and I. García-Moreno, *Nat. Photonics*, 2012, **6**, 621–626; (b) N. B. Ahamed and P. K. Kalanisamy, *Opt. Commun.*, 2002, **213**, 67–80; (c) B. J. Scott, M. H. Bartl, G. Wirnsberger and G. D. Stucky, *J. Phys. Chem. A*, 2003, **107**, 5499–5502; (d) L. Cerdán, A. Costela and I. García-Moreno, *Org. Electron.*, 2012, **13**, 1463–1469; (e) L. Cerdán, A. Costela, G. Durán-Sampedro and I. García-Moreno, *Appl. Phys. B: Lasers Opt.*, 2012, **108**, 839–850; (f) L. Cerdán, E. Enciso, L. Gartzia-Rivero, J. Bañuelos, I. López-Arbeloa, A. Costela and I. García-Moreno, *RSC Adv.*, 2014, **4**, 22115–22122; (g) L. Gartzia-Rivero, L. Cerdán, J. Bañuelos, E. Enciso, I. López-Arbeloa, A. Costela and I. García-Moreno, *J. Phys. Chem. C*, 2014, **118**, 13107–13117.
- 10 (a) N. C. Jeong, H.-J. Son, C. Prasittichai, C. Y. Lee, R. A. Jensen, O. K. Farha and J. T. Hupp, *J. Am. Chem. Soc.*, 2012, **134**, 19820–19827; (b) J. Fan, M. Hu, P. Zhan and X. Peng, *Chem. Soc. Rev.*, 2013, **42**, 29–43; (c) D. K. Panda, F. S. Goodson, S. Ray and S. Saha, *Chem. Commun.*, 2014, **50**, 5358–5360; (d) S. Kuhri, V. Engelhardt, R. Fausi and D. M. Guidi, *Chem. Sci.*, 2014, **5**, 2580–2588; (e) G. Durán-Sampedro, A. R. Agarrabeitia, I. Garcia-Moreno, L. Gartzia-Rivero, S. de la Moya, J. Bañuelos, I. López-Arbeloa and M. J. Ortiz, *Chem. Commun.*, 2015, **51**, 11382–11385.
- 11 (a) S. Speiser, *Chem. Rev.*, 1996, **96**, 1953–1976; (b) A. C. Benniston and A. Harriman, *Coord. Chem. Rev.*, 2008, **252**, 2528–2539; (c) C. Curutchet, F. A. Feist, B. Van Averbeke, B. Menucci, J. Jacob, K. Müllen, T. Basché and D. Beljonne, *Phys. Chem. Chem. Phys.*, 2010, **12**, 7378–7385; (d) A. Olaya-Castro and G. D. Scholes, *Int. Rev. Phys. Chem.*, 2011, **30**, 49–77.
- 12 (a) M. D. Yilmaz, O. A. Bozdemir and E. U. Akkaya, *Org. Lett.*, 2006, **8**, 2781–2873; (b) J. H. Hurenkamp, W. R. Browne, R. Augulis, P. H. M. Van Loosdrecht, J. H. Van Esch and B. L. Feringa, *Org. Biomol. Chem.*, 2007, **5**, 3354–3362; (c) O. A. Bozdemir, M. D. Yilmaz, O. Buyukcakir, A. Siemiarzczuk, M. Tutas and E. U. Akkaya, *New J. Chem.*, 2010, **34**, 151–155; (d) Z. Mahmood, K. Xu, B. Küçüköz, X. Cui, J. Zhao, Z. Wang, A. Karatay, H. G. Yaglioglu, M. Hayvali and A. Elmali, *J. Org. Chem.*, 2015, **80**, 3036–3049.
- 13 (a) H. Langhals, J. Karolin and L. B.-A. Johansson, *J. Chem. Soc., Faraday Trans.*, 1998, **94**, 2919–2922; (b) F. Castiglione, G. Lanzani, A. Mele, A. Monguzzi, M. Passarello, A. Ruggirello, F. Scotognella and V. T. Liveri, *J. Mater. Sci.*, 2011, **46**, 6402–6407.
- 14 B. Valeur, *Molecular fluorescence: principles and applications*, Wiley-VCH, Weinheim, Germany, 2001.
- 15 F. López Arbeloa, T. López Arbeloa and I. López Arbeloa, *Trends Photochem. Photobiol.*, 1994, **3**, 145–155.
- 16 J. Bañuelos, *Chem. Rec.*, 2016, **16**, 335–348.
- 17 I. Esnal, I. Valois-Escamilla, C. F. A. Gómez-Durán, A. Urías-Benavides, M. L. Betancourt-Mendiola, I. López-Arbeloa, J. Bañuelos, I. García-Moreno, A. Costela and E. Peña-Cabrera, *ChemPhysChem*, 2013, **14**, 4134–4142.
- 18 I. Esnal, G. Durán-Sampedro, A. R. Agarrabeitia, J. Bañuelos, I. García-Moreno, M. A. Macías, E. Peña-Cabrera, I. López-Arbeloa, S. de la Moya and M. J. Ortiz, *Phys. Chem. Chem. Phys.*, 2015, **17**, 8239–8247.

- 19 (a) C. F. A. Gómez-Durán, I. García-Moreno, A. Costela, V. Martín, R. Sastre, J. Bañuelos, F. López Arbeloa, I. López Arbeloa and E. Peña-Cabrera, *Chem. Commun.*, 2010, **46**, 5103–5105; (b) J. Bañuelos, V. Martín, C. F. A. Gómez-Durán, I. J. Arroyo Córdoba, E. Peña-Cabrera, I. García-Moreno, A. Costela, M. E. Pérez-Ojeda, T. Arbeloa and I. López Arbeloa, *Chem. – Eur. J.*, 2011, **17**, 7261–7270.
- 20 (a) R. Ziessel and A. Harriman, *Chem. Commun.*, 2011, **47**, 611–631; (b) D. Bai, A. C. Benniston, J. Hagon, H. Lemmetyinen, N. V. Tkachenko, W. Clegg and R. W. Harrington, *Phys. Chem. Chem. Phys.*, 2012, **14**, 4447–4456; (c) M. A. H. Alamiry, J. P. Hagon, A. Harriman, T. Bura and R. Ziessel, *Chem. Sci.*, 2012, **3**, 1041–1048.
- 21 D. Escudero, *Acc. Chem. Res.*, 2016, **49**, 1816–1824.



## Dyes/Pigments

## Towards Efficient and Photostable Red-Emitting Photonic Materials Based on Symmetric All-BODIPY-Triads, -Pentads, and -Hexads

Edurne Avellanal-Zaballa,<sup>[a]</sup> Juan Ventura,<sup>[b]</sup> Leire Gartzia-Rivero,<sup>[a]</sup> Jorge Bañuelos,<sup>\*,[a]</sup> Inmaculada García-Moreno,<sup>[c]</sup> Clara Uriel,<sup>[b]</sup> Ana M. Gómez,<sup>\*,[b]</sup> and J. Cristobal Lopez<sup>\*,[b]</sup>

**Abstract:** The development of efficient and stable red and near-IR emitting materials under hard radiation doses and/or prolonged times is a sought-after task due to their widespread applications in optoelectronics and biophotonics. To this aim, novel symmetric all-BODIPY-triads, -pentads, and -hexads have been designed and synthesized as light-harvesting arrays. These photonic materials are spectrally active in the 655–730 nm region and display high molar absorption across UV–visible region. Furthermore, they provide, to the best of our knowledge, the highest lasing efficiency (up to

68%) and the highest photostability (tolerance > 1300 GJ mol<sup>-1</sup>) in the near-IR spectral region ever recorded under drastic pumping conditions. Additionally, the modular synthetic strategy to access the cassettes allows the systematic study of their photonic behavior related to structural factors. Collectively, the outstanding behavior of these multichromophoric photonic materials provides the keystone for engineering multifunctional systems to expedite the next generation of effective red optical materials.

## Introduction

Red and near-infrared (NIR) fluorescent dyes are required in relevant technological fields ranging from laser, information storage, or solar power conversion to labeling and photosensing.<sup>[1]</sup> To boost these advanced applications, fluorophores with high absorption over a broad spectral window and bright red-fluorescent emission are required. Even so, the keystone promoting its workability is surely a high resistance against photodegradation especially under strong conditions, such as hard radiation laser doses and/or prolonged exposure times.<sup>[2]</sup> In spite of the efforts of modern chemistry in synthesizing highly efficient and stable fluorophores with emission deeply shifted towards the red edge of the visible spectral region, they still present some important drawbacks: low absorption at stan-

dard laser wavelength, poor stability under intense irradiation, and/or limited chemical versatility for post-functionalization.<sup>[3]</sup>

In recent years, photonic materials based on the difluoroboron dipyrromethene (BODIPY) chromophore have surfaced as chromophores of choice,<sup>[4]</sup> since their unique spectroscopic and photophysical properties can be easily fine-tuned by synthetic post-modifications on its skeleton to meet all the above-outlined requirements (Figure 1).<sup>[5]</sup> In fact, the real power of the BODIPYs is closely related to their ability to undergo a wavelength shift upon selective chemical or biological functionalization of the diaza-indacene core. Thereby, different synthetic post-modifications<sup>[6,7]</sup> have been applied to bathochromically shift the absorption and emission wavelength from the parent BODIPYs, for example, **1**,<sup>[8]</sup> **2**<sup>[4a]</sup> (≈ 500 nm) up to the red spectral region (> 650 nm), for instance, extension of the  $\pi$ -system through incorporation of peripheral alkynyl or distyryl substituents (e.g., **3**,<sup>[9]</sup> **4**,<sup>[10]</sup> **5**<sup>[11]</sup> in Figure 1),<sup>[12]</sup> and/or fusion of aromatic rings.<sup>[13]</sup> In this context, compounds **3b** and **4** had already shown remarkable behavior, in terms of efficiency and photostability, as laser dyes.<sup>[14]</sup>

An additional approach to photonic materials, also based on the chemical versatility of the dipyrroin core, has focused on the design of multichromophoric systems enabling effective excitation energy transfer (EET) through covalently linked BODIPY building blocks acting as either energy-donor and/or energy-acceptor units.<sup>[15]</sup> This last strategy is very appealing since such multichromophoric organic architectures allow a more versatile selection of the excitation source and energy, ensure a better exploitation of the incoming light and avoid photodegradation since the final emitting chromophoric subunit is not directly

[a] E. Avellanal-Zaballa, Dr. L. Gartzia-Rivero, Dr. J. Bañuelos  
Dpto. Química Física, Universidad del País Vasco (UPV/EHU)  
Aptdo. 644, 48080 Bilbao (Spain)  
E-mail: jorge.banuelos@ehu.es

[b] Dr. J. Ventura, Dr. C. Uriel, Dr. A. M. Gómez, Prof. J. C. Lopez  
Instituto de Química Orgánica General (IQOG-CSIC)  
Juan de la Cierva 3, 28006 Madrid (Spain)  
E-mail: ana.gomez@csic.es  
jc.lopez@csic.es

[c] Prof. I. García-Moreno  
Instituto Química-Física "Rocasolano" (IQFR-CSIC)  
Serrano 119, 28006 Madrid (Spain)

Supporting information and the ORCID identification number(s) for the author(s) of this article can be found under:  
<https://doi.org/10.1002/chem.201903804>

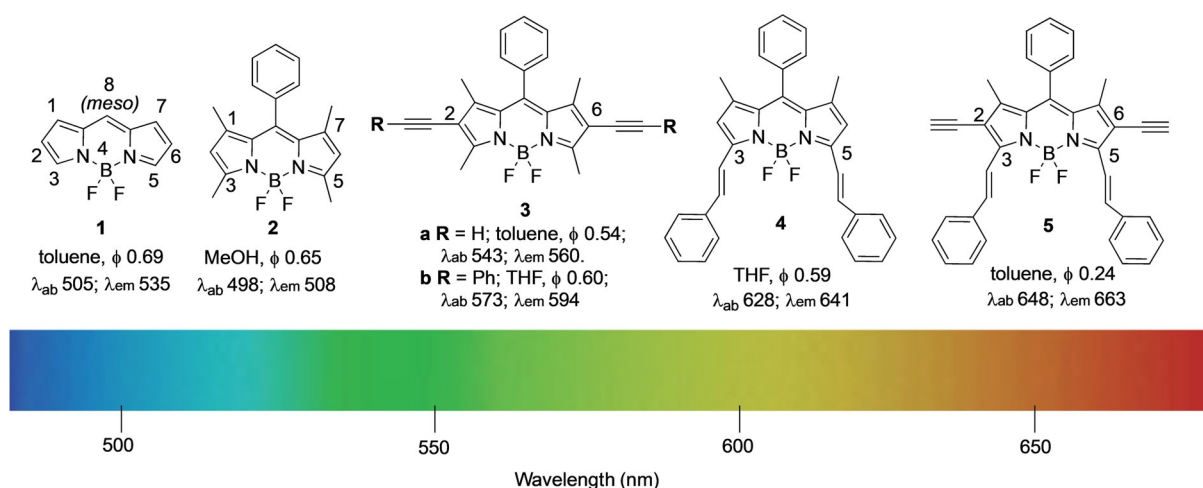


**Figure 1.** BODIPY (1), 1,3,5,7-tetramethyl-8-phenyl BODIPY (2), 2,6-dialkynyl BODIPY (3) and 3,5-distyryl BODIPY (4), superimposed onto a portion of the visible light spectrum.  $\lambda_{ab}$  = absorption maximum (nm),  $\lambda_{em}$  = emission maximum (nm),  $f$  = fluorescence quantum yield.

pumped, but is indirectly excited through EET from the donor units yielding in this way long-lasting and glow emission.<sup>[16]</sup>

Even though many supramolecular cassettes based on BODIPY scaffolds have been described, light-harvesting systems with effective emission in the red-edge of the spectral region are still scarce.<sup>[5b,15,16]</sup> Most of these assembled architectures, rather than involving a long-wavelength BODIPY as energy acceptor, incorporate less efficient and/or photostable chromophoric skeletons such as perylene diimides,<sup>[16c]</sup> porphyrins<sup>[17]</sup> and also aza-BODIPYs,<sup>[18]</sup> among others.<sup>[19]</sup> To the best of our knowledge, the photonic behavior of these structures under a strong irradiation regime, as well as their dependence on the number and position of fluorophores acting as donor and acceptor units have never been described.

In an attempt to simultaneously address all these challenges, and searching for the development of highly efficient and stable red-emitting photonic materials, here we disclose the synthesis, the photophysical signatures (aided by computational simulations), and the laser characterization of novel multichromophoric all-BODIPY materials,<sup>[15a,b,g,20]</sup> that is, BODIPY-triads **6**, **7**, and **8**; BODIPY-pentad **9** and BODIPY-hexad **10** (Figure 2). The acceptor unit(s) in these multichromophores (highlighted in red in Figure 2) is a BODIPY, the absorption and emission of which has been bathochromically shifted up to the red-edge spectral region by extension of its  $\pi$ -conjugation through the combination of styryl substituents at C-3 and C-5, and either alkynyl substituents or, previously unexplored, triazolyl units at C-2 and C-6. Thus, acceptor- and peripheral-donor-BODIPYs were connected through *ortho*-aryl C-8 substituents by way of: i) styryl moieties, for example, **6**, **7**; ii) triazole residues, for example, **8**, or iii) through both, in the case of BODIPY pentad **9** (Figure 2). The presence of the *ortho*-C8 aryl-substituent combined with the presence of the C-1 and C-7 methyl groups was key to ensure the required orthogonal orientation (by rotational restriction) between the C-8 aromatic residue and the BODIPY core, thus avoiding resonant electronic interactions. This set of derivatives differ in the number of donor and acceptor BODIPY subunits as well as in their linkage

positions. Accordingly, i) two donors and one acceptor are present in triads **6–8**, with multichromophores **7** and **8** differing in the attachment points of the BODIPY donor elements; ii) four donors and one acceptor in BODIPY pentad **9**, and finally iii) four donors and two acceptors in bis-urea dimer **10**.

In this way, the new ensemble of all-BODIPY multichromophores becomes the first example of: a) a straightforward synthetic strategy for all-BODIPY cassettes using one single BODIPY progenitor, that is, **11** (Figure 2), which makes use of copper(I)-catalyzed alkyne-azide cycloaddition (CuAAC) reactions,<sup>[21–23]</sup> chemoselective Knoevenagel condensations of 2,6-dialkynyl BODIPYs,<sup>[24]</sup> and an efficient ureation protocol recently described by us (synthetic disconnections **A**, **B**, **C**, respectively, Figure 2);<sup>[25]</sup> b) a systematic analysis of the photonic behavior of red-emitting cassettes based on structural factors such as the number of donor and acceptor units, and the position and the spacers connecting the building blocks; and c) remarkable red-emitting laser cassettes endowed with an effective absorption in the UV–visible spectral region, and, particularly one of the highest emission efficiencies and photostability described to date, key parameters to guarantee long-lasting emission in any advanced applications.

## Results and Discussion

### Synthesis and characterization

As previously mentioned, our approach to multichromophores **6–10**, started from a single precursor, 8-phenyl *ortho*-hydroxymethyl BODIPY **11**, readily available by a one-pot protocol previously described in our laboratory.<sup>[26]</sup> In this context, synthetic transformations on the hydroxymethyl moiety of **11** paved the way to azidomethyl and formyl BODIPYs **12** and **13**, respectively.<sup>[26]</sup> Subsequent synthetic post-modifications on the dipyrromethene core of **11** allowed access to differently 2,6-disubstituted derivatives **14**,<sup>[26]</sup> **15a**, **15b**<sup>[26]</sup> and **16** (Figure 3). Compounds **15** and **16**, with  $\pi$ -extended conjugation, displayed

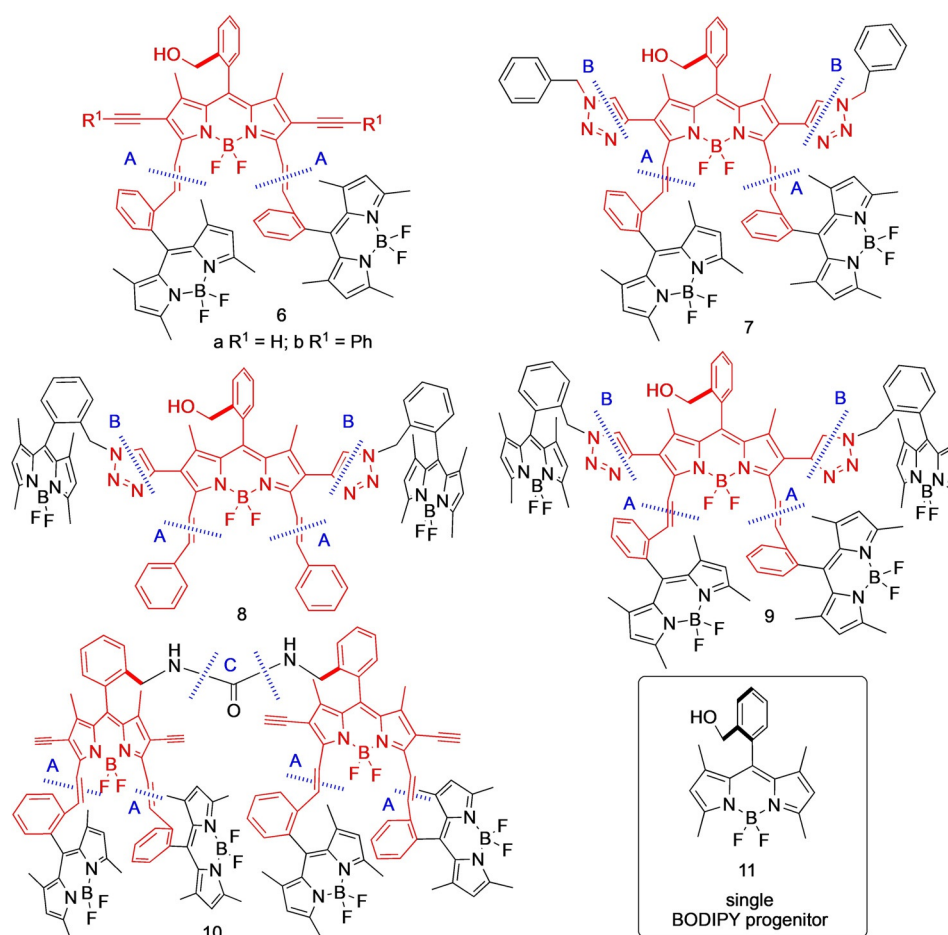


**Figure 2.** All-BODIPY multichromophores 6–10, studied in this work. Single BODIPY starting material (11). Key retrosynthetic disconnections: A) Knoevenagel condensation; B) copper azido alkyne cycloaddition (CuAAC) reaction; C) bis-urea dimerization.

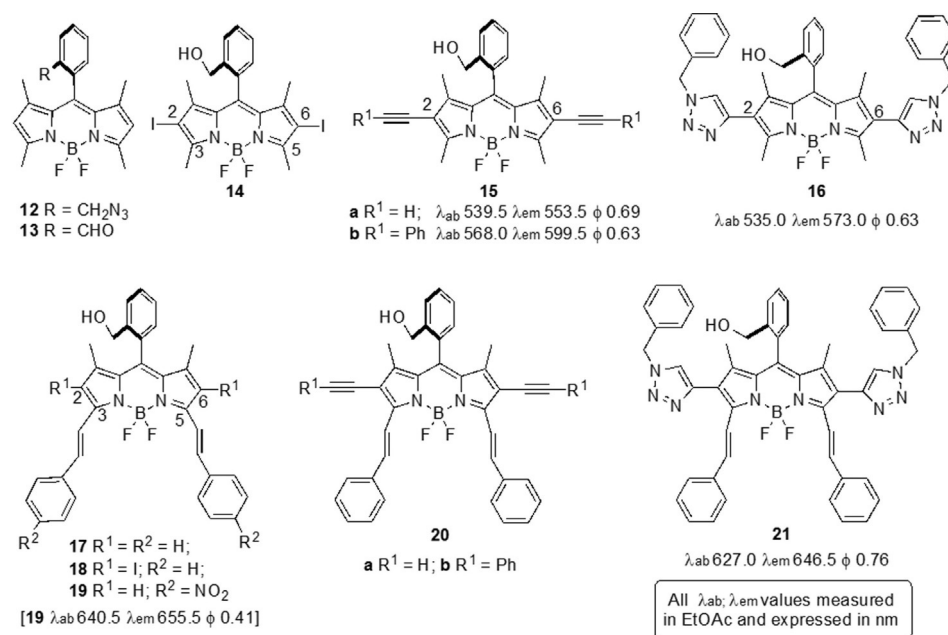


**Figure 3.** Differently 2,6-disubstituted 1,3,5,7-tetramethyl 8-phenyl *ortho*-hydroxymethyl BODIPYs 14–16, and their Knoevenagel-condensation products with benzaldehyde 17–21. Dye concentration: 2 mM. Absorption ( $\lambda_{ab}$ ) and fluorescence emission maxima ( $\lambda_{em}$ ) wavelengths (nm); fluorescence quantum yield ( $\phi$ ). Values measured in EtOAc.

red-shifted absorption and emission in agreement with literature precedents.<sup>[7b]</sup>

Next, we carried out investigations on the chemoselective Knoevenagel condensation of aldehyde **13** with BODIPYs **15** and **16** (rather than self-condensation of **13**). These studies emanated from the observation by Akkaya's group<sup>[12a,27]</sup> that electron-withdrawing substituents (at C-2 and C-6) in 1,3,5,7-tetramethyl BODIPYs experienced a clear enhancement on the acidity of the methyl groups compared to the parent unsubstituted derivatives. They, had taken advantage of this finding for the preparation of 1,3,5,7-tetraaryl-BODIPY dyes.<sup>[12a]</sup> However, to the best of our knowledge, this reactivity difference had not been used to date in eliciting chemoselective Knoevenagel condensations involving formyl BODIPYs<sup>[28]</sup> (see Supporting Information for details).

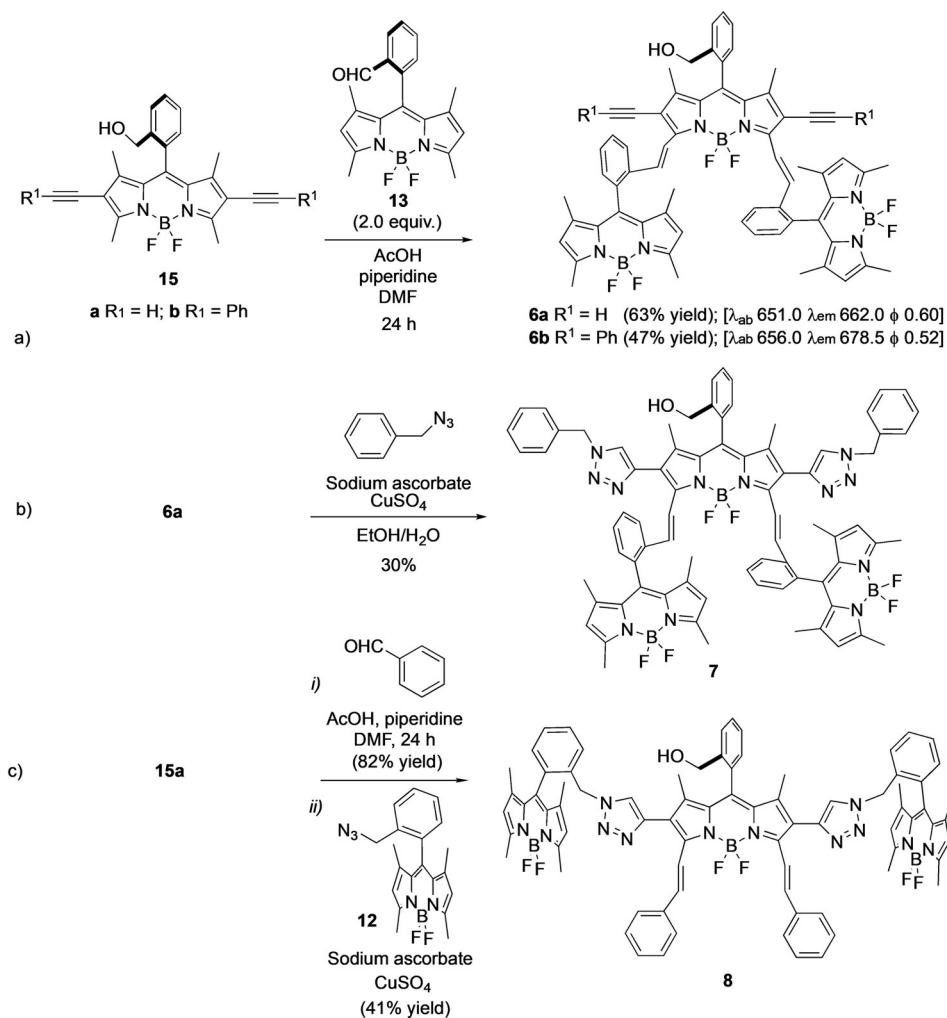
As a result of our studies, we found that chemoselective Knoevenagel condensation of formyl-BODIPY **13** with "activated" BODIPYs **15a,b** takes place at room temperature in DMF, in the presence of piperidine and AcOH, to give distyryl derivatives **6a** and **6b**, in fairly acceptable yields, without traces of self-condensation products arising from **13** (Scheme 1a). Compound **7**, was then easily accessed from **6a** by CuAAC reaction

with benzyl azide. On the other hand, access to BODIPY triad **8**, involved Knoevenagel condensation of dialkynyl derivative **15a** with benzaldehyde (AcOH, piperidine, DMF, 24 h, room temperature) followed by CuAAC reaction of the ensuing distyryl BODIPY **20a** with azidomethyl BODIPY **12** (Scheme 1c).

Final access to BODIPY-pentad **9**, and -hexad **10** was straightforward from BODIPY trimer **6a**. Thus, CuAAC reaction of dialkynyl BODIPY **6a** with azidomethyl BODIPY **12**<sup>[23]</sup> (Scheme 2) led to pentameric BODIPY **9**. Conversely, dimerization of azidomethyl BODIPY trimer **22**,<sup>[25]</sup> obtained from **6a** upon treatment with 2-azido-1,3-dimethylimidazolinium hexafluorophosphate (ADMP) in the presence of DBU,<sup>[29]</sup> yielded dimeric bisurea trimer **10**.

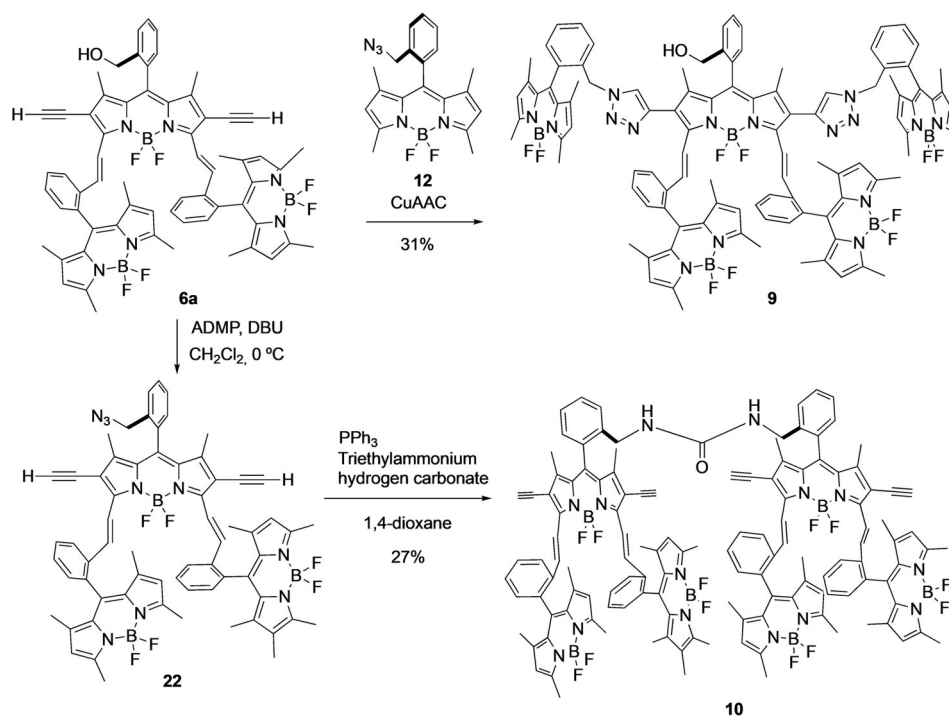
### Photophysical properties

The absorption profile of the molecular cassettes **6–10** featured three well-resolved bands (Figure 4). The long wavelength absorption was assigned to the  $\pi$ -extended central BODIPY subunit matching the spectrum recorded for the isolated dye **21**. This band became bathochromically shifted up to 655 nm when the triazol group grafted at position C-2 and



**Scheme 1.** a) Chemoselective Knoevenagel condensation of 2,6-dialkynyl BODIPYs **15a,b** with BODIPY aldehyde **13**. b) CuAAC Reaction of **6a** with benzyl azide leading to BODIPY-triad **7**. c) Synthesis of bis-triazolyl BODIPY **8**.





Scheme 2. Synthetic routes to multichromophores **9** and **10**, from BODIPY-triad **6a**.

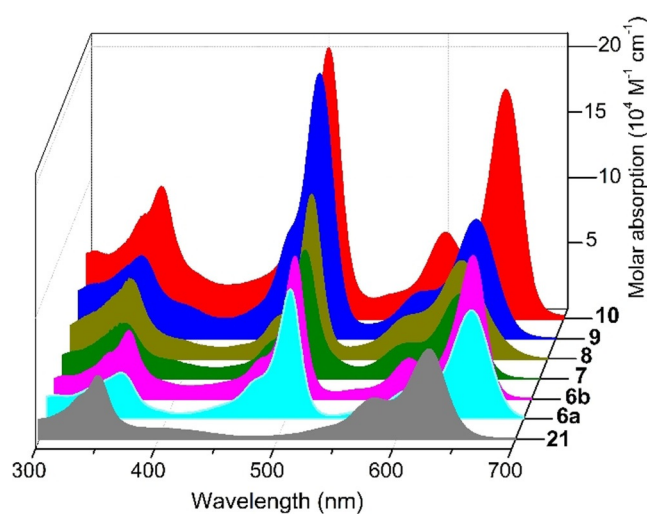


Figure 4. Absorption spectra of the all-BODIPY-based cassettes **6–10** in diluted solutions of diethyl ether. The corresponding spectrum of the isolated red-emitting dye **21** is also included for comparison.

C-6 of the BODIPY in dyes **7**, **8** and **9** was replaced by an acetylene group (in **6a** and **10**) or by an acetylenophenyl group (**6b**). With respect to the triazol functionalization, these latter groups allowed a stronger electronic coupling to the central BODIPY unit inducing the red-shifted of the corresponding absorption band.

A strong and dominating absorption band was registered at the green–yellow region (around 505 nm) and was attributed to the absorption of the peripheral tetramethylated BODIPYs. The molar absorption coefficient of the new dyes in the

green–red spectral region increased progressively with the number of BODIPY units covalently linked (Figure 4). Thus, the extinction coefficient at the red-edge maximum wavelength reached up to  $170\,000\text{ M}^{-1}\text{ cm}^{-1}$  for compound **10**, bearing two  $\pi$ -extended central BODIPYs, whereas this absorption coefficient at the green–yellow maximum wavelength became even higher than  $200\,000\text{ M}^{-1}\text{ cm}^{-1}$  for dyes **9** and **10**, bearing four pendant peripheral BODIPYs (Figure 4). Finally, an absorption band placed at the ultraviolet edge (360 nm in Figures 4) was recorded and was attributed to the interaction of the styryl arm at positions C-3 and C-5 with the pyrrole groups of the central BODIPY.<sup>[6d]</sup> In addition, the peripheral BODIPYs should be contributing to increase the absorption in this spectral region even though they weakly absorbed at this UV wavelength, but owing to the number of chromophoric units linked this contribution was no longer residual and became significant.

The computational simulation of the absorption spectra supported this assignment (see simulated spectra for the triads in Figure S3 in the Supporting Information). The molecular orbitals involved in the long-wavelength transition (HOMO  $\rightarrow$  LUMO) were placed exclusively into the central BODIPY (see the molecular orbitals for the cassettes in Figures S4–S8 in the Supporting Information). The molecular orbitals responsible of the absorption in the green spectral region involved electronic configurations energetically close (for example HOMO-2  $\rightarrow$  LUMO + 1 and HOMO-1  $\rightarrow$  LUMO + 2 in trimeric **6b**, Figure S4 in the Supporting Information) and were located just at each peripheral BODIPY (Figures S4–S8 in the Supporting Information). The UV transition resulted from the simultaneous contribution of multiple electronic configurations involving

molecular orbitals placed at the peripheral BODIPYs and mainly at the central BODIPY with the electronic density mostly located at the C-3 and C-5 styryl groups. Therefore, the molecular design and the imposed geometrical hindrance were suitable to span the electronic delocalization through the aromatic functionalization without reaching the peripheral BODIPYs. As a result, each chromophoric subunit retained its molecular identity after the covalent linkage, contributing almost additively to the whole absorption spectrum. Moreover, this rational molecular design avoids excitonic coupling between the chromophoric subunits, which usually leads to loss of photon energy or poorly emissive aggregates.

The fluorescence spectra of the new cassettes, regardless of the excitation wavelength, featured mainly a unique band shifted to the red-edge, around 650–680 nm depending on the aromatic group grafted at positions C-2 and C-6 (Figure 5, S1

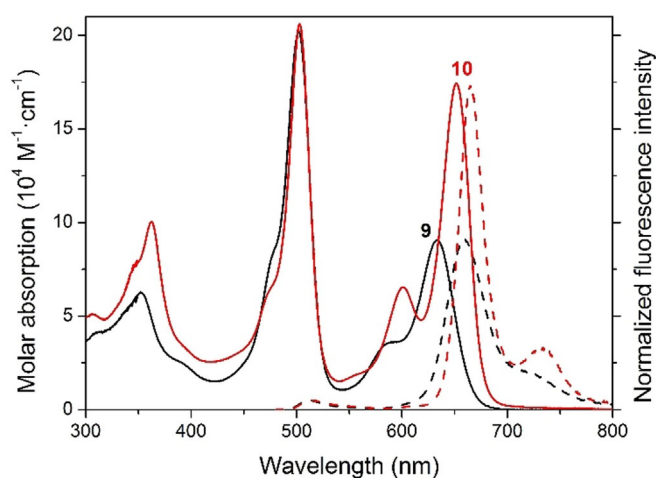


**Figure 5.** Absorption (solid line) and fluorescence (dashed, under selective excitation at 475 nm) of the representative cassettes **9** (black) and **10** (red) in diluted solutions of diethyl ether. The corresponding spectra of cassettes **6–8** are collected in Figures S1 and S2 in the Supporting Information.

and S2 in the Supporting Information). Moreover, the excitation spectra monitored at such red emissions matched nicely with the absorption profile (Figures S1 and S2 in the Supporting Information). These trends support the suggestion that these cassettes underwent highly efficient intramolecular EET (intra-EET) from the peripheral BODIPY donors to the central p-extended BODIPY acting as acceptor unit. Indeed, the emission from the donor units (placed at around 510–515 nm) was drastically quenched (being almost residual, see Figure 5, with a fluorescence efficiency lower than 1%) promoting the growth of the predominant red emission (fluorescence efficiency up to 68% in apolar media, Table 1).

Based on the decline of the fluorescence quantum yield of the donor upon binding to the acceptor, an intra-EET efficiency of more than 98% in all the media and cassettes was estimated. This high efficiency is related to the short donor–acceptor distance and the high spectral overlap between the donor fluorescence and the acceptor absorption. Both factors enhance and allow the required dipole–dipole coupling to under-

**Table 1.** Photophysical properties of the energy transfer cassettes in diluted solutions (2 mM) of apolar (diethyl ether, Et<sub>2</sub>O) and polar (methanol, MeOH) solvents. Full photophysical data in different solvents are listed in Table S1 in the Supporting Information.

		$\lambda_{ab}$ <sup>[a]</sup> (nm)	$\epsilon_{max}$ <sup>[b]</sup> (10 <sup>4</sup> M <sup>-1</sup> cm <sup>-1</sup> )	$\lambda_{fl}$ <sup>[c]</sup> (nm)	$\phi_f$ <sup>[d,f]</sup>	$\tau$ <sup>[e,f]</sup> (ns)
<b>6a</b>	Et <sub>2</sub> O	652.0	10.4	662.5	0.65	4.72
		501.5	10.6			
		361.5	5.3			
	MeOH	649.5	8.4	660.5	0.016	0.14 (97%) –0.47 (3%)
		500.5	9.3			
		360.5	4.9			
<b>6b</b>	Et <sub>2</sub> O	655.0	8.8	676.5	0.65	4.50
		504.0	10.2			
		361.5	4.0			
	MeOH	657.5	8.1	682.0	0.030	0.26 (99%) –1.81 (1%)
		503.5	9.7			
		361.5	4.0			
<b>7</b>	Et <sub>2</sub> O	632.5	7.2	654.5	0.54	4.39
		503.0	10.2			
		350.5	5.4			
	MeOH	629.0	7.0	651.0	0.024	0.22 (90%) –0.92 (10%)
		502.5	10.2			
		350.5	6.1			
<b>8</b>	Et <sub>2</sub> O	627.0	8.6	652.0	0.68	4.32
		502.5	13.6			
		349.5	6.8			
	MeOH	624.5	8.7	649.5	0.45	2.78
		502.0	12.8			
		347.5	7.2			
<b>9</b>	Et <sub>2</sub> O	633.5	9.0	657.5	0.69	4.25
		502.0	20.2			
		352.0	6.2			
	MeOH	631.0	9.5	655.5	0.042	0.44 (91%) –1.13 (9%)
		501.0	19.6			
		349.0	7.1			
<b>10</b>	Et <sub>2</sub> O	651.5	17.4	664.5	0.65	4.56
		503.0	20.6			
		362.0	10.0			
	MeOH	650.5	15.4	666.0	0.018	0.12 (77%) –0.48 (23%)
		501.5	20.0			
		362.0	8.8			

[a] Absorption wavelength. [b] Molar absorption coefficient. [c] Fluorescence wavelength. [d] Fluorescence quantum yield. [e] Fluorescence lifetime. [f] The fluorescence lifetimes and quantum yields are independent on the excitation wavelength.

go through-space EET via Förster mechanism. Moreover, the  $\pi$ -system of the central acceptor BODIPY, extended through the aromatic substituents at positions 3 and 5, as well as through the functional groups grafted at positions 2 and 6, could enable a through-bond mediated EET<sup>[20c]</sup> since the donors were directly and adequately connected to such moieties allowing the required electronic superexchange mechanism. As a consequence of the viability and simultaneous contribution of both mechanisms, the transfer of excitation energy from the donor moieties to the central energy-trap is almost absolute.

The multichromophoric systems bearing a donor BODIPY grafted at the *ortho* position of the 3,5-styryl groups (**6**, **7**, **9** and **10**) exhibited a fluorescent efficiency strongly dependent on the solvent polarity. In apolar media, they were characterized by a bright red emission peaked at 650–680 nm, with an efficiency ranging from 55% to 70%, and a monoexponential

decay curve leading to a lifetime around 4.5 ns regardless of the excitation wavelength (Table 1). An increase of the solvent polarity led to a drastic reduction of the emission efficiency and a shortening of the lifetime (Figures 6 and Figures 7, and

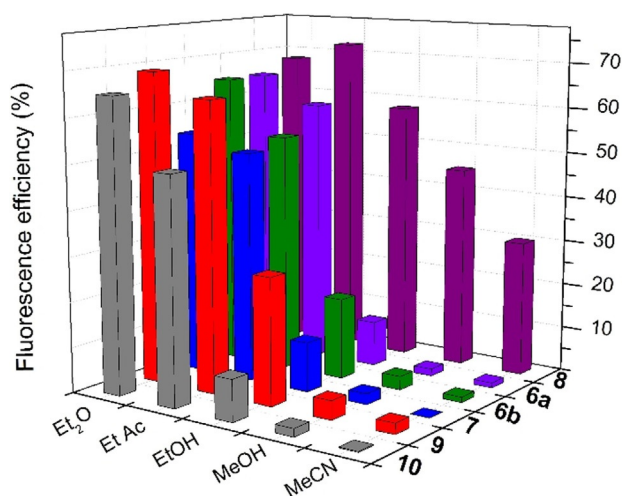


**Figure 6.** Comparative evolution of the fluorescence quantum yields of all the cassettes on the solvent polarity. Full data are collected in Table S1 in the Supporting Information.

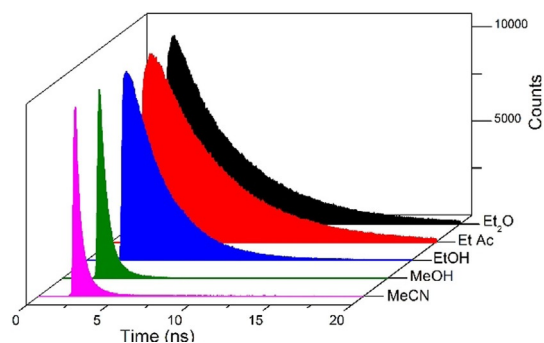


**Figure 7.** Evolution of the fluorescence decay curve with the solvent polarity for the representative pentad **9**. Full data are collected in Table S1 in the Supporting Information.

Table 1). Indeed, the fluorescence decay curves acquired a biexponential character with a main and fast component of few hundred picoseconds (Figure 7). Moreover, in the most polar media such as methanol and acetonitrile the emission was almost negligible revealing that the solvent polarity switched on in these molecular assemblies an effective non-radiative deactivation channel (Figure 6). This sensitivity of the fluorescent capacity on the solvent polarity is usually related to a non-emissive intramolecular charge transfer (ICT) process.<sup>[22]</sup> As the polarity of the solvent increases the charge separation inherent to this ICT becomes more stabilized, strongly quenching the fluorescence from the locally excited (LE) state, regardless of its excitation pathway (direct absorption and/or via EET).

The only exception to this behavior was the photophysical signatures of cassette **8**, which showed a lower dependence

on the solvent polarity. Comparison of the photophysical properties of the structurally related trimers **7** and **8** allowed the influence of the molecular design on the effectiveness of this ICT process to be established. In fact, these cassettes just differ in the linkage position of the donor BODIPY units, which were grafted at the 3,5-stryryl groups in **7** while they were linked at the 2,6-phenyl groups in **8** (Figure 2). Thus, whereas the emission from **7** clearly dropped as the solvent polarity increased, the fluorescent efficiency of **8** remained as high as 45% even in the most polar solvent (Figure 6). This finding unambiguously backs up the ability of the BODIPY grafted to 3,5-stryryl groups to induce effective ICT processes. Furthermore, in cassette **10** the urea spacer linking the acceptor BODIPYs was itself able to induce an effective ICT owing to its electron donor ability, as was reported previously in symmetric bis-BODIPYs.<sup>[25]</sup> The viability of two pathways to induce effective ICT processes in **10** led to the lowest fluorescent quantum yield and the shortest lifetime in polar media among the cassettes herein synthesized (Table 1). These results highlight the complex excited state dynamics of these multichromophoric systems in polar solvents where, besides the ongoing intra-EET, ICT processes were also directing their emission response.

Therefore, the molecular design of these multichromophoric dyes fulfilled all the desirable features of an optimal photonic cassette. This strategy ensures broad and extremely efficient light harvesting, large “pseudo” Stokes shift, and competitive excitation energy transport to the final emitting trap, which displayed glow emission in all the tested media regardless of the pumping spectral region. Moreover, the high synthetic versatility of these multichromophoric systems allowed us to modulate and understand the influence of the molecular structure (number of donor and acceptor subunits, as well as the donor–acceptor linkage positions) into the photophysical signatures of the final cassettes.

### Laser properties

According to the absorption properties of the new BODIPYs their lasing properties were studied under transversal pumping at standard laser wavelengths such as 355 nm and 532 nm. Since the new multichromophoric systems were designed to behave as highly efficient and photostable photonic materials, to properly assess their long-term stability as well as the dependence of their lasing properties on the number and position of the linked BODIPY units, we selected strong pumping conditions such as 8 mJ per pulse and 15 Hz, as pumping energy and repetition rate, respectively. It is worth noting that these pumping conditions are more drastic than those we usually select for the laser characterization of BODIPY dyes (i.e., 5 mJ per pulse and 5 or 10 Hz repetition rate).<sup>[30]</sup> The concentration that optimized the laser efficiency in ethyl acetate solution, understood as the ratio of the output and input (pump) energies, depended on both the given dye and the pumping wavelength, and ranged from 0.09 to 2 mM. The lasing properties of the new monomeric and multichromophoric BODIPYs analyzed under these experimental conditions are reported in Table 2.

**Table 2.** Lasing properties of the monomeric and multichromophoric dyes in ethyl acetate solution pumped at wavelengths 355 and 532 nm.

Dye	% Eff. <sup>[a]</sup>	532 nm		% Eff.	355 nm	
		$\lambda_{la}$ <sup>[b]</sup> (nm)	$E_{dose}$ <sup>[c]</sup> (GJ mol <sup>-1</sup> )		$\lambda_{la}$ (nm)	$E_{dose}$ (GJ mol <sup>-1</sup> )
<b>6a</b>	52	720	308	49	716	265
<b>6b</b>	47	710	342	50	704	294
<b>7</b>	51	703	388	52	700	327
<b>8</b>	62	705	524	58	699	445
<b>9</b>	68	715	993	65	710	843
<b>10</b>	57	730	1137	56	722	938
<b>15a</b>	33	580	51			
<b>15b</b>	35	622	35			
<b>16</b>	36	610	58			
<b>21</b>				30	690	55

[a] Lasing wavelength. [b] Lasing efficiency. [c] Photostability, defined as the amount of pumping energy absorbed by the dye to retain 50% of its initial emission.

The monomeric BODIPYs **15a**, **15b** and **16** were only pumped at 532 nm due to its low absorption at 355 nm and rendered broad-band laser emission peaked at 580 nm, 622 nm and 610 nm, respectively, with a pump energy threshold of 0.9 mJ, and lasing efficiencies of up to 35%. On the other hand, the dye **21** was only pumped at 355 nm due to its low absorption at 532 nm, rendering red-edge laser emission peaked at 690 nm with an efficiency of 30%.

In terms of traceability and feasibility of photonic materials, efficiency is not the only crucial variable to be considered. A further important parameter is the photostability of the emission over long operation times. Ideally, a high resistance to active medium photodegradation under repeated pumping is sought after. A reasonable evaluation of the photostability of laser materials can be obtained by irradiating a small amount of solution with exactly the same pumping energy and geometry as used in the laser experiments, and monitoring the evaluation of the laser-induced fluorescence intensity with respect to the number of pump pulses (see the Experimental Section). To properly compare the intrinsic photodegradation rate of the active media irrespective of the cavity configuration/parameters and sample concentrations used, we introduced a normalized photostability parameter such as the accumulated pump energy absorbed by the system, per mole of dye, before the output energy falls to a 50% its initial value ( $E_{dose}$  in GJ mol<sup>-1</sup>). The monomeric BODIPYs (**15a**, **15b** and **16**) exhibited good photostability (Table 2) particularly considering that they have been pumped at high repetition rate (15 Hz). It is well-established that the accumulation of heat into the active medium increases significantly with the pumping repetition rate resulting in a rapid decrease of the lasing photostability.

More interesting was the laser behavior of the new multichromophoric systems, which was a significant improvement on those exhibited individually by the corresponding donor and acceptor components. The photophysical behavior of **6–10** dyes as effective EET cassettes allowed them to lase efficiently in the red spectral region when they were transversally

pumped at 355 nm as well as at 532 nm. In fact, the covalent linkage of BODIPY units into the cassettes **6–10** led to a significant increase of the absorption at both pumping wavelengths compared to those exhibited individually by the related monomeric parent dyes. This is a key factor from the point-of-view of the laser action, since it allows significant reduction of the required gain-media concentrations, avoiding consequent dye-solubility problems, or emission quenching and/or aggregation processes, all of which have detrimental effects on laser action.

Firstly, cassettes **6–10** were transversely pumped at 532 nm, the wavelength at which only absorbed the BODIPYs acting as donor units. Under these experimental conditions, the exhibited lasing emission peaked in the red-edge of the visible spectrum, ranging from 705 nm to 730 nm, with a pump energy threshold as low as 0.04 mJ, an efficiency of up to 68% and a very high photostability since up to 1300 GJ mol<sup>-1</sup> were required for a 50% decrease of its initial emission (Table 2). The enhancement of the photonic behavior on going from the monomeric dyes to the multichromophoric cassettes strongly depended on the molecular design following the rule: the higher the number of peripheral BODIPYs acting as donor units the lower the pump energy threshold, and the higher the lasing efficiency and photostability. In this regard, the lasing emission of the new multichromophoric cassettes **9** and **10** stand out by a pump energy threshold of up to 22-fold lower, and an efficiency and photostability of up to two- and 20-fold higher than those recorded from the corresponding monomeric BODIPY **21** acting as acceptor unit (Table 2 and Figure 8). The outstanding laser behavior of **6–10** has to be related to the molecular design, which led to, on the one hand, a high dipole moment presumably leading to high transition dipole moments and allowing the molecular alignment with respect to the polarization of the exciting laser beam to enhance the emission efficiency of the media,<sup>[30]</sup> and, on the other hand, an effective EET from the peripheral BODIPYs to the central red-emitting BODIPY, which significantly reduced the rate and extension of the photodegradation processes.

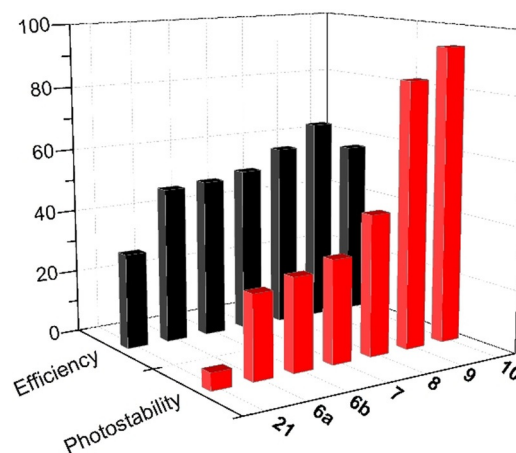


**Figure 8.** Lasing efficiency and photostability (10<sup>10</sup> J mol<sup>-1</sup>) of the cassettes **6–10** under pumping at 355 nm with respect to the isolated red-emitting energy acceptor dye **21**.

Another advantage of the molecular design of these cassettes that increases their photonic applicability is the versatility to be pumped in the UV region. In fact, under laser pumping at 355 nm, cassettes **6–10** exhibited also red laser emission with a threshold and efficiency similar to those recorded at 532 nm (Table 2 and Figure 8). It should be noted that at 355 nm the BODIPY acting as acceptor partially absorbed the pumping radiation although with a coefficient lower than the multiple BODIPYs acting as donor units. The direct excitation of the acceptor could reduce the photostability of the final system. However, this deleterious effect in cassettes **6–10** became balanced by a “pseudo” Stokes shift that increased up to  $14470\text{ cm}^{-1}$  thus ensuring long operation times regardless of the laser excitation wavelength. These outstanding results point out the rational design of multichromophoric BODIPY cassettes as a smart skeleton for developing highly efficient and photostable photonic materials with emission in the red-edge region of the visible spectrum.

## Conclusions

Hitherto, photonic performance and resistance under intense irradiation of red-emitting optical materials were either too limited or unreported or at least not well documented. Herein we describe a concise entry to symmetric all-BODIPY-triads, -pentads, and -hexads as artificial light-harvesting systems in which up to four energy donors surround and are covalently linked to one or two central red-emitting energy acceptors. The design and characterization of these multichromophoric systems entailed major achievements in widespread knowledge fields spanning organic synthesis, computer-assisted photophysics to photonics.

From a synthetic viewpoint a novel and efficient protocol was designed to develop all multichromophoric systems studied herein. The new synthetic approach makes use of *one single BODIPY progenitor 11*, and takes advantage of the acidity enhancement of the 3,5-methyl groups in 1,3,5,7-tetramethyl BODIPYs bearing electron-withdrawing substituents (at C-2 and C-6) in eliciting chemoselective Knoevenagel condensations. Additionally, we have demonstrated the effectiveness of dimerization as a synthetic short-cut in the generation of valuable light-harvesting derivatives. Thus, the generation of multichromophore **10**, by dimerization of BODIPY-triad **22** (Scheme 2) compares well in terms of synthetic efficiency with the preparation of BODIPY-pentad **9** from **6a** (Scheme 2). Multichromophores **9** and **10**, comprising four BODIPY donor units each, although differing in the number of acceptor elements (one and two, respectively) displayed comparable lasing properties (see Figure 8).

From the standpoint of computational-aided photophysical characterization, the new BODIPY cassettes showed efficient light-harvesting properties across the ultraviolet–visible spectral region owing to the orthogonal donor–acceptor disposition, which assured the required steric hindrance to avoid both resonant electronic interactions as well as supramolecular aggregation by  $\pi$ – $\pi$  stacking interactions, with deleterious effects on the emission efficiency. Regardless of the excitation wave-

length, the new multichromophoric BODIPYs exhibited bright fluorescence mainly in the red-edge spectral region due to the ongoing effective intramolecular EET process. The high synthetic versatility of the multichromophoric BODIPYs allowed the first systematic and in-depth study of the photophysical behavior of red-emitting cassettes on the solvent polarity as well as on structural factors such as number of donor and acceptor units, and position and spacers connecting the corresponding building blocks.

From the photonic viewpoint, the new BODIPY cassettes lased beyond 700 nm with, to the best of our knowledge this is the highest lasing efficiency and photostability ever recorded under strong pumping conditions such as hard radiation laser doses and prolonged times mimicking those applied in the most advanced photonic and biophotonic applications. In these materials, the enhancement of its photonic behavior strongly depended on the molecular design following the rule: the higher the number of peripheral BODIPYs acting as donor units the lower the pump energy threshold, and the higher the lasing efficiency and photostability. In this way, the new cassettes make it possible to achieve near-IR lasing emission with efficiencies as high as 68%, pump energy thresholds as low as 0.04 mJ, and most crucially, outstanding photostabilities requiring pump energy doses as high as  $1300\text{ GJ mol}^{-1}$  to drop just 50% its initial emission. Collectively, the improved understanding of the processes governing the synthesis and outstanding photonic behavior of the new library of BODIPYs related to their structure should facilitate and speed up the rational design of advanced red-emitting optical materials.

## Experimental Section

### General experimental methods

All solvents and reagents were obtained commercially and were used as received unless stated otherwise. Residual water was removed from starting compounds by repeated co-evaporation with toluene. Reactions were executed at ambient temperatures unless stated otherwise. All moisture-sensitive reactions were performed in dry flasks fitted with glass stoppers or rubber septa under a positive pressure of argon. Air- and moisture-sensitive liquids and solutions were transferred by syringe or stainless steel cannula. Anhydrous  $\text{MgSO}_4$  or  $\text{Na}_2\text{SO}_4$  were used to dry organic solutions during workup, and evaporation of the solvents was performed under reduced pressure using a rotary evaporator. Flash column chromatography was performed using 230–400 mesh silica gel. Thin-layer chromatography was conducted on Kieselgel 60 F254. Spots were observed under UV irradiation (254 nm).  $^1\text{H}$  and  $^{13}\text{C}$  NMR spectra were recorded in  $\text{CDCl}_3$  at 300, 400 or 500 MHz and 75, 101 or 126 MHz, respectively. Chemical shifts are expressed in parts per million ( $\delta$  scale) downfield from tetramethylsilane with the residual protium ( $\text{CHCl}_3$ ;  $\delta = 7.25\text{ ppm}$ ) and carbon ( $\text{CDCl}_3$ ;  $\delta = 77.0\text{ ppm}$ ) solvent resonances as internal references. Coupling constants ( $J$ ) are given in Hz. All presented  $^{13}\text{C}$  NMR spectra are proton-decoupled. Mass spectra were recorded by direct injection with an Accurate Mass Q-TOF LC/MS spectrometer equipped with an electrospray ion source in positive mode. BODIPY monomers **11**, **12**, **13**, **14**, **15b**, **17** and **18** were prepared according to previously reported methods.<sup>[26]</sup>

## General procedures

**General method for Knoevenagel reaction. a) At 80 °C under microwave (MW) irradiation:** To a solution of the corresponding BODIPY 14–16 (0.1 mmol) and the aromatic aldehyde (4 equiv) in dry DMF (25 mL mmol<sup>-1</sup>) were added piperidine (0.1 mL) and acetic acid (0.1 mL). The condensation reaction was performed under MW irradiation for 2 h at 80 °C. The resulting crude mixture was then partitioned between CH<sub>2</sub>Cl<sub>2</sub> and water, and the aqueous layer was re-extracted. The organic phase was dried over MgSO<sub>4</sub>, concentrated and purified on a silica gel column. **b) At room temperature:** To a solution of the corresponding BODIPY (0.1 mmol) and the appropriate aldehyde (2–4 equiv) in dry DMF (25 mL mmol<sup>-1</sup>) were added piperidine (0.1 mL) and acetic acid (0.1 mL) at room temperature (usually 24 h). The resulting crude mixture was then partitioned between CH<sub>2</sub>Cl<sub>2</sub> and water, and the aqueous layer was re-extracted. The organic phase was dried over MgSO<sub>4</sub>, concentrated and purified on a silica gel column.

**General method for copper(I)-catalyzed alkyne-azide cycloaddition reaction (CuAAC):** The corresponding azide (2 equiv), sodium ascorbate (3 equiv), and CuSO<sub>4</sub> (1.5 equiv) were added to a solution of the appropriate alkyne-BODIPY (50 mg, 0.1 mmol) in EtOH/H<sub>2</sub>O (1:1, v/v, 50 mL mmol<sup>-1</sup>). The solution was subjected to MW irradiation at 80 °C until no starting materials were left. The reaction mixture was then concentrated under reduced pressure and the residue was purified by silica gel column chromatography.

**General method for ureation reaction:** The appropriate azidomethylphenyl-BODIPY (0.1 mmol) was added to a mixture of 1 M triethylammonium hydrogen carbonate buffer (2.6 equiv) and 1,4-dioxane (60 mL mmol<sup>-1</sup>). Triphenylphosphine (1.3 equiv) was added, and the reaction was monitored by TLC. After disappearance of the starting material, the solvent was evaporated in vacuo to dryness. The obtained BODIPY dimer was purified by flash chromatography on silica gel.

## Spectroscopic data of multichromophoric all-BODIPY materials

**Trimer 6a:** <sup>1</sup>H NMR (500 MHz, CDCl<sub>3</sub>): δ = 8.48 (d, *J* = 16.3 Hz, 2H), 8.16 (d, *J* = 8 Hz, 2H), 7.89 (d, *J* = 16.3 Hz, 2H), 7.68–7.48 (m, 6H), 7.29–7.25 (m, 3H), 7.10–7.07 (m, 1H), 5.98 (s, 4H), 4.48 (s, 2H), 3.47 (s, 2H), 2.55 (s, 12H), 1.40 (s, 12H), 1.38 ppm (s, 6H); <sup>13</sup>C NMR (125 MHz, CDCl<sub>3</sub>): δ = 155.6, 152.5, 146.3, 143.4, 139.9, 138.7, 138.1, 135.4, 135.2, 135.1, 132.3, 132.2, 131.6, 130.2, 129.6, 128.8, 128.7, 128.5, 128.0, 125.5, 121.4, 119.8, 113.8, 88.6, 88.5, 68.0, 62.3, 14.6, 14.0, 12.5 ppm; <sup>19</sup>F NMR (376 MHz, CDCl<sub>3</sub>): δ = -138.97 (m), -145.34 (m), -146.88 ppm (m). HRMS (ESI-TOF): *m/z* calcd for C<sub>64</sub>H<sub>55</sub>N<sub>6</sub>O<sub>3</sub>F<sub>6</sub> [M+NH<sub>4</sub>]<sup>+</sup>; 1093.45403; found 1093.45519.

**Trimer 6b:** <sup>1</sup>H NMR (500 MHz, CDCl<sub>3</sub>): δ = 8.04 (d, *J* = 16.0 Hz, 2H), 7.93 (d, *J* = 7.8 Hz, 2H), 7.71–7.38 (m, 12H), 7.31–7.06 (m, 10H), 5.70 (s, 2H), 5.66 (s, 2H), 4.59 (s, 2H), 2.43 (s, 6H), 2.42 (s, 6H), 1.45 (s, 6H), 1.36 ppm (s, 12H); <sup>13</sup>C NMR (125 MHz, CDCl<sub>3</sub>): δ = 155.7, 155.6, 152.2, 145.8, 142.9, 139.6, 139.2, 138.3, 136.9, 136.2, 134.4, 132.7, 132.6, 131.6, 131.5, 131.0, 130.2, 129.8, 129.0, 128.9, 128.7, 128.5, 128.2, 128.1, 127.0, 123.0, 122.3, 121.5, 114.8, 98.3, 82.0, 68.3, 62.5, 14.8, 14.0, 13.0 ppm. <sup>19</sup>F NMR (376 MHz, CDCl<sub>3</sub>): δ = -140.12 (m), -146.94 (m), -147.99 ppm (m). HRMS (ESI-TOF): calcd for C<sub>76</sub>H<sub>67</sub>B<sub>3</sub>F<sub>6</sub>N<sub>7</sub>O [M+NH<sub>4</sub>]<sup>+</sup>; 1240.55942; found 1240.56160.

**Trimer 7:** <sup>1</sup>H NMR (500 MHz, CDCl<sub>3</sub>): δ = 8.00 (dd, *J* = 8.1, 1.2 Hz, 2H), 7.80 (d, *J* = 16.4 Hz, 2H), 7.65–7.52 (m, 3H), 7.43 (tdd, *J* = 7.6, 5.0, 1.3 Hz, 3H), 7.38–7.21 (m, 10H), 7.16–7.03 (m, 7H), 6.71 (d, *J* = 16.4 Hz, 2H), 6.04 (s, 2H), 6.02 (s, 2H), 5.33 (s, 4H), 4.57 (s, 2H), 2.62 (s, 6H), 2.61 (s, 6H), 1.38 (s, 6H), 1.37 (s, 6H), 1.26 ppm (s, 6H);

<sup>13</sup>C NMR (125 MHz, CDCl<sub>3</sub>): δ = 155.3, 151.0, 143.8, 142.2, 140.1, 139.8, 139.0, 138.2, 135.8, 135.4, 134.4, 134.0, 132.8, 132.6, 131.5, 130.9, 129.8, 129.6, 129.0, 128.7, 128.4, 128.0, 127.5, 126.1, 123.0, 122.5, 121.4, 121.3, 62.3, 53.6, 14.8, 14.0, 13.9 ppm. HRMS (ESI-TOF) *m/z* calcd for C<sub>78</sub>H<sub>69</sub>B<sub>3</sub>F<sub>6</sub>N<sub>12</sub>NaO [M+Na]<sup>+</sup>; 1359.58244, found: 1359.57729.

**Trimer 8:** <sup>1</sup>H NMR (500 MHz, CDCl<sub>3</sub>): δ = 7.80–7.66 (m, 3H), 7.61–7.19 (m, 31H), 7.04 (d, *J* = 16.5 Hz, 2H), 5.97 (s, 2H), 5.93 (s, 2H), 5.47 (s, 4H), 4.70 (s, 2H), 2.54 (s, 6H), 2.51 (s, 6H), 1.27–1.22 ppm (m, 18H); <sup>13</sup>C NMR (125 MHz, CDCl<sub>3</sub>): δ = 156.8, 156.5, 151.7, 142.7, 142.4, 142.1, 140.8, 138.8, 138.7, 137.8, 136.6, 133.6, 132.8, 132.7, 132.6, 130.9, 130.6, 130.2, 129.9, 129.4, 128.9, 128.7, 128.6, 128.4, 127.6, 124.4, 122.1, 121.8, 118.6, 62.2, 51.2, 14.7, 14.0, 12.4 ppm. HRMS (ESI-TOF) *m/z* calcd for C<sub>78</sub>H<sub>70</sub>B<sub>3</sub>F<sub>6</sub>N<sub>12</sub>O [M+H]<sup>+</sup>; 1337.60050, found: 1337.60301.

**Pentamer 9:** <sup>1</sup>H NMR (500 MHz, CDCl<sub>3</sub>): δ = 7.96 (d, *J* = 8.0 Hz, 2H), 7.75 (d, *J* = 16.4 Hz, 2H), 7.70–7.60 (m, 1H), 7.51 (dtd, *J* = 10.6, 7.7, 1.6 Hz, 4H), 7.45–7.30 (m, 8H), 7.26 (s, 10H), 7.21–7.15 (m, 1H), 7.10 (s, 2H), 7.06 (dd, *J* = 7.6, 1.4 Hz, 2H), 7.00–6.94 (m, 2H), 6.65 (s, 1H), 6.62 (s, 1H), 5.99 (s, 2H), 5.96 (s, 2H), 5.83 (d, *J* = 2.3 Hz, 4H), 5.17 (d, *J* = 4.3 Hz, 4H), 4.64 (s, 2H), 2.55 (s, 12H), 2.36 (s, 12H), 1.23–1.27 ppm (m, 30H). <sup>13</sup>C NMR (125 MHz, CDCl<sub>3</sub>): δ = 156.5, 156.4, 155.4, 151.1, 143.4, 143.0, 142.8, 141.9, 139.7, 139.4, 138.4, 138.2, 135.5, 134.6, 134.1, 133.5, 132.9, 132.5, 131.3, 130.9, 130.0, 129.9, 129.6, 129.5, 129.2, 128.7, 128.6, 128.5, 128.1, 125.9, 123.7, 122.3, 121.7, 121.2, 121.1, 62.3, 50.4, 14.6, 14.3, 13.9, 13.8, 13.7, 12.2 ppm. HRMS (ESI-TOF) *m/z* calcd for C<sub>104</sub>H<sub>95</sub>B<sub>5</sub>F<sub>10</sub>N<sub>16</sub>NaO [M+Na]<sup>+</sup>; 1851.81289, found: 1851.81945.

**Hexamer 10:** <sup>1</sup>H NMR (400 MHz, CDCl<sub>3</sub>): δ = 8.47 (d, *J* = 16.3 Hz, 4H), 8.16 (d, *J* = 8.0 Hz, 4H), 7.88 (d, *J* = 16.3 Hz, 5H), 7.63 (m, 4H), 7.57–7.46 (m, 4H), 7.47–7.37 (m, 3H), 7.12–6.97 (m, 2H), 5.97 (s, 4H), 5.95 (s, 4H), 4.37 (t, *J* = 6.0 Hz, 2H), 4.05–4.12 (m, 4H), 3.46 (s, 2H), 3.45 (s, 2H), 2.55 (s, 12H), 2.53 (m, 12H), 1.40–1.35 ppm (m, 36H). <sup>13</sup>C NMR (125 MHz, CDCl<sub>3</sub>): δ = 166.2, 155.7, 152.4, 149.3, 149.0, 146.2, 143.3, 139.8, 135.6, 135.3, 132.1, 131.5, 130.2, 129.6, 128.8, 125.5, 121.4, 119.7, 113.8, 110.0, 88.8, 81.4, 58.8, 41.7, 14.6, 14.0, 12.5 ppm. HRMS (ESI-TOF) *m/z* calcd for C<sub>129</sub>H<sub>110</sub>B<sub>6</sub>F<sub>12</sub>N<sub>14</sub>O [M+H]<sup>+</sup>; 2164.95073, found: 2164.95431.

## Photophysical properties

Spectroscopic properties were registered in diluted solutions (around 2 × 10<sup>-6</sup> M), prepared by adding the corresponding solvent (spectroscopic grade) to the residue from the adequate amount of a concentrated stock solution in acetone, after vacuum evaporation of this solvent. UV/Vis absorption spectra were recorded on a Varian model CARY 4E spectrophotometer, whereas the fluorescence and excitation spectra, as well as the decay curves were registered in an Edinburgh Instruments spectrofluorimeter (model FLSP 920). Fluorescence quantum yields (*φ*<sup>f</sup>) were obtained using as reference commercial cresyl violet (*φ*<sup>f</sup> = 0.54 in methanol), for the long-wavelength emission of the energy acceptor, and commercial PM546 (*φ*<sup>f</sup> = 0.81 in methanol) to account for the green, and quenched emission owing to energy transfer, of the energy donor subunit. The values were corrected by the refractive index of the solvent. Radiative decay curves were registered with the time correlated single-photon counting technique using a multi-channel plate detector with picosecond time-resolution. Fluorescence emission was monitored at the maximum emission wavelength after excitation by means of a wavelength-tunable Fianium Supercontinuum laser. The fluorescence lifetime (*τ*) was obtained after the deconvolution of the instrumental response signal from the recorded decay curves by means of an iterative method. The

decay curve was essentially the same regardless of the excited visible absorption band. The goodness of the exponential fit was controlled by statistical parameters (chi-square and the analysis of the residuals). The radiative ( $k_{\text{r}}$ ) and non-radiative ( $k_{\text{nr}}$ ) rate constants were calculated from the fluorescence quantum yield and lifetime;  $k_{\text{r}} = \phi/\tau$  and  $k_{\text{nr}} = (1 - \phi)/\tau$ .

### Quantum mechanical calculations

Ground state geometries were optimized at the density functional theory (DFT) using range-separated hybrid wB97XD method. The vertical Franck–Condon electronic transition was predicted by the time dependent (TD) method and the same functional. In both cases the double valence basis set with one polarization functions (6–31g\*) was used owing to the large size of the computed chromophoric molecules. The geometries were considered as energy minimum when the corresponding frequency analysis did not give any negative value. The solvent effect (cyclohexane) was considered in the conducted theoretical simulations by means of the polarizable continuum model (PCM). All the calculations were performed using the Gaussian 16 software (Revision C.01)<sup>[31]</sup> as implemented in the computational cluster “arina” of the UPV/EHU.

### Laser properties

Laser efficiency was evaluated from concentrated solutions (millimolar) of dyes in ethyl acetate contained in 1 cm optical-path rectangular quartz cells carefully sealed to avoid solvent evaporation during experiments. The liquid solutions were transversely pumped with 8 mJ, 8 ns FWHM pulses from the third harmonic (355 nm) or the second harmonic (532 nm) of a Q-switched Nd:YAG laser (Lotis TII 2134) at a repetition rate of 1 Hz. The excitation pulses were line-focused onto the cell using a combination of positive and negative cylindrical lenses ( $f = 15$  cm and  $f = -15$  cm, respectively) perpendicularly arranged. The plane parallel oscillation cavity (2 cm length) consisted of a 90% reflectivity aluminum mirror acting as back reflector, and the lateral face of the cell acting as output coupler (4% reflectivity). The pump and output energies were detected by a GenTec powermeter. The photostability of the dyes in ethyl acetate solution was evaluated by using a pumping energy and geometry exactly equal to that of the laser experiments. We used spectroscopic quartz cuvettes with 0.1 cm optical to allow for the minimum solution volume ( $V_s = 40 \mu\text{L}$ ) to be excited. The lateral faces were grounded, whereupon no laser oscillation was obtained. Information about photostability was obtained by monitoring the decrease in laser-induced fluorescence (LIF) intensity. In order to facilitate comparisons independently of the experimental conditions and sample, the photostability figure of merit was defined as the accumulated pump energy absorbed by the system ( $E_{\text{dose}}$ ), per mole of dye, before the output energy falls to a 50% its initial value. In terms of experimental parameters, this energy dose, in units of  $\text{GJ mol}^{-1}$ , can be expressed as [Eq. (1)]:

$$E_{\text{dose}}^{50\%} (\text{GJ mol}^{-1}) = \frac{E_{\text{pump}} (\text{GJ}) (1 - 10^{-\epsilon C L}) \sum_{\# \text{pulse}} f}{C V_s} \quad (1)$$

where  $E_{\text{pump}}$  is the energy per pulse,  $C$  is the molar concentration,  $\epsilon$  is the molar absorption coefficient in units of  $\text{m}^{-1} \text{cm}^{-1}$ ,  $L$  is the depth of the cuvette expressed in cm,  $V_s$  is the solution volume, in liters, within the cuvette, and  $f$  is the ratio between the LIF intensity after #pulses and the LIF intensity in the first pulse. To speed up the experiment the pump repetition rate was increased up to 15 Hz. The fluorescence emission and laser spectra were monitored

perpendicular to the exciting beam, collected by an optical fiber, and imaged onto a spectrometer (Acton Research corporation) and detected with a charge-coupled device (CCD; SpectruMM:GS128B). The fluorescence emission was recorded by feeding the signal to the boxcar (Stanford Research, model 250) to be integrated before being digitized and processed by a computer. The estimated error in the energy and photostability measurements was 10%.

### Acknowledgements

We gratefully acknowledge the Spanish Ministerio de Economía y Competitividad for financial support (projects CTQ2015-66702-R, MAT2017-83856-C3-1-P and 3-P). We also thank the Ministerio de Ciencia Innovación y Universidades (project RTI2018-094862-B-I00) and the Gobierno Vasco for financial support (project IT912-16) and for a predoctoral fellowship to E.A.Z. The authors thank SGIker of UPV/EHU for technical support with the computational calculations, which were carried out in the “arina” informatic cluster.

### Conflict of interest

The authors declare no conflict of interest.

**Keywords:** all-BODIPY multichromophores · energy transfer · lasers · photophysics · red-emitting materials

- [1] a) M. Vendrell, D. Zhai, J. C. Er, Y. T. Chang, *Chem. Rev.* **2012**, *112*, 4391; b) S. van de Linde, M. Sauer, *Chem. Soc. Rev.* **2014**, *43*, 1076; c) A. J. C. Kuehne, M. C. Gather, *Chem. Rev.* **2016**, *116*, 12823; d) P. Murto, A. Minotto, A. Zampetti, X. Xu, M. R. Andersson, F. Cacialli, E. Wang, *Adv. Opt. Mater.* **2016**, *4*, 2068; e) Y. Zhang, S. Xia, M. Fang, W. Mazi, Y. Zeng, T. Johnston, A. Pap, R. L. Luck, H. Liu, *Chem. Commun.* **2018**, *54*, 7625; f) S. Zhu, Z. Rui, R. Tian, B. C. Yung, Q. Yang, S. Zhao, D. O. Kiesewetter, G. Niu, H. Sun, A. L. Antaris, X. Chen, *Adv. Mater.* **2018**, *30*, 1802546; g) E. Oliveira, E. Bértolo, C. Nuñez, V. Pilla, H. M. Santos, J. Fernandez-Lodeiro, A. Fernandez-Lodeiro, J. Djafari, J. L. Capelo, C. Lodeiro, *ChemistryOpen* **2018**, *7*, 9; h) C. Staudinger, J. Breining, I. Klimant, S. M. Borisov, *Analyst* **2019**, *144*, 2393.
- [2] a) M. Grossi, M. Morgunova, S. Cheung, D. Scholz, E. Conroy, M. Terrile, A. Panarella, J. C. Simpson, W. M. Gallagher, D. F. O’Shea, *Nat. Commun.* **2016**, *7*, 10855; b) X. Wu, Y. Zhang, K. Takle, O. Bilsel, Z. Li, H. Lee, Z. Zhang, D. Li, W. Fan, C. Duan, E. M. Chan, C. Lois, Y. Xiang, G. Han, *ACS Nano* **2016**, *10*, 1060; c) J. Liu, Y.-Q. Sun, H. Zhang, H. Shi, Y. Shi, W. Guo, *ACS Appl. Mater. Interfaces* **2016**, *8*, 22953; d) Y. Zhang, S. A. Autry, L. E. McNamara, S. T. Nguyen, N. Le, P. Brogdon, D. L. Watkins, N. I. Hammer, J. H. Delcamp, *J. Org. Chem.* **2017**, *82*, 5597; e) D. Pfeifer, I. Klimant, S. M. Borisov, *Chem. Eur. J.* **2018**, *24*, 10711; f) A. Adamow, L. Sznitko, E. Chrzumnicka, J. Stachera, A. Szukalski, T. Martynski, J. Mysliwiec, *Sci. Rep.* **2019**, *9*, 2143.
- [3] a) L. Yuan, W. Lin, K. Zheng, L. He, W. Huang, *Chem. Soc. Rev.* **2013**, *42*, 622; b) Q. Zheng, M. F. Juetta, S. Jockusch, M. R. Wassermann, Z. Zhou, R. B. Altman, S. C. Blanchard, *Chem. Soc. Rev.* **2014**, *43*, 1044; c) Z. Yao, L. Yang, Y. Cai, C. Yan, M. Zhang, N. Cai, X. Dong, P. Wang, *J. Phys. Chem. C* **2014**, *118*, 2977; d) A. Dessì, M. Calamante, A. Mordini, M. Peruzzini, A. Sinicropi, R. Basosi, F. Fabrizi, M. Taddei, D. Colonna, A. Di Carlo, G. Reginato, L. Zani, *Chem. Commun.* **2014**, *50*, 13952; e) T. Kowada, H. Maeda, K. Kikuci, *Chem. Soc. Rev.* **2015**, *44*, 4953; f) D. Wu, A. C. Sedgwick, T. Gunnalugsson, E. U. Akkaya, J. Yoon, T. D. James, *Chem. Soc. Rev.* **2017**, *46*, 7105; g) Z. Gao, Y. Hao, M. Zheng, Y. Chen, *RSC Adv.* **2017**, *7*, 7604; h) C. Schwachheimer, F. Röncke, U. Schepers, H. A. Wagenknecht, *Chem. Sci.* **2018**, *9*, 6557; i) S. Basu, L. M. Needham, D. Lando, E. J. R. Taylor, K. J. Wohlfahrt, D. Shah, W. Boucher, Y. L. Tan, L. E. Bates, O. Takchenko, J.

- Cramard, B. C. Lagerholm, C. Eggeling, B. Hendrich, D. Klenerman, S. F. Lee, E. D. Laue, *Nat. Commun.* **2018**, *9*, 2520.
- [4] a) A. Loudet, K. Burgess, *Chem. Rev.* **2007**, *107*, 4891; b) G. Ulrich, R. Ziessel, A. Harriman, *Angew. Chem. Int. Ed.* **2008**, *47*, 1184; *Angew. Chem.* **2008**, *120*, 1202; c) R. Ziessel, G. Ulrich, A. Harriman, *New J. Chem.* **2007**, *31*, 496; d) A. Treibs, F.-H. Kreuzer, *Liebigs Ann. Chem.* **1968**, *718*, 208–223.
- [5] a) A. Kamkaew, S. H. Lim, H. B. Lee, L. V. Kiew, L. Y. Chung, K. Burgess, *Chem. Soc. Rev.* **2013**, *42*, 77; b) J. Fan, M. Hu, P. Zhan, X. Peng, *Chem. Soc. Rev.* **2013**, *42*, 29; c) A. Bessette, G. S. Hanan, *Chem. Soc. Rev.* **2014**, *43*, 3342; d) J. Zhao, J. K. Xu, W. Yang, Z. Wang, F. Zhong, *Chem. Soc. Rev.* **2015**, *44*, 8904; e) Y. Ge, D. F. O'Shea, *Chem. Soc. Rev.* **2016**, *45*, 3846; f) J. Bañuelos, *Chem. Rec.* **2016**, *16*, 355.
- [6] a) Y. Cakmak, E. U. Akkaya, *Org. Lett.* **2009**, *11*, 85; b) V. Lakshmi, R. R. Rao, M. Ravikanth, *Org. Biomol. Chem.* **2015**, *13*, 2501; c) N. Boens, B. Verbelen, W. Dehaen, *Eur. J. Org. Chem.* **2015**, 6577; d) C. F. A. Gómez-Durán, I. Esnal, I. Valois-Escamilla, A. Urias-Benavides, J. Bañuelos, I. Lopez Arbeloa, I. Garcia-Moreno, E. Peña-Cabrera, *Chem. Eur. J.* **2016**, *22*, 1048.
- [7] a) V. Lakshmi, R. Sharma, M. Ravikanth, *Rep. Org. Chem.* **2016**, *6*, 1; b) H. Lu, J. Mack, Y. Yang, Z. Shen, *Chem. Soc. Rev.* **2014**, *43*, 4778.
- [8] a) I. J. Arroyo, R. Hu, G. Merino, B. Z. Tanag, E. Peña-Cabrera, *J. Org. Chem.* **2009**, *74*, 5719; b) K. Tram, H. Yan, H. A. Jenkins, S. Vassiliev, D. Bruce, *Dyes Pigm.* **2009**, *82*, 392; A. Schmitt, B. Hinkeldey, M. Wild, G. Jung, *J. Fluoresc.* **2009**, *19*, 755.
- [9] a) W. Wu, J. Zhao, H. Guo, J. Sun, S. Ji, Z. Wang, *Chem. Eur. J.* **2012**, *18*, 1961, (compound **3a**); D. Zhang, Y. Wang, Y. Xiao, S. Qian, X. Qian, *Tetrahedron* **2009**, *65*, 8099, (compound **3b**).
- [10] L. Huang, X. Cui, B. Therrien, J. Zhao, *Chem. Eur. J.* **2013**, *19*, 17472.
- [11] W. Yang, A. Karatay, J. Zhao, J. Song, L. Zhao, Y. Xing, C. Zhang, C. He, H. G. Yaglioglu, M. Hayvali, A. Elmali, B. Küçüköz, *Inorg. Chem.* **2015**, *54*, 7492.
- [12] a) O. Buyukcikir, O. A. Bozdemir, S. Kolenen, S. Erbas, E. U. Akkaya, *Org. Lett.* **2009**, *11*, 4644; b) D. Frath, J. Massue, G. Ulrich, R. Ziessel, *Angew. Chem. Int. Ed.* **2014**, *53*, 2290; *Angew. Chem.* **2014**, *126*, 2322; c) L. Jiao, Y. Wu, S. Wang, X. Hu, P. Zhang, C. Yu, K. Cong, Q. Meng, E. Hao, M. G. H. Vicent, *J. Org. Chem.* **2014**, *79*, 1830; d) N. L. Bill, J. M. Lim, C. M. Davis, S. Bahring, J. O. Jeppesen, D. Kim, J. L. Sessler, *Chem. Commun.* **2014**, *50*, 6758; e) C. Cheng, N. Gao, C. Yu, Z. Wang, J. Wang, E. Hao, Y. Wei, X. Mu, Y. Tian, C. Ran, L. Jian, *Org. Lett.* **2015**, *17*, 278.
- [13] a) S. P. Singh, T. Gayathri, *Eur. J. Org. Chem.* **2014**, 4689; b) L. Luo, D. Wu, W. Li, S. Zhang, Y. Ma, S. Yan, J. You, *Org. Lett.* **2014**, *16*, 6080; c) C. Yu, L. Jiao, P. Zhang, Z. Feng, C. Cheng, Y. Wei, X. Mu, E. Hao, *Org. Lett.* **2014**, *16*, 3048; d) S. Debnath, S. Singh, A. Bedi, K. Krishnamoorthy, S. S. Zade, *J. Phys. Chem. C* **2015**, *119*, 15859; e) C. Maeda, T. Todaka, T. Ema, *Org. Lett.* **2015**, *17*, 3090; f) S. Yamazawa, M. Nakashima, Y. Suda, R. Nishiyabu, Y. Kubo, *J. Org. Chem.* **2016**, *81*, 1310; g) Z. Zhou, J. Zhou, L. Gai, A. Yuan, Z. Shen, *Chem. Commun.* **2017**, *53*, 6621; h) A. Savoldelli, Q. Meng, R. Paolesse, F. R. Fronczek, K. M. Smith, M. G. H. Vicente, *J. Org. Chem.* **2018**, *83*, 6498; i) Y. Li, Z. Qiao, T. Li, O. Zeika, K. Leo, *ChemPhotoChem* **2018**, *2*, 1017; j) J. L. Belmonte-Vázquez, E. Avellan-Zaballa, E. Enriquez-Palacios, L. Cerdán, I. Esnal, J. Bañuelos, C. Villegas-Gomez, I. Lopez-Arbeloa, E. Peña-Cabrera, *J. Org. Chem.* **2019**, *84*, 2523.
- [14] I. García-Moreno, D. Zhang, A. Costela, V. Martin, R. Sastre, Y. Xiao, *J. Appl. Physiol.* **2010**, *107*, 073105.
- [15] a) T. Bura, P. Retailleau, R. Ziessel, *Angew. Chem. Int. Ed.* **2010**, *49*, 6659; *Angew. Chem.* **2010**, *122*, 6809; b) Altan Bozdemir, S. Erbas-Cakmak, O. O. Ekiz, A. Dana, E. U. Akkaya, *Angew. Chem. Int. Ed.* **2011**, *50*, 10907; *Angew. Chem.* **2011**, *123*, 11099; c) R. Ziessel, G. Ulrich, A. Haeefe, A. Harriman, *J. Am. Chem. Soc.* **2013**, *135*, 11330; d) D. Su, J. Oh, S. C. Lee, J. M. Lim, S. Sahu, X. Yu, D. Kim, Y. T. Chang, *Chem. Sci.* **2014**, *5*, 4812; e) M. A. H. Alamiry, A. Harriman, A. Haeefe, R. Ziessel, *ChemPhysChem* **2015**, *16*, 1867; f) A. Harriman, *Chem. Commun.* **2015**, *51*, 11745; g) C. Azarias, R. Russo, L. Cupellini, B. Mennucci, D. Jacquemin, *Phys. Chem. Chem. Phys.* **2017**, *19*, 6443; h) L. Lin, X. Lin, H. Guo, F. Yang, *Org. Biomol. Chem.* **2017**, *15*, 6006; i) G. Reddy, N. Duvva, S. Seetharaman, F. D'Souza, L. Giribabu, *Phys. Chem. Chem. Phys.* **2018**, *20*, 27418.
- [16] a) L. Cerdán, E. Enciso, V. Martin, J. Bañuelos, I. Lopez-Arbeloa, A. Costela, I. Garcia-Moreno, *Nat. Photonics* **2012**, *6*, 621; b) G. Duran-Sampedro, A. R. Agarrabeitia, I. Garcia-Moreno, L. Gartzia, S. de la Moya, J. Bañuelos, I. Lopez Arbeloa, M. J. Ortiz, *Chem. Commun.* **2015**, *51*, 11382; c) E. Avelanal-Zaballa, G. Duran-Sampedro, A. Prieto-Castañeda, A. R. Agarrabeitia, I. Garcia-Moreno, I. Lopez-Arbeloa, J. Bañuelos, M. J. Ortiz, *Phys. Chem. Chem. Phys.* **2017**, *19*, 13210.
- [17] a) C. Y. Lee, O. K. Farha, B. J. Hong, A. A. Sarjeant, S. T. Nguyen, J. T. Hupp, *J. Am. Chem. Soc.* **2011**, *133*, 15858; b) A. Meares, A. Satraitis, N. Santhanam, Z. Yu, M. Ptaszek, *J. Org. Chem.* **2015**, *80*, 3858; c) G. Hu, R. Liu, E. J. Alexy, A. K. Mandal, D. F. Bocian, D. Holten, J. S. Lindsey, *New J. Chem.* **2016**, *40*, 8032; d) M. D. Weber, V. Nikolaou, J. E. Wittmann, A. Nikolaou, P. A. Angaridis, G. Charalambidis, C. Stangel, A. Kahnt, A. G. Coutsolelos, R. D. Costa, *Chem. Commun.* **2016**, *52*, 1602; e) A. N. Kurnsunlu, *RSC Adv.* **2014**, *4*, 47690; f) H. R. A. Golf, A. M. Oltmanns, D. H. Trieu, H.-U. Reissig, A. Wiehe, *Eur. J. Org. Chem.* **2015**, 4224.
- [18] a) S. Guo, L. Ma, J. Zhao, B. Kucukoz, A. Karatay, M. Hayvali, H. G. Yaglioglu, A. Elmali, *Chem. Sci.* **2014**, *5*, 489; b) V. Bandi, F. P. D'Souza, H. B. Gobeze, F. D'Souza, *Chem. Eur. J.* **2015**, *21*, 2669; c) S. Kumar, H. Gobeze, T. Chatterje, F. D'Souza, M. Ravikanth, *J. Phys. Chem. A* **2015**, *119*, 8338; d) S. Kumar, K. G. Thorat, M. Ravikanth, *J. Org. Chem.* **2017**, *82*, 6568.
- [19] a) M. Galletta, F. Puntoriero, S. Campagna, C. Chiorboli, M. Quesada, S. Goeb, R. Ziessel, *J. Phys. Chem. A* **2006**, *110*, 4348; b) J. Bañuelos, F. Lopez-Arbeloa, T. Arbeloa, S. Salleres, F. Amat-Guerri, M. Liras, I. Lopez-Arbeloa, *J. Phys. Chem. A* **2008**, *112*, 10822; c) C. Dumas-Verdes, F. Mio-mandre, E. Lepicier, O. Galangau, T. T. Vu, G. Clavier, R. Meallet-Renault, P. Audebert, *Eur. J. Org. Chem.* **2010**, 2525; d) F. Puntoriero, F. Nastasi, S. Campagna, T. Bura, R. Ziessel, *Chem. Eur. J.* **2010**, *16*, 8832; e) M. T. Whited, P. I. Djurovich, S. T. Roberts, A. C. Durrell, C. W. Schlenker, S. E. Bradforth, M. E. Thompson, *J. Am. Chem. Soc.* **2011**, *133*, 88; f) T. Lazarides, S. Kuhri, G. Charalambidis, M. K. Panda, D. M. Guldi, A. G. Coutsolelos, *Inorg. Chem.* **2012**, *51*, 4193; g) Q. Hualmé, E. Cece, A. Mirloup, R. Ziessel, *Tetrahedron Lett.* **2014**, *55*, 4953; h) S. Diring, F. Puntoriero, F. Nastasi, S. Campagna, R. Ziessel, *J. Am. Chem. Soc.* **2009**, *131*, 6108; i) J. lehl, J.-F. Nierengarten, A. Harriman, T. Bura, R. Ziessel, *J. Am. Chem. Soc.* **2012**, *134*, 988; j) T. Bura, F. Nastasi, F. Puntoriero, S. Campagna, R. Ziessel, *Chem. Eur. J.* **2013**, *19*, 8900; k) L. Huang, X. Cui, B. Therrien, J. Zhao, *Chem. Eur. J.* **2013**, *19*, 17472.
- [20] All-BODIPY based systems have been studied: a) X. Zhang, Y. Xiao, X. Qian, *Org. Lett.* **2008**, *10*, 29; b) G. Barin, M. D. Yilmaz, E. U. Akkaya, *Tetrahedron Lett.* **2009**, *50*, 1738; c) O. A. Bozdemir, Y. Cakmak, F. Sozmen, T. Odzemir, A. Siemiarzczuk, E. U. Akkaya, *Chem. Eur. J.* **2010**, *16*, 6346; d) Y. Xiao, D. Zhang, X. Qian, A. Costela, I. Garcia-Moreno, V. Martin, M. E. Perez-Ojeda, J. Bañuelos, L. Gartzia, I. Lopez-Arbeloa, *Chem. Commun.* **2011**, *47*, 11513; e) P. Bonaccorsi, M. C. Aversa, A. Barattucci, T. Papalia, F. Puntoriero, S. Campagna, *Chem. Commun.* **2012**, *48*, 10550; f) T. M. Khan, M. S. Shaik, M. Ravikanth, *Dyes Pigm.* **2012**, *94*, 66; g) R. Sharma, H. B. Gobeze, F. D'Souza, M. Ravikanth, *ChemPhysChem* **2016**, *17*, 2516.
- [21] a) S. K. Mamidyala, M. G. Finn, *Chem. Soc. Rev.* **2010**, *39*, 1252; b) M. Galibert, P. Dumy, D. Boturyn, *Angew. Chem. Int. Ed.* **2009**, *48*, 2576; *Angew. Chem.* **2009**, *121*, 2614; M. Meldal, C. W. Tornøe, *Chem. Rev.* **2008**, *108*, 2952.
- [22] J. E. Moses, A. D. Moorhouse, *Chem. Soc. Rev.* **2007**, *36*, 1249.
- [23] a) M. R. Martinez-Gonzalez, A. Urias-Benavides, E. Alvarado-Martinez, J. C. Lopez, A. M. Gómez, M. del Rio, I. Garcia, A. Costela, J. Bañuelos, T. Arbeloa, I. Lopez Arbeloa, E. Peña-Cabrera, *Eur. J. Org. Chem.* **2014**, 5659; b) M. L. Lepage, A. Mirloup, M. Ripoll, F. Stauffert, A. Bodlener, R. Ziessel, P. Compain, *Beilstein J. Org. Chem.* **2015**, *11*, 659–667.
- [24] Styryl-BODIPY derivatives have proven to be remarkable near-IR emitting fluorophores: for the first example of a monostyryl BODIPY, see: a) K. Rurack, M. Kollmannsberger, J. Daub, *Angew. Chem. Int. Ed.* **2001**, *40*, 385; *Angew. Chem.* **2001**, *113*, 396; b) for the first example of a distyryl BODIPY see: Z. Dost, S. Atilgan, E. U. Akkaya, *Tetrahedron* **2006**, *62*, 8484.
- [25] J. Cristóbal López, M. del Rio, A. Oliden, J. Bañuelos, I. Lopez-Arbeloa, I. Garcia-Moreno, A. M. Gomez, *Chem. Eur. J.* **2017**, *23*, 17511.
- [26] M. del Río, F. Lobo, J. C. Lopez, A. Oliden, J. Bañuelos, I. Lopez-Arbeloa, I. Garcia-Moreno, A. M. Gomez, *J. Org. Chem.* **2017**, *82*, 1240.
- [27] E. Deniz, G. C. Isbasar, O. A. Bozdemir, L. T. Yildirim, A. Siemiarzczuk, E. U. Akkaya, *Org. Lett.* **2008**, *10*, 3401.
- [28] A seminal approach to all-BODIPY chromophores based on the chemo-selective Knoevenagel condensation of a pivotal formyl 4,4'-dialkynylboron BODIPY dye with 8-aryl-1,3,5,7-tetramethyl BODIPY derivatives had been described by Ziessel's group. In this process, the selectivity of



the “crossed” condensation over the “self-Knoevenagel condensation” had been ascribed to a reactivity-reduction of the C-3, C-5 methyl groups in the former, induced by the steric congestion around the boron center, see reference [15a] and also: A. Mirloup, P. Retailleau, R. Ziessel, *Tetrahedron Lett.* **2013**, *54*, 4456.

- [29] M. Kitamura, T. Koga, M. Yano, T. Okauchi, *Synlett* **2012**, *23*, 1335.  
 [30] L. Cerdán, A. Costela, I. García-Moreno, J. Bañuelos, I. López Arbeloa, *Laser Phys. Lett.* **2012**, *9*, 426.  
 [31] Gaussian 16, Revision C.01, M. J. Frisch, G. W. Trucks, H. B. Schlegel, G. E. Scuseria, M. A. Robb, J. R. Cheeseman, G. Scalmani, V. Barone, G. A. Petersson, H. Nakatsuji, X. Li, M. Caricato, A. V. Marenich, J. Bloino, B. G. Janesko, R. Gomperts, B. Mennucci, H. P. Hratchian, J. V. Ortiz, A. F. Izmaylov, J. L. Sonnenberg, D. Williams-Young, F. Ding, F. Lipparini, F. Egidi, J. Goings, B. Peng, A. Petrone, T. Henderson, D. Ranasinghe, V. G. Zakrzew-

ski, J. Gao, N. Rega, G. Zheng, W. Liang, M. Hada, M. Ehara, K. Toyota, R. Fukuda, J. Hasegawa, M. Ishida, T. Nakajima, Y. Honda, O. Kitao, H. Nakai, T. Vreven, K. Throssell, J. A. Montgomery, Jr., J. E. Peralta, F. Ogliaro, M. J. Bearpark, J. J. Heyd, E. N. Brothers, K. N. Kudin, V. N. Staroverov, T. A. Keith, R. Kobayashi, J. Normand, K. Raghavachari, A. P. Rendell, J. C. Burant, S. S. Iyengar, J. Tomasi, M. Cossi, J. M. Millam, M. Klene, C. Adamo, R. Cammi, J. W. Ochterski, R. L. Martin, K. Morokuma, O. Farkas, J. B. Foresman, D. J. Fox, Gaussian, Inc., Wallingford CT, **2016**.

---

Manuscript received: August 27, 2019

Accepted manuscript online: September 13, 2019

Version of record online: October 25, 2019

---

